

Tracking inter-particle correlations  
by many-body  
spectroscopies from complex systems

Dissertation

zur Erlangung des Doktorgrades der Naturwissenschaften  
(Dr. rer. nat.)

der

Naturwissenschaftlichen Fakultät II  
Chemie, Physik und Mathematik

der Martin-Luther-Universität  
Halle-Wittenberg

vorgelegt von

Herrn Schüler, Michael  
geb. am 16.07.1988 in Halle (Saale)

Betreuer: PD Dr. Yaroslav Pavlyukh, Prof. Dr. Jamal Berakdar

1. Gutachter: Prof. Dr. Jamal Berakdar
2. Gutachter: Prof. Dr. Ingrid Mertig
3. Gutachter: Prof. Dr. Robert van Leeuwen

Datum der Abgabe: 29. Juni 2016

Datum der öffentlichen Verteidigung: 07. Dezember 2016

Vorsitzender der Promotionskommission: Prof. Dr. Reinhard Krause-Rehberg

---

# Contents

<b>Contents</b>	<b>1</b>
<b>List of abbreviations</b>	<b>3</b>
<b>Publications included in the cumulative thesis</b>	<b>5</b>
<b>1 Introduction</b>	<b>7</b>
<b>2 Quantum mechanics and dynamics of many-body systems</b>	<b>11</b>
2.1 Atomistic Hamiltonian . . . . .	11
2.2 Interaction with the electromagnetic field . . . . .	12
2.3 Nuclear degrees of freedom . . . . .	13
2.4 Electronic degrees of freedom . . . . .	16
2.5 Nonequilibrium Green's functions and many-body perturbation theory . . . . .	23
2.6 Linear response . . . . .	35
<b>3 Insight from spectroscopic techniques</b>	<b>39</b>
3.1 Photon impact . . . . .	39
3.2 Photoemission . . . . .	43
3.3 Electron and photon scattering . . . . .	50
<b>4 Ultra-fast tracing of nuclear wave-packet dynamics by spatially-resolved photoemission</b>	<b>53</b>
4.1 E1: Local ionization dynamics traced by photoassisted scanning tunneling microscopy: a theoretical approach . . . . .	53
4.2 E2: Nuclear-wave-packet dynamics mapped out by two-center interference in the $\text{HeH}^{2+}$ molecule . . . . .	59
<b>5 Many-body spectroscopy from Buckminster fullerene</b>	<b>69</b>
5.1 Symmetry aspects . . . . .	69
5.2 E3: Single-or double-electron emission within the Keldysh nonequilibrium Green's function and Feshbach projection operator techniques . . . . .	71
5.3 E4: Disentangling multipole contributions to collective excitations in fullerenes . . . . .	92
5.4 E5: Electron pair escape from fullerene cage via collective modes . . . . .	99
5.5 E6: Femtosecond dynamics of correlated many-body states in $\text{C}_{60}$ fullerenes . . . . .	107
<b>6 Transient spectroscopy from quantum kinetics</b>	<b>121</b>
6.1 Kadanoff-Baym equations . . . . .	121
6.2 E7: Time-dependent many-body treatment of electron-boson dynamics: application to plasmon-accompanied photoemission . . . . .	122
<b>7 Conclusions and perspectives</b>	<b>139</b>
7.1 Summary . . . . .	139
7.2 Outlook . . . . .	140
<b>Appendix A Geometric classification of many-body states</b>	<b>145</b>

<b>Appendix B Quantum chemistry methods</b>	<b>147</b>
<b>Appendix C Source-field method and Hedin's equations</b>	<b>149</b>
C.1 Hedin's equations . . . . .	149
C.2 Generating functionals for electron-boson models . . . . .	150
C.3 Electron-boson models and screened interaction . . . . .	151
<b>Appendix D Markovian quantum kinetics</b>	<b>153</b>
<b>Bibliography</b>	<b>155</b>
<b>Acknowledgements</b>	<b>165</b>
<b>List of publications</b>	<b>167</b>
<b>Curriculum vitae</b>	<b>169</b>
<b>Eidesstattliche Erklärung</b>	<b>171</b>

---

## Abbreviations and conventions

2PPE	...	Two-photon photoemission
ADT	...	Adiabatic-to-diabatic transformation
AFM	...	Atomic-force microscopy
ARPES	...	Angular-resolved photoemission spectroscopy
BO	...	Born-Oppenheimer
BSE	...	Bethe-Salpeter equation
CC(SD...)	...	Coupled-cluster (singles, doubles ...)
CI(SD...)	...	Configuration-interaction (singles, doubles ...)
DCS	...	Differential cross-section
DD	...	Density-density
DFT	...	Density-functional theory
DOS	...	Density of states
DPE	...	Double photoemission
EB	...	Electron-boson
EELS	...	Electron-energy loss spectroscopy
EKT	...	Extended Koopman's theorem
EOM	...	Equation of motion
FDT	...	Fluctuation-dissipation theorem
FEL	...	Free-electron laser
FPA	...	Feshbach projection algebra
GF	...	Green's function
GGA	...	Generalized gradient approximation
GKBA	...	Generalized Kadanoff-Baym ansatz
GWA	...	GW approximation
HF	...	Hartree-Fock
HHF	...	High harmonic generation
HOMO	...	Highest occupied molecular orbital
IP	...	Ionization potential
IXS	...	Inelastic X-ray scattering
KBEs	...	Kadanoff-Baym equations
KMS	...	Kubo-Martin-Schwinger
KS	...	Kohn-Sham
LDA	...	Local-density approximation
LDOS	...	Local density of states
LUMO	...	Lowest unoccupied molecular orbital
MF	...	Mean-field
NEGF	...	Nonequilibrium Green's function
NMF	...	Non-negative matrix factorization
NWP	...	Nuclear wave-packet

PAD	...	Photoelectron angular distribution
PES	...	Potential-energy surface
$p-h$	...	Particle-hole
QED	...	Quantum electrodynamics
RDM	...	Reduced density matrix
RHF	...	Restricted Hartree-Fock
RPA	...	Random-phase approximation
SAF	...	Symmetry-adapted function
SAMO	...	Super-atom molecular orbital
SCA	...	Semi-classical approximation
SP	...	Single-particle
SPE	...	Single photoemission
STS	...	Scanning-tunneling microscopy
STS	...	Scanning-tunneling spectroscopy
TDDFT	...	Time-dependent density-functional theory
TDPT	...	Time-dependent perturbation theory
TDSE	...	Time-dependent Schrödinger equation
TISE	...	Time-independent Schrödinger equation
TMA	...	$T$ -matrix approximation
TOF	...	Time-of-flight
UHF	...	Unrestricted Hartree-Fock
UV	...	Ultraviolet
XUV	...	Extreme ultraviolet
xc	...	exchange-correlation

In this thesis, atomic units (a. u.) are used throughout, unless state otherwise. The a. u. system is defined by identifying the following quantities by unity:

Symbol	Meaning
$m_0$	electron mass
$e$	elementary charge
$\hbar = h/(2\pi)$	reduced Planck's constant
$4\pi\epsilon_0$	vacuum permittivity

We will be using the following derived units:

Quantity	Definition in a. u.
length (Bohr)	$a_B = 4\pi\epsilon_0/(m_0e^2)$
energy (Hartree)	$E_h = m_0e^4/(4\pi\epsilon_0\hbar)^2$
time	$t_{at} = \hbar/E_h$
fine-structure constant	$\alpha_0 = e^2/(4\pi\epsilon_0\hbar c)$

---

## Publications included in the cumulative thesis

- [E1] M. Schüler, Y. Pavlyukh, and J. Berakdar, *Local Ionization Dynamics Traced by Photoassisted Scanning Tunneling Microscopy: A Theoretical Approach*, J. Phys. Chem. Lett. **4**, 1131 (2013)
- [E2] M. Schüler, Y. Pavlyukh, and J. Berakdar, *Nuclear-wave-packet dynamics mapped out by two-center interference in the  $HeH^{2+}$  molecule*, Phys. Rev. A **89**, 063421 (2014)
- [E3] Y. Pavlyukh, M. Schüler, and J. Berakdar, *Single and double electron emission: combination of projection operator and nonequilibrium Green's function approaches*, Phys. Rev. B **91**, 155116 (2015)
- [E4] M. Schüler, J. Berakdar, and Y. Pavlyukh, *Disentangling multipole contributions to collective excitations in fullerenes*, Phys. Rev. A **92**, 021403 (2015)
- [E5] M. Schüler, Y. Pavlyukh, P. Bolognesi, L. Avaldi, and J. Berakdar, *Electron pair escape from fullerene cage via collective modes*, Sci. Rep. **6**, 24396 (2016)
- [E6] S. Usenko, M. Schüler, A. Azima, M. Jakob, L. L. Lazzarino, Y. Pavlyukh, A. Przystawik, M. Drescher, T. Laarmann and J. Berakdar, *Femtosecond dynamics of correlated many-body states in isolated  $C_{60}$  fullerenes*, New. J. Phys. **18**, 113055 (2016)
- [E7] M. Schüler, J. Berakdar, and Y. Pavlyukh, *Time-dependent many-body treatment of electron-boson dynamics: Application to plasmon-accompanied photoemission*, Phys. Rev. B **93**, 054303 (2016)

- The publication [E1] is reproduced with permission of the American Chemical Society. Copyright (2013) by the American Chemical Society.
- The publications [E2, E3, E4, E7] are reprinted with permission of the American Physical Society. Copyright (2013,2014,2015,2016) by the American Physical Society.
- The publication [E5] is reprinted as permitted by the Creative Commons Attribution 4.0 International License.
- The publications [E6] is reprinted as permitted by the Creative Commons License CC-BY 3.0.





## Introduction

With its fascinating properties, emerging phenomena and derived applications, the quantum world is continuing to transform our daily life. When several quantum-mechanical objects interact, new phenomena emerge, such as quantum entanglement and collective effects. The specific properties of the materials surrounding us are determined by such quantum many-body effects. This includes fundamental phenomena such as magnetism, optical or transport properties, which can only be fully understood by accounting for the interaction or the *correlations* of the participating particles.

Due to the complexity and richness of physics in many-body systems, unveiling the underlying principles in an experimental observation is an intricate task. In an experiment, there is no possibility to directly "see" particle correlations – extracting information is accomplished by detecting the *response* of the system upon a controllable perturbation. This is where spectroscopies – which yield energy-resolved data – come into play. Due to the reciprocal relation of time and energy or frequency in quantum mechanics, full information in energy space provides insight in the dynamics, as well. An overview of the typical energies of excitations in atoms, molecules or solids and the corresponding time scales are given in fig. 1.1. As an example, let us consider the oscillatory collective motion of nearly-free electrons in metals, which takes place on a time scale of  $T \sim 0.5$  fs. In order to excite the corresponding electron dynamics, a perturbation with an energy of  $\omega = 2\pi/T \sim 8$  eV is therefore required. Generally, the dynamics in molecular or solid matter occurs on the ultrafast time scale, spanning around six orders of magnitudes from the picosecond down to the attosecond regime. Consequently, assuming the system is probed with electromagnetic radiation, the corresponding energy scale ranges from infrared (meV) over visible light (eV) up to ultraviolet and X-rays (keV).

With the advent of ultrafast pulses and the attosecond metrology, experiments operating in the time

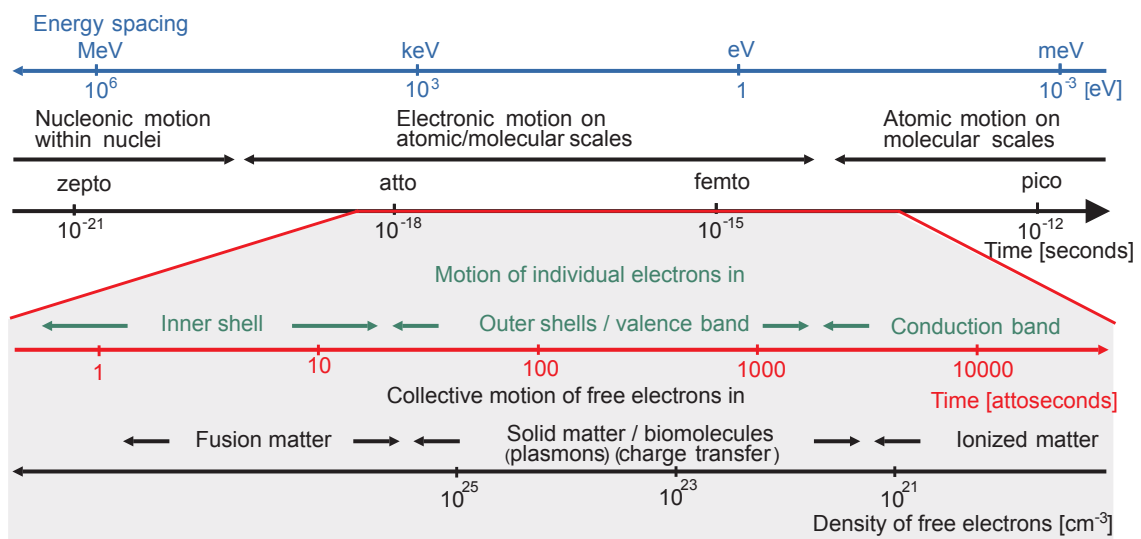


Figure 1.1: The relevant time- and energy scales of fundamental physical processes in atoms, molecules and solids. Reprinted figure from Krausz and Ivanov [1]. Copyright (2009) by the American Physical Society.

domain directly gain more and more popularity. On the one hand, time-resolved studies, even though delivering the equivalent information as compared to energy-resolved measurements, often yield a more intuitive picture and thus fuel new interpretations to facilitate the understanding. A typical example is given by the apparent time delay in photoionization [1]. In the language of spectroscopy, this effect amounts to the rather abstract concept of scattering phases, whereas the time-dependent view provides – to some degree – insight into the dynamics of birth and propagation of photoelectrons. Genuinely new information can be obtained by *transient* spectroscopies, in which the data is recorded in both time- and energy-resolved fashion. This is mostly achieved by the pump-probe setup, i. e., the system is excited (pumped) in a controlled way before a spectroscopic (probe) measurement. The time resolution is often given by the delay between pump and probe. Note that this procedure is not hampered by the time-energy uncertainty principle, since the time- and frequency domain is not accessed simultaneously, reflecting again that substantially more information is contained in transient spectroscopies.

Despite all experimental finesse, not the physical state but only its manifestation in a small set of observables is accessible. In order to still draw conclusions on the system and its correlations, in particular, the support and insight from theory are indispensable. With the idea of spectroscopies in mind, the concept of *linear response* plays an important role. Since probing and so exciting the system is inevitable, the perturbation should be chosen as weak as possible to preserve the initial preparation. The theory of linear response – in accordance with this requirement – allows connecting the initial state and the excitation channels of a many-body system to typical experimental observables such as cross-sections *without* taking the probing field explicitly into account. Transient spectroscopies, on the other hand, go beyond the linear response concept and require a suitable theoretical description to treat the excitations induced by the pump fields.

The interplay of the theory of quantum mechanics and suitable spectroscopies with the goal of accessing the properties of many-body systems governed by their ground state or excitations is the central topic of this thesis. Fig. 1.2 represents the outline of the present work. With a growing number of degrees of freedom as encountered in few- or many-body systems, the practical implementation of the wave-function-based approach quickly exceeds any feasible limits. Hence, suitable ways of reducing the complexity while retaining the pertinent physical information are inevitable. Among the most powerful methods are density-functional theory (DFT) along with the extension to time-dependent DFT (TDDFT) and the many-body perturbation theory (MBPT) based on the Green’s function formulation. Further important concepts are the time-dependent perturbation theory (TDPT), which allows for taking weak probe fields as discussed above into account, and the scattering theory which describes the escape of particles from the system or the time-reversed process (particle impact). All the mentioned theoretical tools have been used to obtain the results presented in this thesis. Besides being compatible with the linear response concept, TDDFT and the nonequilibrium Green’s function (NEGF) approach are particularly suited to capture transient dynamics. Of course, the theories shown in fig. 1.2 should not be considered independent; there are many connections, both on fundamental and on practical level. This aspect is taken into consideration in the introduction of the theoretical concepts in chapter 2.

In chapter 3 the theory from chapter 2 is connected to the description of typical spectroscopic and time-resolved experiments with emphasis on the question which information on the target can be inferred. In particular, the emerging phenomena of many-body systems interacting with weak electromagnetic radiation are discussed. Photoemission – the liberation of one or several electrons upon absorbing photons – will be in the focus of this work. The limitations of the standard approaches for the prediction of photoemission spectra for correlated systems and the need for advanced theoretical tools as discussed in chapter 2 are demonstrated.

Chapters 4–6 summarize the results of this cumulative thesis with a brief topic-specific introduction, providing the scientific context of the included works [E1]–[E7] and underpinning the achievements. The physics we<sup>1</sup> have been interested in are dynamical inter-particle correlations with an intrinsic time scale. Specifically, we consider the coupling of electrons and nuclei in molecules and the dynamical aspects of electron-electron interactions. The mapping of the emerging effects onto observables for prospective experiments has been particularly important. Furthermore, the works [E5] and [E6] are joint theoretical and

---

<sup>1</sup>Since the work summarized by this thesis has been carried out in a collaborative effort, the word ‘we’ is used, as it is usual in joint publications, as a pronoun throughout.

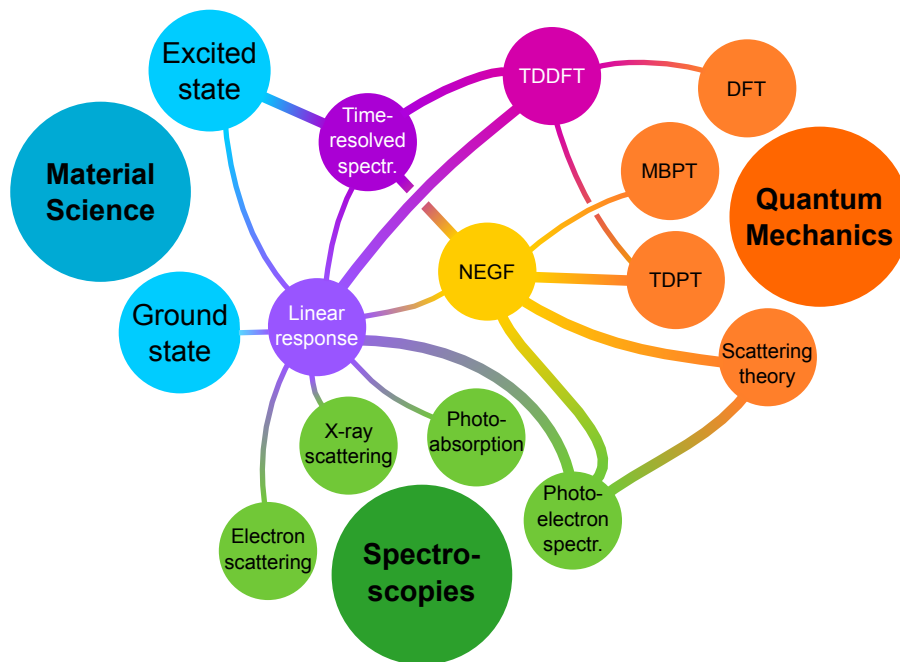


Figure 1.2: Mind map illustrating the close connection of quantum mechanics and major theoretical methods for many-body systems, typical spectroscopies, and ground-state and excited-state properties of materials. The connections where this thesis primarily contributes to are marked by thick lines.

experimental studies.

In [E1] we study the dynamics of small polar molecules adsorbed to an insulating ionic surface such as LiF. Adopting the pump-probe scheme, we show how the vibrations of the molecules can be controlled and mapped out. Based on the spatial distribution of the photoelectrons, an experiment for studying the local dynamics of *single* adsorbed molecules is proposed. The interplay of molecular dynamics and photoemission observables is the topic of [E2]. Here, quantum interference effects in the ionization process are shown to deliver a wealth of information on the atomic dynamics. The principle is demonstrated for the simple  $\text{HeH}^{2+}$  molecule. This allows for exact treatment and for testing the methods we developed to tackle scattering properties.

With [E3] we switch to electronic correlations. We develop a general theory for photoemission with one or, more interestingly, two electrons being ejected from the sample after absorbing one photon (called double photoemission). The latter is a clear indication of correlations as it is excluded in non-interacting systems. Our main motivation is to establish the connection of the general theory to the powerful NEGF formalism. Furthermore, we provide the theory for post-emission effects (electron-electron scattering events the photoelectrons may undergo), which covers a wide range of phenomena.

The works [E4]–[E6] focus on the Buckminster fullerene  $\text{C}_{60}$  molecule and its fascinating properties. We show, based on accurate TDDFT calculations, how the aforementioned collective density oscillations emerge from the electron-electron interaction and provide an efficient scheme for their classification. The impact of the collective excitations on electron-energy-loss spectroscopy (EELS) measurements is clarified and confirmed by comparing to experiments. Based on these results, in [E5] we address how these density fluctuations lead to a dynamical, strong electron-electron interaction which is manifested in double photoemission. The results of our full-fledged *ab initio* calculations are corroborated by dedicated experiments, endorsing the new mechanism suggested by us. In [E6] we consider the dynamics of many-body states for hot (vibrationally excited) molecules by the pump-probe setup outlined above and identify the intrinsic time scales, both theoretically and experimentally.

Our work [E7] focuses on the time-dependent NEGF approach and presents methodological advance-

ments in the treatment of electron-boson models. The latter allows for a unified approach to both electron-nuclei and electron-electron interactions. We apply the methods to transient photoemission spectroscopy from core levels and show how the different interaction channels – which are hard to discern within ordinary spectroscopy – can be separated in the time domain, endorsing yet again the potential of the transient approach.

Finally, chapter 7 summarizes the findings and accomplishments of this thesis and provides an outlook on the directions of future research.

## Quantum mechanics and dynamics of many-body systems

In this chapter, we revisit the basic formulation of the theoretical concepts of matter consisting of electrons and nuclei such as atoms, molecules or clusters (which applies, in principle, to both crystalline and non-crystalline solids, as well). Our intention is a brief presentation which introduces the theoretical background and sketches specific methods employed in the attached publications. Following the concept map fig. 1.2, the emphasis is put onto the theories which are suitable to tackle the many-body problem and have a clear-cut connection to spectroscopies.

We start from the standard Hamiltonian formulation of matter composed of several to many atoms (sec. 2.1) and discuss how to treat the interaction of such systems with external electromagnetic fields (sec. 2.2). As the next step, we employ the usual separation of the energy scale (or, equivalently, the time scale) of the nuclear and the electronic degrees of freedom and point out how the dynamics of the atomic cores can be treated (sec. 2.3), provided that the electronic structure is known. The latter issue is taken up in sec. 2.4, where we briefly introduce typical methods and approximation schemes suitable for our purposes: density-functional theory, quantum chemistry and, with a more extended presentation, the general Green's function approach (sec. 2.5). In view of the excited-state properties that are inherent to many-body spectroscopies, the steady-state and time-dependent formulation are introduced on equal footing. The linear response concept and typical computational schemes for the practical determination of response properties are discussed in sec. 2.6. Important definitions or known facts are highlighted by a shaded background.

The presented theoretical methods are only an excerpt of a multitude of ways to deal with the quantum many-body problem. In places where it is suitable, we remark on alternative approaches and their relation to the main topics covered by this chapter.

### 2.1 Atomistic Hamiltonian

Taking into account the quantum nature of  $N_e$  electrons and  $N_c$  cores, the starting point for theory is the joint wave-function  $\Theta(x_1, \dots, x_{N_e}; \mathbf{R}_1, \dots, \mathbf{R}_{N_c})$ . The coordinates of the electrons  $x_i = \mathbf{r}_i \sigma_i$  ( $i = 1, \dots, N_e$ ) capture both spatial and spin degrees of freedom, while the nuclear spin is neglected here for its weak interaction with the electrons, such that core coordinates  $\mathbf{R}_n$  along with the associated masses  $M_n$  and charges  $Z_n$  ( $n = 1, \dots, N_c$ ) suffice to characterize the nuclear arrangement. For finding static properties, the wave-function is required to obey the time-independent Schrödinger equation (TISE)

$$\hat{H}_0 \Theta(x_1, \dots, x_{N_e}; \mathbf{R}_1, \dots, \mathbf{R}_{N_c}) = \mathcal{E} \Theta(x_1, \dots, x_{N_e}; \mathbf{R}_1, \dots, \mathbf{R}_{N_c}). \quad (2.1)$$

The Hamiltonian  $\hat{H}_0$  consists of the kinetic energy of the electrons ( $\hat{T}_e$ ) and of the cores ( $\hat{T}_c$ ), the electron-electron ( $\hat{V}_{ee}$ ) and the core-core ( $\hat{V}_{cc}$ ) interaction as well as the electron-core attraction ( $\hat{V}_{ec}$ ):

$$\hat{H}_0 = \hat{T}_e + \hat{T}_c + \hat{V}_{ee} + \hat{V}_{ec} + \hat{V}_{cc}. \quad (2.2)$$

The individual contributions to the Hamiltonian (2.2) are defined in the usual way:

$$\hat{T}_e = -\frac{1}{2} \sum_{i=1}^{N_e} \nabla_{\mathbf{r}_i}^2, \quad \hat{T}_c = -\frac{1}{2} \sum_{n=1}^{N_c} \frac{\nabla_{\mathbf{R}_n}^2}{M_n},$$

$$\hat{V}_{ee} = \frac{1}{2} \sum_{\substack{i,j=1 \\ i \neq j}}^{N_e} \frac{1}{|\mathbf{r}_i - \mathbf{r}_j|}, \quad \hat{V}_{cc} = \frac{1}{2} \sum_{\substack{n,m=1 \\ n \neq m}}^{N_c} \frac{Z_n Z_m}{|\mathbf{R}_n - \mathbf{R}_m|}, \quad \hat{V}_{ec} = - \sum_{i=1}^{N_e} \sum_{n=1}^{N_c} \frac{Z_n}{|\mathbf{r}_i - \mathbf{R}_n|}.$$

Note that the Hamiltonian (2.2) does not depend on the spin degrees of freedom explicitly. The reason for this is that we consider the *non-relativistic* Schrödinger equation here. Taking relativistic effects into account (up to second order in  $1/c^2$ ) can be achieved by replacing the Hamiltonian (2.2) by the Breit Hamiltonian [2]. For many applications, adding relativistic correction terms to eq. (2.2) such as the spin-orbit coupling provides an accurate approximation. This extension is then fully compatible with the subsequent considerations. However, we will stay on the level of non-relativistic quantum physics<sup>1</sup>. While the TISE (2.1) describes the stationary states of a given quantum system, the dynamics is governed by the time-dependent Schrödinger equation (TDSE):

$$i\partial_t \Theta(x_1, \dots, x_{N_e}; \mathbf{R}_1, \dots, \mathbf{R}_{N_c}; t) = \hat{H}(t) \Theta(x_1, \dots, x_{N_e}; \mathbf{R}_1, \dots, \mathbf{R}_{N_c}; t). \quad (2.3)$$

The most common scenario is that the time-dependent Hamiltonian  $\hat{H}(t)$  in the TDSE (2.3) arises from some external perturbation such as particle impact or electric and magnetic fields. For their importance for photon-based spectroscopies, we concentrate on the latter case for now. How to treat particle impact is discussed in sec. 3.3.

## 2.2 Interaction with the electromagnetic field

The classical the electric field  $\mathbf{E}(\mathbf{r}, t)$  and the magnetic field  $\mathbf{B}(\mathbf{r}, t)$  are described by Maxwell's equations and derived from the electromagnetic potentials  $\mathbf{A}(\mathbf{r}, t)$  (vector potential) and  $\varphi(\mathbf{r}, t)$  (scalar potential). The influence of the external fields on the quantum system is accounted for by the minimal coupling scheme, according to the replacement rules

$$-i\nabla_{\mathbf{r}_i} \rightarrow -i\nabla_{\mathbf{r}_i} + \mathbf{A}(\mathbf{r}_i, t), \quad -i\nabla_{\mathbf{R}_n} \rightarrow -i\nabla_{\mathbf{R}_n} - Z_n \mathbf{A}(\mathbf{R}_n, t)$$

and the adding the scalar potential to the potential energy<sup>2</sup>. Note that the minimal coupling describes the action of the field on the matter only, whereas the back-action due to induced free charges or currents is not taken into account. While such higher-order effects can often be neglected in the case of isolated systems such as molecules or small clusters, the polarization of the charges and induced currents occurring in solids as the response to the external fields require a modification of the external fields. Such effects can (on classical level) be incorporated by inserting the charge density and current expectation values obtained by the time-dependent many-body wave function  $|\Theta(t)\rangle$  into the inhomogeneous Maxwell's equations and solving them self-consistently with the TDSE (2.3) [3].

However, this pragmatic approach still does not treat the electromagnetic field and the matter on equal footing, as, for instance, the reduction of the field due to absorption is missing. A more fundamental treatment accounts for the quantization of the field into its quasi-particle excitation (photons). The quantum

<sup>1</sup>Relativistic effects become more and more important for heavier elements as the stronger and stronger Coulomb attraction of the core confines the electrons in a narrow region of space and thus increases their kinetic energy. The most prominent example is the yellowish color of gold due to the small energy gap between the 5d and 6s levels. Spin-orbit coupling, in particular, plays an important role in magnetism, as well. A compass needle, for instance, would not adjust itself to the magnetic field in the hypothetical case of vanishing spin-orbit coupling.

<sup>2</sup>The direct coupling of the spin degrees of freedom the magnetic field needs, in principle, to be taken into account, too. For electromagnetic waves, which we will concentrate on, the influence of this coupling is, however, weaker (by the factor  $1/c$ ) and is hence omitted.

description of the photon field then requires field-theoretical methods. The combination of the theory of the quantized electromagnetic field (quantum electrodynamics, QED) with state-of-the-art approximation schemes for treating electrons is, in fact, the topic of very recent research [4, 5] and is also addressed by our own work [E7]. A typical physical scenario where the QED is required is given by cavity geometries [6–9] (often referred to as cavity QED).

Let us now assume that the classical picture of the electromagnetic field is applicable and that both the vector potential and the scalar potential are subject to the (possibly inhomogeneous) Maxwell's equations. Working out the minimal coupling scheme explicitly, the full time-dependent Hamiltonian  $\hat{H}(t)$  governing the TDSE (2.3) can be written as

$$\hat{H}(t) = \hat{H}_0 + \hat{V}_{e,\text{ext}}(t) + \hat{V}_{c,\text{ext}}(t), \quad (2.4)$$

where the electrons (cores) are subject to  $\hat{V}_{e,\text{ext}}(t)$  ( $\hat{V}_{c,\text{ext}}(t)$ ). The coupling attains the form

$$\hat{V}_{e,\text{ext}}(t) = \sum_{i=1}^{N_e} \left[ -i\mathbf{A}(\mathbf{r}_i, t) \cdot \nabla_{\mathbf{r}_i} - \frac{i}{2} \left( \nabla_{\mathbf{r}_i} \cdot \mathbf{A}(\mathbf{r}_i, t) \right) + \frac{1}{2} |\mathbf{A}(\mathbf{r}_i, t)|^2 - \varphi(\mathbf{r}_i, t) \right] \quad (2.5)$$

and, analogously,

$$\hat{V}_{c,\text{ext}}(t) = \sum_{n=1}^{N_c} \left[ iZ_n \mathbf{A}(\mathbf{R}_n, t) \cdot \nabla_{\mathbf{R}_n} + \frac{iZ_n}{2} \left( \nabla_{\mathbf{R}_n} \cdot \mathbf{A}(\mathbf{R}_n, t) \right) + \frac{Z_n^2}{2} |\mathbf{A}(\mathbf{R}_n, t)|^2 + Z_n \varphi(\mathbf{R}_n, t) \right]. \quad (2.6)$$

Note that divergence operation in the round brackets in eq. (2.5) and (2.6) acts on the vector potential only and can thus, depending on the gauge, be eliminated<sup>3</sup>. In the typical situation of a small molecule interacting with electromagnetic radiation with a wavelength much larger than the spatial extent of the system, the *dipole approximation* simplifies the expressions (2.5) and (2.6) significantly. The spatial dependence of the potentials is neglected hereby, reducing (after dropping pure phase factors) the external field contributions to

$$\hat{V}_{e,\text{ext}}^{\text{VG}}(t) = -i\mathbf{A}(t) \cdot \sum_{i=1}^{N_e} \nabla_{\mathbf{r}_i}, \quad \hat{V}_{c,\text{ext}}^{\text{VG}}(t) = i\mathbf{A}(t) \cdot \sum_{n=1}^{N_c} Z_n \nabla_{\mathbf{R}_n}. \quad (2.7)$$

The above form, the so-called *velocity gauge*, can be mapped on the well-known *length gauge*

$$\hat{V}_{e,\text{ext}}^{\text{LG}}(t) = -\mathbf{E}(t) \cdot \sum_{i=1}^{N_e} \mathbf{r}_i, \quad \hat{V}_{c,\text{ext}}^{\text{LG}}(t) = \mathbf{E}(t) \cdot \sum_{n=1}^{N_c} Z_n \mathbf{R}_n, \quad (2.8)$$

by applying a unitary transformation. Even though it yields an adequate picture of light-matter interaction, a treatment beyond the dipole approximation becomes necessary for, for example, (i) high-energy incident radiation, (ii) light propagation close to metallic nanostructures due to near-field effects [10], or (iii) the interaction with new types of structured light [11, 12].

## 2.3 Nuclear degrees of freedom

The TISE (2.1) with the Hamiltonian (2.2) completely describes the physical state (within the limits discussed at the beginning of sec. 2) of an  $N_e$ -electron and  $N_c$ -nuclei system. It is obvious that for any realistic molecule or even atom, besides the simplest cases, obtaining the exact solution of the TISE is beyond reach and one has to resort to suitable approximations. For systems composed of electrons and the much heavier nuclei, the first approximation usually bases on the separation of the time-, or, equivalently, the energy scales of both types of subsystems. Let us for now assume the purely electronic TISE for fixed nuclear configuration as the collection of core coordinates (denoted by  $\{\mathbf{R}\}$ ) can be solved:

$$\begin{aligned} \hat{H}_e \Psi_\alpha(x_1, \dots, x_{N_e}; \{\mathbf{R}\}) &\equiv [\hat{T}_e + \hat{V}_{ec} + \hat{V}_{ee} + \hat{V}_{cc}] \Psi_\alpha(x_1, \dots, x_{N_e}; \{\mathbf{R}\}) \\ &= E_\alpha(\{\mathbf{R}\}) \Psi_\alpha(x_1, \dots, x_{N_e}; \{\mathbf{R}\}). \end{aligned} \quad (2.9)$$

<sup>3</sup>The Coulomb gauge is defined by  $\nabla \cdot \mathbf{A}(\mathbf{r}, t) = 0$ . However, with electromagnetic waves in mind one usually employs the Lorentz gauge as it leads to a wave equation for the potentials directly. In this case the divergence of the vector potential is linked to the scalar potential by  $\nabla \cdot \mathbf{A}(\mathbf{r}, t) + (1/c^2) \partial_t \varphi(\mathbf{r}, t) = 0$ .

Here, the core coordinates are to be understood as parameters, such that both the electronic eigenstates and eigenvalues parametrically depend on  $\{\mathbf{R}\}$ . Then the full wave-function can be expanded into

$$\Theta(x_1, \dots, x_{N_e}; \mathbf{R}_1, \dots, \mathbf{R}_{N_c}) = \sum_{\alpha} \chi_{\alpha}(\{\mathbf{R}\}) \Psi_{\alpha}(x_1, \dots, x_{N_e}; \{\mathbf{R}\}), \quad (2.10)$$

where  $\chi_{\alpha}(\{\mathbf{R}\})$  represent the nuclear wave-functions. Eq. (2.10) is nothing else than the expansion over the a complete electronic basis set. In principle, there is no fundamental reason why one could not go the other way around and expand the full wave-function with parametrically fixed *electron arrangement*. Indeed, this approach turned out to be useful if the roles of nuclei and electrons are reversed regarding their time scales, which occurs for almost classical, highly-excited Rydberg states [13]. Returning to the usual case where the cores can be considered as slow as compared to the electrons, one can insert the expansion (2.10) into the TISE (2.1) and project out electronic degrees of freedom in order to obtain an effective TISE for the nuclei. This procedure yields

$$\sum_{\beta} [\delta_{\alpha\beta} (\hat{T}_c + E_{\alpha}(\{\mathbf{R}\})) + \hat{W}_{\alpha\beta}] \chi_{\beta}(\{\mathbf{R}\}) = \mathcal{E} \chi_{\alpha}(\mathbf{R}_1, \dots, \mathbf{R}_{N_c}), \quad (2.11)$$

where

$$\hat{W}_{\alpha\beta} = \sum_{n=1}^{N_c} \frac{1}{M_n} \left[ \langle \Psi_{\alpha} | \nabla_{\mathbf{R}_n} | \Psi_{\beta} \rangle_e \nabla_{\mathbf{R}_n} + \frac{1}{2} \langle \Psi_{\alpha} | \nabla_{\mathbf{R}_n}^2 | \Psi_{\beta} \rangle_e \right] \equiv \hat{W}_{\alpha\beta}^{(1)} + \hat{W}_{\alpha\beta}^{(2)}. \quad (2.12)$$

Here, the subscript  $\langle \dots \rangle_e$  stands for quantum averaging over the electron subspace only. As we can see from eq. (2.11), the total electronic energy  $E_{\alpha}$  as a function of the core arrangement plays the role of the potential energy for the nuclei. For this reason,  $E_{\alpha}(\{\mathbf{R}\})$  is known as *potential energy surface* (PES) for the electronic state  $|\Psi_{\alpha}\rangle$ . The second part where electronic properties enter the nuclear TISE (2.11) is by the off-diagonal operator (2.12), which takes the electron-nuclei interaction in terms of electronic transitions upon changing nuclear configuration into account. In absence of  $\hat{W}_{\alpha\beta}$ , the PESs decouple and can be treated separately, i. e. no electronic transitions in the sense  $|\Psi_{\alpha}(\{\mathbf{R}\})\rangle \rightarrow |\Psi_{\beta}(\{\mathbf{R}\})\rangle$ ,  $\alpha \neq \beta$ , can occur due to moving nuclei for any configuration  $\{\mathbf{R}\}$ . In other words, the off-diagonal elements of  $\hat{W}_{\alpha\beta}$  represent *non-adiabatic* coupling between the different PESs<sup>4</sup>.

In order to treat the time-dependent case as governed by the TDSE (2.3), the separation ansatz (2.10) is extended to

$$\Theta(x_1, \dots, x_{N_e}; \{\mathbf{R}\}, t) = \sum_{\alpha} \chi_{\alpha}(\{\mathbf{R}\}, t) \Psi_{\alpha}(x_1, \dots, x_{N_e}; \{\mathbf{R}\}), \quad (2.13)$$

where  $\chi_{\alpha}(\{\mathbf{R}\}, t)$  now play the dual role of nuclear wave-functions, on the one hand, and time-dependent expansion coefficients for the electronic states, on the other hand. Following the analogous steps as for the TISE, one obtains the effective nuclear TDSE

$$i\partial_t \chi_{\alpha}(\{\mathbf{R}\}; t) = \sum_{\beta} [\delta_{\alpha\beta} (\hat{T}_c + E_{\alpha}(\{\mathbf{R}\})) + \hat{V}_{c,\text{ext}}(t) + \hat{W}_{\alpha\beta} + \hat{V}_{\alpha\beta}(t)] \chi_{\beta}(\{\mathbf{R}\}; t). \quad (2.14)$$

Here,  $\hat{V}_{\alpha\beta}(t) = \langle \Psi_{\alpha} | \hat{V}_{e,\text{ext}}(t) | \Psi_{\beta} \rangle$  defines the electronic transition matrix elements (which still depends on the nuclear configuration).

### 2.3.1 Born-Oppenheimer approximation

Revisiting the non-adiabatic coupling terms (2.12) we notice that they scale as one over the mass of the cores. Hence, non-adiabatic effects are expected to be small for heavier nuclei. A more accurate criterion on the importance of the non-adiabatic coupling is can be obtained from the Hellmann-Feynman theorem [14]. It is straightforward to see that the first term in eq. (2.12) (usually  $\hat{W}_{\alpha\beta}^{(1)} \gg \hat{W}_{\alpha\beta}^{(2)}$ ) can be expressed as

$$\hat{W}_{\alpha\beta}^{(1)} = \frac{1}{E_{\alpha}(\{\mathbf{R}\}) - E_{\beta}(\{\mathbf{R}\})} \sum_{n=1}^{N_c} \mathbf{a}_{\alpha\beta,n} \cdot \nabla_{\mathbf{R}_n}.$$

<sup>4</sup>The diagonal contribution  $\hat{W}_{\alpha\alpha} = \hat{W}_{\alpha\alpha}^{(2)} = \langle \Psi_{\alpha} | \hat{T}_c | \Psi_{\alpha} \rangle$  can be incorporated into the PESs.



Here,  $\mathbf{a}_{\alpha\beta,n}$  denotes the acceleration of the  $n^{\text{th}}$  core due to the electrostatic force due to the *transition density*<sup>5</sup> given by the two states  $|\Psi_\alpha(\{\mathbf{R}\})\rangle$  and  $|\Psi_\beta(\{\mathbf{R}\})\rangle$ . As a conclusion, non-adiabatic coupling effects only play a subsidiary role if (i) the acceleration of the cores is small, and (ii) if the PESs are well-separated. Assuming that both (i) and (ii) are valid amounts to the *Born-Oppenheimer* (BO) approximation [15]. While (i) turns out to be a good approximation for most systems, (ii) fails in typical cases such as avoided crossings or conical intersections [16]. However, as long as the PESs are not too close to each other, the BO approximation yields a reliable picture.

The major significance of the BO approximation lies in completely decoupling the spectrum and the dynamics of the electrons from the nuclei, which turned out to be a cornerstone for subsequent simplifications, numerical schemes and a great deal of applications. For instance, nuclear motion affects the electrons only adiabatically within the BO picture – a fact that can be utilized to extract the nuclear dynamics (e. g. after a laser excitation) from the electrons by means of ultrafast spectroscopy [17, 18]. Studying chemical bonds in this way is right at the heart of the field of femtochemistry [19–21]. We will come back to this point when discussing our own work based on this principle [E1, E2] in chapter 4.

The PESs  $E_\alpha(\{\mathbf{R}\})$  depend on the arrangement of the atoms and thus form high-dimensional hyper-surfaces for larger molecules. To be precise, after eliminating the translational and rotational motion, a general molecule possesses  $3N_c - 6$  independent degrees of freedom<sup>6</sup> – the normal modes of vibration. In the case the atoms in the system are vibrationally cold, that is, the (possibly thermal) ensemble of nuclear wave-functions is predominantly consists of states close to the respective ground state, expanding the corresponding PES around the potential minima provides some insight into the potential energy landscape. Denoting the core positions at which the PESs are minimized (equilibrium positions) by  $\mathbf{R}_n^{(0)}$ , the  $M = 3N_c - 6$  reduced coordinates can be expressed in terms of the displacement vectors<sup>7</sup>:

$$X_\mu = \sum_{n=1}^{N_c} \mathbf{S}_{n,\mu} \cdot (\mathbf{R}_n - \mathbf{R}_n^{(0)}), \quad \nu = 1, \dots, M, \quad (2.15)$$

where  $\mathbf{S}_{n,\mu}$  are known as Wilson vectors [22–24]. After Taylor-expanding the PESs,

$$E_\alpha(\mathbf{R}_1, \dots, \mathbf{R}_{N_c}) - E_\alpha(\mathbf{R}_1^{(0)}, \dots, \mathbf{R}_{N_c}^{(0)}) \simeq \frac{1}{2} \sum_{\mu,\nu} A_{\mu\nu} X_\mu X_\nu, \quad (2.16)$$

and expressing the kinetic energy in terms of the derivatives  $\dot{X}_\mu$ , the resulting Hamiltonian needs to be transformed into a diagonal form with respect to the momenta and coordinates. This is accomplished by a linear transformation connecting the coordinates  $X_\mu$  to the normal modes (vibrational eigenmodes)  $\hat{Q}_\nu = \sum_\mu L_{\nu\mu} X_\mu$ . The transformation matrix elements  $L_{\nu\mu}$  are obtained by solving Wilson’s equation [25]. The nuclear Hamiltonian is then cast into the simple form

$$\hat{H}_{\text{nuc}} = \frac{1}{2} \sum_{\nu=1}^M \left[ \frac{\hat{P}_\nu^2}{m_\nu} + m_\nu \Omega_\nu^2 \hat{Q}_\nu^2 \right], \quad (2.17)$$

where  $\hat{P}_\nu$  denotes the momentum operator conjugated to the eigenmodes  $\hat{Q}_\nu$ , while  $m_\nu$  and  $\Omega_\nu$  stand for the effective mass and the eigenfrequency of the eigenmode. The Wilson method is used in [E1] and [E6]. Rescaling  $(m_\nu \Omega_\nu)^{-1/2} \hat{P}_\nu \rightarrow \hat{P}_\nu$ ,  $(m_\nu \Omega_\nu)^{1/2} \hat{Q}_\nu \rightarrow \hat{Q}_\nu$  makes the Hamiltonian (2.17) completely symmetric and provides a convenient starting point for further treatment of electron-vibron interactions (see subsec. 2.5.6).

### 2.3.2 Non-adiabatic treatment

Despite the wide range of applicability of the BO approximation, incorporating effects beyond the adiabatic picture is inevitable if different PESs get close to each other. Typical examples are photoexcited dynamics and charge-transfer processes. The expansion (2.10) (or (2.13) in the time-dependent case) cannot be

<sup>5</sup>The transition density is defined as  $\rho_{\alpha\beta}(\mathbf{r}) = \langle \Psi_\alpha | \hat{n}(\mathbf{r}) | \Psi_\beta \rangle - \delta_{\alpha\beta} \langle \Psi_\alpha | \hat{n}(\mathbf{r}) | \Psi_\alpha \rangle$ . Here,  $\hat{n}(\mathbf{r})$  denotes the charge-density operator. In first quantization, the latter reads  $\hat{n}(\mathbf{r}) = \sum_{i=1}^{N_e} \delta(\mathbf{r} - \mathbf{r}_i)$ .

<sup>6</sup>For the special case of linear molecules, the number of normal modes is  $3N_c - 5$ .

<sup>7</sup>We assume small elongations and consider a linear dependence only.

reduced to a single dominant term (the ground-state PES, for example), but has to include all the relevant states. In principle, the exact properties or dynamics is guaranteed if the non-adiabatic coupling matrix elements (2.12) are taken into account. Their direct implementation can, however, be quite tedious, since they entail off-diagonal coupling connected to the momentum operator. The analogy to a spatially-dependent vector potential (see sec. 2.2) gives rise to the idea of performing a gauge transformation to shift the non-adiabatic coupling from kinetic-energy-type terms (eq. (2.12)) into the potential energy. The transformation is accomplished by switching the electronic basis set to the *diabatic* basis  $\tilde{\Psi}_\alpha(\mathbf{r}_1, \dots, \mathbf{r}_{N_e}; \{\mathbf{R}\})$  with

$$\Psi_\alpha(\mathbf{r}_1, \dots, \mathbf{r}_{N_e}; \{\mathbf{R}\}) = \sum_\beta \hat{U}_{\alpha\beta} \tilde{\Psi}_\beta(\mathbf{r}_1, \dots, \mathbf{r}_{N_e}; \{\mathbf{R}\}),$$

such that the expansion of the full wave-function (2.10) is modified into

$$\Theta(x_1, \dots, x_{N_e}; \{\mathbf{R}\}) = \sum_\alpha \tilde{\chi}_\alpha(\{\mathbf{R}\}) \tilde{\Psi}_\alpha(x_1, \dots, x_{N_e}; \{\mathbf{R}\}). \quad (2.18)$$

The unitary transformation  $\hat{U}_{\alpha\beta}$  is required to give rise to the modified nuclear TISE

$$\sum_\beta [\delta_{\alpha\beta}(\hat{T}_c + \hat{V}_{cc}) + U_{\alpha\beta}(\{\mathbf{R}\})] \tilde{\chi}_\beta(\{\mathbf{R}\}) = \mathcal{E} \tilde{\chi}_\alpha(\{\mathbf{R}\}), \quad (2.19)$$

where the coupling term  $U_{\alpha\beta}(\{\mathbf{R}\})$  does not contain derivatives with respect to the nuclear coordinates any more. This transition is known as adiabatic-to-diabatic transformation (ADT) [26]. It is important to notice that the transformation into the diabatic basis is, mathematically speaking, only possible if the curl of effective vector potential vanishes. This condition is however often violated. In practice, the ADT is carried out approximately, for instance by an interpolation scheme. More details for the special case of two PESs are given by [E2].

We briefly mention that recent studies showed that the full wave-function can be factored exactly into a single-term expression [27] as in the BO approximation, but including all non-adiabatic effects. The resulting coupled electronic and nuclear TISEs (or TDSEs, respectively) have to be solved self-consistently and give rise to the notion of the *exact* (time-dependent) PES [28].

In the scenario of small vibrational excitations and weak interaction of the electrons with the vibrons (the quanta of the vibrational excitations), an expansion of the PESs (as discussed in subsec. 2.3.1) and the electronic wave-functions around the equilibrium geometry is feasible. Taking only the first term into account gives rise to a single coupling term linear in the eigenmode coordinates  $\hat{Q}_v$ . This approximation might seem rather crude at first glance, but represents the only feasible way of treating electron-vibron interaction in larger molecules or clusters. Especially for solids, the linear approximation to the electron-phonon interaction constitutes the standard approach [29–31]. The equal-footing treatment of coupled electron-vibron or electron-phonon dynamics is revisited in [E7], whereas the electron dynamics in presence of an excited vibronic bath is the topic of [E6] and, in more detail, appendix D.

## 2.4 Electronic degrees of freedom

In sec. 2.3 we explained how to explore the atomic core structure and dynamics based on the knowledge of electronic properties. In particular, the key quantities are (i) the eigenenergies  $E_\alpha$  of the many-body states  $|\Psi_\alpha\rangle$ , (ii) non-adiabatic coupling matrix elements (eq. (2.12)), and (iii) matrix elements with respect to the interaction with the electromagnetic field (cf. eq. (2.5)). All the quantities (i)–(iii) are, of course, functions of the nuclear configuration. Let us now focus on the electronic TISE or TDSE, keeping mind the solution has to be obtained for any configuration  $\{\mathbf{R}\}$ .

Noting that the electronic Hamiltonian (2.2) along with the coupling to external fields, eq. (2.5) depends, within first quantization, on the number of electrons  $N_e$  explicitly, the second-quantized form proves to be advantageous for later purposes. Introducing the standard field operators  $\hat{\psi}^\dagger(x)$  ( $\hat{\psi}(x)$ ), creating (annihilating) an electron with the spin-space coordinate  $x = \mathbf{r}\sigma$ , the electronic Hamiltonian attains the form

$$\hat{H}_e(t) = \int dx \int dx' \hat{\psi}^\dagger(x) \langle x | \hat{h}(t) | x' \rangle \hat{\psi}(x') + \frac{1}{2} \int dx \int dx' v(x, x') \hat{\psi}^\dagger(x) \hat{\psi}^\dagger(x') \hat{\psi}(x') \hat{\psi}(x). \quad (2.20)$$

Here,

$$\hat{h}(t) = -\frac{1}{2} \nabla^2 - \sum_{n=1}^{N_c} \frac{Z_n}{|\mathbf{r} - \mathbf{R}_n|} + \hat{v}_{e,\text{ext}}(t) \quad (2.21)$$

denotes the one-body or single-particle (SP), that is, the non-interacting part of the Hamiltonian, whereas

$$v(x, x') = \delta_{\sigma\sigma'} v(\mathbf{r} - \mathbf{r}') = \delta_{\sigma\sigma'} \frac{1}{|\mathbf{r} - \mathbf{r}'|}$$

is the Coulomb interaction. The last term in eq. (2.21) captures the coupling to external electromagnetic fields and is defined analogously to eq. (2.5) (but as one-body operator). Instead of working with the position-spin basis, one can also represent the Hamiltonian based on the complete set of SP states  $\{|\varphi_{i\sigma}\rangle = |\varphi_i\rangle \otimes |\sigma\rangle\}$  (product states in position and spin space), which are typically eigenstates of some reference SP Hamiltonian  $\hat{h}_{\text{ref}}$ <sup>8</sup>. In accordance with the change of the basis, the creation (annihilation) operators are transformed into  $\hat{c}_{i\sigma}^\dagger$  ( $\hat{c}_{i\sigma}$ ). The electronic Hamiltonian (2.20) is thus expressed equivalently as

$$\hat{H}_e(t) = \sum_{ij} \sum_{\sigma\sigma'} h_{ij}^{\sigma\sigma'}(t) \hat{c}_{i\sigma}^\dagger \hat{c}_{j\sigma} + \frac{1}{2} \sum_{ijkl} \sum_{\sigma\sigma'} v_{ijkl} \hat{c}_{i\sigma}^\dagger \hat{c}_{j\sigma'}^\dagger \hat{c}_{k\sigma'} \hat{c}_{l\sigma}, \quad (2.22)$$

where the one-body matrix elements are defined as

$$h_{ij}^{\sigma\sigma'}(t) = \langle \varphi_{i\sigma} | \hat{h}(t) | \varphi_{j\sigma'} \rangle, \quad (2.23)$$

while the two-body Coulomb integrals, also known as electron-repulsion integrals, read

$$v_{ijkl} = \int d\mathbf{r} \int d\mathbf{r}' \phi_i^*(\mathbf{r}) \phi_j^*(\mathbf{r}') v(\mathbf{r} - \mathbf{r}') \phi_k(\mathbf{r}') \phi_l(\mathbf{r}). \quad (2.24)$$

With the basic notation introduced, we now proceed to theoretical tools to tackle the electronic TISE or TDSE as governed by the Hamiltonian (2.20). Accent is put on those methods which are employed in the publications comprised by this thesis.

### 2.4.1 Scattering theory

The quantum mechanical treatment of a single electron subject to the realistic potential  $v(\mathbf{r})$ , such as in the hydrogen atom or related models, leads to different types of solutions. Denoting the corresponding one-body Hamiltonian by  $\hat{h}$ , we consider its eigenstates  $\hat{h}|\psi_a\rangle = \varepsilon_a|\psi_a\rangle$  (the spin degree of freedom does not play an important role here) and classify them according to their spatial character. Eigenstates are called bound ( $a \in \mathcal{B}$ ) if for any small number  $\delta > 0$  there is a compact set  $B \subset \mathbb{R}^3$  such that

$$\int_{B^c} d\mathbf{r} |\langle \mathbf{r} | e^{-i\hat{h}t} | \psi_a \rangle|^2 = \int_{B^c} d\mathbf{r} n_a(\mathbf{r}, t) < \delta, \quad B^c = \mathbb{R}^3 \setminus B. \quad (2.25)$$

In other words, the bound wave-functions (and the corresponding density  $n_a(\mathbf{r}, t)$ ) stays in the compact set  $B$  and does not propagate to infinity. Conversely, a wave-function is called a scattering state, if

$$\lim_{T \rightarrow \infty} \frac{1}{2T} \int_{-T}^T dt \int_B d\mathbf{r} |\langle \mathbf{r} | e^{-i\hat{h}t} | \psi_a \rangle|^2 = 0 \quad (2.26)$$

<sup>8</sup>The most popular choices are the Kohn-Sham or the Hartree-Fock Hamiltonians (see subsec 2.4.2 and subsec 2.4.3).

for any compact set  $B$ , which means scattering states fill the complete three-dimensional space. The RAGE theorem [32] provides a link of these definitions to the spectrum of  $\hat{h}$ . It can be shown that states belonging to the discrete spectrum are bound, while continuum states are scattering states. For the latter, one identifies the quantum number with the wave vector  $a = \mathbf{k}$  indicating (i) the asymptotic propagation direction of the electron and (ii) the energy by  $\epsilon_{\mathbf{k}} = \epsilon_k = k^2/2$ . As  $\psi_{\mathbf{k}}(\mathbf{r})$  does not tend to zero (in the above sense) as  $|\mathbf{r}| \rightarrow \infty$ , the asymptotic boundary conditions need to be fixed. One distinguishes between *outgoing* (*incoming*) boundary conditions by adding the superscript (+) ((-)). For a short-ranged potential  $v(\mathbf{r})$ <sup>9</sup>, the outgoing scattering wave-function fulfills the asymptotic behavior

$$\psi_{\mathbf{k}}^{(+)}(\mathbf{r}) \rightarrow A \left( e^{i\mathbf{k}\cdot\mathbf{r}} + f(\hat{\mathbf{k}}) \frac{e^{ikr}}{r} \right), \quad r \rightarrow \infty, \quad (2.27)$$

where  $A$  is a normalization constant and  $f(\hat{\mathbf{k}})$  denotes the scattering amplitude. The latter yields the probability amplitude for the electron to be scattered into a certain direction with respect to the incoming wave vector  $\mathbf{k}$ . For potentials behaving as  $v(\mathbf{r}) \sim Z/r$  for  $r \rightarrow \infty$  (which is the normal case for atoms or molecules), on the other hand, the outgoing scattering wave-function has the form [33]

$$\psi_{\mathbf{k}}^{(+)}(\mathbf{r}) \rightarrow \tilde{A} \left( \exp[i\mathbf{k}\cdot\mathbf{r} + i\eta \log(kr - \mathbf{k}\cdot\mathbf{r})] + \tilde{f}(\hat{\mathbf{k}}) \frac{\exp[ikr - i\eta \log(2kr)]}{r} \right), \quad r \rightarrow \infty, \quad (2.28)$$

with the Sommerfeld parameter  $\eta = Z/k$ . The incoming scattering wave-functions are obtained by time inversion which, in absence of the spin degree of freedom, is identical to complex conjugation.

**Partial-wave expansion.** A very useful approach to compute scattering wave-functions explicitly is offered by the partial-wave expansion in terms of spherical harmonics  $Y_{\ell m}(\hat{\mathbf{r}})$ . Suppose the potential  $v(\mathbf{r})$ , which behaves as  $v(\mathbf{r}) \sim Z/r$  for  $r \rightarrow \infty$ , is efficiently represented by

$$v(\mathbf{r}) = \sum_{\ell m} v_{\ell m}(r) Y_{\ell m}(\hat{\mathbf{r}}), \quad \int d\hat{\mathbf{r}} Y_{\ell m}^*(\hat{\mathbf{r}}) v(\mathbf{r}) Y_{\ell' m'}(\hat{\mathbf{r}}) = \sum_{pq} G(pq\ell' m' | \ell m) v_{pq}(r) \equiv v_{\ell m \ell' m'}(r). \quad (2.29)$$

Here,

$$G(\ell_1 m_1 \ell_2 m_2 | LM) = (-1)^M \sqrt{\frac{c_{\ell_1} c_{\ell_2} c_L}{4\pi}} \begin{pmatrix} \ell_1 & \ell_2 & L \\ 0 & 0 & 0 \end{pmatrix} \begin{pmatrix} \ell_1 & \ell_2 & L \\ m_1 & m_2 & -M \end{pmatrix} \quad (2.30)$$

defines the Gaunt coefficients by the Wigner 3j-symbols [34] and  $c_{\ell} = (2\ell + 1)$ . Likewise, the scattering wave-functions are expanded in partial waves as

$$\psi_{\mathbf{k}}^{(\pm)}(\mathbf{r}) = \sum_{\ell m} \sum_{\ell' m'} (\mp i)^{\ell'} e^{\pm i\sigma_{\ell'}(k)} \frac{\zeta_{\ell m \ell' m'}^{(\pm)}(k; r)}{r} Y_{\ell m}(\hat{\mathbf{r}}) Y_{\ell' m'}^*(\hat{\mathbf{k}}), \quad \sigma_{\ell}(k) = \arg[\Gamma(\ell + 1 + i\eta)]. \quad (2.31)$$

Inserting the eq. (2.29) and (2.31) into the one-body TISE results in the coupled-channel radial TISE

$$\sum_{pq} \left[ \left( -\frac{1}{2} \partial_r^2 + \frac{\ell(\ell+1)}{2r^2} \right) \delta_{\ell k} \delta_{mq} + v_{\ell mpq}(r) \right] \zeta_{pq\ell' m'}^{(\pm)}(k; r) = \epsilon_k \zeta_{\ell m \ell' m'}^{(\pm)}(k; r), \quad (2.32)$$

which is to be solved along with the asymptotic boundary condition

$$\zeta_{\ell m \ell' m'}^{(-)}(k; r) \sim \delta_{\ell \ell'} \delta_{mm'} H_{\ell}^+(kr; \eta) - S_{\ell m \ell' m'}(k)^* H_{\ell'}^-(kr; \eta), \quad \zeta_{\ell m \ell' m'}^{(+)}(k; r) = (\zeta_{\ell m \ell' m'}^{(-)}(k; r))^*. \quad (2.33)$$

$S_{\ell m \ell' m'}(k)$  is the complex  $S$ -matrix containing the scattering phase shifts originating from the short-ranged parts of the potential. It is determined by requiring the wave-function to behave regularly at the origin. The functions  $H_{\ell}^{\pm}(kr; \eta)$  are the Hankel functions, conforming the NIST DLMF [35]. The minus superscript for the continuum wave-function becomes clear from eq. (2.33): the outgoing contribution ( $H_{\ell}^+$ ) is unperturbed and contains only pure s,p, ..., waves, while the incoming part ( $H_{\ell}^-$ ) is a mixture of different partial waves.

An efficient method to compute exact SP scattering wave-functions based on the one-centre expansion (2.31) is presented in [E2] and used in [E5] and [E6].

<sup>9</sup>Short-range potentials are defined by  $r v(\mathbf{r}) \rightarrow 0$  for  $r \rightarrow \infty$ .

**Many-body scattering states.** The intricacy of the scattering problem becomes even more pronounced on the many-body level because any number of electrons can be incoming or outgoing scattering waves. While many-body bound states can be defined by a generalization of the criterion (A.1) (see appendix A), a mathematically rigorous definition of  $n$ -electron scattering states is not directly possible. However, in view of experiments that detect exactly  $n$  continuum electrons, we would like to classify the generic eigenstates of the Hamiltonian (2.20) (assuming it to be time-independent)  $\hat{H}_e |\Psi_\lambda\rangle = E_\lambda |\Psi_\lambda\rangle$  accordingly. We consider states associated with  $\lambda \in \Lambda_{N_e}$  and decompose the set of quantum numbers into

$$\Lambda_{N_e} = \mathcal{B}_{N_e} \cup (\mathcal{B}_{N_e-1} \cup \mathcal{C}) \cup (\mathcal{B}_{N_e-2} \cup \mathcal{C}_2) \cup \dots \cup (\mathcal{B}_1 \cup \mathcal{C}_{N_e-1}) \cup \mathcal{C}_{N_e}, \quad (2.34)$$

where  $\mathcal{B}_n$  ( $\mathcal{C}_n$ ) denotes a set of quantum numbers with  $n$  electrons bound (in the continuum). The mathematical background for this classification provided in appendix A in terms of the Feshbach projection algebra (FPA). It is clear that  $\mathcal{B}_n$  is a discrete set, while  $\mathcal{C}_n \subset \mathbb{R}^{3n}$ . In contrast to the single-electron case, an electron emanating from a many-body system still interacts with the remaining electrons in a correlated way, which leads to a considerable difficulty of constructing corresponding many-body wave-functions. In the asymptotic region, at least, a clear definition is possible. For the case of a single scattering electron  $\lambda = (\alpha, \mathbf{k}) \in \mathcal{B}_{N_e-1} \cup \mathcal{C}$ , one defines

$$\Psi_{\alpha, \mathbf{k}}^{(\pm)}(x_1, \dots, x_{N_e}) \sim \Phi_{\alpha, \mathbf{k}}^{(\pm)}(x_1, \dots, x_{N_e}) \equiv \hat{\mathcal{A}} \left[ \psi_{\mathbf{k}}^{(\pm)}(x_1) \Psi_\alpha^+(x_2, \dots, x_{N_e}) \right], \quad r_1, \dots, r_{N_e} \rightarrow \infty. \quad (2.35)$$

The state  $|\Psi_\alpha^+\rangle$  is an eigenstate of the  $(N_e - 1)$ -electron Hamiltonian, indicated by the superscript  $+$  as positively ionized system. The operator  $\hat{\mathcal{A}}$  anti-symmetrizes the full many-body wave-function with respect to the scattering state. This definition (2.35) can, in principle, be generalized in a straightforward manner. For two scattering electrons one finds

$$\Psi_{\alpha, \mathbf{k}_1 \mathbf{k}_2}^{(\pm)}(x_1, \dots, x_{N_e}) \sim \Phi_{\alpha, \mathbf{k}_1 \mathbf{k}_2}^{(\pm)}(x_1, \dots, x_{N_e}) \equiv \hat{\mathcal{A}} \left[ \psi_{\mathbf{k}_1 \mathbf{k}_2}^{(\pm)}(x_1, x_2) \Psi_\alpha^{2+}(x_3, \dots, x_{N_e}) \right], \quad r_1, \dots, r_{N_e} \rightarrow \infty. \quad (2.36)$$

Analogous to the above,  $|\Psi_\alpha^{2+}\rangle$  is an eigenstate of the  $(N_e - 2)$ -particle Hamiltonian. Eqs. (2.35) and (2.36) demonstrate that for  $n$  continuum electrons, the  $n$ -body TISE has to be solved. Even for  $n = 2$  this is a formidable task. There has been a surge of recent works on solving the two-body TISE for scattering states  $\psi_{\mathbf{k}_1 \mathbf{k}_2}^{(\pm)}(x_1, x_2)$  *exactly* [36–39], which also allows modelling the emission of two electrons from atoms [40] based on eq. (2.36).

**Møller operators.** The wave-functions (2.35) and (2.36) are only defined in the asymptotic region. We can think of a laser pulse exciting the system which evolves into the asymptotic states as  $t \rightarrow \infty$ . Therefore, by propagating backwards in time, one should be able to recover, at least on a formal level, the exact many-body wave-functions in any point in space. Formally, this is accomplished by the Møller operators

$$\hat{\Omega}^{(\pm)} = \mp \lim_{\epsilon \rightarrow 0^+} \epsilon \int_0^{\mp\infty} dt e^{\pm\epsilon t} e^{i\hat{H}_\epsilon t} e^{-i\hat{H}_\epsilon^{(0)} t}, \quad (2.37)$$

where  $\hat{H}_\epsilon^{(0)}$  is obtained by switching off the Coulomb interaction between the scattering and the remaining electrons<sup>10</sup>. With the help of the Møller operators, the asymptotic states can be converted into actual eigenstates of  $\hat{H}_\epsilon$ :

$$|\Psi_{\alpha, \mathbf{k}}^{(\pm)}\rangle = \hat{\Omega}^{(\pm)} |\Phi_{\alpha, \mathbf{k}}^{(\pm)}\rangle, \quad |\Psi_{\alpha, \mathbf{k}_1 \mathbf{k}_2}^{(\pm)}\rangle = \hat{\Omega}^{(\pm)} |\Phi_{\alpha, \mathbf{k}_1 \mathbf{k}_2}^{(\pm)}\rangle.$$

The concept of the Møller operators reaches, however, even deeper. Suppose, for instance, we construct an asymptotic state by  $|\Phi_{\alpha, \mathbf{k}}\rangle = \hat{c}_{\mathbf{k}\sigma}^\dagger |\Psi_\alpha^+\rangle$  with some continuum wave-function  $\phi_{\mathbf{k}}(\mathbf{r})$  and spin  $\sigma$  as a part of the SP basis. Regardless of the asymptotic boundary conditions which  $\phi_{\mathbf{k}}(\mathbf{r})$  might fulfill (a mix between incoming and outgoing is possible),  $\hat{\Omega}^{(\pm)}$  acts as a projection operator onto the fully interacting many-body

<sup>10</sup>This is accomplished by replacing the electron-repulsion integral  $v_{ijkl}$  by zero if any of the indices corresponds to a scattering state.

state  $|\Psi_{\alpha,\mathbf{k}}^{(\pm)}\rangle = \hat{\Omega}^{(\pm)}\hat{c}_{\mathbf{k}\sigma}^\dagger|\Psi_\alpha^+\rangle$  with incoming or outgoing boundary condition. For two continuum electrons, one can redefine  $\hat{H}_e^{(0)}$  such that also the Coulomb interaction between the two electrons is switched off, i. e.  $|\Phi_{\alpha,\mathbf{k}_1\mathbf{k}_2}\rangle = \hat{c}_{\mathbf{k}_1\sigma_1}^\dagger\hat{c}_{\mathbf{k}_2\sigma_2}^\dagger|\Psi_\alpha^{2+}\rangle$  is an eigenstate of  $\hat{H}_e^{(0)}$ . Nevertheless, the correlated state with correct incoming or outgoing boundary conditions is recovered by  $|\Psi_{\alpha,\mathbf{k}_1\mathbf{k}_2}^{(\pm)}\rangle = \hat{\Omega}^{(\pm)}\hat{c}_{\mathbf{k}_1\sigma_1}^\dagger\hat{c}_{\mathbf{k}_2\sigma_2}^\dagger|\Psi_\alpha^{2+}\rangle$ .

A general perturbative treatment of the emission of one or two electrons from many-body compounds is the subject of [E3].

## 2.4.2 Hartree-Fock approximation

The Hartree-Fock (HF) method can be regarded as the root of all treatments of correlated many-body systems, both from conceptual as well as from historical point of view<sup>11</sup>. Respecting the anti-symmetry, from which the Pauli principle follows, the many-body wave-function is approximated by a Slater determinant (which would be exact in case of non-interacting electrons). In second quantization, the HF wave-function is generated from the vacuum state  $|0\rangle$  by

$$|\Psi_0^{\text{HF}}\rangle = \left( \prod_{i=1}^{N_e^\uparrow} \hat{d}_{i\uparrow}^\dagger \right) \left( \prod_{i=1}^{N_e^\downarrow} \hat{d}_{i\downarrow}^\dagger \right) |0\rangle, \quad (2.38)$$

where  $\hat{d}_{i\sigma}^\dagger = \int d\mathbf{r} \psi_{i\sigma}^{\text{HF}}(\mathbf{r}) \hat{\psi}^\dagger(\mathbf{r}\sigma)$  creates an electron in the HF orbital  $\psi_{i\sigma}^{\text{HF}}(\mathbf{r})$ . The latter is determined by requiring  $\langle \Psi_0^{\text{HF}} | \hat{H}_e | \Psi_0^{\text{HF}} \rangle$  to be minimal under the constraint  $\langle \Psi_0^{\text{HF}} | \Psi_0^{\text{HF}} \rangle = 1$ . This yields the HF equations for the HF orbitals:

$$\left[ -\frac{1}{2}\nabla^2 + v_0(\mathbf{r}) + v_{\text{H}}(\mathbf{r}) \right] \psi_{i\sigma}^{\text{HF}}(\mathbf{r}) + \int d\mathbf{r}' v_x^\sigma(\mathbf{r}, \mathbf{r}') \psi_{i\sigma}^{\text{HF}}(\mathbf{r}') = \varepsilon_{i\sigma} \psi_{i\sigma}^{\text{HF}}(\mathbf{r}). \quad (2.39)$$

$v_0(\mathbf{r})$  is the one-body potential accounting for the electron-core attraction and  $v_{\text{H}}(\mathbf{r})$  is the electrostatic potential generated by the electron density (Hartree potential). The last term on the left-hand side of the HF equation (2.39) constitutes the non-local exchange potential

$$v_x^\sigma(\mathbf{r}, \mathbf{r}') = - \sum_{j\sigma'} \delta_{\sigma\sigma'} v(\mathbf{r} - \mathbf{r}') (\psi_{j\sigma'}^{\text{HF}}(\mathbf{r}'))^* \psi_{j\sigma'}^{\text{HF}}(\mathbf{r}). \quad (2.40)$$

The HF methods yields an effective (but non-local) one-body Schrödinger equation for the SP orbitals. The exchange potential reflecting the anti-symmetry leads to electrons with the same spin avoiding each other (exchange hole). In contrast to the exchange, the Coulombic correlations are not captured correctly by the HF theory. This typically leads to a significant overestimation of the ground state energy, band gaps and ionization potentials.

Since there is no restriction with regard to the spin degree of freedom, eq. (2.39) is referred to as unrestricted HF (UHF). The orbitals associated to  $1 \leq i \leq N_e^\uparrow$  ( $1 \leq i \leq N_e^\downarrow$ ) are called occupied spin-up (spin-down) orbitals; other (higher) orbitals are unoccupied and addressed as virtual. Presuming the orbitals for the different spin projections to be equal and taking  $N_e^\uparrow = N_e^\downarrow$  results in the restricted Hartree-Fock (RHF) equations.

Representing the HF states by the SP (typically truncated) basis set  $\psi_{n\sigma}^{\text{HF}}(\mathbf{r}) = \sum_i A_i^{n\sigma} \phi_i(\mathbf{r})$ , the HF equation (2.39) is transformed to the Hall-Roothaan equation

$$\sum_l \left[ h_{il}^{(0)} + \sum_{jkl} \left( v_{ijkl} \gamma_{jk} - v_{ijlk} \gamma_{jk}^{\sigma\sigma} \right) \right] A_l^{n\sigma} \equiv \sum_l h_{il}^{\text{HF}} A_l^{n\sigma} = \varepsilon_{n\sigma} \sum_j S_{ij} A_j^{n\sigma}, \quad (2.41)$$

where  $\gamma_{mn}^{\sigma\sigma'} = \langle \Psi_0^{\text{HF}} | \hat{c}_{m\sigma}^\dagger \hat{c}_{n\sigma'} | \Psi_0^{\text{HF}} \rangle \equiv \langle \hat{c}_{m\sigma}^\dagger \hat{c}_{n\sigma'} \rangle$  stands for the RDM;  $\gamma_{mn} = \sum_\sigma \gamma_{mn}^{\sigma\sigma}$  represents the spin-traced-out RDM.  $h_{il}^{(0)}$  captures the non-interacting part and  $S_{ij} = \langle \phi_i | \phi_j \rangle$  accounts a possibly non-orthogonal

<sup>11</sup>The self-consistent field method developed by Fock as an extension of the works of Hartree [41, 42] were the starting point of the reduction principle – the mapping of the many-body problem onto an effective independent particle picture [43].

basis. Eq. (2.41) underlines the HF method as *mean-field* (MF) approximation: if  $\hat{c}_{j\sigma}^\dagger$  is contracted with  $\hat{c}_{k\sigma'}$  or (with different sign)  $\hat{c}_{l\sigma}$  (replaced by the expectation value  $\langle \hat{c}_{j\sigma}^\dagger \hat{c}_{k\sigma'} \rangle$  or  $\langle \hat{c}_{j\sigma}^\dagger \hat{c}_{l\sigma} \rangle$ , that is), the SP part is equivalent to the HF Hamiltonian in eq. (2.41).

The HF eigenvalues  $\varepsilon_{i\sigma}$  arise as Lagrangian multipliers and have, *a priori*, no physical meaning. Their standard interpretation as orbital energies is, however, supported by the Koopmans's theorem [44–46] and, more generally, by the extended Koopmans's theorem (EKT) [47], according to which the energy difference  $E_{i\sigma}^{(N_e-1)} - E_0^{(N_e)}$  with  $\hat{H}_e |\Psi_0^{\text{HF}}\rangle = E_0^{(N_e)} |\Psi_0^{\text{HF}}\rangle$  and  $E_i^{(N_e-1)}$  denoting the energy if one electron has been removed from the  $i^{\text{th}}$  HF orbital with spin  $\sigma$  (excluding orbital relaxation effects), amounts to  $-\varepsilon_{i\sigma}$ . An analogous statement can be made for adding an electron. In practice, the ionization potential (IP) is usually quite well described by the EKT because systematic errors of the HF method are compensated to some extent, while electron affinities differ significantly from experimental values.

The HF Hamiltonian excludes spurious self-interactions<sup>12</sup> and guarantees the correct  $1/r$ -behavior of the effective non-local potential. It is therefore suitable to construct scattering wave-functions, as well. The HF Hamiltonian is the first-order contribution to a systematic treatment of electron scattering from many-body systems, as presented in [E3].

Since the Slater determinants form a basis in the  $N_e$ -electron Hilbert space, provided a complete set of SP orbitals is used for their construction, a systematic improvement of the many-body wave-function is most conveniently based on the HF determinant and orbitals. This is the starting point of the machinery of quantum chemistry. Some background on the specific methods used for our work [E1] is provided in appendix B.

### 2.4.3 Density-functional theory

Density-functional theory (DFT) can be regarded as one of the most successful theoretical tools. Especially for crystalline solids, DFT is *the* standard tool for computing band structures and other properties. The conceptual breakthrough of DFT arises from mapping the many-body problem, as described by the Hamiltonian (2.20), onto an effective system of non-interacting electrons. The mathematical background is provided by the Hohenberg-Kohn theorems [48], stating that (i) the total energy of any many-electron system is uniquely determined by the ground-state (spin) density

$$n_\sigma(\mathbf{r}) = \langle \Psi_0 | \hat{\psi}^\dagger(x) \hat{\psi}(x) | \Psi_0 \rangle, \quad \underline{n}(\mathbf{r}) = (n_\uparrow(\mathbf{r}), n_\downarrow(\mathbf{r})) \quad (2.42)$$

and (ii) the exact ground-state density minimizes the total energy. The one-to-one correspondence between the spin-resolved density and total energy ensures the existence of the functional

$$E[\underline{n}] = T[\underline{n}] + V_0[\underline{n}] + E_{\text{H}}[\underline{n}] + E_{\text{xc}}[\underline{n}]. \quad (2.43)$$

Here,  $V_0[\underline{n}]$  captures the electron-core interaction and static external fields;  $E_{\text{H}}[\underline{n}]$  denotes the electrostatic energy (Hartree energy). Both terms are obtained in a straightforward way from evaluating  $\langle \Psi_0 | \hat{H}_e | \Psi_0 \rangle$  ( $\hat{H}_e$  is defined by eq. (2.20) with the last term in eq. (2.21) being time-independent). It is slightly less obvious to see that the kinetic energy  $T[\underline{n}]$  can be expressed in terms of the density only. From the time-independent version of the Hamiltonian (2.20) one obtains the kinetic energy as functional of the reduced density matrix (RDM)

$$\gamma^{\sigma\sigma'}(\mathbf{r}, \mathbf{r}') = \langle \Psi_0 | \hat{\psi}^\dagger(x) \hat{\psi}(x') | \Psi_0 \rangle$$

instead.

All remaining contributions to the total energy arising from the electron-electron interaction are captured by the exchange-correlation (xc) function  $E_{\text{xc}}[\underline{n}]$ . It is usually unknown and is replaced by a suitable approximation in practice. First attempts were inspired by the Thomas-Fermi model, resulting in the local density approximation (LDA). By incorporating the gradient of the density the generalized-gradient approximation (GGA) is obtained. Further extending this generalization leads to meta-GGA functionals, including spatial

<sup>12</sup>The electrostatic potential acting on a particular electron does not include the its own charge density due to the exchange term.

derivatives of the density up to second order. Usually, the exchange and correlation part of the xc-functional are separated into two terms. As the exchange is treated exactly within the HF approach (see subsec. 2.4.2), the idea of mixing the Fock exchange arose, yielding hybrid functionals such as the popular B3LYP [49].

Employing the Ritzian variational principle for minimizing the total energy using the KS parameterization

$$n_\sigma(\mathbf{r}) = \sum_{i=1}^{N_e^\sigma} |\psi_{i\sigma}^{\text{KS}}(\mathbf{r})|^2, \quad N_e^\sigma = \int d\mathbf{r} n_\sigma(\mathbf{r})$$

yields the KS equations

$$\left[ -\frac{1}{2}\nabla^2 + v_0(\mathbf{r}) + v_{\text{H}}(\mathbf{r}) + v_{\text{xc}}^\sigma(\mathbf{r}) \right] \psi_{i\sigma}^{\text{KS}}(\mathbf{r}) = \varepsilon_{i\sigma} \psi_{i\sigma}^{\text{KS}}(\mathbf{r}), \quad i = 1, \dots, N_e^\sigma. \quad (2.44)$$

In eq. (2.44),  $v_0(\mathbf{r})$  captures all static external fields and the electron-core interaction,  $v_{\text{H}}(\mathbf{r})$  stands for the electrostatic potential generated by the electrons density  $n(\mathbf{r}) = \sum_\sigma n_\sigma(\mathbf{r})$ , whereas the xc potential  $v_{\text{xc}}^\sigma(\mathbf{r})$  is given by the functional derivative

$$v_{\text{xc}}^\sigma(\mathbf{r}) = \frac{\delta E_{\text{xc}}[n]}{\delta n_\sigma(\mathbf{r})}. \quad (2.45)$$

Summarizing all potentials defines the KS potential  $v_{\text{KS}}^\sigma(\mathbf{r})$ , which plays the role of an effective (spin-dependent), local one-body potential comprising the influence of the surrounding electrons. Note that the kinetic energy is expressed in terms of the KS orbitals, which in turn uniquely depend on the density via the KS potential. Hence, the kinetic energy can be expressed as functional of the density only.

The KS eigenvalues  $\varepsilon_{i\sigma}$  appear as Lagrangian parameters and have, in principle, no physical meaning. Nevertheless, they are usually interpreted as orbital energies, which is justified by Koopman's theorem for DFT: suppose  $|\Psi_0\rangle$  and  $|\Psi_0^+\rangle$  is the  $N_e$ -electron and  $(N_e - 1)$ -electron ground state, respectively, then the IP  $E_{\text{IP}} = E_0^+ - E_0$  equals the negative KS eigenvalue of the highest occupied molecular orbital (HOMO),  $\varepsilon_{\text{HOMO}}$ . The reason for the identity  $E_{\text{IP}} = -\varepsilon_{\text{HOMO}}$  lies in the equivalence of the densities for the real and the KS system, respectively, allowing to match their (exponential) behavior as  $r \rightarrow \infty$ . This has important implications for approximating the xc-functional: any functional which does not guarantee the correct asymptotic behavior  $v_{\text{KS}}^\sigma(\mathbf{r}) \sim -1/r$  for  $r \rightarrow \infty$  invalidates Koopman's theorem and does not permit the interpretation of the KS eigenvalues as binding energies [50]. For this reason, methods restoring the  $1/r$ -behavior of the KS potential have been developed, such as self-interaction corrections (SIC) [51], electrostatic corrections [52] or appropriate functionals [53–55]. The correct transition to a Coulomb potential is also important for constructing scattering wave-functions as solutions of the KS equation (2.44), which we use in [E5] and [E6].

The KS theorems make a statement on the ground-state (spin) density and the ground-state energy. Insight into excited-state properties can be gained by time-dependent DFT (TDDFT) [56–58]. The mathematical foundation is the Runge-Gross theorem<sup>13</sup>, which guarantees a unique map between time-dependent external potentials and the electronic (spin) density  $n_\sigma(\mathbf{r}, t)$ . The KS construction yields an effective system of non-interacting electrons with  $n_\sigma(\mathbf{r}, t)$  amounting exactly to the time-dependent density of the fully-interacting system. The KS equations attain the form of a set of one-body TDSEs:

$$i\partial_t \psi_{i\sigma}^{\text{KS}}(\mathbf{r}, t) = \left[ -\frac{1}{2}\nabla^2 + v_{\text{KS}}^\sigma(\mathbf{r}, t) \right] \psi_{i\sigma}^{\text{KS}}(\mathbf{r}, t). \quad (2.46)$$

While the time-dependent counterparts of the external and the Hartree potential are defined in a straightforward fashion, it is, in principle, unclear how to characterize the time-dependent xc-potential  $v_{\text{xc}}^\sigma(\mathbf{r}, t)$ <sup>14</sup>. However, the standard approach to TDDFT is to use the xc-functionals known from ground-state DFT and insert  $n_\sigma(\mathbf{r}, t)$ , treating  $t$  as parameter. For these reasons, (i) memory effects are lacking within this so-called *adiabatic* TDDFT, and (ii) TDDFT fails at very short time scales. Nevertheless, adiabatic TDDFT is a very successful method for predicting time-resolved dynamics and excitation properties [61]. Having said that, the extension beyond adiabatic functionals is an ongoing field of research [62, 63].

<sup>13</sup>The proof of the theorem presented in ref. [59] was however not completely correct, as causality was not guaranteed. This point was clarified later by van Leeuwen [60].

<sup>14</sup>The existence of a local xc-potential is however guaranteed by the time-dependent Sham-Schlüter relation [60].



## 2.5 Nonequilibrium Green's functions and many-body perturbation theory

The Green's function (GF) formalism has a long history. Emerging from nuclear and particle physics [64], where most of the formal foundation was developed, the methodology has expanded into almost all branches of theoretical many-body physics. Its success is mostly based on two advantages. First, the method offers an extraordinary flexibility. Treatment of systems at finite temperatures, under the influence of time-dependent fields and in the presence of an external bath is covered by the same formalism. In addition the GF formalism can describe open systems and hence is well suited for quantum transport, especially on the nano-scale [65]. A further advantage is the so-called conserving approximations. The GF formalism provides a systematic way to approximate the electron-electron interaction while basic conservation laws like energy, charge or momentum conservation are built in automatically.

The GF formalism has been developed for systems at zero [66–68] and at finite temperature (Matsubara GF [69]), for steady-state nonequilibrium conditions (Keldysh GF [70]) and for time-dependent scenarios (Kadanoff-Baym equations [71–73]). Instead of regarding all these approaches as separate, we follow the unified contour-based formulation from ref. [74] and specialize when necessary.

This introduction of the nonequilibrium Green's function (NEGF) formalism is given more space than the electronic structure methods in sec. 2.4. There are two reasons for this choice. On the one hand, the NEGF formalism is more fundamental as outlined above. Furthermore, GFs are not limited to objects describing electrons. Even though we mostly focus on the case of spin-1/2 fermions in this section for the sake of concreteness, one can also define GF for bosons such as atoms with integer nuclear spin or even for bosonic quasi-particle excitations such as photons, phonons, magnons and so on [E7]. Hence, treating the GFs for both electronic and nuclear degrees of freedom allows, in principle, to treat both subsystems on equal footing. The whole machinery is furthermore compatible with general two-body interactions, making it suitable to treat, for example, Hubbard models [73]. Secondly, while DFT and quantum chemistry methods are mostly employed as tools to obtain physical properties of particular systems, this thesis includes contributions to NEGF formalism on conceptual level, as well [E3, E7, E5].

### 2.5.1 Contour formulation

Let us now return to the case of electrons subject to the Hamiltonian (2.20). Different types of electron-electron interaction can be incorporated by substituting the Coulomb interaction  $v(\mathbf{r})$  by any two-body potential. The special case of bosonic GFs is addressed in subsec. 2.5.6.

In general, the GFs are objects depending on position-spin and time arguments. The latter does not only account for an explicit time-dependence of observables such as the density or the current, but contain information on the characteristic energies contained in the system, as well. These dependencies can be treated on equal footing if the time arguments are chosen to follow a specific contour  $z \in C$  in the complex plane (fig. 2.1).

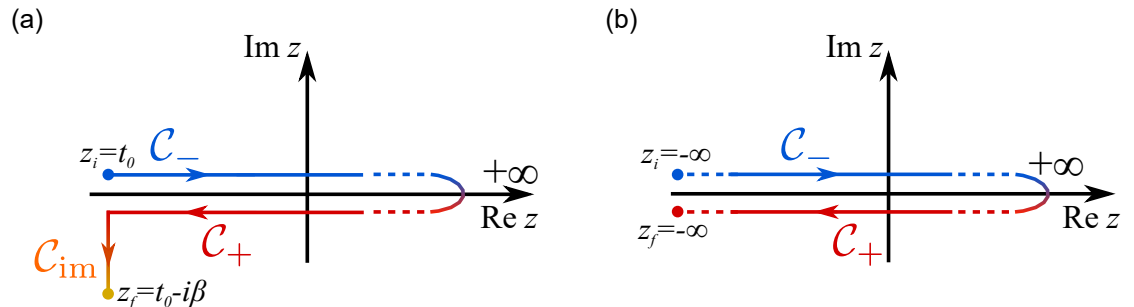


Figure 2.1: Different contours for the notion of the time arguments for the GF formalism, running from the initial point  $z_i$  to the final point  $z_f$  in the directions indicated by the arrows. (a) The (most general) Konstantinov-Perel' contour, running from a finite start time  $z_i = t_0$ , back to  $t_0$  and down the imaginary track to  $t_0 - i\beta$ . (b) The Keldysh contour with  $z_i = -\infty$  progressing to  $+\infty$  and back to  $z_f = -\infty$ , which is often used for steady-state transport calculations.

The directions of the arrows in fig. 2.1 define the induced ordering of time arguments  $z \in C$ : we call  $z_2$  later than  $z_1$  (denoted by the binary relation  $z_2 \succ z_1$ ) if  $z_2$  can be reached by progressing along  $C$  following the arrow directions. In particular, contour arguments  $z_2 \in C_+$  are always later than  $z_1 \in C_-$ . The explicit time-dependence of the Hamiltonian (2.20) is now to be understood as

$$\hat{H}_e(z) = \begin{cases} \hat{H}_e(t_\pm) & : z = t_\pm \in C_\pm \\ \hat{H}_e(t_0) - \mu \hat{N} & : z = -i\tau \in C_{\text{im}}, \end{cases} \quad (2.47)$$

where  $\hat{N}$  stands for the particle-number operator and is  $\mu$  the chemical potential. A commonly used abbreviation that we are adopting is that  $z_+$  denotes a time argument on the contour which is infinitesimally later than  $z$ . Let us define a contour-ordering symbol  $\mathcal{T}$  analogously to the time-ordering symbol for purely real times by

$$\mathcal{T} \hat{A}_H(z_1) \hat{B}_H(z_2) = \begin{cases} \hat{A}_H(z_1) \hat{B}_H(z_2) & : z_1 \succ z_2 \\ -\hat{B}_H(z_2) \hat{A}_H(z_1) & : z_2 \succ z_1. \end{cases} \quad (2.48)$$

The time dependence of the operators is to be understood in the generalized contour Heisenberg picture (subscript H), which we define by the contour time-evolution operator

$$\hat{U}_C(z_1, z_2) = \mathcal{T} \exp \left[ -i \int_{z_2}^{z_1} d\bar{z} \hat{H}_e(\bar{z}) \right], \quad (2.49)$$

where the integration runs along either contours. The Heisenberg representation of an operator is then defined as

$$\hat{A}_H(z) = \hat{U}_C(z_f, z) \hat{A} \hat{U}_C(z, z_i). \quad (2.50)$$

The expectation values of any operator or correlator can be expressed as

$$\langle \hat{A}_H(z) \rangle = \frac{\text{Tr} [\hat{U}_C(z_f, z) \hat{A} \hat{U}_C(z, z_i)]}{\text{Tr} [\hat{U}_C(z_f, z_i)]}. \quad (2.51)$$

In the case the contour fig. 2.1(a) is used, by  $\hat{U}_C(z_f, z_i) = \exp[-\beta(\hat{H}_e(t_0) - \mu \hat{N})]$  the denominator in eq. (2.51) is thus identified as the grand-canonical partition function. It is easy to see that for  $z \in C_{\text{im}}$  the numerator amounts to  $\text{Tr}[\exp[-\beta(\hat{H}_e(t_0) - \mu \hat{N})] \hat{A}]$ , such that eq. (2.51) yields the ensemble average in thermal equilibrium, while for  $z = t \in C_\pm$  the corresponding time-dependent ensemble average is obtained from eq. (2.51). For the zero-temperature case, the contour fig. 2.1(b) is used, transforming the denominator into unity, while the contour time-evolution operator  $\hat{U}_C(z_1, z_2)$  turns into the standard propagator for real times. The trace in eq. (2.51) is then replaced by the ground-state expectation value.

Let us use the convention to skip the subscript H for any annihilation or creation operators and assume that the appearance of a contour argument indicates the Heisenberg picture. Furthermore, we denote the combined time and position-spin basis argument with arabic numbers, i. e. we refer to  $(\mathbf{x}_1 z_1)$  as  $1$ , to  $(\bar{\mathbf{x}}_1 \bar{z}_1)$  as  $\bar{1}$  and so on. Now we define the  $N$ -particle GF as

$$G_N(1, \dots, N; \bar{1}, \dots, \bar{N}) = (-i)^N \frac{\text{Tr} [\mathcal{T} \hat{\psi}(1) \dots \hat{\psi}(N) (\hat{\psi}(\bar{1}) \dots \hat{\psi}(\bar{N}))^\dagger]}{\text{Tr} [\hat{U}_C(z_f, z_i)]}. \quad (2.52)$$

Using the Heisenberg equation of motion (EOM) for the field operators with respect to  $\hat{H}_e(t_0)$ , the EOM for the  $N$ -particle GF is derived:

$$\begin{aligned} \left[ i\partial_{z_k} - h(k) \right] G_N(1, \dots, N; \bar{1}, \dots, \bar{N}) &= -i \int d\tilde{1} v(k, \tilde{1}) \left[ G_{N+1}(1, \dots, N, \tilde{1}; \bar{1}, \dots, \bar{N}, \tilde{1}+) \right. \\ &\quad \left. + \sum_{j=1}^N (-1)^{k+j} \delta(k, \bar{j}) G_{N-1}(1, \dots, \cancel{k}, \dots, N; \bar{1}, \dots, \bar{j}, \dots, \bar{N}) \right]. \end{aligned} \quad (2.53)$$

In eq. (2.53) we have denoted the missing arguments in the  $(N - 1)$ -particle GF by crossing them out. Furthermore, we have used the contour  $\delta$ -function

$$\delta(1, 2) \equiv \delta(x_1, x_2)\delta(z_1, z_2), \quad \delta(x_1, x_2) = \delta_{\sigma_1\sigma_2}\delta(\mathbf{r}_1 - \mathbf{r}_2).$$

Eq. (2.53) is called Martin-Schwinger hierarchy for its structure, which connects the  $N$ -particle GF with the  $(N + 1)$ - and the  $(N - 1)$ -particle GF. Provided we can solve eq. (2.53), we obtain the full information about the  $N$ -particle system, that is, we can compute any correlator or expectation value.

Due to the two-body structure of the Coulomb (or any pairwise) interaction, the most important cases are the one-body and two-body GFs, containing all the information on SP properties and electron-electron correlations. Specializing to the one-body GF (and dropping the subscript), the corresponding EOM reads

$$\left[ i\partial_{z_1} - h(1) \right] G(1; 2) = \delta(1, 2) - i \int d3 \nu(1, 3) G_2(1, 3; 2, 3+) \equiv \delta(1, 2) + \int d3 \Sigma(1; 3) G(3; 2). \quad (2.54)$$

The EOM (2.54) is formally closed by the notion of the self-energy  $\Sigma(1; 2)$ , which is implicitly defined by requiring the last two expressions to be equal. In the case of vanishing Coulomb interaction, eq. (2.54), which simplifies to  $[i\partial_z - h(1)] g(1; 2) = \delta(1, 2)$ , is readily solved for the non-interacting GF  $g(1; 2)$ . The latter allows for representing the integro-differential equation (2.54) in terms of an integral equation

$$\begin{aligned} G(1; 2) &= g(1; 2) + \int d(34) g(1; 3) \Sigma(3; 4) G(4; 2) \\ &= g(1; 2) + \int d(34) g(1; 3) \Sigma(3; 4) g(4; 2) + \int d(3456) g(1; 3) \Sigma(3; 4) g(4; 5) \Sigma(5; 6) g(6; 2) + \dots, \end{aligned} \quad (2.55)$$

which is known as the contour Dyson equation – it amounts to an infinite series in powers of the non-interacting reference GF and the self-energy. The corresponding diagrammatic representation is shown in fig. 2.2.

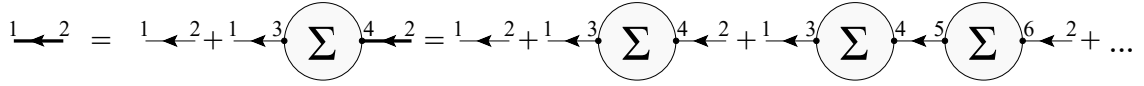


Figure 2.2: Diagrammatic representation of the Dyson equation in terms of the reference GF  $g(1; 2)$  (thin lines), the full GF  $G(1; 2)$  (thick lines) and the self-energy  $\Sigma(1; 2)$  (grey circle). The time contour arguments match eq. (2.55).

### 2.5.2 Electronic self-energy

The self-energy is an extremely useful concept in many-body physics, both from theoretical point of view as well as for the physical interpretation of the information contained in the GFs. The Martin-Schwinger hierarchy for the one-body GF, eq. (2.54), together with the Kubo-Martin-Schwinger (KMS) boundary conditions [75], has a formal solution provided by Wick's theorem [66], expanding the "dressed" GF  $G(1; 2)$  in a power series of  $g(1; 2)$  and the Coulomb interaction. This expansion produces a considerable number of diagrams and is often mathematically ill-posed. Hence it is desirable to reduce the number of diagrams and resum a convergent series of diagrams. This is accomplished by incorporating repeated structures into the self-energy. By virtue of the Dyson equation (2.55), an *infinite* series of diagrams of a certain kind (self-energy insertions) is thus taken into account, while the convergence issue for the GF is circumvented. The diagrammatic expansion is then encapsulated in the self-energy as a functional  $\Sigma[g, \nu]$ . By definition, the self-energy comprises all diagrams with two external vertices which do not separate into disjoint pieces of the same type by removing a single GF line. However, the number of diagrams can be reduced even further by replacing self-energy insertions by virtue of the Dyson equation by the dressed GF  $G$ . In this way, the self-energy turns into a functional of the type  $\Sigma[G, \nu]$ . Let us now have a look at typical approximations for  $\Sigma[G, \nu]$ , whose diagrammatic representation is shown in fig. 2.3. The simplest possible approximation is first order in  $\nu$ . There are exactly two such contributions (first two diagrams in fig. 2.3(a) and (b)). Translating back into mathematical expressions (prefactors are obtained from the Feynman rules [74]) and inserting

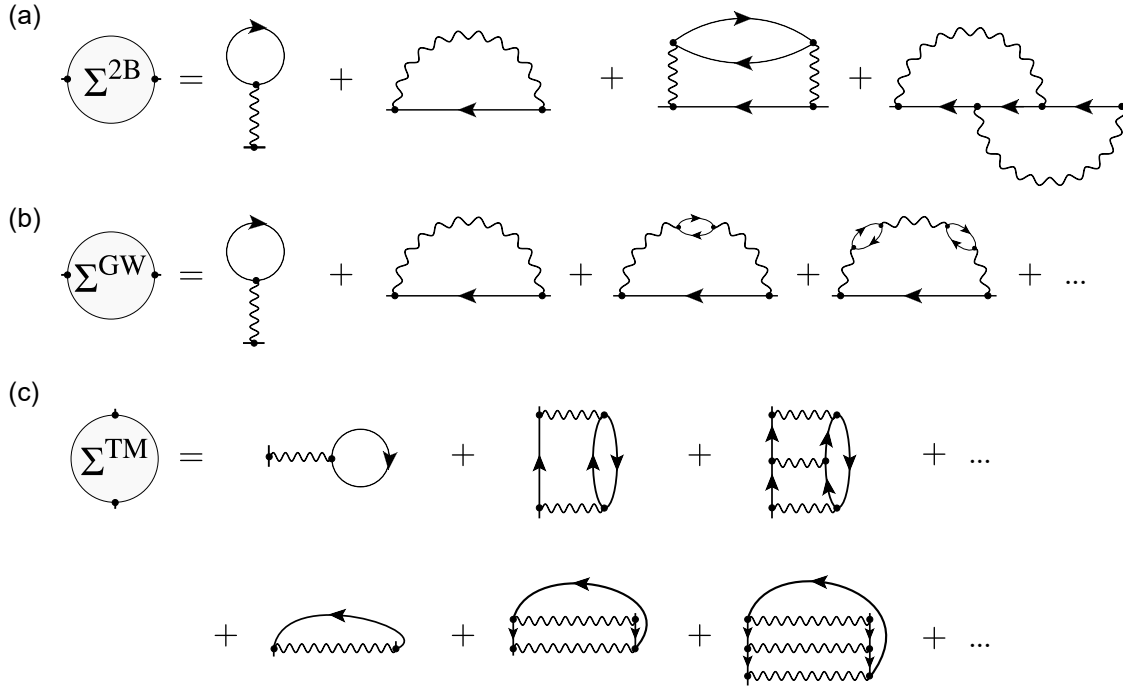


Figure 2.3: Typical approximation to the self-energy in a diagrammatic representation. (a) Second-Born, (b) GW, and (c)  $T$ -matrix approximation. The wiggly line denotes the Coulomb interaction, whereas the solid lines with arrows represent the dressed GF. The self-energies (a)–(c) are conserving approximations [76], i. e. basic conservation laws are not broken. The transformation of the diagrams into mathematical expressions is accomplished by the Feynman rules [74].

the definition of the GF, eq. (2.52), yields

$$\begin{aligned} \Sigma^{(1)}(1; 2) &= -i\delta(1; 2) \int d3 v(1, 3)G(3, 3+) + i\nu(1, 2)G(1, 2+) \\ &= \delta_{\sigma_1\sigma_2}\delta(z_1, z_2) \left[ \delta(\mathbf{r}_1 - \mathbf{r}_2) \int d\mathbf{r}_3 v(\mathbf{r}_1 - \mathbf{r}_3)n(\mathbf{r}_3, z_1) - \nu(\mathbf{r}_1 - \mathbf{r}_2)\gamma^{\sigma_1\sigma_1}(\mathbf{r}_2, \mathbf{r}_1) \right]. \end{aligned}$$

$n(\mathbf{r}, z) = \langle \hat{n}(\mathbf{r}, z) \rangle$  is the charge density and  $\gamma^{\sigma\sigma'}(\mathbf{r}, \mathbf{r}')$  is the RDM. The density operator is defined by  $\hat{n}(\mathbf{r}) = \sum_{\sigma} \hat{\rho}(\mathbf{r}\sigma)$  with  $\hat{\rho}(x) = \hat{\psi}^{\dagger}(x)\hat{\psi}(x)$ . The expectation value of the latter is directly obtained from the GF by  $\langle \hat{\rho}(x_1, z_1) \rangle = -iG(1, 1+)$ . Thus, the contributions to  $\Sigma^{(1)}(1; 2)$  are identified as the Hartree and the exchange potential. The EOM for GF, eq. (2.54) attains a particularly simple form due to the  $\delta$ -function with respect to the contour arguments  $z_1, z_2$  and can hence be reduced to the EOM for a non-interacting problem by modifying the non-interacting Hamiltonian into the HF Hamiltonian. In other words, the first-order approximation to the self-energy amounts to a MF approximation and is completely equivalent to the HF approximation (see subsec. 2.4.2).

Any higher-order self-energy term goes beyond the MF treatment. Including second-order contributions with respect to the Coulomb interaction leads to the so-called second-Born approximation  $\Sigma(1; 2) \approx \Sigma^{2B}(1; 2)$ , shown in fig. 2.3(a). A more sophisticated and much more successful approximation to the self-energy is the GW approximation (GWA)  $\Sigma(1; 2) \approx \Sigma^{GW}(1; 2)$  (fig. 2.3(b)). The first two terms (as it is the case for any self-energy) are MF parts, while all higher diagrams comprise so-called polarization bubbles. Note that an infinite series of diagrams needs to be summed within the GW approximation. This is accomplished by solving an additional Dyson-type equation (see subsec. 2.5.3). Generally, both the second-Born and the GWA are applicable for moderate to high electronic densities, as the influence of the Coulomb interaction is reduced in this scenario. A quite different approximation to the self-energy is given by the ladder or  $T$ -matrix approximation (TMA)  $\Sigma(1; 2) \approx \Sigma^{TM}(1; 2)$ , depicted diagrammatically in fig. 2.3(c). Similarly to the GWA, the TMA entails solving a Dyson equation for an effective interaction (the  $T$ -matrix [70]) in

order to include an infinite series of a certain type of diagrams. The TMA provides an accurate description for low electron density (but independent of the interaction strength). It is hence mainly applied for effective interaction in superconductors [77] and for Hubbard models [73, 78, 79].

So far we have discussed contributions to the self-energy arising due to the electron-electron interaction. The concept of the self-energy has much wider range of applicability, though. An important scenario is a (correlated) subsystem coupled to a larger reservoir. Typical examples are molecular or nano-junctions or molecules adsorbed on a surface. In these cases the interaction between the local system and the reservoir is incorporated into the SP Hamiltonian. For concreteness, we assume an electronic system (described by the Hamiltonian (2.20)) is coupled to a second, uncorrelated electronic system (associated with the field operators  $\hat{\xi}(x)$ ):

$$\hat{H}_{\text{tot}}(z) = \hat{H}_e(z) + \int dx \int dx' (\langle x | \hat{u}(z) | x' \rangle \hat{\psi}^\dagger(x) \hat{\xi}(x') + \text{h. c.}) + \int dx \int dx' \langle x | \hat{h}_{\text{res}}(z) | x' \rangle \hat{\xi}^\dagger(x) \hat{\xi}(x'),$$

where  $\hat{u}(z)$  describes the coupling on SP level. The reservoir is described by the SP Hamiltonian  $\hat{h}_{\text{res}}(z)$  and the GF

$$G_{\text{res}}(1; 2) = G_{\text{res}}(x_1 z_1; x_2 z_2) = -i \langle \mathcal{T} \hat{\xi}(1) \hat{\xi}^\dagger(2) \rangle.$$

Solving the EOM of the bath GF implicitly and substituting the result back into the EOM for the system's GF yields

$$\left[ i\partial_{z_1} - h(1) \right] G(1; 2) = \delta(1, 2) + \int d3 \left[ \Sigma(1; 3) + \Sigma^{\text{em}}(1; 3) \right] G(3; 2), \quad (2.56)$$

with the embedding self-energy

$$\Sigma^{\text{em}}(1; 2) = \int dx_3 \int dx_4 \langle x_1 | \hat{u}(z_1) | x_3 \rangle G_{\text{res}}(x_3 z_1; x_4 z_2) \langle x_4 | \hat{u}^\dagger(z_2) | x_2 \rangle. \quad (2.57)$$

Hence, the embedding self-energy is completely determined by the reservoir GF (and the coupling Hamiltonian), which, in turn, is easily found in the non-interacting case.

### 2.5.3 Density fluctuations and screened interaction

The rearrangement of the nearly-free charges in metals – electrostatic induction – *screens* external electric fields. On a quantum mechanical level, the screening of external potentials upon separating electrons and holes (particle-hole ( $p$ - $h$ ) excitations) is described by the screened interaction  $W(1; 2)$ . This is a genuine many-body effect – it vanishes when neglecting the Coulomb interaction.

On a diagrammatic level, we have already seen (subsec. 2.5.2) that dressing the GF, that is, summing over certain diagrams up to infinite order by virtue of the Dyson equation, leads to a significant reduction of the number of diagrams. Continuing this idea, one can also dress the Coulomb interaction, by summing over all so-called polarization insertions<sup>15</sup>. Gathering all polarization terms in the (irreducible) polarization  $P(1; 2)$  (the lowest two terms are shown in fig 2.4(a)), this procedure gives rise to a Dyson equation for screened interaction  $W(1; 2)$ :

$$W(1; 2) = v(1; 2) + \int d(34) v(1; 3) P(3; 4) W(4; 2), \quad (2.58)$$

depicted in fig. 2.4(b) in diagrammatic language. As inferred from eq. (2.58), the bare Coulomb interaction is modified (screened) by the polarization. The latter can be interpreted as separation of electrons and holes in the medium, consistent with the classical picture. Taking only the first term for the polarization (first diagram in fig. 2.4(a)) into account,  $P(1; 2) \approx -iG(1; 2)G(2; 1)$ , we see that the series of interaction lines and polarization bubbles generated by the Dyson equation (2.58) corresponds exactly to all diagrams for the self-energy in fig. 2.3(b) beyond the Hartree term. Therefore, all these terms can be replaced by a single

<sup>15</sup>All diagrams with two external vertices which can be cut away by removing two interaction lines.

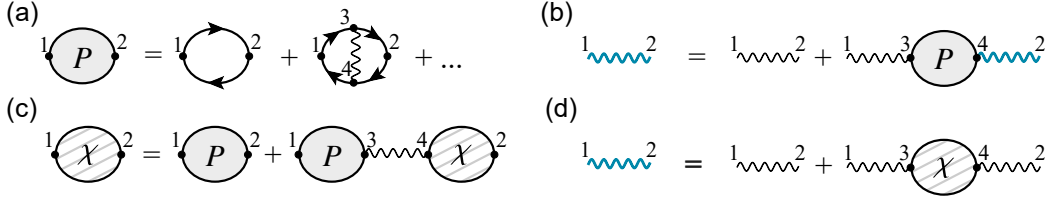


Figure 2.4: (a) Lowest-order diagrams for the polarization propagator  $P(1;2)$ . (b) Diagrammatic representation of the Dyson equation for the screened interaction (thick turquoise wiggly line) in terms of the polarization  $P(1;2)$  and the bare Coulomb interaction (thin wiggly line). (c) Diagrams for the Dyson equation for the DD response function (reducible polarizability)  $\chi(1;2)$ . (d) Representation of the screened interaction by the DD response function.

one in terms of the screened interaction instead of the Coulomb interaction. Expressed in formulae, the GW self-energy simplifies to

$$\Sigma^{\text{GW}}(1;2) = \Sigma^{\text{H}}(1;2) + iG(1;2)W(1;2),$$

where we have denoted the Hartree contribution by the first term on the right-hand side. The structure of the second term explains the naming of the GWA. The GWA has proven incredibly useful, especially for the calculation of band structures of solids. Mostly based on constructing a reference GF (including MF contributions) by DFT, which typically underestimates band gaps, the GF obtained by solving the Dyson equation with  $\Sigma^{\text{GW}}(1;2)$  often yields a quite accurate description of the electronic structure [61, 80, 81]. The GW method is thus one of the most popular ways of introducing electronic correlations beyond DFT in extended systems<sup>16</sup>.

From physical point of view it is clear that screening phenomena have a close relation to fluctuations of the electronic density. A propagator which quantifies these fluctuations can be defined as

$$\chi(1;2) = -i\langle \mathcal{T} \delta\hat{\rho}(1)\delta\hat{\rho}(2) \rangle, \quad \delta\hat{\rho}(1) = \hat{\psi}^\dagger(1)\hat{\psi}(1) - \langle \hat{\psi}^\dagger(1)\hat{\psi}(1) \rangle, \quad (2.59)$$

which is known as *reducible* polarization or density-density (DD) response function<sup>17</sup>. As can be inferred from the number of field operators, it is a genuine two-body quantity and has, in fact, a very close connection to the two-body GF (see appendix C.1). The connection between the two quantities is given by the Dyson equation

$$\chi(1;2) = P(1;2) + \int d(34) P(1;3)v(3,4)\chi(4;2), \quad (2.60)$$

which is shown in fig. 2.4(c) in diagrammatic form. Invoking again the simplest approximation  $P(1;2) \approx -iG(1;2)G(2;1)$  yields the so-called random-phase approximation [61] (RPA), transforming eq. (2.60) into an integral equation which can be solved for  $\chi(1;2)$  once the GF is (approximately) known. Provided the reducible polarization has been obtained or approximated sufficiently well, one can also find the screened interaction via

$$W(1;2) = v(1;2) + \int d(34) v(1;3)\chi(3;4)v(4,2). \quad (2.61)$$

The corresponding diagrams are shown in fig. 2.4(d). The relations between the quantities discussed here are explained in more detail in appendix C.1 by Hedin's equations, an alternative, variational approach to the many-body problem.

### 2.5.4 Keldysh components

The formal notion of the GF and the self-energy on the basis of contour arguments allowed for a general introduction of the EOM, the Dyson equation and the diagrammatic representation. For any practical application, however, the contour arguments have to be projected onto observable times or the imaginary axis.

<sup>16</sup>Only a few alternative methods are available at the moment: quantum chemistry after localization of the SP basis [82, 83] or in combination with embedding techniques and the related Korringa-Kohn-Rostoker (KKR) GF method [84].

<sup>17</sup>Strictly speaking,  $\chi(1;2)$  describes the fluctuations of the spin-resolved density.

Revisiting the contour in fig. 2.1, separating the GF into parts with the contour arguments situated on  $C_+$ / $C_-$ / $C_{\text{im}}$  yields nine possibilities, which are referred to as Keldysh components. For a generic object with two contour arguments  $X(z_1, z_2)$  (position-spin coordinates are omitted for brevity), the Keldysh components, which are marked by superscripts, are summarized in tab. 2.1 along with their proper name. Note that the Keldysh components are functions of two real time (or effective time) arguments.

Table 2.1: Keldysh components of a generic two-argument function  $X(z_1, z_2)$  belonging to the Keldysh space.

	$z_2 = t_2 \in C_-$	$z_2 = t_2 \in C_+$	$z_2 = -i\tau_2 \in C_{\text{im}}$
$z_1 = t_1 \in C_-$	causal, $X^{--}(t_1, t_2)$	lesser, $X^{<}(t_1, t_2)$	left, $X^{\downarrow}(t_1, \tau_2)$
$z_1 = t_1 \in C_+$	greater, $X^{>}(t_1, t_2)$	anti-causal, $X^{++}(t_1, t_2)$	left, $X^{\downarrow}(t_1, \tau_2)$
$z_1 = -i\tau_1 \in C_{\text{im}}$	right, $X^{\uparrow}(\tau_1, t_2)$	right, $X^{\uparrow}(\tau_1, t_2)$	Matsubara, $X^{\text{M}}(\tau_1 - \tau_2)$

Furthermore, the GF and the self-energy are usually represented in a SP basis:

$$G_{i\sigma, j\sigma'}(z_1, z_2) = \int d\mathbf{r}_1 \int d\mathbf{r}_2 \phi_i^*(\mathbf{r}_1) G(x_1 z_1, x_2 z_2) \phi_j(\mathbf{r}_2) = -i \langle \mathcal{T} \hat{c}_{i\sigma}(z_1) \hat{c}_{j\sigma'}^\dagger(z_2) \rangle, \quad (2.62)$$

$$\Sigma_{i\sigma, j\sigma'}(z_1, z_2) = \int d\mathbf{r}_1 \int d\mathbf{r}_2 \phi_i^*(\mathbf{r}_1) \Sigma(x_1 z_1, x_2 z_2) \phi_j(\mathbf{r}_2). \quad (2.63)$$

For the GF in particular, the different Keldysh components have a clear meaning. The causal GF  $G_{i\sigma, j\sigma}^{--}(t_1, t_2)$  is identical to the GF encountered in the zero-temperature treatment [66] (time-ordered formalism). The greater GF  $G_{i\sigma, j\sigma}^{>}(t_1, t_2) = -i \langle \hat{c}_{i\sigma}(t_1) \hat{c}_{j\sigma'}^\dagger(t_2) \rangle$  on the other hand is defined by the creation of an electron in the SP state  $|\phi_j\rangle$  with spin  $\sigma'$  at time  $t_2$ , while an electron in state  $|\phi_i\rangle$  with spin  $\sigma$  is annihilated at time  $t_1$ . In other words, the greater GF describes the propagation of an electron in an interacting medium. Closely related, the lesser GF  $G_{i\sigma, j\sigma}^{<}(t_1, t_2) = i \langle \hat{c}_{j\sigma'}^\dagger(t_2) \hat{c}_{i\sigma}(t_1) \rangle$  contains the dynamics of hole states. Moreover, since  $G_{i\sigma, j\sigma}^{<}(t, t) = i\gamma_{ji}^{\sigma'\sigma}(t)$  the one-body RDM is readily extracted from the lesser GF. Hence, the expectation value of any one-body operator can be computed once the lesser GF is known. The special case when both contour argument lie on the imaginary branch  $C_{\text{im}}$  defines the Matsubara GF  $G_{i\sigma, j\sigma}^{\text{M}}(\tau)$ . Note that due to  $\hat{H}_e(-i\tau) \equiv \hat{H}_e(t_0) - \mu \hat{N}$  the Matsubara GF depends on the difference of imaginary time arguments only. As (i) the definition of  $C_{\text{im}}$  entails fixing a finite temperature by  $\beta = 1/k_{\text{B}}T$  and (ii) the Hamiltonian contains the chemical potential  $\mu$ , the Matsubara GF describes an electronic system in a grand-canonical ensemble. Another type of Keldysh components is the retarded (advanced) function  $X^{\text{R/A}}(t_1, t_2)$  ( $X^{\text{A}}(t_1, t_2)$ ), defined by

$$X^{\text{R/A}}(t_1, t_2) = \pm \theta(\pm(t_1 - t_2)) [X^{>}(t_1, t_2) - X^{<}(t_1, t_2)]. \quad (2.64)$$

We proceed by formulating the EOM for the Keldysh components of the GF. For a more compact notation, we gather the dependence on the indices into matrices. As pointed out in subsec. 2.5.2, the MF part of the self-energy can be incorporated into the HF Hamiltonian  $\mathbf{h}^{\text{HF}}(z)$  – its matrix elements are the same as in eq. (2.41) (but with time-dependent RDMs). The remaining contribution to the self-energy, including the correlation and possibly embedding, is denoted by  $\tilde{\Sigma}$ . In terms of contour arguments, the EOM reads

$$\left[ i\partial_{z_1} - \mathbf{h}^{\text{HF}}(z_1) \right] \mathbf{G}(z_1, z_2) = \mathbf{I}\delta(z_1, z_2) + \int_C dz \tilde{\Sigma}(z_1, z) \mathbf{G}(z, z_2) \equiv \mathbf{I}\delta(z_1, z_2) + \mathbf{J}(z_1, z_2). \quad (2.65)$$

Here, the convolution of the self-energy and GF over  $C$  defines the collision integrals  $\mathbf{J}(z_1, z_2)$ . Projecting now on the Keldysh components, one obtains

$$\left[ i\partial_{t_1} - \mathbf{h}^{\text{HF}}(t_1) \right] \mathbf{G}^{\lessgtr}(t_1, t_2) = \mathbf{J}^{\lessgtr}(t_1, t_2), \quad (2.66a)$$

$$\left[ i\partial_t - \mathbf{h}^{\text{HF}}(t) \right] \mathbf{G}^{\uparrow}(t, \tau) = \mathbf{J}^{\uparrow}(t, \tau), \quad (2.66b)$$

which, together with the corresponding adjoint equations and the symmetries resulting from the definitions and eq. (2.64), defines the so-called Kadanoff-Baym equations (KBEs). Depending on the choice for the self-energy, they constitute a coupled set of non-linear partial integro-differential equations as an initial-value

problem. The KBEs predict the time evolution of an electronic system under the influence of external fields and many more effects, provided the corresponding equilibrium problem has been solved (the Matsubara GF is known, that is). In a hypothetical scenario where the self-energy is known exactly, the exact dynamics of, e. g., the RDM can be obtained from the KBEs. The dynamical aspect adds a new dimension to the assessment of typical approximation schemes for the self-energy, as not only the accuracy of the equilibrium configuration, but also of the time evolution is an important criterion. More background on the KBEs is provided in sec. 6.1, while conceptual as well as numerical details are included in [E7].

Let us now assume the Hamiltonian  $\hat{H}_e$  has no explicit time dependence. In this case all GFs depend on the time difference only, allowing for switching to frequency space by Fourier transformation. The retarded and advanced GFs turn out to be particularly convenient objects to work with in this case. As pointed out before, the HF Hamiltonian plays the role of the reference one-body Hamiltonian, while all further interactions are included in  $\tilde{\Sigma}$ . It is thus convenient to redefine the reference GF by  $[i\partial_{z_1} - \mathbf{h}^{\text{HF}}(z_1)]\mathbf{g}(z_1, z_2) = \mathbf{I}\delta(z_1, z_2)$ . Specifically for the retarded/advanced component  $\mathbf{g}^{\text{R/A}}(t_1, t_2) = \mathbf{g}^{\text{R/A}}(t_1 - t_2)$ , this means

$$[i\partial_t - \mathbf{h}^{\text{HF}}] \mathbf{g}^{\text{R/A}}(t) = \pm \mathbf{I}\delta(t) \quad \leftrightarrow \quad \mathbf{g}^{\text{R/A}}(\omega) = \int_{-\infty}^{\infty} dt e^{i\omega t} \mathbf{g}^{\text{R/A}}(t) = \frac{1}{\omega - \mathbf{h}^{\text{HF}} \pm i\eta}, \quad (2.67)$$

where the positive infinitesimal  $\eta$  arises from the Fourier representation of the Heaviside function. Using the rules for the Keldysh components of products and convolutions (Langreth rules [74]), one finds

$$[i\partial_t - \mathbf{h}^{\text{HF}}] \mathbf{G}^{\text{R/A}}(t) = \pm \mathbf{I}\delta(t) + \int_{-\infty}^{\infty} dt' \tilde{\Sigma}^{\text{R/A}}(t - t') \mathbf{G}^{\text{R/A}}(t').$$

Multiplying by the reference GF, using eq. (2.67) and Fourier-transforming yields the Dyson equation in frequency space

$$\mathbf{G}^{\text{R/A}}(\omega) = \mathbf{g}^{\text{R/A}}(\omega) + \mathbf{g}^{\text{R/A}}(\omega) \tilde{\Sigma}^{\text{R/A}}(\omega) \mathbf{G}^{\text{R/A}}(\omega). \quad (2.68)$$

Due to the Fourier transformation, the convolution has turned into a simple multiplication for the frequency-dependent GFs. Hence, the Dyson equation (2.68) amounts to, for fixed  $\omega$ , a matrix equation for the interacting retarded/advanced GF. Note that retarded self-energy  $\tilde{\Sigma}^{\text{R/A}}(\omega)$  might depend on the greater and lesser Keldysh components. For this reason, they need to be determined self-consistently with eq. (2.68) – which is accomplished by considering the solution of the KBEs (2.66a) in the asymptotic limit  $t_1, t_2 \rightarrow \infty$  and subsequent Fourier transformation. This procedure yields

$$\mathbf{G}^{\gtrless}(\omega) = \mathbf{G}^{\text{R}}(\omega) \tilde{\Sigma}^{\gtrless}(\omega) \mathbf{G}^{\text{A}}(\omega), \quad (2.69)$$

which is sometimes called Keldysh equation. The self-consistent solution of eqs. (2.68) and (2.69) provides a description of an electronic system not only in equilibrium, but in a steady-state configuration, as well. The latter makes eqs. (2.68) and (2.69) suitable for studying transport in correlated systems. The coupling to leads, for instance, can be incorporated in a straightforward way by adding the corresponding embedding self-energy to the correlation part.

### 2.5.5 Quasiparticle picture

We have already said a few words on the physical meaning of the GFs in subsec 2.5.4. Let us pick up the thread by the following gedankenexperiment: an electron is injected into a medium (an electronic system) with the specific state  $\phi_i(\mathbf{r})$  and spin  $\sigma$  at time  $t = 0$ . After a time  $t$  an electron with spatial orbital  $\phi_j(\mathbf{r})$  and spin  $\sigma'$  is removed. What is the probability amplitude that the time-evolved state of the injected electron equals the removal state? Assuming that the system is initially prepared in the ground state  $|\Psi_0\rangle$  and not exposed to time-dependent fields, the answer to this question is given by

$$\frac{\langle \Psi_0 | \hat{c}_{j\sigma'} e^{-i\hat{H}_e t} \hat{c}_{i\sigma}^\dagger | \Psi_0 \rangle}{\langle \Psi_0 | e^{-i\hat{H}_e t} | \Psi_0 \rangle} = \langle \Psi_0 | e^{i\hat{H}_e t} \hat{c}_{j\sigma'} e^{-i\hat{H}_e t} \hat{c}_{i\sigma}^\dagger | \Psi_0 \rangle = iG_{j\sigma', i\sigma}^>(t, 0).$$

Hence, the greater GF plays the role of a conditional probability amplitude for the setup stated above. Analogously, one can show that  $-iG_{i\sigma, j\sigma'}^<(0, t)$  amounts to the conditional probability amplitude of observing a



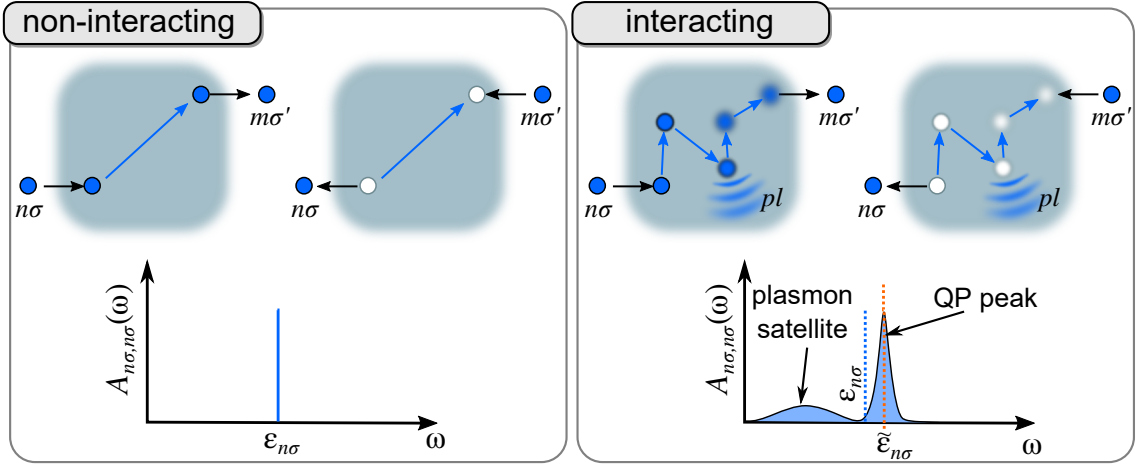


Figure 2.5: Illustration of the physical meaning of the GFs in the non-interaction (left-hand side) and in the interacting (right-hand side) case. The schematic graphs sketch the typical behavior of the spectral function (see text).

hole (i. e., a missing electron) in the state  $\phi_j(\mathbf{r})$  with spin  $\sigma'$  after time  $t$ , if an electron in with state  $\phi_i(\mathbf{r})$  and spin  $\sigma$  had been removed at  $t = 0$ . Hence, the lesser (greater) GF contains the structure and dynamics of particle (hole) states.

The trivial propagation of particles or holes in a non-interacting medium is sketched in fig. 2.5. For clarity, the SP basis is chosen as the the eigenstates of the non-interacting problem:  $\hat{h}|n\sigma\rangle = \varepsilon_{n\sigma}|n\sigma\rangle$ . As no scattering events occur the final state of the electron (hole) is identical to the one of the injected (removed) electron<sup>18</sup>. The situation changes substantially in the case of fully-interacting systems (illustrated on the right-hand side of fig. 2.5). At variance with the non-interacting case, a series of scattering events may alter the state of the injected (removed) electron upon time evolution.

For a more quantitative discussion we switch to the frequency domain to gain access to the spectral characteristics of particle or hole propagation. From the definition of the greater/lesser GF and taking the Fourier transform with respect to the time difference of the two arguments, one obtains

$$G_{n\sigma, m\sigma'}^>(\omega) = -2\pi i \langle \Psi_0 | \hat{c}_{n\sigma} \delta(\omega + E_0 - \hat{H}_e) \hat{c}_{m\sigma'}^\dagger | \Psi_0 \rangle, \\ G_{n\sigma, m\sigma'}^<(\omega) = 2\pi i \langle \Psi_0 | \hat{c}_{m\sigma'}^\dagger \delta(\omega - E_0 + \hat{H}_e) \hat{c}_{n\sigma} | \Psi_0 \rangle.$$

Inserting a completeness relation in the  $(N_e + 1)$ -particle Hilbert space for the greater GF (provided that  $|\Psi_0\rangle$  is a  $N_e$ -particle state) defines the so-called Lehmann representation. The steps for the lesser GF are analogous (but we have to insert the completeness relation in the  $(N_e - 1)$ -particle Hilbert space). Let us define

$$\phi_{0,\alpha}^{(p)}(x) = \langle \Psi_0 | \hat{\psi}(x) | \Psi_\alpha^{(N_e+1)} \rangle, \quad \phi_{0,\alpha}^{(h)}(x) = \langle \Psi_\alpha^{(N_e-1)} | \hat{\psi}(x) | \Psi_0 \rangle \quad (2.70)$$

for brevity. Using this short-hand notation, we find

$$G_{n\sigma, m\sigma'}^>(\omega) = -2\pi i \sum_\alpha \langle n\sigma | \phi_{0,\alpha}^{(p)} \rangle \langle \phi_{0,\alpha}^{(p)} | m\sigma' \rangle \delta(\omega + E_0 - E_\alpha^{(N_e+1)}), \quad (2.71a)$$

$$G_{n\sigma, m\sigma'}^<(\omega) = 2\pi i \sum_\alpha \langle n\sigma | \phi_{0,\alpha}^{(h)} \rangle \langle \phi_{0,\alpha}^{(h)} | m\sigma' \rangle \delta(\omega - E_0 + E_\alpha^{(N_e-1)}). \quad (2.71b)$$

The SP orbital  $\phi_{0,\alpha}^{(p)}(x)$  is called particle-type Dyson orbital with respect to the two states  $|\Psi_0\rangle$  and  $|\Psi_\alpha^{(N_e+1)}\rangle$ , whereas  $\phi_{0,\alpha}^{(h)}(x)$  is referred to as hole-type Dyson orbital. Together with the singular points in the energy

<sup>18</sup>One obtains  $G_{n\sigma, m\sigma'}^>(t_1, t_2) = -i\delta_{\sigma\sigma'}\delta_{nm}(1 - f_{n\sigma})\exp[-i\varepsilon_{n\sigma}(t_1 - t_2)]$  and  $G_{n\sigma, m\sigma'}^<(t_1, t_2) = i\delta_{\sigma\sigma'}\delta_{nm}f_{n\sigma}\exp[-i\varepsilon_{n\sigma}(t_1 - t_2)]$ , where  $f_{n\sigma}$  is the occupation of the SP state  $|n\sigma\rangle$ .

domain in eq. (2.71a) and (2.71b), the physical meaning of the greater/lesser GF becomes clear: the greater GF describes adding particles to the system along with the respective change in energy ( $E_\alpha^{(N_e+1)} - E_0$ ), while the lesser GF contains information on the removal of particles, or, equivalently, the creation of holes. A concept that is closely related to this interpretation is the *spectral function*, defined as

$$A_{n\sigma,m\sigma'}(\omega) = i \left[ G_{n\sigma,m\sigma'}^>(\omega) - G_{n\sigma,m\sigma'}^<(\omega) \right] = i \left[ G_{n\sigma,m\sigma'}^R(\omega) - G_{n\sigma,m\sigma'}^A(\omega) \right]. \quad (2.72)$$

Let us for a moment switch off any particle-particle interactions. The diagonal element of the spectral function would be  $A_{n\sigma,n\sigma}(\omega) = 2\pi\delta(\omega - \varepsilon_{n\sigma})$  in this scenario – a quantity that can be interpreted as the probability density of finding the state  $|n\sigma\rangle$  at the energy  $\omega = \varepsilon_{n\sigma}$  (see illustration in fig. 2.5). In an interacting system however, any SP-type excitation can no longer be an eigenstate. However, one can still ask the question how much of a SP state  $|n\sigma\rangle$  is contained in the many-body system at energy  $\omega$ . The answer to this equation is exactly  $A_{n\sigma,n\sigma}(\omega)$ . The typical structure of the spectral function resembles a peak-like structure which is broadened and shifted due to the interaction. The peak positions (like in the non-interacting case) contain information on the energy of the SP-like (*quasiparticle*, QP) excitations. Their exact values, as can be seen from eqs. (2.71), corresponds to the particle removal or addition energies. The second generic feature of the spectral function are plasmon satellites (see fig. 2.5). They arise due to inelastic scattering processes which induce collective excitations in the system (indicated by *pl* in fig. 2.5). More details can be found in sec. 6.2. The spectral function is a versatile tool to analyze spectral properties. For instance, the density of states (DOS) is given by  $D(\omega) = (1/2\pi) \sum_{n\sigma} A_{n\sigma,n\sigma}(\omega)$  (spin-resolved DOS is obtained by omitting the sum over  $\sigma$ ), while, similarly, the local DOS (LDOS) can be computed by  $\rho(\mathbf{r}, \omega) = (1/2\pi) \sum_{n\sigma} |\langle \mathbf{r} | n\sigma \rangle|^2 A_{n\sigma,n\sigma}(\omega)$ . As injecting/removing a particle does not yield an eigenstate of the system, QP excitations are subject to dephasing and relaxation. This is reflected in the finite width of the QP peaks. One can show that in lowest order, the latter is proportional to  $\Gamma_{n\sigma} = \text{Im}[\Sigma_{n\sigma,n\sigma}^R(\tilde{\varepsilon}_{n\sigma})]$ , whereas the shifted QP energy is found from  $\tilde{\varepsilon}_{n\sigma} = \varepsilon_{n\sigma} + \text{Re}[\Sigma_{n\sigma,n\sigma}^R(\tilde{\varepsilon}_{n\sigma})]$ .

The Lehmann representation eqs. (2.71) does not only underpin the QP picture, but also provides an alternative route of calculating the GFs by, e. g., quantum chemistry methods (see appendix B), via the Dyson orbitals eq. (2.70). One might ask why the explicit construction of the GFs is useful, as all information can be extracted from the many-body wave-functions. The answer lies in the accessibility of the exact self-energy via the Dyson equation (2.68). This offers a way of assessing different approximation schemes, on the one hand, but also allows studying QP properties such as the lifetime of molecular states [85], on the other hand.

Although the spectral function is a standard tool to characterize equilibrium or steady-state systems, a generalization towards time-dependent scenarios is possible. Importantly, the greater/lesser GFs intrinsically depend on two time arguments that can not be reduced to a difference. Hence, the transition to the frequency domain is not straightforward. In analogy to the definition of the Wigner function in quantum mechanics, it is feasible to define the time-dependent spectral function as

$$A_{n\sigma,m\sigma'}(\omega, T) = i \int_{-\infty}^{\infty} dt e^{i\omega t} \left[ G_{n\sigma,m\sigma'}^>(T + \frac{t}{2}, T - \frac{t}{2}) - G_{n\sigma,m\sigma'}^<(T + \frac{t}{2}, T - \frac{t}{2}) \right]. \quad (2.73)$$

Eq. (2.73) represents an optimal compromise between spectral ( $\Delta\omega$ ) and time resolution ( $\Delta t$ ), i. e. the uncertainty product  $(\Delta t)(\Delta\omega) = 1$  is minimal<sup>19</sup>. It also demonstrates again the meaning of the two time arguments of the GFs: while the dynamics connected to the observable time  $T$  is encoded in the time-diagonal  $t_1 = t_2 = T$ , the orthogonal direction  $t_1 - t_2 = t$  contains the spectral information. Typical applications where the time-dependent spectral function (2.73) plays an important role are time-resolved photoemission [86], transient absorption [87] or transmission [88, 89].

## 2.5.6 Electron-boson models

The presentation of the (NE)GF formalism so far was oriented towards electronic systems with Coulomb-type particle-particle interaction (even though with slight modifications it applies to bosonic particles, too).

<sup>19</sup>We refer to the inequality between time and frequency resolution  $(\Delta t)(\Delta\omega) \geq 1$  arising from the Fourier transformation. In spite of the formal relation, this needs to be distinguished from the uncertainty principle for quantum fluctuations, because the time has no operator character.

In this subsection we briefly introduce a different type of interacting system: electrons linearly coupled to bosonic QP excitations. In particular, we consider bosons which can be emitted or absorbed<sup>20</sup> (quasi-bosons [90]), mediating an effective electron-electron interaction. The generic Hamiltonian reflecting this situation is given by

$$\begin{aligned}\hat{H}(t) &= \sum_{ij} h_{ij}(t) \hat{c}_i^\dagger \hat{c}_j + \sum_{\nu} \sum_{ij} \Gamma_{ij}^{\nu} \hat{c}_i^\dagger \hat{c}_j \hat{Q}_{\nu} + \frac{1}{2} \sum_{\nu} \Omega_{\nu} (\hat{P}_{\nu}^2 + \hat{Q}_{\nu}^2) \\ &= \hat{H}_e(t) + \hat{H}_{e-b} + \hat{H}_b.\end{aligned}\quad (2.74)$$

Note that we omitted the spin index here for the sake of a more compact notation. The explicit dependence on the spin degree of freedom can be retained by replacing the SP indices as  $i \rightarrow i\sigma$ . The bosons modes, labelled by  $\nu$ , are described by their characteristic frequencies  $\Omega_{\nu}$ , the coordinate and momentum operators

$$\hat{Q}_{\nu} = \frac{1}{\sqrt{2}}(\hat{a}_{\nu} + \hat{a}_{\nu}^{\dagger}), \quad \hat{P}_{\nu} = \frac{1}{i\sqrt{2}}(\hat{a}_{\nu} - \hat{a}_{\nu}^{\dagger}). \quad (2.75)$$

Here,  $\hat{a}_{\nu}^{\dagger}$  ( $\hat{a}_{\nu}$ ) stands for the bosonic creation (annihilation) operators. The electron-boson (EB) Hamiltonian (2.74) has a range of applications:

- As discussed in subsec. 2.3.2, eq. (2.74) can describe electrons coupled to the vibrational modes in molecules or phonons modes in crystalline solids. This approach is limited to the linear coupling regime, though. In this context, the Fröhlich Hamiltonian [91–93] and the Holstein model [94–96] represent some of the most relevant model systems. A systematic way how to obtain a EB model of the type (2.74) from the molecular Hamiltonian (2.2) is presented in ref. [30].
- If the electromagnetic field is treated on QED level the photon field is quantized, yielding a photon Hamiltonian similar to  $\hat{H}_b$  and a total Hamiltonian of the form of eq. (2.74) [4]. Similarly, the near-field induced by charge-density oscillations in metallic nano-junctions are typically quantized. The electron dynamics of, e. g., molecules in the vicinity is then subject to the Hamiltonian (2.74) [97, 98].
- Many-body excitations can often be represented by quasi-bosons. In particular, collective (long-wavelength) charge density fluctuations display oscillatory behavior, as shown by Pines and Bohm for the homogeneous electron gas [99]. Quantizing these density fluctuations gives rise to an effective Hamiltonian [100] as eq. (2.74). In this way, the (Coulomb) electron-electron interaction is mapped onto an effective interaction due to exchanging quasi-bosons. More details can be found in appendix C.3.

We assume the system has been prepared in a grand-canonical ensemble with chemical potential  $\mu_e = \mu$  for the electrons, while the chemical potential for the quasi-bosons is zero<sup>21</sup>. The one-body electronic GF is defined, analogously to eq. (2.52), as

$$G_{ij}(z_1, z_2) = -i \langle \mathcal{T} \hat{c}_i(z_1) \hat{c}_j^{\dagger}(z_2) \rangle \equiv -i \frac{\text{Tr} \left[ \mathcal{T} \hat{c}_i(z_1) \hat{c}_j^{\dagger}(z_2) \right]}{\text{Tr} \left[ \hat{U}_{\mathcal{C}}(z_f, z_i) \right]}, \quad z_1, z_2 \in \mathcal{C}, \quad (2.76)$$

where the trace is carried out over eigenstates of  $\hat{H}(t_0) - \mu \hat{N}_e$  ( $\hat{N}_e = \sum_i \hat{c}_i^{\dagger} \hat{c}_i$ ). The contour evolution operator  $\hat{U}_{\mathcal{C}}(z_1, z_2)$  is defined with respect to the full Hamiltonian (2.74). Therefore, the time-dependent electronic creation and annihilation operators entail the bosonic dynamics, too.

<sup>20</sup>Bosonic particles like atoms with integer nuclear spin are excluded at this point.

<sup>21</sup>This is a typical assumption for excitations such as photons, phonons, ..., reflecting that, in principle, an infinite amount of these quasi-bosons can be created.

It is not clear *a priori* what should be the bosonic counterpart to the electronic GF (2.76). This is by no means a trivial point, since the spectral properties of the bosonic GFs should be quite different from the electron case. Unlike electrons, the quasi-bosons can be absorbed and emitted, resulting in two peaks at  $\pm\Omega_\nu$  in the spectral function for a single mode  $\nu$ . Furthermore, exchanging the bosonic quasi-particle excitations gives rise to an effective interaction between the electrons. Hence a propagator characterizing the boson fluctuations is necessary. Reflecting these requirements, the most convenient objects to work with are fluctuation correlators with respect to bosonic coordinates  $\hat{Q}_\nu$ :

$$D_{\mu\nu}(z_1, z_2) = -i \left[ \langle \hat{Q}_\mu(z_1) \hat{Q}_\nu(z_2) \rangle - \langle \hat{Q}_\mu(z_1) \rangle \langle \hat{Q}_\nu(z_2) \rangle \right]. \quad (2.77)$$

As discussed in appendix C.2, using the boson correlator (2.77), one can readily define the effective electron-electron interaction by

$$\mathcal{W}_{ijkl}(z_1, z_2) = \sum_{\mu\nu} \Gamma_{il}^\nu D_{\mu\nu}(z_1, z_2) \Gamma_{jk}^\mu. \quad (2.78)$$

In fact, the notion of  $\mathcal{W}_{ijkl}(z_1, z_2)$  by eq. (2.78) allows for applying the diagrammatic machinery analogous to subsec. 2.5.2. Specifically, the diagrammatic representation of the self-energy based on the interaction (2.78) is completely parallel to the diagrammatics in terms of the screened interaction beyond the Hartree term. With an appropriate approximation to the EB self-energy  $\Sigma^{e-b}(z_1, z_2)$  (we again employ the matrix notation for self-energy and GF), the EOM for the GF attains the familiar form

$$\left[ i\partial_{z_1} - \mathbf{h}^{\text{MF}}(z_1) \right] \mathbf{G}(z_1, z_2) = \mathbf{I}\delta(z_1, z_2) + \int_C dz \Sigma^{e-b}(z_1, z) \mathbf{G}(z, z_2). \quad (2.79)$$

The explicit form of the self-energy can be found in appendix C.2. The MF Hamiltonian is given by the intuitive modification of the ony-body Hamiltonian:  $\mathbf{h}^{\text{MF}}(z) = \mathbf{h}(z) + \sum_\nu \Gamma^\nu \langle \hat{Q}_\nu(z) \rangle$ , which can also be obtained by taking the expectation value of the Hamiltonian (2.74) in the bosonic subspace only. The EOM (2.79) can, as explained in subsec. 2.5.4, be separated into the various Keldysh components in order to obtain the respective Dyson equation or the KBEs.

How does the electron dynamics act on the quasi-bosons? One can imagine that any electronic excitation ( $p$ - $h$  excitations in this context) drains the quasi-bosons, while recombination processes of electrons with holes leads to the generation of bosons. In other words, the polarization  $P(1; 2)$  of the electronic medium (see subsec. 2.5.3) should play a dominant role for the boson dynamics. Indeed, one can show that the bosonic self-energy is directly proportional to the electron polarization, which needs to be computed self-consistently to treat the electrons and bosons on equal footing. The explicit expressions for both the electronic and the bosonic self-energy along with a full derivation are presented in appendix C.2 and [E7], where we also discuss the peculiarities of the EOM of the bosonic propagator (2.77).

On a more fundamental level we note the connection between the EB model and a purely electronic system. The fluctuations (of the bosonic coordinates or the charge density, respectively) mediate the effective electron-electron interaction, while the polarization, measuring the excitations of the electrons, influences these fluctuations. As a matter of fact, a direct link between the two scenarios can be established – at least in equilibrium, as shown in appendix C.3 with the appropriate choice of the coupling matrix elements  $\Gamma_{ij}^\nu$  and the mode energies  $\Omega_\nu$ . In this case, the dynamical part of the screened interaction is precisely reproduced [101] by the effective interaction (2.78). This is the reason why specific versions of the EB Hamiltonian (2.74), in particular the  $S$ -model introduced by Lundqvist [102], have been introduced. The  $S$ -model possesses an analytical solution [103] and thus offers an ideal test system for challenging the MBPT [104]. We continue this discussion in sec. 6.2.

In case the quasi-bosons describe photons, vibrons, phonons or similar QP excitations that do not emerge from the electronic system, the treatment outlined in this subsection is compatible with the NEGF formalism for Coulomb-interacting electronic systems, as well. The different interaction channels can be incorporated by taking the sum of the respective self-energies. This is, in fact, the standard approach to describe phonon-driven relaxation in excited correlated systems [105–107].

## 2.6 Linear response

Let us consider a quantum system and two operators: an observable  $\hat{A}$  we are interested in and a perturbation  $\hat{B}$  which acts on the system. We are interested in the time-dependent expectation value  $A(t) = \langle \hat{A}_H(t) \rangle$  (subscript indicates the Heisenberg picture) in the presence of a time-dependent driving of the type  $\hat{B}f(t)$ . Provided the excitation is sufficiently weak,  $A(t)$  is given by the *retarded* linear response function

$$A(t) = \int_{-\infty}^{\infty} dt' \chi_{AB}^R(t, t') f(t'). \quad (2.80)$$

The response function in eq. (2.80) is identified by virtue of the Kubo formula [108] as

$$\chi_{AB}^R(t, t') = -i\theta(t - t') \langle [\hat{A}_H(t), \hat{B}_H(t')] \rangle. \quad (2.81)$$

The expectation values  $\langle \dots \rangle$  are defined with respect to an initial preparation of eigenstates of the Hamiltonian  $\hat{H}_0$  of the system. For concreteness, we consider the electronic degrees of freedom here and assume  $\hat{H}_0 = \hat{H}_e(t_0)$  with some reference time  $t_0$ . Already at this stage an important conclusion can be drawn from eq. (2.80) and (2.81): in order to compute the response upon a weak perturbation, knowledge of only the *initial* configuration of the system is required, as this completely suffices to define the corresponding response function. Hence, the properties of the initial configuration is inherent to the concept of linear response. The excitations of the system enter in the time dependence of the operators  $\hat{A}_H(t)$  and  $\hat{B}_H(t)$ .

The superscript R indicates a connection to the retarded Keldysh component of correlators defined on the complex contour (see subsec. 2.5.4). The connection becomes immediately clear from the reducible polarization introduced in subsec. 2.5.3: if we identify  $\hat{A} = \hat{B} = \delta\hat{\rho}(x)$ , the retarded component of reducible polarization  $\chi(1; 2)$  matches the definition (2.81).

### 2.6.1 Fluctuation-dissipation theorem

Assuming the system to be prepared in the thermodynamical equilibrium (inverse temperature  $\beta$ ) implies  $\chi_{AB}^R(t_1, t_2) = \chi_{AB}^R(t_1 - t_2)$ , which allows to perform the Fourier transformation with respect to the time difference,

$$\chi_{AB}^R(\omega) = \int_{-\infty}^{\infty} dt e^{i\omega t} \chi_{AB}^R(t) = \int_0^{\infty} dt e^{i\omega t} \chi_{AB}^R(t). \quad (2.82)$$

One of the most important cases is given if the perturbation and the response are described by the same type of operator, i. e.  $\hat{B} = \hat{A}^\dagger$ . It is straightforward to see that the corresponding response function is related to a dissipation of energy. Suppose the system is driven by the time-dependent perturbation  $\hat{H}(t) = \hat{H}_0 + \hat{V}(t)$  with  $\hat{V}(t) = f_0 (e^{-i\omega t} \hat{A}^\dagger + \text{h. c.})$ . For the energy transfer to the system within the time interval  $[0, T]$  one finds

$$\begin{aligned} \frac{dE}{dt} &= \frac{1}{T} \int_0^T dt \partial_t \langle \Psi(t) | \hat{H}(t) | \Psi(t) \rangle = \frac{1}{T} \int_0^T dt \langle \Psi(t) | \partial_t \hat{H}(t) | \Psi(t) \rangle = \frac{1}{T} \int_0^T dt (-i\omega f_0 e^{i\omega t} A(t))^* + \text{c. c.} \\ &= -2\omega \text{Im}[\chi_{AA^\dagger}^R(\omega)] |f_0|^2 > 0 \quad \text{for } \omega > 0 \end{aligned}$$

as  $T \rightarrow \infty$ . The property  $\text{Im}[\chi_{AA^\dagger}^R(\omega)] < 0$  ( $\omega > 0$ ) follows directly from the definition (2.81) and (2.82). Hence, the system absorbs, in other words dissipates the energy originating from the driving fields. Conversely,  $dE/dt < 0$  for  $\omega < 0$ , corresponding to emission from the system.

A closely related concept is the fluctuation correlator

$$S_{AA^\dagger}(\omega) = \frac{1}{2\pi} \int_{-\infty}^{\infty} dt e^{i\omega t} \langle \hat{A}_H(t) \hat{A}^\dagger \rangle = A_{\text{eq}} \delta(\omega) + \frac{1}{2\pi} \int_{-\infty}^{\infty} dt e^{i\omega t} \langle \delta \hat{A}_H(t) \delta \hat{A}^\dagger \rangle, \quad (2.83)$$

where  $A_{\text{eq}} = \langle \hat{A} \rangle$  with respect to the initial preparation and  $\delta \hat{A} = \hat{A} - A_{\text{eq}}$ . The quantity (2.83) is also known as *dynamical structure factor*.

In thermodynamical equilibrium, the important fluctuation-dissipation theorem (FDT), which is a consequence of a detailed balance of quantum transitions [108], holds:

$$\text{Im}[\chi_{AA^\dagger}^{\text{R}}(\omega)] = -\pi (1 - e^{-\beta\omega}) S_{AA^\dagger}(\omega). \quad (2.84)$$

Although the correctness of the FDT (2.84) might seem trivial, it breaks down if the system is out of equilibrium. This has important implications for time-resolved spectroscopies where the system is probed after driving it to an excited state.

### 2.6.2 Typical response functions

Let us revisit the way the coupling to external electromagnetic fields is introduced (sec. 2.2) and specify the time-dependent one-body part  $\hat{h}(t)$  of the Hamiltonian (2.20). In the presence of the (weak) vector ( $\delta \mathbf{A}(\mathbf{r}, t)$ ) and the scalar ( $\delta \varphi(\mathbf{r}, t)$ ) potentials, the linear coupling scheme yields

$$\hat{h}(t) = \hat{h}_0 + \int d\mathbf{r} \hat{\mathbf{j}}(\mathbf{r}) \cdot \delta \mathbf{A}(\mathbf{r}, t) - \int d\mathbf{r} \hat{n}(\mathbf{r}) \delta \varphi(\mathbf{r}, t). \quad (2.85)$$

Here,  $\hat{h}_0$  denotes the static part comprising the electron-core interactions. Hence, for describing the action of electromagnetic fields within linear response, two types of perturbation operators play a role: (i) coupling to the density  $\hat{n}(\mathbf{r}) = \sum_{\sigma} \hat{\rho}(\mathbf{r}\sigma)$ , and (ii) to the current operator

$$\hat{\mathbf{j}}(\mathbf{r}) = \frac{1}{2i} \sum_{\sigma} [\hat{\psi}^\dagger(\mathbf{r}\sigma)(\nabla \hat{\psi}(\mathbf{r}\sigma)) - (\nabla \hat{\psi}^\dagger(\mathbf{r}\sigma))\hat{\psi}(\mathbf{r}\sigma)]. \quad (2.86)$$

On the other hand, the density and the current are the most typical observables to look at when driving the system with electromagnetic fields. It is thus natural to define response functions with respect to these operators. The DD response function

$$\chi^{\text{R}}(\mathbf{r}, \mathbf{r}'; t, t') = -i\theta(t - t') \langle [\delta \hat{n}(\mathbf{r}, t), \delta \hat{n}(\mathbf{r}', t')] \rangle \quad (2.87)$$

allows for computing the change of the density and thus any spatially-local observable upon driving by external scalar potentials. For instance, the time-dependent dipole moment induced by a laser pulse (within the dipole approximation and the length gauge, see sec. 2.2) can be readily computed from the DD response function (2.87). If the system evolves under the influence of possibly time-dependent magnetic fields, the current operator (2.86) plays the role of the perturbation. One might still be interested in the variation of the density, which is then described by the density-current response function. The converse case (system driven by scalar potential, current as the observable) can be employed to compute the flux of scattering electrons emanating from a sample, or the conductivity in a solid. For magnetic systems, response functions based on the notion of the spin density  $\hat{\mathbf{S}}(\mathbf{r})$ <sup>22</sup> plays an important role. Tab. 2.2 summarizes the response functions mentioned here. We remark that the concept of linear response is even more general and allows the construction of response functions for very different setups.

Returning to the DD response function, its general structure can, similarly to the one-body GFs (see subsec 2.5.5), be better understood in terms of the Lehmann representation by inserting a complete set of many-body eigenstates  $|\Psi_\lambda\rangle$  of  $\hat{H}_0$ . Assuming the system to be prepared in the ground state, this procedure yields

$$\chi^{\text{R}}(\mathbf{r}, \mathbf{r}'; t) = -i \sum_{\lambda} [\rho_\lambda(\mathbf{r})\rho_\lambda^*(\mathbf{r}')e^{-i(E_\lambda - E_0)t} - \rho_\lambda(\mathbf{r}')\rho_\lambda^*(\mathbf{r})e^{i(E_\lambda - E_0)t}] \quad (2.88)$$

where  $\rho_\lambda(\mathbf{r}) = \langle \Psi_0 | \hat{n}(\mathbf{r}) | \Psi_\lambda \rangle$  defines the so-called *fluctuation density*. Abbreviating the excitation energies by  $\Omega_\lambda = E_\lambda - E_0$ ,  $\lambda \neq 0$ , the DD response function in the frequency domain reads

$$\chi^{\text{R}}(\mathbf{r}, \mathbf{r}'; \omega) = \sum_{\lambda} \left[ \frac{\rho_\lambda(\mathbf{r})\rho_\lambda^*(\mathbf{r}')}{\omega - \Omega_\lambda + i\eta} - \frac{\rho_\lambda(\mathbf{r}')\rho_\lambda^*(\mathbf{r})}{\omega + \Omega_\lambda + i\eta} \right] = \sum_{\lambda} \frac{2\Omega_\lambda}{(\omega + i\eta)^2 - \Omega_\lambda^2} \rho_\lambda(\mathbf{r})\rho_\lambda(\mathbf{r}'), \quad (2.89)$$

<sup>22</sup>The spin-density operator is defined by  $\hat{\mathbf{S}}(\mathbf{r}) = \hat{\psi}^\dagger(\mathbf{r})\hat{\boldsymbol{\sigma}}\hat{\psi}(\mathbf{r})$ , where  $\hat{\boldsymbol{\sigma}}$  is the vector of the Pauli matrices and  $\hat{\psi}(\mathbf{r})$  denotes the spinor of the field operators.

Table 2.2: Examples of response functions by classification according to perturbation ( $\hat{B}$ ) and observable ( $\hat{A}$ ).

$\hat{A}$	$\hat{B}$	response function
$\hat{n}(\mathbf{r})$	$\hat{n}(\mathbf{r})$	density-density
$\hat{\mathbf{j}}(\mathbf{r})$	$\hat{\mathbf{j}}(\mathbf{r})$	current-current
$\hat{n}(\mathbf{r})$	$\hat{\mathbf{j}}(\mathbf{r})$	density-current
$\hat{\mathbf{j}}(\mathbf{r})$	$\hat{n}(\mathbf{r})$	current-density (conductivity)
$\hat{\mathbf{S}}(\mathbf{r})$	$\hat{\mathbf{S}}(\mathbf{r})$	spin-spin (magnetic susceptibility)

where the second equality holds for real fluctuation densities. As usual  $\eta \rightarrow 0+$ . The first term in the square brackets in eq. (2.89) is associated with absorption, as it becomes dominant if the driving frequency  $\omega$  approaches the excitation energies of the system. The second term on the other hand describes the inverse process. A generalization of eq. (2.89) to the more general case of a (grand) canonical ensemble is straightforward.

### 2.6.3 Calculation of the response function

With the formal definition of the response functions at our disposal, we can briefly discuss some typical ways of computing the response functions which have been used to obtain the results included in this thesis. We focus on the DD response function here.

**Time propagation.** Employing the definition (2.80) for the variation of the density  $\delta n(\mathbf{r}, t)$  upon excitation by a scalar potential  $\delta\varphi(\mathbf{r}, t)$  gives

$$\delta n(\mathbf{r}, t) = - \int_{-\infty}^{\infty} dt' \int d\mathbf{r}' \chi^{\text{R}}(\mathbf{r}, \mathbf{r}'; t - t') \delta\varphi(\mathbf{r}', t'). \quad (2.90)$$

On the other hand,  $\delta n(\mathbf{r}, t)$  can be computed by some other suitable method which allows to predict the real-time evolution. Besides solving the KBEs for the one-body GF and thus the time-dependent density, TDDFT offers a practical way by solving the time-dependent KS equations (2.46). It is particularly useful to choose the perturbation as  $\delta\varphi(\mathbf{r}, t) = \delta\varphi(\mathbf{r})\delta(t)$  – all frequencies are contained in this excitation. Fourier transforming the density variation, one obtains

$$\delta n(\mathbf{r}, \omega) = - \int d\mathbf{r}' \chi^{\text{R}}(\mathbf{r}, \mathbf{r}'; \omega) \delta\varphi(\mathbf{r}'). \quad (2.91)$$

Hence, the complete frequency dependence of the DD response function can be extracted by a single time propagation [109]. The accuracy of the so computed response properties depends on the level of approximation for the self-energy (in case the KBEs are solved) or the xc-functional (for TDDFT).

Accessing the non-local spatial information encoded in  $\chi^{\text{R}}(\mathbf{r}, \mathbf{r}'; \omega)$  turns out to be more intricate. A possible approach is to insert the Lehmann representation (2.89) and choose suitable perturbation potentials  $\delta\varphi(\mathbf{r})$ , such that conclusions on the fluctuation densities  $\rho_{\lambda}(\mathbf{r})$  can be drawn. This method is utilized in [E4] to characterize the response function of a complex many-body system.

**Time-dependent density-functional theory in frequency space.** An alternative formulation avoiding the explicit time propagation is the Casida method [110], which is based on the frequency-space formulation of TDDFT. The DD response function can be shown to obey the Dyson equation

$$\chi^{\text{R}}(\mathbf{r}, \mathbf{r}'; \omega) = \chi_0^{\text{R}}(\mathbf{r}, \mathbf{r}'; \omega) + \int d\mathbf{r}_1 \int d\mathbf{r}_2 \chi_0^{\text{R}}(\mathbf{r}, \mathbf{r}_1; \omega) K_{\text{xc}}(\mathbf{r}_1, \mathbf{r}_2, \omega) \chi^{\text{R}}(\mathbf{r}_2, \mathbf{r}'; \omega). \quad (2.92)$$

Here,  $\chi_0^{\text{R}}(\mathbf{r}, \mathbf{r}'; \omega)$  denotes the response function of the non-interacting fictitious KS system defined by

$$\chi_0^{\text{R}}(\mathbf{r}, \mathbf{r}'; \omega) = \sum_{i \in \text{occ}} \sum_{p \in \text{virt}} \left[ \frac{\rho_{ip}(\mathbf{r}) \rho_{ip}^*(\mathbf{r}')}{\omega - \Omega_{ip} + i\eta} - \frac{\rho_{ip}(\mathbf{r}') \rho_{ip}^*(\mathbf{r})}{\omega + \Omega_{ip} + i\eta} \right], \quad \Omega_{ip} = \epsilon_p - \epsilon_i, \quad (2.93)$$

with the fluctuation densities  $\rho_{ip}(\mathbf{r}) = \phi_i^*(\mathbf{r})\phi_p(\mathbf{r})$ .  $K_{xc}$  is defined by  $K_{xc}(\mathbf{r}, \mathbf{r}'; \omega) = v(\mathbf{r} - \mathbf{r}') + f_{xc}(\mathbf{r}, \mathbf{r}'; \omega)$ , where  $f_{xc}$  stands for the xc-kernel obtained by the second functional derivative of the xc-functional with respect to the density. Inserting adiabatic functionals, the frequency dependence disappears; employing functionals which depend on the density only (not its gradients) like the LDA, the xc-kernel becomes local in space. Ignoring the xc-kernel corresponds to the RPA. Instead of the expressing the density variation caused by an external potential in terms of the full response function as in eq. (2.90), one can introduce the modified (screened) potential

$$\tilde{V}(\mathbf{r}, \omega) = \delta\varphi(\mathbf{r}, \omega) + \int d\mathbf{r}' K_{xc}(\mathbf{r}, \mathbf{r}'; \omega)\delta n(\mathbf{r}', \omega). \quad (2.94)$$

The induced density variation is then given by the non-interacting response function:

$$\delta n(\mathbf{r}, \omega) = \int d\mathbf{r}' \chi_0^R(\mathbf{r}, \mathbf{r}'; \omega)\tilde{V}(\mathbf{r}', \omega). \quad (2.95)$$

Inserting eq. (2.94) into eq. (2.95) yields a self-consistent equation for  $\delta n(\mathbf{r}, \omega)$ . For the eigenmodes of the system  $\omega = \Omega_\lambda$  (i. e. the poles of the exact DD response function), the external potential can be neglected due to the singular behavior. Expanding the density variation in particle-hole (occupied-unoccupied) pairs,

$$\delta n(\mathbf{r}, \Omega_\lambda) = \sum_\sigma \sum_{i \in \text{occ}} \sum_{p \in \text{virt}} A_{ip\sigma}^\lambda \psi_{i\sigma}^{\text{KS}}(\mathbf{r}) \psi_{p\sigma}^{\text{KS}}(\mathbf{r}),$$

yields the effective eigenvalue equation

$$\mathbf{R}\mathbf{F}^\lambda = \Omega_\lambda^2 \mathbf{F}^\lambda, \quad (2.96)$$

where the components  $(ip\sigma)$  are compressed in vector notation. The excitation matrix  $\mathbf{R}$  is comprised of the KS eigenvalues and the two-body matrix elements of the kernel  $K_{xc}(\mathbf{r}, \mathbf{r}'; \Omega_\lambda)$ . The Casida excitation amplitudes  $A_{ip\sigma}^\lambda$  are obtained by the eigenvectors  $\mathbf{F}^\lambda$  by linear transformation and allow for constructing approximate many-body states by

$$|\Psi_\lambda\rangle = \sum_\sigma \sum_{i \in \text{occ}} \sum_{p \in \text{virt}} A_{ip\sigma}^\lambda \hat{c}_{p\sigma}^\dagger \hat{c}_{i\sigma} |\Psi_0\rangle, \quad (2.97)$$

where  $|\Psi_0\rangle$  stands for the Slater determinant of the ground-state KS orbitals. Similarly to the quantum chemistry methods, the number of virtual orbitals to be included is a crucial factor. Restricting the virtual states subspace limits the energy range where reliable predictions of the response properties can be expected. We employ the Casida method in [E6].

**Semi-classical approximation.** The semi-classical approximation (SCA) allows for a significant simplification of calculation of the DD response function within the RPA in the limit of high-frequency driving. As the basic ingredient to the Dyson equation (2.92), we again consider the reference DD response function (2.93). Assuming  $\omega \gg \Omega_{ip}$  simplifies the denominators in eq. (2.93) by the high-frequency approximation  $1/(\omega - \Omega_{ip} + i\eta) \approx (1 - \Omega_{ip}/\omega)/\omega$ . Importantly, the non-interaction DD response function so becomes a functional of the ground-state density  $n_0(\mathbf{r})$  only. In particular, for any function  $f(\mathbf{r})$  one finds [111]

$$\int d\mathbf{r}' \chi_0^R(\mathbf{r}, \mathbf{r}'; \omega) f(\mathbf{r}') = \frac{1}{\omega^2} [\nabla n_0(\mathbf{r}) \cdot \nabla f(\mathbf{r}) - n_0(\mathbf{r}) \nabla^2 f(\mathbf{r})]. \quad (2.98)$$

Using eq. (2.98), it is straightforward to obtain a simple integral equation for the density fluctuation  $\delta n(\mathbf{r}, \omega) = \int d\mathbf{r}' \chi^R(\mathbf{r}, \mathbf{r}'; \omega) \delta\varphi(\mathbf{r}', \omega)$  induced by the external driving field  $\delta\varphi(\mathbf{r}', \omega)$ . After a short derivation one finds

$$(\omega^2 - \omega_p(\mathbf{r})^2) \delta n(\mathbf{r}, \omega) + \nabla n_0(\mathbf{r}) \cdot \Phi(\mathbf{r}, \omega) = \nabla n_0(\mathbf{r}) \cdot \nabla \delta\varphi(\mathbf{r}, \omega) - n_0(\mathbf{r}) \nabla^2 \delta\varphi(\mathbf{r}, \omega), \quad (2.99)$$

where  $\omega_p(\mathbf{r}) = (4\pi n_0(\mathbf{r}))^{1/2}$  denotes the local plasmon frequency and  $\Phi(\mathbf{r}, \omega) = \int d\mathbf{r}' v(\mathbf{r} - \mathbf{r}') \delta n(\mathbf{r}', \omega)$  is the self-induced electrostatic potential. Equivalently, the integral equation (2.99) can also be derived from purely classical considerations by coupling the hydrodynamical Euler equation to the self-induced potential generated by the density fluctuations [112]. Our work [E4] compares the predictions of the SCA and the full quantum (TDDFT) treatment of the DD response function for complex molecular system.



## Insight from spectroscopic techniques

This chapter is organized in the following way: first (sec. 3.1) we introduce the relevant quantities for photoabsorption spectroscopy and discuss the most important excitation mechanisms due to the interaction with the photons provided by the probing electromagnetic radiation. The special case of the liberation of electrons from a sample as one important manifestation of photo-induced excitations – the photoemission – is given room in sec. 3.2. We introduce the concepts of standard single-electron photoemission and explain the intricacies of the non-sequential emission of an electron pair, a process that is particularly sensitive to the correlations in the system. As an important example of (transient) nonlinear spectroscopies, the (time-resolved) two-photon photoemission is briefly explained. Finally, spectroscopies with photons or electrons (or other particles) which undergo inelastic scattering from the target are considered (sec. 3.3).

### 3.1 Photon impact

Spectroscopies and time-resolved studies using laser sources are a major tool for studying atomic, molecular and solid-state systems. The flexibility and tunability offered by the different type of light sources<sup>1</sup> allow for controlling, steering and probing quantum systems. Depending on the requirements for the intensity, pulse duration, spatial and temporal coherence, different laser sources may be employed in a complementary way. Let us have a brief look at laser sources which are relevant for the theory included in this thesis.

Ti:Sa lasers emitting infrared radiation at 800 nm wavelength are a standard tabletop source providing continuous output or femtosecond pulses. Using non-linear effects such as second-harmonic generation or frequency mixing, the wavelength can be tuned over a wide range. This laser source is used in our joint experimental-theoretical work [E6].

Using the principle of high-harmonic generation (HHG) [113], extreme ultraviolet (XUV) or soft X-ray pulse trains can be produced. Triggering the HHG mechanism with few-cycle pulses allows for the generation of isolated, ultrafast XUV pulses [1]. Using suitable energy filters, HHG represents the state-of-the-art method to generate short XUV pulse with a pulse duration as short as 67 attoseconds [114]. Such short pulses are required for the attosecond time resolution as provided by the streaking technique, a standard approach to time-resolved photoemission [115]. Among the many applications, attosecond streaking allows for tracing time-dependent build-up of screening in metals [116] which is addressed by [E7].

Tunable electromagnetic radiation (UV, XUV, soft and hard X-rays) is delivered by synchrotron beamlines [117]. The basic principle relies on accelerating electrons to relativistic velocities and injecting them into a storage ring, where the electrons move in circular orbits. By passing the electrons through strong magnetic fields and thus forcing a rapid change of the direction of motion results in the emission of (high-energy) photons. The femtosecond time scale can be reached, as well, using the slicing technique [118]. The experiments in [E5] have been conducted using the synchrotron beamline Elettra [119].

#### 3.1.1 Photoabsorption cross-section

We now assume a general molecule, described by the TISE (2.1), is exposed to high-energy, but low-intensity, electromagnetic radiation. For the sake of a clear presentation, we assume the laser to act on

<sup>1</sup>We use the term light source even though the energy of the photons is typically in ultraviolet or X-ray regime.

the electrons only<sup>2</sup>. Furthermore, the molecule is described in BO approximation (see subsec. 2.3.1). In compact bra-ket notation, the ground state of the system is

$$\hat{H}_0|\Theta_0\rangle \equiv \hat{H}_0(|\Psi_0\rangle \otimes |\chi_0^{(0)}\rangle) = \mathcal{E}_0(|\Psi_0\rangle \otimes |\chi_0^{(0)}\rangle), \quad (3.1)$$

where the total energy is given by both the PES, reflecting the electronic contribution, and the energy of the nuclei:  $\mathcal{E}_0 = \langle \chi_0^{(0)} | \hat{T}_c + E_0(\{\mathbf{R}\}) | \chi_0^{(0)} \rangle$ . Similarly to the ground state (3.1), excited states of the whole system are denoted by  $|\Theta_{\alpha,\mu}\rangle = |\Psi_\alpha\rangle \otimes |\chi_\mu^{(\alpha)}\rangle$  with eigenenergy  $\mathcal{E}_{\alpha,\mu}$ . In order to compute the response of the molecule to continuous electromagnetic radiation with frequency  $\omega$ , described by the perturbation operator

$$\hat{V}_{e,\text{ext}}(t) = \hat{V}_0 e^{-i\omega t} e^{-\eta t} + \text{h. c.}, \quad (3.2)$$

where  $\eta \rightarrow 0+$ , one can employ the method of adiabatic switching. Since for  $t \rightarrow -\infty$  the initial state  $|\Theta_0\rangle$  is an eigenstate of the Hamiltonian, letting the state evolve adiabatically up to  $t = 0$  transforms it to a fully-interacting state  $|\tilde{\Theta}\rangle$  by virtue of the Gell-Mann and Low theorem [120]. Resorting to first-order time-dependent perturbation theory (TDPT), one obtains

$$|\tilde{\Theta}\rangle = |\Theta_0\rangle + \frac{1}{\omega + \mathcal{E}_0 - \hat{H}_0 + i\eta} \hat{V}_0 |\Theta_0\rangle. \quad (3.3)$$

Using eq. (3.3) the transition probability to access the excited eigenstates  $|\Theta_{\beta,\nu}\rangle$  follows as

$$P_{\beta,\nu}(\omega) = \left| \langle \Theta_{\beta,\nu} | \tilde{\Theta} \rangle \right|^2 = \frac{1}{(\omega + \mathcal{E}_0 - \mathcal{E}_{\beta,\nu}) + \eta^2} \left| \langle \Theta_{\beta,\nu} | \hat{V}_0 | \Theta_0 \rangle \right|^2. \quad (3.4)$$

Normalizing to the effective interaction time  $(2\eta)^{-1}$ , the transition rate  $p_{\beta,\nu} = 2\eta P_{\beta,\nu}$  yields, taking the limit  $\eta \rightarrow 0$ , the Fermi Golden rule

$$p_{\beta,\nu}(\omega) = 2\pi \left| \langle \Theta_{\beta,\nu} | \hat{V}_0 | \Theta_0 \rangle \right|^2 \delta(\omega + \mathcal{E}_0 - \mathcal{E}_{\beta,\nu}). \quad (3.5)$$

The matrix element in eq. (3.5) is conveniently split into

$$\langle \Theta_{\beta,\nu} | \hat{V}_0 | \Theta_0 \rangle = \langle \chi_\nu^{(\beta)} | \chi_0^{(0)} \rangle \langle \Psi_\beta | \hat{V}_0 | \Psi_0 \rangle \equiv C_{\nu,0}^{(\beta,0)} M_{\beta,0}. \quad (3.6)$$

The overlap of the nuclear wave-functions  $C_{\nu,\mu}^{(\beta,\alpha)}$  is known as Franck-Condon factor [121]. The electric matrix elements  $M_{\beta,\alpha}$  contain all the symmetry properties which the respective states possess and thus might result in selection rules. Assuming the dipole approximation to be applicable, that is

$$\hat{V}_0^{\text{VG}} = -i\mathbf{A}_0 \cdot \sum_{i=1}^{N_e} \nabla_{\mathbf{r}_i} \equiv \mathbf{A}_0 \cdot \hat{\mathbf{D}}^{\text{VG}}, \quad \hat{V}_0^{\text{LG}} = \mathbf{E}_0 \cdot \sum_{i=1}^{N_e} \mathbf{r}_i \equiv \mathbf{E}_0 \cdot \hat{\mathbf{D}}^{\text{LG}}, \quad (3.7)$$

a straightforward classification of dipole-allowed transitions is possible by the corresponding symmetry analysis [122].

A universal quantity to characterize the photoabsorption probability, which is independent of a concrete experimental setup, is given by the concept of the total or differential (i. e., resolved with respect to final state quantum numbers) cross-section. The photoabsorption cross-section is obtained from the transition rates (3.5) by normalizing to the flux of the incoming photons  $F = I/\omega$ , with  $I = E_0^2/(8\pi\alpha_0) = \omega^2 A_0^2/(8\pi\alpha_0)$  denoting the intensity:

$$\begin{aligned} \sigma(\omega) &= \frac{1}{4F} \sum_{\beta,\nu} p_{\beta,\nu}(\omega) = \frac{4\pi^2\alpha_0}{\omega} \sum_{\beta,\nu} \left| C_{\nu,0}^{(\beta,0)} \right|^2 \left| \langle \Psi_\beta | \mathbf{u} \cdot \hat{\mathbf{D}}^{\text{VG}} | \Psi_0 \rangle \right|^2 \delta(\omega + \mathcal{E}_0 - \mathcal{E}_{\beta,\nu}) \\ &= 4\pi^2\alpha_0\omega \sum_{\beta,\nu} \left| C_{\nu,0}^{(\beta,0)} \right|^2 \left| \langle \Psi_\beta | \mathbf{u} \cdot \hat{\mathbf{D}}^{\text{LG}} | \Psi_0 \rangle \right|^2 \delta(\omega + \mathcal{E}_0 - \mathcal{E}_{\beta,\nu}). \end{aligned} \quad (3.8)$$

<sup>2</sup>For sufficiently high photon energy, resonant transitions between vibrational states can be excluded by energy conservation.

Here,  $\mathbf{u} = \mathbf{A}_0/|\mathbf{A}_0| = -\mathbf{E}_0/|\mathbf{E}_0|$  is the polarization vector. The prefactor 1/4 is convention. In many cases, the photoionization process is much faster than the characteristic time scale for transitions between nuclear wave-functions on the different PESs. This gives rise to the frozen-core approximation which amounts to neglecting the nuclear degrees of freedom. The cross-section so attains the form

$$\begin{aligned}\sigma(\omega) &= \frac{4\pi^2\alpha_0}{\omega} \sum_{\beta} \left| \langle \Psi_{\beta} | \mathbf{u} \cdot \hat{\mathbf{D}}^{\text{VG}} | \Psi_0 \rangle \right|^2 \delta(\omega + E_0 - E_{\beta}) \\ &= 4\pi^2\alpha_0\omega \sum_{\beta} \left| \langle \Psi_{\beta} | \mathbf{u} \cdot \hat{\mathbf{D}}^{\text{LG}} | \Psi_0 \rangle \right|^2 \delta(\omega + E_0 - E_{\beta}).\end{aligned}\quad (3.9)$$

The absorption cross-section (3.9) should have a close relation to the response functions defined in sec. 2.6, since the first-order TDPT is equivalent to linear response. The correspondence is easily seen by expressing the cross-section in terms of the dynamical structure factor (2.83):

$$\sigma(\omega) = \frac{\pi}{2F} S_{V_0 V_0^\dagger}(\omega) = \frac{4\pi^2\alpha_0}{\omega} S_{D^{\text{VG}}(D^{\text{VG}})^\dagger}(\omega) = 4\pi^2\alpha_0\omega S_{D^{\text{LG}}(D^{\text{LG}})^\dagger}(\omega), \quad (3.10)$$

where  $\hat{D}^{\text{VG/LG}} = \mathbf{u} \cdot \hat{\mathbf{D}}^{\text{VG/LG}}$ . Under the same conditions that are required for the FDT (2.84) (see subsec. 2.6.1), expressing the cross-section in terms of the DD (LG) or the current-current (VG) response function is thus straightforward. For the LG one finds

$$\sigma(\omega) = -2\pi\alpha_0\omega \int d\mathbf{r} \int d\mathbf{r}' (\mathbf{u} \cdot \mathbf{r}) \text{Im}[\chi^{\text{R}}(\mathbf{r}, \mathbf{r}'; \omega)] (\mathbf{u} \cdot \mathbf{r}'), \quad \omega > 0. \quad (3.11)$$

Experimentally, the total photoabsorption cross-section is determined by measuring the flux of transmitted photons normalized to the input flux [123].

### 3.1.2 Photoexcitation processes

As inferred from the Fermi Golden rule (3.9) or the Lehmann representation of the DD response function (eq. (2.89)), a *complete* set of many-body excited states needs to be included to describe the absorption of the incoming photons. In other words, any photoexcitation of the system contributes to optical absorption. Employing the classification of the many-body states according to their geometric character (see subsec. 2.4.1) allows the categorization of the excitation channels according to the charge of the system after absorbing a photon. Expanding the absorption part ( $\omega > 0$ ) of the DD response function in this way yields

$$\begin{aligned}\chi^{\text{R}}(\mathbf{r}, \mathbf{r}'; \omega) &= \sum_{\alpha \in \mathcal{B}_{N_e}} \frac{\rho_{\alpha}(\mathbf{r})\rho_{\alpha}^*(\mathbf{r}')}{\omega - \Omega_{\alpha} + i\eta} + \sum_{\alpha \in \mathcal{B}_{N_e-1}} \int d\mathbf{k} \frac{\rho_{\alpha\mathbf{k}}^{(-)}(\mathbf{r})(\rho_{\alpha\mathbf{k}}^{(-)}(\mathbf{r}'))^*}{\omega - \epsilon_{\mathbf{k}} - \Omega_{\alpha}^+ + i\eta} \\ &+ \sum_{\alpha \in \mathcal{B}_{N_e-2}} \int d\mathbf{k}_1 \int d\mathbf{k}_2 \frac{\rho_{\alpha\mathbf{k}_1\mathbf{k}_2}^{(-)}(\mathbf{r})(\rho_{\alpha\mathbf{k}_1\mathbf{k}_2}^{(-)}(\mathbf{r}'))^*}{\omega - \epsilon_{\mathbf{k}_1} - \epsilon_{\mathbf{k}_2} - \Omega_{\alpha}^{2+} + i\eta} + \dots\end{aligned}\quad (3.12)$$

Here, the super- and subscripts of the fluctuation densities match the corresponding many-body excited states in subsec. 2.4.1, while  $\Omega_{\alpha} = E_{\alpha} - E_0$  are the neutral electronic excitation energies,  $\Omega_{\alpha}^+ = E_{\alpha}^+ - E_0$  the electron removal energies,  $\Omega_{\alpha}^{2+} = E_{\alpha}^{2+} - E_0$  the two-electron removal energies and so on. Let us now discuss the typical processes contributing to each of the individual terms in the general expansion of the DD response function (3.12).

**Single-particle excitations.** In finite systems, typical charge-conserving excitations include the transition from occupied valence states to virtual orbitals (see fig. 3.1(a) for an illustration). The electronic subsystem absorbs photons with energy  $\omega$  larger than the gap between the HOMO and lowest unoccupied molecular orbital (LUMO), unless electron-vibron interaction plays an important role<sup>3</sup>. Increasing the photon energy might drive the transition of core electrons to unoccupied valence states.

<sup>3</sup>Electronic transitions may be vibrationally-assisted, i.e. the energy is partly taken from the vibrons, lowering the threshold for photoabsorption.

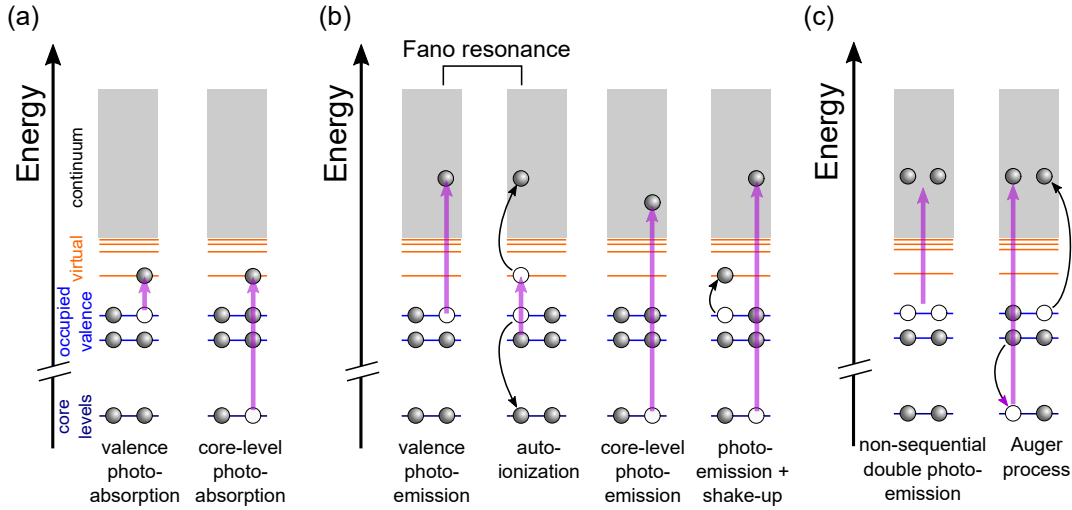


Figure 3.1: Photoexcitation processes of finite systems: (a) neutral excitations, (b) excitations involving the emission of single electrons, and (c) excitations resulting in the emission of two electrons.

For  $\omega > \omega_{\text{IP}}$ , the liberation of a single electron – called photoemission or photoionization<sup>4</sup> – can occur (sketched in fig. 3.1(b)). For weakly-interacting systems the most dominant channels will be the direct ionization of valence states, or, provided the photon energy is sufficiently large, ionization of the core levels. For interacting systems, this simple SP picture of photoemission, often referred to as single-active electron approximation, needs to be extended to include many-body effects. A typical process in this context is autoionization. Suppose the Coulomb interaction is scaled down  $v \rightarrow \epsilon v(\mathbf{r})$ . In many cases there are bound excited states  $|\tilde{\Psi}_{\alpha'}\rangle$  for this hypothetical system ( $\epsilon < 1$ ) above the ionization threshold of the actual system ( $\epsilon = 1$ ). This results in the virtual excitation of  $|\tilde{\Psi}_{\alpha'}\rangle$  during the photoabsorption process; however, as they are not an eigenstate of the real system, a coupling to the continuum occurs due to  $\langle \tilde{\Psi}_{\alpha'} | \Psi_{\alpha, \mathbf{k}}^{(-)} \rangle \neq 0$ . Hence, a photoelectron is released. Since at a given photon energy this process might compete with direct ionization from the valence states, the resulting quantum pathway interference gives rise to so-called Fano resonances [124]. Other many-body effects include the reorganization of the valence shell upon removing a core electron (shake-up mechanism). A few more details on experimental techniques and the theoretical description of single photoemission (SPE) is provided in subsec. 3.2.1.

If the photon energy exceeds the double ionization threshold, the emission of two electrons as a result of the sample absorbing one photon is possible, even though the probability as compared to SPE is reduced considerably. Generally, the double photoemission (DPE) can be separated into non-sequential events, where two electrons are liberated almost at once (via electron-electron scattering, for instance), and the Auger process. The latter can be regarded as a shake-up process, where the excess energy is converted into the emission of a second electron. As compared to DPE, the Auger process is a sequential double ionization event.

**Collective excitations.** The physical picture outlined so far and summarized in fig. 3.1 applies for the photoexcitation of small systems (atoms or molecules), where the SP picture still is a useful concept. With growing system size, however, more degrees of freedom for many-body excitations emerge. In particular, the collective, self-sustained charge density oscillations in nearly-free electron systems (called plasmons) should be mentioned in this context. For the homogeneous electron gas, plasmons are elementary excitations occurring at short wavelength. Their energy, the plasmon frequency, is given by  $\omega_{\text{pl}} = (4\pi n)^{1/2}$  with  $n$  denoting the electron density<sup>5</sup> They interact with  $p$ - $h$  pairs and decay if allowed by momentum and energy conservation (Landau damping). In many cases, plasmons dominate the excitation channels and

<sup>4</sup>The term photoionization is typically used for atoms or molecules and expresses that the system is left in an ionized state (which can be evidenced by detecting the ions). The term photoemission, on the other hand, emphasizes on the photoelectrons is hence more used for condensed matter.

<sup>5</sup>The dependence of the plasmon frequency on the wave vector  $\mathbf{q}$  has the form  $\omega(\mathbf{q}) = \omega_{\text{pl}}(1 + Aq^2)$  for small  $q$ .

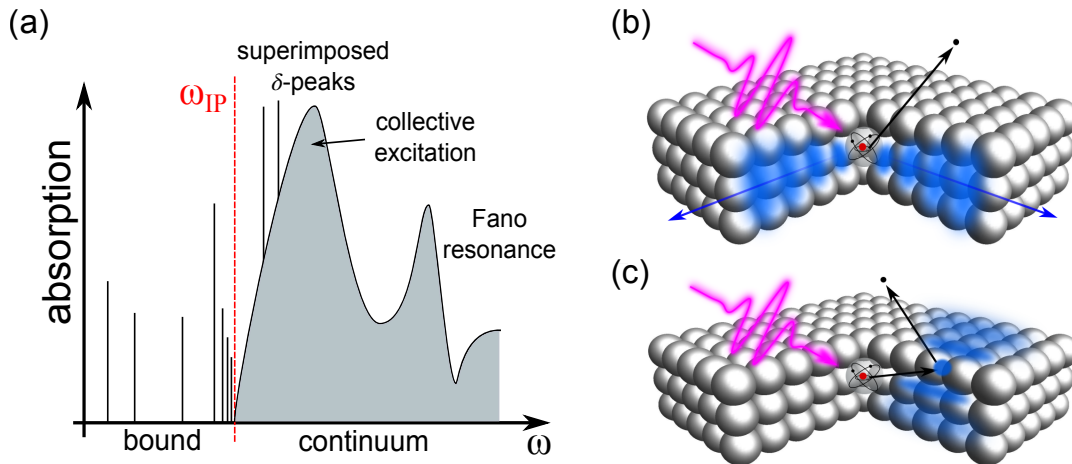


Figure 3.2: (a) Generic behavior of the total absorption of a many-body system.  $\omega_{IP}$  marks the ionization potential. (b) Illustration of intrinsic losses in extended systems: a hole created by ultrafast photoemission is screened by  $p$ -hor collective excitations in surrounding electron density. (c) Illustration of extrinsic losses: the photoelectron scatters inelastically upon inducing electronic excitations.

thus the DD response function. Due to eq. (2.61), the dynamical screening of the Coulomb interaction and external electric fields then driven via plasmon excitation<sup>6</sup>. Many-body excitations with a strongly collective character may exist in larger molecular systems or clusters, as well. In fact, the field of engineering nanostructures with strong plasmonic response has experienced a surge of research [125–128].

In an optical absorption spectrum, plasmons are manifest by strong peaks with a finite width, reflecting their finite lifetime due to the Landau damping mechanism. Fig. 3.2(a) sketches a generic absorption spectrum including all the features discussed so far: below  $\omega_{IP}$ , only discrete excitations (represented by  $\delta$ -peaks) are possible, albeit they get infinitely close due to the Rydberg series existing in any Coulombic system. After crossing the IP, the absorption spectrum becomes continuous and may include plasmon peaks<sup>7</sup> or Fano resonances.

The interplay of the excitation of plasmons and the emission of electrons adds a new dimension of complexity to the photoemission process and is the focus of [E3], [E7] and [E5], where these processes are discussed in detail. For illustration purposes, let us consider the emission from a core level. The positive charge of the hole may excite plasmons – hence, the emission process and the collective degrees of freedom are strongly coupled. If the photon energy  $\omega$  is partly converted into a plasmon upon removing the electron, the energy of the photoelectron will be reduced as compared to direct emission from the core level [101] – this process constitutes *intrinsic* losses<sup>8</sup>, which are illustrated in fig. 3.2(b). A competing process is the direct emission from the core level, where the photoelectron undergoes scattering within the sample and loses a part of its energy upon creating a plasmon [101]. This is the mechanism for *extrinsic* losses (see sketch in fig. 3.2(c)). Both channels may lead to the same final state, resulting in quantum pathway interference [90]. In principle, intrinsic and extrinsic losses can occur in any system where inelastic scattering channels are present. A typical example, besides plasmon losses, is the electron-vibron or electron-phonon interaction beyond the BO approximation [129]. For relatively weak electron-phonon interaction, the EB Hamiltonian eq. (2.74) is a suitable starting point to incorporate such effects.

## 3.2 Photoemission

Measuring the absorption cross-section delivers a wealth of information, as all the various photoexcitation channels discussed subsec. 3.1.2 may contribute. Consequently, discerning some of the individual processes

<sup>6</sup>For most metals, the plasmon frequency is in the range of visible light. Therefore, the electric field of visible light is most effectively screened, resulting in a strong reflectivity.

<sup>7</sup>Bound states may also cluster and thus form a collective excitation (which is still comprised by discrete peaks).

<sup>8</sup>In some sense, intrinsic losses can be seen as shake-up process where the internal excitation possesses collective character.

can be a substantial task. It is thus desirable to resolve the cross-section with respect to selected final channels. In this section, we focus on the emission of electrons, in particular on SPE and DPE. We point out how the theories presented in chapter 2 can be employed to compute photoemission spectra and explain the connection to typical experimental setups.

### 3.2.1 Photoelectron spectroscopy

Let us assume the final state of a system (we focus on the electronic degrees of freedom here) after absorbing a photon is of the type  $|\Psi_{\alpha,\mathbf{k}}^{(-)}\rangle$ ,  $\alpha \in \mathcal{B}_{N_e-1}$ , i. e. exactly one electron is emitted. The projection into this SPE subspace is achieved experimentally by detecting the energy of the photoelectron  $\varepsilon_{\mathbf{k}}$  and its direction  $\hat{\mathbf{k}}$  – the wave-vector  $\mathbf{k}$  is thus completely determined. Analogous to subsec. 3.1.1, resolving the final-state channels with respect to  $\mathbf{k}$  leads to the definition of the *differential* cross-section (DCS):

$$\frac{d\sigma}{d\mathbf{k}} = 4\pi^2\alpha_0\omega \sum_{\alpha} \left| M_{\alpha,0}^{\text{LG}}(\mathbf{k}) \right|^2 \delta(\omega - \Omega_{\alpha}^{+} - \varepsilon_{\mathbf{k}}) = \frac{4\pi^2\alpha_0}{\omega} \sum_{\alpha} \left| M_{\alpha,0}^{\text{VG}}(\mathbf{k}) \right|^2 \delta(\omega - \Omega_{\alpha}^{+} - \varepsilon_{\mathbf{k}}), \quad (3.13)$$

where we have abbreviated the matrix elements in length (LG) and velocity (VG) gauge, respectively:

$$M_{\alpha,0}^{\text{LG}}(\mathbf{k}) = \langle \Psi_{\alpha,\mathbf{k}}^{(-)} | \mathbf{u} \cdot \hat{\mathbf{D}}^{\text{LG}} | \Psi_0 \rangle, \quad M_{\alpha,0}^{\text{VG}}(\mathbf{k}) = \langle \Psi_{\alpha,\mathbf{k}}^{(-)} | \mathbf{u} \cdot \hat{\mathbf{D}}^{\text{VG}} | \Psi_0 \rangle. \quad (3.14)$$

An equivalent picture is obtained by measuring the number of photoelectrons  $\hat{N}_{\mathbf{k}} = \sum_{\sigma} \hat{c}_{\mathbf{k}\sigma}^{\dagger} \hat{c}_{\mathbf{k}\sigma}$  in the perturbed state. Applying again the first-order TDPT as in subsec. 3.1.1, the initial state  $|\Psi_0\rangle$  transforms by the adiabatic switching into  $|\tilde{\Psi}\rangle = |\Psi_0\rangle + |\delta\Psi_{\eta}\rangle$  with  $[\omega + E_0 - \hat{H}_e + i\eta]|\delta\Psi_{\eta}\rangle = \hat{V}_0|\Psi_0\rangle$ . In [E2] this inhomogeneous TISE is solved directly for the one-electron case. An intuitive observable to characterize the photoemission is given by the photocurrent  $\mathbf{J}_{\mathbf{k}} = 2\eta\langle\delta\Psi_{\eta}|\hat{N}_{\mathbf{k}}|\delta\Psi_{\eta}\rangle$  with  $\eta \rightarrow 0+$ . Inserting the completeness relation in the  $(N_e - 1)$ -electron Hilbert space, the photocurrent is transformed into

$$\begin{aligned} \mathbf{J}_{\mathbf{k}} &= 2\eta \sum_{\sigma} \langle \Psi_0 | \hat{V}_0^{\dagger} \frac{1}{\omega + E_0 - \hat{H}_e - i\eta} \hat{c}_{\mathbf{k}\sigma}^{\dagger} \hat{c}_{\mathbf{k}\sigma} \frac{1}{\omega + E_0 - \hat{H}_e + i\eta} \hat{V}_0 | \Psi_0 \rangle \\ &= 2\eta \sum_{\sigma} \sum_{\alpha} \left| \langle \Psi_{\alpha}^{+} | \hat{c}_{\mathbf{k}\sigma} \frac{1}{\omega + E_0 - \hat{H}_e + i\eta} \hat{V}_0 | \Psi_0 \rangle \right|^2 \end{aligned}$$

The correspondence to eigenstates  $|\Psi_{\alpha,\mathbf{k}}^{(-)}\rangle$  is found from the Møller operator (cf. eq. (2.37)):

$$|\Psi_{\alpha,\mathbf{k}}^{(-)}\rangle = \hat{\Omega}^{(-)} \hat{c}_{\mathbf{k}\sigma}^{\dagger} |\Psi_{\alpha}^{+}\rangle = \eta \int_0^{\infty} dt e^{-\eta t} e^{i\hat{H}_e t} e^{-i(\varepsilon_{\mathbf{k}} + E_{\alpha}^{+})t} \hat{c}_{\mathbf{k}\sigma}^{\dagger} |\Psi_{\alpha}^{+}\rangle = \frac{-i\eta}{\varepsilon_{\mathbf{k}} + E_{\alpha}^{+} - \hat{H}_e + i\eta} \hat{c}_{\mathbf{k}\sigma}^{\dagger} |\Psi_{\alpha}^{+}\rangle, \eta \rightarrow 0+.$$

With the energy balance  $\omega + E_0 = \varepsilon_{\mathbf{k}} + E_{\alpha}^{+}$  it is thus straightforward to see  $\mathbf{J}_{\mathbf{k}} = 4F d\sigma/d\mathbf{k}$ . Besides  $\alpha \in \mathcal{B}_{N_e-1}$ , the sum over the many-body states also includes further continuum electrons, i. e. multiple ionization is not excluded (a typical example is the Auger effect, see subsec. 3.2.2). For explicitly studying SPE, the projection into the subspace  $\mathcal{B}_{N_e-1}$  has to be performed (see appendix A), as discussed in [E3].

Inspecting the mathematical structure of eq. (3.13) along with eq. (3.14), one realizes a significant difference to the total cross-section (3.11) – the latter can be written in response formulation, i. e. by the symmetric contraction of a single object with appropriate matrix element (also called closed-loop formulation). At variance, the SPE DCS (3.13) is asymmetric and can not be expressed by the DD response function – a response formulation of SPE turned out to be a lot more involved. First approaches to SPE from extended systems were based on empirical theories: according to Berglund and Spicer [130], photoemission can be regarded as a three-stage process: (i) photoexcitation, (ii) transport to the surface (the electron might undergo inelastic scattering hereby), and (iii) the transformation into a scattering state at the surface. For SPE from atoms or molecules the intricacies arising due to the (possibly inelastic) propagation of a quasi-free electron to the surface do not play a role; step (ii) and (iii) coalesce into the notion of the (exact) scattering wavefunction. For few-body systems, wave-functions of the type of  $|\Psi_{\alpha,\mathbf{k}}^{(-)}\rangle$  can be approximated using methods from quantum chemistry [131–133] or specialized methods like the R-matrix approach [131, 134, 135]. A more general approach is provided by the perturbative expansion of the dipole matrix elements (3.14) in

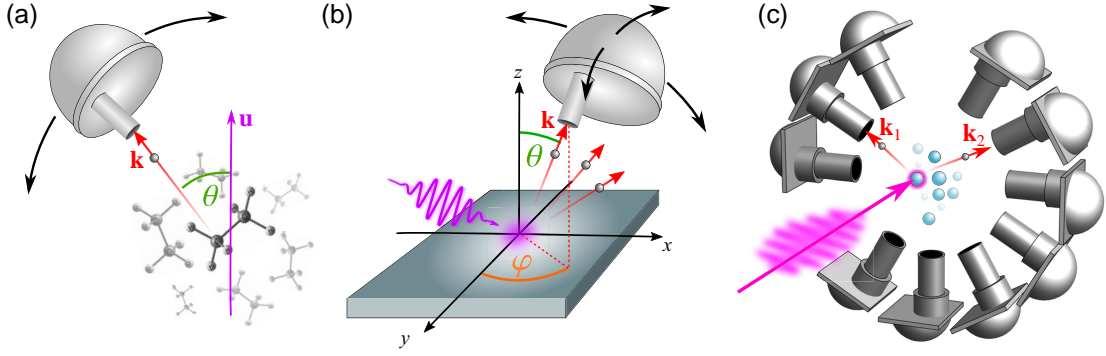


Figure 3.3: (a) Illustration of angle-resolved photoemission from a gas-phase target. The direction of the photoelectron  $\hat{\mathbf{k}}$  is measured against the polarization direction  $\mathbf{u}$ . (b) Schematic of photoemission from a surface of a solid, where the crystallographic directions usually serve as reference for the angular distribution. (c) Example setup for an electron-electron multi-coincidence spectrometer with two turntables with three and seven hemispherical analyzers, respectively (schematic according to ref. [139]).

terms of Coulombic scattering processes [136]. Choosing the diagrammatic representation, the parallels to the MBPT for the polarization  $\chi(1;2)$  become clear; in particular, the specific version of the RPA is widely employed [137].

A general treatment to incorporate many-body scattering events, which is applicable for extended systems, as well, has been introduced by Caroli [129] and is discussed in detail in our work [E3]. For now we resort to the standard approximation for photoemission, the so-called sudden approximation: assuming for the Møller operator  $\hat{\Omega}^{(-)} \approx 1$ , the anti-symmetrized product  $|\Psi_{\alpha,\mathbf{k}}^{(-)}\rangle \approx |\Phi_{\alpha,\mathbf{k}}\rangle = \hat{c}_{\mathbf{k}\sigma}^{\dagger} |\Psi_{\alpha}^{+}\rangle$  (compare subsec. 2.4.1) takes over the role of the final state. One so obtains the matrix elements (3.14) in terms of the hole-Dyson orbitals (see subsec. 2.5.5):

$$M_{\alpha,0}^{\text{LG}}(\mathbf{k}) = \langle \phi_{\mathbf{k}} | \mathbf{u} \cdot \mathbf{r} | \phi_{0,\alpha}^{(h)} \rangle, \quad M_{\alpha,0}^{\text{VG}}(\mathbf{k}) = -i \langle \phi_{\mathbf{k}} | \mathbf{u} \cdot \nabla | \phi_{0,\alpha}^{(h)} \rangle, \quad (3.15)$$

where the SP scattering wave-function  $\phi_{\mathbf{k}}(\mathbf{r})$  is associated to the operator  $\hat{c}_{\mathbf{k}\sigma}^{\dagger}$ . Expressing the many-body matrix elements by the Dyson orbitals as in eq. (3.15) is an enormous simplification, since they reduce to effective one-body matrix elements. Furthermore, it provides a direct link to the lesser GF:

$$\frac{d\sigma}{d\mathbf{k}} = 4\pi^2 \alpha_0 \omega \sum_{ij} m_i^{\text{LG}}(\mathbf{k}) G_{ij}^{<}(\omega - \varepsilon_{\mathbf{k}}) m_j^{\text{LG}}(\mathbf{k})^* = \frac{4\pi^2 \alpha_0}{\omega} \sum_{ij} m_i^{\text{VG}}(\mathbf{k}) G_{ij}^{<}(\omega - \varepsilon_{\mathbf{k}}) m_j^{\text{VG}}(\mathbf{k})^*. \quad (3.16)$$

In contrast to the above, the matrix elements occurring in eq. (3.16) are defined with respect to the SP basis, i. e. the SP states  $|\phi_i\rangle$  replace the Dyson orbitals in eq. (3.15). In some sense, eq. (3.16) represents a closed-loop formula for SPE with the sudden approximation. The lesser GF can hereby be interpreted as the response function upon electron removal. Describing SPE in terms of the GF has the important conceptual and practical advantage of being compatible with the MBPT theory outlined in sec. 2.5. Hence, the correlations within the initial state can be incorporated in a systematic way. A treatment beyond the sudden approximation based on the NEGF formalism has been introduced by the diagrammatic technique by Caroli [129]; a closed-loop generalization of SPE based on the Feshbach projection algebra was presented by Almbadh [138]. Our work [E3] incorporates the different approaches and points out their deep connection.

For measuring DCS of photoionization from atoms or molecules, experiments are usually carried out in the gas phase. The greatly reduced density lowers the interaction effects and thus comes close to the ideal of spectroscopy from isolated molecules. On the other hand, the random orientation needs to be taken into account. As shown by Yang [140], the orientation-averaged DCS within the dipole approximation (not resolved with respect to the spin) amounts to

$$\frac{d\sigma}{d\mathbf{k}} = \frac{\sigma_0(\omega)}{4\pi} [1 + \beta P_2(\cos \theta)], \quad (3.17)$$

where  $\sigma_0(\omega) = \int d\hat{\mathbf{k}} d\sigma/d\mathbf{k}$  is the energy-resolved cross-section;  $P_2$  the second Legendre polynomial. The angle  $\theta$  is the polar angle corresponding to the solid angle  $\hat{\mathbf{k}}$  (see fig. 3.3(a)). It is measured with respect to the only available reference direction – the polarization  $\mathbf{u}$ . The asymmetry parameter  $-1 \leq \beta \leq 2$  characterizes the photoelectron angular distribution (PAD). Experimentally, the DCS (3.17) is determined by turning an electron detector with a small opening angle and thus scanning over all possible directions  $\theta$  (illustrated in fig. 3.3(a)), or by collecting the signal of many multiple detectors arranged in different directions. Typical electron detectors are hemispherical electrostatic analyzers or time-of-flight (TOF) spectrometers [141]. An alternative way of collecting the angular information is to map the photoelectrons on a two-dimensional plane (and measuring their energy) – this is the basic principle of velocity-map imaging (VMI) [142].

For photoemission from extended systems, in contrast to the above, the symmetry of the sample mainly determines the PAD. For solids, the Bloch theorem puts the crystal momentum  $\mathbf{k}$  in the focus as the fundamental quantum number of the Bloch states. This dependence can be extended to the Dyson orbitals, such that the GF has the generic structure  $G_{\mu\nu}(\mathbf{k}; z_1, z_2)$  ( $\mu, \nu$  are band indices or refer to lattice sites within the unit cell). Beside matrix element effects, measuring the energy and angular dependence with respect to  $\mathbf{k}$  – called angular-resolved photoemission spectroscopy (ARPES), sketched in fig. 3.3(b) – accesses the quasi-hole energies and their dispersion with respect to  $\mathbf{k}$  as constituents of the one-body GF. Hence, ARPES provides a direct experimental link to the QP band structure of the solid [143].

### 3.2.2 Double photoemission and Auger spectroscopy

DPE and the Auger effect are two types of processes that result in the liberation of two correlated electrons from the same target after it absorbed exactly one photon. This needs to be distinguished from a sequential mechanism similar to two SPE events upon the absorption of two photons. After promoting two electrons to the continuum, the final state of the many-body system is of the type  $|\Psi_{\alpha, \mathbf{k}_1 \mathbf{k}_2}^{(-)}\rangle$ . Employing the Fermi Golden rule for the emission of two electrons defines the DCS

$$\frac{d\sigma}{d\mathbf{k}_1 d\mathbf{k}_2} = 4\pi\alpha_0\omega \sum_{\alpha} \left| M_{\alpha,0}^{\text{LG}}(\mathbf{k}_1, \mathbf{k}_2) \right|^2 \delta(\omega - \Omega_{\alpha}^{2+} - \varepsilon_{\mathbf{k}_1} - \varepsilon_{\mathbf{k}_2}) \quad (3.18)$$

$$= \frac{4\pi\alpha_0}{\omega} \sum_{\alpha} \left| M_{\alpha,0}^{\text{VG}}(\mathbf{k}_1, \mathbf{k}_2) \right|^2 \delta(\omega - \Omega_{\alpha}^{2+} - \varepsilon_{\mathbf{k}_1} - \varepsilon_{\mathbf{k}_2}). \quad (3.19)$$

The matrix elements are defined, in analogy to subsec. 3.2.1, as

$$M_{\alpha,0}^{\text{LG}}(\mathbf{k}_1, \mathbf{k}_2) = \langle \Psi_{\alpha, \mathbf{k}_1 \mathbf{k}_2}^{(-)} | \mathbf{u} \cdot \hat{\mathbf{D}}^{\text{LG}} | \Psi_0 \rangle, \quad M_{\alpha,0}^{\text{VG}}(\mathbf{k}_1, \mathbf{k}_2) = \langle \Psi_{\alpha, \mathbf{k}_1 \mathbf{k}_2}^{(-)} | \mathbf{u} \cdot \hat{\mathbf{D}}^{\text{VG}} | \Psi_0 \rangle. \quad (3.20)$$

Following the analogous steps as in subsec. 3.2.1, a link between the DPE DCS (3.18) and the two-electron current

$$J_{\mathbf{k}_1 \mathbf{k}_2} = 2\eta \langle \delta\Psi_{\eta} | \hat{N}_{\mathbf{k}_1} \hat{N}_{\mathbf{k}_2} - \delta_{\mathbf{k}_1 \mathbf{k}_2} \hat{N}_{\mathbf{k}_1} | \delta\Psi_{\eta} \rangle, \quad \eta \rightarrow 0+ \quad (3.21)$$

can be established by  $J_{\mathbf{k}_1 \mathbf{k}_2} = 4F d\sigma/d\mathbf{k}_1 d\mathbf{k}_2$ . The operator  $\hat{N}_{\mathbf{k}_1} \hat{N}_{\mathbf{k}_2} - \delta_{\mathbf{k}_1 \mathbf{k}_2} \hat{N}_{\mathbf{k}_1}$  excludes uncorrelated SPE events.

As already briefly discusses in subsec. 2.4.1, constructing two-body scattering wave-functions is possible for the simplest cases only. The methods of incorporating SP scattering wave-functions into an approximate description of the many-body states (mentioned in subsec. 3.2.1) are, in principle, still applicable and allow for taking two continuum electrons into account. However, the Coulomb interaction between the two liberated electrons is not captured by such approaches. It turned out that the missing repulsion has profound impact on the angular distribution of the two photoelectrons [144–146].

Nevertheless, employing the sudden approximation  $|\Psi_{\alpha, \mathbf{k}_1 \mathbf{k}_2}^{(-)}\rangle \approx \hat{c}_{\mathbf{k}_1 \sigma_1}^{\dagger} \hat{c}_{\mathbf{k}_2 \sigma_1}^{\dagger} |\Psi_{\alpha}^{2+}\rangle$  leads to a significant simplification, as the matrix elements (3.20) can be expressed in terms of the *two-hole* Dyson orbitals:

$$M_{\alpha,0}^{\text{LG}}(\mathbf{k}_1, \mathbf{k}_2) = \langle \Phi_{\mathbf{k}_1 \mathbf{k}_2} | \mathbf{u} \cdot (\mathbf{r}_1 + \mathbf{r}_2) | \Phi_{0,\alpha}^{(2h)} \rangle, \quad M_{\alpha,0}^{\text{VG}}(\mathbf{k}_1, \mathbf{k}_2) = -i \langle \Phi_{\mathbf{k}_1 \mathbf{k}_2} | \mathbf{u} \cdot (\nabla_{\mathbf{r}_1} + \nabla_{\mathbf{r}_2}) | \Phi_{0,\alpha}^{(2h)} \rangle. \quad (3.22)$$



Here,  $|\Phi_{\mathbf{k}_1, \mathbf{k}_2}\rangle$  denotes the anti-symmetrized two-body scattering state built by the one-body scattering wave-functions  $|\phi_{\mathbf{k}_1}\rangle$  and  $|\phi_{\mathbf{k}_2}\rangle$ . In principle, it is also possible to incorporate the Coulomb repulsion into  $|\Phi_{\mathbf{k}_1, \mathbf{k}_2}\rangle$  [147]. The double-hole Dyson orbitals are defined, in analogy to the one-hole case (eq. (2.70)) as

$$\Phi_{0, \alpha}^{(2h)}(x_1, x_2) = \langle \Psi_{\alpha}^{2+} | \hat{\psi}(x_1) \hat{\psi}(x_2) | \Psi_0 \rangle. \quad (3.23)$$

The notion of the two-hole Dyson orbitals (3.23) establishes, similarly to eq. (3.16), a link to a suitable GF. For DPE, this is the two-body GF [148]. Hence, DPE allows for direct insight in genuine two-body quantities and thus opens a window for studying electron-electron correlations. This statement is underpinned by observing that the DPE event is excluded if the Coulomb interaction is switched off. The two-hole Dyson orbitals are then given by anti-symmetrized products of the occupied SP orbitals. Taking the generic dipole operator  $\hat{D} = \hat{d}_1 + \hat{d}_2$  ( $\hat{d}_{1/2}$  acts on electron 1/2), one finds

$$\langle \Phi_{\mathbf{k}_1 \mathbf{k}_2} | \hat{D} | \Phi_{0, \alpha=(ij)}^{(2h)} \rangle = \langle \phi_{\mathbf{k}_1} | \hat{d} | \phi_i \rangle \delta_{\mathbf{k}_2 j} + \langle \phi_{\mathbf{k}_2} | \hat{d} | \phi_j \rangle \delta_{\mathbf{k}_1 i} - \langle \phi_{\mathbf{k}_1} | \hat{d} | \phi_j \rangle \delta_{\mathbf{k}_2 i} - \langle \phi_{\mathbf{k}_2} | \hat{d} | \phi_i \rangle \delta_{\mathbf{k}_1 j} = 0.$$

In other words, it is the electronic correlations which coalesce in the emission of two electrons – systems with stronger (effective) electron-electron interaction are thus much more likely to be double-ionized. This has been confirmed experimentally [149], as well.

From theoretical point of view, a general treatment of DPE within and, in an even more pronounced manner, beyond the sudden approximation is a highly demanding task. One possibility is given by, as for SPE, the diagrammatic expansion of the two-body matrix elements (3.20) in terms of the Coulomb interaction in both the initial and the final state channels [136]. Although formally exact, its practical applicability is limited to cases where the bare Coulomb interaction can be treated as a small quantity – typically small to moderate-size atoms. A link between the NEGF formalism and the powerful machinery of MBPT would be beneficial in a more general setup. This link is the topic of [E3].

As pointed out in subsec. 3.1.2, the Auger decay leads to the emission of two electrons, as well. The Auger decay involves an intermediate (shake-up) stage which results in different characteristics of the mechanism as compared to, for instance, DPE due to direct electron-electron scattering (knock-out). These kinds of indirect emission channels typically result in a time delay between the ionization of the core level and the shake-up ionization. Recent experiments [150] and theories [151] focus on the *time-resolved* Auger effect, where these questions can be addressed. The kinematics of an Auger experiment is usually different from DPE. The photon energy  $\omega$  has to suffice to promote a core electron (binding energy  $-\varepsilon_C$ ) to the continuum:  $\varepsilon_{\mathbf{k}_1} = \varepsilon_C + \omega$ . The energy of the first electron  $\varepsilon_{\mathbf{k}_1}$  needs not to be detected as it is completely determined by the photon energy and the known energetic position of the core level<sup>9</sup>. By detecting the secondary electron with energy  $\varepsilon_{\mathbf{k}_2}$ , the binding energy  $\varepsilon_B$  of the valence orbital (see fig. 3.1(c)) where the Auger electron is liberated from can be determined:  $\varepsilon_B = -\varepsilon_C - \varepsilon_{\mathbf{k}_2}$ . The theoretical description of Auger spectra, similarly to DPE, entails the two-body GF [153].

A typical experimental setup with which both DPE and the Auger effect can be measured [139] is sketched in fig. 3.3(c). An array of hemispherical analyzers collects electrons in (ideally) the full solid angle. Importantly, the case of two uncorrelated emission events from two different targets needs to be excluded. This is achieved by coincidence detection [154]. Taking the autocorrelation of the electron's TOF measured by the individual detectors, correlated emission events can be singled out. Auger and DPE spectra are discussed and paralleled for the  $C_{60}$  molecule in [E5].

### 3.2.3 Two-photon photoemission

Two-photon photoemission (2PPE) goes beyond the perturbative regime as governed by the Fermi Golden rule. In general, 2PPE is a sequential ionization process where electrons are promoted from occupied to virtual states by the first photon, from which they are liberated by absorbing a second photon. It is clear already at this point that both the spectral properties of the occupied and of the virtual states play an important role hereby. Moreover, it explicitly probes excited state properties. 2PPE thus differs from the linear-response

<sup>9</sup>Still, detecting the primary electron in coincidence with the Auger electrons improves the resolution of the overall experiment [152].

philosophy, which relies on transitions from the ground state. Accounting for the coupling of two independent laser fields to the system, the total Hamiltonian (we restrict consider electronic transitions only here) reads

$$\hat{H}(t) = \hat{H}_0 + (\hat{D}f_1(t)e^{-i\omega_1 t} + \hat{D}f_2(t)e^{-i\omega_2 t} + \text{h. c.}) . \quad (3.24)$$

Here,  $\hat{D}$  denotes the dipole operator in either gauge;  $f_1(t)$  ( $f_2(t)$ ) is the envelop function characterizing the temporal structure of the first (second) incident field. For  $\hat{H}_0$  we think of the electronic Hamiltonian  $\hat{H}_e(t_0)$  (eq. (2.20)).

**Steady-state two-photon photoemission.** For a steady-state scenario (continuous laser fields), one chooses  $f_1(t) = f_1^{(0)}e^{-\eta t}$ ,  $f_2(t) = f_2^{(0)}e^{-\delta t}$ . We assume that the respective frequencies  $\omega_1, \omega_2$  are adjusted such that the population of the intermediates states is due to the first laser. Furthermore, the intensity of both lasers is assumed to lie in the perturbative regime. Employing second-order TDPT (and the limit  $\delta \rightarrow 0+$ ) the differential 2PPE DCS attains the form [155]

$$\begin{aligned} \frac{d\sigma_{2\text{PPE}}}{d\mathbf{k}} \propto 2\eta\omega \sum_{\beta \in \mathcal{B}_{N_e-1}} \left| \sum_{\alpha \in \mathcal{B}_{N_e}} (\omega_1 - \Omega_\alpha + i\eta)^{-1} \langle \Psi_{\beta, \mathbf{k}}^{(-)} | \hat{D} | \Psi_\alpha \rangle \right. \\ \left. \times \langle \Psi_\alpha | \hat{D} | \Psi_0 \rangle \delta(\omega_1 + \omega_2 - \Omega_\beta^+ - \varepsilon_{\mathbf{k}}) \right|^2, \quad \eta \rightarrow 0+ . \end{aligned} \quad (3.25)$$

The fraction in the modulus square ensures the energy conservation  $\omega_1 = \Omega_\alpha = E_\alpha - E_0$ , while the  $\delta$ -function represents the total energy conservation. As eq. (3.25) demonstrates, 2PPE compares to the photoemission of the excited states, which are populated with some probability by absorbing the first photon. Note that pathway interference prevents to factor out the individual probabilities to obtain an overall rate expression.

**Time-resolved two-photon photoemission.** 2PPE does not only allow for accessing the virtual states to study their spectral properties, but their time-resolved dynamics, as well, by operating with two pulses rather than continuous lasers. Ideally, the first pulse excites the system resonantly by a short pulse at time  $t = 0$ . The resonance condition has to be balanced against the pulse duration; let us assume a typical number of ten optical cycles. The system undergoes free evolution including relaxation channels such as electron-phonon scattering. After a time  $t = \tau$ , a second (probe) pulse ionizes the system. For a good time resolution, the probe pulse should be as short as possible, but must also allow for ionizing selectively from the virtual states. A suitable observable would be the photoelectron spectrum or photoemission probability at fixed energies. Carrying out this pump-probe experiment as a function of the pulse delay  $\tau$  (illustrated in fig. 3.4(a)) delivers information on the dephasing and relaxation dynamics of the excited states. From theoretical point of view, describing time-resolved 2PPE is achievable by few approaches:

(i) Explicitly solving the TDSE according to the time-dependent Hamiltonian (3.24) for the (many-body) states  $|\Psi(t)\rangle$ . Projecting on the final states with one continuum electron allows us to define the time-resolved photoionization rate  $P_{\beta, \mathbf{k}}(t; \tau) = |\langle \Psi_{\beta, \mathbf{k}}^{(-)} | \Psi(t) \rangle|^2$ , which parametrically depends on  $\tau$ . For  $t \rightarrow \infty$ , the total photoemission probability as a function of the delay can thus be obtained. In practice, one uses a basis-set representation

$$|\Psi(t)\rangle = \sum_{\alpha \in \mathcal{B}_{N_e}} C_\alpha(t) |\Psi_\alpha\rangle + \sum_{\beta \in \mathcal{B}_{N_e-1}} \int d\mathbf{k} \tilde{C}_{\beta, \mathbf{k}}(t) |\Psi_{\beta, \mathbf{k}}^{(-)}\rangle$$

with a suitably reduced number of the involved states. The continuum  $\mathbf{k} \in \mathbb{R}^3$  is typically discretized. We employ this approach in [E1]. Alternatively, one can employ TDDFT in real space and determine the time-dependent photocurrent directly by computing the flux of particles emerging from the system [156] Instead of solving the finite-level TDSE for the amplitudes  $C_\alpha(t)$  and  $\tilde{C}_{\beta, \mathbf{k}}(t)$ , one can also propagate the time-dependent Liouville equation for the density matrix instead. This approach has the advantage that relaxation mechanisms can be incorporated by extending to, e. g., the Lindblad master equation (see appendix D) as in [E6].

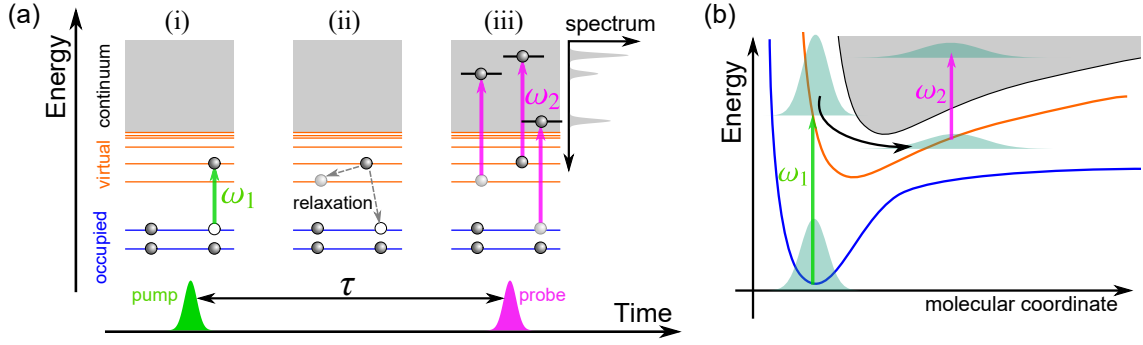


Figure 3.4: (a) Sketch of a time-resolved 2PPE experiment for measuring the lifetime of virtual states in the SP picture. (i) The system is resonantly driven to an excited state by pump pulse. (ii) During free time evolution, dephasing and relaxation effects due to interactions take place. (iii) A photoelectron spectrum upon probing is recorded with varying pump-probe delay  $\tau$ . (b) Illustration of the two-photon femtochemistry: a molecule is vertically excited from the ground-state PES. The corresponding nuclear wave-packet undergoes vibrational or dissociative dynamics, until an electron is emitted by the second photon.

(iii) The time-dependent NEGF formalism. Assuming the photon energy of the probe pulse is sufficiently large, the pulse duration required to accommodate a few optical cycles can be very short as compared to the dynamics induced upon pumping. While the notion of the time-dependent wave-function as used in (i) excludes, in principle, spectral information, the two-times NEGF contains the full information. This leads to the definition of the time-dependent 2PPE DCS, analogously to the SPE case (3.16), as

$$\frac{d\sigma_{2\text{PPE}}(\tau)}{d\mathbf{k}} \propto \sum_{ij} m_i(\mathbf{k}) G_{ij}^<(\omega_2 - \varepsilon_{\mathbf{k}}, \tau) m_j(\mathbf{k})^*. \quad (3.26)$$

Here, the frequency and the time dependence of the GF are as in eq. (2.73). The one-body matrix elements can be in either gauges. Some slight modifications make eq. (3.26) compatible with a finite duration of the probe pulse [86]. Transferring the interpretation of ARPES in terms of the crystal momentum as ingredient to the NEGFs (see subsec. 3.2.1), the pump-probe setup allows for tracing the evolution of the band structure<sup>10</sup> in the time domain – known as time-resolved ARPES [157–159].

**Two-photon femtochemistry.** For molecular systems, the principle of time-resolved 2PPE is closely related to the ideas of femtochemistry. Imagine the following scenario: a short pump pulse drives a resonant electronic transition, while the nuclei can be considered as frozen on the time scale of the pulse (called vertical transition). Revisiting the TDSE for the nuclear wave-functions, eq. (2.14), a vertical transition amounts to neglecting the kinetic energy of the cores. Assuming the molecule to be well-described by the BO approximation, the time evolution is governed by

$$i\partial_t \chi_\alpha(\{\mathbf{R}\}; t) = \sum_\beta \left[ E_\alpha(\{\mathbf{R}\}) \delta_{\alpha\beta} + (f_1(t) e^{-i\omega_1 t} D_{\alpha\beta}(\{\mathbf{R}\}) + \text{h. c.}) \right] \times \chi_\beta(\{\mathbf{R}\}; t), \quad (3.27)$$

where  $D_{\alpha\beta}(\{\mathbf{R}\}) = \langle \Psi_\alpha | \hat{D} | \Psi_\beta \rangle$  and, as in sec. 2.3,  $\{\mathbf{R}\} = (\mathbf{R}_1, \dots, \mathbf{R}_{N_c})$ . After the nuclear wave-function associated with the ground-state PES  $E_0(\{\mathbf{R}\})$  has been promoted to an excited-state PES  $E_\alpha(\{\mathbf{R}\})$  by the pump pulse, a non-trivial time evolution of the nuclear-wave packet (NWP) is triggered since the NWP is no longer an eigenstate with respect to  $E_\alpha(\{\mathbf{R}\})$ . Fig. 3.4(b) shows a sketch of this process. In order to map out the NWP dynamics, a probe pulse can be applied to ionize the molecule. It is known [160] that the information on the NWP can be extracted from the photoelectron spectrum or – in the case of a break up of the molecule – from the molecular fragments [161]. Especially for the latter scenario, called Coulomb explosion, it is more or less established how to reconstruct the dynamics of the NWP [162–164]. Our works [E1] and [E2], on the other hand, explore how comparable information is obtained from the manifestation of the nuclear arrangement on the photoemission properties.

<sup>10</sup>For a correlated system, the band structure as  $\mathbf{k}$ -dependent manifestation of the quasi-particle energies depends on the electron configuration. Promoting electrons to higher bands or the continuum might alter the band structure significantly.

### 3.3 Electron and photon scattering

The photon impact events and the resulting physics discussed in sec. 3.1 and 3.2 were focused on the absorption of a photon. In this section we consider the *inelastic* scattering of photons and electrons from an electronic system and work out the connection to the charge density fluctuations.

#### 3.3.1 Electron-energy loss spectroscopy

In the electron-energy loss spectroscopy (EELS) setup, a high-energy (keV regime) electron (wave vector  $\mathbf{k}$ , energy  $\varepsilon_{\mathbf{k}}$ ) is directed at the target. By measuring (for instance with a hemispherical analyzer, see subsec. 3.2.1) both the energy  $\varepsilon_{\mathbf{k}'}$  and the angle  $\theta$  (with respect to  $\mathbf{k}$ ) under which the electron is scattered from the sample, the momentum transfer  $\mathbf{q} = \mathbf{k} - \mathbf{k}'$  and the energy loss  $\omega = \varepsilon_{\mathbf{k}} - \varepsilon_{\mathbf{k}'}$  become control variables for the experiment. In contrast to the scattering of other particles, the *indistinguishability* of the electrons needs to be accounted for and complicates the theoretical description (see subsec. 2.4.1). However, due to the high energy, exchange effects can often be neglected, such that the scattered electron can be treated as *distinguishable* projectile. Let us thus extend the electronic Hamiltonian (2.22) (any time-dependence in  $\hat{H}_e$  is omitted) by

$$\hat{H}_{ep} = \hat{H}_e + \hat{h}_p + \hat{V}_{ep}, \quad \hat{V}_{ep} = \frac{1}{2} \sum_{ij} \sum_{\mathbf{pp}'} \sum_{\sigma\sigma'} v_{i\mathbf{p}\mathbf{p}'j} \hat{c}_{i\sigma}^\dagger \hat{a}_{\mathbf{p}\sigma'}^\dagger \hat{a}_{\mathbf{p}'\sigma'} \hat{c}_{j\sigma}, \quad \hat{h}_p = \sum_{\mathbf{p}\sigma} \varepsilon_{\mathbf{p}} \hat{a}_{\mathbf{p}\sigma}^\dagger \hat{a}_{\mathbf{p}\sigma}, \quad (3.28)$$

where the projectile degrees of freedom are represented by the creation/annihilation operators  $\hat{a}_{\mathbf{p}\sigma}^\dagger / \hat{a}_{\mathbf{p}\sigma}$  (which are to be distinguished from the electronic operators). Similarly to the treatment of the light-matter interaction (see subsec. 3.1.1), the Coulomb interaction  $\hat{V}_{ep}$  between the projectile and the target is turned on adiabatically. Within first-order TDPT (first Born approximation in this context [33]), the initial state  $\hat{a}_{\mathbf{k}\sigma}^\dagger |\Psi_0\rangle$  (energy  $E_0 + \varepsilon_{\mathbf{k}}$ ) transforms into

$$|\tilde{\Psi}^{(N_e+1)}\rangle = \hat{a}_{\mathbf{k}\sigma}^\dagger |\Psi_0\rangle + \frac{1}{E_0 + \varepsilon_{\mathbf{k}} - \hat{H}_e - \hat{h}_p + i\eta} \hat{V}_{ep} \hat{a}_{\mathbf{k}\sigma}^\dagger |\Psi_0\rangle. \quad (3.29)$$

Projecting onto the final state  $\hat{a}_{\mathbf{k}'\sigma}^\dagger |\Psi_\alpha\rangle$  (as the outgoing momentum  $\mathbf{k}'$  is fixed by the measurement) and normalizing by the effective switch-on time  $(2\eta)^{-1}$  yields the transition rates in form of the Fermi Golden rule

$$p_\alpha(\mathbf{k}, \mathbf{k}') = 2\pi \left| \langle \Psi_\alpha | \hat{a}_{\mathbf{k}'\sigma}^\dagger \hat{V}_{ep} \hat{a}_{\mathbf{k}\sigma}^\dagger |\Psi_0\rangle \right|^2 \delta(E_0 + \omega - E_\alpha) = 2\pi \left| \langle \Psi_\alpha | \hat{V}_{\text{eff}}(\mathbf{k}, \mathbf{k}') |\Psi_0\rangle \right|^2 \delta(E_0 + \omega - E_\alpha)$$

with the effective interaction  $\hat{V}_{\text{eff}}(\mathbf{k}, \mathbf{k}') = (1/2) \sum_{ij} \sum_{\sigma} v_{i\mathbf{k}\mathbf{k}'j} \hat{c}_{i\sigma}^\dagger \hat{c}_{j\sigma}$ , which attains the form of a one-body operator. Further approximating the projectile scattering states by plane waves, the effective interaction becomes a function of the momentum transfer only:

$$\hat{V}_{\text{eff}}(\mathbf{q}) = \frac{4\pi}{q^2} \int d\mathbf{r} e^{i\mathbf{q}\cdot\mathbf{r}} \hat{n}(\mathbf{r}) = \frac{4\pi}{q^2} \sum_{i=1}^{N_e} e^{i\mathbf{q}\cdot\mathbf{r}_i}. \quad (3.30)$$

Expressing the Fermi Golden rule as in subsec. 3.1.1 by the dynamical structure factor gives rise to the definition of the EELS cross-section [165]

$$\frac{d\sigma_{\text{EELS}}}{d\omega d\hat{\mathbf{q}}} = \frac{4\gamma^2}{q^4} \frac{k'}{k} S(\mathbf{q}, \omega), \quad S(\mathbf{q}, \omega) = \int d\mathbf{r} \int d\mathbf{r}' e^{i\mathbf{q}\cdot(\mathbf{r}-\mathbf{r}')} S_{n(\mathbf{r})n(\mathbf{r}')}(r, r', \omega). \quad (3.31)$$

The FDT (2.84) provides again a direct link to the DD response function in momentum space. The prefactor  $\gamma$  is the Lorenz factor, incorporating relativistic corrections to first order. In the high-energy limit one can approximate  $k \approx k'$  and so  $q^2 \approx 2k^2(1 - \cos\theta)$ . The EELS cross-section thus assumes the form

$$\frac{d\sigma_{\text{EELS}}}{d\omega d\hat{\mathbf{q}}} = \frac{d\sigma_{\text{Rh}}}{d\hat{\mathbf{q}}} S(\mathbf{q}, \omega), \quad \frac{d\sigma_{\text{Rh}}}{d\hat{\mathbf{q}}} = \left( \frac{e^2}{8\pi\epsilon_0\varepsilon_{\mathbf{k}}^2} \right)^2 \frac{1}{\sin^4(\theta/2)}, \quad (3.32)$$

where  $d\sigma_{\text{Rh}}/d\hat{\mathbf{q}}$  is the Rutherford cross-section for an electron scattering from a  $1/r$  potential.

EELS can be paralleled to photoabsorption to some extent, as similar photoexcitation processes (see subsec. 3.1.2) may take place. On the other hand, the energy loss  $\omega$  can be chosen selectively. Scanning over  $\omega$  allows to access very different regimes and the corresponding loss channels. For instance, for  $\omega$  in the meV range, phonon or vibron excitation are dominant inelastic channels, while EELS with  $\omega$  in the range of eV targets valence electron or collective excitations. Furthermore, the transition operator  $\hat{V}_{\text{eff}}(\mathbf{q})$ , at variance to optical absorption which is restricted to dipole transitions only, EELS may break the dipole selection rules for  $q > 0$ . As  $e^{i\mathbf{q}\cdot\mathbf{r}} \approx 1 + i\mathbf{q}\cdot\mathbf{r}$  for  $q \rightarrow 0$ , the restriction to dipole transitions is recovered in this case – the case of small  $q$  is called the optical limit. In gas-phase experiments, the orientation of the targets is random – one has only access to the spherically-averaged dynamical structure factor  $S(q, \omega) = (1/4\pi) \int d\hat{\mathbf{q}} S(\mathbf{q}, \omega)$ .

The prefactor  $q^{-4}$  suppresses transitions far from the optical limit significantly. A different perspective on this dependence is gained by substituting the DD response function for the structure factor via the FDT:

$$\begin{aligned} \frac{(4\pi)^2}{q^4} S(\mathbf{q}, \omega) &= -\frac{1}{\pi} \text{Im} \int d\mathbf{r} \int d\mathbf{r}' \int d\mathbf{r}_1 \int d\mathbf{r}_2 e^{i\mathbf{q}\cdot(\mathbf{r}-\mathbf{r}')} v(\mathbf{r}-\mathbf{r}_1) \chi^{\text{R}}(\mathbf{r}_1, \mathbf{r}_2; \omega) v(\mathbf{r}_2-\mathbf{r}') \\ &= -\frac{1}{\pi} \text{Im} \int d\mathbf{r} \int d\mathbf{r}' e^{i\mathbf{q}\cdot(\mathbf{r}-\mathbf{r}')} \delta W^{\text{R}}(\mathbf{r}, \mathbf{r}'; \omega) = -\frac{1}{\pi} \text{Im}[\delta W^{\text{R}}(\mathbf{q}, \omega)]. \end{aligned} \quad (3.33)$$

Here, we have employed the relation between the DD response function and the screened interaction (2.61). Note that only the dynamical (frequency-dependent, that is) part  $\delta W^{\text{R}}(\mathbf{r}, \mathbf{r}'; \omega)$  enters eq. (3.33). The EELS cross-section (3.31) is thus proportional to  $\text{Im}[\delta W^{\text{R}}(\mathbf{q}, \omega)]$ . Therefore, EELS directly probes dynamical screening properties of the target. Physically one can imagine this as follows: the electric field of a passing electron causes the dynamical rearrangement of the electrons in the sample. The energy for this process is taken from the scattering electron. In the case the screening is very ineffective ( $\text{Im}[\delta W^{\text{R}}(\mathbf{q}, \omega)] \approx 0$ ), the scattering is elastic and the EELS cross-section approaches zero.

The EELS setup can be conveniently incorporated into the transmission electron microscope (TEM) [166, 167], allowing for spatially-resolved energy-loss spectroscopy [168]. Moreover, recent applications include angular momentum by producing so-called vortex beams [169]. A corresponding application is addressed in [E4].

### 3.3.2 Inelastic X-ray scattering

Inelastic X-ray scattering (IXS) is a photon-based spectroscopy with many parallels to EELS. Already from classical point of view it is clear that the laser-excited electrons undergo oscillations as driven by the incident radiation, which, in turn, leads to the emission of dipole radiation. Effectively, the incident wave is thus scattered from the electronic system. In the case of elastic scattering – called Thomson scattering – the cross-section, resolved with respect to the scattering solid angle  $\hat{\mathbf{q}}$  ( $\mathbf{q} = \mathbf{k}' - \mathbf{k}$  is the difference vector of the incident ( $\mathbf{k}$ ) and scattered ( $\mathbf{k}'$ ) photon), is given [170] by

$$\frac{d\sigma_{\text{Th}}}{d\hat{\mathbf{q}}} = \frac{1}{16\pi^2 \epsilon_0 m_0^2 c^4} \frac{1 + \cos^2 \theta}{2} = \alpha_0^2 \frac{1 + \cos^2 \theta}{2}. \quad (3.34)$$

The second equality uses, as usual, atomic units. The photon scattering can, however, also be inelastic and thus provide information on internal excitation channels. Treating the photon scattering process within the first Born approximation<sup>11</sup>, one finds [171] for the IXS DCS

$$\frac{d\sigma_{\text{IXS}}}{d\omega d\hat{\mathbf{q}}} = \frac{d\sigma_{\text{Th}}}{d\hat{\mathbf{q}}} S(\mathbf{q}, \omega), \quad (3.35)$$

where  $\omega$  denotes the energy loss.

Comparing the cross-section of EELS (3.32) and for IXS (eq. (3.35)), both techniques establish a direct link to the inelastic scattering processes as described by the dynamical structure factor  $S(\mathbf{q}, \omega)$ , albeit with some restrictions for large  $q$  [172] due to the different prefactor (Rutherford vs. Thomson scattering).

<sup>11</sup>The Fermi Golden rule is obtained similarly as in subsec. 3.3.1, but the perturbation term is given by the non-linear  $A^2$  term [170] arising due to the light-matter interaction (see sec. 2.2)



## Ultra-fast tracing of nuclear wave-packet dynamics by spatially-resolved photoemission

In this chapter we introduce our works [E1] and [E2]. The common feature is the correlation between the nuclear dynamics of small molecules – induced by resonantly tuned laser pulses – and the photoionization process. Emphasis is put on identifying particular features of the photoelectrons reflecting the nuclear degrees of freedom as clearly as possible – with the ultimate goal of finding a direct map between experimentally accessible observables and the vibrational dynamics.

### 4.1 E1: Local ionization dynamics traced by photoassisted scanning tunneling microscopy: a theoretical approach

Spectroscopy of *single* molecules adsorbed on a substrate delivers valuable information on the specific chemical environment and the influence on the electronic and the vibronic properties [173]. Scanning-tunneling microscopy (STM) [174–176] or scanning-tunneling spectroscopy (STS) [177–179] are important techniques in this context. STM provides a map of the LDOS with unrivaled spatial resolution; STS provides insight into the excitation channels of single molecules or atoms. In the time domain, both STM- and STS-type experiments are limited to the nanosecond to picosecond regime [180, 181].

Photoionization, on the other hand, is a process taking place on the attosecond to femtosecond time scale and is so well suited to map out the time-dependent dynamics of adsorbed molecules – provided the photoelectrons are collected such that a single molecule can be pinpointed as the origin. This requirement is, in principle, fulfilled by reversing the principle of STM: instead of measuring the local tunneling current, the photoelectrons originating from the surface due to laser-driven ionization are chosen as the observable. This basic principle of photoemission microscopy has been improved considerably by using an atomic-force microscopy (AFM) tip as high-resolution (up to 5 nm) photoelectron detector [182]. Hence, detecting photoelectrons from a single adsorbed molecule becomes feasible.

Motivated by these developments, we propose in our work [E1] a setup for pump-probe photoemission from single molecules on the surface. For a proof-of-principle, we have chosen the HCN molecule bound to the LiF(001) surface. HCN is an organic molecule with a remarkably strong permanent dipole moment, resulting in a strong hydrogen bond to the polar surface. The very large IP of LiF suppresses limits the ionization of the surface itself (which would result in a large background otherwise) and so allows singling out the adsorbates. We demonstrate that, due an almost linear dependence of the photoionization dipole moment to the relevant vibrational modes of the molecule, a one-to-one correspondence between the vibrations and the photoionization probability can be established. These findings are corroborated by the simulation of a pump-probe scenario: molecular vibrations excited by an infrared pump pulse are paralleled to the photoelectron current driven by a femtosecond UV laser pulse.

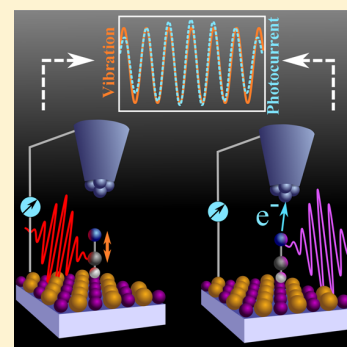
# Local Ionization Dynamics Traced by Photoassisted Scanning Tunneling Microscopy: A Theoretical Approach

Michael Schüler,\* Yaroslav Pavlyukh, and Jamal Berakdar

Institute for Physics, Martin-Luther University Halle-Wittenberg, Heinrich-Damerow-Straße 4, 06120 Halle

W Web-Enhanced Feature S Supporting Information

**ABSTRACT:** For tracing the spatiotemporal evolution of electronic systems, we suggest and analyze theoretically a setup that exploits the excellent spatial resolution based on scanning tunneling microscopy techniques combined with the temporal resolution of femtosecond pump–probe photoelectron spectroscopy. As an example, we consider the laser-induced, local vibrational dynamics of a surface-adsorbed molecule. The photoelectrons released by a laser pulse can be collected by the scanning tip and utilized to access the spatiotemporal dynamics. Our proof-of-principle calculations are based on the solution of the time-dependent Schrödinger equation supported by the ab initio computation of the matrix elements determining the dynamics.



**SECTION:** Spectroscopy, Photochemistry, and Excited States

The impressive advances made in generating and utilizing subfemtosecond laser pulses<sup>1–6</sup> for time-resolving the dynamics of electronic systems are paralleled with the fascinating versatility of scanning tunneling microscopy (STM)<sup>7–10</sup> that allows for atomic spatial resolution. STM also accesses spectroscopic information that is related, under certain assumptions, to the local density of states of the probe. The transport through single molecules<sup>11–16</sup> provides, for instance, insight into the analysis and manipulation of the molecular properties like the conformation<sup>17–19</sup> or the characterization of magnetic systems.<sup>20–22</sup>

To explore the subpicosecond local dynamics, there have been proposals for inducing and probing the electron dynamics by means of focused femtosecond laser pulses applied within the STM context.<sup>23–26</sup> The experimental limitations and issues experienced by previous attempts (mainly due to the thermal expansion of the tip)<sup>23–25</sup> have been shown to be possible to be circumvented by ultrafast two-photon schemes.<sup>26,27</sup>

We propose in this contribution a new model system that demonstrates the feasibility for tracing the femtosecond dynamics of adsorbed atoms or molecules by means of two-photon<sup>28–30</sup> ultrafast STM-based photoelectron detection. As a concrete example (Figure 1), we consider a metal substrate coated with the LiF overlayer, where a single HCN molecule is adsorbed. The LiF layer has the important advantage of a large band gap  $E_g$  (for the bulk at zero temperature,  $E_g = 14.2$  eV, ref 31). Provided the ionization energy of adsorbate is smaller than the LiF work function, the dynamics of the molecule can be accessed selectively. Furthermore, the strongly ionic character gives rise to a particular strong bonding of the HCN molecule (which also has a large permanent dipole moment of  $1.172$  au<sup>32,33</sup>) to the surface. Our molecule serves as a test object

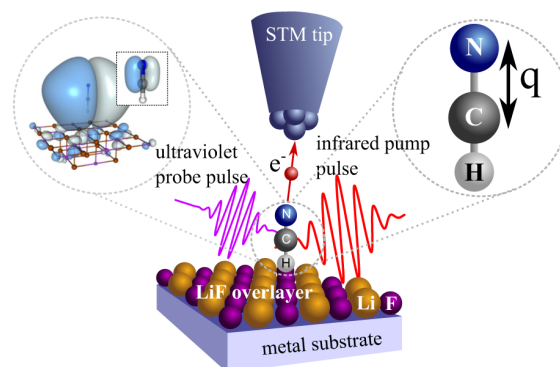


**Figure 1.** Model system proposed to investigate the local vibrational dynamics of a single HCN molecule adsorbed on the LiF(001) surface. After an infrared (IR) pump pulse has induced the vibrational dynamics, a second laser pulse photoionizes the molecule. The released electron collected by a STM tip can then be employed for tracing the transient dynamics.

representing the simplest organic molecule and has some further convenient properties, which will be elucidated by the analysis of the electronic properties.

Our goal is to study the transient vibrational dynamics induced by an infrared (IR) laser pulse (the pump pulse) of moderate intensity and the vibronic coherent motion that can be imaged by utilizing the STM tip for recording the

**Received:** February 1, 2013

**Accepted:** March 19, 2013

**Published:** March 19, 2013



photocurrent (see WEO1 for the video illustration). This approach is, strictly speaking, not identical to the STM setup in the tunneling regime. Recent experiments<sup>34</sup> have, however, demonstrated the feasibility and the potential of the local photoelectron detection with the tip apex, reaching a spatial resolution in range of 5 nm. The photoelectron is released by a second laser pulse (the probe pulse) that ionizes the molecule and is applied at a time delay  $\tau$  with respect to the pump pulse. We remark that the laser intensities and frequencies are chosen such that only a single electron can be released at a time. The delay before launching a second pump–probe sequence is large enough to allow electrons from the metal substrate to tunnel to the  $\text{HCN}^+$  molecule (characteristic time scale in the range of femtoseconds to picoseconds). The molecule has to relax to the initial vibrational state (time scale of picoseconds to nano-second). Considering both of these aspects, we estimate the maximal repetition frequency of  $\sim 10$  MHz for the experiment.

On the basis of a cluster approach for representing the LiF surface, we have found that the most stable equilibrium configuration of HCN is to stand upright on surface, with the positively charged hydrogen atom directly above a F site (further details in the Supporting Information) by bonding to the surface. The comparison with cluster computations reveals that the C–N and the H–C stretching modes of the isolated HCN molecule<sup>35</sup> are hardly altered. (See the Supporting Information.) This result is also expected from the chemical point of view due to the strongly ionic character of both subsystems. Similarly, we found that the highest occupied molecular orbital (HOMO) of the HCN molecule (twice degenerated  $\pi$  orbital in the isolated case) is hardly changed by the presence of the surface (inset in Figure 1) and possesses the same symmetry.

The shape of the HOMO suggests that the excitation of the C–N stretching mode is closely related to contracting or expanding the orbital. Because the HOMO strongly influences the photoionization properties, we expect that a particularly clear connection between the vibrational dynamics and the photocurrent can be established when analyzing the C–N stretching eigenmode. We thus choose as the (1D) vibrational coordinate  $q$  the distance between the carbon and the nitrogen atom (inset in Figure 1). The hydrogen atom also participates in the vibration but with a much smaller amplitude.

For describing the laser-induced vibronic dynamics as well as the photoionization process, we need the  $q$ -dependent energy levels. We have computed all the corresponding potential energy surfaces (PESs) within the range of 15 eV from the ground state and accounted only for those states with a nonzero transition matrix element while exploiting the dipole selection rules for the case of a linear polarization of the laser field set parallel to the molecule axis (Figure 2). The incident laser fields are assumed to enter under small angle such that the components of the polarization perpendicular to the molecule axis can be ignored. Because the molecular dynamics is slow compared with the electronic transitions driven by the probe pulse, we can assume the bond angle to be constant for the photoionization process and thus neglect a transition to PESs associated with a bent conformation of the molecule.<sup>36,37</sup> The computations yield the transitions pathways for the light-molecule interaction: photoionization and the electronic excitation of the neutral system (no contribution to the photocurrent). Because both channels influence each other, including the neutral excited states is required for quantitative insights.

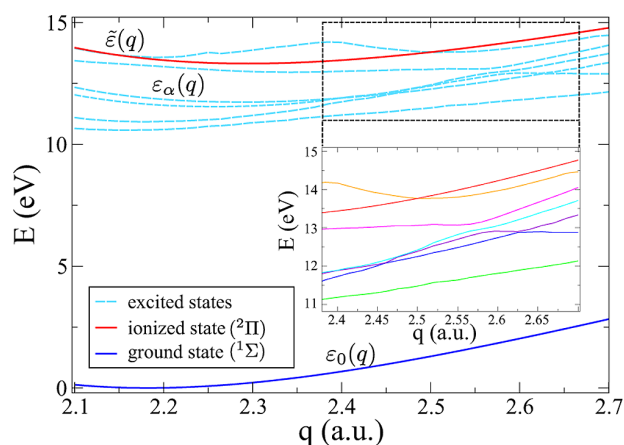


**Figure 2.** PESs of the neutral ground state (blue), the neutral excited states (light blue, dashed), and the ground state of  $\text{HCN}^+$  (red) as a function of the vibrational coordinate  $q$ . The inset magnifies the region where the neutral excited states display energies very close to each other and shows the occurrence of avoided crossings.

We solved the time-dependent Schrödinger equation (TDSE) governing the vibrational dynamics in the presence of the IR laser field  $E(t)$ . For the latter, we assume a Gaussian form  $E(t) = E_0 \exp(-t^2/2T_{\text{IR}}^2) \cos(\omega_{\text{IR}}t)$  with  $T_{\text{IR}} = 20$  fs and  $\omega_{\text{IR}} = 329.2$  meV (This value matches the transition energy from the ground state to the first excited state with respect to the potential  $\epsilon_0(q)$  (Figure 2). The corresponding wavelength is  $\lambda_{\text{IR}} = 3.77$   $\mu\text{m}$ .) The field amplitude derives from the intensity  $I_{\text{IR}} = 1.06 \times 10^{13}$  W/cm<sup>2</sup>.

With this specific choice of the parameters, the population transfer is primarily induced from the vibronic ground state to the first excited state, but the pulse spectral width due to the short pulse duration may allow higher levels to participate in the dynamics. (See Figure 3, top panel, where the states are labeled with the vibrational quantum number  $\lambda$ .) The corresponding coherent motion of the wave packet is represented by the time-dependent expectation value of  $q$  (the middle panel in Figure 3), displaying an oscillation with an

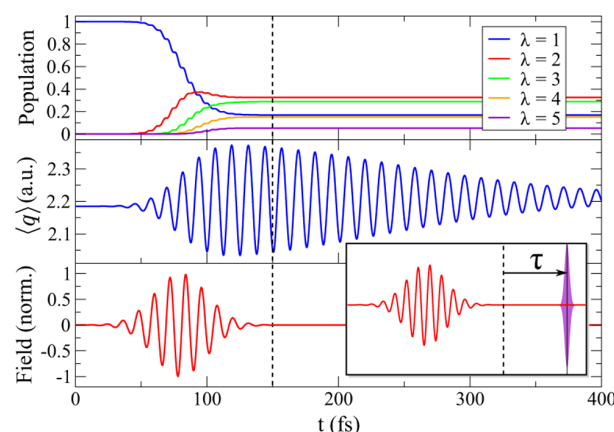


**Figure 3.** Vibrational dynamics of the HCN molecule in the presence of the infrared laser field (shown in the bottom panel) in terms of the level population (top panel) and the time-dependent expectation value of  $q$  (panel in the middle). The inset illustrates the definition of the pump–probe delay  $\tau$ .

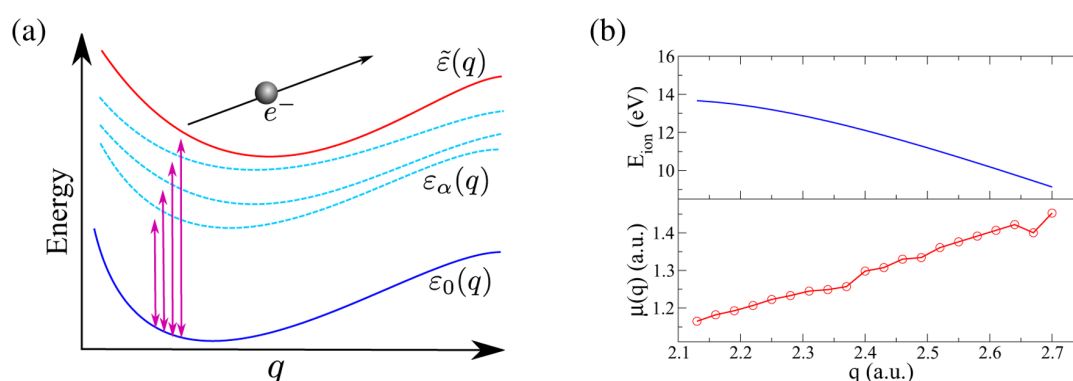


**Figure 4.** (a) Simplifying model for the ionization process: the spectral properties of the laser field only allow for the transitions from the ground state to the excited states or the ionic ground state (indicated by the purple double arrows). (b)  $q$ -dependent ionization energy and the momentum-integrated transition strength.

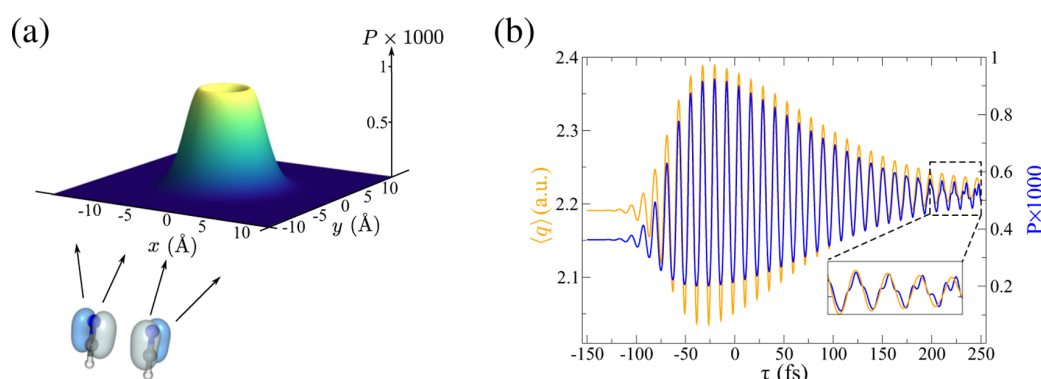


**Figure 5.** (a) Spatial dependence of the detection probability  $P$  in the shifted  $x$ - $y$  plane placed  $\sim 4.5$  Å above the molecule for fixed  $\tau = -150$  fs. Both possible orientation directions of the degenerated Dyson orbital  $\phi_0$  are taken into account. (b) Comparison of the expectation value  $\langle q \rangle$  from Figure 3 with the detection probability  $P$  as a function of the pump-probe delay  $\tau$ . The point in space for the detection is the same plane as in panel a such that  $P$  has the maximal amplitude.

amplitude of 10% around the equilibrium value. The laser field  $E(t)$  is shown in the bottom panel in Figure 3.

To unravel how the vibronic wave packet characterized in Figure 3 can be traced in the quantities of interest, we analyzed the respective many-body TDSE and derived a coupled set of equations including the bound-state dynamics and the release and propagation of exactly one photoelectron to the tip in the presence of the probe pulse. We assume an ultraviolet (UV) Gaussian-shaped laser pulse (central wavelength  $\lambda_{UV} = 100$  nm, peak intensity  $I_{UV} = 3.5 \times 10^{14}$  W cm $^{-2}$  and pulse length  $T_{UV} = 1.97$  fs fwhh). A detailed derivation is provided in the Supporting Information, along with the necessary additional approximations: (i) we ignore correlation effects of the photoelectron with the remaining ones, (ii) we ignore second-order overlap terms of well-localized orbitals with the continuum wave function of the released electron, and (iii) we employ the Born–Oppenheimer (BO) approximation.<sup>38</sup> For the latter, we spend a few words more on the justification for our model system. Because the diabatic coupling matrix elements of the electronic wave functions sandwiching the derivatives with respect to the vibrational coordinate are related to the velocity (the kinetic energy) of the nuclei (slow on the electronic time scale) divided by the energy level spacing of the states, these matrix elements play only a minor role as long as the electronic levels are well-separated. This is, for example, the case for the ground state in Figure 2 but not for the excited

states. However, the physical picture of the slow nuclei implies that the diabatic coupling elements have only a minor influence on the short-time dynamics; that is, when restricting the pulse length of the probing electrical field to a small time scale compared with the characteristic time scale for the vibrations, the BO approximation is still valid. This assumption is tolerable in view of the fact that  $T_{UV}/T_{vib} \approx 0.1$ . We furthermore specialize to the scenario sketched in Figure 4a; that is, we assume that no transitions between the neutral excited state occur, which is ensured by the spectral properties of the probe pulse.

Apart from the approximations stated above, our treatment of the coupled population dynamics of the involved electronic states of the neutral molecule the released electron is exact. The photoelectron wave function is represented on a real-space grid; that is, it does need to be constructed invoking additional approximations. The charge interaction of the photoelectron with the ionized molecule and the time-dependent laser field is taken into account as well.

The experimentally measurable quantity is the photoionization current. Our studies have elucidated that the key quantity connecting the vibrations in the ground state PES  $\varepsilon_0(q)$  and the photocurrent is the transition matrix element of the Dyson orbital with the photoelectron wave function. The Dyson orbital  $\phi_0$ <sup>39,40</sup> is defined as the overlap of the  $N$  electron wave function with the  $(N - 1)$  electron wave function of the

ionized system. We computed  $\phi_0$  by approximating the dominant configurations of the ground states of both the neutral and the ionized molecule by the Hartree–Fock determinants. The (expected) result reveals that this Dyson orbital overlaps by  $\sim 90\%$  with the HOMO. Because the C–N stretching vibration directly contracts or expands the HOMO, we expect an almost linear dependence of the transition strength on the vibrational coordinate. This scenario is supported by the calculation of the transition matrix element (integrated over the momentum of the photoelectron), depicted in Figure 4.

Solving the corresponding time-dependent Schrödinger equation yields the photoelectron wave function and thus the measurable current density  $j$ . For the pump–probe experiment, the time-integrated current (i.e., a probability) rather than the actual time-dependent current  $j$  contains the desired information. Taking the projection in the direction of the tip yields the spatioresolved probability  $P$  of detecting a photoelectron in a plane parallel to the surface and entails the information on the initial vibrational wave packet. We consider a plane with a distance of  $d = 4.5 \text{ \AA}$  above the nitrogen atom ( $x$ – $y$  plane) and compute the detection probability as a function of the position and the time delay  $\tau$  between the pump and the probe pulse. For  $\tau = 0$ , the maximum of the UV pulse is centered at  $t = 150 \text{ fs}$ . (See the inset in Figure 3.)

The spatial dependence of  $P$  is shown in Figure 5a. Because the photoelectron primarily originates from the Dyson orbital  $\phi_0$ , we can expect that the spatial structure of the detection probability in the detection plane is related to a cut through the  $x$ – $y$  plane of  $\phi_0$ . At this point, we have to take for the degeneracy of the HOMO and add the probability contributions according to the two orientations of the Dyson orbital, resulting in a radially symmetric spatial dependence. Interestingly, the probability displays a minimum directly above the molecule because the Dyson orbital has a nodal plane along the molecule axis. We thus infer that the dependence of  $P$  on  $x$  and  $y$  yields a probability map that is closely related to viewing the Dyson orbital “from above”.

We proceed by fixing  $x$  and  $y$  such that the detection probability is maximal and study the dependence on  $\tau$ . As we have already discussed, we expect an approximately linear mapping of the coherent vibrational dynamics to the detection probability for two reasons: the dependence of (i) the ionization energy and (ii) the transition strength to the continuum on  $q$  is almost linear. The result is presented in Figure 5b, where the expectation value of the vibrational coordinate is also shown for a comparison. Both curves are very similar, although some higher frequency components occur evidencing nonlinear contributions. As an outcome of this study, an animation (WEO2) illustrates the time evolution of the vibronic wave packet simultaneously with the  $\tau$ -dependent detection probability (spatially resolved along the  $x$  axis).

In conclusion, we suggested theoretically a novel experimental setup to access the spatiotemporal dynamics of adsorbates. The proposal is based on a combination of pump–probe techniques with a local detection scheme. We illustrated the model by explicitly studying a sample consisting of a HCN molecule adsorbed on a LiF overlayer deposited on a metal substrate. We studied how the molecule is adsorbed on the surface and find that the vibrational as well as the electronic properties are hardly altered. The proposed setup involved (i) the excitation of a coherent vibronic wave packet due to an IR pump pulse, and (ii) the photoionization of the adsorbed

molecule by an ultraviolet probe pulse. (iii) The photoelectrons are detected by the STM tip. We demonstrated by a proof-of-principle calculation how the vibronic wave packet can be mapped onto a probability  $P$  detected by the STM tip. The tip position yields the spatial dependence and can be exploited to image the involved orbitals. The temporal dependence with respect to the pump–probe delay  $\tau$  yields a measurable signal that closely resembles the time-dependent expectation value of the vibrational coordinate  $q$ , characterizing the coherent dynamics. Whereas our proof-of-principle study concentrates on a rather simple molecule, a generalization to more complex systems is conceptually straightforward. The combination of spatial and temporal resolution potentially coalesces in, for example, probing relaxation and decoherence processes or photoinduced conformation switching on single molecules in the time domain.

## THEORETICAL METHODS

All structure computations have been carried out using the Gaussian 03 code. Details (method, basis set) for each of the steps are provided in the Supporting Information. For the time-propagation of the photoelectron wave function, we employed a fourth-order Runge–Kutta scheme and discretized the spatial derivatives to the fourth order.

## ASSOCIATED CONTENT

### Supporting Information

Details of the computations of the vibrational modes and the orbitals of the surface-molecule system, for calculating the PESs and the derivation of Schrödinger equations for the photoemission. Schematic video of the model system and the setup.

Animation of the time-delay dependence of the vibrational wave packet dynamics synchronized with the detection probability. This material is available free of charge via the Internet at <http://pubs.acs.org>.

### Web-Enhanced Features

Web Enhanced Object 1 (WEO1): Schematic video of the model system and the setup. Web Enhanced Object 2 (WEO2): Animation of the time-delay dependence of the vibrational wave-packet dynamics synchronized with the detection probability. Available in the HTML version of the paper.

## AUTHOR INFORMATION

### Corresponding Author

\*E-mail: [michael.schueler@physik.uni-halle.de](mailto:michael.schueler@physik.uni-halle.de).

### Notes

The authors declare no competing financial interest.

## ACKNOWLEDGMENTS

This research is supported financially by the DFG through SFB 762.

## REFERENCES

- (1) Goulielmakis, E.; Schultze, M.; Hofstetter, M.; Yakovlev, V. S.; Gagnon, J.; Uiberacker, M.; Aquila, A. L.; Gullikson, E. M.; Attwood, D. T.; Kienberger, R.; Krausz, F.; Kleineberg, U. Single-Cycle Nonlinear Optics. *Science* **2008**, *320*, 1614–1617.
- (2) Schultze, M.; Fieß, M.; Karpowicz, N.; Gagnon, J.; Korbman, M.; Hofstetter, M.; Neppel, S.; Cavalieri, A. L.; Komninos, Y.; Mercouris, Th.; et al. Delay in Photoemission. *Science* **2010**, *328*, 1658–1662.
- (3) Haessler, S.; Caillat, J.; Boutou, W.; Giovanetti-Teixeira, C.; Ruchon, T.; Auguste, T.; Diveki, Z.; Breger, P.; Maquet, A.; Carré, B.;

- Taieb, R.; Salières, P. Attosecond Imaging of Molecular Electronic Wavepackets. *Nat. Phys.* **2010**, *6*, 200–206.
- (4) Shafir, D.; Mairesse, Y.; Villeneuve, D. M.; Corkum, P. B.; Dudovich, N. Atomic Wavefunctions Probed through Strong-Field Light-Matter Interaction. *Nat. Phys.* **2009**, *5*, 412–416.
- (5) Krausz, F.; Ivanov, M. Attosecond Physics. *Rev. Mod. Phys.* **2009**, *81*, 163–234.
- (6) Cavalieri, A. L.; Müller, N.; Uphues, Th.; Yakovlev, V. S.; Baltuška, A.; Horvath, B.; Schmidt, B.; Blümel, L.; Holzwarth, R.; Hendel, S.; et al. Attosecond Spectroscopy in Condensed Matter. *Nature* **2007**, *449*, 1029–1032.
- (7) Oka, H.; Ignatiev, P. A.; Wedekind, S.; Rodary, G.; Niebergall, L.; Stepanyuk, V. S.; Sander, D.; Kirschner, J. Spin-Dependent Quantum Interference Within a Single Magnetic Nanostructure. *Science* **2010**, *327*, 843–846.
- (8) Wiesendanger, R. Spin Mapping at the Nanoscale and Atomic Scale. *Rev. Mod. Phys.* **2009**, *81*, 1495–1550.
- (9) Fu, Y.-S.; Schwöbel, J.; Hla, S.-W.; Dilullo, A.; Hoffmann, G.; Klyatskaya, S.; Ruben, M.; Wiesendanger, R. Reversible Chiral Switching of Bis(phthalocyaninato) Terbium(III) on a Metal Surface. *Nano Lett.* **2012**, *12*, 3931–3935.
- (10) Schwöbel, J.; Fu, Y.; Brede, J.; Dilullo, A.; Hoffmann, G.; Klyatskaya, S.; Ruben, M.; Wiesendanger, R. Real-Space Observation of Spin-Split Molecular Orbitals of Adsorbed Single-Molecule Magnets. *Nat. Commun.* **2012**, *3*, 953.
- (11) Müllegger, S.; Schöfberger, W.; Rashidi, M.; Reith, L. M.; Koch, R. Spectroscopic STM Studies of Single Gold(III) Porphyrin Molecules. *J. Am. Chem. Soc.* **2009**, *131*, 17740–17741.
- (12) Katano, S.; Kim, Y.; Kagata, Y.; Kawai, M. Single-Molecule Vibrational Spectroscopy and Inelastic-Tunneling-Electron-Induced Diffusion of Formate Adsorbed on Ni(110). *J. Phys. Chem. C* **2010**, *114*, 3003–3007.
- (13) Burema, S. R.; Bocquet, M.-L. Resonance Charges to Encode Selection Rules in Inelastic Electron Tunneling Spectroscopy. *J. Phys. Chem. Lett.* **2012**, *3*, 3007–3011.
- (14) Jiang, N.; Foley, E. T.; Klingsporn, J. M.; Sonntag, M. D.; Valley, N. A.; Dieringer, J. A.; Seideman, T.; Schatz, G. C.; Hersam, M. C.; Van Duyne, R. P. Observation of Multiple Vibrational Modes in Ultrahigh Vacuum Tip-Enhanced Raman Spectroscopy Combined with Molecular-Resolution Scanning Tunneling Microscopy. *Nano Lett.* **2012**, *12*, 5061–5067.
- (15) Zhao, J.; Feng, M.; Yang, J.; Petek, H. The Superatom States of Fullerenes and Their Hybridization into the Nearly Free Electron Bands of Fullerites. *ACS Nano* **2009**, *3*, 853–864.
- (16) Jorn, R.; Zhao, J.; Petek, H.; Seideman, T. Current-Driven Dynamics in Molecular Junctions: Endohedral Fullerenes. *ACS Nano* **2011**, *5*, 7858–7865.
- (17) Braun, K.-F.; Hla, S.-W. Probing the Conformation of Physisorbed Molecules at the Atomic Scale Using STM Manipulation. *Nano Lett.* **2005**, *5*, 73–76.
- (18) Alemani, M.; Peters, M. V.; Hecht, S.; Rieder, K.-H.; Moresco, F.; Grill, L. Electric Field-Induced Isomerization of Azobenzene by STM. *J. Am. Chem. Soc.* **2006**, *128*, 14446–14447.
- (19) Kuck, S.; Hoffmann, G.; Bröring, M.; Fecht, M.; Funk, M.; Wiesendanger, R. “Naked” Iron-5,10,15-triphenylcorrole on Cu(111): Observation of Chirality on a Surface and Manipulation of Multiple Conformational States by STM. *J. Am. Chem. Soc.* **2008**, *130*, 14072–14073.
- (20) Loth, S.; Etzkorn, M.; Lutz, C. P.; Eigler, D. M.; Heinrich, A. J. Measurement of Fast Electron Spin Relaxation Times with Atomic Resolution. *Science* **2010**, *329*, 1628–1630.
- (21) Loth, S.; Baumann, S.; Lutz, C. P.; Eigler, D. M.; Heinrich, A. J. Bistability in Atomic-Scale Antiferromagnets. *Science* **2012**, *335*, 196–199.
- (22) Robles, R.; Lorente, N.; Isshiki, H.; Liu, J.; Katoh, K.; Breedlove, B. K.; Yamashita, M.; Komeda, T. Spin Doping of Individual Molecules by Using Single-Atom Manipulation. *Nano Lett.* **2012**, *12*, 3609–3612.
- (23) Pfeiffer, W.; Sattler, F.; Vogler, S.; Gerber, G.; Grand, J. Y.; Möller, R. Photoelectron Emission in Femtosecond Laser Assisted Scanning Tunneling Microscopy. *Appl. Phys. B: Laser Opt.* **1997**, *64*, 265–268.
- (24) Gerstner, V.; Knoll, A.; Pfeiffer, W.; Thon, A.; Gerber, G. Femtosecond Laser Assisted Scanning Tunneling Microscopy. *J. Appl. Phys.* **2000**, *88*, 4851–4859.
- (25) Grafstrom, S. Photoassisted Scanning Tunneling Microscopy. *J. Appl. Phys.* **2002**, *91*, 1717–1754.
- (26) Lee, J.; Perdue, S. M.; Whitmore, D.; Apkarian, V. A. Laser-Induced Scanning Tunneling Microscopy: Linear Excitation of the Junction Plasmon. *J. Chem. Phys.* **2010**, *133*, 104706.
- (27) Dolocan, A.; Acharya, D. P.; Zahl, P.; Sutter, P.; Camillone, N. Two-Color Ultrafast Photoexcited Scanning Tunneling Microscopy. *J. Phys. Chem. C* **2011**, *115*, 10033–10043.
- (28) Knoesel, E.; Hertel, T.; Wolf, M.; Ertl, G. Femtosecond Dynamics of Electronic Excitations of Adsorbates Studied by Two-Photon Photoemission Pulse Correlation: CO/Cu(111). *Chem. Phys. Lett.* **1995**, *240*, 409–416.
- (29) Gruebele, M.; Zewail, A. H. Femtosecond Wave Packet Spectroscopy: Coherences, the Potential, and Structural Determination. *J. Chem. Phys.* **1993**, *98*, 883.
- (30) Petel, H.; Ogawa, S. Surface Femtochemistry: Observation and Quantum Control of Frustrated Desorption of Alkali Atoms from Noble Metals. *Annu. Rev. Phys. Chem.* **2002**, *53*, 507–531.
- (31) Tran, F.; Blaha, P. Accurate Band Gaps of Semiconductors and Insulators with a Semilocal Exchange-Correlation Potential. *Phys. Rev. Lett.* **2009**, *102*, 226401.
- (32) Thomas, J. R.; DeLeeuw, B. J.; Vacek, G.; Crawford, T. D.; Yamaguchi, Y.; Schaefer, H. F. The Balance between Theoretical Method and Basis Set Quality: A Systematic Study of Equilibrium Geometries, Dipole Moments, Harmonic Vibrational Frequencies, and Infrared Intensities. *J. Chem. Phys.* **1993**, *99*, 403.
- (33) Bündgen, P.; Grein, F.; Thakkar, A. J. Dipole and Quadrupole Moments of Small Molecules. An Ab Initio Study using Perturbatively Corrected, Multi-Reference, Configuration Interaction Wave Functions. *J. Mol. Struct.* **1995**, *334*, 7–13.
- (34) Yu, P.; Kirschner, J. Nanoscale Imaging of Photoelectrons using an Atomic Force Microscope. *Appl. Phys. Lett.* **2013**, *102*, 063111.
- (35) Mellau, G. C. The  $\nu_1$  Band System of HNC. *J. Mol. Spectrosc.* **2010**, *264*, 2–9.
- (36) Schwenzer, G. M.; O’Neil, S. V.; Schaefer, H. F., III; Baskin, C. P.; Bender, C. F. Geometries of the Excited Electronic States of HCN. *J. Chem. Phys.* **1974**, *60*, 2787.
- (37) Nayak, M. K.; Chaudhuri, R. K.; Krishnamachari, S. N. L. Theoretical Study on the Excited States of HCN. *J. Chem. Phys.* **2005**, *122*, 184323.
- (38) Drake, G. W. F. *Springer Handbook of Atomic, Molecular, and Optical Physics*; Springer: New York; 2005.
- (39) Oana, C. M.; Krylov, A. I. Dyson Orbitals for Ionization from the Ground and Electronically Excited States Within Equation-of-Motion Coupled-Cluster Formalism: Theory, Implementation, and Examples. *J. Chem. Phys.* **2007**, *127*, 234106.
- (40) Oana, C. M.; Krylov, A. I. Cross Sections and Photoelectron Angular Distributions in Photodetachment from Negative Ions using Equation-of-Motion Coupled-Cluster Dyson orbitals. *J. Chem. Phys.* **2009**, *131*, 124114.

## 4.2 E2: Nuclear-wave-packet dynamics mapped out by two-center interference in the $\text{HeH}^{2+}$ molecule

Interference effects are omnipresent in quantum mechanics and also play a fundamental role for the photoemission process. For instance, the constructive or destructive interference of the scattering pathways of the emitted electrons gives rise to typical oscillations in the absorption cross-section. One prominent example are the oscillations in the X-ray absorbance for a photon energy exceeding the threshold of core-level ionization, called extended X-ray absorption fine structure [183–185].

Photoemission from valence states is considerably more difficult to address, for the hybridization into molecular states (for molecules) or bands (for extended systems). The photoionization process can no longer be completely understood as the emission from one highly localized atomic orbital, but from the whole molecular wave-function, for which additional quantum numbers as the parity and the overall symmetry play a significant role. This leads not only to oscillations [186] in the total photoemission (or photoabsorption) cross-section, but also modifies the angular distribution of the emitted photoelectrons. The experimental observation of impact of interference effects on the PAD was reported in [187–190].

Our work [E2] focuses on how the molecular geometry is reflected in the PAD. Accurate calculations of the photoionization DCS are required hereby. In order to demonstrate the principles, we have chosen the  $\text{HeH}^{2+}$  molecule – in this case, the electronic (both bound and scattering) wave-functions can be treated exactly. Following the pump-probe scheme from subsec. 3.2.3, we compute the dynamics of the NWP after a resonant electronic transition and establish a direct link to the PAD. In particular, we demonstrate that the time-dependent NWP can be reconstructed from the angle-resolved photoelectron spectra. Even though the spatial interference is always present for photoemission from such molecules and is thus always included in an appropriate description, we specifically focus on this aspect as the main ingredient for the spatial resolution of the NWP dynamics. We propose that for more complex targets, the information extracted from the PAD can complement and assist other methods such as Coulomb explosion [162, 163, 191].

From the theoretical and computational point of view, most high-precision calculations for diatomic molecules rely on the expansion in prolate spheroidal coordinates that explicitly make use of the cylindrical symmetry. In view of more general applications, we do not constrain the representation of the electronic states to any symmetry, but use a general one-center expansion, albeit the convergence works best for targets whose symmetry deviates little from spherical symmetry. The advantage of this method is the direct availability of the PAD. In this respect, our work [E2] also served as proof-of-principle for our variant of computing the scattering amplitude – achieved by a generalization of the renormalized Numerov method – which we applied to more complex molecules, as well [E5].

**Nuclear-wave-packet dynamics mapped out by two-center interference in the  $\text{HeH}^{2+}$  molecule**

M. Schüler, Y. Pavlyukh, and J. Berakdar\*

*Institut für Physik, Martin-Luther-Universität Halle-Wittenberg, 06120 Halle, Germany*

(Received 18 February 2014; published 30 June 2014)

Photoemission from diatomic molecules closely resembles the Young-type double-slit experiment where each of the two atomic sites represents a coherent emission source. When the photoelectron wavelength becomes commensurate with the effective interatomic distance, the resulting spatial interference gives rise to oscillations in the photoionization total and differential cross sections. This phenomenon provides detailed information on the molecular geometry, a fact that can be utilized for probing the nuclear dynamics triggered by the interaction with a laser field. We demonstrate how this coherent wave-packet evolution can be traced by observing the photoelectron angular distribution. Based on *ab initio* scattering calculations we perform a proof-of-principle reconstruction of the nuclear-wave-packet evolution in the  $\text{HeH}^{2+}$  molecule.

DOI: [10.1103/PhysRevA.89.063421](https://doi.org/10.1103/PhysRevA.89.063421)

PACS number(s): 33.80.Be, 33.60.+q, 31.15.A-, 73.22.Dj

**I. INTRODUCTION**

The impressive experimental advance over recent years in generating ultrashort, high-energy coherent x-ray laser pulses enabled new insight in the electronic structure of extended solid-state systems, large biomolecules down to small molecules, and atoms, allying submolecular spatial with femtosecond temporal resolution [1–6]. In particular, the x-ray absorption (XAS) reveals detailed structural information, especially at the photon energy high enough to eject a core electron to the continuum. The subsequent multiple scattering of the photoelectron from the neighboring atoms and its interference gives rise to an oscillatory behavior of the x-ray absorbance, known as extended x-ray absorption fine structure, whose period is directly related to the structural arrangement of the sample [7,8].

Similar interference effects have also been predicted for the photoemission cross section of diatomic molecules [9], highlighting the analogy to the Young-type double-slit experiment. However, due to the typically smaller internuclear distance, tracing those oscillations has been a challenge, for it requires tuning the photon energy over several hundred electron volts [10–14]. Moreover, the hybridization of the atomic wave functions into molecular states gives rise to new effects, such as oscillations in the *angle-resolved* distribution of the emitted electrons as a function of energy, as well. The photoelectron angular distribution (PAD) strongly depends on the parity of the electron wave function and thus contains the signature of the respective angular momentum [14] or exhibits asymmetries due to the superposition of gerade and ungerade states [15,16].

On the other hand, diatomic molecules are convenient testing systems where important insights [17–19] in the nuclear dynamics can be gained either by means of (e.g., two-color) pump-probe techniques [20–22] or by recolliding electrons giving rise to higher harmonics generation [23]. For both scenarios, the fragmentation of the molecule after electron ejection by an ultrashort laser pulse—the Coulomb explosion (CE)—provides rich information on the initial or excited molecular configuration and even allows for reconstructing the

corresponding nuclear wave packet (NWP) [17,20–22,24,25]. Mapping out the NWP can be ambiguous for more complex targets due to the variety of accessible electronic channels; additionally measuring the PAD narrows down the number of pathways and improves the NWP reconstruction [25].

The simplest systems proving this kind of physics are the homonuclear dihydrogen cation  $\text{H}_2^+$  and the heteronuclear helium hydrogen double cation  $\text{HeH}^{2+}$ . Whereas the former allows for investigating the interference from identical atoms [26–28], the  $\text{HeH}^{2+}$  system provides an example of interference from different emission centers [29,30]. From the theoretical point of view, highly precise methods exploiting the axial symmetry of these molecules can further be employed as a basis for two-or-more-electron systems as, for example, for studying the ro-vibrational photodissociation of the  $\text{HeH}^+$  molecule [31–33].

The  $\text{HeH}^{2+}$  molecule, which is the system studied in this contribution, has a number of interesting electronic properties. Its ground electronic state ( $1s\sigma$ ) potential energy surface (PES) does not possess a minimum, such that the molecule dissociates right away in this state. In contrast, the first excited state ( $2p\sigma$ ) shows a metastable potential minimum (with the lifetime of 3.9 ns [34]). The equilibrium atom-atom separation of  $R = R_0 = 3.89$  a.u.  $\simeq 2.06$  Å [35,36] is twice as large as for the  $\text{H}_2^+$  molecule and thus requires only one-fourth of the photoelectron energy to achieve the same interference effects.

Our goal is to analyze the asymmetry of the photoemission probability in the direction of the hydrogen or the helium atom, respectively. Such asymmetries have also been observed for homonuclear systems (due to the Fano resonance of competing channels) and exploited for probing molecular wave-packet dynamics [16]. We demonstrate how the impact of the Young-type interference to the PAD can be related to the nuclear dynamics of the  $\text{HeH}^{2+}$  molecule upon optimized laser-induced electronic transitions, including the reconstruction of the dissociative wave functions (Sec. III). The latter becomes possible because of the rich information encoded in the PAD (compared to angle-independent quantities like the total photoabsorption cross section). Large-scale numerical studies of the coupled electron and nuclear and laser field degrees of freedom are accomplished by invoking the renormalized Numerov method [37], which we have employed for computing accurate bound states of large fullerene molecules in

\*jamal.berakdar@physik.uni-halle.de

previous studies [38]. We have extended the method (presented in Sec. II) to efficiently deal with unbounded states, making it well suited for a variety of scattering problems. We adopt atomic units consistently throughout the text.

## II. COMPUTATIONAL METHODS

Invoking the adiabatic approximation, the wave function in the combined electronic and nuclear Hilbert space can be expanded as [39]

$$\Psi(\mathbf{r}, R, t) = \sum_{\alpha} \chi_{\alpha}(R, t) \psi^{(\alpha)}(\mathbf{r}; R), \quad (1)$$

where  $\alpha$  labels electronic states parametrically dependent on the interatomic distance  $R$ . Inserting Eq. (1) into the time-dependent Schrödinger equation (TDSE) with the Hamiltonian [39]

$$H(t) = H_0 + V(t) = T_c(R) + T_e(\mathbf{r}) + V_{ec}(\mathbf{r}, R) + V_{cc}(R) + V_{el}(\mathbf{r}, t) + V_{cl}(R, t) \quad (2)$$

and projecting out the electronic part yields a standard coupled-channel evolution equation,

$$i \partial_t \chi_{\alpha}(R, t) = \sum_{\beta} \langle \psi^{(\alpha)} | H(t) | \psi^{(\beta)} \rangle \chi_{\beta}(R, t). \quad (3)$$

The first two terms in Eq. (2) describe the kinetic energy of the cores and electrons, respectively, whereas the next two terms stand for the Coulombic electron-core and the core-core interactions. Remaining time-dependent terms represent the interaction of the particles with the laser field, which is treated on the level of the dipole interaction. The matrix element  $\langle \psi^{(\alpha)} | H(t) | \psi^{(\beta)} \rangle$  in Eq. (3) (with the integration over  $\mathbf{r}$  only) reads

$$\langle \psi^{(\alpha)} | H(t) | \psi^{(\beta)} \rangle = -\frac{1}{2\mu} \frac{d^2}{dR^2} \delta_{\alpha\beta} + \mathcal{E}_{\alpha\beta}(R) - \mathcal{D}_{\alpha\beta}(R) E(t), \quad (4)$$

where the first term corresponds to the kinetic energy  $T_c(R)$  of the two-nuclei system with the reduced mass  $\mu$  and  $\mathcal{E}_{\alpha\beta}(R)$  captures three other time-independent operators in Eq. (2), while  $\mathcal{D}_{\alpha\beta}(R)$  describes the dipole elements and  $E(t)$  the electric field. The adiabatic approximation ignores derivatives of the electronic wave functions with respect to  $R$ , such that  $\mathcal{E}_{\alpha\beta}(R)$  become diagonal with the diagonal elements  $\mathcal{E}_{\alpha}(R)$  fulfilling the purely electronic eigenvalue condition for fixed  $R$ . The validity of the adiabatic approximation is constrained by the energy separation between different PESs [given by the  $R$ -dependent eigenvalues  $\mathcal{E}_{\alpha}(R)$ ]. Hence, a modification of this scheme becomes necessary in the vicinity of avoided crossings.

### A. Electronic states

As outlined above, finding the electronic eigenstates  $\psi^{(\alpha)}$  for all (fixed) values of  $R$  is the basic ingredient for solving for the molecular dynamics. We expand the wave functions in terms of the spherical harmonics:

$$\psi^{(\alpha)}(\mathbf{r}) = \sum_{\ell m} \frac{\phi_{\ell m}^{(\alpha)}(r)}{r} Y_{\ell m}(\hat{\mathbf{r}}). \quad (5)$$

Note that the dependence on  $R$  has been omitted for brevity. The origin of coordinate system is set at the geometric center of the molecule and the zenith is in the direction of the He atom. Inserting Eq. (5) into the Schrödinger equation yields the coupled-channel eigenvalue equation

$$\sum_{\ell' m'} \left[ -\frac{1}{2} \frac{d^2}{dr^2} \delta_{\ell \ell'} \delta_{m m'} + V_{\ell m \ell' m'}(r) \right] \phi_{\ell' m'}^{(\alpha)}(r) = \mathcal{E}_{\alpha} \phi_{\ell m}^{(\alpha)}(r), \quad (6)$$

where  $V_{\ell m \ell' m'}(r) = V_{cc}(R) \delta_{\ell \ell'} \delta_{m m'} + \langle \ell m | V_{ec} | \ell' m' \rangle$  is evaluated by expanding the Coulombic potentials in terms of Legendre polynomials followed by the Clebsch-Gordan algebra [40]. We note that the cylindrical symmetry of the molecule implies that the Hamiltonian is diagonal with respect to  $m$ , such that electronic states can be classified spectroscopically according to their phase change when rotating around the molecular axis.

In what follows, we represent all wave functions and operators by vectors and matrices which are spanned in the  $(\ell, m)$  space (marked as bold face). Thus, Eq. (6) can be cast into a general multichannel form,

$$\left\{ \frac{d^2}{dr^2} \mathbf{I} + 2[\mathcal{E} \mathbf{I} - \mathbf{V}(r)] \right\} \boldsymbol{\phi}(r) = 0. \quad (7)$$

The renormalized Numerov method [37] is then implemented as follows: The vector  $\boldsymbol{\phi}(r)$  expressed as a product of the fundamental solution matrix  $\boldsymbol{\Phi}(r)$  with a constant vector  $\mathbf{c}$  (to be determined). The coordinate  $r$  is now represented by an equidistant grid with the step size  $h$ . The basic idea is to eliminate the wave-function-like quantity  $\boldsymbol{\Phi}_n \equiv \boldsymbol{\Phi}(r_n)$  in favor of the ratio matrix  $\mathbf{R}_n$  relating the function's values at adjacent grid points. Let us denote

$$\mathbf{T}_n = -\frac{h^2}{6} [\mathcal{E} - \mathbf{V}(r_n)] \quad \text{and} \\ \mathbf{U}_n = (\mathbf{I} - \mathbf{T}_n)^{-1} (2\mathbf{I} + 10\mathbf{T}_n).$$

Applying Numerov's finite differences formula and substituting  $\mathbf{F}_n = [\mathbf{I} - \mathbf{T}_n] \boldsymbol{\Phi}_n$ , one finds

$$\mathbf{F}_{n+1} = \mathbf{R}_n \mathbf{F}_n, \quad (8)$$

where the ratio matrix obeys the recurrence relation,

$$\mathbf{R}_n = \mathbf{U}_n - \mathbf{R}_{n-1}. \quad (9)$$

Similar recursion relations can also be written for the backward propagation, as discussed in detail by Johnson [37]. Importantly, propagation of the ratio matrix is a very stable procedure, unlike working with the wave function itself. The benefits become evident in classically forbidden regions: Whereas the wave function contains an exponentially growing term that can possibly lower the precision, the ratio matrix varies only slowly. This can also be understood by the close relationship between the ratio matrix and the logarithmic derivative.

The energy eigenvalues are then found by choosing a matching point  $r_M$  and solving the recurrence relation Eq. (9) starting from the left and the right boundaries separately until  $r_M$  is reached. The continuity of the wave function and its first derivative at this point are the determining conditions for the energy eigenvalues. The search is performed by the Brent

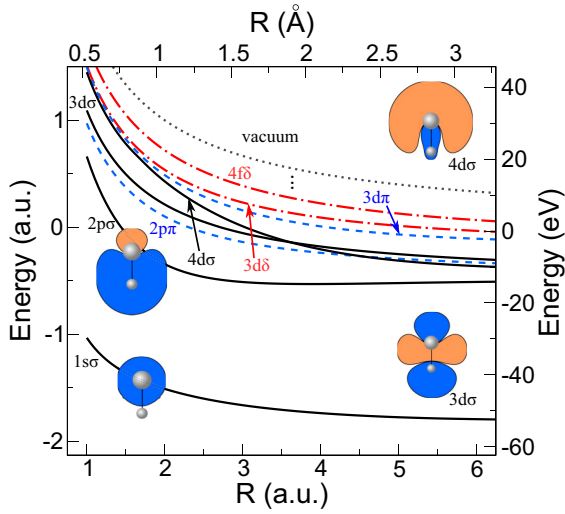


FIG. 1. (Color online) The PES of the first  $\sigma$  (solid black),  $\pi$  (dashed blue), and  $\delta$  (dot-dashed red lines) states along with their spectroscopic labels of the  $\text{HeH}^{2+}$  molecule as a function of interatomic distance  $R$ . The insets depict a cut through the  $\sigma$ -molecular orbitals with a plane parallel to the molecular axis (at the equilibrium distance). Blue color indicates positive values of  $\psi^{(\omega)}$  and orange negative values.

method for nondegenerate states and by the node-counting algorithm otherwise [38]. The actual wave function can easily be obtained from Eq. (8) once the energy is fixed.

Using the renormalized Numerov method, we have computed the first four eigenstates  $\psi^{(\omega)}(\mathbf{r}; R)$  for  $m = 0$  and lowest energy states for  $m = 1, 2$  for various values for  $R$ . The sum over  $\ell$  in Eq. (5) has been truncated at  $\ell_{\max} = 24$ , providing an accuracy of at least five digits for all eigenvalues. The PES  $\mathcal{E}_\alpha(R)$  for these states is shown in Fig. 1, along with an orbital representation of the corresponding wave functions.

## B. Scattering properties

In order to describe the photoemission from an (general) electronic state  $|\psi_0\rangle$  (initial energy  $\mathcal{E}_0$ ) within the weak-field approximation, an expansion in terms of the photon numbers proves to be particularly useful, which is nothing else but the Floquet series. Suppose the time-dependent Hamiltonian reads  $H(t) = H_0 + \{\delta H e^{-i\omega t} + \delta H^\dagger e^{i\omega t}\}$ , the projection on the different laser-dressed states with a particular photon number  $N$  yields the Floquet hierarchy [41],

$$[\mathcal{E}_0 + N\omega - H_0]|\psi_N\rangle = \delta H|\psi_{N-1}\rangle + \delta H^\dagger|\psi_{N+1}\rangle. \quad (10)$$

Note that the operator  $\delta H$  in Eq. (10) only allows for single-photon transitions. For low laser field intensity, Eq. (10) can be truncated at  $N = 1$ , such that we obtain the inhomogeneous or *driven Schrödinger equation* (DSE),

$$[\mathcal{E}_0 + \omega - H_0]|\psi^+\rangle = \delta H|\psi_0\rangle. \quad (11)$$

Here  $|\psi^+\rangle$  denotes the first-order correction to the initial wave function upon the irradiation with the laser field. Equation (11) is consistent with the standard time-dependent perturbation theory [42]. Solving DSE (11) with *outgoing boundary conditions* [42] (the superscript  $+$  has been added

for this reason) reproduces the scattering amplitude without the necessity of computing the transition matrix elements in perturbative treatments. Thus, it represents a very economical tool to study photoemission and related processes [43–45]. The only ingredient required is the asymptotic behavior of the scattering solution  $|\psi^+\rangle$ . For an electron subject to spherically symmetric short-range  $V_{\text{sh}}(r)$  and Coulomb  $Z/r$  potentials the asymptotic solution of Eq. (11) for a particular set  $(\ell, m)$  of angular momentum quantum numbers reads

$$\psi_{\ell m}^+(\mathbf{r}) \stackrel{V_{\text{sh}}(r) \rightarrow 0}{\sim} i^{-\ell} e^{-i\sigma_\ell(k)} \mathcal{F}_{\ell m}(k) H_\ell^+(kr; \eta) Y_{\ell m}(\hat{\mathbf{r}}), \quad (12)$$

where  $k = \sqrt{2(\mathcal{E}_0 + \omega)}$  is the photoelectron momentum,  $\sigma_\ell = \arg \Gamma(\ell + 1 + i\eta)$  the Coulomb phase shift, and  $\eta = Z/k$  the Sommerfeld parameter. The Hankel function [46], Sec. 32.2.11  $H_\ell^+(kr; \eta) = iF_\ell(kr; \eta) + G_\ell(kr; \eta)$  (where  $F_\ell$  and  $G_\ell$  are the regular and the irregular Coulomb functions, respectively) ensures the purely outgoing asymptotic properties. The scattering amplitude  $\mathcal{F}_{\ell m}(k)$  includes all the scattering phase shifts from  $V_{\text{sh}}(r)$  and therefore completely determines the PAD.

For our specific case of the  $\text{HeH}^{2+}$  molecule, asymptotic solutions can also be easily constructed: At sufficiently large distances  $r > r_C$  from the molecule the one-center approximation is valid and it suffices to take the first term  $-3/r$  from the multipole expansion of the Coulomb potential. The outgoing wave takes a form of Eq. (12) with  $Z = 3$ . A particular choice of  $r_C$  was found to have little influence on the final results, and we set  $r_C = 80$  a.u. as the cutoff distance.

In order to numerically determine for a given initial state  $\psi_0(\mathbf{r})$  the yet unknown scattering amplitude  $\mathcal{F}_{\ell m}(k)$ , we generalize (similar to Ref. [48]) the renormalized Numerov method from Sec. II A to incorporate the driving term [cf. Eq. (11)]. This can easily be achieved by extending Eq. (8) to

$$\mathbf{F}_{n+1} = \mathbf{R}_n \mathbf{F}_n + \mathbf{b}_n, \quad (13)$$

with the ratio matrix  $\mathbf{R}_n$  still obeying Eq. (9), whereas the additional vector  $\mathbf{b}_n$  satisfies the recurrence relation

$$\mathbf{b}_n = \frac{\hbar^2}{12} [\mathbf{s}(r_{n+1}) + 10\mathbf{s}(r_n) + \mathbf{s}(r_{n-1})] - \mathbf{R}_{n-1}^{-1} \mathbf{b}_{n-1}. \quad (14)$$

The function  $\mathbf{s}(r)$  is the vector representation (with respect to the spherical harmonics) of  $\delta H \psi_0(\mathbf{r}) = -(\mathbf{E}_0 \cdot \mathbf{r}) \psi_0(\mathbf{r})$ ; i.e., it describes the interaction of the electron with linearly polarized light with the electrical field of amplitude  $\mathbf{E}_0$  within the dipole approximation. Note that instead of propagating all linearly independent vectors spanning the space of possible initial derivatives as in Eq. (8), for the driven equation it is sufficient to start with already known bound state and, thus, propagate only *one* vector [Eq. (13)]. This is consistent with the loss of arbitrariness of the normalization in the case of DSE.

The numerical scheme now runs as follows. (i) Equations (9) and (14) are propagated from  $r = 0$  to  $r = r_C$ . This procedure yields  $\mathbf{R}_C$  and  $\mathbf{b}_C$ . (ii) The scattering amplitude  $\mathcal{F}_{\ell m}(k)$  can now be found by comparing  $\mathbf{R}_C$  with known asymptotic solutions  $\tilde{\mathbf{R}}_C$ . As Eq. (12) demonstrates the ratio matrix  $\tilde{\mathbf{R}}_C$  in the asymptotic limit does not mix different components; i.e., it is diagonal. Therefore, it can be constructed from the known asymptotic solution at two adjacent grid



points,

$$\begin{aligned}\tilde{\mathbf{R}}_C &= \tilde{\mathbf{F}}_{C+1} \tilde{\mathbf{F}}_C^{-1} \\ &= [\mathbf{I} - \mathbf{T}_{C+1}] \text{diag} \left\{ \frac{H_\ell^+(kr_{C+1}; \eta)}{H_\ell^+(kr_C; \eta)} \right\}_{\ell m} [\mathbf{I} - \mathbf{T}_C]^{-1}.\end{aligned}$$

(iii) Imposing the continuity condition yields

$$\mathbf{F}_{C+1} = \tilde{\mathbf{R}}_C \mathbf{F}_C = \mathbf{R}_C \mathbf{F}_C + \mathbf{b}_C. \quad (15)$$

This equation makes it possible to determine  $\mathbf{F}_C$  and thus the scattering wave function at  $r_C$ . The desired scattering amplitude  $\mathcal{F}_{\ell m}(k)$  is then obtained by the comparison with Eq. (12).

Hence, the outlined procedure does not require exact scattering wave functions for the calculation of scattering amplitudes. Only a single outward propagation (for fixed photoelectron energy) is necessary to compute  $\mathcal{F}_{\ell m}(k)$ .

### C. Diabatic representation

Figure 1 reveals the existence of a crossing point at  $R_{\text{cr}} = 3.595$  a.u. between the  $\psi^{(3d\sigma)}$  and the  $\psi^{(4d\sigma)}$  states, which is in fact an avoided crossing with a gap energy  $\mathcal{E}_{4d\sigma}(R_{\text{cr}}) - \mathcal{E}_{3d\sigma}(R_{\text{cr}}) = 2.6467 \times 10^{-3} \simeq 72$  meV. The small energy separation hence necessitates a transformation from the adiabatic to the diabatic representation to account for the coupling of the two PESs. The adiabatic transition of the state  $\psi^{(3d\sigma)}$  to  $\psi^{(4d\sigma)}$  can be pictured by the upper negative (orange) lobe of the orbital corresponding to  $\psi^{(3d\sigma)}$  (see Fig. 1) moving downwards, as the negative lobe is “squeezed” out to resemble the shape of  $\psi^{(4d\sigma)}$ . We determine the diabatic surfaces  $\mathcal{E}_{ij}^D(R)$ ,  $i, j = 1, 2$ , by a simple interpolation technique; that is, we impose  $\mathcal{E}_{11}^D(R_{\text{cr}}) = \mathcal{E}_{22}^D(R_{\text{cr}}) = [\mathcal{E}_{4d\sigma}(R_{\text{cr}}) + \mathcal{E}_{3d\sigma}(R_{\text{cr}})]/2$  and  $\mathcal{E}_{11}^D(R)[\mathcal{E}_{22}^D(R)] \rightarrow \mathcal{E}_{3d\sigma}(R)[\mathcal{E}_{4d\sigma}(R)]$  as  $|R - R_{\text{cr}}|$  grows. The actual transformation is accomplished by the rotation

$$\mathcal{U}^\dagger(R) \begin{pmatrix} \mathcal{E}_{11}^D(R) & \mathcal{E}_{12}^D(R) \\ \mathcal{E}_{12}^D(R) & \mathcal{E}_{22}^D(R) \end{pmatrix} \mathcal{U}(R) = \begin{pmatrix} \mathcal{E}_{3d\sigma}(R) & 0 \\ 0 & \mathcal{E}_{4d\sigma}(R) \end{pmatrix}, \quad (16)$$

where

$$\mathcal{U}(R) = \begin{pmatrix} \cos \Omega(R) & \sin \Omega(R) \\ -\sin \Omega(R) & \cos \Omega(R) \end{pmatrix}. \quad (17)$$

Together with the aforementioned conditions, solving Eq. (16) allows for interpolating  $\Omega(R)$  and thus yields the diagonal and off-diagonal diabatic PESs. Once  $\mathcal{U}(R)$  is known, calculations can be performed within the diabatic basis. Observables are computed by the corresponding backwards transformation.

All following calculations are carried out in cylindrical symmetry, as we take the laser polarization  $\mathbf{E}_0$  along the molecular axis. Hence, the (not avoided) crossing of the  $\sigma$  orbitals with the  $2p\pi$  state does not require special treatment as  $\pi \leftrightarrow \sigma$  dipolar transitions are forbidden by the symmetry selection rules.

### III. PUMP-PROBE INTERFERENCE SPECTROSCOPY

Within a simple LCAO model [49] for the initial states and plane waves (PWs) as the final states, the PAD takes the form

$$\frac{dP}{d\Omega} \propto (\boldsymbol{\epsilon} \cdot \mathbf{k})^2 [A(\mathbf{k}) + B(\mathbf{k}) \cos(\mathbf{k} \cdot \mathbf{R})], \quad (18)$$

where  $\boldsymbol{\epsilon}$  denotes the polarization direction of the laser field,  $\mathbf{k}$  is the photoelectron momentum, while  $\mathbf{R}$  is a vector along the molecular axis with length  $R$ . The parameters  $A(\mathbf{k})$  and  $B(\mathbf{k})$  are determined by shape of orbitals in momentum space. The interference term in Eq. (18) suggests a close connection between the PAD and the molecular geometry, a dependence that can be exploited for tracing the nuclear dynamics. Additionally, the photoelectron energy can also be tuned, providing even more information. We stress that an accurate treatment of both the initial and moreover the final states is required for correct angular distributions [27]; projecting on PWs excludes a class of transition channels due to the wrong parity properties [30].

We invoke two approximations for the photoionization process: (i) the sudden approximation, that is, the photoelectron is not influenced by the molecule dynamics after the liberation, and (ii) the spectral resolution of laser pulse is fine enough to resonantly separate the different PESs. Under these assumptions, the PAD for the total state  $\Psi_\alpha(\mathbf{r}, R, t) = \chi_\alpha(R, t) \psi^{(\alpha)}(\mathbf{r}; R)$  reads

$$\frac{dP_\alpha}{d\Omega d\mathbf{k}} = \int dR \left| \sum_{\ell m} (-i)^\ell e^{i\sigma_\ell(k)} \mathcal{F}_{\ell m}^{(\alpha)}(k; R) Y_{\ell m}(\hat{\mathbf{k}}) \right|^2 n_\alpha(R, t), \quad (19)$$

where the scattering amplitude  $\mathcal{F}_{\ell m}^{(\alpha)}(k; R)$  for an initial electronic state  $\psi^{(\alpha)}$  is computed using the methods from Sec. II B.  $n_\alpha(R, t) = |\chi_\alpha(R, t)|^2$  is the probability density of finding the NWP at the position  $R$  at time  $t$  when electronic state of the system is given by  $\psi^{(\alpha)}$ .

For utilizing the interference phenomenon to probe the molecule wave function, we take the laser polarization axis along the molecule axis and consider photoemission in a small cone around that direction. In this way, the emitted electrons are most likely influenced by *one* of the atoms as they propagate to infinity (Fig. 2). In order to follow the nuclear dynamics we propose to use a typical pump-probe scheme [18, 19, 50]: A femtosecond laser pulse induces electronic transitions that subsequently drive the vibrational or dissociative dynamics of the molecule. The latter is then probed by a short pulse that promotes the electron in a scattering state. The probe-pulse needs to contain a sufficient number of optical cycles in order to address the system resonantly. Varying the delay  $\Delta t$  between the two pulses then makes it possible to monitor the evolution of  $n_\alpha(R, \Delta t)$ . As the observable we chose the integrated probability to detect a photoelectron within the detector angle  $\theta_D$  either in the forward or the backward direction (see Fig. 2):

$$P_\alpha^F = \int_0^{2\pi} d\phi \int_0^{\theta_D} \sin \theta \frac{dP_\alpha}{d\Omega d\mathbf{k}}, \quad (20a)$$

$$P_\alpha^B = \int_0^{2\pi} d\phi \int_{\pi-\theta_D}^\pi \sin \theta \frac{dP_\alpha}{d\Omega d\mathbf{k}}. \quad (20b)$$

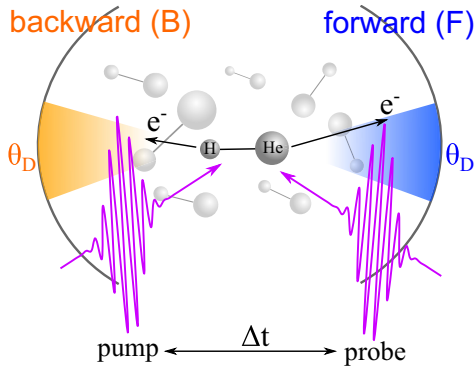


FIG. 2. (Color online) In the proposed setup for the pump-probe interference spectroscopy we only consider oriented molecules and allow for the photoelectron detection only within the acceptance angle  $\theta_D$ . The time delay  $\Delta t$  between the pump and the probe pulses serves as the reference time for the induced dynamics.

In what follows we fix  $\theta_D = 0.2\pi = 36^\circ$ .

### A. Interference profiles

Before we describe how the NWP dynamics triggered by the electronic excitation is reflected in the PAD, it is instructive to discuss the photoemission properties for a *fixed* geometry first [i.e., the averaging with respect to the nuclear wave function in Eq. (19) is ignored]. The forward (backward) emission probability  $P_\alpha^F$  ( $P_\alpha^B$ ) for  $1s\sigma$ ,  $2p\sigma$ , and  $3d\sigma$  and  $4d\sigma$  states is depicted in Figs. 3–5, respectively. The magnitude of the electrical field is set to  $|\mathbf{E}_0| = 0.01$  a.u., which corresponds to an intensity of  $\sim 3.5 \times 10^{12}$  W cm $^{-2}$ . Conceptually, the pulse is infinitely long; estimating, however, that the resonance condition is matched within ten optical cycles, the minimum temporal length is about 1.0 fs for the photoelectron energies

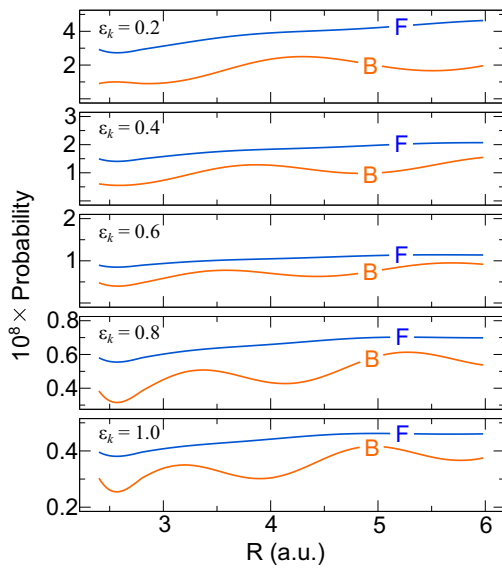


FIG. 3. (Color online) The emission probability  $P_{1s\sigma}^F$  (blue lines, marked with F) and  $P_{1s\sigma}^B$  (orange lines, marked with B) according to Eq. (20) for fixed values of  $R$ . The photoelectron energy  $\varepsilon_k$  is displayed in each panel.

studied here. Let us consider the photoemission from the  $1s\sigma$  state first (Fig. 3). Depending on the energy of the photoelectron  $\varepsilon_k = k^2/2$ , the probability for the emission in the direction of the hydrogen atom shows an oscillatory behavior for varying  $R$ . In contrast, the emission in the He direction demonstrates only slight increase of probability with increasing  $R$ . These features are easily understood in terms of the wave function  $\psi^{(1s\sigma)}$  (cf. the inset in Fig. 1). The helium atom carries most of the electron density; as  $R \rightarrow \infty$  the electron becomes completely localized around its nucleus ( $\text{He}^+ + \text{H}^+$ ). This density localization leads to an enhanced photoemission probability. On the other hand, the photoelectrons are not subject to any additional scattering when being emitted in the forward direction (i.e., no interference effects occur); interference effects come into play only for the backward (hydrogen) direction. The distance between the minima and the maxima is reduced with raising  $\varepsilon_k$  (as expected physically). The dependence is, in fact, square-root-like, but deficiencies of the explanation provided by the LCAO + PW model [Eq. (18)] become immediately apparent.

The situation is reversed for the  $2p\sigma$  state (Fig. 4). Unlike the  $1s\sigma$  state, the  $2p\sigma$  PES asymptotically describes the dissociation into  $\text{H} + \text{He}^{2+}$ ; i.e., the electron remains bound to the hydrogen atom. As a consequence, the photoemission in the backward direction is slightly larger than in the helium direction and shows more pronounced interference features. However, the localization of the electron density is not as strong as for the  $1s\sigma$  state for the internuclear distance around the equilibrium value. Therefore, the forward emission is subject to the spatial interference as well. Even though the  $\text{HeH}^{2+}$  molecule lacks the inversion symmetry, certain parity effects that occur for inversion-symmetric systems ( $\text{H}_2^+$ , for example) can also be observed here. Comparing Fig. 4 to Fig. 3 shows a phase shift between the two sets of curves. If we

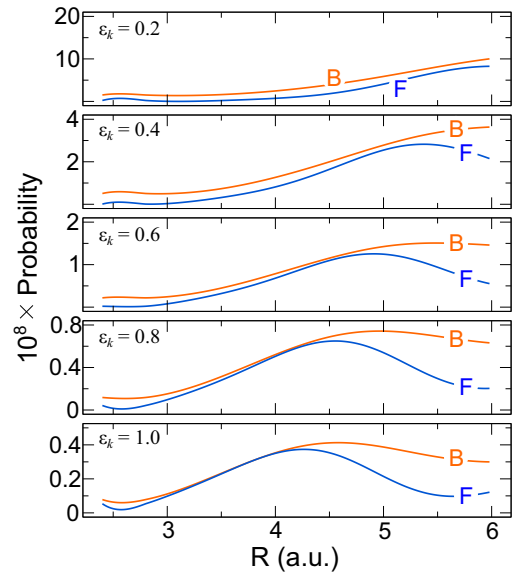


FIG. 4. (Color online) The emission probability  $P_{2p\sigma}^F$  (blue lines, marked with F) and  $P_{2p\sigma}^B$  (orange lines, marked with B) according to Eq. (20) for fixed values of  $R$ . The photoelectron energy  $\varepsilon_k$  is displayed in each panel.

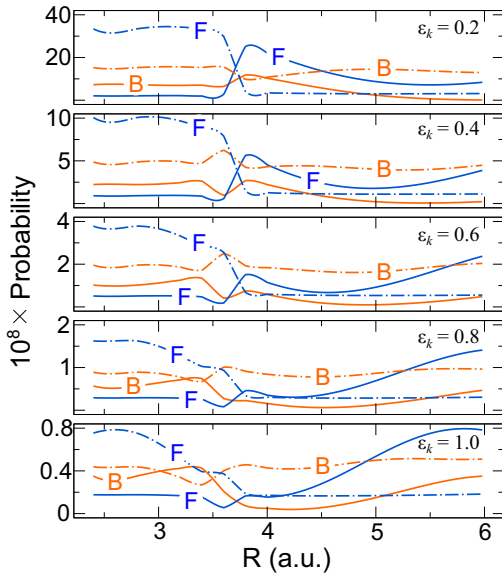


FIG. 5. (Color online) The emission probability  $P_{\alpha}^F$  (blue lines, marked with F) and  $P_{\alpha}^B$  (orange lines, marked with B) for the  $3d\sigma$  (solid lines) and the  $4d\sigma$  initial state (dot-dashed lines) for fixed values of  $R$ . The diabatic representation (Sec. II C) has been used to interpolate in the vicinity of the crossing point. The photoelectron energy  $\varepsilon_k$  is displayed in each panel.

follow, for instance, the first maximum of  $P_{1s\sigma}^B$  upon increasing  $\varepsilon_k$  we notice that  $P_{2p\sigma}^F$  has an almost sine-like behavior at those  $R$  points. This is consistent with a phase change of the wave function from positive to negative values when going along the molecule axis (cf. Fig. 1). However, as the parity is not defined for  $\text{HeH}^{2+}$ , the explained dependence is only approximate.

The behavior of probability profiles for the  $3d\sigma$  and the  $4d\sigma$  states (Fig. 5) can be understood as a mixture of the profiles of the two lower states. For  $R > R_{\text{cr}}$ ,  $P_{3d\sigma}^F$  and  $P_{3d\sigma}^B$  are almost parallel, but with  $P_{3d\sigma}^F > P_{3d\sigma}^B$ . This becomes clear by noting that  $\psi^{(3d\sigma)}$  is almost symmetrical with respect to the geometric center of the molecule (Fig. 1), while the majority of the localization probability is situated in the lower half. Interpreting the phase relation as for the  $2p\sigma$  state is, however, not feasible since the electron emission can also take place the “middle” of the molecule and not only from the atom sites. The  $4d\sigma$  state, on the other hand, has a node close to the position of the He atom, that is, positive and negative phase contributions close to each other that reduce the interference variations.

### B. Nuclear-wave-packet dynamics

With the physical understanding of the interference phenomenon for photoionization of the  $\sigma$  states (Sec. III A) at our disposal, we can now draw our attention to the manifestation of the NWP dynamics. The molecule is assumed to be initially in the  $\Psi_{2p\sigma}(\mathbf{r}, R) = \chi_{2p\sigma}(R)\psi^{(2p\sigma)}(\mathbf{r}; R)$  quantum state where  $\chi_{2p\sigma}(R)$  is the nuclear ground state with respect to  $\mathcal{E}_{2p\sigma}$  PES. With the laser polarization oriented along the molecule axis, the only possible excitation channels are the  $\sigma$  states. We solve Eq. (3) inserting a Gaussian-shaped pump laser pulse  $E(t) = E_{\text{pump}}e^{-(t-t_m)^2/2T_p^2} \cos[\omega(t-t_m)]$  such that the central

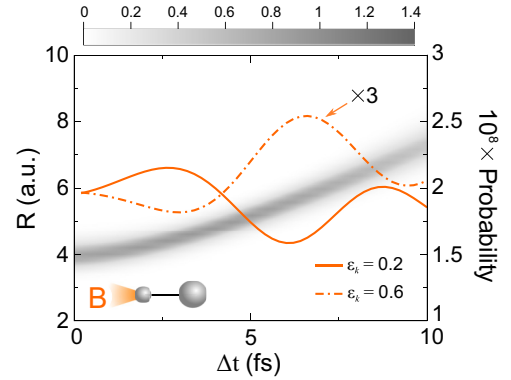


FIG. 6. (Color online) The NWP evolving in the PES  $\mathcal{E}_{1s\sigma}$  after the pump pulse (see text). The grayscale map in the background depicts the NWP density  $n_{1s\sigma}(R, \Delta t)$ , while the overlaid graphs show the emission probability  $P_{1s\sigma}^B$  evaluated by Eq. (20) for  $\varepsilon_k = 0.2$  a.u. (solid line) and  $\varepsilon_k = 0.6$  a.u. (dot-dashed line). The latter has been multiplied by 3.0 to make it comparable with the solid line.

frequency  $\omega$  matches the  $2p\sigma \rightarrow 1s\sigma$  resonant transition at  $R = R_0 = 3.89$  a.u. The pulse duration  $T_p$  was chosen to be as small as possible under the constraint that only the target PES lies in its spectral range. The laser amplitude was optimized to have the largest possible population transfer.

For transition  $\psi^{(2p\sigma)} \rightarrow \psi^{(1s\sigma)}$  the pump field amplitude amounts to  $E_{\text{pump}} = 0.5$  a.u. (corresponds to peak intensity  $I_{\text{pump}} = 8.8 \times 10^{15} \text{ W cm}^{-2}$ ) and  $T_p = 0.5$  fs. With these parameters, the population transfer takes place in about 0.8 fs, a time scale on which the nuclear dynamics is basically frozen. For this reason, we present only the wave-packet dynamics after the population has been transferred; i.e., the origin of the time delay  $\Delta t$  (see Fig. 2) is set to 1.0 fs. As  $\mathcal{E}_{1s\sigma}(R)$  is purely repulsive, the resulting wave-packet dynamics (Fig. 6) is dissociative.

Within 10 fs, the NWP moves outwards in an almost classical fashion (that is, the spreading remains approximately constant). Therefore, the expectation value  $\langle \chi_{1s\sigma}(\Delta t) | R | \chi_{1s\sigma}(\Delta t) \rangle$  is a suitable quantity that can be compared to the interference profiles in Fig. 3. For  $\varepsilon_k = 0.2$  a.u., the emission probability has a maximum around  $R = 4.2$  a.u. and a minimum around  $R = 5.5$  a.u., which can also be seen in Fig. 6, as the wave packet evolves. Taking  $\varepsilon_k = 0.6$  a.u. instead turns the minimum (approximately) into a maximum, as present in Fig. 6, too. Hence, selecting certain values for the energy of the photoelectron makes it possible to focus on distinct regions in the  $R$  space where the photoemission is enhanced.

Even with optimal parameters, only about 90% of the ground-state population is transferred to the  $1s\sigma$  state. Due to the  $R$  dependence of the transition matrix element and the energy separation, the remaining nuclear wave function  $\chi_{2p\sigma}(R, \Delta t = 0)$  is (apart from having a smaller norm) shifted with respect to the vibronic ground state, launching a purely bound oscillatory dynamics (Fig. 7).

Within the region  $3.0 < R < 5.0$ , both the forward and the back emission probability have an almost linear slope for  $\varepsilon_k = 0.4$  a.u. (see Fig. 4). Therefore, the detected signal is a good measure of the expectation value

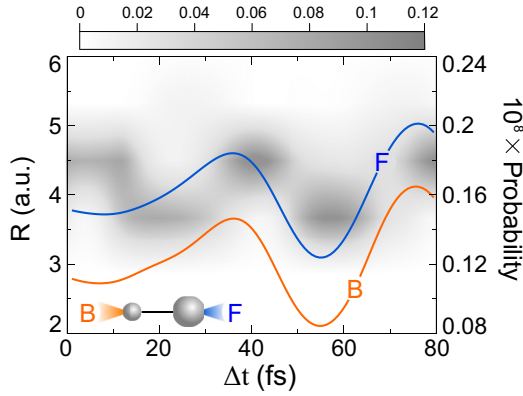


FIG. 7. (Color online) The NWP evolving in the PES  $\mathcal{E}_{2p\sigma}$  after the pump pulse (see text). The grayscale map in the background depicts the nuclear wave function density  $n_{2p\sigma}(R, \Delta t)$ , while the overlaid graphs show the forward (blue) and backward (orange) emission probability according to Eq. (20). The photoelectron energy amounts to  $\varepsilon_k = 0.4$ .

$\langle \chi_{2p\sigma}(\Delta t) | R | \chi_{2p\sigma}(\Delta t) \rangle$ , which should undergo a nearly harmonic time dependence. This is confirmed by Fig. 7 (overlaid graphs), which depicts  $P_{2p\sigma}^{F/B}$  as a function of  $\Delta t$ .

In order to target the  $3d\sigma$  state instead one needs to account for a smaller energy separation between the PESs and correspondingly adjust the pump-pulse parameters. Because it is not possible to separately address  $\psi^{(3d\sigma)}$  and  $\psi^{(4d\sigma)}$  states, Eq. (3) is solved using the *diabatic* representation, taking  $\omega = [\mathcal{E}_{11}^D(R_0) + \mathcal{E}_{22}^D(R_0)]/2$ . We found that  $T_p = 1.0$  fs provides a good compromise between a fast transfer and sufficient spectral sharpness, while  $E_{\text{pump}} = 0.08$  a.u. ( $I_{\text{pump}} \simeq 2.2 \times 10^{14}$  W cm $^{-2}$ ) serves for an optimal population transfer. However, the electron remains with more than 70% probability in the  $2p\sigma$  state. The transition can be imagined as “drilling” a Gaussian-shaped hole into the nuclear ground state, separating  $\chi_{2p\sigma}(R, \Delta t)$  into an “inner” and an “outer” wave packet. The latter one is dissociating, whereas the inner wave packet performs small oscillations. Because both  $3d\sigma$  and  $4d\sigma$  PESs are strongly repulsive, the transferred wave packets quickly propagate out of the crossing region, and we can safely identify them with  $\chi_{3d\sigma}(R, \Delta t)$  [or  $\chi_{4d\sigma}(R, \Delta t)$ ] corresponding to the electronic state  $\psi^{(3d\sigma)}$  (or  $\psi^{(4d\sigma)}$ ). The majority of the population is found in the  $3d\sigma$  state, which, similarly to Fig. 6, gives rise to a fast dissociation dynamics (Fig. 8). Since we can no longer regard the nuclei as frozen during the time when the pump field is switched on, Fig. 8 depicts the full dynamics starting from zero population in the  $3d\sigma$  state. The time delay  $\Delta t$  is in this case measured from 3.0 fs before the peak field is reached (bottom panel in Fig. 8). The photoemission requires a sufficient separation between the initial states in order to be able to resolve them. Therefore, the population transfer dynamics for  $\Delta t < 5$  fs in Fig. 8 cannot be observed in such an experiment (Fig. 8 only includes the  $3d\sigma$  state). For  $\Delta t > 5$  fs the NWP completely leaves the crossing region and can be treated within the *adiabatic* approximation. Again, we can pick certain values for  $\varepsilon_k$  in order to extract different features of the wave packet (see Fig. 5). Choosing  $\varepsilon_k = 0.2$  a.u. allows for tracing the evolving wave function in the region around

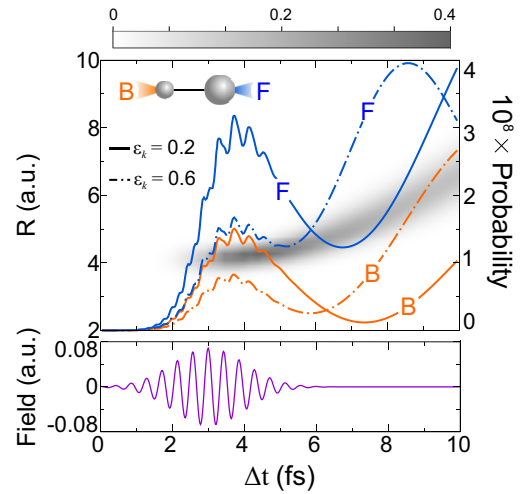


FIG. 8. (Color online) The electronic population and the NWP dynamics in the coupled-channel diabatic PES  $\mathcal{E}_{ij}^D$ ,  $i, j = 1, 2$  as functions of time. The grayscale map in the background depicts the nuclear wave function density  $n_1(R, \Delta t)$  [which is identical to  $n_{3d\sigma}(R, \Delta t)$  for  $\Delta t \gtrsim 5$  fs], while the overlaid graphs show the forward (blue) and backward (orange) emission probability according to Eq. (20). The photoelectron energy amounts to  $\varepsilon_k = 0.2$  a.u. (solid lines) and  $\varepsilon_k = 0.6$  a.u. (dot-dashed lines).

$R = 5.5$  a.u., where the emission probability shows a dip, and to observe the respective increase when moving outwards. Similarly, setting  $\varepsilon_k = 0.6$  a.u. shifts the emission maximum in the forward direction to smaller values of  $R$ , such that the region around  $R = 7$  a.u. is probed.

### C. Nuclear-wave-packet reconstruction

The dependence of the photoemission probabilities on the photoelectron energy enables us to extract even richer information, provided the laser frequency  $\omega$  can be tuned fine enough. We demonstrate here that not only certain expectation values, but the whole NWP density can be reconstructed from the mentioned energy dependence. This procedure works well when a bounded region where the wave packet is currently localized, can be estimated. This can be achieved by the analysis of Secs. III A and III B. Choosing  $\varepsilon_k$  such that the  $R$  dependence of the interference profiles is adequately described by a parabola, the corresponding photoemission probabilities with respect to a NWP  $\chi_\alpha(R, t)$  allow for determining the expectation values of  $R$  and  $R^2$ , from which the width of the wave packet can be estimated. Once this is done, the function  $n_\alpha(R, t) = |\chi_\alpha(R, t)|^2$  (for a fixed time) can be obtained by solving the integral equation corresponding to Eq. (19). We, however, found it more convenient to work with the relative forward photoemission rate

$$\tilde{P}_\alpha^F = \frac{P_\alpha^F}{P_\alpha^F + P_\alpha^B} \quad (21)$$

instead, in order to eliminate the reduction of the probability for increasing  $\varepsilon_k$ . Equations (19) and (20) imply the integral

equation

$$\tilde{\mathcal{P}}_{\alpha}^{\text{F}}(\varepsilon_k) = \int dR K^{\text{F}}(\varepsilon_k, R) n_{\alpha}(R, t) \quad (22)$$

with a kernel

$$K^{\text{F}}(\varepsilon_k, R) = \frac{\mathcal{P}_{\alpha}^{\text{F}}(\varepsilon_k, R)}{\mathcal{P}_{\alpha}^{\text{F}}(\varepsilon_k, R) + \mathcal{P}_{\alpha}^{\text{B}}(\varepsilon_k, R)}. \quad (23)$$

The functions  $\mathcal{P}_{\alpha}^{\text{F/B}}$  in Eq. (23) are defined as

$$\begin{aligned} \mathcal{P}_{\alpha}^{\text{F}}(\varepsilon_k, R) &= \int_0^{2\pi} d\phi \int_0^{\theta_{\text{D}}} d\theta \sin\theta \\ &\times \left| \sum_{\ell m} (-i)^{\ell} e^{i\sigma_{\ell}(k)} \mathcal{F}_{\ell m}^{(\alpha)}(k; R) Y_{\ell m}(\hat{\mathbf{k}}) \right|^2 \end{aligned} \quad (24)$$

(and  $\mathcal{P}_{\alpha}^{\text{B}}$  analogously). In order solve Eq. (22) for the NWP density, we discretize the  $R$  coordinate (into  $N$  points) in the region  $R_{\text{min}} \leq R \leq R_{\text{max}}$ , where the wave packet is localized and approximate the integration (22) by the trapezoidal rule in order to obtain a system of  $M$  linear equations,

$$\tilde{\mathcal{P}}_{\alpha}^{\text{F}}(\varepsilon_{k_i}) = \sum_{j=1}^N w_j K^{\text{F}}(\varepsilon_{k_i}, R_j) n_{\alpha}(R_j, t), \quad i = 1, \dots, M, \quad (25)$$

where the weights  $w_1 = w_N = (R_{\text{max}} - R_{\text{min}})/2N$  and  $w_j = (R_{\text{max}} - R_{\text{min}})/N$  otherwise. It is clear that we need  $M \geq N$  values for  $\varepsilon_k$  to solve Eq. (25).

We have approximated the kernel Eq. (23) by a simple fifth-order polynomial in  $\varepsilon_k$  and  $R$  and computed  $\tilde{\mathcal{P}}_{\alpha}^{\text{F}}(\varepsilon_k)$  for  $M = 40$  values for the photoelectron energy, distributed equidistantly in the interval  $0.2 \leq \varepsilon_k \leq 1.0$ . Solving Eq. (25) directly is, however, troublesome due to a nearly singular coefficient matrix  $K^{\text{F}}(\varepsilon_{k_i}, R_j)$ . This problem can be avoided by reformulating Eq. (25) in terms of a minimization problem, where we have added a term suppressing oscillatory solutions. This leads to a numerically stable procedure for the reconstruction of the dissociative wave packets. A typical result is presented in Fig. 9. Unfortunately, finer structures could not be resolved, as can be seen, for instance, by  $|\chi_{3d\sigma}(R, t = 4 \text{ fs})|^2$  and the respective reconstructed density. However, more observables (possibly the complete PAD) can be added to the reconstruction algorithm to improve its accuracy. We propose it as a new technique for mapping NWP or to complement and support CE experiments.

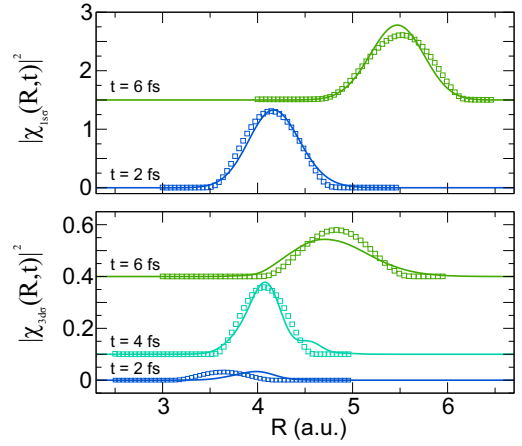


FIG. 9. (Color online) Comparison between the original NWP densities and the reconstruction for the  $1s\sigma$  (top panel) and the  $3d\sigma$  state (bottom panel) (see also Figs. 6 and 8) for different times. The solid lines are the original wave packets, whereas the squares in the corresponding color represent the reconstructed solutions. The curves for  $t > 2$  fs have been shifted upwards for better visibility.

#### IV. CONCLUSIONS

In summary, a detailed study of the photoionization of the  $\text{HeH}^{2+}$  molecule in the weak-field regime has been performed. We have shown how the forward and backward photoemission rates (with respect to the molecular axis parallel to the laser polarization) depend on the interatomic distance and explained their oscillatory behavior by the interference effects. For the proposed pump-probe experimental setup we have computed the evolution of the NWP triggered by electron transitions (pump pulse) and its manifestation in the photoemission (probe pulse). Provided that the probe-pulse frequency can be tuned over a moderate energy range, the relative forward emission rate contains even more information and allows for reconstructing the NWP dynamics. Our proof-of-principle calculations demonstrate the feasibility of such an approach provided scattering cross sections can be precisely computed and measured.

#### ACKNOWLEDGMENTS

This work is supported by the DFG under Grants No. SFB762 and No. PA 1698/1-1. Consultation with R. Moshhammer is gratefully acknowledged.

- 
- [1] T. Pfeifer, C. Spielmann, and G. Gerber, *Rep. Prog. Phys.* **69**, 443 (2006).  
 [2] E. Goulielmakis, M. Schultze, M. Hofstetter, V. S. Yakovlev, J. Gagnon, M. Uiberacker, A. L. Aquila, E. M. Gullikson, D. T. Attwood, R. Kienberger, F. Krausz, and U. Kleineberg, *Science* **320**, 1614 (2008).  
 [3] D. Shafir, Y. Mairesse, D. M. Villeneuve, P. B. Corkum, and N. Dudovich, *Nat. Phys.* **5**, 412 (2009).  
 [4] F. Krausz and M. Ivanov, *Rev. Mod. Phys.* **81**, 163 (2009).  
 [5] S. Haessler, J. Caillat, W. Boutu, C. Giovanetti-Teixeira, T. Ruchon, T. Auguste, Z. Diveki, P. Breger, A. Maquet, B. Carré, R. Taïeb, and P. Salières, *Nat. Phys.* **6**, 200 (2010).  
 [6] M. Schultze *et al.*, *Science* **328**, 1658 (2010).  
 [7] J. J. Rehr and R. C. Albers, *Rev. Mod. Phys.* **72**, 621 (2000).  
 [8] S. Pabst, *Eur. Phys. J. Spec. Top.* **221**, 1 (2013).  
 [9] H. D. Cohen and U. Fano, *Phys. Rev.* **150**, 30 (1966).  
 [10] E. Shigemasa, J. Adachi, M. Oura, and A. Yagishita, *Phys. Rev. Lett.* **74**, 359 (1995).

- [11] X.-J. Liu, N. A. Cherepkov, S. K. Semenov, V. Kimberg, F. Gel'mukhanov, G. Prümper, T. Lischke, T. Tanaka, M. Hoshino, H. Tanaka, and K. Ueda, *J. Phys. B* **39**, 4801 (2006).
- [12] B. Zimmermann, D. Rolles, B. Langer, R. Hentges, M. Braune, S. Cvejanovic, O. Geßner, F. Heiser, S. Korica, T. Lischke, A. Reinköster, J. Viehhaus, R. Dörner, V. McKoy, and U. Becker, *Nat. Phys.* **4**, 649 (2008).
- [13] D. Akoury *et al.*, *Science* **318**, 949 (2007).
- [14] M. Ilchen, L. Glaser, F. Scholz, P. Walter, S. Deinert, A. Rothkirch, J. Seltmann, J. Viehhaus, P. Decleva, B. Langer, A. Knie, A. Ehresmann, O. M. Al-Dossary, M. Braune, G. Hartmann, L. C. Tribedi, A. Meissner, M. AlKhalidi, and U. Becker, *Phys. Rev. Lett.* **112**, 023001 (2014).
- [15] B. Fischer, M. Kremer, T. Pfeifer, B. Feuerstein, V. Sharma, U. Thumm, C. D. Schröter, R. Moshhammer, and J. Ullrich, *Phys. Rev. Lett.* **105**, 223001 (2010).
- [16] A. Fischer, A. Sperl, P. Cörlin, M. Schönwald, H. Rietz, A. Palacios, A. González-Castrillo, F. Martín, T. Pfeifer, J. Ullrich, A. Senftleben, and R. Moshhammer, *Phys. Rev. Lett.* **110**, 213002 (2013).
- [17] J. H. Posthumus, *Rep. Prog. Phys.* **67**, 623 (2004).
- [18] M. Gruebele and A. H. Zewail, *J. Chem. Phys.* **98**, 883 (1993).
- [19] A. H. Zewail, *J. Phys. Chem. A* **104**, 5660 (2000).
- [20] A. D. Bandrauk and S. Chelkowski, *Phys. Rev. Lett.* **87**, 273004 (2001).
- [21] S. Chelkowski and A. D. Bandrauk, *Phys. Rev. A* **65**, 023403 (2002).
- [22] S. Barmaki and H. Bachau, *J. Phys. B* **40**, 463 (2007).
- [23] M. Lein, *J. Phys. B* **40**, R135 (2007).
- [24] H. Stapelfeldt, E. Constant, and P. B. Corkum, *Phys. Rev. Lett.* **74**, 3780 (1995).
- [25] M. Magrakvelidze, O. Herrwerth, Y. H. Jiang, A. Rudenko, M. Kurka, L. Foucar, K. U. Kühnel, M. Kübel, N. G. Johnson, C. D. Schröter, S. Dusterer, R. Treusch, M. Lezius, I. Ben-Itzhak, R. Moshhammer, J. Ullrich, M. F. Kling, and U. Thumm, *Phys. Rev. A* **86**, 013415 (2012).
- [26] J. Colgan, A. Huetz, T. J. Reddish, and M. S. Pindzola, *J. Phys. B* **41**, 085202 (2008).
- [27] R. D. Picca, P. D. Fainstein, M. L. Martiarena, and A. Dubois, *J. Phys. Conf. Ser.* **141**, 012006 (2008).
- [28] R. Della Picca, P. D. Fainstein, and A. Dubois, *Phys. Rev. A* **84**, 033405 (2011).
- [29] G. L. Yudin, S. Patchkovskii, and A. D. Bandrauk, *J. Phys. B* **39**, 1537 (2006).
- [30] X. Guan, E. B. Secor, R. C. DuToit, and K. Bartschat, *Phys. Rev. A* **86**, 053425 (2012).
- [31] H. B. Pedersen, S. Altevogt, B. Jordon-Thaden, O. Heber, M. L. Rappaport, D. Schwalm, J. Ullrich, D. Zajfman, R. Treusch, N. Guerassimova, M. Martins, J.-T. Hoefft, M. Wellhöfer, and A. Wolf, *Phys. Rev. Lett.* **98**, 223202 (2007).
- [32] J. Loreau, J. Lecointre, X. Urbain, and N. Vaeck, *Phys. Rev. A* **84**, 053412 (2011).
- [33] D. Ursrey, F. Anis, and B. D. Esry, *Phys. Rev. A* **85**, 023429 (2012).
- [34] I. Ben-Itzhak, Z. Chen, B. D. Esry, I. Gertner, O. Heber, C. D. Lin, and B. Rosner, *Phys. Rev. A* **49**, 1774 (1994).
- [35] I. Ben-Itzhak, I. Gertner, O. Heber, and B. Rosner, *Phys. Rev. Lett.* **71**, 1347 (1993).
- [36] H. Miyagi, T. Morishita, and S. Watanabe, *Phys. Rev. A* **85**, 022708 (2012).
- [37] B. R. Johnson, *J. Chem. Phys.* **69**, 4678 (1978).
- [38] Y. Pavlyukh and J. Berakdar, *Phys. Rev. A* **81**, 042515 (2010).
- [39] R. Schinke, *Photodissociation Dynamics: Spectroscopy and Fragmentation of Small Polyatomic Molecules* (Cambridge University Press, Cambridge, UK, 1995).
- [40] A. R. Edmonds, *Angular Momentum in Quantum Mechanics* (Princeton University Press, Princeton, NJ, 1996).
- [41] G. W. F. Drake, *Springer Handbook of Atomic, Molecular, and Optical Physics* (Springer, Berlin, 2006).
- [42] C. J. Joachain, *Quantum Collision Theory* (North-Holland, Amsterdam, 1975).
- [43] C. W. McCurdy, M. Baertschy, and T. N. Rescigno, *J. Phys. B* **37**, R137 (2004).
- [44] M. Baertschy, T. N. Rescigno, W. A. Isaacs, X. Li, and C. W. McCurdy, *Phys. Rev. A* **63**, 022712 (2001).
- [45] D. M. Mitnik, G. Gasaneo, and L. U. Ancarani, *J. Phys. B* **46**, 015202 (2013).
- [46] DLMF, *NIST Digital Library of Mathematical Functions*, <http://dlmf.nist.gov/>, Release 1.0.7 of 2014-03-21, online companion to [47].
- [47] F. W. J. Olver, D. W. Lozier, R. F. Boisvert, and C. W. Clark (eds.), in *NIST Handbook of Mathematical Functions* (Cambridge University Press, New York, 2010), print companion to [46].
- [48] M. L. Du, *Comput. Phys. Commun.* **77**, 229 (1993).
- [49] R. McCarroll and B. L. Moiseiwitsch, *Proc. Phys. Soc., London, Sect. A* **70**, 507 (1957).
- [50] M. Schüler, Y. Pavlyukh, and J. Berakdar, *J. Phys. Chem. Lett.* **4**, 1131 (2013).

## Many-body spectroscopy from Buckminster fullerene

Fullerenes are medium- to macro-sized molecular allotropes of carbon. Their general shape can be quite different: they appear as hollow spheres, ellipsoids or tubes. Besides the cylindrical carbon nanotubes, spherical fullerenes (buckyballs), have gained a great deal of attention. The first fullerene structure – the famous  $C_{60}$  – was prepared in 1985 [192] and named Buckminster fullerene after the Richard Buckminster Fuller, who had introduced an analogous geodesic dome structure in architecture. The Buckminster fullerene, which has the structure of a football (see fig. 5.1(a)), is the subject of our subsequent studies. It is the smallest, quasi-spherical fullerene <sup>1</sup> and possesses a number of remarkable properties, including:

- The ability to efficiently accommodate an extra electron. Due to the peculiarities of the electronic structure, an extra electron can be bound to the molecule by localizing a part of its charge in the hollow sphere. State-of-the-art quantum chemistry calculations are required for an accurate description [193–195]. This particularly pronounced electron affinity makes the  $C_{60}$  molecule a good acceptor for organic photovoltaic molecules [196].
- Strong collective excitations. In the UV regime, the optical absorption is completely dominated by plasmon-type excitations [197], arising from dipolar oscillations of the electronic density. The various plasmon modes also determine the EELS [198–201] and photoemission spectra [202, 203]. A detailed discussion is provided in sec. 5.3 and in [E4].
- Super-atom molecular orbitals (SAMOs). Experimentally discovered by means of STS by Feng *et al.* [204], the SAMOs turned out to be molecular states which closely resemble hydrogen-type  $s$ ,  $p$ ,  $d$ , ... orbitals. The stability of the SAMOs [85] towards electronic perturbations hints at extraordinary prospective transport in the solid phase [205] and has thus triggered a surge of research [206–208].

As we can see from this overview, the Buckminster fullerene entails rich phenomena in the transition regime between molecular and solid-state physics. Hence, it represents an ideal system for many-body theories and spectroscopies. In particular, we are interested in the manifestation of dynamical correlation effects <sup>2</sup>.

Our contribution to the physics of the  $C_{60}$  molecule is given by [E4], [E5], [E6] and, partly by [E3]. After revisiting some general symmetry aspects of  $C_{60}$  (sec. 5.1), we discuss the collective excitations and present our state-of-the-art treatment (sec. 5.3). This also yields a very accurate characterization of dynamical screening effects. Their role for DPE (see subsec. 3.2.2) is mapped out rigorously in sec. 5.4. Finally, we consider the time-resolved relaxation dynamics of many-body states due to electron-vibron interaction beyond the BO approximation (sec. 5.5).

### 5.1 Symmetry aspects

The geometric structure of  $C_{60}$  is shown in fig. 5.1(a). It possess  $I_h$  (icosahedric) symmetry, comprised of discrete rotations around symmetry axes and inversion symmetry. The quasi-spherical behavior of many

<sup>1</sup>Other spherical carbon fullerenes are  $C_{240}$  and  $C_{540}$ .

<sup>2</sup>We are referring to frequency and thus time dependence in quantities such as the self-energy or the screened interaction.

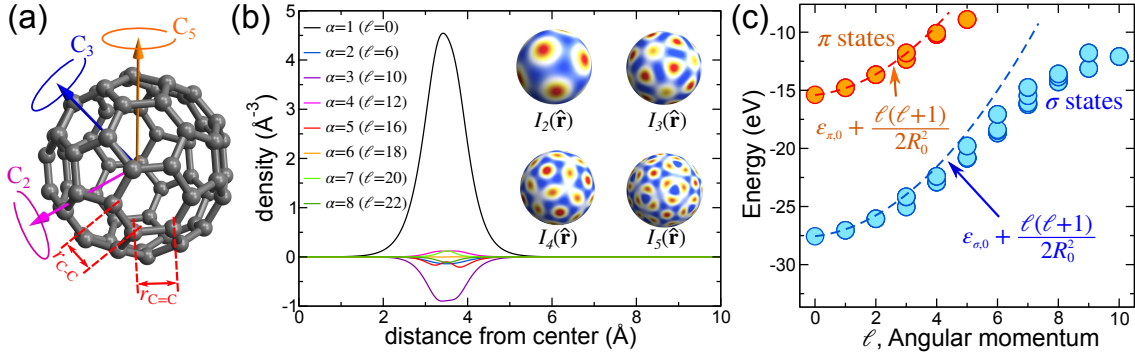


Figure 5.1: (a) Equilibrium molecular structure of the  $C_{60}$  molecule. One representative of the two-fold ( $C_2$ ), the three-fold ( $C_3$ ) and the five-fold ( $C_5$ ) symmetry axis, respectively, is shown. The bonds on the border of the pentagons and the hexagons has double-bonding (C=C) character, while the border between two hexagons is of C-C type. The respective bond length is  $r_{C-C} = 1.455 \text{ \AA}$  and  $r_{C-C} = 1.391 \text{ \AA}$ . (b) The SAF expansion of the electronic density, computed by DFT using the LB94 functional. The inset shows the SAFs on the unit sphere. Red color corresponds the maxima, blue to the minima. (c) Energy spectrum of KS eigenvalues. The corresponding KS orbitals have been projected onto the angular momentum eigenstates. The states have been classified according to their nodal character as  $\sigma$  or  $\pi$  orbitals. The dashed lines show the dispersion of electrons on a sphere with optimized radius  $R_0$ .

properties can be expressed by the symmetry-adapted functions (SAFs) of the  $I_h$  group in terms of spherical harmonics. The SAFs, denoted by  $I_\alpha(\hat{\mathbf{r}})$ , are expanded as

$$I_\alpha(\hat{\mathbf{r}}) = \sum_{|m| \geq \ell_\alpha} C_{\alpha,m} Y_{\ell_\alpha m}(\hat{\mathbf{r}}). \quad (5.1)$$

There is a one-to-one correspondence of the SAF order  $\alpha$  and the associated angular momentum:  $\ell_1 = 0, \ell_2 = 6, \ell_3 = 10, \ell_3 = 12, \dots$ . The first few SAFs are depicted in the inset in fig. 5.1(b). Any quantity with icosahedric symmetry such as the ground-state electron density or any SP potential is conveniently expanded in terms of the SAFs. The representation of the valence electron density

$$n_0(\mathbf{r}) = \sqrt{4\pi} \sum_{\alpha} n_{\alpha}(r) I_{\alpha}(\hat{\mathbf{r}}) \quad (5.2)$$

is shown in fig. 5.1(b), which illustrates that the deviation from spherical symmetry is rather small. This important implications on the SP structure. Both HF or KS states  $\psi_i(\mathbf{r})$ <sup>3</sup> can be (approximately) classified by a corresponding angular momentum  $\ell$ . The electronic structure (the eigenvalues  $\epsilon_i$ ) obtained by the DFT (details in ref. [E6]) as a function of the angular momentum<sup>4</sup> is shown in fig. 5.1(c). A symmetry classification of the SP orbitals prevails for many-body quantities such as the Dyson orbitals or the fluctuation densities. The small deviation from spherical symmetry inspired the application of jellium model, according to which the electronic density is homogeneously distributed in a spherical shell characterized by two radii  $R_1, R_2$  [209, 210]. More refined versions include a spherically-symmetric model potential [211, 212]. In any case, the angular momentum  $\ell$  becomes an exact quantum number and hence allows for an expansion of the density-density response function

$$\chi^R(\mathbf{r}, \mathbf{r}'; \omega) = \sum_{\ell m} \chi_{\ell}(r, r'; \omega) Y_{\ell m}^*(\hat{\mathbf{r}}) Y_{\ell m}(\hat{\mathbf{r}}'). \quad (5.3)$$

Hence, any many-body excitation, be it SP-like or collective excitations, can be classified according to their angular momentum. Despite the practical simplicity and the qualitatively correct physical picture, jellium-type models display a number of shortcomings. Most pronounced effects include the lack of level splitting, leading to a wrong electronic configuration (which is sometimes corrected "by hand"). It is thus a non-trivial task to decide in which steps the approximation of spherical symmetry can be invoked. We

<sup>3</sup>As the molecule is a closed-shell system, the spin degree of freedom is suppressed in the notation.

<sup>4</sup>One defines the weights  $W_{i,\ell} = \sum_m \left| \int d\mathbf{r} \psi_i(\mathbf{r}) Y_{\ell m}(\hat{\mathbf{r}}) \right|^2$  and plots the pair  $(\ell, \epsilon_i)$  for the largest weight.



advocate the following scheme: ground- and excited-state calculations are carried out in full  $I_h$  symmetry, ensuring the correct electronic structure; the map on spherical symmetry is – if needed – applied only after the first-principle calculations. In [E4] we apply this principle to obtain an accurate spherical model of the density-density response function in the form of eq. (5.3) based on a full-fledged *ab initio* TDDFT scheme.

## 5.2 E3: Single-or double-electron emission within the Keldysh nonequilibrium Green's function and Feshbach projection operator techniques

In full generality, photoemission is a complicated process. Neglecting the possible scattering events after the liberation of the photoelectron (sudden approximation), the basic ingredient to SPE are the Dyson orbitals and the quasi-hole energies. For their computation, the knowledge about the ground state *and* of the excited states of the ionized system is required, for the system can be left in any, possibly excited state (albeit restricted by the energy conservation). This includes collective excited states such as plasmons (see subsec. 3.1.2). The QP properties, possibly in presence of collective or dissipative excitation channels, are most conveniently captured by NEGF formalism and the associated MBPT (see sec. 2.5). For these reasons, a general NEGF theory for photoemission is highly desirable. This is the topic of [E3].

For SPE, the standard formulation in this context was introduced by Caroli *et al.* [129] in terms of a diagrammatic expansion which includes extrinsic effects<sup>5</sup>. These inelastic scattering processes can, in principle, be described by a one-body TISE for the photoelectron alone, if a non-local and non-hermitian potential – the so-called optical potential – is used [33]. The question of how to obtain the optical potential is formally answered by the Feshbach projection algebra (FPA) [138], which is outlined in appendix A. Projecting in the subspace of exactly one photoelectron yields a formal definition of the optical potential, or, in the GF language, its self-energy. The connection between the NEGF formulation and the notion of the self-energy as the basic object for the MBPT, on the one hand, and the Feshbach-projected self-energy, on the other hand, was, however, not completely understood. This is where our work [E3] starts. We demonstrate the direct correspondence between the FPA and the self-energy by decomposing the GFs, according to subsec. 2.4.1, into bound and scattering contributions and thus provide a practical way to compute optical potentials *systematically*.

After clarifying these points for SPE, we extend the theory to DPE. The first theory for the emission of two electrons upon absorbing one photon based on the NEGF formalism was proposed by Fominykh *et al.* [147]. Consistent with these findings, we extend our theory for SPE by introducing suitable Feshbach projection operators for the two-electron case. Furthermore, the diagrammatic perturbation theory for the main DPE observable – the coincidence two-electron current or cross-section – is developed. We apply the theory to explore the physics of plasmon-assisted DPE: a photoexcited electron undergoes extrinsic losses by scattering from the parent system upon creating a plasmon. As discussed in subsec. 3.3.1, this is due to the dynamical screening of the remaining electron cloud due to the emanating electron. Another way to look at this process is to consider it as a collective shake-up process. The decay of the collective excitation into  $p$ - $h$  pairs may give rise to the emission of a second electron<sup>6</sup>. The concrete calculations are carried out for the  $C_{60}$  molecule. A more detailed discussion of the results and the associated physics is presented in sec. 5.4.

<sup>5</sup>We remark that a equivalent diagrammatic technique for expression scattering amplitudes has been introduced earlier [136]

<sup>6</sup>Classically, one can imagine the second electron liberated due to the electric field which accompanies the charge density oscillations.

# Single- or double-electron emission within the Keldysh nonequilibrium Green's function and Feshbach projection operator techniques

Y. Pavlyukh,<sup>\*</sup> M. Schüler, and J. Berakdar*Institut für Physik, Martin-Luther-Universität Halle-Wittenberg, 06120 Halle, Germany*

(Received 24 November 2014; revised manuscript received 20 February 2015; published 13 April 2015)

This work provides a unified theoretical treatment of the single- and correlated double-electron emission from a general electronic system. Using Feshbach projection method, the states of interest are selected by the projection operator; the Feshbach-Schur map determines the effective Hamiltonian and the optical potential for the emitted electrons. On the other hand, the nonequilibrium Green's functions method is demonstrated to be a complementary approach, and an explicit correspondence between both methods is established. For a self-contained exposition, some results on single-electron emission are rederived using both formalisms. New insights and results are obtained for the correlated electron-pair emission: This includes the effective two-electron Hamiltonian, the explicit form of the Feshbach self-energy in terms of the many-body self-energies, and the diagrammatic expansion of the two-particle current. As an illustration of the diagrammatic technique, the process of the two-particle emission assisted by the excitation of plasmons is explicitly worked out.

DOI: 10.1103/PhysRevB.91.155116

PACS number(s): 71.10.-w, 79.60.-i, 32.80.-t, 31.15.A-

## I. INTRODUCTION

Scattering experiments deliver the most detailed information on the structure of matter. For instance, the fully resolved spectra of an electron emitted from an electronic system upon photon or particle impact encode the spin and momentum-resolved spectral properties of the sample [1–5]. For direct information on the two-particle properties, the detection of a correlated electron pair is necessary which is usually performed in a one-photon double-electron emission [4] or in a swift particle-impact double-electron emission experiment [6]. Calculations of the electron emission spectra from atomic and molecular systems [1,4,7–9] as well as from condensed matter [1–3] are done routinely. The underlying theories and techniques differ, however. The issue addressed here concerns the formulation of a unified and numerically accessible theoretical framework of single- and double-photoelectron emission (SPE and DPE) from finite and extended electronic systems. A method of choice for this purpose is the nonequilibrium Green's functions (NEGF) approach [10–13]. In full generality, the response function describing electron emission is more involved than the optical response which is related to *time-ordered* particle-hole (p-h) Green's function (GF) for which well-established approximations exist. Even for a *single*-electron emission the response function can only be defined on the Keldysh contour and after performing the calculations, the times are projected on the real *observable* times. The second complication is that for a fixed energy and momentum of the detected electron, the sample may be left in an excited state. A typical example is the plasmon satellites in core-level photoemission [14]. There, the target is left with one excited plasmon [15]. The conservation of energy and momentum allows us to focus on, e.g., the *no-loss current*. The response function is then determined by the product of two vertex functions and three single-particle Green's functions [16]. If an approximation is made for one of the constituents, it has to be taken over consistently to the others. The notion of a *conserving* approximation is rooted in this requirement.

First theories of electron emission were empirical, e.g., for surfaces, following Berglund and Spicer [17], the photoemission is regarded as a three-stage process: excitation, transport to the surface (during this stage the particle may lose energy), and the transformation into a scattering (detector) state. In 1970, Mahan wrote “we have not yet been able to derive a simple, time-ordered, correlation function which would serve as the starting point for a closed-loop type of calculation. That is, we have not yet found a “Kubo formula for photoemission” [18]. Shortly thereafter, Schaich and Ashcroft [19] and Langreth [20] employed a time-ordered formalism for the response function, and Caroli *et al.* [21] introduced the nowadays standard NEGF formulation. The well-known Fermi golden rule expression for the photocurrent

$$J_{\mathbf{p}} = 2\pi \int_{-\infty}^{\mu} d\varepsilon \delta(\varepsilon_{\mathbf{p}} - \varepsilon - \omega) \langle \chi_{\mathbf{p}}^{(-)} | \hat{\Delta} \hat{A}(\varepsilon) \hat{\Delta}^{\dagger} | \chi_{\mathbf{p}}^{(-)} \rangle$$

derives rigorously from the response-function formalism. In 1985, Almladh obtained the following modifications of the *no-loss* current:

$$J_{\mathbf{p}} = 2\pi \int_{-\infty}^{\mu} d\varepsilon \delta(\varepsilon_{\mathbf{p}} - \varepsilon - \omega) \langle \chi_{\mathbf{p}}^{(-)} | \hat{\Lambda}(\varepsilon + \omega, \varepsilon) \hat{A}(\varepsilon) \times \hat{\Lambda}^{\dagger}(\varepsilon + \omega, \varepsilon) | \chi_{\mathbf{p}}^{(-)} \rangle.$$

In these formulas, an interaction with an electromagnetic field of the frequency  $\omega$  is assumed.  $\chi_{\mathbf{p}}^{(-)}$  denotes the final scattering state with the momentum  $\mathbf{p}$  and energy  $\varepsilon_{\mathbf{p}}$ , and  $\hat{A}(\varepsilon)$  is the spectral function.  $\hat{\Lambda}(\varepsilon + \omega, \varepsilon)$  is the so-called vertex function which, for noninteracting systems, reduces to the operator of the light-matter interaction  $\hat{\Delta}$ . In interacting systems, it describes the screening of the optical field by the sample electrons and the accompanying polarization effects [22].

The physics beyond *no-loss* has many facets. There are two prominent examples: the plasmon satellites [15,23,24] and the Auger effect [25–28]. In both cases, the system is left in an excited state that relaxes subsequently either due many-body effects or results in the emission of a secondary electron. It should be noted, however, that the borderline in such a classification is blurred: one can consider the Auger

\*yaroslav.pavlyukh@physik.uni-halle.de

effect as a two-step process, in which the decay is treated independently from the primary ionization or as the *no-loss* double photoemission [29]. The former point of view yields a description of the Auger effect in terms of an equilibrium two-hole Green's function [26,30,31].

The goal here is to generalize the nonequilibrium approach to treat single- and double-electron emission. We will mostly discuss processes related to the absorption of *one* photon. Particle impact is discussed only in the optical limit as specified in Appendix A. In particular, this work provides a detailed discussion of DPE, a process that was experimentally realized for various systems [4,32]. For a self-contained presentation, we start by defining observables and introducing basic formulas solely based on the time-dependent perturbation theory and the assumption of adiabatic switching of the light-matter interaction (Sec. II A). Already on this level one can reformulate these expressions in the Fermi golden rule form and demonstrate how the sudden approximation can be used to reduce the many-body to two-body description (Sec. II B). Such reduction, however, neglects the energy loss of an emitted electron on its way to detector. These *extrinsic* losses are treated by means of the projection operator technique (Sec. III). For single photoemission (SPE), this approach was established in works of Almladh [16], Bardyszewski and Hedin [33], Fujikawa and Hedin [34], Hedin, Michiels, and Inglesfield [35], and for DPE by Brand and Cederbaum [36]. The notion of the optical potential is central to this approach. While the case of elastic scattering was considered in a classical work of Bell and Squires [37], the inelastic case, which is especially relevant for photoemission, is more involved and has a long history with a recent progress due to Cederbaum [38,39]. In Sec. IV, we closely follow the derivation of Almladh and extend the theory to the two-electron case. There are important differences as compared to the single-electron emission. Under some assumptions, DPE is only possible for interacting systems [40]. We corroborate our findings by performing a diagrammatic expansion of the derived DPE response function in terms of Green's function on the Keldysh contour (Sec. V). We consistently use atomic units.

## II. TWO-ELECTRON CURRENT

For DPE from atomic and molecular systems [41,42] a variety of very successful techniques, based on a full numerical solution or using approximate correlated scattering states of the few-body Schrödinger equation, were put forward. The wavefunction-based methods and, consecutively, the scattering approach are less suitable for extended degenerate fermionic systems. Such DPE experiments were first performed for Cu(001) and Ni(001) crystals [32] and meanwhile for a variety of other samples. Here comes the *response* formalism into play: the expectation values of products of the creation and annihilation operators are computed over the ground state of a (many-body) system, and perturbative expansions are evaluated with the help of Wick's theorem. If the studied process can be regarded as a multistep event, then the rate equations are often a very efficient tool. They can be derived either from the density matrix or from the NEGF formalisms using some additional assumptions. For instance, the generalized Kadanoff-Baym ansatz has been used to derive

the quantum master equations starting from NEGF approach to describe the transport in molecular systems [43].

Here, we present a self-contained derivation of the two-particle current starting from the time-dependent perturbation theory. The resulting formula [Eq. (12)] is, however, less useful for practical applications because it requires (generally unknown) many-body states. One has either a choice to completely neglect the target-ejected particles interaction which still might be relevant for higher energies (Sec. II B) or, as will be demonstrated in the next section (III), to properly reduce the formulations as to work with effective residual interactions (i.e., optical potentials).

### A. Basic definitions

#### 1. Hamiltonian

A system of interacting fermions is considered that has the Hamiltonian

$$\hat{H} = \int dx \hat{\psi}^\dagger(x) h(x) \hat{\psi}(x) + \frac{1}{2} \int dx dx' \hat{\psi}^\dagger(x) \hat{\psi}^\dagger(x') v(x, x') \hat{\psi}(x') \hat{\psi}(x), \quad (1)$$

where the field operator  $\hat{\psi}$  ( $\hat{\psi}^\dagger$ ) with argument  $x \equiv (\mathbf{r}, \sigma)$  annihilates (creates) a fermion in position  $\mathbf{r}$  with spin  $\sigma$ . Needed below is the antisymmetrized interaction

$$V(x_1, x_2, x_3, x_4) = v(\mathbf{r}_1, \mathbf{r}_2) [\delta(x_2 - x_3) \delta(x_1 - x_4) - \delta(x_1 - x_3) \delta(x_2 - x_4)]. \quad (2)$$

One may wish also to change the basis for the representation of creation and annihilation operators via

$$\hat{\psi}(x) = \sum_i \langle x|i \rangle c_i, \quad (3)$$

where the sum runs over a complete set of one-particle states and we consistently skip  $\cdot$  on  $c_i$  and  $c_i^\dagger$ . To study photoemission, we need to further classify the states according to their geometric character. A state will be called *bound* ( $\phi_i \in \mathcal{B}$ ) if for any  $\epsilon > 0$  there is a compact set  $B \subset \mathbb{R}^3$  such that for all times  $t$  the state remains in  $B$ :  $\|\chi_{B^c} e^{it\hat{H}} \phi_i\| < \epsilon$ , where  $B^c$  is the complement of  $B$ ,  $\chi_{B^c}$  denotes the corresponding characteristic function. Analogically for the *scattering* states ( $\phi_{\mathbf{k}} \in \mathcal{C}$ ) we adopt the following definition: they are the vectors for which  $\lim_{T \rightarrow \infty} \frac{1}{2T} \int_{-T}^T \|\chi_B e^{it\hat{H}} \phi_{\mathbf{k}}\| dt = 0$  for all compact sets  $B \subset \mathbb{R}^3$ , i.e., they leave any bounded region. It is clear that  $\mathcal{B} \perp \mathcal{C}$  and according to the RAGE theorem [44] all the states from the discrete (point) spectrum are bound, whereas the continuum states (absolutely continuous and singularly continuous) are the scattering states. Thus, parallels between the geometric and the spectral classification allows us to use continuum and scattering, and point and bound terms interchangeably, although for the purpose of this work the geometric classification is preferred. Finally, we note that if our theory is to be applied to solids, the use of localized Wannier functions [45] is preferred, at least for systems where their existence can be proved [46].

We will use the letters (*abcd*) for general orbitals, (*ijnm*) for bound orbitals, and boldface letters for continuum states.

In these notations

$$\hat{H} = \sum_{ab} t_{ab} c_a^\dagger c_b + \frac{1}{2} \sum_{abcd} v_{abcd} c_a^\dagger c_b^\dagger c_d c_c \quad (4)$$

$$= \sum_{ab} t_{ab} c_a^\dagger c_b + \frac{1}{4} \sum_{abcd} V_{abcd} c_a^\dagger c_b^\dagger c_d c_c. \quad (5)$$

## 2. Initial-state preparation

The above Hamiltonian determines the quantum state of the target (wave function  $|\Psi_0\rangle$ ) with corresponding energy  $E_0$ ) in the remote past ( $t = -\infty$ ). When the system is perturbed by the interaction with external fields, it evolves to a new state. As a typical mechanism we consider here the light-matter interaction

$$\hat{V}(t) = (\hat{\Delta} e^{-i\omega t} + \hat{\Delta}^\dagger e^{i\omega t}) e^{\eta t}, \quad \hat{\Delta} = \sum_{ab} \Delta_{ab} c_a^\dagger c_b. \quad (6)$$

In this expression,  $\hat{V}(t)$  is adiabatically turned on allowing us to introduce a typical interaction time  $\sim (2\eta)^{-1}$ . The form (6) permits generalizations: In Appendix A, we consider the process of impact ionization caused by a charged projectile particle (e.g., an electron) impinging on the target system. At high energy, the projectile can be regarded as distinguishable from electrons of the system. This allows us to average the projectile-target interaction over the projectile's states and write the perturbation in essentially the same form as in Eq. (6), i.e., as a single-particle operator.

From the first-order time-dependent perturbation theory we obtain the *approximate* eigenstate  $|\tilde{\Psi}^{(+)}\rangle$  of the full Hamiltonian  $\hat{H} + \hat{V}(t)$  at time  $t = 0$ :

$$|\tilde{\Psi}^{(+)}\rangle = |\Psi_0\rangle + \lim_{\eta \rightarrow 0} \frac{1}{E_0 + \omega - \hat{H} + i\eta} \hat{\Delta} |\Psi_0\rangle. \quad (7)$$

Readers will immediately notice parallels of Eq. (7) with the scattering theory where the Møller operators  $\hat{\Omega}^{(\pm)}$  convert an eigenstate of  $\hat{H}$  (the Hamiltonian of the target system) at  $t = \mp\infty$ , into an eigenstate of  $\hat{H} + \hat{V}(0)$  (the full Hamiltonian)  $|\Psi_\alpha^{(\pm)}\rangle = \hat{\Omega}^{(\pm)} |\Psi_\alpha\rangle$  at time  $t = 0$  [cf. Eqs. (14.66) of Joachain [47]]. The scattering theory is required when electromagnetic fields are quantized. For classical fields, Eq. (7) follows from the first-order expansion (in  $\hat{\Delta}$ ) of the Møller operator  $\hat{\Omega}^{(+)}$ . To emphasize the similarity, we denote the state given by Eq. (7) as the scattering state. In what follows, we omit the tilde which we used to denote its approximate character.

## 3. Observables

Assuming we know the quantum state of the target at  $t = 0$ , some observables can be computed. Since we are interested in the electron emission these are the expectation values of current operators. The safe way to introduce them is to use the continuity equation which is gauge invariant. The one-electron current  $J_{\mathbf{k}}$  is defined as the number of electrons  $N_{\mathbf{k}}$  with a given momentum  $\mathbf{k}$  outside the target divided by the effective interaction time  $(2\eta)^{-1}$ . There is a detailed discussion [16] on why electrons in the sample give a negligible contribution to the current. The same arguments are valid for the two-electron case. Thus, we analogically define the two-electron current as

$$J_{\mathbf{k}_1, \mathbf{k}_2} = \lim_{\eta \rightarrow 0} 2\eta \langle \hat{N}_{\mathbf{k}_1} \hat{N}_{\mathbf{k}_2} - \delta_{\mathbf{k}_1, \mathbf{k}_2} \hat{N}_{\mathbf{k}_1} \rangle. \quad (8)$$

In the expression above (and all subsequent derivations), we do not explicitly spell out the spin quantum numbers. The dependence on the spin can be recovered by substituting the continuum quantum numbers like  $\mathbf{k}$  by  $\mathbf{k}\sigma$  (likewise for bound indices). The second term excludes the one-electron current in the case when two momenta are equal. Equation (8) gives access to the differential cross section through the following relation:

$$\frac{d^2\sigma}{d\mathbf{k}_1 d\mathbf{k}_2} = \frac{\omega}{I} J_{\mathbf{k}_1, \mathbf{k}_2}, \quad (9)$$

where  $I/\omega$  is the photon flux density [48]. For the velocity gauge  $\hat{\Delta} = \frac{1}{c} \mathbf{A}_0 \cdot \hat{\mathbf{p}}$ ,  $I = \frac{\omega^2 A_0^2}{2\pi c}$ , where  $A_0$  is the amplitude of the vector potential and  $\hat{\mathbf{p}}$  is the momentum operator. Similar expressions can be given for the length gauge.

The average in Eq. (8) is performed over the perturbed state (7):

$$J_{\mathbf{k}_1, \mathbf{k}_2} = \lim_{\eta \rightarrow 0} 2\eta \langle \Psi_0 | \hat{\Delta}^\dagger \frac{1}{E_0 + \omega - \hat{H} - i\eta} c_{\mathbf{k}_1}^\dagger c_{\mathbf{k}_2}^\dagger c_{\mathbf{k}_2} c_{\mathbf{k}_1} \times \frac{1}{E_0 + \omega - \hat{H} + i\eta} \hat{\Delta} | \Psi_0 \rangle, \quad (10)$$

where we used the usual anticommutation relations for the fermionic operators. The current is quadratic in  $\hat{\Delta}$  or linear in the number of absorbed photons. The first order in  $\hat{\Delta}$  gives the linear conductivity current and is of no interest here [21].

To derive the Fermi golden rule for DPE we insert a complete set of the  $(N-2)$ -particle states and use the scattering theory to evaluate matrix elements of the type:

$$M_{\mathbf{k}_1, \mathbf{k}_2, \beta}^* = \langle \Psi_0 | \hat{\Delta}^\dagger \frac{1}{E_0 + \omega - \hat{H} - i\eta} c_{\mathbf{k}_1}^\dagger c_{\mathbf{k}_2}^\dagger | \Psi_\beta^{2+} \rangle.$$

We will generally use lower indices to distinguish quantum states and upper indices to indicate the charge of the system or the nature of the state ( $\pm$ ), i.e., incoming or outgoing wave. For a scattering process with the following energy balance

$$E_i = E_0 + \omega \rightarrow E_f = \varepsilon_{\mathbf{k}_1} + \varepsilon_{\mathbf{k}_2} + E_\beta^{2+},$$

the Møller operator  $\hat{\Omega}^{(-)}$  translates a wave function in the remote future into an *incoming* [they are sometimes called inverted low-energy electron diffraction (LEED) states [35]] scattering state at  $t = 0$ :

$$|\Psi_\beta^{(-)}\rangle = \hat{\Omega}^{(-)} c_{\mathbf{k}_1}^\dagger c_{\mathbf{k}_2}^\dagger |\Psi_\beta^{2+}\rangle = \lim_{\eta \rightarrow 0} \frac{-i\eta}{E_f - \hat{H} - i\eta} c_{\mathbf{k}_1}^\dagger c_{\mathbf{k}_2}^\dagger |\Psi_\beta^{2+}\rangle.$$

Following Almladh [16], we obtain

$$M_{\mathbf{k}_1, \mathbf{k}_2, \beta}^* = \frac{1}{E_i - E_f - i\eta} \langle \Psi_0 | \hat{\Delta}^\dagger | \Psi_\beta^{(-)} \rangle, \quad (11)$$

resulting in the Fermi golden rule for DPE for an adiabatic switching of  $\hat{V}(t)$ :

$$J_{\mathbf{k}_1, \mathbf{k}_2} = \lim_{\eta \rightarrow 0} 2\eta \sum_{\beta} |M_{\mathbf{k}_1, \mathbf{k}_2, \beta}|^2 = 2\pi \sum_{\beta} \delta(E_i - E_f) |\langle \Psi_\beta^{(-)} | \hat{\Delta} | \Psi_0 \rangle|^2. \quad (12)$$

This is essentially an exact equation if strong field effects are neglected, i.e., if the first-order perturbation theory in

field strength is adequate. Now, we discuss some common approximations. In the *sudden approximation*, the Møller operator is set to be the identity operator and it follows  $|\Psi_\beta^{(-)}\rangle \approx c_{\mathbf{k}_1}^\dagger c_{\mathbf{k}_2}^\dagger |\Psi_\beta^{2+}\rangle$  leading, e.g., to Eq. (1) of Napitu and Berakdar [49]. The sudden approximation is broadly used to interpret the single photoemission. However, it is easy to construct an example when it completely fails: consider photoemission from a system surrounded by an impenetrable potential barrier. Irrespective of the photon energy there will be zero current in the detector. Thus, it is *extrinsic losses* [35] that are missing in the sudden approximation.

### B. Sudden approximation

In the sudden approximation for SPE it is possible to reduce the many-body description to a single-particle picture which also allows us to approximately treat the Møller operator and accommodate extrinsic losses. The central objects in such an approach are the *Dyson orbitals* [50]. The *hole* Dyson orbital is defined as an overlap of  $(N - 1)$  many-particle states with the  $N$ -particle initial state:

$$\begin{aligned} \phi_\alpha(x_1) &= \sqrt{N} \int d(x_2 \dots x_N) [\Psi_\alpha^+(x_2, \dots, x_N)]^* \\ &\quad \times \Psi_0(x_1, \dots, x_N) \\ &= \langle \Psi_\alpha^+ | \hat{\psi}(x_1) | \Psi_0 \rangle. \end{aligned} \quad (13)$$

A rather extensive review of such overlap operators as well as the proof on the last “dressed in the fancy outfit of the occupation number formalism” identity can be found in Ref. [51]. Practical approaches for their computation are overviewed in Refs. [52,53]. By introducing a similar *two-hole Dyson orbital*

$$\begin{aligned} \phi_\beta^{(2)}(x_1, x_2) &= \sqrt{\frac{N(N-1)}{2!}} \int d(x_3 \dots x_N) [\Psi_\beta^{2+}(x_3, \dots, x_N)]^* \\ &\quad \times \Psi_0(x_1, \dots, x_N) \\ &= \frac{1}{\sqrt{2}} \langle \Psi_\beta^{2+} | \hat{\psi}(x_1) \hat{\psi}(x_2) | \Psi_0 \rangle, \end{aligned} \quad (14)$$

and neglecting the Møller operator, we obtain for the two-particle current (12)

$$J_{\mathbf{k}_1, \mathbf{k}_2} = 2\pi \sum_\beta \delta(E_i - E_f) |\langle \mathbf{k}_1 \mathbf{k}_2 | \hat{\Delta} | \phi_\beta^{(2)} \rangle|^2, \quad (15)$$

where  $|\mathbf{k}_1 \mathbf{k}_2\rangle$  is asymptotic two-particle state, i.e., antisymmetrized product of two plane waves. The two-hole orbital is antisymmetric with respect to the interchange of particle coordinates and in general has a norm  $\leq 1$ . To derive (15) it is instructive to consider at first the corresponding matrix element for SPE:

$$M_{\mathbf{k}, \alpha} \approx \frac{1}{E_i - E_f + i\eta} \sum_{ab} \Delta_{ab} \langle \Psi_\alpha^+ | c_{\mathbf{k}} c_a^\dagger c_b | \Psi_0 \rangle.$$

Now, we have  $c_{\mathbf{k}} c_a^\dagger c_b | \Psi_0 \rangle = \delta_{\mathbf{k}, a} c_b | \Psi_0 \rangle + c_a^\dagger c_b c_{\mathbf{k}} | \Psi_0 \rangle$  and it is time to make another very important assumption:

$$c_{\mathbf{k}} | \Psi_0 \rangle \approx 0. \quad (16)$$

It is not valid in general, however, one can use the same arguments as Almladh [see discussion around his Eq. (11)] to

demonstrate that it gives a vanishing contribution. For homogeneous electron gas, this is even a generally valid statement. Aside from allowing us to compute the matrix elements, the assumption (16) also justifies why terms resulting from the second-order perturbation theory give vanishing contributions to the current.

In this way (see Appendix D),  $M_{\mathbf{k}, \alpha} = \frac{1}{E_i - E_f + i\eta} \langle \mathbf{k} | \hat{\Delta} | \phi_\alpha \rangle$  and

$$J_{\mathbf{k}} = 2\pi \sum_\alpha \delta(E_i - E_f) |\langle \mathbf{k} | \hat{\Delta} | \phi_\alpha \rangle|^2.$$

For DPE, we analogously analyze the matrix element entering Eq. (11) and neglect terms with two holes at momenta  $\mathbf{k}_1$  and  $\mathbf{k}_2$  (i.e.,  $c_{\mathbf{k}_2} c_{\mathbf{k}_1} | \Psi_0 \rangle \approx 0$ ) as compared to the terms with only one hole (Appendix D). Notice that for SPE we neglected one hole term as compared to zero hole contribution [cf. Eq. (16)].

It is obvious that the sudden approximation is only valid for large momenta  $k_{1,2}$  and it is indifferent to the state in which the system is left in (the final double-ionized state can be an excited state). Thus, it is desirable to generate improved approximations to Eq. (12) by rewriting it in the two-particle form, but with an improved final state [such as Eq. (4) of Fominykh *et al.* [54] or Eq. (2) of Fominykh *et al.* [55]].

## III. EXTRINSIC EFFECTS

A many-body target interacts with light such that a certain number of electrons are emitted. Here, the fundamental question is whether it is legitimate to describe the process in such a way that only quantum numbers of ejected particles are considered and remaining degrees of freedom are traced out, i.e., put into some effective interactions. The projection operator formalism is a general method to treat this kind of problem. In this section, we introduce the basic concepts of this theory and demonstrate to the reader that a deep connection with the nonequilibrium Green’s function formalism exist. We conclude this rather mathematical section by considering two examples. Based on these examples, the Fermi golden rule is derived in the subsequent section.

### A. Nonequilibrium Green’s functions

In the Keldysh formalism [13], the field operators evolve on the time-loop contour  $\mathcal{C}$  shown in Fig. 1. Operators on the *minus* branch are ordered chronologically while operators on the *plus* branch are ordered antichronologically. Letting  $z_1$  and  $z_2$  be two contour times, the Green’s function  $G(x_1 z_1, x_2 z_2)$  can be divided into different components  $G^{\alpha\beta}(x_1 t_1, x_2 t_2)$  depending on the branch  $\alpha, \beta = +/-$  to which  $z_1$  and  $z_2$  belong. As before,  $x_i$  denote a composite coordinate comprising space and spin variables. For  $\alpha = \beta = -$ , we have the *time-ordered*

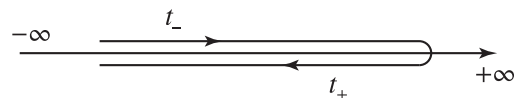


FIG. 1. The Keldysh time-loop contour  $\mathcal{C}$ . The forward branch is denoted with a “-” label while the backward branch is denoted by a “+” label.

Green's function

$$G^{--}(x_1 t_1, x_2 t_2) = -i \langle T[\hat{\psi}_H(x_1 t_1) \hat{\psi}_H^\dagger(x_2 t_2)] \rangle. \quad (17)$$

In this expression, the average  $\langle \dots \rangle$  is taken over a given density matrix  $\hat{\rho}$  and  $T$  is the time-ordering operator. The subscript “ $H$ ” attached to a general operator  $\hat{O}$  signifies that the operator is in the Heisenberg picture

$$\hat{O}_H(t) = \hat{U}(t_0, t) \hat{O} \hat{U}^\dagger(t, t_0), \quad (18)$$

where  $\hat{U}(t_1, t_2)$  is the time-evolution operator and  $t_0$  is an arbitrary initial time. Reversing the time arrow the  $G^{--}$  is converted into the *anti-time-ordered* Green's function

$$G^{++}(x_1 t_1, x_2 t_2) = -i \langle \bar{T}[\hat{\psi}_H(x_1 t_1) \hat{\psi}_H^\dagger(x_2 t_2)] \rangle, \quad (19)$$

where  $\bar{T}$  orders the operators antichronologically. Finally, choosing  $z_1$  and  $z_2$  on different branches we have

$$G^{-+}(x_1 t_1, x_2 t_2) = i \langle \hat{\psi}_H^\dagger(x_2 t_2) \hat{\psi}_H(x_1 t_1) \rangle, \quad (20a)$$

$$G^{+-}(x_1 t_1, x_2 t_2) = -i \langle \hat{\psi}_H(x_1 t_1) \hat{\psi}_H^\dagger(x_2 t_2) \rangle. \quad (20b)$$

The last two components are equivalently written as  $G^{-+} = G^<$  (*lesser* Green's function) and  $G^{+-} = G^>$  (*greater* Green's function), and describe the propagation of an added hole ( $G^<$ ) or particle ( $G^>$ ) in the medium.

It is often convenient in addition to time-ordered and anti-time-ordered functions to introduce the retarded and advanced components

$$G^R(x_1, x_2; t) = \theta(t)[G^>(x_1, x_2; t) - G^<(x_1, x_2; t)], \quad (21a)$$

$$G^A(x_1, x_2; t) = \theta(-t)[G^<(x_1, x_2; t) - G^>(x_1, x_2; t)]. \quad (21b)$$

In order to find their representation in frequency space, we multiply the retarded GF by  $e^{-\eta t}$  with  $\eta \rightarrow 0+$  in order to enforce the convergence and compute the Fourier integral

$$G^R(x_1, x_2; \omega) = \left\langle \hat{\psi}(x_1) \frac{1}{\omega + E_0 - \hat{H} + i\eta} \hat{\psi}^\dagger(x_2) \right\rangle + \left\langle \hat{\psi}^\dagger(x_2) \frac{1}{E_0 - \omega - \hat{H} - i\eta} \hat{\psi}(x_1) \right\rangle. \quad (22)$$

Let us further introduce (for general  $z \in \mathbb{C}$ ) the particle-type and hole-type GF by

$$G^{(p)}(x_1, x_2; z) = \left\langle \hat{\psi}(x_1) \frac{1}{z - \hat{H}} \hat{\psi}^\dagger(x_2) \right\rangle, \quad (23a)$$

$$G^{(h)}(x_1, x_2; z) = \left\langle \hat{\psi}^\dagger(x_2) \frac{1}{z - \hat{H}} \hat{\psi}(x_1) \right\rangle. \quad (23b)$$

From Eqs. (23) follows

$$G^{R/A}(x_1, x_2; \omega) = G^{(p)}(x_1, x_2; E_0 + \omega \pm i\eta) - G^{(h)}(x_1, x_2; E_0 - \omega \mp i\eta).$$

Finally, let us present the equation of motion (EOM) for the retarded GF in the form

$$(\omega + i\eta)G^R(x_1, x_2; \omega) = \delta(x_1 - x_2) + \left\langle [\hat{\psi}(x_1), \hat{H}] \frac{1}{E_0 + \omega - \hat{H} + i\eta} \hat{\psi}^\dagger(x_2) \right\rangle - \left\langle \hat{\psi}^\dagger(x_2) \frac{1}{E_0 + \omega - \hat{H} + i\eta} [\hat{\psi}(x_2), \hat{H}] \right\rangle. \quad (24)$$

The two-particle Green's functions are much more diverse. However, we will only need those containing creation operators with the same time argument and the same holds for annihilation operators. To specify the relative order of creation (or annihilation) operators infinitesimally small times are added. Because such Green's functions depend on two times only, the same nomenclature as in the single-particle case can be used. Thus, we define

$$G^{(pp)}(x_1, x_2; \bar{x}_1, \bar{x}_2; z) = \left\langle \hat{\psi}(x_1) \hat{\psi}(x_2) \frac{1}{z - \hat{H}} \hat{\psi}^\dagger(\bar{x}_2) \hat{\psi}^\dagger(\bar{x}_1) \right\rangle, \\ G^{(hh)}(x_1, x_2; \bar{x}_1, \bar{x}_2; z) = \left\langle \hat{\psi}^\dagger(\bar{x}_2) \hat{\psi}^\dagger(\bar{x}_1) \frac{1}{z - \hat{H}} \hat{\psi}(x_1) \hat{\psi}(x_2) \right\rangle.$$

They are the constituents of the retarded and advanced two-particle Green's functions

$$iG^{R/A}(x_1, x_2; \bar{x}_1, \bar{x}_2; \omega) = G^{(pp)}(x_1, x_2; \bar{x}_1, \bar{x}_2; E_0 + \omega \pm i\eta) - G^{(hh)}(x_1, x_2; \bar{x}_1, \bar{x}_2; E_0 - \omega \mp i\eta).$$

For the retarded function, the following equation of motion can be derived:

$$(\omega + i\eta)G^R(x_1, x_2; \bar{x}_1, \bar{x}_2; \omega) = \delta(x_1 - \bar{x}_1)G^<(x_2, \bar{x}_2, 0) - \delta(x_1 - \bar{x}_2)G^>(x_2, \bar{x}_1, 0) + \delta(x_2 - \bar{x}_2)G^>(x_1, \bar{x}_1, 0) - \delta(x_2 - \bar{x}_1)G^<(x_1, \bar{x}_2, 0) - i \left\langle [\hat{\psi}(x_1) \hat{\psi}(x_2), \hat{H}] \frac{1}{E_0 + \omega - \hat{H} + i\eta} \hat{\psi}^\dagger(\bar{x}_2) \hat{\psi}^\dagger(\bar{x}_1) \right\rangle - i \left\langle \hat{\psi}^\dagger(\bar{x}_2) \hat{\psi}^\dagger(\bar{x}_1) \frac{1}{E_0 - \omega - \hat{H} - i\eta} [\hat{\psi}(x_1) \hat{\psi}(x_2), \hat{H}] \right\rangle. \quad (25)$$

## B. Two projection operators

In the previous section, we have seen that relevant types of Green's functions can be written in the form of a *resolvent*  $\langle (z - \hat{H})^{-1} \rangle$ ,  $z \in \mathbb{C}$ . To be more specific about the state over which the averaging is performed, we select from all possible states of the target and emitted particles the relevant ones for the effect of interest by employing projection operators. In the following, we consistently skip  $\hat{\cdot}$  when writing these operators and use 1 to denote the identity operator. Hence,  $P + Q = 1$  are two complementary projection operators with the idempotence ( $P^2 = P$ ,  $Q^2 = Q$ ) as their defining property and the basis formula for computing resolvents

$$P \frac{1}{z - \hat{H}} = \frac{P}{z - \hat{H}_P - \hat{\Sigma}_P(z)} \times \left[ 1 + PHQ \frac{1}{z - \hat{H}_Q} \right], \quad (26)$$

where  $\hat{H}_P = P\hat{H}P$ ,  $\hat{H}_Q = Q\hat{H}Q$ , and the self-energy operator is defined as

$$\hat{\Sigma}_P(E) = P\hat{H}Q \frac{1}{E - \hat{H}_Q} Q\hat{H}P. \quad (27)$$

The map  $F_p : \hat{H} \rightarrow \hat{H}_p + \hat{\Sigma}_p(E)$  is called the Feshbach-Schur map, it relates the eigenvalue problem on the full Hilbert space to that on its subspace. We summarize relevant matrix identities in Appendix C. Due to the presence of the bath Hamiltonian  $\hat{H}_Q$  in Eq. (27), this definition cannot be used for practical computation of the self-energy. Fortunately, a connection with the many-body perturbation theory (MBPT) exists [56,57]. If, for example, starting from the  $N$ -particle Schrödinger equation  $\hat{H}|\Psi_0\rangle = E_0|\Psi_0\rangle$  we use a projector

$$P = \hat{\psi}^\dagger(\mathbf{r})|\Psi_\alpha^+\rangle \frac{1}{\bar{n}_\alpha(\mathbf{r})} \langle\Psi_\alpha^+|\hat{\psi}(\mathbf{r}),$$

where  $\bar{n}(\mathbf{r})$  is the hole density of ionized state  $\alpha$ , i.e.,  $\bar{n}(\mathbf{r}) \equiv \langle\Psi_\alpha^+|\hat{\psi}(\mathbf{r})\hat{\psi}^\dagger(\mathbf{r})|\Psi_\alpha^+\rangle$ , the eigenvalue problem on the  $P$  subspace (C3)  $\{\langle\Psi_\alpha^+|\hat{\psi}(\mathbf{r})[\hat{H}_P + \hat{\Sigma}_P(E) - EI_P]P|\Psi_0\rangle = 0\}$  is the Lippmann-Schwinger equation for the hole Dyson orbital (13). Notice that  $\hat{H}_P$  contains the electrostatic and exchange part of self-energy, whereas  $\hat{\Sigma}_P(E) \rightarrow 0$  for  $E \rightarrow \pm\infty$ . Similarly, in 1959 Bell and Squires [37] considered a one-body potential for the scattering of a particle incident on a complex (many-body) target. They demonstrated that this *optical potential* is exactly given by the sum of all proper linked diagrams, i.e., many-body self-energy in the *time-ordered* formulation. In fact, their Eq. (7) directly corresponds to Eq. (C3) when  $P$  is a projection yielding a *particle* Dyson orbital.

In order to study single and double photoemission, we introduce two special projection operators. The main goal of this section is to establish an equivalence between the abstractly defined self-energy [Eq. (27)] and the self-energy of the many-body perturbation theory. We consider the expression appearing in the first line of Eq. (26), i.e., resolvents of the type

$$P \frac{1}{z - \hat{H}} P = P \frac{1}{z - \hat{H}_P - \hat{\Sigma}_P(z)} P.$$

We will demonstrate that the formalism of nonequilibrium Green's functions is directly paralleled with the Feshbach projection algebra (FPA). The basic relation for the subsequent derivations are the operator identities

$$(\hat{A} - \hat{B})^{-1} = \hat{A}^{-1} + \hat{A}^{-1}\hat{B}(\hat{A} - \hat{B})^{-1}, \quad (28a)$$

$$(\hat{A} - \hat{B})^{-1} = \hat{A}^{-1} + (\hat{A} - \hat{B})^{-1}\hat{B}\hat{A}^{-1}. \quad (28b)$$

We will show following that with

$$\hat{A} = z - P\hat{H}P \equiv z - \hat{H}_P, \quad (29a)$$

$$\hat{B} = Q\hat{H}P + P\hat{H}Q + Q\hat{H}Q, \quad (29b)$$

the operator identities (28) have a structure of the Dyson equation for certain Green's functions.

For SPE, we consider the projection operator

$$P_\alpha = \sum_{\mathbf{k}} c_{\mathbf{k}}^\dagger |\Psi_\alpha^+\rangle \langle\Psi_\alpha^+| c_{\mathbf{k}}, \quad (30)$$

where the sum runs over scattering states. It is common to select these single-particle states  $|\varphi_{\mathbf{k}}\rangle$  to be eigenfunctions of some reference Hamiltonian with proper boundary conditions. We request that  $|\Psi_\alpha^+\rangle$  is a completely bound remainder of the ionization event and does not emit a second electron at a later stage (Auger electrons is a typical example). There are many equivalent ways to impose this restriction, for instance, we will assume

$$c_{\mathbf{k}}|\Psi_\alpha^+\rangle = 0, \quad (31)$$

i.e., implying  $|\Psi_\alpha^+\rangle$  is a vacuum state for photoelectrons. From the assumption follows the idempotency ( $P_\alpha^2 = P_\alpha$ , see Appendix D for proof) and, thus,  $P_\alpha$  represents a true projection operator. The application of  $P_\alpha$  restricts the possible processes which might occur upon excitation to the definite emission of *one* photoelectron, whereas the ionized system is left in a (possibly excited) bound state  $|\Psi_\alpha^+\rangle$ . From the assumption Eq. (31) follows another restriction

$$\lim_{r \rightarrow \infty} \hat{\psi}(x, t) |\Psi_\alpha^+\rangle = \lim_{r \rightarrow \infty} \sum_i \langle x|i \rangle c_i(t) |\Psi_\alpha^+\rangle + \lim_{r \rightarrow \infty} \sum_{\mathbf{k}} \langle x|\mathbf{k} \rangle c_{\mathbf{k}}(t) |\Psi_\alpha^+\rangle = 0, \quad (32)$$

where the first term is equal to zero because each bound state ( $i$ ) is necessarily given by a square integrable function (converse is not true). In the following, we will use another consequence of the assumptions (31) and (32):

$$G_{\mathbf{k}\alpha}^<(\omega) = 0, \quad G_{\alpha\mathbf{k}}^<(\omega) = 0, \quad (33)$$

$$\lim_{r_1 \rightarrow \infty} G^<(x_1 t_1, x_2 t_2) = \lim_{r_1 \rightarrow \infty} G^<(x_2 t_2, x_1 t_1) = 0. \quad (34)$$

The projection operator for DPE we define as

$$P_\beta = \frac{1}{2} \sum_{\mathbf{p}\mathbf{p}'} c_{\mathbf{p}}^\dagger c_{\mathbf{p}'}^\dagger |\Psi_\beta^{2+}\rangle \langle\Psi_\beta^{2+}| c_{\mathbf{p}'} c_{\mathbf{p}}. \quad (35)$$

Here,  $|\Psi_\beta^{2+}\rangle$  is the doubly ionized reference state, to which two photoelectrons with continuum quantum numbers  $\mathbf{p}$  and  $\mathbf{p}'$  are added. We can easily show the idempotency of the projection operator (35) if we require, similar to Eq. (31),

$$c_{\mathbf{p}} |\Psi_\beta^{2+}\rangle = 0. \quad (36)$$

## C. Example of SPE

### 1. Equation of motion (EOM)

As a starting point, let us use the following operator identity which can be derived from Eq. (28a) or verified by direct computation:

$$(z - E_\alpha^+) P_\alpha \frac{1}{z - \hat{H}} P_\alpha = P_\alpha + P_\alpha (\hat{H} - E_\alpha^+) \frac{1}{z - \hat{H}} P_\alpha.$$

With the definition of the SPE projection operator  $P_\alpha$  in Eq. (30), we find

$$\begin{aligned} P_\alpha \frac{1}{z - \hat{H}} P_\alpha &= \sum_{\mathbf{p}\mathbf{q}} c_{\mathbf{p}}^\dagger |\Psi_\alpha^+\rangle \langle\Psi_\alpha^+| c_{\mathbf{p}} \frac{1}{z - \hat{H}} c_{\mathbf{q}}^\dagger |\Psi_\alpha^+\rangle \langle\Psi_\alpha^+| c_{\mathbf{q}} \\ &= \sum_{\mathbf{p}\mathbf{q}} c_{\mathbf{p}}^\dagger |\Psi_\alpha^+\rangle G_{\mathbf{p}\mathbf{q}}^{(\mathbf{p})}(z) \langle\Psi_\alpha^+| c_{\mathbf{q}}, \end{aligned}$$

where we applied the definition of the particle-type GF (23a). Note that the GF is defined for a particular subspace spanned by the operator  $P_\alpha$  and should therefore always be understood as the GF associated with  $|\Psi_\alpha^+\rangle$ . For brevity, however, we omit labeling GF by  $\alpha$ .

Using these notations, the operator identity reads as

$$\begin{aligned} (z - E_\alpha^+) \sum_{\mathbf{pq}} c_{\mathbf{p}}^\dagger |\Psi_\alpha^+\rangle G_{\mathbf{pq}}^{(p)}(z) \langle \Psi_\alpha^+ | c_{\mathbf{q}} \\ = \sum_{\mathbf{k}} c_{\mathbf{k}}^\dagger |\Psi_\alpha^+\rangle \langle \Psi_\alpha^+ | c_{\mathbf{k}} + \sum_{\mathbf{pq}} c_{\mathbf{p}}^\dagger |\Psi_\alpha^+\rangle \langle \Psi_\alpha^+ | c_{\mathbf{p}} (H - E_\alpha^+) \\ \times \frac{1}{z - \hat{H}} c_{\mathbf{q}}^\dagger |\Psi_\alpha^+\rangle \langle \Psi_\alpha^+ | c_{\mathbf{q}}. \end{aligned}$$

With the help of our assumption (31) we can now remove the sum by applying  $\langle \Psi_\alpha^+ | c_{\mathbf{p}'}$  from the left and  $c_{\mathbf{q}'}^\dagger |\Psi_\alpha^+\rangle$  from the right as Eq. (31) implies  $\langle \Psi_\alpha^+ | c_{\mathbf{p}'} c_{\mathbf{p}}^\dagger |\Psi_\alpha^+\rangle = \delta_{\mathbf{pp}'}$ . Furthermore, we note that  $\langle \Psi_\alpha^+ | c_{\mathbf{p}} (\hat{H} - E_\alpha^+) = \langle \Psi_\alpha^+ | [c_{\mathbf{p}}, \hat{H}]$  because of  $\hat{H} |\Psi_\alpha^+\rangle = E_\alpha^+ |\Psi_\alpha^+\rangle$ . Hence, we obtain

$$(z - E_\alpha^+) G_{\mathbf{pq}}^{(p)}(z) = \delta_{\mathbf{pq}} + \langle \Psi_\alpha^+ | [c_{\mathbf{p}}, \hat{H}] \frac{1}{z - \hat{H}} c_{\mathbf{q}}^\dagger |\Psi_\alpha^+\rangle. \quad (37)$$

As stated above, we can think of  $|\Psi_\alpha^+\rangle$  as a vacuum state for free particles [cf. Eq. (31)]. The hole-type GF is identically zero. Therefore,

$$G_{\mathbf{pq}}^{(p)}(E_\alpha^+ + \omega + i\eta) = G_{\mathbf{pq}}^R(\omega).$$

Substituting  $z = E_\alpha^+ + \omega + i\eta$  in Eq. (37) we realize its equivalence to Eq. (24). In other words, by applying the FPA we can derive EOM for the retarded Green's function.

## 2. Effective Hamiltonian

In Eq. (28a),  $\hat{A}^{-1}$  plays the role of the reference Green's function. Correspondingly,  $P \hat{H} P$  is the effective Hamiltonian. Using the standard anticommutation algebra and the assumption (31), we find

$$\begin{aligned} \langle \Psi_\alpha^+ | c_{\mathbf{p}} \hat{H} c_{\mathbf{q}}^\dagger | \Psi_\alpha^+ \rangle \\ = E_\alpha^+ \delta_{\mathbf{pq}} + \langle \Psi_\alpha^+ | [c_{\mathbf{p}}, \hat{H}] c_{\mathbf{q}}^\dagger | \Psi_\alpha^+ \rangle \\ = E_\alpha^+ \delta_{\mathbf{pq}} + t_{\mathbf{pq}} + \sum_{nm} (v_{\mathbf{pnmq}} - v_{\mathbf{npmq}}) \langle \Psi_\alpha^+ | c_n^\dagger c_m | \Psi_\alpha^+ \rangle \\ = E_\alpha^+ \delta_{\mathbf{pq}} + \tilde{t}_{\mathbf{pq}}, \end{aligned} \quad (38)$$

i.e., it consists of the total energy of the ionized system and the Hartree-Fock Hamiltonian for continuum states. The latter is computed with the density matrix of the target:

$$\tilde{t}_{\mathbf{pq}} = t_{\mathbf{pq}} + \sum_{nm} V_{\mathbf{pnmq}} \langle c_n^\dagger c_m \rangle. \quad (39)$$

Let  $\hat{h}$  be an operator acting on the subspace of continuum states with matrix elements given by Eq. (38). Its resolvent

$$g_{\mathbf{pq}}^{(p)}(z) = \langle \Psi_\alpha^+ | c_{\mathbf{p}} \frac{1}{z - \hat{h}} c_{\mathbf{q}}^\dagger | \Psi_\alpha^+ \rangle \quad (40)$$

relates to the reference retarded GF as  $g_{\mathbf{pq}}^R(\omega) = g_{\mathbf{pq}}^{(p)}(E_\alpha^+ + \omega + i\eta)$ .

## 3. Self-energy and the Dyson equation

The second correlator in EOM (37) amounts to

$$\begin{aligned} \langle \Psi_\alpha^{(1)} | [c_{\mathbf{p}}, \hat{H}] \frac{1}{z - \hat{H}} c_{\mathbf{q}}^\dagger | \Psi_\alpha^+ \rangle \\ = \sum_a t_{\mathbf{pa}} \langle \Psi_\alpha^+ | c_a \frac{1}{z - \hat{H}} c_{\mathbf{q}}^\dagger | \Psi_\alpha^+ \rangle \\ + \sum_n \sum_{ab} v_{\mathbf{pnab}} \langle \Psi_\alpha^+ | c_n^\dagger c_a c_b \frac{1}{z - \hat{H}} c_{\mathbf{q}}^\dagger | \Psi_\alpha^+ \rangle. \end{aligned}$$

With Eq. (29) inserted into the identity (28a) we apply  $P_\alpha$  from left and right, use the same trick to multiply with suitable states from left and right, and find

$$\begin{aligned} G_{\mathbf{pq}}^{(p)}(z) = g_{\mathbf{pq}}^{(p)}(z) - \sum_{\mathbf{kk}'} g_{\mathbf{pk}}^{(p)}(z) \tilde{t}_{\mathbf{kk}'} G_{\mathbf{k}'\mathbf{q}}^{(p)}(z) \\ + \sum_{\mathbf{k}} \sum_a g_{\mathbf{pk}}^{(p)}(z) t_{\mathbf{ka}} G_{\mathbf{aq}}^{(p)}(z) \\ + \sum_{\mathbf{k}} \sum_n \sum_{ab} g_{\mathbf{pk}}^{(p)}(z) v_{\mathbf{knab}} \langle \Psi_\alpha^+ | c_n^\dagger c_a c_b \frac{1}{z - \hat{H}} c_{\mathbf{q}}^\dagger | \Psi_\alpha^+ \rangle. \end{aligned} \quad (41)$$

With  $z = E_\alpha^+ + \omega + i\eta$ , Eq. (41) has a structure of a Dyson equation for the retarded Green's function in the subspace of continuum states:

$$G_{\mathbf{pq}}^R(\omega) = g_{\mathbf{pq}}^R(\omega) + \sum_{\mathbf{ka}} g_{\mathbf{pk}}^R(\omega) \Sigma_{\mathbf{ka}}^R(\omega) G_{\mathbf{aq}}^R(\omega). \quad (42)$$

The second sum runs over the full set of orbitals (bound and continuum). This is the most general form and without additional analysis it cannot be reduced to the Dyson equation with the self-energy from the projection formalism [cf. Eq. (27)]. Let us compare Eqs. (41) and (42). At first we notice that Eq. (39) defines the reference Hamiltonian only on the subspace of scattering states. We might extend the definition and request, for instance, that all the basis functions (bound and scattering) are the eigenstates of the reference Hamiltonian. This implies  $\tilde{t}_{\mathbf{pq}} = \varepsilon_{\mathbf{p}} \delta_{\mathbf{pq}}$  and  $\tilde{t}_{\mathbf{nq}} = 0$ . Thus, mean-field terms of the Hartree-Fock Hamiltonian are then canceled by the frequency-independent part of the last correlator in Eq. (41). In the case when the reference Hamiltonian is not diagonal in the chosen basis the embedding self-energy terms additionally appear. In the simplest case (no interaction), they can be written as  $\Sigma_{\mathbf{pq}}^{\text{em}}(z) = \sum_{mn} t_{\mathbf{pn}} g_{\mathbf{nm}}^{(p)}(z) t_{\mathbf{nq}}$ . Let us now assume that the single-particle basis is such that no embedding self-energy appears. What would be the diagrammatic structure of the self-energy (27)? From the Dyson equation in the bound-continuum sector

$$\begin{aligned} G_{\mathbf{lq}}^R(\omega) = \sum_{\mathbf{mk}} g_{\mathbf{lm}}^R(\omega) \Sigma_{\mathbf{mk}}^R(\omega) G_{\mathbf{kq}}^R(\omega) \\ + \sum_{\mathbf{mn}} g_{\mathbf{lm}}^R(\omega) \Sigma_{\mathbf{mn}}^R(\omega) G_{\mathbf{nq}}^R(\omega), \end{aligned} \quad (43)$$



we determine the Green's function in this sector ( $G_{bc}$ ) and substitute in Eq. (42):

$$G_{pq}^R(\omega) = g_{pq}^R(\omega) + \sum_{kk'} g_{pk}^R(\omega) \times \left[ \Sigma_{cc} + \Sigma_{cb} \frac{g_b}{1 - g_b \Sigma_{bb}} \Sigma_{bc} \right]_{kk'} G_{k'q}^R, \quad (44)$$

where for brevity the subscripts  $b$  and  $c$  denote the bound and the continuum sectors. Expressions in square brackets [Eq. (44)] can now be compared with the self-energy from the projection formalism (27). Notice that the reference Green's function was assumed to be diagonal, i.e.,  $g_b \equiv g_{bb}$  and  $g_{bc} = 0$ .

#### 4. Dominant scattering mechanisms

Let us recapitulate what led us to Eq. (44). We have chosen a projection operator in the form (30). This specifies the state of a system after the photoionization as containing one photoelectron in the scattering state plus the bound ionized target. Next, we obtained an effective Hamiltonian (38) acting on the  $P$  subspace and used it to define the reference Green's function (40). We want to understand what is the diagrammatic content of the Feshbach self-energy (27). It is not possible to use this equation directly because it involves the effective Hamiltonian on the complementary  $Q$  subspace. However, it is possible to use another matrix identity (28a) and to formulate the Dyson equation for the full Green's function in the  $P$  subspace (41) avoiding the use of the  $Q\hat{H}Q$  resolvent. This equation can be put in a direct correspondence with the Dyson equation for the retarded GF from the many-body perturbation theory. The difference between them is the domain where the self-energies are defined: the Feshbach self-energy operates on the continuum sector only, whereas many-body perturbation theory does not impose such a restriction. By writing another Dyson equation (43) in the bound-continuum sector, we can finally obtain the Dyson equation with an effective self-energy in the continuum-continuum sector. This self-energy is an exact counterpart of the Feshbach self-energy (27). Critical for our derivation was the choice of the single-particle basis. We have demonstrated that it is the projection operator that determines the effective Hamiltonian, and if the basis is such that the Hamiltonian is diagonal the embedding self-energy vanishes and one arrives at Eq. (44). No further assumptions have been made and Eq. (44) is so far exact.

Let us analyze the meaning of different terms of the photoelectron self-energy (Fig. 2). As discussed in details by Bardyszewski and Hedin [33], Almbladh [16], and Fujikawa and Hedin [34], scattering states that vanish in the sample (damped) represent the real photoelectron states more precisely. One can derive explicitly the residual interaction which they experience. The reasoning is easier to perform in real space where the Coulomb interaction depends on two coordinates only [cf. Eq. (2)] as opposite to the Coulomb matrix elements which are four index quantities. Since the scattering states are damped in the sample, there are only two nonvanishing Green's functions  $G_{vv}$  and  $G_{VV}$  operating exclusively in the inner ( $v$ ) and outer ( $V$ ) spaces, respectively. The Green's function starting in the sample and ending outside of it ( $G_{vV}$ ) and the reverse ( $G_{Vv}$ ) vanish. We can rewrite

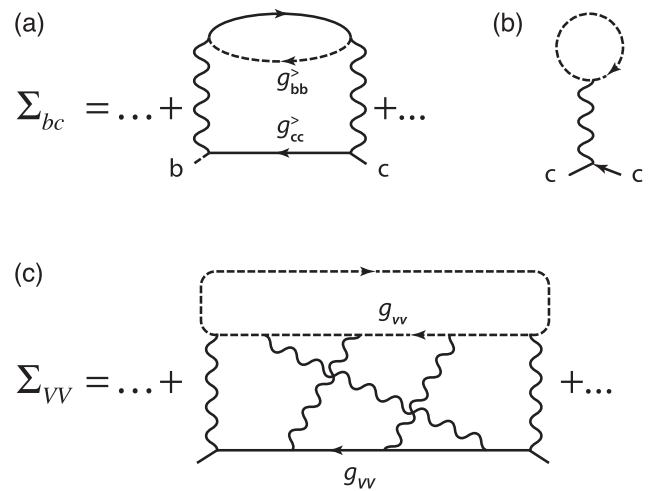


FIG. 2. (a) Example of self-energy diagram that mixes bound and continuum states and is the building block of the second term in brackets in Eq. (44); (b) mean-field Hartree contribution to the effective Hamiltonian (38); (c) a typical contribution to the electron self-energy in continuum-continuum sector in the case when the photoelectron is completely screened in the sample.

Eq. (44) in these new notations, however, it is not even necessary as it amounts to the mere replacement  $b \rightarrow v$  and  $c \rightarrow V$ . What has changed is the interaction lines in the diagrammatic expansion of the self-energy. They can connect  $v$  and  $V$  domains and generate therefore nonzero contributions. It is easy to see, however, that the second self-energy term vanishes: a diagrammatic expansion of  $\Sigma_{vV}$  necessarily contains at least one  $g_{vV}$  line which is zero according to our assumption. Thus, only  $\Sigma_{VV}$  needs to be analyzed. By explicitly forbidding the particle exchange with the sample, we arrived exactly at the case of *elastic* electron scattering considered in the seminal paper of Bell and Squires [37]. We will see below that the structure of  $\Sigma_{VV}$  is quite general and appears in the diagrammatic consideration of other processes, remarkably, in the parquet diagram treatment of the Fermi edge singularities [58]. There, however, a similar diagrammatic expansion arises due to the specific choice of the interaction between the deep hole (labeled by  $m$ ) and the conduction electrons:  $\hat{H}_I = \sum_{kk'} V_{kk'} c_{k'}^\dagger c_k c_m^\dagger c_m$ . In contrast to their work, what induces a special structure of diagrams for  $\Sigma_{VV}$  is not a specific form of the interaction matrix elements, but rather the absence of the off-diagonal blocks in  $g$ . It is easy to construct the electron self-energy fulfilling these restrictions: it consists of *one* open photoelectron line (depicted as solid line on Fig. 2) and a number of closed bound electron loops (depicted as dashed lines). Because of the restriction (33) there are no photoelectron loops.

The topic of the present section is quite extensive, and such an aspect as the Lehmann representation of the Green's functions mentioned here was completely left out of our discussion. This is, however, very relevant for the treatment of finite systems, with important recent progress, e.g., [59].

### D. Example of DPE

#### 1. Equation of motion

The derivation for the two-particle case goes along the same lines. We insert the definition of the projection operator [Eq. (35)] in the identity

$$(z - E_\beta^{2+})P_\beta \frac{1}{z - \hat{H}} P_\beta = P_\beta + P_\beta (\hat{H} - E_\beta^{2+}) \frac{1}{z - \hat{H}} P_\beta,$$

replace  $\langle \Psi_\beta^{2+} | c_{\mathbf{p}'} c_{\mathbf{p}} (\hat{H} - E_\beta^{2+}) = \langle \Psi_\beta^{2+} | [c_{\mathbf{p}'} c_{\mathbf{p}}, \hat{H}]$ , and as for SPE compute the matrix elements of the whole expression. The final results read as

$$\begin{aligned} (z - E_\beta^{2+})G_{\mathbf{p}\mathbf{p}'\mathbf{q}\mathbf{q}'}^{(\text{pp})}(z) &= \delta_{\mathbf{p}\mathbf{q}}\delta_{\mathbf{p}'\mathbf{q}'} - \delta_{\mathbf{p}\mathbf{q}'}\delta_{\mathbf{p}'\mathbf{q}} \\ &+ \langle \Psi_\beta^{2+} | [c_{\mathbf{p}'} c_{\mathbf{p}}, H] \frac{1}{z - \hat{H}} c_{\mathbf{q}'}^\dagger c_{\mathbf{q}}^\dagger | \Psi_\beta^{2+} \rangle. \end{aligned} \quad (45)$$

The prefactor  $\frac{1}{4}$  originating from the product of two projection operators is canceled because of the symmetries of the particle-particle GF and of the second term on the right-hand side of Eq. (45):

$$G_{\mathbf{p}'\mathbf{p}\mathbf{q}\mathbf{q}'}^{(\text{pp})}(z) = G_{\mathbf{p}\mathbf{p}'\mathbf{q}\mathbf{q}'}^{(\text{pp})}(z) = -G_{\mathbf{p}\mathbf{p}'\mathbf{q}\mathbf{q}'}^{(\text{pp})}(z) = -G_{\mathbf{p}'\mathbf{p}\mathbf{q}\mathbf{q}'}^{(\text{pp})}(z). \quad (46)$$

Inserting  $z = E_\beta^{2+} + \omega + i\eta$  shows the equivalence of Eq. (45) to the equation of motion (25).

#### 2. Effective two-particle Hamiltonian

Analogically to the SPE case we consider the Feshbach-projected Hamiltonian in the subspace defined by  $P_\beta$  and describing two electrons including their interaction and their mean-field interaction with the ionized system:

$$\begin{aligned} \langle \Psi_\beta^{2+} | c_{\mathbf{p}'} c_{\mathbf{p}} \hat{H} c_{\mathbf{q}}^\dagger c_{\mathbf{q}'}^\dagger | \Psi_\beta^{2+} \rangle \\ = E_\beta^{2+} (\delta_{\mathbf{p}\mathbf{q}}\delta_{\mathbf{p}'\mathbf{q}'} - \delta_{\mathbf{p}\mathbf{q}'}\delta_{\mathbf{p}'\mathbf{q}}) + \langle \Psi_\beta^{2+} | [c_{\mathbf{p}'} c_{\mathbf{p}}, H] c_{\mathbf{q}}^\dagger c_{\mathbf{q}'}^\dagger | \Psi_\beta^{2+} \rangle, \end{aligned} \quad (47)$$

where the last term can be expressed as follows:

$$\begin{aligned} \langle \Psi_\beta^{2+} | [c_{\mathbf{p}'} c_{\mathbf{p}}, H] c_{\mathbf{q}}^\dagger c_{\mathbf{q}'}^\dagger | \Psi_\beta^{2+} \rangle \\ = t_{\mathbf{p}\mathbf{q}}\delta_{\mathbf{p}'\mathbf{q}'} + t_{\mathbf{p}'\mathbf{q}}\delta_{\mathbf{p}\mathbf{q}} - t_{\mathbf{p}\mathbf{q}'}\delta_{\mathbf{p}'\mathbf{q}} - t_{\mathbf{p}'\mathbf{q}'}\delta_{\mathbf{p}\mathbf{q}} + v_{\mathbf{p}\mathbf{p}'\mathbf{q}\mathbf{q}'} - v_{\mathbf{p}'\mathbf{p}\mathbf{q}\mathbf{q}'} \\ + \sum_n \sum_{ab} [v_{\mathbf{p}nab} \langle \Psi_\beta^{2+} | c_n^\dagger c_{\mathbf{p}'} c_a c_b c_{\mathbf{q}}^\dagger c_{\mathbf{q}'}^\dagger | \Psi_\beta^{2+} \rangle \\ - v_{\mathbf{p}'nab} \langle \Psi_\beta^{2+} | c_n^\dagger c_{\mathbf{p}} c_a c_b c_{\mathbf{q}}^\dagger c_{\mathbf{q}'}^\dagger | \Psi_\beta^{2+} \rangle]. \end{aligned} \quad (48)$$

The first correlator in the square brackets evaluates in terms of the density matrix with respect to  $|\Psi_\beta^{2+}\rangle$  with bound state indices to

$$\sum_{nm} [V_{\mathbf{p}n\mathbf{q}m} \delta_{\mathbf{p}'\mathbf{q}'} - V_{\mathbf{p}n\mathbf{q}'m} \delta_{\mathbf{p}\mathbf{q}}] \langle c_n^\dagger c_m \rangle.$$

Here, we have written it in terms of the matrix elements of the antisymmetrized Coulomb interaction (2)  $V_{abcd} \equiv v_{abcd} - v_{abdc}$ . Similarly, the second correlator is obtained from this expression by the index exchange  $\mathbf{p} \leftrightarrow \mathbf{p}'$ . The effective two-particle Hamiltonian (47) is so expressible as a Hartree-Fock Hamiltonian (39) for two independent electrons

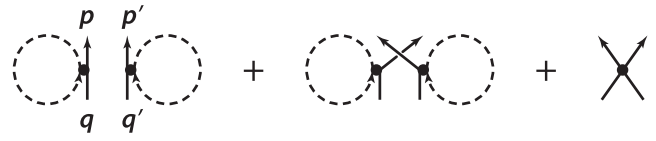


FIG. 3. Interaction between the photoelectrons incorporated in the effective Hamiltonian (49). Dashed lines denote bare bound-state propagators. Dots denote the antisymmetrized Coulomb interaction (2).

plus the interaction (Fig. 3):

$$\begin{aligned} h_{\mathbf{p}'\mathbf{p}\mathbf{q}\mathbf{q}'} &= E_\beta^{2+} (\delta_{\mathbf{p}\mathbf{q}}\delta_{\mathbf{p}'\mathbf{q}'} - \delta_{\mathbf{p}\mathbf{q}'}\delta_{\mathbf{p}'\mathbf{q}}) + (\tilde{t}_{\mathbf{p}\mathbf{q}}\delta_{\mathbf{p}'\mathbf{q}'} + \tilde{t}_{\mathbf{p}'\mathbf{q}}\delta_{\mathbf{p}\mathbf{q}}) \\ &- (\tilde{t}_{\mathbf{p}\mathbf{q}'}\delta_{\mathbf{p}'\mathbf{q}} + \tilde{t}_{\mathbf{p}'\mathbf{q}'}\delta_{\mathbf{p}\mathbf{q}}) + V_{\mathbf{p}'\mathbf{p}\mathbf{q}\mathbf{q}'}. \end{aligned} \quad (49)$$

#### 3. Kernel and Dyson equation

We return to the matrix identity (28a) and insert the splitting (29) with  $P = P_\beta$  [Eq. (35)]:

$$\begin{aligned} P_\beta \frac{1}{z - \hat{H}} P_\beta &= P_\beta \frac{1}{z - \hat{h}} P_\beta + P_\beta \frac{1}{z - \hat{h}} P_\beta \hat{H} \frac{1}{z - \hat{H}} P_\beta \\ &- P_\beta \frac{1}{z - \hat{h}} P_\beta \hat{H} P_\beta \frac{1}{z - \hat{H}} P_\beta, \end{aligned}$$

and define the reference two-particle GF

$$g_{\mathbf{p}\mathbf{p}'\mathbf{q}\mathbf{q}'}^{(\text{pp})}(z) = \langle \Psi_\beta^{2+} | c_{\mathbf{p}} c_{\mathbf{p}'} \frac{1}{z - \hat{h}} c_{\mathbf{q}}^\dagger c_{\mathbf{q}'}^\dagger | \Psi_\beta^{2+} \rangle. \quad (50)$$

Invoking again the symmetries (46), which also holds true for the reference GF, and applying the same states from left and right, we obtain

$$\begin{aligned} G_{\mathbf{p}\mathbf{p}'\mathbf{q}\mathbf{q}'}^{(\text{pp})}(z) &= g_{\mathbf{p}\mathbf{p}'\mathbf{q}\mathbf{q}'}^{(\text{pp})}(z) + \sum_{\mathbf{k}\mathbf{k}'} g_{\mathbf{p}\mathbf{p}'\mathbf{k}\mathbf{k}'}^{(\text{pp})}(z) \\ &\times \left[ \langle \Psi_\beta^{2+} | [c_{\mathbf{k}} c_{\mathbf{k}'}, \hat{H}] \frac{1}{z - \hat{H}} c_{\mathbf{q}}^\dagger c_{\mathbf{q}'}^\dagger | \Psi_\beta^{2+} \rangle \right. \\ &\left. - \frac{1}{2} \sum_{\mathbf{nn}'} \langle \Psi_\beta^{2+} | [c_{\mathbf{k}} c_{\mathbf{k}'}, \hat{H}] c_{\mathbf{n}}^\dagger c_{\mathbf{n}'}^\dagger | \Psi_\beta^{2+} \rangle G_{\mathbf{nn}'\mathbf{q}\mathbf{q}'}^{(\text{pp})}(z) \right]. \end{aligned} \quad (51)$$

It is instructive to divide the kernel entering the equation of motion [second line of Eq. (45)] or the Dyson equation [second line of Eq. (51)] into the terms containing higher correlation functions and those expressible in terms of two-particle GFs:

$$\begin{aligned} \langle \Psi_\beta^{2+} | [c_{\mathbf{k}} c_{\mathbf{k}'}, \hat{H}] \frac{1}{z - \hat{H}} c_{\mathbf{q}}^\dagger c_{\mathbf{q}'}^\dagger | \Psi_\beta^{2+} \rangle \\ = T_{\mathbf{k}\mathbf{k}'\mathbf{q}\mathbf{q}'}(z) + \sum_b (t_{\mathbf{k}'b} G_{\mathbf{k}b\mathbf{q}\mathbf{q}'}^{(\text{pp})}(z) - t_{\mathbf{k}b} G_{\mathbf{k}'b\mathbf{q}\mathbf{q}'}^{(\text{pp})}(z)) \\ + \sum_{ab} v_{\mathbf{k}\mathbf{k}'ab} G_{\mathbf{a}b\mathbf{q}\mathbf{q}'}^{(\text{pp})}(z). \end{aligned}$$

The latter gives rise to the particle-particle embedding self-energy. We can now formally introduce the correlated

frequency-dependent and the static kernels:

$$\begin{aligned}
T_{\mathbf{k}\mathbf{k}'\mathbf{q}\mathbf{q}'}(z) &= \sum_{\mathbf{nn}'} \left[ \mathcal{K}_{\mathbf{k}\mathbf{k}'\mathbf{nn}'}^c(z) + \frac{1}{2} \mathcal{K}_{\mathbf{k}\mathbf{k}'\mathbf{nn}'}^\infty \right] G_{\mathbf{nn}'\mathbf{q}\mathbf{q}'}^{(\text{pp})}(z) \\
&= \sum_n \sum_{ab} v_{\mathbf{k}nab} \langle \Psi_\beta^{2+} | c_n^\dagger c_{\mathbf{k}'} c_a c_b \frac{1}{z - \hat{H}} c_{\mathbf{q}'}^\dagger c_{\mathbf{q}}^\dagger | \Psi_\beta^{2+} \rangle \\
&\quad - \sum_n \sum_{ab} v_{\mathbf{k}'nab} \langle \Psi_\beta^{2+} | c_n^\dagger c_{\mathbf{k}} c_a c_b \\
&\quad \times \frac{1}{z - \hat{H}} c_{\mathbf{q}'}^\dagger c_{\mathbf{q}}^\dagger | \Psi_\beta^{2+} \rangle. \quad (52)
\end{aligned}$$

The static part is exactly canceled by the density-dependent part of the effective Hamiltonian:

$$\begin{aligned}
\mathcal{K}_{\mathbf{k}\mathbf{k}'\mathbf{q}\mathbf{q}'}^\infty &= \sum_n \langle c_n^\dagger c_m \rangle [V_{\mathbf{k}n\mathbf{q}m} \delta_{\mathbf{k}'\mathbf{q}'} + V_{\mathbf{k}'n\mathbf{q}'m} \delta_{\mathbf{k}\mathbf{q}} \\
&\quad - V_{\mathbf{k}n\mathbf{q}'m} \delta_{\mathbf{k}'\mathbf{q}} - V_{\mathbf{k}'n\mathbf{q}m} \delta_{\mathbf{k}\mathbf{q}'}]. \quad (53)
\end{aligned}$$

The embedding self-energy originates from the kernel as well as from the effective Hamiltonian (49):

$$\begin{aligned}
&\sum_{\mathbf{nn}'} \mathcal{K}_{\mathbf{k}\mathbf{k}'\mathbf{nn}'}^{\text{em}} G_{\mathbf{nn}'\mathbf{q}\mathbf{q}'}^{(\text{pp})}(z) \\
&= \sum_m (\tilde{t}_{\mathbf{k}'m} G_{\mathbf{k}m\mathbf{q}\mathbf{q}'}^{(\text{pp})}(z) - \tilde{t}_{\mathbf{k}m} G_{\mathbf{k}'m\mathbf{q}\mathbf{q}'}^{(\text{pp})}(z)) \\
&\quad + \sum_{ab} v_{\mathbf{k}\mathbf{k}'ab} G_{ab\mathbf{q}\mathbf{q}'}^{(\text{pp})}(z) - \sum_{\mathbf{pp}'} v_{\mathbf{k}\mathbf{k}'\mathbf{p}\mathbf{p}'} G_{\mathbf{p}\mathbf{p}'\mathbf{q}\mathbf{q}'}^{(\text{pp})}(z). \quad (54)
\end{aligned}$$

With the results (49), (52), (53), and (54) we can cast the Dyson equation (51) in the final form

$$\begin{aligned}
G_{\mathbf{p}\mathbf{p}'\mathbf{q}\mathbf{q}'}^R(\omega) &= g_{\mathbf{p}\mathbf{p}'\mathbf{q}\mathbf{q}'}^R(\omega) + \sum_{\mathbf{k}\mathbf{k}'} \sum_{\mathbf{nn}'} g_{\mathbf{p}\mathbf{p}'\mathbf{k}\mathbf{k}'}^R(\omega) \\
&\quad \times [\mathcal{K}_{\mathbf{k}\mathbf{k}'\mathbf{nn}'}^{\text{em}} + \mathcal{K}_{\mathbf{k}\mathbf{k}'\mathbf{nn}'}^c(\omega)] G_{\mathbf{nn}'\mathbf{q}\mathbf{q}'}^R(\omega). \quad (55)
\end{aligned}$$

Equation (55) has a form of the Dyson equation for the two-particle Green's function, however, the reference GF  $g_{\mathbf{p}\mathbf{p}'\mathbf{q}\mathbf{q}'}^R(\omega)$  is not given as a product of fully interacting single-particle GFs, but rather is the full two-particle GF: the resolvent of the effective Hamiltonian (47) which includes the full electron-electron repulsion and the mean-field contribution from the ionized system.

#### IV. FERMI GOLDEN RULE

##### A. Single photoemission

SPE was treated by several authors. We recapitulate the main points. The total observed current is proportional to the expectation value of the electron number operator  $\hat{N}_{\mathbf{k}} = c_{\mathbf{k}}^\dagger c_{\mathbf{k}}$ . Out of all possible final states of the target we discard all unbound states, i.e.,  $c_{\mathbf{k}} |\Psi_\alpha^+\rangle = 0$  and choose only those relevant for a specific experiment. Let  $\lambda_\alpha$  be a corresponding distribution function. For instance, when the target is left in the ground state we can set  $\lambda_0 = 1$  and  $\lambda_\alpha = 0$  for all excited states. Modified particle-number operator for this process reads as

$$\hat{N}_{\mathbf{k}} = \sum_\alpha \lambda_\alpha c_{\mathbf{k}}^\dagger |\Psi_\alpha^+\rangle \langle \Psi_\alpha^+| c_{\mathbf{k}} = \sum_\alpha \lambda_\alpha P_\alpha c_{\mathbf{k}}^\dagger c_{\mathbf{k}} P_\alpha.$$

The same expression can be obtained from the Langreth approach starting from the Wigner distribution function [20]. Let now the SPE current be the expectation value of this operator:

$$\begin{aligned}
J_{\mathbf{k}} &= \lim_{\eta \rightarrow 0} 2\eta \sum_\alpha \lambda_\alpha \langle \Psi_0 | \hat{\Delta}^\dagger \frac{1}{E_0 + \omega - \hat{H} - i\eta} P_\alpha c_{\mathbf{k}}^\dagger c_{\mathbf{k}} P_\alpha \\
&\quad \times \frac{1}{E_0 + \omega - \hat{H} + i\eta} \hat{\Delta} | \Psi_0 \rangle. \quad (56)
\end{aligned}$$

We only consider the case

$$P_\alpha \frac{1}{E_i - \hat{H} + i\eta} \approx \frac{P_\alpha}{E_i - \hat{H}_P - \hat{\Sigma}_P^{(+)}(E_i)}, \quad (57)$$

where we neglect the off-diagonal term in Eq. (26) and define  $\hat{\Sigma}_P^{(\pm)}(\omega) = \hat{\Sigma}_P(\omega \pm i\eta)$ . We omit the subscript  $\alpha$  where it does not cause a confusion. A simple calculation leads to the modified matrix element

$$M_{\mathbf{k},\alpha} = \langle \Psi_\alpha^+ | c_{\mathbf{k}} \frac{1}{E_i - \hat{H}_P - \hat{\Sigma}_P^{(+)}(E_i)} P_\alpha \hat{\Delta} | \Psi_0 \rangle. \quad (58)$$

Using the same assumption for the computation of the matrix element of  $\hat{\Delta}$ ,  $\langle \Psi_\alpha^+ | c_{\mathbf{p}} \hat{\Delta} | \Psi_0 \rangle = \langle \mathbf{p} | \hat{\Delta} | \phi_\alpha \rangle$  and the definition of the Green's function on the  $P_\alpha$  subspace

$$G_{\mathbf{p}\mathbf{k},\alpha}^{(\text{p})}(\omega + \varepsilon_\alpha \pm i\eta) = \langle \Psi_\alpha^+ | c_{\mathbf{p}} \frac{1}{E_i - \hat{H}_P - \hat{\Sigma}_P^{(\pm)}(E_i)} c_{\mathbf{k}}^\dagger | \Psi_\alpha^+ \rangle,$$

we obtain for the current

$$\begin{aligned}
J_{\mathbf{k}} &= \lim_{\eta \rightarrow 0} 2\eta \sum_\alpha \lambda_\alpha \sum_{\mathbf{p}\mathbf{q}} \langle \phi_\alpha | \hat{\Delta}^\dagger | \mathbf{p} \rangle G_{\mathbf{p}\mathbf{k},\alpha}^{(\text{p})}(\omega + \varepsilon_\alpha - i\eta) \\
&\quad \times G_{\mathbf{k}\mathbf{q},\alpha}^{(\text{p})}(\omega + \varepsilon_\alpha + i\eta) \langle \mathbf{q} | \hat{\Delta} | \phi_\alpha \rangle, \quad (59)
\end{aligned}$$

where  $\varepsilon_\alpha = E_0 - E_\alpha^+$ . As shown in Appendix B, we can express the particle Green's functions in terms of Møller operators

$$G_{\mathbf{p}\mathbf{k},\alpha}^{(\text{p})}(\omega + \varepsilon_\alpha - i\eta) = \frac{1}{\omega + \varepsilon_\alpha - \varepsilon_{\mathbf{k}} - i\eta} \langle \mathbf{p} | \chi_{\mathbf{k},\alpha}^{(-)} \rangle, \quad (60a)$$

$$G_{\mathbf{k}\mathbf{q},\alpha}^{(\text{p})}(\omega + \varepsilon_\alpha + i\eta) = \frac{1}{\omega + \varepsilon_\alpha - \varepsilon_{\mathbf{k}} + i\eta} \langle \chi_{\mathbf{k},\alpha}^{(-)} | \mathbf{q} \rangle. \quad (60b)$$

This finally leads to the current

$$J_{\mathbf{k}} = 2\pi \sum_\alpha \lambda_\alpha \langle \chi_{\mathbf{k},\alpha}^{(-)} | \hat{\Delta} | \phi_\alpha \rangle \delta(\omega + \varepsilon_\alpha - \varepsilon_{\mathbf{k}}) \langle \phi_\alpha | \hat{\Delta}^\dagger | \chi_{\mathbf{k},\alpha}^{(-)} \rangle.$$

A standard definition of the spectral function entails to

$$\hat{A}(\zeta) = \sum_\alpha |\phi_\alpha\rangle \delta(\zeta - \varepsilon_\alpha) \langle \phi_\alpha|.$$

Therefore, we can recast the expression for the current in a more familiar response form

$$J_{\mathbf{k}} = 2\pi \int_{-\infty}^{\mu} d\zeta \delta(\omega + \zeta - \varepsilon_{\mathbf{k}}) \langle \chi_{\mathbf{k},\alpha}^{(-)} | \hat{A}(\zeta) \hat{\Delta}^\dagger | \chi_{\mathbf{k},\alpha}^{(-)} \rangle,$$

where the tilde denotes a spectral function with restrictions imposed by the weighting factors  $\lambda_\alpha$  and  $\mu$  is the chemical potential, or in the Fermi golden rule form

$$J_{\mathbf{k}} = 2\pi \sum_\alpha \lambda_\alpha \delta(\omega + \varepsilon_\alpha - \varepsilon_{\mathbf{k}}) |\langle \chi_{\mathbf{k},\alpha}^{(-)} | \hat{\Delta} | \phi_\alpha \rangle|^2.$$

The major distinction from other approaches is that both initial and final states are dependent on the final state of the target  $\alpha$ . Formally,  $|\chi_{\mathbf{k},\alpha}^{(-)}\rangle$  is the incoming scattering state of an electron in the optical potential of the ionized target in the state  $|\Psi_{\alpha}^{+}\rangle$ .

### B. Double photoemission

The total observed current is given in terms of the expectation value of the electron-number operators  $\hat{N}_{\mathbf{k}_1\mathbf{k}_2} = \hat{N}_{\mathbf{k}_1}\hat{N}_{\mathbf{k}_2} - \delta_{\mathbf{k}_1,\mathbf{k}_2}\hat{N}_{\mathbf{k}_1}$ , viz., Eq. (8). Out of all possible final states of the target we discard all unbound states, i.e.,  $c_{\mathbf{k}}|\Psi_{\beta}^{2+}\rangle = 0$  and introduce weights  $\lambda_{\beta}$  selecting the relevant ones. The modified observable reads as

$$\begin{aligned}\hat{N}_{\mathbf{k}_1\mathbf{k}_2} &= \sum_{\beta} \lambda_{\beta} c_{\mathbf{k}_1}^{\dagger} c_{\mathbf{k}_2}^{\dagger} |\Psi_{\beta}^{2+}\rangle \langle \Psi_{\beta}^{2+}| c_{\mathbf{k}_2} c_{\mathbf{k}_1} \\ &= \sum_{\beta} P_{\beta} c_{\mathbf{k}_1}^{\dagger} c_{\mathbf{k}_2}^{\dagger} c_{\mathbf{k}_2} c_{\mathbf{k}_1} P_{\beta}.\end{aligned}\quad (61)$$

This allows us to improve upon Eq. (15):

$$\begin{aligned}J_{\mathbf{k}_1,\mathbf{k}_2} &= \lim_{\eta \rightarrow 0} 2\eta \sum_{\beta} \lambda_{\beta} \langle \Psi_0 | \hat{\Delta}^{\dagger} \frac{1}{E_0 + \omega - \hat{H} - i\eta} \\ &\quad \times P_{\beta} c_{\mathbf{k}_1}^{\dagger} c_{\mathbf{k}_2}^{\dagger} c_{\mathbf{k}_2} c_{\mathbf{k}_1} P_{\beta} \frac{1}{E_0 + \omega - \hat{H} + i\eta} \hat{\Delta} | \Psi_0 \rangle.\end{aligned}\quad (62)$$

Using assumption (57), Eq. (62) can be written in the Fermi golden rule form with a modified matrix element

$$M_{\mathbf{k}_1\mathbf{k}_2,\beta} = \langle \Psi_{\beta}^{2+} | c_{\mathbf{k}_2} c_{\mathbf{k}_1} \frac{1}{E_i - \hat{H}_P - \hat{\Sigma}_P^{(+)}(E_i)} P_{\beta} \hat{\Delta} | \Psi_0 \rangle.$$

Using the matrix elements of  $\hat{\Delta}$ ,  $\langle \Psi_{\beta}^{2+} | c_{\mathbf{q}} c_{\mathbf{p}} \hat{\Delta} | \Psi_0 \rangle = \langle \mathbf{p}\mathbf{q} | \hat{\Delta} | \phi_{\beta}^{(2)} \rangle$  [cf. Eq. (D8)], and the properties of the two-particle Green's functions (Appendix B)

$$\begin{aligned}G_{\mathbf{p}\mathbf{q},\mathbf{k}_1\mathbf{k}_2,\beta}^{(\text{pp})}(\omega + \varepsilon_{\beta}^{(2)} \pm i\eta) &= \langle \Psi_{\beta}^{2+} | c_{\mathbf{p}} c_{\mathbf{q}} \frac{1}{E_i - \hat{H}_P - \hat{\Sigma}_P^{(+)}(E_i)} c_{\mathbf{k}_2}^{\dagger} c_{\mathbf{k}_1}^{\dagger} | \Psi_{\beta}^{2+} \rangle \\ &= \frac{1}{\omega + \varepsilon_{\beta}^{(2)} - \varepsilon_{\mathbf{k}_1} - \varepsilon_{\mathbf{k}_2} \pm i\eta} \langle \mathbf{p}\mathbf{q} | \psi_{\mathbf{k}_1\mathbf{k}_2,\beta}^{(-)} \rangle,\end{aligned}\quad (63)$$

we finally obtain for Eq. (10)

$$\begin{aligned}J_{\mathbf{k}_1,\mathbf{k}_2} &= 2\pi \int_{-\infty}^{\mu^{(2)}} d\zeta \delta(\omega + \zeta - \varepsilon_{\mathbf{k}_1} - \varepsilon_{\mathbf{k}_2}) \\ &\quad \times \langle \psi_{\mathbf{k}_1\mathbf{k}_2,\beta}^{(-)} | \hat{\Delta} A^{(2)}(\zeta) \hat{\Delta}^{\dagger} | \psi_{\mathbf{k}_1\mathbf{k}_2,\beta}^{(-)} \rangle,\end{aligned}\quad (64)$$

where  $\mu^{(2)} = \max_{\beta} (E_0 - E_{\beta}^{2+})$  is the negative of second ionization potential,  $|\psi_{\mathbf{k}_1\mathbf{k}_2,\beta}^{(-)}\rangle$  is the incoming damped two-electron scattering state in the optical potential of doubly ionized target and  $A^{(2)}(\zeta)$  is the two-particle spectral function, which can be written in terms of two-hole Dyson orbitals

$$\hat{A}^{(2)}(\zeta) = \sum_{\beta} \delta(\zeta - \varepsilon_{\beta}^{(2)}) |\phi_{\beta}^{(2)}\rangle \langle \phi_{\beta}^{(2)}|,\quad (65)$$

with  $\varepsilon_{\beta}^{(2)} = E_0 - E_{\beta}^{2+}$ .

Notice that the current has been obtained using the approximation (57). Exact calculation leads to the appearance of

the vertex functions resulting from  $Q_{\beta} \hat{\Delta} | \Psi_0 \rangle$  and describing a screening of the optical field by the electrons of the target [16].

In valence shell DPE electron correlations in the valence band are important, viz., the correlated two-particle spectral function entering (64). In contrast, when core electrons are involved, a dominant mechanism for DPE is due to the final-state relaxation (so-called shake-off). Multiple stages are then described by introducing corresponding projection operators for each intermediate stage. In the following, we focus on the diagrammatic approach because it allows us to treat all these effects on equal footing.

## V. DIAGRAMMATIC APPROACH

Treatment of the off-diagonal part of the Hamiltonian resolvent is the main difficulty of the Feshbach projection algebra. It is even more aggravated in the two-particle case. The diagrammatic technique provides a natural and practical solution to this problem.

### A. Derivation

Equation (10) when transformed to the time domain gives rise to the following ground-state correlator:

$$\begin{aligned}Z(t,t') &= \langle \Psi_0 | c_b^{\dagger}(t) c_a(t) c_{\mathbf{k}_1}^{\dagger}(0) c_{\mathbf{k}_2}^{\dagger}(0) c_{\mathbf{k}_2}(0) c_{\mathbf{k}_1}(0) \\ &\quad \times c_c^{\dagger}(t') c_d(t') | \Psi_0 \rangle,\end{aligned}\quad (66)$$

where the field operators are in the Heisenberg representation and  $t, t' \in (-\infty, 0]$  are *physical* times. For clarity, we omitted the indices in the notation of the correlator. It can be evaluated diagrammatically by adiabatically switching on the interaction in the remote past, i.e.,  $\hat{H}_{\delta} = \hat{H}_0 + e^{-\delta|t|} \hat{H}_1$ . Now, the average is performed over the noninteracting ground state  $|\Phi_0\rangle$  and the times  $t_2^- < t_1^+$  lie on forward and backward branches of Keldysh contour  $\gamma$  (Fig. 1), respectively:

$$\begin{aligned}Z(t,t') &= \langle \Phi_0 | \mathcal{T} \{ e^{-i \int_{\gamma} \hat{H}_{\delta}(t) dt} c_b^{\dagger}(t_+) c_a(t_+) \\ &\quad \times c_{\mathbf{k}_1}^{\dagger}(0) c_{\mathbf{k}_2}^{\dagger}(0) c_{\mathbf{k}_2}(0) c_{\mathbf{k}_1}(0) c_c^{\dagger}(t_-) c_d(t_-) \} | \Phi_0 \rangle.\end{aligned}\quad (67)$$

$\mathcal{T}$  here is the usual contour ordering operator [13] with the order relation  $\prec$ .  $\hat{H}_{\delta}$  is such that it is equal to the Hamiltonian of noninteracting system  $H_0$  in the remote past and is identical to  $\hat{H}$  at  $t = 0$ . Notice that it is different from adiabatic switching on of the electromagnetic field in Eq. (7).  $|\Phi_0\rangle$  is the ground state of  $\hat{H}_0$ . Using Wick's theorem, we can contract the product of field operators in order to express the correlator in terms of products of single-particle Green's functions. Zeroth order obviously yields four fermionic lines. However, if we use the same assumption as in Sec. IV B, any zeroth-order diagram vanishes. This is easy to understand by comparing with SPE case. There, no-zero contributions are coming from the following contraction:

$$\overbrace{\langle c_b^{\dagger}(t_+) c_a(t_+) c_{\mathbf{p}}^{\dagger}(0) c_{\mathbf{p}}(0) c_c^{\dagger}(t_-) c_d(t_-) \rangle}.$$

This is the only combination that results in greater GFs when one of the arguments is a scattering state [and is compatible with (33)]. In particular, the above contraction equals to

$$g_{ap}^>(t)g_{db}^<(t'-t)g_{pc}^>(-t').$$

In DPE, two creation operators with continuum state indices need to be contracted with two annihilation operators on the positive track. However, there is only one such operator. Hence, zeroth order in interaction is zero. The argument that excludes the first-order diagram is slightly different and is based on the fact that bare interaction is instantaneous, i.e., corresponding time arguments necessarily lie on the same, positive or negative, track.

Second-order nonvanishing contributions contain products of two Coulomb interaction operators (e.g., at contour times  $\bar{t}_+$  and  $\bar{t}_-$ ) and already a familiar product of six operators as in Eq. (67). From all possible contractions (they yield eight fermionic lines), we have to exclude many terms. Some of them immediately vanish because of the assumption (33) for noninteracting GF. Others represent the Hartree-Fock renormalization of two fermionic lines and likewise vanish because of the same assumption for the full fermionic propagators [Fig. 4 (a)]. Then, there are diagrams [Fig. 4 (b)] containing isolated islands of pluses and minuses which also vanish because otherwise the two-particle current cannot be written in the Fermi golden rule form [60,61]. Finally, there

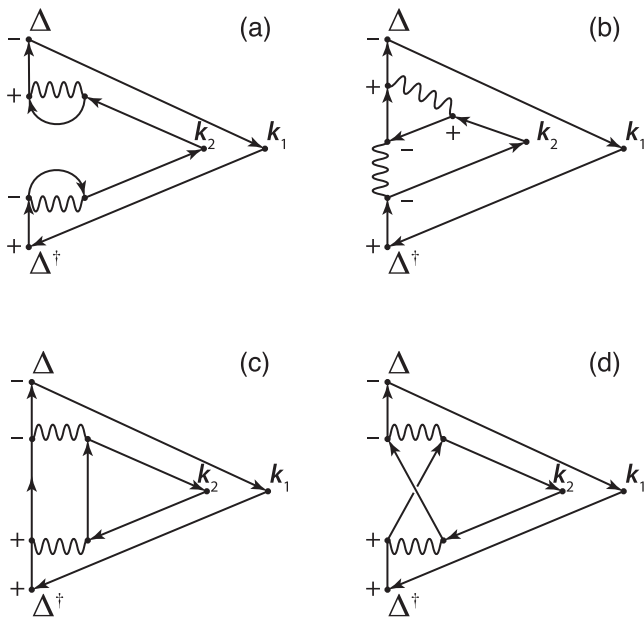


FIG. 4. Second-order diagrams (in bare Coulomb interaction) representing the DPE process. The dots labeled  $\mathbf{k}_1$  and  $\mathbf{k}_2$  correspond to the scattering state of two electrons observed in a coincidence measurement by the detector. Notice that not all combinations of pluses and minuses are possible because Coulomb interaction can only connect vertices on the same branch of the Keldysh contour. (a) Diagram vanishes according to the assumption (33) for dressed GFs. (b) Diagram vanishes because it contains an isolated island of minuses. (c) and (d) are the lowest-order nonzero diagrams. The remaining two are obtained by permuting  $\mathbf{k}_1$  and  $\mathbf{k}_2$ .

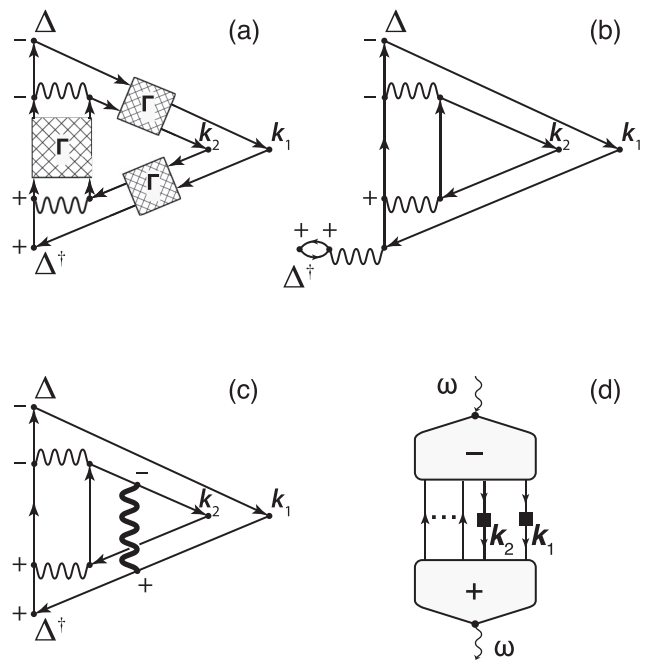


FIG. 5. (a) Diagram for the two-particle current involving dressed two-particle propagators. (b) Simplest diagram where the optical field is screened. (c) Example of a diagram describing external losses. Thick wavy line denotes the screened Coulomb interaction. (d) Generic diagram for the two-particle current.

are only four (times two for exchange) nonzero diagrams. Two of them are depicted at Figs. 4(c) and 4(d).

It is clear now how more general diagrams for the two-electron current can be constructed: (i) One replaces all bare fermionic propagators and interaction lines with the dressed ones. (ii) Each pair of parallel fermionic lines are replaced by the corresponding two-particle propagator [Fig. 5(a)]. In doing so, one obtains, in principle, diagrams given by Fig. 1(b) of Fominykh *et al.* [54] with a small correction that zeroth- and the first-order two-particle GF should be excluded from the vertical track. (iii) Next class of the diagrams are those that describe the screening of the optical field [Fig. 5(b)]. (iv) Processes involving intrinsic or extrinsic losses are given by the diagrams with interaction lines connecting points on different tracks, i.e., “+−,” “+0,” “−0.” They cannot be obtained by the renormalization of fermionic or bosonic propagators; one such example shown in Fig. 5(c) reveals a process with extrinsic losses.

Finally, we give a description of a general diagram for the photoemission process. Examining SPE and DPE diagrams we see that all of them are constructed from the common ancestor: the density-density response function  $\chi^{\equiv} \chi^{-+}$  having a form of two islands with time arguments belonging to either forward or backward tracks of the Keldysh contour. Now, we introduce detectors [shown as black squares at Fig. 5(d)] measuring  $J_{\mathbf{k}_1, \mathbf{k}_2}$ . As explained before, (i) the lesser GF with one of the indices being a continuum state vanishes because of the assumptions (31) and (32); and (ii) observation is made at the rightmost point of the contour (i.e., at  $t_- = t_+ = 0$  in our notations), thus, each detector measuring particle numbers  $N_{\mathbf{k}_i}$

is connected to two greater GF. In view of this, the detectors “lie” on the fermionic lines flowing from the “-” (forward track) to “+” (backward track) islands. Each response function constructed in this way has an important property that it can be represented in the Fermi golden rule form, such construction obviously generalizes to an arbitrary number ( $n$ ) of emitted particles. Simple counting shows that these processes are of at least  $2(n - 1)$  order in the Coulomb interaction.

The diagram in Fig. 5(d) is a generic one describing all the DPE processes including the ones with losses such as shown in Fig. 5(c). One can go a step further and give a prescription for classes of lossless diagrams. A detailed analysis of this particular situation is possible and will be done elsewhere. Here, we mention without a derivation that such diagrams can be split into the scattering part [the two-particle propagators can be written in terms of the scattering states  $|\psi_{\mathbf{k}_1\mathbf{k}_2,\beta}^{(-)}\rangle$ , cf. Eq. (63)] and the spectral part [containing the two-particle spectral function, Eq. (65)].

### B. Example of plasmon-assisted DPE

As an example, we consider the processes depicted in Fig. 6. The diagrams show a very common situation where a primary electron excited by the laser pulse is losing its energy on the way to the detector by exciting a secondary electron. There could be either bare or screened Coulomb interaction between the two electrons. In the latter case, some resonant phenomena related to the excitation of, e.g., plasmon are expected. The SPE case [Figs. 6(a) and 6(b)] is identical to the process of secondary electron excitation considered by Caroli *et al.* [21]. All DPE processes covered by the diagram in Fig. 6(c) form a subset of the SPE process. The only difference between the two scenarios is whether primary, secondary, or both electrons are observed in the detector.

Since we do not take into account the interaction between the two emitted electrons [as given, for, instance by two  $\Gamma$  blocks in Fig. 5(a)], one can express the final result for the current as a matrix element over the direct product of two single-particle scattering states. This is typically a good approximation for the case when two electrons have different energies (momenta), or for approximately equal  $\mathbf{k}_1$  and  $\mathbf{k}_2$  in the case of larger energies [48].

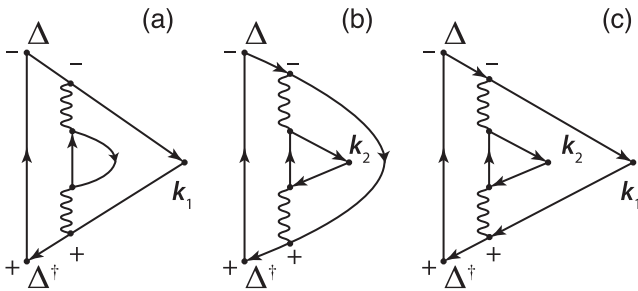


FIG. 6. Diagrams for the plasmon-assisted photoemission. SPE setup: only the primary (a), secondary electron (b) is observed, the fate of another electron is not specified. (c) DPE setup: both primary and secondary electrons are observed in coincidence.

To work this out, consider a part of the DPE diagram that contains a product of two GFs involving the external momentum  $\mathbf{k}$ . Introducing the Fourier representations for each of the GFs  $G_{\mathbf{a}\mathbf{k}}^>(\tau) = \int_{-\infty}^{\infty} \frac{d\nu'}{2\pi} e^{-i\nu'\tau} G_{\mathbf{a}\mathbf{k}}^>(\nu')$ ,  $G_{\mathbf{k}\mathbf{b}}^>(-\tau') = \int_{-\infty}^{\infty} \frac{d\nu''}{2\pi} e^{i\nu''\tau'} G_{\mathbf{k}\mathbf{b}}^>(\nu'')$ , expressing the interacting GF as a product of the Møller operator and the free-particle Green's function (see Appendix B), we obtain expressions similar to Eqs. (60). Thus, in the time domain the product of two interacting single-particle GFs reduces to a simple propagator computed on the scattering states with incoming boundary conditions:

$$G_{\mathbf{a}\mathbf{k}}^>(\tau)G_{\mathbf{k}\mathbf{b}}^>(-\tau') = \langle \chi_{\mathbf{k}}^{(-)} | b \rangle e^{-i\varepsilon_{\mathbf{k}}(\tau-\tau')} \langle a | \chi_{\mathbf{k}}^{(-)} \rangle \times \theta(-\tau)\theta(-\tau')e^{\delta(\tau+\tau')}. \quad (68)$$

As an exercise, let us evaluate the diagram in Fig. 7(a) describing the SPE process with extrinsic plasmon losses. The current is given by the following expression in the time domain:

$$J_{\mathbf{k}} = \lim_{\eta \rightarrow 0} 2\eta \lim_{\delta \rightarrow 0} \sum_{abcd} \int d(x x') \int_{-\infty}^0 d(t t') e^{\eta(t+t')} \int_{-\infty}^0 d(\tau \tau') \times e^{i\omega(t-t')} \Delta_{cd} G_{db}^<(t', t) G_{x'c}^{--}(\tau', t') W_{xx'}^>(\tau, \tau') \times G_{\mathbf{k}x'}^>(0, \tau') G_{x\mathbf{k}}^>(\tau, 0) G_{ax}^{++}(t, \tau) (\Delta_{ab})^\dagger. \quad (69)$$

Representing the lesser Green's function on the vertical track in terms of the electron spectral function [normalized as  $\sum_b \int_{-\infty}^{\mu} \frac{d\zeta}{2\pi} A_{bb}(\zeta) = N$ ,  $N$  is the number of electrons in the system]

$$G_{db}^<(t', t) = i \int_{-\infty}^{\mu} \frac{d\zeta}{2\pi} A_{db}(\zeta) e^{-i\zeta(t'-t)}, \quad (70)$$

and the greater component of the screened interaction in terms of the plasmon spectral function

$$W_{xx'}^>(\tau, \tau') = -i \int_0^{\infty} \frac{d\xi}{2\pi} B_{xx'}(\xi) e^{-i\xi(\tau-\tau')}, \quad (71)$$

representing time-ordered  $G_{x'c}^{--}(\tau', t')$  and anti-time-ordered  $G_{ax}^{++}(t, \tau)$  as Fourier integrals and using expression (68), we

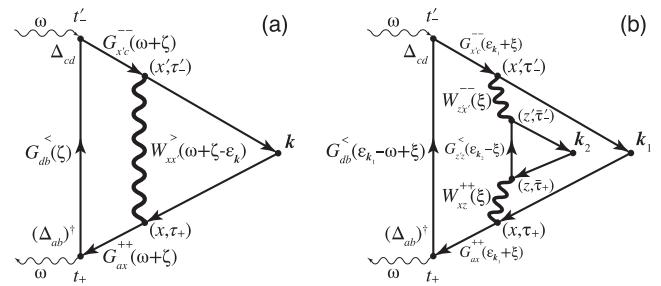


FIG. 7. Energy flows in (a) SPE diagram with external plasmonic losses, (b) DPE diagram describing a related plasmon-assisted process. Analytical expressions corresponding to these diagrams are first written in the time domain, then the integrations are performed by Fourier transforming all the propagators, and lastly the limits  $\eta \rightarrow 0$  and  $\delta \rightarrow 0$  are taken.

obtain

$$\begin{aligned}
J_{\mathbf{k}} &= \lim_{\eta \rightarrow 0} \lim_{\delta \rightarrow 0} \sum_{abcd} \int d(x x') \int_{-\infty}^{\mu} \frac{d\zeta}{2\pi} \int_0^{\infty} \frac{d\xi}{2\pi} B_{xx'}(\xi) \\
&\times \int d(\omega_1 \omega_2) 2\eta \frac{1}{\omega + \zeta - \omega_1 - i\eta} \frac{1}{\omega + \zeta - \omega_2 + i\eta} \\
&\times \frac{1}{\omega_1 - \xi - \varepsilon_{\mathbf{k}} - i\delta} \frac{1}{\omega_2 - \xi - \varepsilon_{\mathbf{k}} + i\delta} G_{x'c}^{--}(\omega_2) G_{ax}^{++}(\omega_1) \\
&\times \langle \chi_{\mathbf{k}}^{(-)} | x' \rangle \Delta_{cd} A_{db}(\zeta) (\Delta_{ab})^\dagger \langle x | \chi_{\mathbf{k}}^{(-)} \rangle. \quad (72)
\end{aligned}$$

Now, the limits can be taken making use of an identity discovered by Almladh [16] (see Appendix E). It transforms the product of four fractions in the equation above into the product of three  $\delta$  functions  $(2\pi)^3 \delta(\omega_1 - \omega - \zeta) \delta(\omega_2 - \omega - \zeta) \delta(\xi + \varepsilon_{\mathbf{k}} - \omega + \zeta)$ , and after the frequency integration we obtain

$$\begin{aligned}
J_{\mathbf{k}} &= 2\pi \int_{-\infty}^{\mu} \frac{d\zeta}{2\pi} \int_0^{\infty} \frac{d\xi}{2\pi} \delta(\xi + \varepsilon_{\mathbf{k}} - \omega - \zeta) \\
&\times \int d(x x') \langle \chi_{\mathbf{k}_1}^{(-)} | x' \rangle B_{xx'}(\xi) \langle x | \chi_{\mathbf{k}_1}^{(-)} \rangle \\
&\times [\hat{G}^{--}(\omega + \zeta) \hat{\Delta} \hat{A}(\zeta) \hat{\Delta}^\dagger \hat{G}^{++}(\omega + \zeta)]_{x'x}. \quad (73)
\end{aligned}$$

The two-particle current is obtained along the same lines using the energy flow as shown on Fig. 7(b):

$$\begin{aligned}
J_{\mathbf{k}_1 \mathbf{k}_2} &= 2\pi \int_{-\infty}^{\mu} \frac{d\zeta}{2\pi} \int_{-\infty}^{\mu} \frac{d\bar{\zeta}}{2\pi} \int_0^{\infty} \frac{d\xi}{2\pi} \delta(\xi + \varepsilon_{\mathbf{k}_1} - \omega - \zeta) \\
&\times \int d(x x' z z') \langle \chi_{\mathbf{k}_1}^{(-)} | x' \rangle W_{z'x'}^{--}(\xi) W_{xz}^{++}(\xi) \langle x | \chi_{\mathbf{k}_1}^{(-)} \rangle \\
&\times \langle \chi_{\mathbf{k}_2}^{(-)} | z' \rangle A_{z'z}(\bar{\zeta}) \langle z | \chi_{\mathbf{k}_2}^{(-)} \rangle \delta(\varepsilon_{\mathbf{k}_2} - \xi - \bar{\zeta}) \\
&\times [\hat{G}^{--}(\omega + \zeta) \hat{\Delta} \hat{A}(\zeta) \hat{\Delta}^\dagger \hat{G}^{++}(\omega + \zeta)]_{x'x}. \quad (74)
\end{aligned}$$

Similarly to the previous case, the limits  $\eta \rightarrow 0$ ,  $\delta \rightarrow 0$  yield a product (of five)  $\delta$  function which were subsequently used to perform three frequency integrations here (see Appendix E). All the quantities in Eqs. (73) and (74) can be expressed in terms of the spectral functions. We can, for instance, start with a general expression for the time-ordered and anti-time-ordered functions in terms of the functions on the Keldysh contour:

$$\hat{f}^{--}(\tau) = \hat{f}^\delta \delta(\tau) + \theta(\tau) \hat{f}^>(\tau) + \theta(-\tau) \hat{f}^<(\tau), \quad (75a)$$

$$\hat{f}^{++}(\tau) = -\hat{f}^\delta \delta(\tau) + \theta(-\tau) \hat{f}^>(\tau) + \theta(\tau) \hat{f}^<(\tau), \quad (75b)$$

where in the first equation  $\tau \equiv t_- - t'_-$  is equal to the time difference on the forward branch of the contour, and  $\tau \equiv t_+ - t'_+$  is equal to the time difference on the backward branch of the contour in the second equation. After the Fourier transform  $\hat{f}(\omega) = \int_{-\infty}^{\infty} d\tau e^{i\omega\tau} \hat{f}(\tau)$ , we have

$$\hat{f}^{--}(\omega) = \hat{f}^\delta + \int_{-\infty}^{\infty} \frac{d\omega'}{2\pi} \left[ \frac{i \hat{f}^>(\omega')}{\omega - \omega' + i\delta} - \frac{i \hat{f}^<(\omega')}{\omega - \omega' - i\delta} \right]. \quad (76)$$

The fluctuation-dissipation theorem at zero temperature allows us to express the lesser and greater propagators in terms of the corresponding spectral functions [Kubo-Martin-Schwinger

(KMS) conditions [10]]:

$$\hat{G}^<(\omega) = i\theta(\mu - \omega) \hat{A}(\omega), \quad \hat{G}^>(\omega) = -i\theta(\omega - \mu) \hat{A}(\omega).$$

The screened interaction obeys KMS conditions for bosonic propagators

$$\hat{W}^<(\omega) = i\theta(-\omega) \hat{B}(\omega), \quad \hat{W}^>(\omega) = -i\theta(\omega) \hat{B}(\omega),$$

with the symmetry property for the spectral function  $\hat{B}(-\omega) = -\hat{B}(\omega)$  [follows, e.g., from the fact that  $\hat{W}^R(t, t')$  is a real function or, more precisely, a Hermitian matrix]. We have already used these equations [cf. Eqs. (70) and (71)] to express SPE current in terms of spectral functions. Using Eq. (76), we can write the spectral representation of the fermionic propagator

$$\hat{G}^{--}(\omega) = \int_{-\infty}^{\infty} \frac{d\omega'}{2\pi} \hat{A}(\omega') \left[ \frac{\theta(\mu - \omega')}{\omega - \omega' - i\delta} + \frac{\theta(\omega' - \mu)}{\omega - \omega' + i\delta} \right],$$

where  $\mu$  is the Fermi energy. The anti-time-ordered GF is obtained similarly  $G^{++}(\omega) = -[G^{--}(\omega)]^\dagger$ . The screened interaction is expressed as an integral over the positive frequencies:

$$\hat{W}^{--}(\omega) = \hat{v} + \int_0^{\infty} \frac{d\omega'}{2\pi} \hat{B}(\omega') \frac{2\omega'}{\omega^2 - (\omega' - i\delta)^2},$$

while  $\hat{W}^{++}(\omega) = -[\hat{W}^{--}(\omega)]^\dagger$ .

Let us consider plasmon-mediated DPE. This process is of relevance for metallic and large molecular systems. Since plasmon is a long-wavelength or small-momentum electronic excitation, it is useful to go from the abstract basis to momentum representation and write  $W^{--}(k, \omega)$  in a short form as

$$W(k, \omega) = v_k \left[ 1 + \frac{\omega_p^2}{\omega^2 - \omega_p^2(k)} \right], \quad (77)$$

where  $\omega_p(k)$  is the plasmon dispersion,  $\omega_p \equiv \omega_p(0)$  is the classical plasmon frequency, and  $v_k = \frac{4\pi}{k^2}$  is the matrix element of Coulomb interaction. It is clear that in this form the plasmon peak completely exhausts the  $f$ -sum rule. Such plasmon pole approximation for the screened interaction is broadly used in the electronic-structure calculation when full-fledged calculations are not feasible. Similarly, it can be used to simplify Eq. (74).

### C. Numerical results

Let us make some simplifications. Usually, it is a good approximation to start with the mean-field Green's functions

$$G_{xy}^{--}(\omega) = \sum_{a \in \text{occ}} \frac{\langle x|a \rangle n_a \langle a|y \rangle}{\omega - \varepsilon_a - i\delta} + \sum_{a \in \text{unocc}} \frac{\langle x|a \rangle \bar{n}_a \langle a|y \rangle}{\omega - \varepsilon_a + i\delta}, \quad (78)$$

where  $n_a$  is the occupation number of the state  $a$  and  $\bar{n}_a \equiv 1 - n_a$ . After straightforward, but tedious, calculation the frequency integrations in Eq. (74) can be performed [for technical reasons it is better to start from the time rather than frequency expression, and it can be obtained by directly transcribing the diagram in Fig. 7(b) using standard rules]

yielding the following expression for the two-particle current:

$$J_{\mathbf{k}_1\mathbf{k}_2} = 4\pi \sum_{abcd} \frac{n_b n_d \Delta_{cb} \Delta_{ba} \delta(\omega + \varepsilon_b + \varepsilon_d - \varepsilon_{\mathbf{k}_1} - \varepsilon_{\mathbf{k}_2})}{(\varepsilon_c + \varepsilon_d - \varepsilon_{\mathbf{k}_1} - \varepsilon_{\mathbf{k}_2})(\varepsilon_{\mathbf{k}_1} + \varepsilon_{\mathbf{k}_2} - \varepsilon_a - \varepsilon_d)} \\ \times \sum_{\mathbf{q}_1\mathbf{q}_2} \left[ \frac{f_{\mathbf{k}_1c}^{\mathbf{q}_1} (f_{\mathbf{k}_2d}^{\mathbf{q}_1})^* v_{\mathbf{q}_1} \omega_p^2}{(\varepsilon_d - \varepsilon_{\mathbf{k}_2})^2 - \omega_p^2(q_1)} \right] \\ \times \left[ \frac{f_{a\mathbf{k}_1}^{\mathbf{q}_2} (f_{d\mathbf{k}_2}^{\mathbf{q}_2})^* v_{\mathbf{q}_2} \omega_p^2}{(\varepsilon_d - \varepsilon_{\mathbf{k}_2})^2 - \omega_p^2(q_2)} \right], \quad (79)$$

with the following matrix elements:

$$f_{a\mathbf{k}}^{\mathbf{q}} = \int d^3r \langle a|r \rangle e^{-i\mathbf{q}\cdot\mathbf{r}} \langle r|\chi_{\mathbf{k}}^{(-)} \rangle. \quad (80)$$

Notice that it is not necessary to separately treat the bare Coulomb interaction; it can be recovered as  $\omega_p \rightarrow \infty$  limit as explained in [62].

Let us compare Eq. (79) with the general result obtained using the Feshbach projection formalism (64). For the mean-field approximation (78), the two-particle spectral function is diagonal and is given by the convolution of two single-particle spectral densities:

$$A_{bd}^{(2)}(\zeta) = \int d\bar{\zeta} A_{bb}(\zeta - \bar{\zeta}) A_{dd}(\bar{\zeta}) \\ = \int d\bar{\zeta} n_b n_d \delta(\zeta - \bar{\zeta} - \varepsilon_b) \delta(\bar{\zeta} - \varepsilon_d) \\ = n_b n_d \delta(\varepsilon_b + \varepsilon_d - \zeta). \quad (81)$$

The energy conservation for the whole process, which is given by the  $\delta$  function in the numerator of (79), is expressed in terms of the two-particle spectral function  $A^{(2)}(\varepsilon_{\mathbf{k}_1} + \varepsilon_{\mathbf{k}_2} - \omega)$  [cf. Eq. (65)]. The denominator of the first line reflects the resonant character of the considered two-step process. From the resonance conditions (zeros of the denominator) we see that the double photoemission is enhanced when  $a$  and  $c$  are continuum states and therefore we denote them as  $\mathbf{k}_a$  and  $\mathbf{k}_c$ . We replace the scattering states  $|\chi_{\mathbf{k}_1}^{(-)}\rangle$  and  $|\chi_{\mathbf{k}_2}^{(-)}\rangle$  entering the matrix elements (80) by the plane waves and perform the integration yielding  $f_{\mathbf{k}_k}^{\mathbf{q}} = \delta(\mathbf{k} - \mathbf{k}_a - \mathbf{q})$ . Combining all together we obtain the following concise expression for the plasmon-assisted DPE process:

$$J_{\mathbf{k}_1\mathbf{k}_2} = 4\pi \sum_{\mathbf{k}_a\mathbf{k}_c} \sum_{bd} \Delta_{\mathbf{k}_c b} \Delta_{b\mathbf{k}_a} A_{bd}^{(2)}(\varepsilon_{\mathbf{k}_1} + \varepsilon_{\mathbf{k}_2} - \omega) \\ \times \frac{\langle \mathbf{k}_1 + \mathbf{k}_2 - \mathbf{k}_a | d \rangle \langle d | \mathbf{k}_1 + \mathbf{k}_2 - \mathbf{k}_c \rangle}{(\varepsilon_{\mathbf{k}_c} + \varepsilon_d - \varepsilon_{\mathbf{k}_1} - \varepsilon_{\mathbf{k}_2})(\varepsilon_{\mathbf{k}_1} + \varepsilon_{\mathbf{k}_2} - \varepsilon_{\mathbf{k}_a} - \varepsilon_d)} \\ \times W(\mathbf{k}_1 - \mathbf{k}_c, \varepsilon_d - \varepsilon_{\mathbf{k}_2}) W(\mathbf{k}_1 - \mathbf{k}_a, \varepsilon_d - \varepsilon_{\mathbf{k}_2}). \quad (82)$$

We have seen that the plane-wave approximation for the scattering states (i.e., the Møller operator is given by the identity operator) results in a great simplification for the two-particle current: it is given by a sum over two bound states (they correspond to two lesser propagators in the diagrammatic representation of this process) and by the two momentum integrals corresponding to the propagators of the secondary electron. In contrast, in the full-fledged calculations based on Eq. (79), the momenta of the secondary electron and the emitted electrons are not rigidly related. Therefore, in

general, two additional momentum integrations are required. This will be the subject of a forthcoming publication where this formalism is applied to a large molecular system.

The DPE process described by Eq. (82) is suited to probe the plasmon dispersion and damping. First, let us look at the classical plasmon that carries vanishing momentum and otherwise is strongly damped. This leads us to consider the case  $\mathbf{k}_a \approx \mathbf{k}_c \approx \mathbf{k}_1$ , and  $\varepsilon_d - \varepsilon_{\mathbf{k}_2} = \omega_p$  is the condition for the plasmon resonance. In this case, the second line reduces to  $|\langle \mathbf{k}_2 | d \rangle|^2 / \omega_p^2$ , and is clearly off resonance. The situation greatly changes if we allow for the plasmon to carry finite momentum  $q_c$  and consider a large momentum of the secondary electron  $\mathbf{k}_a \approx \mathbf{k}_c \approx \mathbf{k}_1 > \sqrt{\omega_p}$ . For simplicity, take a symmetric situation when both screened interaction lines carry approximately the same energy and momentum and denote  $\mathbf{K} \approx \frac{1}{2}(\mathbf{k}_a + \mathbf{k}_1) \approx \frac{1}{2}(\mathbf{k}_c + \mathbf{k}_1)$  and  $\mathbf{q} \approx \mathbf{k}_a - \mathbf{k}_1 \approx \mathbf{k}_c - \mathbf{k}_1$ . In this case, one achieves the resonant enhancement when

$$\varepsilon_{\mathbf{k}_a} - \varepsilon_{\mathbf{k}_1} \approx \varepsilon_{\mathbf{k}_c} - \varepsilon_{\mathbf{k}_1} = 2(\mathbf{q} \cdot \mathbf{K}) = \omega_p.$$

Thus, for collinear  $\mathbf{k}_a$ ,  $\mathbf{k}_c$ , and  $\mathbf{k}_1$  the probability for the plasmon-assisted emission of the secondary electron is enhanced when  $K$  reaches the value of  $\omega_p/q_c$ .

In order to illustrate the features arising due to the plasmon-assisted process in an experiment, we computed the current for a simple model system. To be concrete, we consider the basic jellium model for the  $C_{60}$  molecule (treated as spherically symmetric) [63,64], which is known for its pronounced (dipolar) plasmon resonance at  $\omega_p \sim 22$  eV. Inserting a smoothed boxlike potential as approximation to the Kohn-Sham potential, we solved the Schrödinger equation for the 120 orbitals required (240 electrons in total). This procedure yields the single-particle energies  $\varepsilon_d$  associated to the orbitals  $\phi_d(\mathbf{r})$ , from which we can compute all quantities in Eq. (82). Because of the spherical symmetry, we can separate the radial and the angular dependence, that is,  $\phi_d(\mathbf{r}) = \frac{u_d(r)}{r} Y_{\ell m}(\hat{r})$  [ $Y_{\ell m}(\hat{r})$  are the spherical harmonics] and only solve the radial Schrödinger equation. For the optical matrix elements, we choose the length gauge and assume a linear polarization along the  $z$  axis ( $\hat{\Delta} = z$ ). Since we are not interested in the absolute scale, a prefactor proportional to the field strength will not be included. The matrix elements  $\Delta_{\mathbf{k}b}$  attain the form

$$\Delta_{\mathbf{k}b} = 4\pi \sum_{\ell m} C_{\ell m \ell_b m_b} s_{b\ell}(k) Y_{\ell m}(\hat{\mathbf{k}}), \\ s_{b\ell}(k) = \int_0^\infty dr r^2 u_b(r) j_\ell(kr),$$

where  $j_\ell$  denotes the spherical Bessel function. The coefficients  $C_{\ell m \ell_b m_b}$  are obtained from the standard Clebsch-Gordan algebra [65,66]. Similarly, the Fourier-transformed orbitals  $\langle \mathbf{k} | d \rangle = \tilde{\phi}_d(\mathbf{k})$  can be expressed in terms of the Bessel transformation:  $\tilde{\phi}_d(\mathbf{k}) = 4\pi \tilde{u}_d(k) Y_{\ell m}(\hat{\mathbf{k}})$  with  $\tilde{u}_d(k) = \int_0^\infty dr r u_d(r) j_\ell(kr)$ .

Next, we transform the summation over  $\mathbf{k}_a$  and  $\mathbf{k}_c$  into integrations and substitute them by the integration over the momentum transfer vectors  $\mathbf{q}_{a,c} = \mathbf{k}_1 - \mathbf{k}_{a,c}$ . At this stage, no further simplification can be made, such that the six-dimensional integral has to be evaluated. However, it is



reasonable to consider  $\mathbf{q}_{a,c}$  as small since the plasmon branch enters the particle-hole continuum for growing momentum, where it is strongly damped. Hence, we introduce the momentum cutoff  $q_{\max}$  and assume  $k_1, k_2 \gg q_{\max}$ . Thus, we approximate  $\Delta_{\mathbf{k}_{a,c}b} = \Delta_{\mathbf{k}_1 - \mathbf{q}_{a,c}b} \approx \Delta_{\mathbf{k}_1 b}$  and  $\phi_d(\mathbf{k}_1 + \mathbf{k}_2 - \mathbf{k}_{a,c}) = \tilde{\phi}_d(\mathbf{k}_2 + \mathbf{q}_{a,c}) \approx \tilde{\phi}_d(\mathbf{k}_2)$ . Furthermore, we integrate over the spherical angles of  $\mathbf{k}_1$  and  $\mathbf{k}_2$ , keeping only the dependence on their magnitude. Thus, the two-electron current can be written as

$$J_{k_1, k_2} \propto \sum_{bd} \sum_{\ell m} |C_{\ell m \ell_b m_b} S_{b\ell}(k_1)|^2 |\tilde{u}_d(k_2)|^2 \times \left( 1 + \text{Re} \frac{\omega_p^2}{(\varepsilon_d - \varepsilon_{k_2} - i\Gamma)^2 - \omega_p^2} \right)^2 F_d(k_1, k_2), \quad (83)$$

where

$$F_d(k_1, k_2) = \left( \int_0^{q_{\max}} dq \frac{1}{q^2 + 2k_1 q - k_2^2 + 2\varepsilon_d} \right)^2.$$

Note that we inserted the imaginary shift  $i\Gamma$  in the energy argument accounting for a finite width (lifetime in the time domain) of the plasmon resonance (which is assumed dispersionless for simplicity).

In an experiment, the distinction between primary ( $\mathbf{k}_1$ ) and secondary electron ( $\mathbf{k}_2$ ) is, of course, not possible. For this reason, the photocurrent needs to be symmetrized (let us denote it by  $J^{\text{sym}}$ ). Representing the  $J^{\text{sym}}$  as a function of  $\varepsilon_{\mathbf{k}_1}$  and  $\varepsilon_{\mathbf{k}_2}$  yields the typical energy-sharing diagrams (Fig. 8). Spectral properties of the system [dominated by  $A^{(2)}(\varepsilon)$ ] display themselves along the main diagonal, as only the sum  $\varepsilon_{\mathbf{k}_1} + \varepsilon_{\mathbf{k}_2}$  enters. Dominant scattering events mediated by the (screened) interaction on the other hand are visible along lines  $\varepsilon_{\mathbf{k}_1} = \text{const}$  (or  $\varepsilon_{\mathbf{k}_2} = \text{const}$ ). As Eq. (83) indicates, the two-particle current contains contributions from (i) the bare Coulomb [two interacting lines in Fig. 7(b) are not screened], (ii) plasmonic scattering (both lines are screened), and the interference terms. (i), (ii), and the total contribution are shown at Figs. 8(a), 8(b), and 8(c), respectively. For vanishing  $\Gamma$ , the current is dominated by sharp plasmonic resonances. For finite damping parameter such as used for the present simulations ( $\Gamma = 0.1$ , we use a realistic value as in Ref. [67]), the interference terms are important: we still have a large plasmonic contribution [viz., Fig. 7(b)], however, the bare Coulomb contributes with the opposite sign. Therefore, in total current the large peak at  $\varepsilon_{\mathbf{k}_2} \approx 0.15$  becomes less pronounced and additional peaks at higher energies (e.g., at  $\varepsilon_{\mathbf{k}_2} \approx 0.5$ ) appear. The whole spectral width of the signal is limited by the two-particle spectral function shown in Fig. 7(d) as a shaded curve.

## VI. CONCLUSIONS

There are a large number of theoretical works devoted to the interaction of light and matter which involve the emission of one or more electrons. This contribution is meant to expose parallels between the single- and the double-electron photoemission in a formal way. We started by defining corresponding observables and deriving expressions for one- and two-particle currents based on the first-order time-dependent perturbation theory. These expressions are suitable if exact

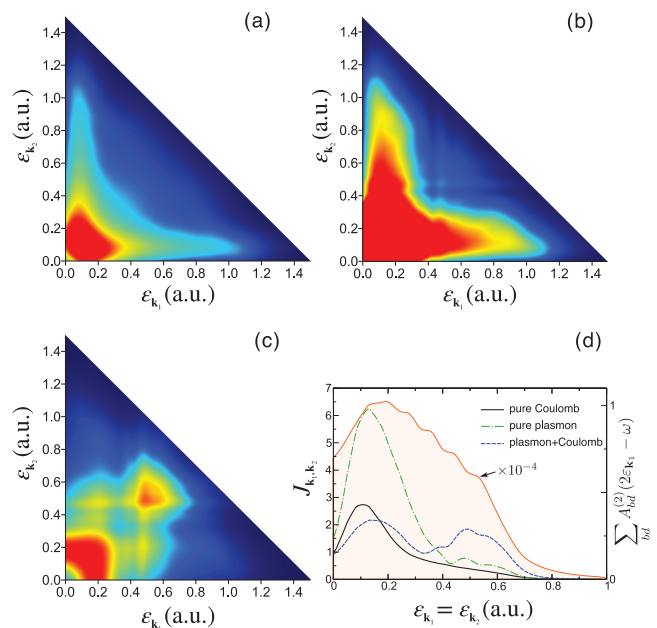


FIG. 8. (Color online) The symmetrized two-electron current as a function of the photoelectron energies (energy-sharing diagram) for typical parameters:  $\omega = 2.0$  and  $\omega_p = 0.8$ . The color scale is the same for all three panels and runs from dark blue to red, indicating increasing values. (a) The process is mediated by the pure Coulomb interaction. (b) Pure plasmonic contribution. (c) Total (bare Coulomb and plasmonic contributions) signal including the interference terms. (d) Equal energy sharing ( $\varepsilon_{\mathbf{k}_1} = \varepsilon_{\mathbf{k}_2}$ ) for the current and trace of the two-particle spectral density (shaded curve).

formulas in terms of many-body states are required. In order to obtain computationally useful expressions, many-body effects should also be accounted for in a perturbative fashion. Thus, in the first part of the paper we applied the projection operator formalism. Starting from the explicit form of the projection operators dividing the whole Hilbert space of the system into that of the emitted electron(s) and the target, we derived the effective one- and two-particle Hamiltonian, discussed integral equations for the Green's functions describing emitted particles, and demonstrated a close connection of this formalism to the nonequilibrium Green's function theory. For the latter, one can easily derive the diagrammatic expansions for one- and two-particle currents starting from the time-dependent perturbation theory and using the adiabatic switching of the electron-electron interaction. Hence, we have electromagnetic field switched on at the remote past (as  $e^{i\eta t}$ ) and independently adiabatically switched on the interaction such that the total Hamiltonian takes a form  $\hat{H}_\delta = \hat{H}_0 + e^{-\delta|t|} \hat{H}_1$ . We analyzed in details the diagrammatic structure of one- and two-particle currents. It is surprisingly simple: one starts with the density-density response function  $\chi^<$  which necessarily contains two blocks associated with the forward (“−”) and backward (“+”) parts of the Keldysh contour. Requesting that one or two lines flowing from “−” to “+” blocks are associated with scattering states (with momenta  $\mathbf{k}_i$ ), one obtains exactly the diagrams for SPE and DPE currents showing the close connection between these types of light-matter interaction. It is not difficult to generalize

this approach to an arbitrary number of particles. Finally, we presented a detailed analysis of the plasmon-assisted DPE and showed that if one of the emitted particles is unobserved, its diagrammatic representation reduces to the one describing external losses in the SPE process considered by Caroli *et al.* [21]. Plasmon pole approximation was employed to derive computationally manageable expressions. We illustrated the distinct features to be expected in an experiment by analyzing the simple and yet realistic jellium model for the C<sub>60</sub> molecule. This will be used in the forthcoming paper devoted to the *ab initio* treatment of this large molecular system.

### ACKNOWLEDGMENT

This work is supported by the German Research Foundation (DFG) Grants No. SFB 762 and No. PA 1698/1-1.

### APPENDIX A: PARTICLE-IMPACT IONIZATION

Under some circumstances, the formalism developed in the main text can be extended to other mechanisms of ionization, e.g., particle-impact ionization. The basic requirement we impose is the *distinguishability* of the projectile from the target electrons. This applies also for a projectile electron if the impact energy is high and the small-momentum transfer is small (optical limit).

The target we describe by the Hamiltonian (4). The Coulomb interaction between the projectile (with charge  $Z$ ) and the sample reads as

$$\hat{V} = \frac{Z}{2} \sum_{ab} \sum_{\nu\mu} v_{ab\nu\mu} c_a^\dagger d_\nu^\dagger d_\mu c_b. \quad (\text{A1})$$

$d_\nu$  ( $d_\nu^\dagger$ ) is the annihilation (creation) operator of the projectile states  $|\nu\rangle$ . These states can be chosen as the eigenstates of the projectile Hamiltonian  $\hat{h}_p$  with energy  $\varepsilon_\nu$ .

Assuming that the projectile initially possesses the momentum  $\mathbf{k}_i$ , we can construct the asymptotic state prior to the interaction (that is, at  $t = -\infty$ ) as the product state

$$|\Psi_{0,\mathbf{k}_i}\rangle = |\mathbf{k}_i\rangle \otimes |\Psi_0\rangle.$$

$\hat{V}$  is switched on reaching its full strength at  $t = 0$ . Assuming that its average value is much smaller than the kinetic energy of the projectile, we can apply the first-order perturbation theory (i.e., the first Born approximation in the projectile-target interaction [47]). Denoting the full Hamiltonian by  $\hat{H} + \hat{h}_p$ , one may write

$$|\tilde{\Psi}^{(+)}\rangle = |\Psi_{0,\mathbf{k}_i}\rangle + \lim_{\eta \rightarrow 0} \frac{1}{E_0 + \varepsilon_{\mathbf{k}_i} - \hat{H} - \hat{h}_p + i\eta} \hat{V} |\Psi_{0,\mathbf{k}_i}\rangle. \quad (\text{A2})$$

The projectile has a well defined final momentum  $\mathbf{k}_f$ . In analogy to Sec. IV A, we introduce the particle-number operator

$$\hat{N}_{\mathbf{k}} \rightarrow P_f \hat{N}_{\mathbf{k}} P_f$$

with  $P_f = |\mathbf{k}_f\rangle \langle \mathbf{k}_f|$  projecting only onto the projectile space.  $\hat{N}_{\mathbf{k}}$  acts on the system's states only (including the ejected electrons upon particle impact). Evaluating then the current as in Sec. II A and approximating the projectile states by plane

waves  $\langle \mathbf{r} | \mathbf{k} \rangle = e^{i\mathbf{k}\cdot\mathbf{r}}$  yields

$$\begin{aligned} J_{\mathbf{k}} &= \lim_{\eta \rightarrow 0} 2\eta \langle \Psi_{0,\mathbf{k}_i} | \hat{V}^\dagger \frac{1}{E_0 + \varepsilon_{\mathbf{k}_i} - \hat{H} - \hat{h}_p - i\eta} P_f c_{\mathbf{k}}^\dagger c_{\mathbf{k}} P_f \\ &\quad \times \frac{1}{E_0 + \varepsilon_{\mathbf{k}_i} - \hat{H} - \hat{h}_p + i\eta} \hat{V} |\Psi_{0,\mathbf{k}_i}\rangle \\ &= \lim_{\eta \rightarrow 0} 2\eta \langle \Psi_0 | \hat{V}^{\text{eff}}(\mathbf{q})^\dagger \frac{1}{E_0 + \varepsilon_{\mathbf{k}_i} - \varepsilon_{\mathbf{k}_f} - \hat{H} - i\eta} c_{\mathbf{k}}^\dagger c_{\mathbf{k}} \\ &\quad \times \frac{1}{E_0 + \varepsilon_{\mathbf{k}_i} - \varepsilon_{\mathbf{k}_f} - \hat{H} + i\eta} \hat{V}^{\text{eff}}(\mathbf{q}) |\Psi_0\rangle, \end{aligned} \quad (\text{A3})$$

where  $\mathbf{q} = \mathbf{k}_i - \mathbf{k}_f$  is the *momentum transfer*, and  $\hat{V}^{\text{eff}}(\mathbf{q})$  is the effective single-particle operator acting on the target wave function, explicitly

$$\hat{V}^{\text{eff}}(\mathbf{k}_i - \mathbf{k}_f) = \langle \mathbf{k}_i | \hat{V} | \mathbf{k}_f \rangle = \frac{Z}{2} \sum_{ab} v_{a\mathbf{k}_f b\mathbf{k}_i} c_a^\dagger c_b. \quad (\text{A4})$$

In this optical limit,

$$\hat{V}^{\text{eff}}(\mathbf{q}) = \frac{4\pi Z}{q^2} e^{i\mathbf{q}\cdot\mathbf{r}} \quad (\text{A5})$$

acts similar to the light-matter interaction  $\hat{\Delta}$ ; the transferred energy (or *energy loss*)  $\varepsilon_{\mathbf{k}_i} - \varepsilon_{\mathbf{k}_f}$  resembles the photon energy.

### APPENDIX B: GREEN'S FUNCTIONS

Let us recast the following many-body correlators from Sec. IV A,

$$G_{\mathbf{p}\mathbf{q},\alpha}^{(\text{p})}(z) = \langle \Psi_\alpha^+ | c_{\mathbf{p}} \frac{1}{z - \hat{H}_p - \hat{\Sigma}_p(z)} c_{\mathbf{q}}^\dagger | \Psi_\alpha^+ \rangle,$$

in the form of one-particle averages. We define the particle propagator of one-particle system in the presence of optical potential  $\hat{W}(z)$ :

$$\mathcal{G}_{\mathbf{p}\mathbf{q}}(z) = \langle \mathbf{p} | \frac{1}{z - \hat{H}_f - \hat{W}(z)} | \mathbf{q} \rangle.$$

Consider  $G_{\mathbf{p}\mathbf{q},\alpha}^{(\text{p})}(\omega + E_0 \pm i\eta)$ . The matrix element of the effective Hamiltonian operator in its definition can be simplified to

$$\langle \Psi_\alpha^+ | c_{\mathbf{p}} [\hat{H}_p + \hat{\Sigma}_p(z)] c_{\mathbf{q}}^\dagger | \Psi_\alpha^+ \rangle = E_\alpha^+ + \langle \mathbf{p} | \hat{H}_f + \hat{W}_\alpha(z) | \mathbf{q} \rangle,$$

where we decompose the total  $N$ -particle Hamiltonian  $H$  as a sum of three terms:

$$\hat{H} = \hat{H}_f + \hat{H}^+ + \hat{V}.$$

Here,  $\hat{H}_f$  is the free-particle Hamiltonian,  $\hat{H}^+$  is the Hamiltonian of ionized system

$$\hat{H}^+ | \Psi_\alpha^+ \rangle = E_\alpha^+ | \Psi_\alpha^+ \rangle,$$

and  $\hat{V}$  is the frequency-independent part of the self-energy. If the optical potential is identified with the self-energy, then we can relate two propagators

$$G_{\mathbf{p}\mathbf{q},\alpha}^{(\text{p})}(\omega + E_0 \pm i\eta) = \mathcal{G}_{\mathbf{p}\mathbf{q},\alpha}^{(\pm)}(\omega + \varepsilon_\alpha),$$

where we introduced the Green's functions  $\mathcal{G}_{\mathbf{p}\mathbf{q}}^{(\pm)}(\omega) = \mathcal{G}_{\mathbf{p}\mathbf{q}}^{(\pm)}(\omega \pm i\eta)$  and  $\varepsilon_\alpha = E_0 - E_\alpha^+$ . From the formal scattering

theory (see Sec. 20 of Joachain [47]) and independent of the concrete choice of the representation, we can express them in terms of the Møller operator and the free-particle Green's function

$$\mathcal{G}^\pm(\omega) = \hat{\Omega}^{(\pm)} \mathcal{G}_0^{(\pm)}(\omega). \quad (\text{B1})$$

*Two-particle case.* For DPE, the two-particle Green's function over the excited state  $\Psi_\beta^{2+}$  is required:

$$G_{\mathbf{p}\mathbf{q}, \mathbf{k}_1 \mathbf{k}_2, \beta}^{(\text{pp})}(z) = \langle \Psi_\beta^{2+} | c_{\mathbf{p}} c_{\mathbf{q}} \frac{1}{z - \hat{H}_p - \hat{\Sigma}_P(z)} c_{\mathbf{k}_1}^\dagger c_{\mathbf{k}_2}^\dagger | \Psi_\beta^{2+} \rangle,$$

where the projection operator is defined by Eq. (35). This propagator can be related to the scattering Green's function of the two-particle system in the presence of the optical potential of doubly ionized target

$$G_{\mathbf{p}\mathbf{q}, \mathbf{k}_1 \mathbf{k}_2, \beta}^{(\text{pp})}(\omega + E_0 \pm i\eta) = \mathcal{G}_{\mathbf{p}\mathbf{q}, \mathbf{k}_1 \mathbf{k}_2, \beta}^{(\pm)}(\omega + \varepsilon_\beta^{(2)}),$$

with  $\varepsilon_\beta^{(2)} = E_0 - E_\beta^{2+}$ .  $\mathcal{G}_{\mathbf{p}\mathbf{q}, \mathbf{k}_1 \mathbf{k}_2, \beta}^{(\pm)}$  can be likewise expressed in the form (B1).

### APPENDIX C: MATRIX IDENTITIES

The formalism presented here works in finite- as well as in infinite-dimensional Hilbert spaces. For illustration we formulate it in the matrix form. Given  $\mathcal{M}$  is square block matrix

$$\mathcal{M} = \begin{bmatrix} \mathcal{A} & \mathcal{B} \\ \mathcal{C} & \mathcal{D} \end{bmatrix}, \quad (\text{C1})$$

where  $\mathcal{D}$  is square invertible matrix, the Schur complement [68] (also known in physics as the Feshbach map [57,69,70]) is defined as

$$\tilde{\mathcal{A}} = \mathcal{A} - \mathcal{B}\mathcal{D}^{-1}\mathcal{C}.$$

We might think of  $\mathcal{M}$  as a Hamiltonian operator acting in some larger Hilbert space, whereas  $\mathcal{A}$  is the same operator, but acting in a physically relevant subspace.  $P$  is the projection operator onto this subspace ( $P\mathcal{M}P = \mathcal{A}$ ) and  $Q = I - P$  is its complement ( $Q\mathcal{M}Q = \mathcal{D}$ ). For definiteness we may take  $\mathcal{M}$  to be a compact self-adjoint operator on the Hilbert space describing an  $N$ -fermion system  $\mathcal{H}^{(N)}$  and  $\mathcal{A}$  its projection upon the Hilbert space of two particles  $\mathcal{H}^{(2)}$ . Because of the couplings between subspaces (for physical Hamiltonians obviously holds  $\mathcal{B} = \mathcal{C}^\dagger$ ),  $\mathcal{M}$  and  $\mathcal{A}$  have different spectral properties. Nonetheless, one can show the following equivalence:

$$\mathcal{M}V = 0 \iff \tilde{\mathcal{A}}PV = 0 \quad (\text{C2})$$

for a vector  $V \in \mathcal{H}^{(N)}$ . If  $\mathcal{M} \equiv H - EI$ , the first part implies that  $V$  is an eigenvector of  $H$  with the energy  $E$ . The second part implies that  $PV$  is a corresponding eigenvector of  $\tilde{\mathcal{A}}(E)$  with the same energy:

$$[H_P + \Sigma_P(E) - EI_P]PV = 0. \quad (\text{C3})$$

Expression for the self-energy (27) is derived for instance in Sec. 20.2.3 of Joachain [47]. A mathematically rigorous proof of the theorem (C2) as well as other properties of the Feshbach-Schur map can be found in Chap. 11 of Gustafson

and Sigal [71]. It is further possible to write the inverse of the matrix  $\mathcal{M}$  explicitly:<sup>1</sup>

$$\mathcal{M}^{-1} = \begin{bmatrix} \tilde{\mathcal{A}}^{-1} & -\tilde{\mathcal{A}}^{-1}\mathcal{B}\mathcal{D}^{-1} \\ -\mathcal{D}^{-1}\mathcal{C}\tilde{\mathcal{A}}^{-1} & \mathcal{D}^{-1} + \mathcal{D}^{-1}\mathcal{C}\tilde{\mathcal{A}}^{-1}\mathcal{B}\mathcal{D}^{-1} \end{bmatrix}. \quad (\text{C4})$$

This identity is natural to apply to compute resolvents. For instance, Eq. (26) is given the first line of Eq. (C4). This formula can also be found in Almladh as Eq. (19) [16].

### APPENDIX D: PROPERTIES OF PROJECTION OPERATORS

Our basic assumptions for operators with continuum indices  $c_{\mathbf{p}}|\Psi_\alpha^+\rangle = 0$  and  $c_{\mathbf{p}}|\Psi_\beta^{2+}\rangle = 0$  imply that final states of the target are the vacuum states for these operators. Thus, standard Wick's theorem can be used for the calculation of various correlators. It follows

$$c_{\mathbf{p}} c_{\mathbf{q}}^\dagger |\Psi_\alpha^+\rangle = \delta_{\mathbf{p}\mathbf{q}} |\Psi_\alpha^+\rangle, \quad (\text{D1})$$

$$c_{\mathbf{k}_2} c_{\mathbf{k}_1} c_{\mathbf{p}}^\dagger c_{\mathbf{q}}^\dagger |\Psi_\beta^{2+}\rangle = (\delta_{\mathbf{k}_1\mathbf{p}} \delta_{\mathbf{k}_2\mathbf{q}} - \delta_{\mathbf{k}_1\mathbf{q}} \delta_{\mathbf{k}_2\mathbf{p}}) |\Psi_\beta^{2+}\rangle. \quad (\text{D2})$$

These equations lead to the idempotency relations  $P_\alpha P_\alpha = P_\alpha$  and  $P_\beta P_\beta = P_\beta$  and to the properties

$$c_{\mathbf{k}}^\dagger |\Psi_\alpha^+\rangle \langle \Psi_\alpha^+ | c_{\mathbf{k}} = P_\alpha c_{\mathbf{k}}^\dagger c_{\mathbf{k}} P_\alpha, \quad (\text{D3})$$

$$c_{\mathbf{k}_1}^\dagger c_{\mathbf{k}_2}^\dagger |\Psi_\beta^{2+}\rangle \langle \Psi_\beta^{2+} | c_{\mathbf{k}_2} c_{\mathbf{k}_1} = P_\beta c_{\mathbf{k}_1}^\dagger c_{\mathbf{k}_2}^\dagger c_{\mathbf{k}_2} c_{\mathbf{k}_1} P_\beta. \quad (\text{D4})$$

The matrix element of a one-particle operator  $\hat{O} = \hat{O}(x_1) + \hat{O}(x_2)$  over the determinant two-particle states  $\langle x_1 x_2 | ab \rangle = \frac{1}{\sqrt{2}} [\phi_a(x_1) \phi_b(x_2) - \phi_b(x_1) \phi_a(x_2)]$  can be verified by direct evaluation:

$$\begin{aligned} \langle ab | \hat{O} | cd \rangle &= \langle a | \hat{O} | c \rangle \delta_{bd} + \langle b | \hat{O} | d \rangle \delta_{ac} \\ &\quad - \langle a | \hat{O} | d \rangle \delta_{bc} - \langle b | \hat{O} | c \rangle \delta_{ad}. \end{aligned} \quad (\text{D5})$$

If one of the states is a two-hole Dyson orbital, the matrix element is computed similarly:

$$\begin{aligned} \langle ab | \hat{O} | \varphi_\beta^{(2)} \rangle &= \frac{1}{2} \sum_{cd} \langle ab | \hat{O} | cd \rangle \langle \Psi_\beta^{2+} | c_c c_d | \Psi_0 \rangle \\ &= \sum_{cd} (\langle a | \hat{O} | c \rangle \delta_{bd} - \langle b | \hat{O} | c \rangle \delta_{ad}) \langle \Psi_\beta^{2+} | c_c c_d | \Psi_0 \rangle. \end{aligned} \quad (\text{D6})$$

Using this result and the vacuum assumption for the initial states, we can compute a matrix element entering the Fermi golden rule formula for SPE,

$$\begin{aligned} \langle \Psi_\alpha^+ | c_{\mathbf{k}} \hat{\Delta} | \Psi_0 \rangle &= \sum_{ab} \Delta_{ab} \langle \Psi_\alpha^+ | c_{\mathbf{k}} c_a^\dagger c_b | \Psi_0 \rangle \\ &\approx \sum_b \langle \mathbf{k} | \hat{\Delta} | b \rangle \langle \Psi_\alpha^+ | c_b | \Psi_0 \rangle = \langle \mathbf{k} | \hat{\Delta} | \phi_\alpha \rangle, \end{aligned} \quad (\text{D7})$$

<sup>1</sup>According to Zhang [68], it was a Polish astronomer Banachiewicz who obtained this formula for the first time. However, it was reinvented many times (see a short historical review at the top of p. 699 of Ref. [72] where the authors suggest to use the name Schur-Livsic-Feshbach-Grushin for the equation).

and DPE,

$$\begin{aligned} \langle \Psi_{\beta}^{2+} | c_{\mathbf{k}_1} c_{\mathbf{k}_2} \hat{\Delta} | \Psi_0 \rangle &= \sum_{ab} \Delta_{ab} \langle \Psi_{\beta}^{2+} | c_{\mathbf{k}_1} c_{\mathbf{k}_2} c_a^{\dagger} c_b | \Psi_0 \rangle \approx \sum_{bc} [ \langle \mathbf{k}_1 | \hat{\Delta} | b \rangle \delta_{\mathbf{k}_2 c} - \langle \mathbf{k}_2 | \hat{\Delta} | b \rangle \delta_{\mathbf{k}_1 c} ] \langle \Psi_{\beta}^{2+} | c_b c_c | \Psi_0 \rangle \\ &= \langle \mathbf{k}_1 \mathbf{k}_2 | \hat{\Delta} | \phi_{\beta}^{(2)} \rangle. \end{aligned} \quad (\text{D8})$$

We used an assumption  $c_{\mathbf{k}} | \Psi_0 \rangle \approx 0$  to derive (D7) and  $c_{\mathbf{k}_1} c_{\mathbf{k}_2} | \Psi_0 \rangle \approx 0$  to derive (D8).

#### APPENDIX E: SOKHOTSKI-PLEMELJ-TYPE IDENTITIES

The following identities were used to perform frequency integrations leading to Eqs. (73) and (74):

$$\lim_{\eta \rightarrow 0} \lim_{\delta \rightarrow 0} 2\eta \frac{1}{\omega_1 - z_1 - i\eta} \frac{1}{\omega_2 - z_2 + i\eta} \frac{1}{z_3 - \omega_3 - i\delta} \frac{1}{z_3 + z_2 - z_1 - \omega_3 + i\delta} = \prod_{i=1}^3 2\pi \delta(z_i - \omega_i) \quad (\text{E1})$$

for  $\omega_1 = \omega_2$ , and

$$\begin{aligned} \lim_{\eta \rightarrow 0} \lim_{\delta \rightarrow 0} 2\eta \frac{1}{\omega_1 - z_1 - i\eta} \frac{1}{\omega_2 - z_2 + i\eta} \frac{1}{z_3 - z_2 + \omega_2 - \omega_3 - i\delta} \frac{1}{z_4 - z_1 + \omega_1 - \omega_4 + i\delta} \frac{1}{\omega_4 + \omega_5 - z_4 - z_5 + i\delta} \\ \times \frac{1}{\omega_3 + \omega_5 - z_3 - z_5 - i\delta} = \prod_{i=1}^5 2\pi \delta(z_i - \omega_i) \end{aligned} \quad (\text{E2})$$

for  $\omega_1 = \omega_2$ ,  $\omega_3 = \omega_4$ . The first equation appears in [16]. To the best of our knowledge the second equation has not been addressed in the literature. These identities can be verified by the Fourier transformation with respect to  $z_i$  variables.

- 
- [1] M. Cardona and L. Ley, eds., *Photoemission in Solids I General Principles* (Springer, Berlin, 1978).
- [2] S. Hüfner, *Photoelectron Spectroscopy: Principles and Applications*, 3rd ed., Advanced Texts in Physics (Springer, Berlin, 2003).
- [3] *Solid-State Photoemission and Related Methods: Theory and Experiment*, edited by W. Schattke and M. A. Van Hove (Wiley-VCH, Weinheim, 2002).
- [4] V. Schmidt, *Electron Spectrometry of Atoms Using Synchrotron Radiation*, Cambridge Monographs on Atomic, Molecular, and Chemical Physics No. 6 (Cambridge University Press, Cambridge, 1997).
- [5] E. Weigold, *Electron Momentum Spectroscopy*, Physics of Atoms and Molecules (Kluwer, New York, 1999).
- [6] J. Berakdar, A. Lahmam-Bennani, and C. Dal Cappello, *Phys. Rep.* **374**, 91 (2003).
- [7] S. T. Manson and A. F. Starace, *Rev. Mod. Phys.* **54**, 389 (1982).
- [8] M. Y. Amusia, *Atomic Photoeffect*, Physics of Atoms and Molecules (Plenum, New York, 1990).
- [9] J. H. D. Eland, in *Advances in Chemical Physics*, edited by S. A. Rice (Wiley, Hoboken, NJ, 2009), pp. 103–151.
- [10] L. Kadanoff and G. Baym, *Quantum Statistical Mechanics Green's Function Methods in Equilibrium and Nonequilibrium Problems* (Benjamin, New York, 1962).
- [11] D. C. Langreth, in *Linear and Nonlinear Electron Transport in Solids*, Advanced Study Institutes Series, Vol. 17, edited by J. Devreese and V. Doren (Springer, New York, 1976), pp. 3–32.
- [12] P. Danielewicz, *Ann. Phys. (NY)* **152**, 239 (1984).
- [13] G. Stefanucci and R. van Leeuwen, *Nonequilibrium Many-Body Theory of Quantum Systems: A Modern Introduction* (Cambridge University Press, Cambridge, 2013).
- [14] M. N. R. Wohlfarth and L. S. Cederbaum, *Phys. Rev. A* **65**, 052703 (2002).
- [15] J. E. Inglesfield, *J. Phys. C: Solid State Phys.* **16**, 403 (1983).
- [16] C.-O. Almbladh, *Phys. Scr.* **32**, 341 (1985).
- [17] C. N. Berglund and W. E. Spicer, *Phys. Rev.* **136**, A1030 (1964).
- [18] G. D. Mahan, *Phys. Rev. B* **2**, 4334 (1970).
- [19] W. L. Schaich and N. W. Ashcroft, *Phys. Rev. B* **3**, 2452 (1971).
- [20] D. C. Langreth, *Phys. Rev. B* **3**, 3120 (1971).
- [21] C. Caroli, D. Lederer-Rozenblatt, B. Roulet, and D. Saint-James, *Phys. Rev. B* **8**, 4552 (1973).
- [22] C.-O. Almbladh, *Phys. Rev. B* **34**, 3798 (1986).
- [23] L. Campbell, L. Hedin, J. J. Rehr, and W. Bardyszewski, *Phys. Rev. B* **65**, 064107 (2002).
- [24] M. Guzzo, G. Lani, F. Sottile, P. Romaniello, M. Gatti, J. J. Kas, J. J. Rehr, M. G. Silly, F. Sirotti, and L. Reining, *Phys. Rev. Lett.* **107**, 166401 (2011).
- [25] M. Cini, *Solid State Commun.* **20**, 605 (1976).
- [26] G. A. Sawatzky, *Phys. Rev. Lett.* **39**, 504 (1977).
- [27] F. Tarantelli, A. Sgamellotti, and L. S. Cederbaum, *J. Chem. Phys.* **94**, 523 (1991).
- [28] F. Tarantelli, A. Sgamellotti, and L. S. Cederbaum, *Phys. Rev. Lett.* **72**, 428 (1994).
- [29] C. Verdozzi, M. Cini, and A. Marini, *J. Electron. Spectrosc. Relat. Phenom.* **117-118**, 41 (2001).
- [30] M. Cini, *Phys. Rev. B* **17**, 2486 (1978).
- [31] F. Tarantelli, A. Tarantelli, A. Sgamellotti, J. Schirmer, and L. S. Cederbaum, *J. Chem. Phys.* **83**, 4683 (1985).
- [32] R. Herrmann, S. Samarin, H. Schwabe, and J. Kirschner, *Phys. Rev. Lett.* **81**, 2148 (1998).
- [33] W. Bardyszewski and L. Hedin, *Phys. Scr.* **32**, 439 (1985).
- [34] T. Fujikawa and L. Hedin, *Phys. Rev. B* **40**, 11507 (1989).
- [35] L. Hedin, J. Michiels, and J. Inglesfield, *Phys. Rev. B* **58**, 15565 (1998).
- [36] J. Brand and L. S. Cederbaum, *Ann. Phys. (NY)* **252**, 276 (1996).
- [37] J. S. Bell and E. J. Squires, *Phys. Rev. Lett.* **3**, 96 (1959).
- [38] L. S. Cederbaum, *Phys. Rev. Lett.* **85**, 3072 (2000).
- [39] L. S. Cederbaum, *Ann. Phys. (NY)* **291**, 169 (2001).

- [40] J. Berakdar, *Phys. Rev. B* **58**, 9808 (1998).
- [41] O. Schwarzkopf, B. Krässig, J. Elmiger, and V. Schmidt, *Phys. Rev. Lett.* **70**, 3008 (1993).
- [42] J. S. Briggs and V. Schmidt, *J. Phys. B: At., Mol. Opt. Phys.* **33**, R1 (2000).
- [43] M. Esposito and M. Galperin, *Phys. Rev. B* **79**, 205303 (2009).
- [44] M. Demuth, *Determining Spectra in Quantum Theory*, Progress in Mathematical Physics No. 44 (Birkhäuser, Boston, 2005).
- [45] N. Marzari, A. A. Mostofi, J. R. Yates, I. Souza, and D. Vanderbilt, *Rev. Mod. Phys.* **84**, 1419 (2012).
- [46] C. Brouder, G. Panati, M. Calandra, C. Mourougane, and N. Marzari, *Phys. Rev. Lett.* **98**, 046402 (2007).
- [47] C. J. Joachain, *Quantum Collision Theory* (North-Holland, Amsterdam, 1975).
- [48] J. Berakdar, *Concepts of Highly Excited Electronic Systems*, 1st ed. (Wiley-VCH, Weinheim, 2003).
- [49] B. D. Napitu and J. Berakdar, *Phys. Rev. B* **81**, 195108 (2010).
- [50] Y. Pavlyukh and J. Berakdar, *J. Chem. Phys.* **135**, 201103 (2011).
- [51] J. M. Bang, F. G. Gareev, W. T. Pinkston, and J. S. Vaagen, *Phys. Rep.* **125**, 253 (1985).
- [52] L. S. Cederbaum, W. Domcke, J. Schirmer, and W. Von Niessen, *Adv. Chem. Phys.* **65**, 115 (1986).
- [53] M. Deleuze and L. Cederbaum, *Adv. Quantum Chem.* **35**, 77 (1999).
- [54] N. Fominykh, J. Henk, J. Berakdar, P. Bruno, H. Gollisch, and R. Feder, *Solid State Commun.* **113**, 665 (2000).
- [55] N. Fominykh, J. Berakdar, J. Henk, and P. Bruno, *Phys. Rev. Lett.* **89**, 086402 (2002).
- [56] W. Domcke, *Phys. Rep.* **208**, 97 (1991).
- [57] F. Capuzzi and C. Mahaux, *Ann. Phys. (NY)* **245**, 147 (1996).
- [58] B. Roulet, J. Gavoret, and P. Nozières, *Phys. Rev.* **178**, 1072 (1969).
- [59] B. Feuerbacher and L. S. Cederbaum, *Phys. Rev. A* **72**, 022731 (2005).
- [60] G. Stefanucci, Y. Pavlyukh, A.-M. Uimonen, and R. van Leeuwen, *Phys. Rev. B* **90**, 115134 (2014).
- [61] A.-M. Uimonen, G. Stefanucci, Y. Pavlyukh, and R. van Leeuwen, *Phys. Rev. B* **91**, 115104 (2015).
- [62] Y. Pavlyukh, A. Rubio, and J. Berakdar, *Phys. Rev. B* **87**, 205124 (2013).
- [63] M. E. Madjet, H. S. Chakraborty, J. M. Rost, and S. T. Manson, *J. Phys. B: At., Mol. Opt. Phys.* **41**, 105101 (2008).
- [64] Y. Pavlyukh and J. Berakdar, *Phys. Rev. A* **81**, 042515 (2010).
- [65] A. R. Edmonds, *Angular Momentum in Quantum Mechanics* (Princeton University Press, Princeton, NJ, 1996).
- [66] D. A. Varshalovich and A. N. Moskalev, *Quantum Theory of Angular Momentum* (World Scientific, Singapore, 1988).
- [67] A. S. Moskalenko, Y. Pavlyukh, and J. Berakdar, *Phys. Rev. A* **86**, 013202 (2012).
- [68] F. Zhang, *The Schur Complement and Its Applications*, Numerical Methods and Algorithms No. 4 (Springer, New York, 2005).
- [69] H. Feshbach, *Ann. Phys. (NY)* **19**, 287 (1962).
- [70] J. Escher and B. K. Jennings, *Phys. Rev. C* **66**, 034313 (2002).
- [71] S. J. Gustafson, *Mathematical Concepts of Quantum Mechanics*, 2nd ed. (Springer, Heidelberg, 2011).
- [72] A. Jensen and G. Nenciu, *Commun. Math. Phys.* **261**, 693 (2006).

### 5.3 E4: Disentangling multipole contributions to collective excitations in fullerenes

Within the jellium picture, the SCA (see subsec. 2.6.3) can already give a hint on how the density fluctuations coalesce into collective modes. The SCA captures some of the essential physics and predicts – for somewhat realistic parameters – a strong plasmonic resonance as observed in experiments [213]. Further refinements incorporate the density oscillations on the outer and inner surface of the spherical shell, allowing a classification of the plasmons by distinguishing with respect to symmetric or anti-symmetric surface plasmons and the corresponding angular momentum  $\ell$ . The anti-symmetric mode with  $\ell = 0$  represents a bulk plasmon. Despite providing a good fitting model for experiments [201], the predictive power of the SCA is limited. Moreover, important physical ingredients are missing:

- (i) The radial profile of the density oscillations has to be guessed and is not the result of the calculation. In particular, restricting the density fluctuations effectively treats the fullerene as an ideal metal. The deviation of the density from this picture (called spill-out density) results in additional degrees of freedom and thus plays an important role.
- (ii) The SCA excludes  $p$ - $h$  excitations by construction. When approaching the nano regime, however, plasmons and  $p$ - $h$  channels coalesce, giving rise to a significant coupling and thus broad plasmon peaks. This width entails atomistic details such as the band width of the SP states and their location in the energy-momentum plane.

All the deficiency of the SCA can, in principle, be overcome by a full-quantum calculation of the DD response function. Among the available options (see subsec. 2.6.3), we have chosen the real-time formulation via TDDFT: using suitable driving fields  $\delta\varphi(\mathbf{r}, t) = \delta(t)\delta\varphi(\mathbf{r})$  and solving the time-dependent KS equations (2.46), the Fourier-transformed density provides a direct link to the DD response function according to eq. (2.91). In particular, by choosing the perturbation potentials to have a specific multipolarity, we obtain an efficient scheme to compute the spherically-averaged dynamical structure factor  $S(q, \omega)$  (see subsec. 3.3.2) via the FDT (2.84). Generally, the time-propagation method offers a number of advantages in our scenario as compared to other methods. Most importantly, the collective excitations have a energy larger than the IP, such that ionization occurs upon plasmon decay. Such effects are efficiently incorporated by propagating the KS equations in real space and adding absorbing boundary conditions <sup>7</sup>.

Even though the structure factor obtained from TDDFT might be quite precise, all the different excitations are mixed and hard to disentangle. Intuitively, one would still expect the DD response to be reminiscent of the semi-classical picture to some degree. But how to bridge TDDFT and the semi-classical physics? The classification according to multipolarity, on the one hand, is achieved by projection both the driving potentials and the time-dependent density onto spherical harmonics. The remaining question is how to discern various excitation channels in the  $(q, \omega)$  plane. Within the SCA, this dependence is given by a set of plasmon frequencies  $\omega_{\ell, \nu}$  ( $\nu$  classifies the radial oscillation profile in symmetric/anti-symmetric) and  $q$ -dependence directly related to the spatial oscillation profile of the density. In order to converge to a similar picture from the TDDFT side, we employ a useful mathematical tool which is typically used for face-recognition algorithms [214]– the non-negative matrix factorization (NMF). In general, it decomposes a non-negative matrix into  $M_{ij} \approx \sum_{k=1}^r W_{ik} H_{kj}$  with small rank  $r$  and is thus well suited to find the few special features the matrix is composed of <sup>8</sup>. The idea of our work [E4] is the following: initializing the NMF algorithm with the SCA, we are able to decompose the rich TDDFT results into specific collective modes. This provides a practical scheme to bridge the gap between the accuracy from TDDFT and a simple physical interpretation as provided by semi-classical models. With the help of a subsequent fitting procedure we obtain a simple model for the DD response function which agrees, by construction, very well with the TDDFT results and is free of any parameter. Both the full TDDFT calculation and our model are tested against recent experimental data for EELS and show excellent agreement.

<sup>7</sup>For the Casida method, one needs to include a continuum of scattering states in the calculation, which makes the calculations extraordinarily demanding.

<sup>8</sup>Imagine filling a matrix with values  $0 \leq M_{ij} \leq 1$  corresponding to the pixels of a grey-scale photograph of a face. The NMF, if properly converged, decomposes this image into several images containing only specific features of the face such as the eyes, mouth or nose.



## Disentangling multipole contributions to collective excitations in fullerenes

M. Schüler,<sup>\*</sup> J. Berakdar, and Y. Pavlyukh

*Institut für Physik, Martin-Luther-Universität Halle-Wittenberg, 06099 Halle, Germany*

(Received 17 February 2015; published 24 August 2015)

Angular resolved electron energy-loss spectroscopy (EELS) gives access to the momentum and the energy dispersion of electronic excitations and allows one to explore the transition from individual to collective excitations. Dimensionality and geometry thereby play a key role. As a prototypical example we theoretically analyze the case of Buckminster fullerene  $C_{60}$  using *ab initio* calculations based on the time-dependent density-functional theory. Utilizing the non-negative matrix factorization method, multipole contributions to various collective modes are isolated, imaged in real space, and their energy and momentum dependencies are traced. A possible experiment is suggested to access the multipolar excitations selectively via EELS with electron vortex (twisted) beams. Furthermore, we construct an accurate analytical model for the response function. Both the model and the *ab initio* cross sections are in good agreement with recent experimental data.

DOI: 10.1103/PhysRevA.92.021403

PACS number(s): 36.40.Gk, 79.20.Uv, 31.15.A–

Plasmonics, a highly active field at the intersection of nanophotonics, material science, and nanophysics [1], has a long history dating back to the original work of Gustav Mie on light scattering from spherical colloid particles [2,3]. For extended systems the plasmon response occurs at a frequency set by the carrier density while in a finite system topology and finite-size quantum effects play a key role. E.g., for a nanoshell [4–6] in addition to the volume mode, two coupled ultraviolet surface plasmons arise having significant contributions from higher multipoles, as demonstrated below. Such excitations can be accessed by optical means as well as by electron energy-loss spectroscopy (EELS) [7,8]. Particle-hole (p-h) excitations and collective modes may “live” in overlapping momentum-energy domains and couple in a size-dependent way that cannot be understood classically [9–11]. Giant plasmon resonances were measured in buckminsterfullerene  $C_{60}$  [12–17] and explained, e.g., by assuming  $C_{60}$  to have a constant density of electrons confined to a shell with inner ( $R_1$ ) and outer ( $R_2$ ) radii (the spherical shell model) [18–20]. Refinements in terms of a semiclassical approximation (SCA) incorporate the quantum-mechanical density extending out of the shell  $R_1 < r < R_2$  (so-called spill-out density [21]). Time-dependent density-functional theory (TDDFT) [21–23] was also employed in a number of calculations [24–26]; however, most of them use the jellium model, i.e., the ionic structure is smeared out to a uniform positive background.

We present here, an atomistic full-fledged TDDFT calculations for EELS from  $C_{60}$  at *finite* momentum transfer. We demonstrate the necessity of the full *ab initio* approach by unraveling the nature of the various contributing plasmonic modes and their multipolar character. This is achieved by analyzing and categorizing the *ab initio* results by means of the *non-negative matrix factorization* method [27]. The results are in line with recent experimental findings [28]. The analysis also allows for constructing an accurate analytical model response function.

In first Born approximation for the triply differential cross section (TDCS) for detecting an electron with momentum  $\mathbf{p}_f$ ,

i.e., measuring its solid scattering angle  $d\Omega$  and energy  $\epsilon_{\mathbf{p}_f}$  is

$$\frac{d^3\sigma}{d\omega d\Omega} = \frac{4\gamma^2 p_f}{q^4 p_i} S(\mathbf{q}, \omega). \quad (1)$$

Here,  $\mathbf{p}_i$  is the incidence momentum corresponding to an energy  $\epsilon_{\mathbf{p}_i}$ ,  $\gamma$  is the Lorentz factor,  $\mathbf{q} = \mathbf{p}_f - \mathbf{p}_i$  is the momentum transfer, and  $\omega = \epsilon_{\mathbf{p}_f} - \epsilon_{\mathbf{p}_i}$  (atomic units are used throughout).  $S(\mathbf{q}, \omega)$  is the *dynamical structure factor* akin solely to the target [29]. The fluctuation-dissipation [29] theorem links  $S(\mathbf{q}, \omega)$  with the nonlocal, retarded density-density linear response function  $\chi^R(\mathbf{r}, \mathbf{r}'; t - t')$  [29–31] via  $S(\mathbf{q}, \omega) = -(1/\pi)\text{Im}[\chi^R(\mathbf{q}, -\mathbf{q}; \omega)]$  for  $\omega > 0$ . On the other hand,  $\chi^R(\mathbf{r}, \mathbf{r}'; t - t')$  describes the change in the system density  $\delta n(\mathbf{r}, t)$  upon a small perturbing potential  $\delta\varphi(\mathbf{r}, t)$ , i.e.,

$$\delta n(\mathbf{r}, t) = \int_{-\infty}^{\infty} dt' \int d\mathbf{r}' \chi^R(\mathbf{r}, \mathbf{r}'; t - t') \delta\varphi(\mathbf{r}', t'). \quad (2)$$

The response function is determined by evaluating the density variation with tunable perturbations, as accomplished via TDDFT which delivers  $\delta n(\mathbf{r}, t)$  upon solving the time-dependent Kohn-Sham (KS) equations [32].

Along this line, we utilized the OCTOPUS package [33,34], and propagated the KS equations. Kohn-Sham states are represented on a uniform real space grid [35] (0.2 Å grid spacing) confined to a sphere with 10 Å radius. For the ground state we checked the performance of different typical functionals and found that the local-density approximation (LDA) improved by self-interaction correction (SIC) yields fairly good results. The highest occupied molecular orbital (HOMO) (−9.2 eV) is located slightly too low with respect to the experimental value (−7.6 eV) [15]. The bandwidth (which is typically underestimated in DFT) within the LDA+SIC scheme is the largest for the tested functionals [36]. LDA-type Troullier-Martins pseudopotentials are used to incorporate the influence of the two core electrons per C atom, such that only the 240 valence electrons are accounted for. Gaussian smearing has been employed to deal with the degeneracy of the HOMO. In gas phase the molecules are randomly oriented. Hence, we have to evaluate the spherically averaged structure factor  $S(q, \omega)$ . Technically, this can be accomplished by choosing the perturbation  $\delta\varphi(\mathbf{r}, t) = I_0\delta(t)j_\ell(qr)Y_{\ell m}^*(\Omega_{\mathbf{r}})$  [37] where  $j_\ell$  is

<sup>\*</sup>michael.schueler@physik.uni-halle.de

the spherical Bessel function and  $Y_{\ell m}$  is the spherical harmonic. The perturbation strength lies with  $I_0 = 0.01$  a.u. well within the regime of linear response. The perturbed states are then propagated by the approximated enforced time-reversal symmetry (AETRS) propagator [38] up to  $T = 20\hbar/\text{eV}$  with a time step of  $\Delta t = 2 \times 10^{-3}\hbar/\text{eV}$ , covering the range from 0.31 to 3142 eV in frequency space. The large simulation box ensured the adequate representation of excited states. A mask was applied to the Kohn-Sham states at each time step in order to smoothly absorb contributions above the ionization threshold. From the density variation  $\delta n(\mathbf{r}, t) = n(\mathbf{r}, t) - n(\mathbf{r}, t = 0)$ ,  $\delta n_{\ell m}(q, \omega) = \int d\mathbf{r} \delta n(\mathbf{r}, t) j_\ell(qr) Y_{\ell m}(\Omega_{\mathbf{r}})$  is then computed in each time step and Fourier transformed to  $\delta n_{\ell m}(q, \omega)$  allowing one to determine  $S(q, \omega)$  as

$$S(q, \omega) = -\frac{4}{I_0} \sum_{\ell=0}^{\ell_{\max}} \sum_{m=-\ell}^{\ell} \text{Im}[\delta n_{\ell m}(q, \omega)]. \quad (3)$$

The  $m$  dependence is subsidiary. To a good approximation henceforth  $m = 0$ . It is sufficient to consider  $|\text{Im}[\delta n_\ell(q, \omega)]| \equiv -\text{Im}[\delta n_{\ell, m=0}(q, \omega)]$ , which stands for the  $\ell$ -resolved dynamical structure factor depicted in Fig. 1. For  $q \rightarrow 0$  (in the optical limit) the dipolar term is clearly dominant over higher multipoles.

According to the shell model [20] the  $\text{C}_{60}$  molecule possesses a volume plasmon mode ( $\ell = 0$  and radial density oscillation with one node), a symmetric surface mode ( $\ell \geq 1$  and no radial oscillation), and an antisymmetric surface mode ( $\ell \geq 1$  and one radial node). We denote these modes by V, S1 and S2, respectively. The plasmon energies are derived as  $\omega_V = \sqrt{3/r_s^3}$ ,  $\omega_{S(1,2), \ell} = \frac{\omega_V^2}{2} [1 \mp \frac{1}{2\ell+1} \sqrt{1 + 4\ell(\ell+1)(R_1/R_2)^{2\ell+1}}]$ . Inspecting the  $\ell = 1$

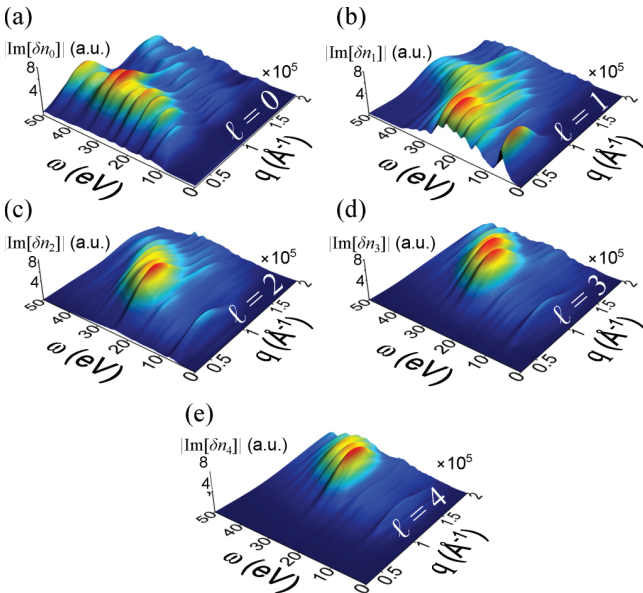


FIG. 1. (Color online) The  $\ell$ -resolved constituents of the dynamical structure factor of  $\text{C}_{60}$ ,  $|\text{Im}[\delta n_\ell(q, \omega)]|$  for (a)  $\ell = 0$ , (b)  $\ell = 1$ , (c)  $\ell = 2$ , (d)  $\ell = 3$ , and (e)  $\ell = 4$ . The  $\text{C}_{60}$  molecule was treated in standard truncated icosahedric geometry with bond lengths  $r_{\text{C-C}} = 1.445 \text{ \AA}$  and  $r_{\text{C-C}} = 1.390 \text{ \AA}$ .

panel the two surface modes may be identified around  $q \sim 0.3 \text{ \AA}^{-1}$ ,  $\omega \sim 20 \text{ eV}$  and  $q \sim 1 \text{ \AA}^{-1}$ ,  $\omega \sim 40 \text{ eV}$ .

As evident from Fig. 1, for higher  $q$  plasmonic modes (S1, S2, V) seem to merge and attain various multipole contributions. This is a manifestation of electronic transitions between the single-particle states with different angular momentum [39–41]. Thus, the question arises of how to disentangle these modes and to unravel their multipolar nature.

A suitable mathematical tool to tackle this task is the non-negative matrix factorization (NMF), which is extensively used, e.g., for face recognition algorithms [27]. Applied to our problem, the NMF delivers two functions  $F_i(\omega) \geq 0$  and  $G_i(q) \geq 0$  that enter the density response as  $|\text{Im}[\delta n_\ell(q, \omega)]| = \sum_i F_i(\omega) G_i(q)$  (see Appendix A). This structure follows, namely, from the Lehmann representation of  $\chi^R(\mathbf{r}, \mathbf{r}'; \omega)$  as

$$\chi^R(\mathbf{r}, \mathbf{r}'; \omega) = \sum_{\alpha} \xi_{\alpha}(\omega) \rho_{\alpha}(\mathbf{r}) \rho_{\alpha}(\mathbf{r}'),$$

$$\xi_{\alpha}(\omega) = \frac{2E_{\alpha}}{(\omega + i\Gamma_{\alpha})^2 - E_{\alpha}^2}, \quad (4)$$

where  $\rho_{\alpha}$  is the real fluctuation density corresponding to a transition from the ground to an excited many-body state labeled by  $\alpha$  (with excitation energy  $E_{\alpha}$ ), and  $\Gamma_{\alpha}$  is the linewidth. Assuming spherical symmetry, excitations have angular ( $\ell$ ) and radial ( $\nu$ ) components. Expanding  $\rho_{\alpha}(\mathbf{r}) \rho_{\alpha}(\mathbf{r}') = \sum_{\ell m} R_{\nu, \ell}(r) R_{\nu, \ell}(r') Y_{\ell m}(\Omega_{\mathbf{r}}) Y_{\ell m}^*(\Omega_{\mathbf{r}'})$ , Eq. (4) implies for the structure factor

$$S(q, \omega) = \sum_{\nu \ell} (2\ell + 1) F_{\nu, \ell}(\omega) G_{\nu, \ell}(q),$$

$$F_{\nu, \ell}(\omega) = -\text{Im}[\xi_{\nu, \ell}(\omega)],$$

$$G_{\nu, \ell}(q) = \left( \int_0^{\infty} dr r^2 R_{\nu, \ell}(r) j_{\ell}(qr) \right)^2.$$

In full generality the sum (4) contains an infinite number of terms corresponding to the infinite number of excited states. For homogeneous electron gas plasmons are strongly damped when their momentum enters the p-h continuum, where the noninteracting structure factor  $S^{(0)}(q, \omega) > 0$ . For electrons confined to a spherical shell the momentum can be represented by a magnitude  $q$  and an angular momentum  $\ell$ . To mark the effective region  $q_{\max}$  and  $\ell_{\max}$  in which plasmon modes exist, we estimate the transverse momentum as  $2\ell\pi/R$  (with radius  $R$ ) and compare it to the critical momentum  $q_{\text{crit}} = 0.559k_{\text{F}}$  [42] [the Fermi momentum is  $k_{\text{F}} = (9\pi/4)^{1/4} r_s^{-1}$ ]. We find so a critical  $\ell \sim 3$ . Thus, any collective excitation beyond  $\ell_{\max} = 4$  will be suppressed. For a complementary picture, we analyzed  $S^{(0)}(q, \omega)$  in SCA [43], for which the electron density enters as a central ingredient [we take the spherically averaged DFT density  $n_0(r)$ ] [44]. This allows one to estimate for which  $q$  the p-h pairs dominate the spectrum for each  $\ell$  separately. For  $\ell_{\max} = 4$  we find the p-h domain at  $q \gtrsim 1.2 \text{ \AA}^{-1}$ . Note that due to geometrical confinement plasmons and p-h excitations intersect each other and couple so significantly.

Now we separate the response into  $\nu = \text{S1}$  (Fig. 2) and  $\nu = \text{S2}$  (Fig. 3) for  $\ell \geq 1$ , while the mode  $\nu = \text{V}$  can be found from  $\ell = 0$  density component (Fig. 4). The onset of p-h excitations is also present in the spectra. The plasmon frequencies  $\omega_{\nu, \ell}$  are identified from the maximum of



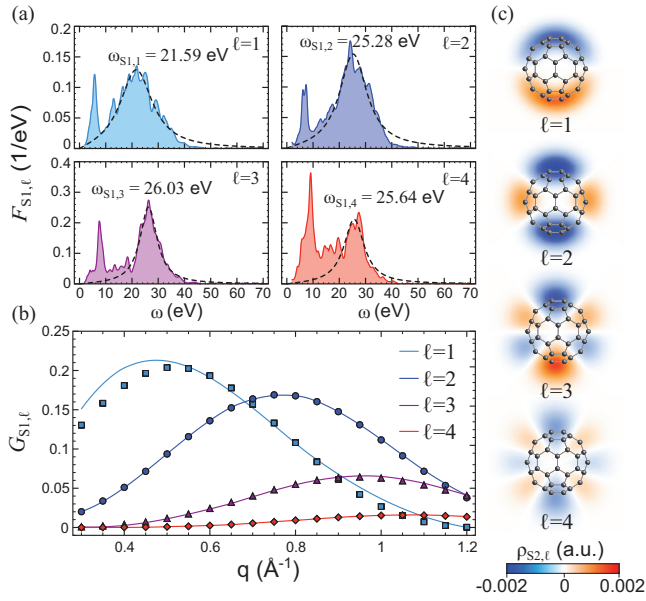


FIG. 2. (Color online) (a) Frequency-dependent part of the S1 modes obtained from the NMF (shaded curves) with fits (dashed lines). For plasmon features we concentrate on the region  $\omega > 18$  eV. (b)  $q$ -dependent part of the S1 modes from the NMF (solid lines) along with fits using the model fluctuation density (symbols). (c) Model fluctuation density  $\rho_{S1,\ell}$  in a plane cut through the center of the molecule for  $\ell$  ranging from 1 (top) to 4 (bottom).

the  $\omega$ -dependence spectra as obtained by the NMF in the form  $F_{v,\ell}^{\text{fit}}(\omega) = -\text{Im}\{2\omega_{v,\ell}/[(\omega + i\Gamma_{v,\ell})^2 - \omega_{v,\ell}^2]\}$ . Inspecting Fig. 2(a), we find the dipole plasmon at  $\omega_{S1,1} \simeq 21.59$  eV; this is a well established value. Increasing  $\ell$  shifts the peak to larger energies (in line with the shell model); the sharp peak around 7.5 eV, which is known to consist of a series of p-h excitations [11], gains spectral weight until it dominates for  $\ell = 4$ . An abundance of large angular momentum states around the HOMO-LUMO gap [41] increases the number of channels for high-multipole electronic transitions and is responsible for the peak's enhancement. The plasmon frequency  $\omega_{S1,4} = 25.64$  eV, on the other hand, is smaller than  $\omega_{S1,3} = 26.03$  eV. This demonstrates the limitations of the SCA.

The radial profile of the density oscillations  $R_{v,\ell}(r)$  can be inferred from  $G_{v,\ell}(q)$  in that we assume  $R_{S1,\ell}^{\text{fit}}(r) = A_\ell r \exp[-(r - r_\ell)^2/2\sigma_\ell^2]$  and extract the parameters  $(A_\ell, r_\ell, \sigma_\ell)$  for which the norm  $\|G_{S1,\ell}(q) - [\int_0^\infty dr r^2 R_{S1,\ell}^{\text{fit}}(r) j_\ell(qr)]^2\|$  is minimized. The effective fluctuation densities are then given by  $\rho_{S1,\ell}(\mathbf{r}) = R_{S1,\ell}(r) Y_{\ell 0}(\Omega_{\mathbf{r}})$  [cf. Fig. 2(c)].

An analogous procedure for S2 modes (Fig. 3) reveals a decrease of the plasmon energies in qualitative agreement with Ref. [14]. However, the dispersion is less pronounced than in the shell model. To characterize the fluctuation densities, we use an ansatz containing a node  $R_{S2,\ell}^{\text{fit}}(r) = A_\ell r(1 - r/r_\ell^{(0)}) \exp[-(r - r_\ell)^2/2\sigma_\ell^2]$  and determine the parameters as to match  $G_{S2,\ell}(q)$  [Fig. 3(b)]. The spatial structure of the plasmon oscillation is shown in Fig. 3(c).

A common and physically intuitive feature of the S1 and S2 modes is that the spatial extent of the fluctuation density

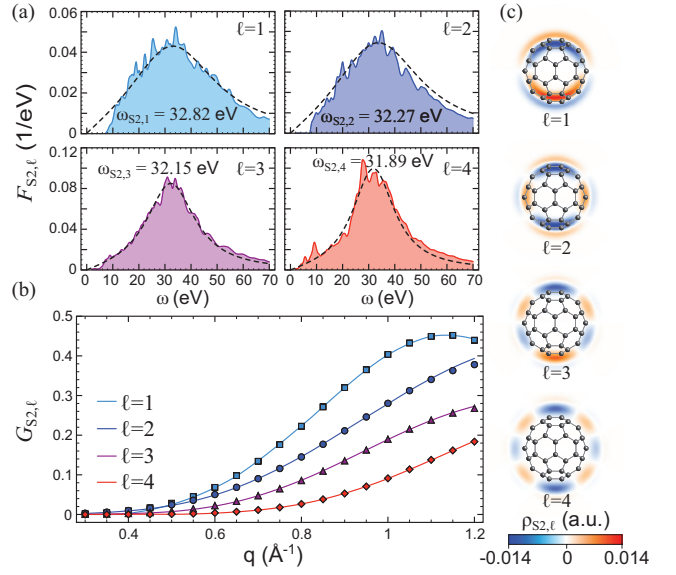


FIG. 3. (Color online) (a) Frequency-dependent part of the S2 modes from the NMF (shaded curves) and corresponding fits (dashed lines). For the latter, no constraint has been imposed on the frequency range. (b)  $q$ -dependent part of the S2 modes from the NMF (solid lines) and fits (symbols). (c) Model fluctuation density  $\rho_{S2,\ell}$  as in Fig. 2.

is growing with  $\ell$ . This is a consequence of the increasing centrifugal force, “pushing” the oscillation away from the center.

Applying the NMF with two components to  $|\text{Im}[\delta n_0(q, \omega)]|$  shows (Fig. 4) that in addition to the expected volume plasmon (labeled by V1) around  $\omega_{V1} = 42.69$  eV (which agrees well with density parameter  $r_s \sim 1$ ), a second resonance peaked around  $\omega_{V2} = 24.17$  eV appears. To clarify its origin

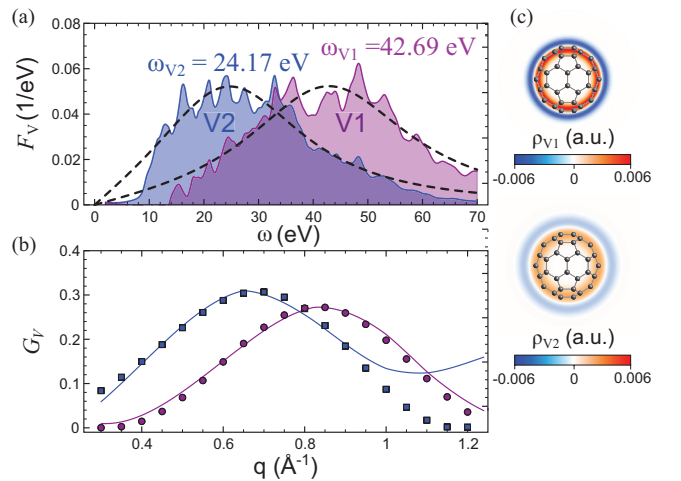


FIG. 4. (Color online) (a) Frequency-dependent part of the V1 (blue shaded curve) and V2 (purple shaded curve) mode from the NMF along with corresponding fits (dashed lines). Fitting has been carried out in the complete frequency range. (b)  $q$ -dependent part of the V1 and V2 modes from the NMF (solid lines) and fits (symbols). (c) Model fluctuation densities in the same plane as in Fig. 2.

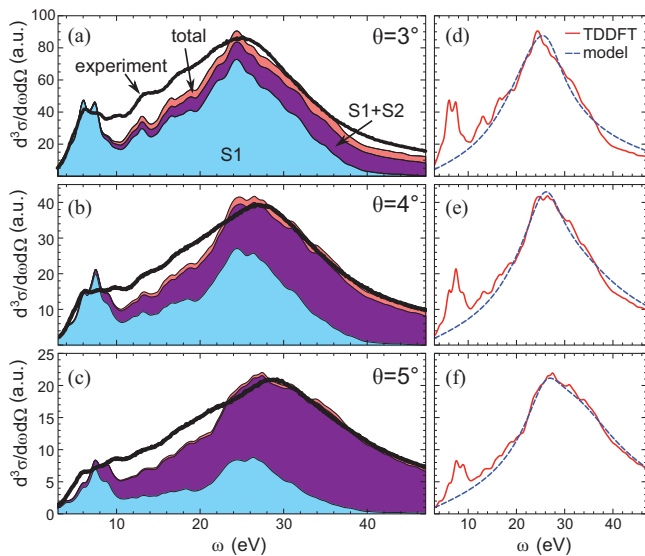


FIG. 5. (Color online) TDCS for EELS of  $C_{60}$  at scattering angles  $\theta = 3^\circ$  (a),  $\theta = 4^\circ$  (b), and  $\theta = 5^\circ$  (c). The energy loss  $\omega$  is with respect to initial beam energy of  $\epsilon_0 = 1050$  eV. Colored curves represent TDDFT calculations resolved in the contribution from S1, S1+S2, and S1+S2+V. The thick curve shows experimental data [28]. (d)–(f) Comparison of full TDDFT and model cross sections.

we computed the response function from its noninteracting counterpart in the random-phase approximation and invoking the SCA (see Appendix B). After obtaining  $|\text{Im}[\delta n_0(q, \omega)]|$  we applied the NMF, as well. This procedure yields very similar spectra including the occurrence of V2. This feature is, however, very sensitive to the details of the density distribution; it vanishes for a discontinuous steplike profile. Thus, it is the oscillations of the spill-out density taking place on the surface of the molecule that form V2. This is a pure quantum effect.

With the dynamical structure factor being fully characterized, we proceed by computing the TDCS [Eq. (1)]. Figure 5 compares calculated and measured [28] EELS spectra as a function of the electron scattering angle  $\theta$  which fixes the momentum transfer. The magnitudes of the measured spectra shown in Fig. 5 are determined up to an overfall factor fixed in Fig. 5(a). Thus, the theory-experiment comparison in Figs. 5(b) and 5(c) is on the absolute scale. The classification of the plasmon modes accomplished by the NMF analysis allows for plotting mode-resolved TDCS curves. As Figs. 5(a)–5(c) demonstrate, the S1 plasmons play the dominant role for small  $\theta$  (which corresponds to the optical limit of small  $q$ ), while the S2 modes becomes increasingly significant for larger  $\theta$  (i.e., larger  $q$ ). The larger energy of the S2 with respect to the S1 plasmons leads to the formation of a shoulder (clearly visible for  $\theta = 4^\circ$ ) and, thus, to the apparent shift of the maximum of the experimental EELS spectrum with growing  $\theta$ . A similar effect is also observed for the S1 modes due to their dispersion with respect to  $\ell$ .

Furthermore, the extracted  $\omega$ -dependencies and the model fluctuation densities can be used to construct an approximate structure factor  $S^{\text{model}}(q, \omega) = \sum_{\nu\ell} (2\ell + 1) F_{\nu,\ell}^{\text{fit}}(\omega) G_{\nu,\ell}^{\text{fit}}(q)$  that reproduces the TDDFT results around the plasmon

resonances in a precise way by construction. Corresponding TDCSs are compared in Figs. 5(d)–5(f).

An important feature of the structure factor is the  $f$ -sum rule  $\int_0^\infty d\omega \omega S(q, \omega) = Nq^2/2$  (number of electrons  $N$ ). Inspecting the (plasmon-dominated)  $S^{\text{model}}(q, \omega)$  shows the discrepancy for larger  $q$ ; a critical value is reached when  $\int_0^\infty d\omega \omega S^{\text{model}}(q, \omega)$  decreases again after quadratic growth. We find  $q_{\text{crit}} \sim 1.2 \text{ \AA}^{-1}$ , which is consistent with the estimation above. Hence, p-h excitations become more important for  $q > q_{\text{crit}}$  and gradually diminish the plasmon contribution. In this context, we note that Eq. (1) is most reliable around the plasmon resonance (similar findings were reported for crystalline  $C_{60}$  [45]) at which screening is more effective and hence the use of a plane wave for the continuum electron, as done here, is justified. Account of post collision interactions might remove some the remaining discrepancies between theory and experiments.

In summary, we presented accurate TDDFT calculations for the dynamical structure factor and EELS spectra for a  $C_{60}$  molecule underlining the role of higher multipole contributions. Using NMF decomposition allowed us to trace the evolution in  $q$  and  $\omega$  of the symmetric and antisymmetric surface and volume plasmons. In addition, we characterized and modeled the fluctuation densities (i.e., the ingredients of the response function) and unveiled their multipolar character. These ingredients may, in principle, be accessed selectively by using electron beams carrying a definite angular momentum (electron vortex beams [46,47]). By measuring the angular momentum of the scattered beam the *angular momentum transfer*  $\Delta\ell$  becomes a control variable which the EELS spectra depend on. Particularly, provided the beam axis coincides with the symmetry axis of spherical system, the plasmonic response upon scattering of such twisted electrons contains multipole contributions for  $\ell \geq |\Delta\ell|$  only [48]. Hence, specific multipoles can be excluded or included by varying  $\Delta\ell$ .

Furthermore, we discussed the limitation of spherical-shell models in describing the quenching of the volume plasmon and identified the electronic density distribution as a key factor determining its energy. We obtained excellent agreement with experimental results and explained how the different plasmon modes contribute to the spectra.

This work is supported by the German Research Foundation (DFG) Collaborative Research Centre SFB 762 Functionality of Oxide Interfaces and Grant Number PA 1698/1-1. We thank Paolo Bolognesi and Lorenzo Avaldi for fruitful discussions and for providing experimental data.

#### APPENDIX A: NON-NEGATIVE MATRIX FACTORIZATION

As dictated by the fluctuation-dissipation theorem, the imaginary part of  $\delta n_\ell(q, \omega)$  for  $\omega > 0$  is purely negative. Thus, the NMF can be applied to  $|\text{Im}[\delta n_\ell(q, \omega)]| = -\text{Im}[\delta n_\ell(q, \omega)]$  to split

$$|\text{Im}[\delta n_\ell(q, \omega)]| = \sum_{\nu=1}^N F_{\nu,\ell}(\omega) G_{\nu,\ell}(q). \quad (\text{A1})$$

Without imposing any restriction on the number of components ( $N$ ) the expansion (A1) is exact and can be paralleled with the

singular value decomposition of a general (complex or real) matrix  $\mathbf{M}$ :  $\mathbf{M} = \mathbf{U}\Sigma\mathbf{V}^*$ . The difference is in the additional requirements of positivity on the vectors forming  $\mathbf{U}$  and  $\mathbf{V}$ . The transition from continuous variables as in Eq. (A1) to the matrix form is provided by discretizing the  $\omega$  and the  $q$  points after smooth interpolation.

We select  $N = 2$  as we expect two dominant surface plasmon modes (S1 and S2). This choice is confirmed by computing the residue norm with respect to the full function  $|\text{Im}[\delta n_\ell(q, \omega)]|$ .

The problem of non-negative matrix factorization can be formulated as a *nonconvex* minimization problem for the residue norm  $r = \|\mathbf{A} - \mathbf{WH}\|^2$ . Thus, the solution is not unique and may lead to *local minima*. Depending on the norm used different algorithms can be formulated. A commonly used method is the *multiplicative update* of Lee and Seung [27]:

$$\mathbf{W}_{ia} \leftarrow \mathbf{W}_{ia} \frac{(\mathbf{A}\mathbf{H}^T)_{ia}}{(\mathbf{W}\mathbf{H}\mathbf{H}^T)_{ia}}, \quad (\text{A2a})$$

$$\mathbf{H}_{aj} \leftarrow \mathbf{H}_{aj} \frac{(\mathbf{W}^T\mathbf{A})_{aj}}{(\mathbf{W}^T\mathbf{W}\mathbf{H})_{aj}}, \quad (\text{A2b})$$

where  $i$  indexes the energy points and  $j$  numbers the time points. The method starts with some suitable guess for matrices  $\mathbf{W}$  and  $\mathbf{H}$ . Additionally, the vectors forming  $\mathbf{W}$  are normalized each step:

$$\mathbf{W}_{ia} \leftarrow \frac{\mathbf{W}_{ia}}{\|\mathbf{W}_a\|}.$$

Upon these prescriptions (A2) the Euclidean distance  $r$  monotonously decreases until the stationary point (local minimum) has been reached. We initialized the vector  $\mathbf{W}_1$  ( $\mathbf{W}_2$ ) with cuts of  $|\text{Im}[\delta n_{\ell m}(q, \omega)]|$  along  $q$  direction at  $\omega = 20$  eV ( $\omega = 40$  eV), while  $\mathbf{H}_1$  ( $\mathbf{H}_2$ ) is constructed by cuts at  $q = 0.5 \text{ \AA}^{-1}$  ( $q = 1.0 \text{ \AA}^{-1}$ ). We found that typically 1000 iterations yield well converged results.

The functions  $F_{v,\ell}(\omega)$  and  $G_{v,\ell}(q)$  are then obtained from interpolating the data from  $\mathbf{H}_v$  and  $\mathbf{W}_v$ , respectively. We normalize the frequency spectra such that fitting by  $F_{v,\ell}^{\text{fit}}(\omega) = -\text{Im}\{2\omega_{v,\ell}/[(\omega + i\Gamma_{v,\ell})^2 - \omega_{v,\ell}^2]\}$  (as explained in the main text) can be performed without any additional prefactor.

$G_{v,\ell}(q)$  is normalized accordingly. This normalization procedure is consistent with the Lehmann representation.

## APPENDIX B: SEMICLASSICAL CALCULATIONS

In order to elucidate the behavior of the volume plasmons, semiclassical calculations provide some insight. The starting point is the Dyson equation for the density-density response function in random-phase approximation:

$$\chi(\mathbf{r}, \mathbf{r}'; z) = \chi^{(0)}(\mathbf{r}, \mathbf{r}'; z) + \int d\mathbf{r}_1 \int d\mathbf{r}_2 \chi^{(0)}(\mathbf{r}, \mathbf{r}_1; z) \times v(\mathbf{r}_1 - \mathbf{r}_2) \chi(\mathbf{r}_2, \mathbf{r}'; z). \quad (\text{B1})$$

We drop the superscript R and consider general complex argument  $z$  here. In SCA, the noninteracting reference response function  $\chi^{(0)}(\mathbf{r}, \mathbf{r}'; z)$  can be expressed in terms of ground-state density  $n_0(\mathbf{r}) [= n_0(r)]$  as we assume spherical symmetry here only. The subsequent derivations and the solution scheme for Eq. (B1) are detailed in the Supplemental Material [49]. The amount of spill-out density can be adjusted by varying the smearing parameter  $\Delta r$  in the model density

$$n_0(r) = N_0[\theta_{\Delta r}(r - R_1) - \theta_{\Delta r}(r - R_2)],$$

$$\theta_{\Delta r}(r) = \frac{1}{1 + \exp[-r/\Delta r]}, \quad (\text{B2})$$

where  $R_1 = R_0 - \Delta R/2$ ,  $R_2 = R_0 + \Delta R/2$  are the inner and outer radii ( $R_0 = 6.5$  a.u.), while the normalization  $N_0$  ensures the correct total valence charge.  $\Delta R$  is fixed to keep the mean density constant. The scenario  $\Delta r \rightarrow 0$  corresponds to a boxlike density profile with sharp boundaries, while  $\Delta r = 0.5$  a.u. is a good approximation to the spherically averaged DFT density. Once Eq. (B1) is solved for certain  $\Delta r$ , the ( $\ell = 0$ ) contribution to the structure factor,  $\text{Im}[\delta n_0(q, z = \omega + i\Gamma)]$  ( $\Gamma = 0.1$  a.u. is a broadening parameter) can be computed. Applying the NMF technique allows again for separating the V1 and V2 modes. We find the position of V1 similar to the TDDFT results, while the behavior of V2 is very sensitive to  $\Delta r$ . While very pronounced for  $\Delta r = 0.5$  a.u., the relative strength of the V2 peak vanishes for  $\Delta r \rightarrow 0$ . More details and graphs of volume plasmon spectra can be found in the Supplemental Material.

- 
- [1] J. A. Schuller, E. S. Barnard, W. Cai, Y. C. Jun, J. S. White, and M. L. Brongersma, *Nat. Mater.* **9**, 368 (2010).  
 [2] G. Mie, *Ann. Phys. (N.Y.)* **330**, 377 (1908).  
 [3] N. J. Halas, S. Lal, W.-S. Chang, S. Link, and P. Nordlander, *Chem. Rev.* **111**, 3913 (2011).  
 [4] L. M. Liz-Marzan, *Langmuir* **22**, 32 (2006).  
 [5] P. K. Jain and M. A. El-Sayed, *Nano Lett.* **7**, 2854 (2007).  
 [6] E. Prodan, C. Radloff, N. J. Halas, and P. Nordlander, *Science* **302**, 419 (2003).  
 [7] R. F. Egerton, *Rep. Prog. Phys.* **72**, 016502 (2009).  
 [8] F. J. García de Abajo, *Rev. Mod. Phys.* **82**, 209 (2010).  
 [9] C. Yannouleas and R. A. Broglia, *Ann. Phys. (N.Y.)* **217**, 105 (1992).  
 [10] F. Alasia, R. A. Broglia, H. E. Roman, L. Serra, G. Colo, and J. M. Pacheco, *J. Phys. B* **27**, L643 (1994).  
 [11] A. S. Moskalenko, Y. Pavlyukh, and J. Berakdar, *Phys. Rev. A* **86**, 013202 (2012).  
 [12] E. Sohmen, J. Fink, and W. Krätschmer, *Z. Phys. B: Condens. Matter* **86**, 87 (1992).  
 [13] A. W. Burose, T. Dresch, and A. M. G. Ding, *Z. Phys. D: At. Mol. Clusters* **26**, 294 (1993).  
 [14] P. Bolognesi, L. Avaldi, A. Ruocco, A. Verkhovtsev, A. V. Korol, and A. V. Solov'yov, *Eur. Phys. J. D* **66**, 254 (2012).  
 [15] I. V. Hertel, H. Steger, J. de Vries, B. Weisser, C. Menzel, B. Kamke, and W. Kamke, *Phys. Rev. Lett.* **68**, 784 (1992).  
 [16] S. W. J. Scully, E. D. Emmons, M. F. Gharaibeh, R. A. Phaneuf, A. L. D. Kilcoyne, A. S. Schlachter, S. Schippers, A. Müller,

- H. S. Chakraborty, M. E. Madjet, and J. M. Rost, *Phys. Rev. Lett.* **94**, 065503 (2005).
- [17] A. Reinköster, S. Korica, G. Prümper, J. Viehhaus, K. Godehusen, O. Schwarzkopf, M. Mast, and U. Becker, *J. Phys. B* **37**, 2135 (2004).
- [18] D. Östling, S. P. Apell, G. Mukhopadhyay, and A. Rosen, *J. Phys. B* **29**, 5115 (1996).
- [19] B. Vasvári, *Z. Phys. B: Condens. Matter* **100**, 223 (1996).
- [20] A. Verkhovtsev, A. V. Korol, and A. V. Solov'yov, *Eur. Phys. J. D* **66**, 253 (2012).
- [21] R. Esteban, A. G. Borisov, P. Nordlander, and J. Aizpurua, *Nat. Commun.* **3**, 825 (2012).
- [22] E. Prodan and P. Nordlander, *Nano Lett.* **3**, 543 (2003).
- [23] M. A. L. Marques and E. K. U. Gross, *Annu. Rev. Phys. Chem.* **55**, 427 (2004).
- [24] R. Bauernschmitt, R. Ahlrichs, F. H. Hennrich, and M. M. Kappes, *J. Am. Chem. Soc.* **120**, 5052 (1998).
- [25] M. E. Madjet, H. S. Chakraborty, J. M. Rost, and S. T. Manson, *J. Phys. B* **41**, 105101 (2008).
- [26] E. Maurat, P.-A. Hervieux, and F. Lépine, *J. Phys. B* **42**, 165105 (2009).
- [27] D. D. Lee and H. S. Seung, *Nature (London)* **401**, 788 (1999).
- [28] A. V. Verkhovtsev, A. V. Korol, A. V. Solov'yov, P. Bolognesi, A. Ruocco, and L. Avaldi, *J. Phys. B* **45**, 141002 (2012).
- [29] G. Giuliani and G. Vignale, *Quantum Theory of the Electron Liquid* (Cambridge University Press, Cambridge, 2005).
- [30] G. Onida, L. Reining, and A. Rubio, *Rev. Mod. Phys.* **74**, 601 (2002).
- [31] M. A. L. Marques, N. T. Maitra, F. M. S. Nogueira, E. K. U. Gross, and A. Rubio, *Fundamentals of Time-Dependent Density Functional Theory* (Springer, New York, 2012).
- [32] The time-propagation method is more efficient than the Casida linear response scheme [31] for larger systems. The computational cost scales cubically with the number of p-h pairs, which is typically large for fullerenes [50].
- [33] M. A. L. Marques, A. Castro, G. F. Bertsch, and A. Rubio, *Comput. Phys. Commun.* **151**, 60 (2003).
- [34] X. Andrade, J. Alberdi-Rodriguez, D. A. Strubbe, M. J. T. Oliveira, F. Nogueira, A. Castro, J. Muguerza, A. Arruabarrena, S. G. Louie, A. Aspuru-Guzik, A. Rubio, and M. A. L. Marques, *J. Phys.: Condens. Matter* **24**, 233202 (2012).
- [35] X. Andrade, D. Strubbe, U. D. Giovannini, A. H. Larsen, M. J. T. Oliveira, J. Alberdi-Rodriguez, A. Varas, I. Theophilou, N. Helbig, M. J. Verstraete, L. Stella, F. Nogueira, A. Aspuru-Guzik, A. Castro, M. A. L. Marques, and A. Rubio, *Phys. Chem. Chem. Phys.* (2015).
- [36] Besides the LDA+SIC scheme, the ground-state calculation was carried out using standard LDA, the generalized-gradient approximation functional LB94, and the hybrid function B3LYP [51].
- [37] A. Sakko, A. Rubio, M. Hakala, and K. Hamalainen, *J. Chem. Phys.* **133**, 174111 (2010).
- [38] A. Castro, M. A. L. Marques, and A. Rubio, *J. Chem. Phys.* **121**, 3425 (2004).
- [39] M. Feng, J. Zhao, and H. Petek, *Science* **320**, 359 (2008).
- [40] Y. Pavlyukh and J. Berakdar, *Chem. Phys. Lett.* **468**, 313 (2009).
- [41] Y. Pavlyukh and J. Berakdar, *J. Chem. Phys.* **135**, 201103 (2011).
- [42] G. Stefanucci and R. v. Leeuwen, *Nonequilibrium Many-Body Theory of Quantum Systems: A Modern Introduction* (Cambridge University Press, Cambridge, 2013).
- [43] Y. Pavlyukh, J. Berakdar, and K. Köksal, *Phys. Rev. B* **85**, 195418 (2012).
- [44] For the noninteracting response  $\chi_0^R(\mathbf{r}, \mathbf{r}'; \omega)$  function SCA,  $\int d\mathbf{r} \chi_0^R(\mathbf{r}, \mathbf{r}'; \omega) \phi(\mathbf{r}) = (1/\omega^2)[\nabla n(\mathbf{r}') \cdot \nabla \phi(\mathbf{r}') - n(\mathbf{r}') \nabla^2 \phi(\mathbf{r}')] holds for any function  $\phi(\mathbf{r})$ . Setting  $\phi(\mathbf{r}) = \exp[-i\mathbf{q} \cdot (\mathbf{r} - \mathbf{r}')] and assuming a spherically symmetric density  $n(r)$  yields for the structure factor  $S^{(0)}(q, \omega) \simeq (4/\omega^2) \sum_{\ell} (2\ell + 1) S_{\ell}^{(0)}(q, \omega)$ , where  $S_{\ell}^{(0)}(q, \omega) = \int_0^{\infty} dr r^2 j_{\ell}(qr) [q^2 n(r) j_{\ell}(qr) + qn'(r) j'_{\ell}(qr)]$ .$$
- [45] P. Koval, M. P. Ljungberg, D. Foerster, and D. Sánchez-Portal, *Nucl. Instrum. Methods Phys. Res. Sect. B* **354**, 216 (2015).
- [46] M. Uchida and A. Tonomura, *Nature (London)* **464**, 737 (2010).
- [47] J. Verbeeck, H. Tian, and P. Schattschneider, *Nature (London)* **467**, 301 (2010).
- [48] Employing the first Born approximation for an incoming electron vortex beam with wave function  $\psi_{k_{\perp,i} \ell_i k_{z,i}}(\mathbf{r}) = \zeta_{k_{\perp,i} \ell_i}(r, \theta) e^{ik_{z,i} r \cos \theta} e^{i\ell_i \phi}$  [52] scattered from a spherical system with response function  $\chi^R(\mathbf{r}, \mathbf{r}'; \omega) = \sum_{\ell m} \chi_{\ell}^R(r, r'; \omega) Y_{\ell m}^*(\Omega_{\mathbf{r}}) Y_{\ell m}(\Omega_{\mathbf{r}'})$  into the final state  $\psi_{k_{\perp,f} \ell_f k_{z,f}}(\mathbf{r})$  yields the cross section proportional to  $\sum_{\ell \geq |\Delta \ell|} \int_0^{\infty} dr r^2 \int_0^{\infty} dr' r'^2 \mathcal{V}_{\ell}(r) \mathcal{V}_{\ell}^*(r') \text{Im}[\chi_{\ell}^R(r, r'; \omega)]$ . Explicit calculations result in
- $$\mathcal{V}_{\ell}(r) = 4\pi A_{\ell, \Delta \ell} \int_0^{\infty} dr' \int_0^{\pi} d\theta' \sin \theta' \zeta_{k_{\perp,i} \ell_i}(r', \theta') \zeta_{k_{\perp,f} \ell_f}(r', \theta')$$
- $$\times e^{i(k_{z,i} - k_{z,f})r' \cos \theta'} (r'_{<}/r'_{>})^{\ell} P_{\ell}^{\Delta \ell}(\cos \theta').$$
- Here,  $Y_{\ell m}(\Omega_{\mathbf{r}}) = A_{\ell, m} P_{\ell}^m(\cos \theta) e^{im\phi}$ , and  $\Delta \ell = \ell_f - \ell_i$ .
- [49] See Supplemental Material at <http://link.aps.org/supplemental/10.1103/PhysRevA.92.021403> for the detailed discussion of the semiclassical approach.
- [50] G. Orlandi and F. Negri, *Photochem. Photobiol. Sci.* **1**, 289 (2002).
- [51] S. F. Sousa, P. A. Fernandes, and M. J. Ramos, *J. Phys. Chem. A* **111**, 10439 (2007).
- [52] J. Verbeeck, H. Tian, and A. Béch e, *Ultramicroscopy* **113**, 83 (2012).

## 5.4 E5: Electron pair escape from fullerene cage via collective modes

As discussed in sec. 5.3 and [E4], the collective excitations dominate the many-body excitation spectrum in the UV regime. Hence, dynamical screening effects play a substantial role for the interaction of a photoelectron emanating from the fullerene and the remaining charge density. The – very probable – case that the photoelectron loses a part of its energy to the screening, i. e., the excitation of plasmons in the parent ion, represents a typical example of an extrinsic loss (compare subsec. 3.1.2). This process is reminiscent of EELS, but with the molecule’s own photoexcited electrons. The lifetime of the plasmons, on the other hand, is rather short (the plasmons peaks in [E4] are very broad), due to the strong coupling to  $p$ – $h$  excitations. Since the typical plasmon energy is much larger than the ionization energy of the singly-ionized system, the Landau decay into  $p$ – $h$  pairs leads to the emission of a second electron (the particle state must be a scattering state).

While for atoms the mechanisms of DPE are well understood [145] in terms of the bare Coulomb interaction, the emission of the second electron via dynamical screening and subsequent plasmon decay represents a genuinely new DPE pathway<sup>9</sup> with substantial relevance for larger molecules or clusters and, especially, for solid-state systems. Our model calculations imposing the plasmon-mediated DPE mechanism based on a jellium-type model [E3] have already yielded results matching experimental data (see fig. 5.2). However, a full-fledged theoretical description, supported by appropriate experiments, was still missing. This is where our work [E5] comes into play.

How can the plasmon-assisted mechanism be pinpointed by a DPE measurement? The energetics of the mechanism, shown in fig. 5.2(c), provide essential hints. The  $\pi$  orbitals (see fig. 5.1(c)) form a narrow peak in the DOS. Hence, the DPE signal will be most pronounced if both electrons originate from the  $\pi$  band. Estimating the energy of the plasmons by  $\omega_{\text{plasmon}} \simeq 25$  eV, the energy of the first electrons  $E_1$  (fixed by the detector) should be around  $E_1 \approx 10$  eV, such that the energy of the intermediate scattering state  $E = E_1 + \omega_{\text{plasmon}}$  corresponds to emission from the  $\pi$  band. For the liberation of the second electron, the finite plasmon energy restricts the plasmon-decay ionization process to emission of the  $\pi$  band. These energetic restrictions should be manifest in significant narrowing of the spectrum if scanned over the photon energy (at fixed  $E_1, E_2$ ).

This study is carried out in our joint experimental and theoretical work [E5], where full-fledged *ab initio* calculations – based on our accurate parameterization of the screened interaction from ref. [E4] – are paralleled to coincidence measurements (see subsec. 3.2.2) of the DPE cross-section as function of the photon energy. We explicitly show that by artificially switching off the dynamical screening effects, the spectrum becomes much broader and disagrees with the experimental data. Hence, the plasmon-assisted DPE process is evidenced as the mechanism for ejecting two electrons in the considered setup.

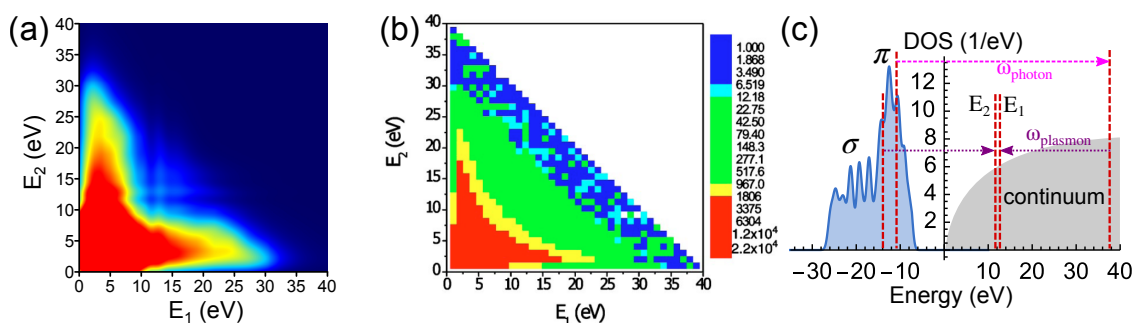


Figure 5.2: Comparison of the DPE cross-section (averaged over the emission angles of the two electrons) as function of the energy of each of the photoelectrons for (a) our calculation, and (b) experimental results by Hillebrecht *et al.*. Reprinted figure with permission from [216]. Copyright (2005) of the American Physical Society. The photon energy was fixed at 65 eV. (c) Sketch of the plasmon-assisted DPE mechanism in the energy picture.

<sup>9</sup>For larger atoms such as Xe, dipolar resonances exist [215] and may lead to DPE, as well. Their excitation upon liberating the first electrons is, however, not due to dynamical screening.

# SCIENTIFIC REPORTS

OPEN

## Electron pair escape from fullerene cage via collective modes

Michael Schüler<sup>1</sup>, Yaroslav Pavlyukh<sup>1</sup>, Paolo Bolognesi<sup>2</sup>, Lorenzo Avaldi<sup>2</sup> & Jamal Berakdar<sup>1</sup>

Received: 10 December 2015

Accepted: 29 March 2016

Published: 18 April 2016

**Experiment and theory evidence a new pathway for correlated two-electron release from many-body compounds following collective excitation by a single photon. Using nonequilibrium Green's function approach we trace plasmon oscillations as the key ingredient of the effective electron-electron interaction that governs the correlated pair emission in a dynamic many-body environment. Results from a full *ab initio* implementation for C<sub>60</sub> fullerene are in line with experimental observations. The findings endorse the correlated two-electron photoemission as a powerful tool to access electronic correlation in complex systems.**

A sample absorbing a single ultraviolet photon may emit a single electron having energy and momentum distributions that reflect the spectral properties of the material<sup>1</sup>. It is also possible, though usually less probable, that two electrons escape. How can one photon “kick out” two electrons? For few-electron atoms, it is established<sup>2</sup> that the Coulomb repulsion plays a key role. A possible scenario is that the photon is absorbed by one bound electron that approaches the other electron while undergoing multiple scattering from the residual ion or the other electron. Mediated by electron-electron Coulomb interaction, the two electrons exchange momentum while leaving the sample and interacting mutually and with the residual ion, in principle to infinite distances. This physical picture, often referred to as *knock-out* mechanism, dominates for photon energies close to double ionization threshold, whereas for larger photon energies different processes (e.g. *shake-off*) become important<sup>3</sup>. When detecting the two electrons in coincidence (called double photoemission (DPE) spectroscopy<sup>4–6</sup>), depending on the selected energies and angles, one may zoom into some of these processes, albeit with restrictions imposed by symmetry<sup>2,7</sup>.

The situation changes with a growing number of electrons in the system. The effective electron-electron interaction is not even known *a priori* as it is determined by the dynamic behavior of its active surrounding, meaning that the *e–e* interaction builds up during the photoexcitation process. Thereby, dimensionality is a key factor<sup>8</sup>. In fact, for electronic systems strongly confined to one dimension (e.g., a one channel quantum wire) *e–e* interaction gives rise to a new form of excitations (Luttinger liquid<sup>9</sup>) with features distinct from those akin to Fermi liquids, i.e. most three-dimensional systems. As DPE experiments are available for weakly and moderately correlated surfaces and bulk materials (e.g. Cu, NiO or CoO<sup>10–12</sup>), it is valuable to consider DPE for nano-sized systems that bridges the extended and atomic cases.

A possible scenario of DPE is that the photon excites one electron which senses its environment for accessible scattering channels (elastic, phononic, magnonic, etc). DPE at a fixed incident photon energy via the selection of the energy sharing and relative angles between the two escaping electrons zooms into those channels, where electron-electron (*e–e*) interaction is operational. The focus here is on *e–e* interaction mediated by charge density fluctuations in confined geometry. On the other hand, electronic correlations are at the heart of diverse fundamental phenomena such as superconductivity and plasmon formation which underlines the relevance of the information encoded in the DPE spectra. Theoretically, the treatment of two-particle correlations is a central problem in many-body physics<sup>13–16</sup>.

For the electron gas in particular, focus was put on two aspects affecting the two-particle interaction. 1) Long wave-length density fluctuations which are characterized by the presence of classical excitations (plasmons) and are well captured, for instance by the time-dependent density functional theory (TDDFT) or the random phase approximation<sup>17,18</sup>. 2) Short wave-length effects (exhibited in the on-top pair distribution function<sup>19–21</sup>) which are captured by the ladder diagrams<sup>22,23</sup>. Exploiting the tunability of synchrotron radiation, DPE (cf. Fig. 1(a)) can be tuned to an energy region where the dynamic and non-local field of collective excitations (plasmons) is the main driving for secondary electron emission whilst short-range effects govern the formation of two-particle scattering states.

<sup>1</sup>Institut für Physik, Martin-Luther-Universität Halle-Wittenberg, 06099 Halle, Germany. <sup>2</sup>CNR-ISM, Area della Ricerca di Roma 1, CP10, 00016 Monterotondo Scalo, Italy. Correspondence and requests for materials should be addressed to M.S. (email: michael.schueler@physik.uni-halle.de)

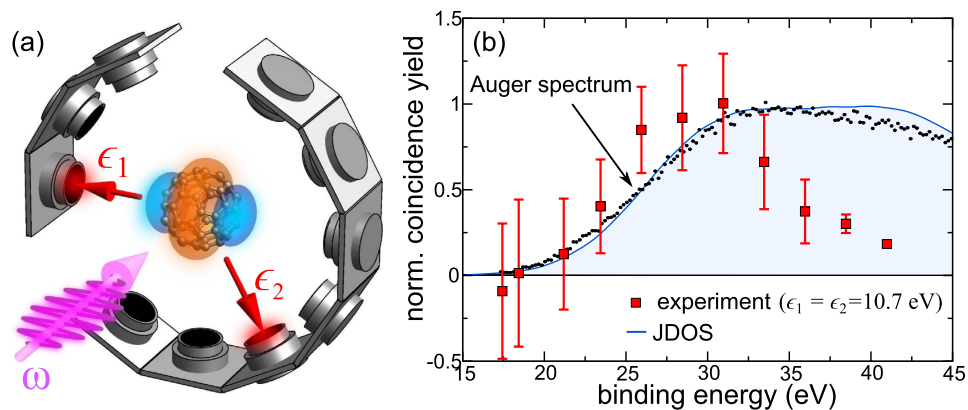


**Figure 1.** (a) DPE Setup: upon absorbing one photon with energy  $\hbar\omega$ , two correlated electrons are emitted non-sequentially from the  $C_{60}$  molecule and detected in coincidence. Charge-density fluctuations play the key role for the correlation hereby. (b) For equal energies of the emitted electrons  $\epsilon_1 = \epsilon_2 = 10.7$  eV, the normalized coincidence yield versus  $C_{60}$  binding energy (red squares with error bars) is compared to the Auger spectrum with  $\hbar\omega = 340$  eV (black dots). The latter is compared to our calculations of the joint density of states (JDOS) (shaded blue line).

A standard single photoemission (SPE) theory usually relies on the hole spectral density, which accommodates so-called *intrinsic* energy losses, and the optical matrix elements. Plasmon-mediated processes are typical for *extrinsic* losses. These refer to all scattering events which the photoelectron undergoes before detection<sup>24</sup>. Formulating a theory for SPE valid for all types of electronic systems, proved to be an involved task. The perturbation theory for the transition dipole, as employed for atoms or molecules<sup>25</sup> is in principle able to incorporate both electron-electron scattering processes and also collective effects<sup>26</sup>. One may also attempt at a direct diagrammatic expansion of the observable photocurrent, as was put forward in ref. 27. A formal theory of DPE entails the use of many-body perturbation theory (MBPT) for two-particle propagators<sup>15</sup> and is thus even more involved. Based on the direct diagrammatic approach for the observable coincidence yield<sup>28</sup> we present here the first fully *ab initio* implementation for DPE accompanied by charge density fluctuations and compare with the first experiments of this kind on  $C_{60}$ . Our approach is applicable to complex atoms such as Xe possessing strong collective resonances<sup>29</sup>, as well.

The emerging physical picture is illustrated in Fig. 2(a): (i) Photoabsorption promotes a valence electron to a high-energy state. (ii) This electron scatters inelastically from charge-density fluctuations (plasmon creation) that (iii) decay emitting a second valence electron (whose energy and angular correlations with the first one is measured in a coincidence set up, revealing so how charge-density fluctuations mediate  $e-e$  interaction). This three-step mechanism (3SM) emerges from a diagrammatic nonequilibrium Green's function (NEGF) approach as detailed in the supplementary information. It is already clear at this stage that DPE is qualitatively different from SPE in that, a) it delivers information on  $e-e$  interaction mediated by charge-density fluctuations, and b) as these plasmonic excitations are triggered by an electron a multitude of modes, e.g. volume plasmons, are involved.

## Results

In Fig. 1(b) the electron pair coincidence yield versus the binding energy  $\epsilon_B = \hbar\omega - \epsilon_1 - \epsilon_2$  of the doubly charged ion is reported and compared with the Auger spectrum. The binding energy of the latter is determined by the energy of the secondary electron and the carbon 1 s core level (see methods). The Auger process, which one might expect to be comparable to DPE when plotting as a function of the binding energy, can be interpreted in terms of the joint density of states (JDOS) as determined by the convolution of the density of occupied states of the neutral system,  $D(\epsilon)$ , and that of the ionized molecule,  $\tilde{D}(\epsilon)$ ,  $J \propto \int_{-\infty}^0 d\zeta \tilde{D}(\epsilon_B + \zeta) D(\zeta)$ . Our *ab initio* calculations in Fig. 1(b) confirm this picture (note, these same  $D(\epsilon)$  and  $\tilde{D}$  are also part of DPE and are calculated with the same code). For plasmon-mediated DPE the situation is different. As inferred from Fig. 2(a), (ii), the spectral width of the plasmon modes is a determining factor for the width of the DPE spectrum. Which mode is active (and what is its multipolar nature) is set by the momentum balance that in turn points to the momentum region of the involved plasmons. The full *ab initio* calculations of multipolar plasmons in  $C_{60}$  in ref. 30 enter as a part (i.e. steps (ii)–(iii) Fig. 2(a)) of our DPE calculations.

The electron pair coincidence yield is calculated following the derivation in the supplementary information. From Fig. 2 one infers that the non-local, frequency dependent screened electron-electron interaction  $W = v + v\chi v$  is a central quantity for DPE ( $v$  is the bare Coulomb interaction). As expected from the scheme in Fig. 2 the density-density response function  $\chi(\mathbf{r}, \mathbf{r}'; \xi)$  is also the key factor for the electron energy loss experiments<sup>31–33</sup> and also for the screening of the optical field<sup>34,35</sup> by charge-density fluctuations in SPE (in our experiment this effect is negligible because the optical frequency is higher than the relevant plasmon resonances). We write the effective  $e-e$  interaction in the form

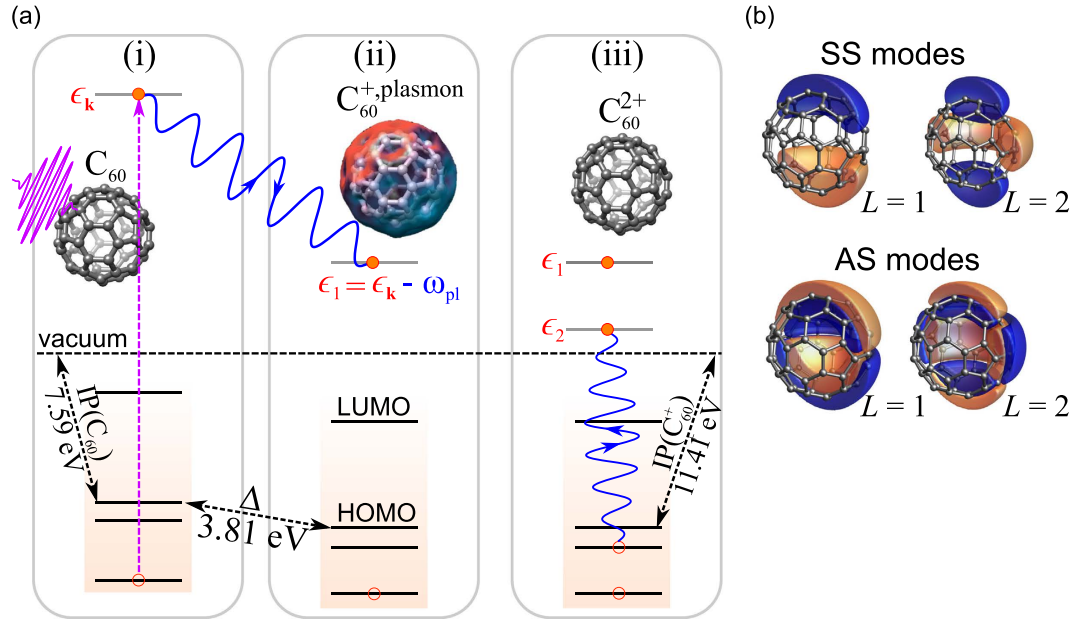


**Figure 2.** (a) Energy level scheme for DPE mediated by charge-density fluctuations in three steps: (i) A valence electron is photo-promoted to an intermediate state with energy  $\epsilon_k$ . (ii) This electron scatters inelastically from excited  $C_{60}$  to an energy state  $\epsilon_1 = \epsilon_k - \omega_{pl}$  while creating multipolar plasmonic modes with energy  $\omega_{pl}$  that (iii) decay on the attosecond time scale<sup>32</sup>, leading to the coherent emission of a second electron (energy  $\epsilon_2$ ) if  $\omega_{pl}$  is larger than the ionization potential (IP) of  $C_{60}^+$ . (b) A cut through fullerene center of the calculated fluctuation densities  $\rho_{\nu LM}(\mathbf{r})$  of the symmetric (SS) and anti-symmetric (AS) surface plasmon modes.  $L(M)$  characterizes the multipolarity (and its azimuthal behavior) and  $\nu$  is a radial quantum number (here  $M = 0$ ). Colored regions represent  $\rho_{\nu LM}(\mathbf{r}) > 5 \times 10^{-4}$  a.u. (light orange) and  $\rho_{\nu LM}(\mathbf{r}) < -5 \times 10^{-4}$  a.u. (dark blue).

$$W(\mathbf{r}, \mathbf{r}'; \xi) = W_{\lambda}^{(0)}(\mathbf{r}, \mathbf{r}') + \delta W(\mathbf{r}, \mathbf{r}'; \xi),$$

$$\delta W(\mathbf{r}, \mathbf{r}'; \xi) = \int d\mathbf{r}_1 \int d\mathbf{r}_2 v(\mathbf{r} - \mathbf{r}_1) \chi(\mathbf{r}, \mathbf{r}'; \xi) v(\mathbf{r}_2 - \mathbf{r}'). \quad (1)$$

Here,  $\xi$  denotes the frequency dependence, while  $\lambda$  represents a screening parameter discussed below. The collective modes are well characterized by the multipolarity  $L$  and a radial quantum number  $\nu$ <sup>30,36</sup>. We account for symmetric surface (SS), the anti-symmetric surface (AS) and volume (V) modes ( $L = 0$ ). The Lehmann representation of the response function is expressible as

$$\chi(\mathbf{r}, \mathbf{r}'; \xi) = \sum_{\nu=SS,AS,V} \sum_{LM} B_{\nu,L}(\xi) R_{\nu,L}(r) R_{\nu,L}(r') Y_{LM}(\hat{\mathbf{r}}) Y_{LM}^*(\hat{\mathbf{r}}'). \quad (2)$$

$Y_{LM}(\hat{\mathbf{r}})$  are the spherical harmonics.  $\rho_{\nu LM}(\mathbf{r}) = R_{\nu,L}(r) Y_{LM}(\hat{\mathbf{r}})$  are known as fluctuation densities, which can be interpreted as the spatial distribution of the density oscillation associated to a particular plasmon (Fig. 2(b)). The corresponding frequency spectrum is represented by  $B_{\nu,L}(\xi)$ . For the radial profiles  $R_{\nu,L}(r)$  and plasmon spectra  $B_{\nu,L}(\xi)$  we utilize our recent approach from ref. 30 that yielded EELS spectra in very good agreement to experiments<sup>33</sup>. The static part in eq. (1) is written as  $W_{\lambda}^{(0)}(\mathbf{r} - \mathbf{r}') = e^{-\lambda|\mathbf{r}-\mathbf{r}'|} v(\mathbf{r} - \mathbf{r}')$ . Previous calculations<sup>37</sup> provided an insight into the value of  $\lambda$ . The two-electron coincidence yield, averaged over the initial orientations of  $C_{60}$ , reads

$$J_{\epsilon_1, \epsilon_2} \propto \frac{1}{\omega} \sum_{n \in \text{occ}} \int_{-\infty}^0 d\zeta \int_0^{\infty} d\xi \delta(\xi + \epsilon_1 - \hbar\omega - \zeta) \tilde{A}_n(\epsilon_2 - \xi) \times \int_0^{\infty} dk k U_{k_2, k_1, nk}(\xi) \sigma_0(\epsilon_k, \omega) \delta(\hbar\omega + \zeta - \epsilon_k). \quad (3)$$

Here,  $\sigma_0(\epsilon_k, \omega)$  is the partial single-ionization cross section for a photoelectron with energy  $\epsilon_k$ . The momenta of the two photoelectrons are denoted by  $k_1$  and  $k_2$ . The sum over  $n$  runs over all occupied states of the singly ionized molecule and  $\tilde{A}_n(\epsilon) = \delta(\epsilon - \epsilon_n + \Delta)$  is the corresponding spectral function.  $U_{k_2, k_1, nk}(\xi) = (4\pi)^{-1/2} \int d\hat{\mathbf{k}}_1 \int d\hat{\mathbf{k}}_2 \int d\hat{\mathbf{k}} \langle |W_{\mathbf{k}_2, \mathbf{k}_1, nk}(\xi)|^2 \rangle$  is proportional to the angle-integrated and orientation-averaged (indicated by  $\langle \dots \rangle$ ) electron-impact ionization cross section<sup>25,38</sup> as calculated from the two-body matrix elements  $W_{\mathbf{k}_2, \mathbf{k}_1, nk}(\xi) = \langle \mathbf{k}_2, \mathbf{k}_1 | W(\xi) | nk \rangle$ . Inspecting eq. (3) one identifies the steps (i)–(iii) sketched in Fig. 2(a). Note, due to rearrangement of the ionic core, the energy levels of the neutral molecule ( $\epsilon_n$ ) are lowered by  $\Delta$  when



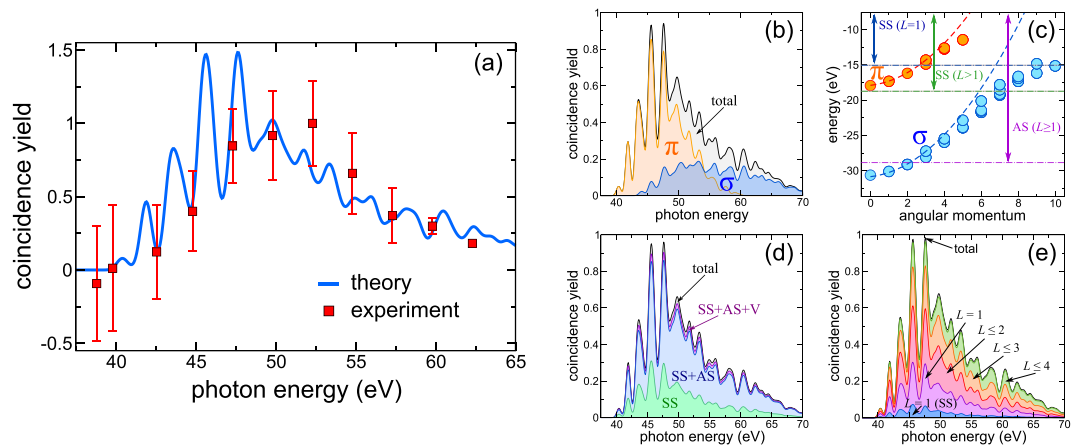


**Figure 3.** (a) Comparison of theoretical prediction of the coincidence spectrum to experimental data. Curves have been normalized to each other at one point. Gaussian broadening of the electronic states is set to  $\eta = 0.25$  eV. (b) Normalized coincidence yield resolved in emission of the second electron from  $\sigma$  and  $\pi$  states, respectively. (c) Single-particle energies of the  $C_{60}^+$  molecule as function of the dominant angular momentum. Dot-dashed lines: accessible energy range of the plasmon modes (FWHM of the plasmon spectra  $B_{\nu,L}(\xi)$ , shifted by the photoelectron energy  $\epsilon_2$ ). Thick dashed lines: ideal dispersion for non-interacting particles on a sphere with radius  $R_0 = 3.57$  Å. Coincidence yield resolved with respect to plasmon modes (d), and multipolarity (e).

removing one electron, such that the IP increases [see Fig. 2(a)]. Overall energy conservation follows from the restrictions (i)  $\epsilon_k = \hbar\omega + \zeta$ , (ii)  $\epsilon_1 = \hbar\omega + \zeta - \xi = \epsilon_k - \xi$ , and (iii)  $\epsilon_2 = \epsilon_n - \Delta + \xi$ .

The computed coincidence photocurrent for the experimental setup of  $\epsilon_1 = \epsilon_2 = 10.7$  eV is presented in Fig. 3(a) along with the data from the experiment. The equal energy-sharing case has been chosen by the experience on atoms, where this represents the case where the effects of the correlation and symmetry play a dominant role. Further tests (see supplementary information) show that, in contrast to the Auger process [Fig. 1(b)], all ingredients of Eq. (3) (and hence all steps in Fig. 2) are essential: matrix elements encoded in  $\sigma_0(\epsilon_k, \omega)$ , plasmon dispersions  $B_{\nu,L}(\xi)$ , radial profiles of the fluctuations densities  $R_{\nu,L}(r)$ , and density of states  $\tilde{A}_n(\epsilon)$ . Hence, DPE in the present case adds new aspects to DPE from, e.g., atomic targets, and is a useful sensor for the  $e-e$  interaction mediated by charge-density fluctuations.

## Discussion

The mechanism behind the narrowing of the DPE as compared to the Auger spectrum [Fig. 1(b)] can be unraveled by analyzing the electronic structure and the individual plasmon modes as they contribute to DPE [Fig. 3(b–e)]. Resolving the DPE yield with respect to either  $\sigma$  or  $\pi$  orbitals<sup>39</sup> [Fig. 3(b)] one realizes that the emission from the  $\sigma$  band [Fig. 3(c)], which is mainly responsible for the DPE signal at photon energies  $\hbar\omega \gtrsim 55$  eV, is suppressed by the energy selectivity of the plasmon excitation. In particular, the plasmon giving rise to the emission of the second electron at stage (iii) needs to provide sufficient energy to promote a certain initial state of the  $C_{60}^+$  molecule [Fig. 3(c)] to the continuum. Hence, the limited spectral width of the SS plasmon modes suppresses the emission from deeper  $\sigma$  states [Fig. 3(b)]. A test calculation replacing the plasmon spectra  $B_{\nu,L}(\xi)$  by a constant produced a significantly broader DPE spectrum. This confirms the picture outlined above.

Our theory permits also to selectively include different plasmonic modes in the calculation. It is known that plasmon excitation upon photoabsorption obeys optical dipole selection rules and allows for exciting the SS plasmon with  $L = 1$  only (the dipolar resonance mostly addressed in the literature and manifested e.g. in plasmon-assisted SPE<sup>40</sup>). On the contrary, the electron scattering (as in EELS) transfers a finite momentum meaning that SS and AS plasmons with any multipolarity can be excited<sup>30,33,36</sup>. In agreement with this Fig. 3(d) underpins the significant contribution of the AS plasmons and thus substantiates the physical picture of the 3SM, according to which the step ii) can be regarded as an inelastic electron scattering event that is inherent to the plasmon-assisted DPE process. Similarly, SS dipolar plasmon transitions play only a minor role, while the multipolar plasmons are responsible to a large extent for the coincidence yield [Fig. 3(e)]. All these facets endorse that DPE mediated by charge-density fluctuations as the predominant channel for  $e-e$  correlations represents a new facet to the information what is extractable from SPE and Auger spectra.

To summarize, an *ab initio* scheme for this process has been implemented with results in line with the first DPE experiment resolved with respect to the electron pair energies. We identified the dominant pathway as the following: a valence electron absorbs the photon and rescatters inelastically from *multipolar* collective modes that mediate the coherent emission of a second electron. The dwell time for this quasi-resonant scattering may be accessed by attosecond time-delay experiments<sup>41</sup>. For plasmon-assisted DPE the average electronic density plays a decisive role. For metals the plasmonic energies (which can be estimated using a classical expression  $\omega_{pl} = \sqrt{3e^2/m_e r_s^3}$  with  $r_s$  being the Wigner-Seitz radius) are too low for plasmons to lead to a direct electron emission, although these modes may likely contribute to the loss channel for DPE. In contrast, for confined systems such as Carbon-based fullerenes the density is much higher ( $r_s \approx 1.0$  a<sub>B</sub>) resulting in plasmonic peaks in the XUV range. Thus,

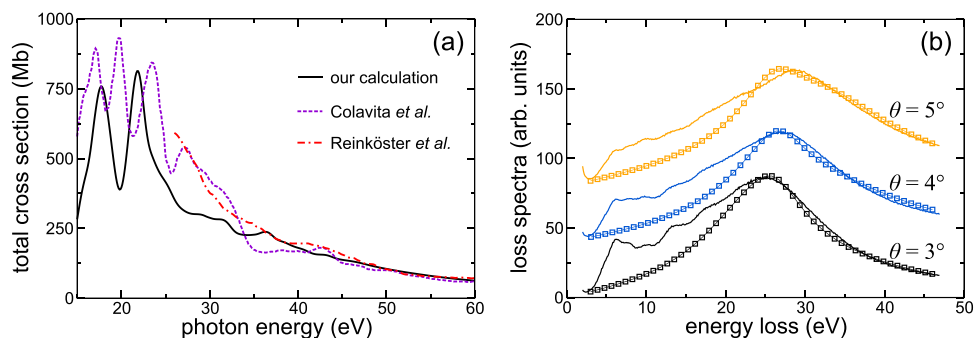


**Figure 4.** (a) Comparison of our calculation of the total SPE cross section with the calculations from Colavita *et al.*<sup>50</sup> and the experiment from Reinköster *et al.*<sup>51</sup> on the absolute scale. (b) EELS spectra computed with our model response function eq. (2) (symbols) compared to experimental data<sup>33</sup> (solid lines) for different scattering angles  $\theta$ . The prefactor between theory and experiment was fixed for  $\theta = 3^\circ$  and kept constant for  $\theta = 4^\circ$  and  $\theta = 5^\circ$ .

energy- and angle resolved DPE experiments open the opportunity to explore different regimes of electronic correlation, including Coulombic scattering, local field effects and dynamical screening.

## Methods

**Experiment.** The experiments have been performed using the multi-coincidence end station<sup>42</sup> of the Gas Phase Photoemission beam line<sup>43</sup> at Elettra, where fully linearly polarized radiation in the photon energy range 13–1000 eV is available. The vacuum chamber hosts two independent turntables, holding respectively three and seven electrostatic hemispherical analyzers at  $30^\circ$  with respect to each other (Fig. 1(a)). The three spectrometers of the smaller turntable, are mounted at  $0^\circ$ ,  $30^\circ$ , and  $60^\circ$  with respect to the polarization vector of the light in the plane perpendicular to the propagation direction of the radiation. The larger turntable rotates in the same plane and its seven analyzers can be used to measure the angular distribution of the correlated electrons. The ten analyzers have been set to detect electrons of kinetic energy  $\epsilon_1 = \epsilon_2 = 10.7$  eV. The energy resolution and the angular acceptance were  $\Delta\epsilon = 300$  meV and  $\Delta\theta_{1,2} = \pm 3^\circ$ , respectively. The photon energy resolution was about 150 meV. At variance with previous works<sup>44–46</sup> where the di-cation yield was measured versus photon energy, here the energy spectrum of the  $C_{60}$  di-cation states is reconstructed by detection of photoelectron-photoelectron pairs in coincidence as the photon energy is scanned. In order to improve the statistical accuracy of the experimental results, the coincidence signals were added up, after a careful energy calibration of the non-coincidence spectra independently collected by the ten analyzers. The  $C_{60}$  source is collinear with the photon beam<sup>47</sup>, which passes through the hollow core of the source before interacting with the molecular beam and ending up on the photodiode. Six apertures drilled into the closure piece of the crucible and pointing to the interaction region increase the molecule density therein.

In the Auger measurements the photon energy was fixed at  $\hbar\omega = 340$  eV and Auger electrons with kinetic energy  $\epsilon_{\text{Auger}} = \epsilon_{\text{C1s}} - \epsilon_{\text{B}}$ , where  $\epsilon_{\text{C1s}}$  is the binding energy of the carbon 1s core state and  $\epsilon_{\text{B}}$  stands for the binding energy in Fig. 1(b) ranging from 15 to 45 eV, were measured.

**Theory.** Equation (3) is derived from the diagrammatic approach to photoemission<sup>28</sup> based on the nonequilibrium Green's function formalism. The full derivation is presented in the supplementary information. For an *ab initio* implementation of eq. (3) we rely on density functional theory (DFT) to compute the Kohn-Sham (KS) bound orbitals and their energies  $\epsilon_n$ . We used the local density approximation (LDA) with self-interaction corrections. They improve the asymptotic behavior of the KS potential that is utilized to compute scattering states. The IPs and the core rearrangement shift  $\Delta$  enter as experimentally determined<sup>44,48</sup>. The SPE cross section  $\sigma_0(\epsilon_{\mathbf{k}}, \omega)$  is computed by the driven-scattering approach<sup>49</sup>, yielding excellent agreement with literature data<sup>50,51</sup> in the relevant energy range [Fig. 4(a)] of  $\hbar\omega \gtrsim 40$  eV. Note that incorporating many-body effects is not required here (as they mainly influence the cross section around the plasmon resonances). The multipolar plasmon modes entering eq. (2) needed for computing the effective interaction (1) is parameterized according to previous calculations<sup>30</sup> and tested against EELS measurements in Fig. 4(b). Describing the Auger spectrum in Fig. 1(b) simply by the JDOS, thus neglecting plasmonic and other correlation effects, is justified by the large kinetic energy of the Auger electron, ruling out matrix-element effects in the considered energy window. Particularly, dynamical screening effects are strongly suppressed for a swift Auger electron due to the momentum-dependence of the density-density response function.

The accurate description of these central ingredients for describing DPE endorses the predictive power of the current theory. Full details on the calculations is provided by the supplementary information.

## References

- Hüfner, S. *Photoelectron Spectroscopy: Principles and Applications* (Springer Science & Business Media, 2003).
- Briggs, J. S. & Schmidt, V. Differential cross sections for photo-double-ionization of the helium atom. *J. Phys. B* **33**, R1 (2000).
- Knapp, A. *et al.* Mechanisms of Photo Double Ionization of Helium by 530 eV Photons. *Phys. Rev. Lett.* **89**, 033004 (2002).
- Berakdar, J. & Kirschner, J. *Correlation Spectroscopy of Surfaces, Thin Films, and Nanostructures* (John Wiley & Sons, 2006).

5. Schattke, W. & Hove, M. A. V. *Solid-State Photoemission and Related Methods: Theory and Experiment* (John Wiley & Sons, 2008).
6. Ullrich, J. & Shevelko, V. *Many-Particle Quantum Dynamics in Atomic and Molecular Fragmentation* (Springer Science & Business Media, 2013).
7. Avaldi, L. & Huetz, A. Photodouble ionization and the dynamics of electron pairs in the continuum. *J. Phys. B* **38**, S861 (2005).
8. Efros, A. L. & Pollak, M. *Electron-Electron Interactions in Disordered Systems* (Elsevier, 2012).
9. Gogolin, A. O., Nersesyan, A. A. & Tselik, A. M. *Bosonization and Strongly Correlated Systems* (Cambridge University Press, 2004).
10. Herrmann, R., Samarin, S., Schwabe, H. & Kirschner, J. Two Electron Photoemission in Solids. *Phys. Rev. Lett.* **81**, 2148–2151 (1998).
11. Schumann, F. O., Winkler, C., Kerhervé, G. & Kirschner, J. Mapping the electron correlation in two-electron photoemission. *Phys. Rev. B* **73**, 041404 (2006).
12. Schumann, F. O., Behnke, L., Li, C. H. & Kirschner, J. Exploring highly correlated materials via electron pair emission: the case of NiO/Ag(100). *Journal of Physics: Condensed Matter* **25**, 094002 (2013).
13. Mahan, G. D. *Many-Particle Physics* (Springer Science & Business Media, 2000).
14. Giuliani, G. & Vignale, G. *Quantum Theory of the Electron Liquid* (Cambridge University Press, 2005).
15. Dickhoff, W. H. & Neck, D. V. *Many-body Theory Exposed!: Propagator Description of Quantum Mechanics in Many-body Systems* (World Scientific, 2008).
16. Abrikosov, A. A., Gorkov, L. P. & Dzyaloshinski, I. E. *Methods of Quantum Field Theory in Statistical Physics* (Courier Corporation, 2012).
17. Pines, D. & Bohm, D. A collective description of electron interactions: II. Collective vs individual particle aspects of the interactions. *Phys. Rev.* **85**, 338 (1952).
18. Strinati, G. Application of the Green's functions method to the study of the optical properties of semiconductors. *Riv. Nuovo Cimento* **11**, 1–86 (1988).
19. Niklasson, G. Dielectric function of the uniform electron gas for large frequencies or wave vectors. *Phys. Rev. B* **10**, 3052–3061 (1974).
20. Gori-Giorgi, P. & Perdew, J. P. Short-range correlation in the uniform electron gas: Extended Overhauser model. *Phys. Rev. B* **64**, 155102 (2001).
21. Qian, Z. On-top pair-correlation function in the homogeneous electron liquid. *Phys. Rev. B* **73**, 035106 (2006).
22. Nagano, S., Singwi, K. S. & Ohnishi, S. Correlations in a two-dimensional quantum electron gas: The ladder approximation. *Phys. Rev. B* **29**, 1209–1213 (1984).
23. Nechaev, I. A. & Chulkov, E. V. Variational solution of the  $T$ -matrix integral equation. *Phys. Rev. B* **71**, 115104 (2005).
24. Berglund, C. N. & Spicer, W. E. Photoemission studies of copper and silver: theory. *Phys. Rev.* **136**, A1030 (1964).
25. Amusia, M. Y. *Atomic Photoeffect* (Springer Science & Business Media, 2013).
26. Amusia, M. Y. Collective Effects in Photoionization of Atoms. In Bederson, D. B. a. B. (ed.) *Advances in Atomic and Molecular Physics*, vol. 17, 1–54 (Academic Press, 1982).
27. Caroli, C., Lederer-Rozenblatt, D., Roulet, B. & Saint-James, D. Inelastic Effects in Photoemission: Microscopic Formulation and Qualitative Discussion. *Phys. Rev. B* **8**, 4552–4569 (1973).
28. Pavlyukh, Y., Schüler, M. & Berakdar, J. Single-or double-electron emission within the Keldysh nonequilibrium Green's function and Feshbach projection operator techniques. *Phys. Rev. B* **91**, 155116 (2015).
29. Shiner, A. D. *et al.* Probing collective multi-electron dynamics in xenon with high-harmonic spectroscopy. *Nature Phys.* **7**, 464–467 (2011).
30. Schüler, M., Berakdar, J. & Pavlyukh, Y. Disentangling multipole contributions to collective excitations in fullerenes. *Phys. Rev. A* **92**, 021403 (2015).
31. Sohmen, E., Fink, J. & Krätschmer, W. Electron energy-loss spectroscopy studies on  $C_{60}$  and  $C_{70}$  fullerite. *Z. Phys. B: Condens. Matter* **86**, 87–92 (1992).
32. Burose, A. W., Dresch, T. & Ding, A. M. G. Electron energy loss spectroscopy of free  $C_{60}$  and  $C_{70}$ . *Z. Phys. D: At. Mol. Clusters* **26**, 294–296 (1993).
33. Bolognesi, P. *et al.* Collective excitations in the electron energy loss spectra of  $C_{60}$ . *Eur. Phys. J. D* **66**, 254 (2012).
34. Almladh, C.-O. Importance of vertex corrections for obtaining correct selection rules in the theory of photoemission. *Phys. Rev. B* **34**, 3798 (1986).
35. Hertel, I. V. *et al.* Giant plasmon excitation in free  $C_{60}$  and  $C_{70}$  molecules studied by photoionization. *Phys. Rev. Lett.* **68**, 784–787 (1992).
36. Verkhovtsev, A., Korol, A. V. & Solov'yov, A. V. Formalism of collective electron excitations in fullerenes. *Eur. Phys. J. D* **66** (2012).
37. Kidun, O. & Berakdar, J. Manifestation of Charge-Density Fluctuations in Metal Clusters: Suppression of the Ionization Channel. *Phys. Rev. Lett.* **87**, 263401 (2001).
38. Drake, G. W. F. *Springer Handbook of Atomic, Molecular, and Optical Physics* (Springer, 2006).
39. Pavlyukh, Y. & Berakdar, J. Angular electronic 'band structure' of molecules. *Chem. Phys. Lett.* **468**, 313–318 (2009).
40. Barillot, T. *et al.* Angular asymmetry and attosecond time delay from the giant plasmon resonance in  $C_{60}$  photoionization. *Phys. Rev. A* **91**, 033413 (2015).
41. Bergues, B. *et al.* Attosecond tracing of correlated electron-emission in non-sequential double ionization. *Nature Communications* **3**, 813 (2012).
42. Bolognesi, P. *et al.* Photodouble ionization beyond the helium case. *J. Electron. Spectrosc. Relat. Phenom.* **141**, 105–119 (2004).
43. Blyth, R. R. *et al.* The high resolution Gas Phase Photoemission beamline, Elettra. *J. Electron. Spectrosc. Relat. Phenom.* **101–103**, 959–964 (1999).
44. Steger, H., de Vries, J., Kamke, B., Kamke, W. & Drewello, T. Direct double ionization of  $C_{60}$  and  $C_{70}$  fullerenes using synchrotron radiation. *Chem. Phys. Lett.* **194**, 452–456 (1992).
45. Hillebrecht, F. U., Morozov, A. & Kirschner, J. Direct observation of electronic correlation in  $C_{60}$  by double photoemission. *Phys. Rev. B* **71**, 125406 (2005).
46. Juranić, P. N., Lukić, D., Barger, K. & Wehlitz, R. Multiple photoionization and fragmentation of  $C_{60}$  in the 18–280-eV range. *Phys. Rev. A* **73**, 042701 (2006).
47. Sokell, E. *et al.* Signature of Two-Electron Interference in Angular Resolved Double Photoionization of Mg. *Phys. Rev. Lett.* **110**, 083001 (2013).
48. Steger, H., Holzapfel, J., Hielscher, A., Kamke, W. & Hertel, I. V. Single-photon ionization of higher fullerenes  $C_{76}$ ,  $C_{78}$  and  $C_{84}$ . Determination of ionization potentials. *Chem. Phys. Lett.* **234**, 455–459 (1995).
49. Schüler, M., Pavlyukh, Y. & Berakdar, J. Nuclear-wave-packet dynamics mapped out by two-center interference in the  $HeH^{2+}$  molecule. *Phys. Rev. A* **89**, 063421 (2014).
50. Colavita, P., De Altì, G., Fronzoni, G., Stener, M. & Decleva, P. Theoretical study of the valence and core photoemission spectra of  $C_{60}$ . *Phys. Chem. Chem. Phys.* **3**, 4481–4487 (2001).
51. Reinköster, A. *et al.* The photoionization and fragmentation of  $C_{60}$  in the energy range 26–130 eV. *J. Phys. B* **37**, 2135 (2004).
52. Moskalenko, A. S., Pavlyukh, Y. & Berakdar, J. Attosecond tracking of light absorption and refraction in fullerenes. *Phys. Rev. A* **86**, 013202 (2012).

### Acknowledgements

This work is supported by the German Research Foundation (DFG) Collaborative Research Centre SFB 762 Functionality of Oxide Interfaces (J. B. and Y. P.) and Grant Number PA 1698/1-1 (Y. P.). M.S. acknowledge funding of his position via PA 1698/1-1.

### Author Contributions

P.B. and L.A. performed the experiment. M.S. and Y.P. carried out the calculations. The main text was written by M.S. and Y.P. and edited by J.B. All authors contributed to reviewing and commenting the text.

### Additional Information

**Supplementary information** accompanies this paper at <http://www.nature.com/srep>

**Competing financial interests:** The authors declare no competing financial interests.

**How to cite this article:** Schüler, M. *et al.* Electron pair escape from fullerene cage via collective modes. *Sci. Rep.* **6**, 24396; doi: 10.1038/srep24396 (2016).



This work is licensed under a Creative Commons Attribution 4.0 International License. The images or other third party material in this article are included in the article's Creative Commons license, unless indicated otherwise in the credit line; if the material is not included under the Creative Commons license, users will need to obtain permission from the license holder to reproduce the material. To view a copy of this license, visit <http://creativecommons.org/licenses/by/4.0/>

## 5.5 E6: Femtosecond dynamics of correlated many-body states in $C_{60}$ fullerenes

Ideally, gas-phase experiments are carried out at low temperatures to focus on the electronic properties and minimize the influence of the molecular vibrations. Having said that, spectroscopy from "hot" molecules allows investigating other important effects such as the vibrationally-induced electronic transitions or the decay of electronic excitations. A prominent example where the dissipation of energy from the electronic degrees of freedom is of great importance is the DNA molecule. It is the energy of an absorbed UV photon which needs to be efficiently dissipated [217]. Otherwise, radicals might form, damaging the DNA. In view of using fullerene derivatives as building blocks for solid-state chemistry, it is known that the standard zero-temperature BO approach does not capture essential phenomena and is thus not sufficient to predict the functionality [218].

Our work [E6] combines theory and experiment to elucidate the energy dissipation within the  $C_{60}$  molecule on the femtosecond time scale. The transient pump-probe scheme explained in subsec. 3.2.3 according to the sketch in fig. 3.4(a) is adopted: gas-phase  $C_{60}$  molecules are exposed to a laser pulse as short as 50 fs with variable wavelength, driving the transition to optically accessible excited states below the ionization threshold. After a time delay  $\tau$ , a second pulse is used to ionize the molecule. The detection is achieved by time-resolved TOF mass spectrometers, evidencing the production of  $C_{60}^+$  ions. While the dependence on the central frequency of the laser pulses maps the optically active electronic states (bright states), scanning over  $\tau$  delivers information on their decay dynamics. The initial stage can be identified as electron- interaction effects, whereas the relaxation extending over  $\sim 1$  ps is due to non-adiabatic vibrational coupling.

A theoretical description of the electron-vibron interaction for such large systems is a challenge. Hence, we resort to the harmonic approximation to the BO PESs (see subsec. 2.3.1), which are computed by DFT. The resulting electron-vibron coupling is assumed to be linear. To keep track of the electron-electron interaction – which was found to be essential to obtain photoabsorption spectra [219] – the electronic degrees of freedom are described in the many-body picture. As a useful tool to approximate the relevant many-body states, the Casida method (see subsec. 2.6.3) is employed. With these ingredients, an EB-type model is constructed. Since the considerable energy of about 5 eV is stored in the molecular vibrations (due to temperatures of  $\sim 770$  K in the experiment) and yet the inefficient energy transfer between electrons and vibrations, the latter is treated as heat bath for the electronic degrees of freedom. The quantum dynamics of the electronic excitations and relaxation is then treated on the level of the Lindblad master equation for the density matrix (see appendix D). This approach – based on the Markovian approximation – is considerably simpler than solving the KBEs (see subsec. 2.5.6 and chapter 6), for memory effects are neglected. This is justified by the high temperature of the vibronic bath.

Our findings for the electronic decay are in line with the experimental observations, confirming the physical picture outlined above. Furthermore, we present the first theoretical description of the vibrationally-induced population of the SAMOs. This is an important point since the dipole transition matrix element of the SAMOs with respect to the ground state vanishes. Optical spectroscopy of these special states is so only possible via an indirect population mechanism. Thus, our results are an important contribution to the interpretation of recent experiments on the SAMOs [206, 220].



## PAPER

Femtosecond dynamics of correlated many-body states in C<sub>60</sub> fullerenes

## OPEN ACCESS

## RECEIVED

5 October 2016

## ACCEPTED FOR PUBLICATION

3 November 2016

## PUBLISHED

29 November 2016

Original content from this work may be used under the terms of the [Creative Commons Attribution 3.0 licence](#).

Any further distribution of this work must maintain attribution to the author(s) and the title of the work, journal citation and DOI.



Sergey Usenko<sup>1</sup>, Michael Schüler<sup>2</sup>, Armin Azima<sup>3,4,5</sup>, Markus Jakob<sup>1,5</sup>, Leslie L Lazzarino<sup>3</sup>, Yaroslav Pavlyukh<sup>2,6</sup>, Andreas Przystawik<sup>1</sup>, Markus Drescher<sup>3,4,5</sup>, Tim Laarmann<sup>1,5,7</sup> and Jamal Berakdar<sup>2,7</sup>

<sup>1</sup> Deutsches Elektronen-Synchrotron DESY, D-22607 Hamburg, Germany

<sup>2</sup> Institut für Physik, Martin-Luther-Universität Halle-Wittenberg, D-06099 Halle, Germany

<sup>3</sup> Department of Physics, University of Hamburg, D-22761 Hamburg, Germany

<sup>4</sup> Center for Free-Electron Laser Science CFEL, DESY, D-22607 Hamburg, Germany

<sup>5</sup> The Hamburg Centre for Ultrafast Imaging CUI, D-22761 Hamburg, Germany

<sup>6</sup> Department of Physics and Research Center OPTIMAS, University of Kaiserslautern, D-67653 Kaiserslautern, Germany

<sup>7</sup> Authors to whom any correspondence should be addressed.

E-mail: [tim.laarmann@desy.de](mailto:tim.laarmann@desy.de) and [jamal.berakdar@physik.uni-halle.de](mailto:jamal.berakdar@physik.uni-halle.de)

**Keywords:** fullerene, ionization dynamics, superatom molecular orbitals, TDDFT

## Abstract

Fullerene complexes may play a key role in the design of future molecular electronics and nanostructured devices with potential applications in light harvesting using organic solar cells. Charge and energy flow in these systems is mediated by many-body effects. We studied the structure and dynamics of laser-induced multi-electron excitations in isolated C<sub>60</sub> by two-photon photoionization as a function of excitation wavelength using a tunable fs UV laser and developed a corresponding theoretical framework on the basis of *ab initio* calculations. The measured resonance line width gives direct information on the excited state lifetime. From the spectral deconvolution we derive a lower limit for purely electronic relaxation on the order of  $\tau_{el} = 10_{-3}^{+5}$  fs. Energy dissipation towards nuclear degrees of freedom is studied with time-resolved techniques. The evaluation of the nonlinear autocorrelation trace gives a characteristic time constant of  $\tau_{vib} = 400 \pm 100$  fs for the exponential decay. In line with the experiment, the observed transient dynamics is explained theoretically by nonadiabatic (vibronic) couplings involving the correlated electronic, the nuclear degrees of freedom (accounting for the Herzberg–Teller coupling), and their interplay.

## 1. Introduction

Molecular junctions, molecular transistors and organic solar cells rely on charge transport channels with negligible energy dissipation during the carriers propagation time. In nanostructured materials and molecular complexes the characteristic timescale is determined by the long-range polarization interaction and by the formation and breaking of chemical bonds mediated by the electronic and nuclear motion. Transient structures and dynamics on the femto and sub-femtosecond timescale is the focus of ultrafast spectroscopy. Time-resolved experiments using femtosecond (fs) laser pulses unravel the dynamic response of promising materials that could serve for instance as molecular building blocks for organic photovoltaics. Polymer solar cells are commonly composed of a photoactive film of a conjugated polymer donor and a fullerene derivative acceptor [1–3], which makes use of the fullerenes' unique ability to form stable C<sub>60</sub><sup>−</sup> anions. Electron correlation plays an important role in the formation of four bound states of the fullerene anion [4–6]. In fact, electronic correlations are responsible for the binding of the 2A<sub>g</sub> state, whereas the bindings of the states 2T<sub>1u</sub>, 2T<sub>2u</sub> and 2T<sub>1g</sub> are less affected by electronic correlations (cf [4] and further references therein).

With its special structure consisting of 174 nuclear degrees of freedom, 60 essentially equivalent delocalized  $\pi$  electrons, and 180 structure-defining localized  $\sigma$  electrons, neutral C<sub>60</sub> serves as a large—but still finite—molecular system with many electronic and nuclear degrees of freedom. Because of the large charge conjugation, its finite 'energy gap', and quantum confinement of electronic states, C<sub>60</sub> may be viewed as an

interesting intermediate case between a molecule and a condensed matter system. In fact, applying solid-state concepts to the valence ‘Bloch electrons’ on the  $C_{60}$  sphere results in an ‘angular band structure’ [7] from which other relevant quantities (such as plasma frequencies and group velocities) can be extracted. Photophysical studies of fullerenes using fs laser fields cover the whole range from atomic through molecular to solid state physics [8–10]. The molecular response is truly a multi-scale phenomenon. It ranges from attosecond dynamics in electronic excitation and ionization to statistical physics describing thermalization processes. So, light-induced processes in fullerenes cover more than 15 orders of magnitude in time [11].

Using low-temperature scanning tunneling microscopy (LT-STM) of  $C_{60}$  molecules deposited on copper surfaces Feng *et al* observed tunneling through electronic states that possess nearly atom-like character [12]. These ‘superatom’ molecular orbitals (SAMOs), also discussed below, have a well-defined symmetry and can be characterized by the nodal structure (principle quantum numbers)  $n$  and angular momentum quantum numbers  $L$  [13]. In addition, these virtual states show a remarkable stability [14], i.e., their initial stage of decay proceeds substantially slower than other states (even LUMO or HOMO) which qualifies them as robust channel for hot electron transport. From a molecular physics point of view, SAMOs can be regarded as low-lying, mixed valence Rydberg states [15] that exhibit substantial electron density inside the hollow sphere. They form chemical bonds affected by hybridization when the system is excited optically or probed with STM in deposited nanostructures. The resulting free-electron bands in self-assembled one-dimensional wires or two-dimensional quantum wells are holding great promise for unique applications in molecular electronics [16], but also for new functionalities such as current carrying states and hence nanometer-sized magnetic field generators [17]. We note in passing that recently SAMO states have also been observed in planar, non-fullerene materials [18, 19], as well as in isolated  $C_{60}$  fullerenes [20–22], where they are energetically located below the known high-lying Rydberg states [23, 24].

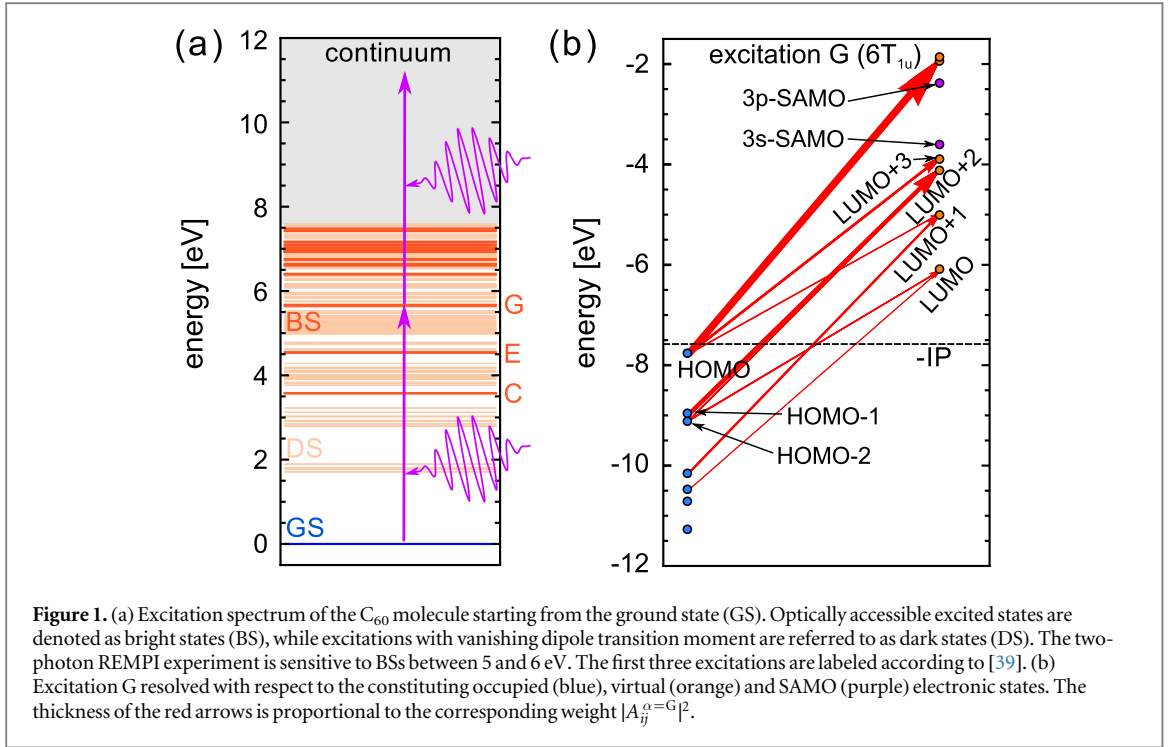
It is of fundamental importance for designing fullerene derivatives as building blocks for solid state chemistry to go beyond the characterization of *static* many-body electronic structure [25]. In particular for optimization and control of the charge flow and energy dissipation, rigorous *dynamic* studies on the fs time scale using ultrafast lasers are indispensable but, still in their infancy [26, 27]. Additionally, time-dependent density-functional theory (TDDFT) calculations of the absorption and photoelectron spectra, accounting for full structural analysis, were performed [28, 29] and constitute the basis for the further development presented below.

Accessing energy dissipation upon the excitation of correlated many-body states in gas phase  $C_{60}$  became feasible recently which allows to connect the coherent quantum [28, 30], classical and statistical mechanisms [31]. It is known from experiments with optical lasers that electron thermalization mediated by inelastic electron–electron collisions takes place on a time scale of 50–100 fs (see [11] and references therein). This is where the present experimental and theoretical work comes into play. Here, the objective is to reduce the complexity of laser-induced multi-photon processes by populating highly-excited many-body states in a resonant one-photon transition in the ultraviolet (UV) spectral range at low laser peak intensity on the order of  $3.5 \times 10^{10} \text{ W cm}^{-2}$ . This allows for a rather detailed probing of the correlated electron dynamics in highly excited states. The study is based on a resonance-enhanced multi-photon ionization (REMPI) scheme, i.e., two-photon photoemission (2PPE) spectroscopy as depicted in figure 1(a). The photoionization yield recorded for resonant excitation is enhanced as compared to an experiment performed in the off-resonance regime. Thereby, we trace the time-dependent electronic structure of intermediate states, which are free from any perturbation caused by metallic substrates affecting the energetics in LT-STM experiments. Furthermore, REMPI on gas phase fullerenes provides information on the neutral molecule whereas 2PPE and LT-STM essentially probe the binding energy and DOS of an anion deposited on a metal surface. Our experiments are compared to *ab initio* calculations.

This paper is organized as follows. In section 2 many-body states below the  $C_{60}$  ionization threshold are calculated as a guideline for the 2PPE experiments. Section 3 describes some experimental details with a focus on the tunable fs laser system in the UV spectral range used for the time-resolved studies. Excitation energy dependent mass spectra are evaluated in section 4.1 and discussed in terms of resonance-enhanced ionization and excited state lifetimes. Section 4.2 concentrates on the time-resolved experiments. A detailed theoretical analysis of the experimental data is given in section 5 followed by a short summary and outlook. In appendix A we provide details on how the electron–vibron coupling matrix elements were computed and the master equation in Lindblad form is derived in appendix B.

## 2. Optical excitations

The first step of a REMPI or 2PPE experiment entails the calculation of excited states, which are typically more difficult to describe than ground-state properties. Often exact diagonalization (full configuration interaction) is



not feasible for large systems in which case one may resort to only a few methods: TDDFT [32], equation-of-motion (EOM) quantum chemistry methods [33], and many-body perturbation theory based on a Green's function formulation [34]. For its reduced computational cost as compared to the other methods, we have employed the linear-response TDDFT approach (Casida's method) [35].

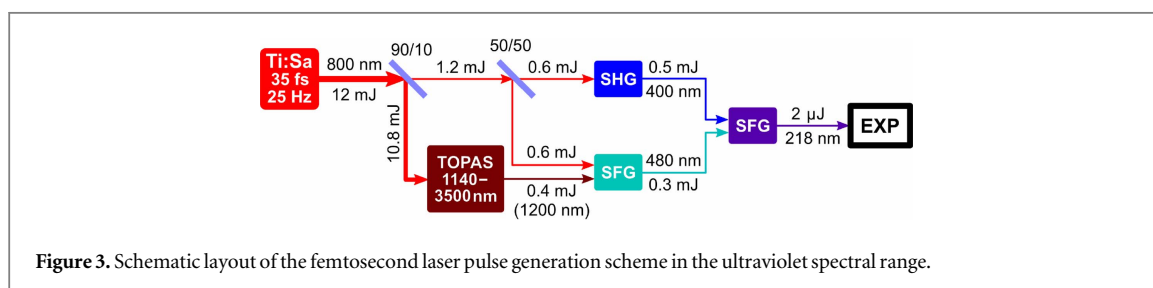
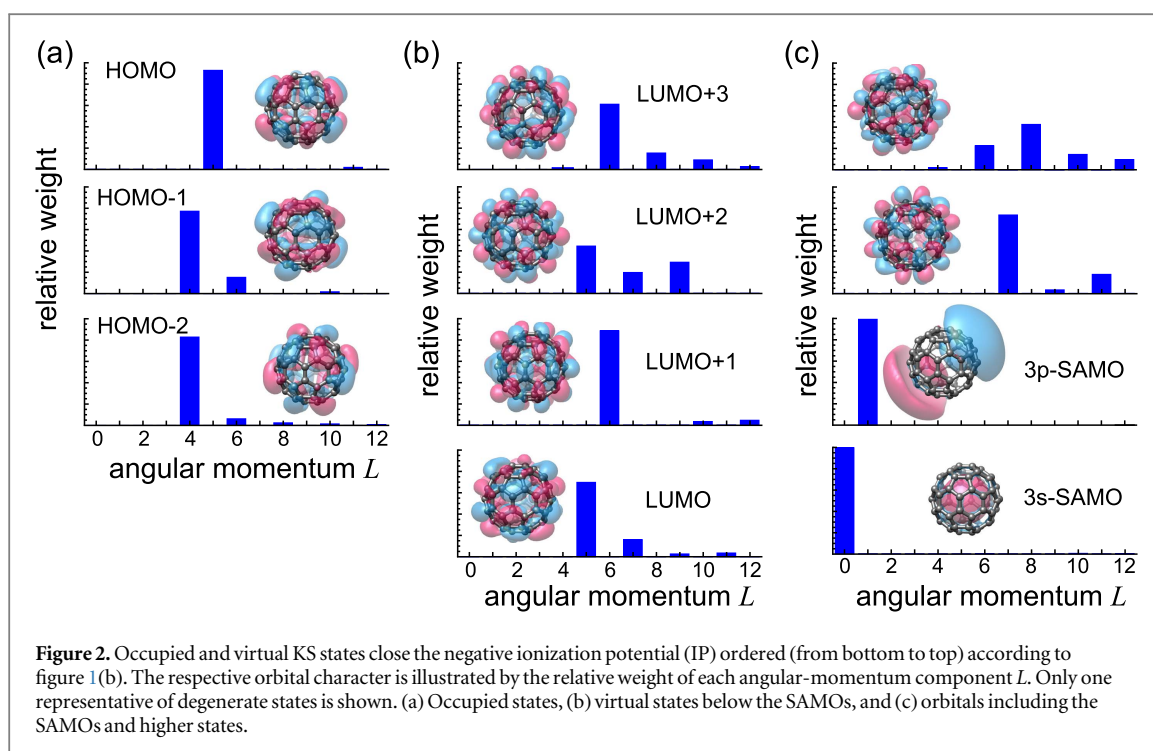
As a first step we calculated the Kohn–Sham (KS) orbitals using the OCTOPUS package [36] with a modified version of the asymptotically corrected functional by Leeuwen and Baerends [37], which was shown to considerably improve excited-state properties [38]. In order to account for a multitude of highly-excited states, we have chosen a relatively large box to which all KS states  $\phi_i(\mathbf{r})$  are confined (a sphere with a radius of 12 Å with uniform grid spacing of 0.15 Å). This ensures that higher virtual orbitals (including the SAMOs) are well represented. After converging the ground-state and computing a sufficient number of virtual orbitals, we computed the singly-excited (i.e., single particle-hole excitations) many-body excitations by Casida's method. Formally this procedure amounts to approximating the excited many-body states  $|\Phi_\alpha\rangle$  by

$$|\Phi_\alpha\rangle = \sum_{i \in \text{occ}} \sum_{j \in \text{virt}} A_{ij}^\alpha \hat{c}_j^\dagger \hat{c}_i |\Phi_0\rangle, \quad (1)$$

where  $|\Phi_0\rangle$  denotes the determinant built by the ground-state KS orbitals and  $\hat{c}_i$  ( $\hat{c}_i^\dagger$ ) is the annihilation (creation) operator with respect to the KS basis. The particle-hole amplitudes  $A_{ij}^\alpha$  are determined by Casida's equation based on linear response. The major approximation hereby is related to the exchange-correlation (xc) kernel  $f_{xc}(\mathbf{r}, \mathbf{r}'; \omega)$ , defined as the functional derivative of the KS potential with respect to the density. We use the local-density approximation for the xc kernel, as it is local and (within adiabatic TDDFT) frequency-independent. Casida's equation is thus transformed into an eigenvalue problem. We computed the Casida vectors  $A_{ij}^\alpha$  with OCTOPUS, taking 75 occupied and 60 virtual orbitals into account, yielding well-converged results for excitation energies up to 10 eV. For testing purposes we also computed the binding energies of the virtual orbitals analogously to [21]. We obtained very similar results for the low-lying states relevant for the present experiments.

The energies of the obtained many-body excitations are shown in figure 1(a), where we distinguish the states with vanishing dipole transition moment (these we refer to as dark states, DS) from the ground state GS, and optically accessible states (bright states, BS). The onset of the visible to UV (UV–vis) optical absorption is well documented (e.g., cf [39] for a review and a comparison with previous experiments). Three distinct absorption peaks (labeled according to literature as C, E and G bands, respectively) are found in the UV–vis region. An overall agreement between our calculations of the optical absorption with the experimental results is found, though the excitation energies are slightly underestimated (which is typical for DFT calculations). Note, the specific experimental conditions may affect the spectral positions of the absorption peaks (as discussed in [39]). In particular, the present experiment probes the optical properties of isolated molecules by ultrafast pulses and thus potentially eliminates energy-loss channels (e.g. collisions and inter- or intra molecular decay) that might shift the absorption peaks to higher energy. For these reasons, we base the subsequent calculations on our DFT





results without any adjustments. As detailed below, very good agreement to the present experiment is achieved, justifying this approach *a posteriori*.

According to our calculations, excitation G represents one triply degenerate many-body state, which is identified as  $6T_{1u}$  excitation [40]. The projection onto the KS basis is depicted in figure 1(b), where we illustrate the relative weight of the excitation from occupied ( $i$ ) to virtual ( $j$ ) orbitals by the thickness of the corresponding arrows. The relevant orbitals are also presented in figure 2. As clear from figures 1(b) and 2, the excitation G is predominantly composed of the transitions (i) from HOMO to virtual states above the first SAMOs with dominant angular momentum of  $L = 8$  and  $L = 6$ , and (ii) from HOMO-1 to LUMO+2. The angular-momentum analysis of the individual orbitals (figure 2) clarifies why the transition to the many-body state associated to excitation G is optically allowed. Analogously one can conclude that neither the 3s-SAMO nor the 3p-SAMO can be populated in a direct single-photon dipole transition from HOMO. This is consistent with a full symmetry analysis of the initial orbitals and the *ab initio* calculations.

### 3. Experimental setup

In order to study electronic transitions into highly excited many-body states close to the ionization potential, fs pulses at UV frequencies are required [41]. The present time-resolved mass-spectrometric study is based on second-order UV autocorrelation making use of a time-of-flight (TOF) mass spectrometer and state-of-the-art nonlinear optics. The laser setup for generating fs pulses in the range of 216–222 nm comprises a Ti:Sa laser system, an optical parametric amplifier (OPA) and several frequency mixing stages. The outline of the system is sketched in figure 3. The Ti:Sa laser (Amplitude Technologies) is the backbone of the overall generation scheme and provides 35 fs (FWHM) pulses with a pulse energy of 12 mJ behind the compressor at a repetition rate of 25 Hz and 800 nm central wavelength. This output is split into several arms. First, the beam is split in a 90:10 ratio. The more intense fraction is sent to a commercial OPA (Light Conversion, TOPAS-C + HE-TOPAS). The OPA

is continuously tunable in the infrared spectral range (1140–3500 nm) and pumped by the Ti:Sa laser. For the subsequent frequency conversion in the UV the output of the OPA is tuned to 1200 nm. The 11 mJ of the 800 nm pump pulse are converted to  $\approx 0.4$  mJ at this wavelength. The low-intensity fraction of the Ti:Sa laser (10%) is equally split into two branches. One half is recombined with the 1200 nm output of the TOPAS in a  $\beta$ -barium borate (BBO, 0.2 mm thick) crystal to generate 480 nm light by sum frequency generation (SFG). The second half is frequency doubled in another BBO, and then together with the 480 nm beam directed to the third SFG stage (BBO, 40  $\mu\text{m}$  thick) to finally generate the 5.7 eV (218 nm) photons. The UV pulse energy was measured using a calibrated XUV photodiode and a pyro detector to be  $\approx 2$   $\mu\text{J}$ .

The output UV beam is directed into a vacuum chamber where it is split into two pulses by a reflective split-and-delay unit (SDU) in order to generate two synchronized pulse replicas. The complete nonlinear optical setup was simulated using the software package LAB2 [42] including dispersion induced by UV pulse propagation in air and through the 2 mm thick entrance window of the vacuum chamber. According to the calculation the 218 nm pulse duration in the interaction region is of the order of 100 fs FWHM with a spectral bandwidth of 2.8 nm. A coarse cross-correlation measurement performed between the 400 nm and 480 nm pulses of 150 fs FWHM supports the derived UV laser beam parameters.

The SDU consists of a Si split-mirror with one half mounted on a delay stage which can displace the mirror along its normal to set the time delay between the pump and the probe pulses. The SDU is followed by a focussing mirror which spatially overlaps the two pulse replicas in the laser–sample interaction area. The laser beams are focused onto the  $\text{C}_{60}$  molecular beam with a spherical mirror ( $f = 300$  mm). Its reflectivity is above 80% in the 200–245 nm range. The beam waist in the interaction area is on the order of 150  $\mu\text{m}$ . The maximum peak intensity reached in the experiments is approximately  $3.5 \times 10^{10} \text{ W cm}^{-2}$ , which is derived from first principles based on Gaussian beam propagation, pulse energy, pulse duration and the far-field laser profile.

The molecular beam is produced by evaporation of  $\text{C}_{60}$  powder (purity >99.5%) in a resistively heated oven at 775 K. The UV laser beams are focused perpendicular to both, the effusive molecular beam and the TOF spectrometer axis. The ions created in the intersection volume are extracted by a static electric field (Wiley–McLaren configuration [43]), directed onto multichannel plates, and finally counted after amplification and discrimination by a digital oscilloscope. The mass resolution of the TOF spectrometer is 0.2% at  $M/q = 720$ .

## 4. Two-photon photoemission

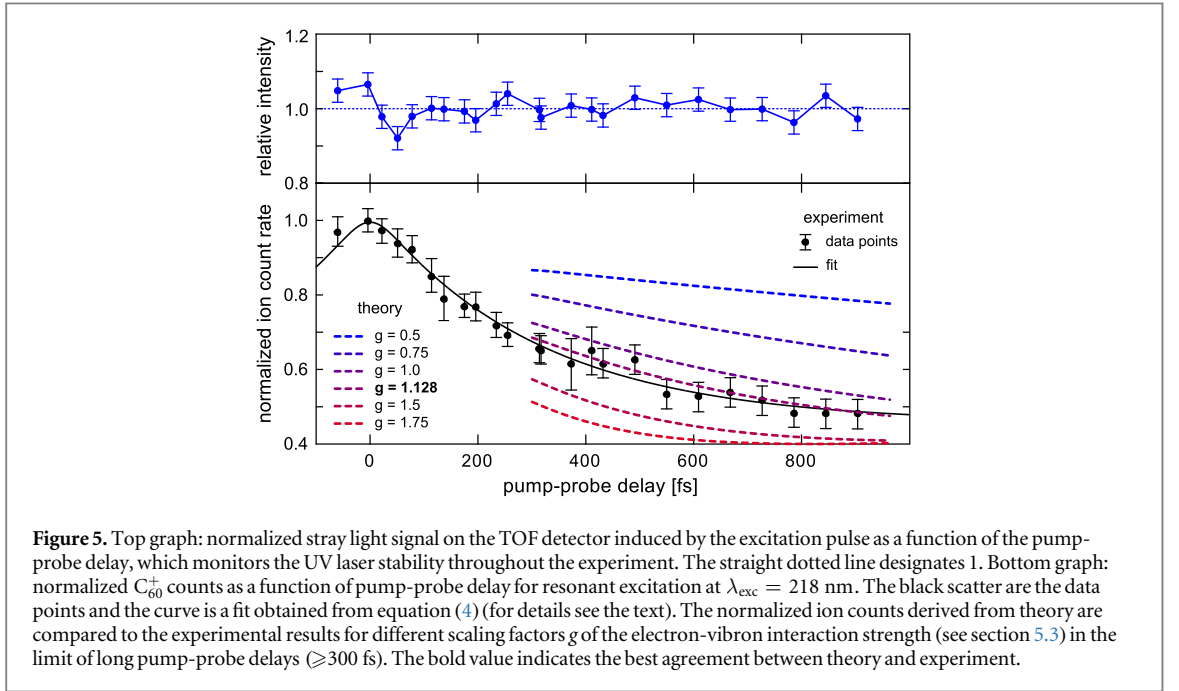
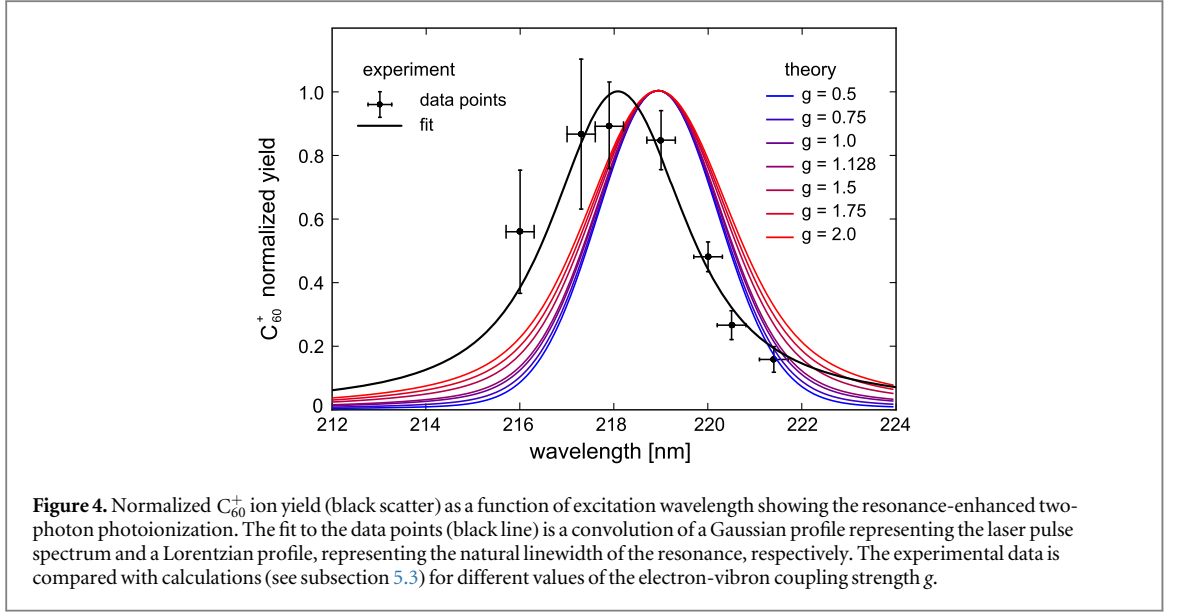
### 4.1. Excitation energy dependence

The photoionization signal recorded for resonant excitation is enhanced compared to an experiment performed off-resonance. The spectral width of the resonance yields information on the excited state lifetime. A UV wavelength scan was performed by tuning the IR wavelength of the OPA. The populated many-body state in the neutral molecule is subsequently ionized during the pulse duration of 100 fs. A full mass spectrum is accumulated over  $\approx 250$  laser shots for each excitation wavelength. The  $\text{C}_{60}^+$  yield was normalized to the relative pulse energy monitored by a photodiode. The  $\text{C}_{60}^+$  ion yield as a function of laser wavelength in the range of 216–222 nm is shown in figure 4. The cut-off at 216 nm corresponds to the OPA's lower wavelength limit of 1140 nm. Relatively large error bars at short wavelengths result from the corresponding low pulse energy and thus poor statistics. The  $\text{C}_{60}^+$  signal disappears for excitation wavelengths longer than 222 nm, thus representing the low-energy threshold of the resonance. The wavelength scan clearly indicates a resonance-enhanced two-photon photoionization at  $\lambda_{\text{exc}} = 218 \pm 0.5$  nm. The observed width of the REMPI signal is of the order of 3.65 nm (94 meV) pointing towards ultrafast ionization within a lifetime that can be as short as  $10_{-3}^{+5}$  fs. The lifetime estimate is derived from the deconvolution of the observed resonance with a Gaussian laser pulse spectrum of 2.8 nm (FWHM) and a Lorentzian describing the homogeneous broadening.

### 4.2. Pump–probe delay dependence

Time-resolved mass spectrometry traces the excited state dynamics in neutral  $\text{C}_{60}$  molecules directly in the time domain. The transient electronic structure is initiated by a UV 100 fs pump pulse and followed (probed) by a delayed pulse replica that photoionizes the molecule (see figure 1(a)). The single-shot mass spectra are taken at varying delay times between the UV pulses ranging from  $-60$  fs to 900 fs with  $\approx 3000$  laser shots per delay point. The time-dependent on-resonance ion signal shown in figure 5 is derived by taking the average number of  $\text{C}_{60}^+$  counts for each delay and normalizing it to the relative pulse energy monitored as the UV stray light peak in the TOF spectrum. The pump–probe scan is repeated two times.

In the most general case the ion signal from a three-level system with a transient intermediate electronic state exposed to resonant excitation will result from two excitation pathways: direct two-photon photoionization from the ground state to the continuum and the ionization via the transient state (REMPI). Therefore, the total ion signal  $S_{\text{tot}}$  can be described as a sum of three components [44]: the coherent term  $S_{\text{ac}}$  (coherent artifact), the



incoherent term  $S_{\text{inc}}$  and a constant background  $a_{\text{bg}}$ . The coherent artifact reflects the direct nonlinear ionization process and is proportional to the autocorrelation (AC) function of the laser pulse:

$$S_{\text{ac}}(\tau) = \int_{-\infty}^{+\infty} I(t - \tau)I(t)dt, \quad (2)$$

where  $I(t)$  is the laser intensity and  $\tau$  is the delay between the pump and probe pulses. The incoherent term  $S_{\text{inc}}$  carries information about the population dynamics of the transient state. It is a convolution of the laser pulse AC with a symmetric decay function. In case of an exponential decay with a characteristic time constant  $\tau_{\text{vib}}$  the incoherent term is given by:

$$S_{\text{inc}}(\tau) = \int_{-\infty}^{+\infty} S_{\text{ac}}(t - \tau) \exp(-|t|/\tau_{\text{vib}}) dt. \quad (3)$$

The constant background  $a_{\text{bg}}$  consists of contributions from each excitation pulse individually and is independent of the pump-probe delay. The total signal reads as:

$$S_{\text{tot}}(\tau) = a_{\text{ac}}S_{\text{ac}}(\tau) + a_{\text{inc}}S_{\text{inc}}(\tau) + a_{\text{bg}} \quad (4)$$

with  $a_i$  being the relative amplitudes of the different components. In general the amplitudes have a ratio depending on the spatial overlap of the two pulses and the ionization pathway of the system. To extract  $\tau_{\text{vib}}$  from

the measurement, the experimental data is fit by the least squares method using expression (4). The background is set to  $a_{\text{bg}} = 1$  and the laser pulses are assumed to be Gaussian with  $\tau_{\text{FWHM}} = 100$  fs. Other variables, i.e.,  $a_{\text{ac}}$ ,  $a_{\text{inc}}$ , and  $\tau_{\text{vib}}$ , are free fit parameters. The best fit curve (black line in the bottom graph of figure 5) yields a time constant  $\tau_{\text{vib}} = 400 \pm 100$  fs (95% confidence band) and an amplitude ratio  $a_{\text{ac}} : a_{\text{inc}} : a_{\text{bg}} = 0.24 : 1.13 : 1$ . The laser intensities in the interaction region in the present experiment are as low as  $3.5 \times 10^{10} \text{ W cm}^{-2}$  which makes the contribution from the direct (nonlinear) two-photon process small. The ratio  $a_{\text{inc}} : a_{\text{bg}}$  is close to 1 as expected for single photon ionization from an occupied transient state.

The observed exponential time constant  $\tau_{\text{vib}} = 400 \pm 100$  fs is significantly longer than the characteristic electron–electron interaction time derived from pump–probe spectroscopy [45] and pulse duration dependent studies [46, 47] in the optical spectral range. It seems that electron thermalization mediated by inelastic electron–electron collisions on a time scale of 50–100 fs does not play a key role when high lying correlated many-body states are excited directly at rather low peak intensity. In the following a detailed theoretical description of the observed resonance and its time-dependent structure is discussed.

## 5. Simulations

To describe the response of the molecule upon pulsed laser irradiation, the interplay between the electronic excitations and the vibrationally hot molecule has to be taken into account (for an overview on this topic we refer to the book [48] and further references therein). In full generality, an *ab initio* description for both the electronic and nuclear degrees of freedom and their coupling is not feasible currently. Hence, one has to rely on suitable approximations. In an Ehrenfest approach the electrons are described on the level of TDDFT and the nuclei are subject to classical equations of motion due to the forces exerted by the electron distribution. Despite the success of this molecular dynamics approach [49] for predicting vibrationally-assisted charge-transfer processes [50] in photovoltaics the Born–Oppenheimer (BO) approximation is an inherent limitation. For excited-state properties, where the nuclear and electronic dynamics are strongly mixed, BO-type molecular dynamics is not predictive. Molecular dynamics beyond the BO approximation [51–53] has been employed for the  $\text{C}_{60}$  molecule [54]; merging such schemes with a treatment of the electronic excitations beyond the KS level is computationally too demanding for our system. Alternatively, one can treat the electrons in a single-particle atomic basis within a tight-binding model [55], removing the adiabaticity constraint with respect to the many-body states. Besides the inevitable empirical ingredient, such theory is also not directly compatible with the *ab initio* description of the many-body states in section 2, i.e. electronic correlations can be taken into account only with great efforts.

### 5.1. Initial laser-induced dynamics

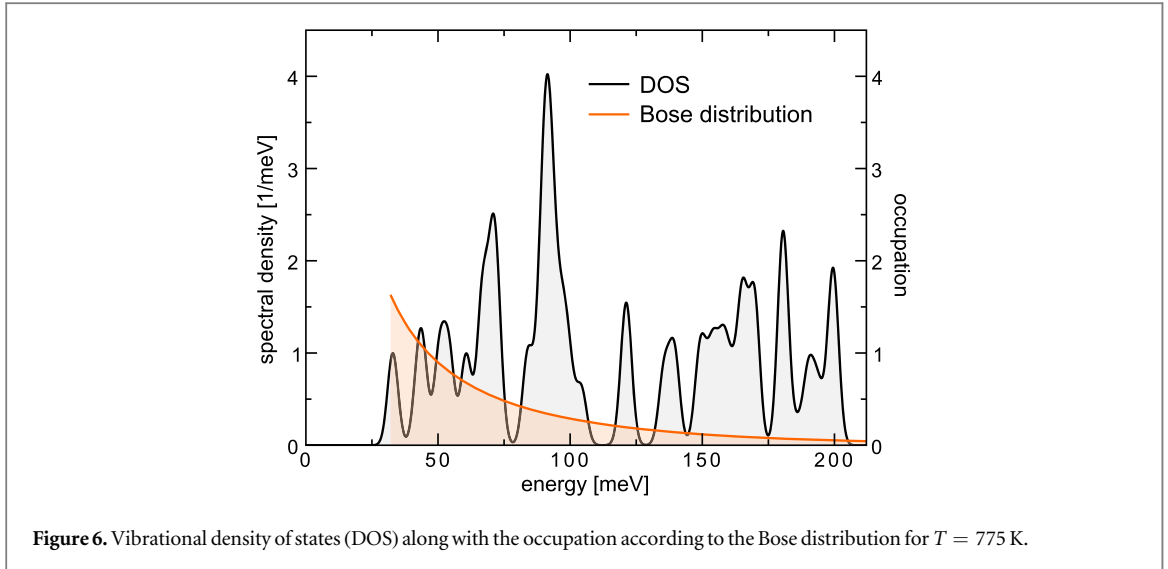
In order to elucidate the laser- and vibration-induced dynamics we take a different angle. Since a considerable amount of energy is stored in thermally activated vibrations, which can only be transferred to the electronic subsystem in small portions, the vibrons can be treated as an effective heat bath for the electrons. A similar model has successfully been employed for incorporating the influence of the vibrations on charge-transfer processes in organic photovoltaic systems based on  $\text{C}_{60}$  [56]. To construct an appropriate model for our case, several ingredients are required. For the vibrations we restrict ourselves to the harmonic approximation of the bottom of the BO surfaces. The vibronic eigenmodes along with their eigenfrequencies and reduced masses were computed using the OCTOPUS code, as well. The resulting density of states (DOS) of the vibronic modes is shown in figure 6. Our results compare very well with those tabulated in the literature, for instance table 6.2 in the book [48].

As inferred from figure 6 the high-energy modes (which affect the electrons at most) are only weakly populated for  $T = 775$  K. Therefore, the oscillations of the nuclei around their equilibrium positions can be considered small. Hence, the Herzberg–Teller (HT) expansion [57] of the full Hamiltonian, including electrons and nuclei, yields a reasonable description for both subsystems and their interaction. The first-order HT Hamiltonian amounts to approximating the electron–vibron coupling as linear in the mode amplitudes  $\hat{Q}_\nu$ . On the KS level, the electron–vibron matrix elements are thus given by

$$k_{ij}^\nu = \langle \phi_i | \frac{\partial V^{\text{KS}}}{\partial Q_\nu} | \phi_j \rangle \Big|_{Q_\nu=0}. \quad (5)$$

Details on the evaluation of equation (5) are provided in appendix A. Since we are opting for a model in the many-body basis of the excitations discussed in section 2, the matrix elements (5) are transformed according to equation (1) (see appendix A). We thus obtain the model Hamiltonian (atomic units are used throughout)

$$\hat{H}(t) = \hat{H}_{\text{el}}(t) + \hat{H}_{\text{el-vib}} + \hat{H}_{\text{vib}}, \quad (6)$$



where

$$\hat{H}_{\text{el}}(t) = \sum_{\alpha} E_{\alpha} |\Phi_{\alpha}\rangle \langle \Phi_{\alpha}| + f(t) \sum_{\alpha\beta} M_{\alpha\beta} |\Phi_{\alpha}\rangle \langle \Phi_{\beta}|, \quad (7)$$

$$\hat{H}_{\text{el-vib}} = g \sum_{\alpha\beta} \sum_{\nu} K_{\alpha\beta}^{\nu} |\Phi_{\alpha}\rangle \langle \Phi_{\beta}| \hat{Q}_{\nu}, \quad (8)$$

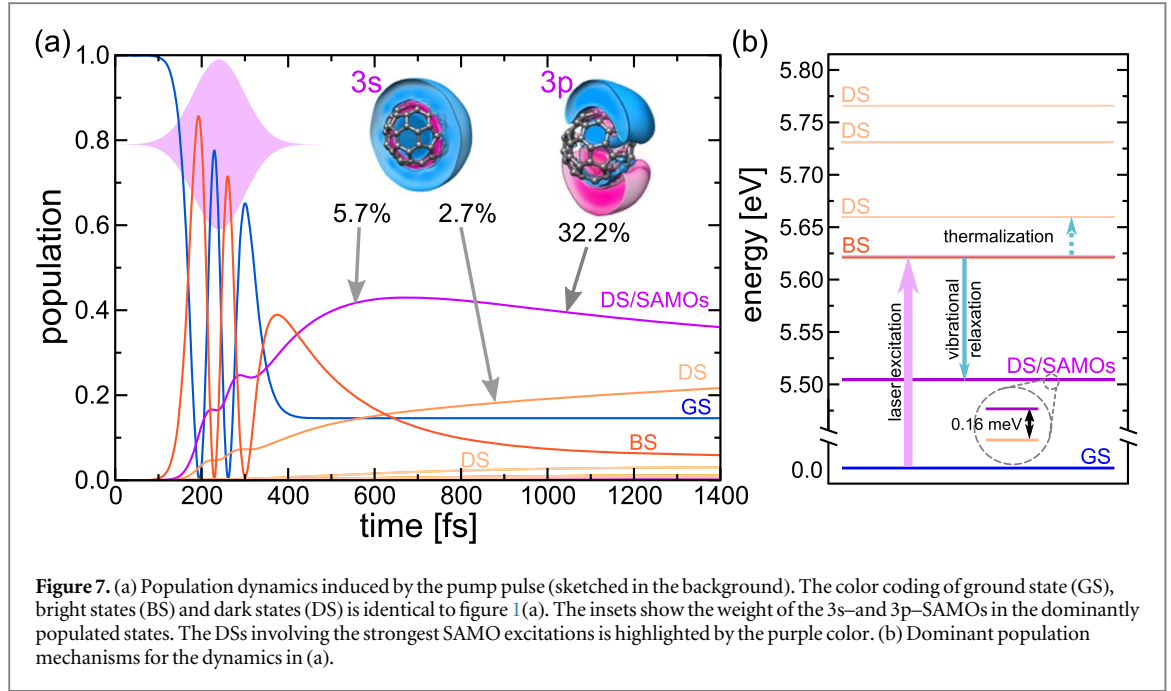
$$\hat{H}_{\text{vib}} = \frac{1}{2} \sum_{\nu} \left( \frac{\hat{P}_{\nu}^2}{M_{\nu}} + k_{\nu} \hat{Q}_{\nu}^2 \right). \quad (9)$$

Here,  $M_{\alpha\beta}$  are the dipole transition matrix elements from our TDDFT calculations, while  $f(t)$  comprises the time-dependent fields. The prefactor  $g$  in equation (8) is introduced as an overall scaling factor for the strength of the vibronic coupling. Ideally,  $g = 1$  should be fixed; however, due to the perturbative description resulting from the HT expansion, the electron-vibron interaction might be underestimated. Hence,  $g$  is kept as a parameter.

Instead of describing the dynamics of the full density matrix according to Hamiltonian (6) (which is a formidable task), we treat the vibrations as a heat bath. This allows to obtain a master equation for the density matrix in the electronic subspace only. Here we assume Markovian dynamics and thus employ the Lindblad master equation, following the standard derivation and formulation from [58]. More details are presented in appendix B. This procedure requires an additional parameter: the vibronic broadening  $\eta$ , which corresponds to the lifetime of the vibrational modes. The laser-induced dynamics is, besides the electron-vibron interaction, treated on *ab initio* level endorsing the predictive power of the approach. Note that the electron-vibron coupling (8) includes, in principle, Jahn–Teller and Herzberg–Teller couplings, which were identified as the main mechanisms for vibrational coupling in fullerenes [59–61].

The time evolution of the occupation of the states depicted in the level scheme figure 1(a) is presented in figure 7(a). The driving pulse  $f(t)$  is chosen as a Gaussian pulse with a FWHM of 100 fs as in the experiment, while the central frequency is adjusted to the vertical excitation energy  $\Delta E = 5.66$  eV between ground state and the BSs corresponding to the G peak. The peak amplitude amounts to the intensity of  $3.5 \times 10^{10}$  W cm<sup>-2</sup>. The values for  $g$  and  $\eta$  are chosen to match the time-dependent pump-probe signal observed in the experiment (see section 5.3).

As one can infer from figure 7, the population transfer between the ground state and the bright excited states is clearly not in the perturbative regime, as two Rabi cycles are apparent during the 100 fs UV pulse interaction. The relaxation dynamics, transferring part of the excitation to the dark states, takes place on two time scales: for short delays one can observe a rapid energy transfer, while for longer times the distribution thermalizes. The depletion dynamics of the laser-excited BS primarily takes place due to the coupling to two lower-energy states at  $\approx 5.5$  eV (see figure 7(b)). Closer inspection reveals that these DSs involve the excitation of the 3s and the 3p SAMOs; the respective weights are given in figure 7(a). This relaxation mechanism is the dominant consequence of the electron-vibron coupling. This behavior is expected, as dissipation pathways are generally preferred compared to bath-induced excitations. These thermalization processes are hence less pronounced and occur on a longer time scale.



## 5.2. Pump-probe dynamics

In order to compute the pump-probe signals from the dynamics of the density matrix  $\rho_{\alpha\beta}(t)$ , as discussed above, an extension to the scattering states is required. However, a straightforward implementation of the Lindblad equation including both bound and unbound many-body states is not feasible. This is due to the large dimension of the Hamiltonian after the inevitable discretization of the continuum. Hence, we opt for a perturbation description which allows to compute the pump-probe dynamics from the time-dependent density matrix without incorporating the ionization dynamics explicitly. This is achieved by a method known from time-resolved photoelectron spectroscopy [62]. Adopting a straightforward derivation for the many-body case, one obtains

$$N_{\mathbf{k}} \propto \text{Re} \sum_{\alpha\beta} \int_{-\infty}^{\infty} dt \int_{-\infty}^t dt' F_{\text{probe}}(t) F_{\text{probe}}(t') e^{-i(E_{\alpha} + \omega - E_{\beta}^+ - \epsilon_{\mathbf{k}})(t-t')} |M_{\beta\mathbf{k},\alpha}|^2 \rho_{\alpha\alpha}(t') \quad (10)$$

for the number  $N_{\mathbf{k}}$  of released photoelectrons with momentum  $\mathbf{k}$  and energy  $\epsilon_{\mathbf{k}}$ . The probe laser pulse is assumed as  $f_{\text{probe}}(t) = F_{\text{probe}}(t)e^{-i\omega t}$  with the pulse envelop  $F_{\text{probe}}$ . The matrix element  $M_{\beta\mathbf{k},\alpha} = \langle \Phi_{\beta,\mathbf{k}} | \hat{D} | \Phi_{\alpha} \rangle$  ( $\hat{D}$  denotes the dipole operator) describes the transition from the intermediate states  $|\Phi_{\alpha}\rangle$  to the final states  $|\Phi_{\beta,\mathbf{k}}\rangle$  with one photoelectron and the ion state labeled by  $\beta$  (energy  $E_{\beta}^+ + \epsilon_{\mathbf{k}}$ ). Note that only the population of excited intermediate states and not the full density matrix enters equation (10). This is an approximation, which relies on the fact that pathway interferences play only a minor role for the considered two-step ionization process.

For the excited state with one electron in the continuum state  $|\mathbf{k}\rangle$ ,  $|\Phi_{\beta,\mathbf{k}}\rangle$ , we write the usual anti-symmetrized product ansatz

$$|\Phi_{\beta,\mathbf{k}}\rangle = \hat{c}_{\mathbf{k}}^{\dagger} |\Phi_{\beta}^+\rangle, \quad (11)$$

where  $|\Phi_{\beta}^+\rangle$  is an eigenstate of the ionized system with energy  $E_{\beta}^+$ . In this case the photoemission matrix element reduces to

$$\langle \Phi_{\beta,\mathbf{k}} | \hat{D} | \Phi_{\alpha} \rangle = \langle \mathbf{k} | \hat{D} | \phi_{\alpha\beta}^{\text{D}} \rangle. \quad (12)$$

Here,  $\phi_{\alpha\beta}^{\text{D}}(\mathbf{r})$  stands for the corresponding Dyson orbital. As the sum over all excited states  $\beta$  is implied, a (computationally expensive) precise calculation of the Dyson orbitals can be omitted by approximating them by simple hole states, i.e., by assuming

$$|\Phi_{\beta=(m,\alpha)}^+\rangle \approx \hat{c}_m |\Phi_{\alpha}\rangle, \quad E_{\beta}^+ \approx E_{\alpha} - \epsilon_m. \quad (13)$$

Here,  $\epsilon_m$  stands for the KS eigenvalue of orbital  $\phi_m(\mathbf{r})$ . The matrix element (12) can thus be evaluated in terms of a superposition of matrix elements with respect to the KS orbitals. The scattering states  $|\mathbf{k}\rangle$  were computed with respect to the spherically averaged KS potential [28], which is known to be an adequate approximation for angle-integrated quantities. Asymptotic corrections ensuring the  $r^{-1}$  behavior are incorporated by smoothly interpolating between the short-range and long-range regimes. Further orthogonalization with respect to the bound KS orbitals is performed.

To reflect the experimental situation, the integration over all photoelectron states has to be performed. Furthermore, we note that equation (10) balances spectral resolution versus temporal resolution in terms of the convolution of the phase factor  $e^{-i\Delta E t}$ ,  $\Delta E = E_\alpha + \omega - E_\beta^+ - \epsilon_{\mathbf{k}}$ , with the envelop function. Due to very long pulses as compared to one oscillation period, this convolution practically yields a Dirac  $\delta$ -function with respect to the energy balance. Taking this into account, the total ionization pump-probe signal  $S(\tau) = \int d\mathbf{k} N_{\mathbf{k}}$  simplifies to

$$S(\tau) \propto \sum_{\alpha\beta} \int_{-\infty}^{\infty} dt \int_{-\infty}^t dt' F_{\text{probe}}(t - \tau) F_{\text{probe}}(t' - \tau) P_{\alpha\beta}(E_\alpha + \omega) \rho_{\alpha\alpha}(t'), \quad (14)$$

where  $P_{\alpha\beta}(\epsilon) = k \int d\Omega_{\mathbf{k}} |M_{\beta\mathbf{k},\alpha}|^2$  with  $k = \sqrt{2\epsilon}$  is proportional to the energy-resolved ionization probability with respect to the initial state  $|\Phi_\alpha\rangle$  and final state  $|\Phi_\beta^+\rangle$ . As in section 4.2,  $\tau$  denotes the pump-probe delay.

### 5.3. Theory versus experiment

The pump-probe signal based on the laser-driven and vibron-coupled dynamics of the density matrix can now be compared to the experiment. We remark that equation (14) assumes that the two pulses can be separated and does not account for the scenario of overlapping pulses. We thus limit the comparison between the theoretical calculations and the experiment, presented in figure 5, to the region of exponential decay for  $\tau \geq 300$  fs.

Furthermore, the dynamics presented in figure 7 indicates that the laser intensity exceeds the perturbative regime. However, even with stronger pulses, the bright states around 5.66 eV are the only accessible channels, as absorbing another photon leads to immediate ionization. This will, however, only affect the background signal. Therefore, we adjust the background  $S_{\text{bg}} = S(\tau \rightarrow \infty)$  to the experiment. After solving the Lindblad master equation for various values of the parameters  $g$  and  $\eta$ , we found the best fit for  $g = 1.128$  and  $\eta = 0.77$  meV. The latter corresponds to a vibrational lifetime of  $\approx 5.4$  ps, which is in accordance with previous experiments [8]. The small deviation of the scaling factor  $g$  from unity underpins the predictive power of our treatment. Note that also  $g = 1$  results in a decay dynamics which closely resembles, apart from the background, the experimental data, whereas varying  $g$  to smaller or larger values clearly deviates from the measurements.

We also calculated the ionization signal for varying photon energy  $\omega$  and compared the resulting spectra in figure 4. To match the laser spectral bandwidth to the experiment, the obtained curves were convolved with a Gaussian having a FWHM of 2.8 nm. The theoretical spectra are centered around the vertical excitation energy, which is lower than what is observed in the experiment. This kind of underestimating bandgaps and thus excitation energies is typical for most DFT calculations and for the  $C_{60}$  molecular, in particular [40]. However, the theoretical and the experimental peak differ only by  $\approx 10$  meV. Generally, both the experimental as well as the theoretical spectra are considerably sharper than in optical absorption measurements. This is a major advantage of the current experimental setup: the dipole excitation dominates over possible loss channels, if the pulse strength is increased, which leads to a narrow resonance.

### 5.4. Steady-state versus time-dependent picture

The interpretation of the present data on the relaxation dynamics requires the full picture including both, correlated electronic and nuclear degrees of freedom and their interactions [63, 64]. It is known that highly excited electronic and vibrational  $C_{60}$  states are strongly mixed [55, 65]. In turn, relaxation channels open up depopulating the electronically excited states by internal conversion close to conical intersections similar to electron-phonon coupling in solid state materials. We note that characteristic fragmentation patterns observed in TOF mass spectra using optical lasers as a function of pump-probe delay revealed (nonadiabatic) vibronic coupling on a time scale of  $\tau_{\text{vib}} = 200\text{--}300$  fs [45], which is in good agreement with the present findings. Furthermore, nonadiabatic coupling of mixed valence and Rydberg states is ubiquitous in polyatomic molecules affecting potential energy surfaces, energy relaxation and dissociation dynamics [21]. Similar processes have been considered to evoke the loss of small neutral fragments from  $C_{60}$  on a picosecond time scale [66].

The identification of vibronic coupling playing a key role in the electronic energy loss of correlated many-body states may open new vistas for optical control of charge-transport phenomena in smart materials containing these nanospheres. For instance, coherently induced radial symmetric ‘breathing’ motion of the cage atoms strongly impacts the structure and dynamics of the molecule [67]. The carbon cage and the electron system start to exchange many eV in energy periodically on a sub-100 fs period timescale. The coherent oscillation prevails for several cycles [67], which might be interesting for novel ultrafast switching applications in molecular electronics.

## 6. Summary and outlook

Ultrashort pulses in the UV spectral range excite correlated many-body states of isolated  $C_{60}$  molecules below the ionization continuum. The population is followed by subsequent UV pulses of the same wavelength that ionize the molecules. By recording the  $C_{60}^+$  ion yield as a function of time delay between the pump and probe pulses we observe an exponential decay with a time constant of  $\tau_{\text{vib}} = 400 \pm 100$  fs which is explained by the coupling of electronic excitation to nuclear motion in the neutral molecule. The initial electronic relaxation can be as fast as  $\tau_{\text{el}} = 10_{-3}^{+5}$  fs according to the evaluation of the resonance line width in single pulse experiments as a function of excitation wavelength. The experimental results are in good agreement with *ab initio* calculation of structure and dynamics including electronic correlation and vibronic coupling. However, the UV pulse duration of 100 fs did not allow to observe pure electron dynamics in time-resolved experiments. Future experimental work making use of shorter UV pulses shall reveal the predicted laser-driven Rabi oscillation and time-resolved transformation of the electronic orbitals, i.e., the coupling between different electronic states.

## Acknowledgments

This research was supported by the Deutsche Forschungsgemeinschaft through the excellence cluster ‘The Hamburg Centre for Ultrafast Imaging (CUI)—Structure, Dynamics and Control of Matter at the Atomic Scale’ (DFG-EXC1074), the collaborative research centres ‘Light induced dynamics and control of correlated quantum systems’ (SFB 925), ‘Functionality of Oxide Interfaces’ (SFB 762), the GrK 1355 and Grant Number PA 1698/1-1.

## Appendix A. Electron-vibron matrix elements

In this appendix we provide the details on how the first-order (Herzberg–Teller) electron-vibron coupling matrix elements, equation (5), were computed. After the calculation of the vibrational eigenmodes  $\nu$ , one readily obtains the associated deformations of the fullerene cage. Denoting the collection of nuclear coordinates in equilibrium by  $\{\mathbf{R}^{(0)}\} = (\mathbf{R}_1^{(0)}, \dots, \mathbf{R}_{60}^{(0)})$ , the vibrational distortion is characterized by

$$\{\mathbf{R}^{(\nu)}(q)\} = (\mathbf{R}_1^{(\nu)}(q), \dots, \mathbf{R}_{60}^{(\nu)}(q)) \quad \text{with} \quad \mathbf{R}_m^{(\nu)}(q) = \mathbf{R}_m^{(0)} + q\mathbf{V}_m^{(\nu)}, \quad (\text{A.1})$$

where  $\mathbf{V}_m^{(\nu)}$  is the displacement eigenvector. Based on equation (A.1), we performed a DFT calculation for each vibrational mode, fixing the magnitude of the distortions at  $\delta q = 0.01$ . Instead of taking derivatives of the KS potential, we employ the equivalent formulation

$$k_{ij}^{\nu} \simeq \frac{1}{\delta q} \langle \phi_i | \hat{h}_{\nu} - \hat{h}_0 | \phi_j \rangle, \quad \hat{h}_{\nu} = -\frac{1}{2} \nabla^2 + v^{\text{KS}}(\mathbf{r}, \{\mathbf{R}^{(\nu)}(\delta q)\}), \quad (\text{A.2})$$

where we have approximated the derivative by finite differences. The KS Hamiltonian describing the molecule in equilibrium is denoted by  $\hat{h}_0$ , while  $\hat{h}_{\nu}$  describes the distorted molecule. For the evaluation of equation (A.2) we insert a (approximate) completeness relation and obtain

$$k_{ij}^{\nu} \simeq \frac{1}{\delta q} [\langle \phi_i | \tilde{\phi}_k^{(\nu)} \rangle \tilde{\epsilon}_k^{(\nu)} \langle \tilde{\phi}_k^{(\nu)} | \phi_j \rangle - \epsilon_i \delta_{ij}],$$

$$\hat{h}_{\nu} | \tilde{\phi}_k^{(\nu)} \rangle = \tilde{\epsilon}_k^{(\nu)} | \tilde{\phi}_k^{(\nu)} \rangle, \quad \hat{h}_0 | \phi_i \rangle = \epsilon_i | \phi_i \rangle. \quad (\text{A.3})$$

Note that the overlaps  $\langle \phi_i | \tilde{\phi}_k^{(\nu)} \rangle$  incorporate the symmetry properties of the vibronically induced transitions.

The transformation into the many-body basis is accomplished by expressing the one-body coupling operator in second quantization,  $\hat{k}^{\nu} = \sum_{ij} k_{ij}^{\nu} \hat{c}_i^{\dagger} \hat{c}_j$ , and evaluating  $\langle \Phi_{\alpha} | \hat{k}^{\nu} | \Phi_{\beta} \rangle$  according to the algebra of the fermionic creation and annihilation operators.

## Appendix B. Lindblad master equation

For the derivation of the Lindblad master equation in the weak-coupling limit, we follow [58]. For the Hamiltonian (7)–(9) one obtains the following EOM for the electronic density matrix

$$\hat{\rho}(t) = \sum_{\alpha\beta} \rho_{\alpha\beta}(t) | \Phi_{\alpha} \rangle \langle \Phi_{\beta} |:$$



$$\begin{aligned} \frac{d}{dt} \hat{\rho}(t) = & -i[\hat{H}_{el}(t), \hat{\rho}(t)] \\ & + \sum_{\alpha\beta\alpha'\beta'} \Gamma_{\alpha\beta\alpha'\beta'} \left( \rho_{\beta\beta'}(t) |\Phi_{\alpha}\rangle \langle \Phi_{\alpha'}| - \frac{1}{2} \{ |\Phi_{\beta'}\rangle \langle \Phi_{\beta}| \hat{\rho}(t) \} \right). \end{aligned} \quad (\text{B.1})$$

The square (curly) brackets denote the commutator (anti-commutator). The vibronic bath enters into

$$\Gamma_{\alpha\beta\alpha'\beta'} = \sum_{\nu} \gamma_{\nu}(E_{\beta} - E_{\alpha}) \delta_{E_{\beta} - E_{\alpha}, E_{\beta'} - E_{\alpha'}} K_{\alpha\beta}^{\nu} K_{\alpha'\beta'}^{\nu}, \quad (\text{B.2})$$

where  $\gamma_{\nu}(E) = (N_{\text{B}}(E) + 1)A_{\nu}(E)$ .  $N_{\text{B}}(E)$  denotes the Bose distribution (displayed in figure 6) which accounts for the occupation of the vibronic modes for the given temperature. The vibrational frequencies determine the spectral function  $A_{\nu}(E) = 2\pi\delta(E - \Omega_{\nu})$ , which we replace by the smeared form

$$A_{\nu}(E) = \sqrt{2\pi/\eta^2} \exp[-(E - \Omega_{\nu})^2/2\eta^2] \quad (\text{B.3})$$

to account for the finite lifetime of the vibrations.

## References

- [1] Sariciftci N S, Smilowitz L, Heeger A J and Wudl F 1992 *Science* **258** 1474–6
- [2] Yu G, Gao J, Hummelen J C, Wudl F and Heeger A J 1995 *Science* **270** 1789–91
- [3] Scholes G D and Rumbles G 2006 *Nat. Mater.* **5** 683–96
- [4] Klaiman S, Gromov E V and Cederbaum L S 2013 *J. Phys. Chem. Lett.* **4** 3319–24
- [5] Klaiman S, Gromov E V and Cederbaum L S 2014 *Phys. Chem. Chem. Phys.* **16** 13287–93
- [6] Voora V K and Jordan K D 2014 *Nano Lett.* **14** 4602–6
- [7] Pavlyukh Y and Berakdar J 2009 *Chem. Phys. Lett.* **468** 313–8
- [8] Hertel I V, Laarmann T and Schulz C P 2005 *Adv. At. Mol. Opt. Phys.* **50** 219–86
- [9] Jacquemin R, Kraus S and Eberhardt W 1998 *Solid State Commun.* **105** 449–53
- [10] Link S, Scholl A, Jacquemin R and Eberhardt W 2000 *Solid State Commun.* **113** 689–93
- [11] Lépine F 2015 *J. Phys. B* **48** 122002
- [12] Feng M, Zhao J and Petek H 2008 *Science* **320** 359–62
- [13] Feng M, Zhao J, Huang T, Zhu X and Petek H 2011 *Acc. Chem. Res.* **44** 360–8
- [14] Pavlyukh Y and Berakdar J 2011 *J. Chem. Phys.* **135** 201103
- [15] Reisler H and Krylov A I 2009 *Int. Rev. Phys. Chem.* **28** 267–308
- [16] Zhao J and Petek H 2014 *Phys. Rev. B* **90** 075412
- [17] Wätzel J, Pavlyukh Y, Schäffer A and Berakdar J 2016 *Carbon* **99** 439–43
- [18] Zoppi L, Martin-Samos L and Baldrige K K 2015 *Phys. Chem. Chem. Phys.* **17** 6114–21
- [19] Dougherty D B, Feng M, Petek H, Yates J T and Zhao J 2012 *Phys. Rev. Lett.* **109** 266802
- [20] Johansson J O, Henderson G G, Remacle F and Campbell E E B 2012 *Phys. Rev. Lett.* **108** 173401
- [21] Mignolet B, Johansson J O, Campbell E E B and Remacle F 2013 *Chem. Phys. Chem* **14** 3332–40
- [22] Bohl E, Sokół K P, Mignolet B, Thompson J O F, Johansson J O, Remacle F and Campbell E E B 2015 *J. Phys. Chem. A* **119** 11504–8
- [23] Boyle M, Hoffmann K, Schulz C P, Hertel I V, Levine R D and Campbell E E B 2001 *Phys. Rev. Lett.* **87** 273401
- [24] Boyle M, Laarmann T, Hoffmann K, Hedén M, Campbell E E, Schulz C P and Hertel I V 2005 *Eur. Phys. J. D* **36** 339–51
- [25] Roy X et al 2013 *Science* **341** 157–60
- [26] Shchatsinin I, Laarmann T, Zhavoronkov N, Schulz C P and Hertel I V 2008 *J. Chem. Phys.* **129** 204308
- [27] Li H et al 2015 *Phys. Rev. Lett.* **114** 123004
- [28] Schüller M, Berakdar J and Pavlyukh Y 2015 *Phys. Rev. A* **92** 021403
- [29] Wopperer P et al 2015 *Phys. Rev. A* **91** 042514
- [30] Schüller M, Pavlyukh Y, Bolognesi P, Avaldi L and Berakdar J 2016 *Sci. Rep.* **6** 24396
- [31] García de Abajo F J 2004 *Phys. Rev. B* **70** 115422
- [32] Marques M A L, Maitra N T, Nogueira F M S, Gross E K U and Rubio A 2012 *Fundamentals of Time-Dependent Density Functional Theory* (Berlin: Springer)
- [33] Bartlett R and MusiaĀ M 2007 *Rev. Mod. Phys.* **79** 291–352
- [34] Aryasetiawan F and Gunnarsson O 1998 *Rep. Prog. Phys.* **61** 237
- [35] Chong D P 1995 *Recent Advances in Density Functional Methods* (Singapore: World Scientific)
- [36] Andrade X et al 2015 *Phys. Chem. Chem. Phys.* **17** 31371–96
- [37] van Leeuwen R and Baerends E J 1994 *Phys. Rev. A* **49** 2421–31
- [38] Schipper P R T, Gritsenko O V, Gisbergen S J A V and Baerends E J 2000 *J. Chem. Phys.* **112** 1344–52
- [39] Smith A L 1996 *J. Phys. B* **29** 4975
- [40] Bauernschmitt R, Ahlrichs R, Hennrich F H and Kappes M M 1998 *J. Am. Chem. Soc.* **120** 5052–9
- [41] Johansson J O, Henderson G G and Campbell E E B 2013 *EPJ Web Conf.* **41** 02015
- [42] Schmidt B, Hacker M, Stobrawa G and Feuer T *LAB2-A Virtual Femtosecond Laser Lab* (<http://lab2.de/>)
- [43] Wiley W C and McLaren I H 1955 *Rev. Sci. Instrum.* **26** 1150–7
- [44] Knoesel E, Hotzel A and Wolf M 1998 *Phys. Rev. B* **57** 12812–24
- [45] Shchatsinin I, Laarmann T, Stibenz G, Steinmeyer G, Stalmashonak A, Zhavoronkov N, Schulz C P and Hertel I V 2006 *J. Chem. Phys.* **125** 194320
- [46] Campbell E E B, Hansen K, Hoffmann K, Korn G, Tchapyguine M, Wittmann M and Hertel I V 2000 *Phys. Rev. Lett.* **84** 2128–31
- [47] Hansen K, Hoffmann K and Campbell E E B 2003 *J. Chem. Phys.* **119** 2513–22
- [48] Chancey C C and O'Brien M C M 1997 *The Jahn-Teller Effect in C<sub>60</sub> and Other Icosahedral Complexes* (Princeton, NJ: Princeton University Press)
- [49] Leszczynski J 2012 *Handbook of Computational Chemistry* (Berlin: Springer)

- [50] Pittalis S, Delgado A, Robin J, Freimuth L, Christoffers J, Lienau C and Rozzi C A 2015 *Adv. Funct. Mater.* **25** 2047–53
- [51] Ben-Nun M, Quenneville J and Martínez T J 2000 *J. Phys. Chem. A* **104** 5161–75
- [52] Nyman G and Yu H G 2000 *Rep. Prog. Phys.* **63** 1001–59
- [53] Schlegel H B 2003 *J. Comput. Chem.* **24** 1514–27
- [54] Fischer M, Handt J, Seifert G and Schmidt R 2013 *Phys. Rev. A* **88** 061403
- [55] Zhang G P, Sun X and George T F 2003 *Phys. Rev. B* **68** 165410
- [56] Tamura H, Martinazzo R, Ruckebauer M and Burghardt I 2012 *J. Chem. Phys.* **137** 22A540
- [57] Köppel H, Yarkony D R and Barentzen H 2009 *The Jahn-Teller Effect: Fundamentals and Implications for Physics and Chemistry* (Berlin: Springer)
- [58] Breuer H P and Petruccione F 2002 *The Theory of Open Quantum Systems* (Oxford: Oxford University Press)
- [59] Sassara A, Zerza G, Chergui M, Negri F and Orlandi G 1997 *J. Chem. Phys.* **107** 8731–41
- [60] Menéndez J and Page J B 2000 *Vibrational spectroscopy of C<sub>60</sub> Light Scattering in Solids VIII* (Berlin: Springer) 27–95
- [61] Orlandi G and Negri F 2002 *Photochem. Photobiol. Sci.* **1** 289–308
- [62] Kemper A F, Sentef M A, Moritz B, Freericks J K and Devereaux T P 2014 *Phys. Rev. B* **90** 075126
- [63] Lezius M, Blanchet V, Rayner D M, Villeneuve D M, Stolow A and Ivanov M Y 2001 *Phys. Rev. Lett.* **86** 51–4
- [64] Lezius M, Blanchet V, Ivanov M Y and Stolow A 2002 *J. Chem. Phys.* **117** 1575–88
- [65] Torralva B, Niehaus T A, Elstner M, Suhai S, Frauenheim T and Allen R E 2001 *Phys. Rev. B* **64** 153105
- [66] Boyle M, Laarmann T, Shchatsinin I, Schulz C P and Hertel I V 2005 *J. Chem. Phys.* **122** 181103
- [67] Laarmann T, Shchatsinin I, Stalmashonak A, Boyle M, Zhavoronkov N, Handt J, Schmidt R, Schulz C P and Hertel I V 2007 *Phys. Rev. Lett.* **98** 058302

## Transient spectroscopy from quantum kinetics

We have already seen that the NEGF formalism represents a particularly useful tool to describe photoemission, both from fundamental (see sec. 5.2) and practical (as demonstrated in sec. 5.4) point of view. The advent of the attosecond metrology (see sec. 3.1) offers genuinely new insights into the dynamics of many-body systems, with the ultimate goal of following the nonequilibrium time evolution – as induced by a tunable excitation – the same way as "watching" a movie. Among the most exciting developments are time- and energy resolved experiments such as time-resolved ARPES (see subsec. 3.2.3). A time-dependent formulation of the NEGF theory of photoemission, which is capable of including the many-body photoexcitation effects discussed in subsec. 3.1.2 would therefore provide powerful tools for exploring electronic correlations in the time domain.

### 6.1 Kadanoff-Baym equations

The dynamics of the GFs is governed by the KBEs (see subsec. 2.5.4). Choosing a suitable SP basis for representing all Keldysh components of the GFs and the self-energy, the KBEs in their usual form read

$$i\partial_{t_1} \mathbf{G}^>(t_1, t_2) = \mathbf{h}^{\text{MF}}(t_1) \mathbf{G}^>(t_1, t_2) + \left[ \boldsymbol{\Sigma}^{\text{R}} \cdot \mathbf{G}^> + \boldsymbol{\Sigma}^> \cdot \mathbf{G}^{\text{A}} + \boldsymbol{\Sigma}^{\text{I}} \star \mathbf{G}^{\text{I}} \right] (t_1, t_2), \quad (6.1a)$$

$$-i\partial_{t_2} \mathbf{G}^<(t_1, t_2) = \mathbf{G}^<(t_1, t_2) \mathbf{h}^{\text{MF}}(t_2) + \left[ \mathbf{G}^{\text{R}} \cdot \boldsymbol{\Sigma}^< + \mathbf{G}^< \cdot \boldsymbol{\Sigma}^{\text{A}} + \mathbf{G}^{\text{I}} \star \boldsymbol{\Sigma}^{\text{I}} \right] (t_1, t_2), \quad (6.1b)$$

$$i\partial_t \mathbf{G}^{\text{I}}(t, \tau) = \left[ \boldsymbol{\Sigma}^{\text{R}} \cdot \mathbf{G}^{\text{I}} + \boldsymbol{\Sigma}^{\text{I}} \star \mathbf{G}^{\text{M}} \right] (t, \tau). \quad (6.1c)$$

The KBEs (6.1) represent the minimal set of equations to propagate in *two* times; all other components can be constructed by symmetry properties. The operations in the square brackets are convolutions on either the real or the imaginary track. The notation is consistent [E7]. The KBEs (6.1) are an initial-value problems with the boundary conditions

$$\mathbf{G}^{\text{I}}(t_0, \tau) = \mathbf{G}^{\text{M}}(-\tau), \quad \mathbf{G}^<(t_0, t_0) = \mathbf{G}^{\text{M}}(0-), \quad \mathbf{G}^>(t_0, t_0) = \mathbf{G}^{\text{M}}(0+). \quad (6.2)$$

Hence, the Matsubara GF has to be known in advance, reflecting the initial preparation of the system in a grand-canonical ensemble. The time derivatives appearing on the left-hand sides of eqs. (6.1) governs the directionality of the time propagation with respect to the two arguments. The derivative  $\partial_{t_1}$  allows to perform the step  $\mathbf{G}^>(t_1, t_2) \rightarrow \mathbf{G}^>(t_1 + \Delta t, t_2)$  ( $\Delta t$  is the time step when discretizing the derivatives), while the KBE (6.1b) for the lesser GF performs the step  $\mathbf{G}^<(t_1, t_2) \rightarrow \mathbf{G}^<(t_1, t_2 + \Delta t)$ . Using the symmetry  $\mathbf{G}^{\lessgtr}(t_1, t_2) = -\mathbf{G}^{\lessgtr}(t_2, t_1)^\dagger$ , the GFs can be thus found in the complete  $(t_1, t_2)$  plane. The left GF obeying eq. (6.1c) is, on the other hand, propagated in  $t_1$ -direction, while  $\tau$  is treated as a parameter. Fig. 6.1(a) illustrates the solution scheme of the KBEs.

The KBEs describe how an interacting fermionic or bosonic system, which is initially prepared in thermal equilibrium, evolves in time upon external driving that enters the MF Hamiltonian  $\mathbf{h}^{\text{MF}}(t)$ . The explicit appearance of the left/right Keldysh components for both the GFs and the self-energy (which contains the

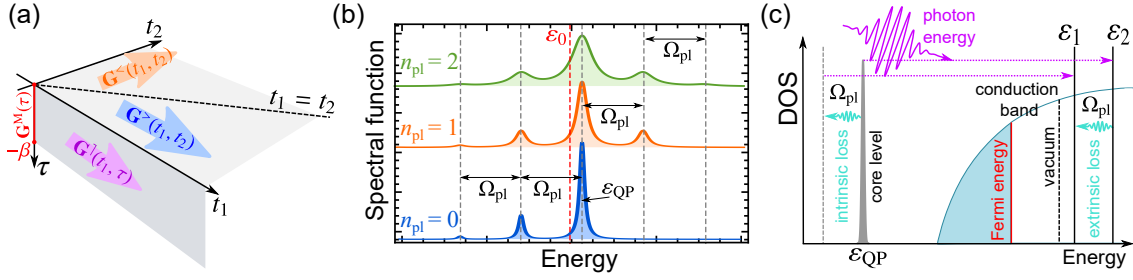


Figure 6.1: (a) Sketch of the solution scheme of the KBEs (6.1). The greater (lesser) GF is propagated in  $t_1$  ( $t_2$ ) direction from the initial point as given by the Matsubara GF, while  $G^<(t_1, \tau)$  is obtained from Matsubara GF as the boundary in the  $t_1$  direction. (b) Typical behavior of the spectral function of the  $S$ -model for different numbers of plasmons in the initial state. (c) Energy scheme of intrinsic and extrinsic plasmon losses for the photoemission from core levels.

full Matsubara GF as boundary conditions) results in the memory of the system of its initial state. As a consequence, the system will return to a thermal equilibrium state, if possible<sup>1</sup> – a dissipation (or dephasing) mechanism is required here. This is typically the case for an open system as encountered in the transport scenario or in extended systems [221]. Note that the reached steady state may depend on the driving history [222].

In full generality, the GFs obtained by solving eqs. (6.1) yield the time-dependent one-body density matrix and time-dependent spectral quantities such as the LDOS (see subsec. 2.5.5). It is clear that the time evolution of such reduced quantities is non-hermitian and entails memory effects [223]. The KBEs thus provide a fundamental description of quantum kinetics, which contains other theories such as, for instance, the Boltzmann equation [70]. In practice, approximations to the correlation part of the self-energy on the right-hand side of eqs. (6.1), which are consistent with the treatment of the Matsubara GF, have to be invoked (see subsec. 2.5.2 for typical approximations). Details of the numerical schemes to solve the KBEs can be found in ref. [71] and in [E7].

## 6.2 E7: Time-dependent many-body treatment of electron-boson dynamics: application to plasmon-accompanied photoemission

Both the typical approximations to the self-energy and the propagation scheme are more or less established for electronic systems, allowing an *ab initio* treatment of atoms and small molecules beyond TDDFT [224–226]. However, less is known for the dynamics of EB systems as introduced in subsec. 2.5.6, where we have already explained their wide range of applications. In view of electron-phonon coupling, where the back-action of the electron dynamics on the phonon subsystem can be disregarded in the usual scenario, the Migdal approximation [105, 106, 159] represents the standard approach, especially in the steady-state regime [227–230]. However, important physical phenomena are missing in this simplified description, such as the polaron formation in the Holstein model [96, 107, 231]. Furthermore, the interaction with bosonic QP excitations on an energy scale comparable to the electrons – as it is typically the case for plasmons – invalidates treating the bosons as frozen. For the advantages the NEGF formalism offers for describing (time-resolved) spectroscopies such as photoemission (see subsec. 3.2.1 and sec. 5.2), treating the appropriate GFs for the electron and bosonic time evolution on equal footing represents an important advance. This is where our – parallel to independent works [232] – pioneering work [E7] comes into play.

The first question that needs to be addressed is how the standard expressions for the self-energy established for the steady-state case translate into a time-dependent scenario. To clarify the subtleties, we have re-derived the counterpart of Hedin’s equations for generalized version of the EB Hamiltonian (2.74) by the source-field method. This provides a systematic way of treating the coupling between the electronic and the bosonic subsystems by corresponding conserving approximations to the self-energy. The parallels to Hedin’s equations for purely fermionic (or bosonic) systems indicate an identical diagrammatic representation of the self-energy. More details on these points are provided by appendix C.

<sup>1</sup>An isolated finite system will, of course, undergo undamped oscillations if a superposition of eigenstates has been excited.

In subsec. 2.5.6 we have already mentioned that EB models represent a very practical way of introducing electron-plasmon interactions. A discussion on the justification is given by appendix C.3. Gaining access to the corresponding dynamics will thus allow for studying the impact of plasmon-accompanied processes on photoemission – which have been a central topic of this thesis – in the time domain. The prototypical model comprising the physics of intrinsic and – with slight extensions – extrinsic plasmon losses is the Lundqvist’s  $S$ -model (see subsec. 2.5.6). It describes a core electron, which is coupled to a single, dispersion-less plasmon mode (frequency  $\Omega_{\text{pl}}$ ) of the conduction band. The Hamiltonian reads

$$\hat{H}_0 = \varepsilon_0 \hat{c}_0^\dagger \hat{c}_0 + \Gamma_0 \hat{c}_0 \hat{c}_0^\dagger \hat{Q} + \frac{1}{2} \Omega_{\text{pl}} (\hat{P}^2 + \hat{Q}^2) . \quad (6.3)$$

It is clear that the coupling between the bosonic and the electronic degrees of freedom vanishes if the core level is occupied; the model thus accommodates intrinsic losses upon photoemission. The spectral function reflecting this process is sketched in fig. 6.1(b). It comprises a QP peak at  $\varepsilon_{\text{QP}} = \varepsilon_0 + \Gamma_0^2 / 2\Omega_{\text{pl}}$  and an infinite series of plasmon satellites. If the core electron is removed from the ground state (no plasmons present:  $n_{\text{pl}} = 0$ ), the photoemission may be direct (originating from the QP) peak or be subject to plasmonic shake-up processes. In the latter case, a part of the energy of the photon is converted into a plasmon; therefore, the corresponding satellite peaks of the spectral function appear at lower energy. In principle, any number  $n_{\text{pl}}$  of plasmon can so be excited, resulting in a infinite series of – with decreasing weights according to a Poisson distribution – plasmon satellites at  $\varepsilon_{\text{QP}} - n_{\text{pl}}\Omega_{\text{pl}}$ . In case  $n_{\text{pl}}$  plasmons are already present in the initial state, transferring their energy to the photoelectron is also possible and reflected by a plasmon satellite on the right-hand side of the QP peak (see fig. 6.1(b)). This plasmon-assisted emission mechanism is closely related to the plasmon-driven photoemission which we have already discussed in sec. 5.4.

Extending the model by adding photoelectron states allows for incorporating extrinsic effects by introducing a coupling operator proportional to the plasmon coordinate  $\hat{Q}$ . A minimal model comprises additionally two photoelectron states with energy  $\varepsilon_1, \varepsilon_2$  (see sketch in fig. 6.1(c)). Besides the no-loss emission from the QP peak (which corresponds to detecting the photoelectron with energy  $\varepsilon_2$ ), there are now two pathways – intrinsic or extrinsic losses – which lead to measuring the photoelectron with reduced energy  $\varepsilon_1 = \varepsilon_2 - \Omega_{\text{pl}}$ . Therefore, quantum interference effects occur [90], which are hard to incorporate into first-principle calculations [233–235]. A better understanding of the interplay of intrinsic and extrinsic losses would hence greatly assist the interpretation of experimental photoemission spectra. How can those two loss channels be disentangled?

In [E7] we suggest to approach this question in the time domain. We consider an EB model similar to the schematic fig. 6.1(c), which delivers a quite realistic picture for the photoemission from core levels in simple metals. In particular, we are motivated by recent attosecond photoemission experiments from the 2p core level in magnesium [116] and adjust the model accordingly. Based on the general treatment of the EB self-energy (discussed above), an efficient propagation scheme of the electron GFs according to the KBEs along with the KBEs for the coordinate-coordinate boson GFs is proposed. The boson correlators – in contrast to the electron case eq. (6.1) – obey a set of *second-order* integro-differential equations (this is also shown in appendix C.2). This reflects the inertia in the plasmon modes associated to the characteristic built-up time scale of screening effects. Computing time-dependent 2PPE spectra (see subsec. 3.2.3), we show that – given suitable parameters of the external laser field – intrinsic losses manifest on a much shorter time scale than extrinsic effects and advocate time-resolved photoemission as a helpful tool to explore the underlying intricacies.



# Time-dependent many-body treatment of electron-boson dynamics: Application to plasmon-accompanied photoemission

M. Schüler,<sup>\*</sup> J. Berakdar, and Y. Pavlyukh

*Institut für Physik, Martin-Luther-Universität Halle-Wittenberg, 06099 Halle, Germany*

(Received 23 October 2015; revised manuscript received 25 January 2016; published 16 February 2016)

Recent experiments access the time-resolved photoelectron signal originating from plasmon satellites in correlated materials and address their buildup and decay in real time. Motivated by these developments, we present the Kadanoff-Baym formalism for the nonequilibrium time evolution of interacting fermions and bosons. In contrast to the fermionic case, the bosons are described by second-order differential equations. Solution of the bosonic Kadanoff-Baym equations—which is the central ingredient of this work—requires substantial modification of the usual two-times electronic propagation scheme. The solution is quite general and can be applied to a number of problems, such as the interaction of electrons with quantized photons, phonons, and other bosonic excitations. Here the formalism is applied to the photoemission from a deep core hole accompanied by plasmon excitation. We compute the time-resolved photoelectron spectra and discuss the effects of *intrinsic* and *extrinsic* electron energy losses and their interference.

DOI: [10.1103/PhysRevB.93.054303](https://doi.org/10.1103/PhysRevB.93.054303)

## I. INTRODUCTION

The impressive advances in the field of time-resolved and, in particular, attosecond metrology [1–4] lead to new insights into the transient electron dynamics in atomic [5], molecular [6], and condensed [7] matter. The attosecond streaking technique, in particular, captures the *time-resolved* photoelectron spectra and thus allows for tracing the pathway of, e.g., plasmon-accompanied photoemission in the time domain [8–10].

Generally, photoemission is an involved process [11] in which several factors are important: the density of states of the unperturbed system, the electron scattering following photoabsorption, and the formation of electron scattering states which are subsequently observed in the detector. The corresponding three stages are known as the classical model of photoemission due to Berglund and Spicer [12]. The last stage is complicated by the presence of long-range Coulomb interaction between the emitted particle and the target. Fortunately, in many cases calculations of the scattering states can be decoupled from the treatment of the many-body effects, which is the main topic of this work.

A deep core hole is created due to the interaction with an XUV photon. The liberated electron interacts with the particle-hole excitations in the conduction band and may also excite collective charge density fluctuations (plasmons). The separation between these scattering mechanisms is only possible in the long wave-length limit where particle-hole excitations shape the threshold profile. The plasmons, by acting as massive bosonic particles, reshape the satellites' features in the spectrum [13]. The latter effect, which is inherently nonequilibrium and known as *extrinsic* losses, should be distinguished from the *intrinsic* losses manifested as, e.g., plasmonic satellites (PSs) in the equilibrium spectral function. The occurrence of quantum interference between these two channels is essential for obtaining accurate photoemission spectra in the vicinity of PSs [14]. A microscopic theory

accounting for intrinsic and extrinsic losses is a challenge even in standard steady-state photoemission theory [15–18], while a time-dependent description is still lacking.

In this work we focus on the time-dependent aspects of photoemission for electronic systems in the case where the interaction is solely mediated by the bosonic excitations. Typical examples are processes involving electron-phonon or electron-photon interactions. Also in pure electronic systems the interaction can often be written in this form: For deep core photoemission the photoelectron at high energies can be treated as a distinguishable particle interacting with the density fluctuations of the system [19]. At metallic densities fluctuations are dominated by plasmonic excitations. This gives rise to the *S*-model originally proposed by Lundqvist [20] and solved by Langreth [13]. Keeping in mind the distinguishability aspect of such a reduction the model can also be applied to more general scenarios such as homogeneous electron gas at metallic densities [21] or solids treated in the plasmon-pole approximation [22]. A sequence of PSs accompanying the main quasiparticle (QP) peak is a generic feature of the density of states of the electron-boson Hamiltonian [23].

A powerful method to deal with time-dependent processes in many body systems is the nonequilibrium Green's function (NEGF) approach. This method provides a link to standard many-body perturbation theory, allowing so for systematic approximation schemes, and also to classical kinetics [24,25]. One important application of the NEGF formalism is the prediction and the interpretation of time- and angular-resolved photoemission spectra (tr-ARPES) [26], a technique that has been employed in recent experiments on ultrafast dynamics of electronic [27] or phononic [28] band structures of correlated materials. Further recent time-resolved experiments such as transient absorption in atoms [5] and transient THz transmission in semiconductors [29,30] are within the scope of the NEGF approach [31–34] as well.

The method relies on solving the equations of motion (EOM) for the Green's functions on the Keldysh time contour [35–37]—the Kadanoff-Baym equations (KBEs)—with a proper choice of the self-energy [38–40], which, in turn, determines the form of the collision integrals. This work

<sup>\*</sup>michael.schueler@physik.uni-halle.de

is devoted to the extension of this formalism to coupled electron-boson Hamiltonians (Sec. II A) and formulation of the bosonic EOM as a second-order equation for massive particles (Sec. II B). The formalism is kept general and is thus applicable to related problems such as pseudoparticles [41], electron-phonon coupling in the steady state [42–46], and time domain [31,47,48], electron-vibron [49,50] or electron-photon [51], or plasmonic nanojunctions [52,53]. In this study we go beyond the frozen boson scheme as often employed for electron-phonon relaxation [31,33,54–56] and treat density oscillations in the system quantum mechanically. Our time-dependent numerical approach (Sec. III) makes it possible to disentangle intrinsic from extrinsic losses in photoemission in a natural way and it complements the steady-state regime studies that have been performed previously [16,17,57–71].

We apply the theory to the time-resolved photoemission from the magnesium  $2p$  core state and discuss the influence of the intrinsic and extrinsic electron-plasmon couplings (Sec. IV). Atomic units are used unless stated otherwise.

## II. THEORY

Our goal is the description of a system of electrons interacting with bosonic QPs that can be emitted or absorbed (sometimes also referred to as quasibosons [14]) and thus mediate an effective electron-electron interaction. As a consequence, the boson propagators must have spectral features that are quite different from (nonrelativistic) electrons: Instead of one QP peak at energy  $\mathcal{E}$ , a bosonic mode with frequency  $\Omega$  is represented by two peaks at  $\pm\Omega$  in the spectral function  $\hat{B}(\omega)$ , corresponding to emission or absorption of the QP, respectively. More generally, this is reflected by the antisymmetry of the boson spectral function  $\hat{B}(\omega) = -\hat{B}^T(-\omega)$ . This is different from that of real bosonic particles (such as atoms with integer nuclear spin) that are not considered here.

The idea of describing the electron-electron interaction in metals by an effective Hamiltonian comprising electronic and bosonic degrees of freedom goes back to Pines and Bohm [72], where it was shown that the collective (long-wavelength) charge density fluctuations (approximately) behave as a harmonic oscillator. Diagrammatically, the long-wavelength regime is captured by the random-phase approximation. For other scenarios other classes of diagrams are relevant (see Ref. [39] for a comparative study).

Second quantization of the density oscillations then leads to the type of electron-boson Hamiltonian discussed below [14,19,73]. Equivalently, the Hamiltonian can be derived from the coupling of electrons to the quantized electromagnetic field [25] within the long-wavelength limit [74]. For nonzero momentum transfer the transversal response as encoded in the correlator of the vector potential function [25] or in the current-current correlation function [75] become important.

### A. Generic Hamiltonian

Let us consider a system characterized by a set of electronic single-particle (SP) states with energies  $\{\mathcal{E}_i\}$  and possessing a number of bosonic modes with corresponding frequencies  $\{\Omega_\nu\}$ . The respective annihilation operators of the electrons (bosons) are denoted by  $\hat{c}_i$  ( $\hat{a}_\nu$ ).

For the electrons we have the noninteracting Hamiltonian

$$\hat{H}_{\text{el}} = \sum_i \mathcal{E}_i \hat{c}_i^\dagger \hat{c}_i, \quad (1)$$

while

$$\hat{H}_{\text{bos}} = \sum_\nu \Omega_\nu \hat{a}_\nu^\dagger \hat{a}_\nu = \frac{1}{2} \sum_\nu \Omega_\nu (\hat{P}_\nu^2 + \hat{Q}_\nu^2) \quad (2)$$

represents the boson Hamiltonian. Instead of working with the bosonic creation or annihilation operators, the coordinate-momentum representation,

$$\hat{Q}_\nu = \frac{1}{\sqrt{2}}(\hat{a}_\nu + \hat{a}_\nu^\dagger), \quad \hat{P}_\nu = \frac{1}{\sqrt{2}i}(\hat{a}_\nu - \hat{a}_\nu^\dagger), \quad (3)$$

is preferred here. Note that electrons and bosons (besides their coupling) are considered as noninteracting here for the sake of clarity. However, additional correlation effects for both subsystems can, in principle, be included without conceptual obstacles.

The electron-boson interaction is taken as

$$\hat{H}_{\text{el-bos}} = \sum_\nu \sum_{ij} \Gamma_{ij}^\nu \hat{c}_i^\dagger \hat{c}_j \hat{Q}_\nu. \quad (4)$$

A coupling where the order of the fermionic operators is interchanged (e.g.,  $\hat{c}_i \hat{c}_j^\dagger$ ) can be treated along the same lines by employing the anticommutator relation  $\hat{c}_i \hat{c}_j^\dagger = \delta_{ij} - \hat{c}_j^\dagger \hat{c}_i$ . The remaining term arising due to the Kronecker  $\delta$ ,  $\sum_{\nu,i} \Gamma_{ii}^\nu \hat{Q}_\nu$  can be removed by shifting bosonic coordinates.

Furthermore, we account for environmental effects such as particle exchange and line broadening by including additional baths. In analogy, we define the environment SP states by the energies  $\{\epsilon_k\}$ , whereas the bosonic bath is characterized by the frequencies  $\{\omega_\alpha\}$ :

$$\hat{H}_{\text{el}}^{\mathcal{B}} = \sum_k \epsilon_k \hat{d}_k^\dagger \hat{d}_k, \quad \hat{H}_{\text{bos}}^{\mathcal{B}} = \frac{1}{2} \sum_\alpha \omega_\alpha (\hat{p}_\alpha^2 + \hat{q}_\alpha^2). \quad (5)$$

The bosonic bath operators  $\hat{p}_\alpha$ ,  $\hat{q}_\alpha$  are defined analogous to Eq. (3), while  $\hat{d}_k$  denotes the annihilation operators with respect to the electron bath. The coupling of the electron-boson system to the environmental degrees of freedom is described by the embedding Hamiltonians

$$\hat{H}_{\text{el-em}} = \sum_{i,k} (V_{ik} \hat{c}_i^\dagger \hat{d}_k + \text{H.c.}) \quad (6)$$

and

$$\hat{H}_{\text{bos-em}} = \sum_{\alpha,\nu} \gamma_{\alpha,\nu} \hat{Q}_\nu \hat{q}_\alpha. \quad (7)$$

The total static Hamiltonian thus reads

$$\hat{H}_0 = \hat{H}_{\text{el}} + \hat{H}_{\text{bos}} + \hat{H}_{\text{el-bos}} + \hat{H}_{\text{el}}^{\mathcal{B}} + \hat{H}_{\text{bos}}^{\mathcal{B}} + \hat{H}_{\text{el-em}} + \hat{H}_{\text{bos-em}}. \quad (8)$$

For later convenience we also introduce

$$\hat{H}'_0(t) = \hat{H}_{\text{el}} + \hat{H}_{\text{bos}} + s(t) \hat{H}_{\text{int}}, \quad (9)$$

where  $\hat{H}_{\text{int}}$  comprises all the interacting contributions from Eq. (8). The modified Hamiltonian (9) makes it possible, by choosing a suitable functional form for the scaling factor  $s(t)$ , to “switch on” the interaction adiabatically in order to obtain

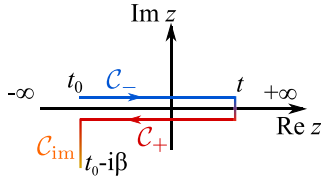


FIG. 1. The general contour  $C$  consisting of the forward branch  $C_-$  on the real axis, the backward branch  $C_+$ , and the imaginary branch  $C_{\text{im}}$ . The arrows indicate the direction of the contour ordering.  $\beta$  denotes the inverse temperature.

fully correlated eigenstates of  $\hat{H}_0$ , while  $s \equiv 1$  retrieves the static case.

To account for the light-matter interaction, we introduce

$$\hat{H}_{\text{el-L}}(t) = \sum_{ij} F_{ij}(t) \hat{c}_i^\dagger \hat{c}_j + \text{H.c.}, \quad (10)$$

where  $F_{ij}(t)$  comprise the transition matrix elements and the time-dependent field. There is no direct coupling of light to bosonic excitations in the minimal coupling scheme. The total time-dependent Hamiltonian is then given by

$$\hat{H}(t) = \hat{H}_0(t) + \hat{H}_{\text{el-L}}(t). \quad (11)$$

### B. Equations of motion

To treat photoemission for the system described by the Hamiltonian (11), we proceed in a standard way by considering the one-particle fermionic and bosonic Green's functions [18,76]. Transient optical absorption requires the use of more complicated two-particle Green's functions [34,77,78] and is outside of the scope of this paper.

Thus, let us introduce the electron GF:

$$G_{ij}(z_1, z_2) = -i \langle \mathcal{T} \hat{c}_i(z_1) \hat{c}_j^\dagger(z_2) \rangle. \quad (12)$$

Here  $z_1$  and  $z_2$  are time arguments on the general contour  $C$  [79] (sketched in Fig. 1), while  $\mathcal{T}$  represents the corresponding contour-ordering operator. All operators are represented in a contour Heisenberg picture. The average  $\langle \dots \rangle$  refers to an initial ensemble of eigenstates of the Hamiltonian  $\hat{H}^M$ . Typical choices here are (i)  $\hat{H}^M = \hat{H}_0 - \mu \hat{n}_{\text{el}}$  ( $\hat{n}_{\text{el}}$  is the electron number operator) or (ii)  $\hat{H}^M = \hat{H}_{\text{el}} + \hat{H}_{\text{bos}} - \mu \hat{n}_{\text{el}}$ . Case (i) prepares the system in an ensemble with initial correlation, whereas in (ii) the noninteracting and thus known basis is used as a reference. Adiabatic switching can then be employed to obtain a correlated state by turning on the interaction along the real time axis [37]. Note that the chemical potential for the bosons is assumed to be zero as, in principle, an infinite number of them can be created.

Next we define the bosonic GF—the coordinate-coordinate correlator—according to

$$\begin{aligned} D_{\mu\nu}(z_1, z_2) &= -i [\langle \mathcal{T} \hat{Q}_\mu(z_1) \hat{Q}_\nu(z_2) \rangle - \langle \hat{Q}_\mu(z_1) \rangle \langle \hat{Q}_\nu(z_2) \rangle] \\ &= -i \langle \Delta \hat{Q}_\mu(z_1) \Delta \hat{Q}_\nu(z_2) \rangle, \end{aligned} \quad (13)$$

with the fluctuation operator  $\Delta \hat{Q}_\nu(z) = \hat{Q}_\nu(z) - \langle \hat{Q}_\nu(z) \rangle$ . Likewise, the momentum-coordinate,

$$D_{\mu\nu}^{PQ}(z_1, z_2) = -i [\langle \mathcal{T} \hat{P}_\mu(z_1) \hat{Q}_\nu(z_2) \rangle - \langle \hat{P}_\mu(z_1) \rangle \langle \hat{Q}_\nu(z_2) \rangle], \quad (14)$$

and momentum-momentum correlators,

$$D_{\mu\nu}^{PP}(z_1, z_2) = -i [\langle \mathcal{T} \hat{P}_\mu(z_1) \hat{P}_\nu(z_2) \rangle - \langle \hat{P}_\mu(z_1) \rangle \langle \hat{P}_\nu(z_2) \rangle], \quad (15)$$

can be defined. We demonstrate below that they are not required for the propagation of  $D_{\mu\nu}(z_1, z_2)$ , but are necessary if one is interested in observables such as the boson occupation number.

In order to elucidate the features of the respective self-energies related to the explicit time dependence, we have rederived the EOM using the source-field method [80]. The full derivation is presented in Appendix A. Here we recapitulate the key points.

The electron GF (represented as matrix) obeys, as usual,

$$\begin{aligned} \left[ i \frac{\partial}{\partial z_1} \mathbf{I} - \mathbf{h}^{\text{MF}}(z_1) \right] \mathbf{G}(z_1, z_2) \\ = \mathbf{I} \delta(z_1, z_2) + \int_C dz_3 \mathbf{\Sigma}(z_1, z_3) \mathbf{G}(z_3, z_2). \end{aligned} \quad (16)$$

The self-energy, comprising many-body effects due to the electron-boson interaction and the coupling to the environment, appears as a mean-field (MF) contribution incorporated into the MF Hamiltonian  $\mathbf{h}^{\text{MF}}$ ,

$$h_{ik}^{\text{MF}}(z) = \mathcal{E}_i \delta_{ik} + F_{ik}(z) + s(z) \sum_v \Gamma_{ik}^v \langle \hat{Q}_v(z) \rangle, \quad (17)$$

and as the time nonlocal correlation self-energy.

The EOM for the boson propagator  $D_{\mu\nu}(z_1, z_2)$  can be derived (details in Appendix A) from the Heisenberg EOM for position and momentum operators:

$$\frac{d}{dz} \hat{Q}_v(z) = \Omega_v \hat{P}_v(z), \quad (18)$$

$$\begin{aligned} \frac{d}{dz} \hat{P}_v(z) &= -\Omega_v \hat{Q}_v(z) - s(z) \sum_{ij} \Gamma_{ij}^v \hat{c}_i^\dagger(z) \hat{c}_j(z) \\ &\quad - s(z) \sum_\alpha \gamma_{\alpha,v} \hat{q}_\alpha(z). \end{aligned} \quad (19)$$

They show that the first-order equation for  $D_{\mu\nu}(z_1, z_2)$  involves momentum-position correlators  $D_{\mu\nu}^{PQ}$  and can only be closed as a second-order equation. The notion of the (bosonic) self-energy  $\Pi_{\mu\nu}(z_1, z_2)$ , in the same spirit as for electronic GFs, results from closing the EOM. Gathering environmental and polarization effects into  $\Pi_{\mu\nu}(z_1, z_2)$ , the contour EOM for the boson GF reads

$$\begin{aligned} -\frac{1}{\Omega_v} \left( \frac{\partial^2}{\partial z_1^2} + \Omega_v^2 \right) D_{\mu\nu}(z_1, z_2) \\ = \delta_{\mu\nu} \delta(z_1, z_2) + \sum_\xi \int_C dz_3 \Pi_{\mu\xi}(z_1, z_3) D_{\xi\nu}(z_3, z_2). \end{aligned} \quad (20)$$

In contrast to the electron case (16), the boson propagators are subject to a second-order EOM.

For examining the spectral properties, we define the different Keldysh components depending on which branch of the contour (Fig. 1) the arguments  $(z_1, z_2)$  are located (we adopt the conventions from Ref. [79]). For example, the greater/lesser boson GF  $D_{\mu\nu}^{\gtrless}(t_1, t_2)$  corresponds to  $D_{\mu\nu}(z_1, z_2)$  with  $z_1 =$



$t_1 \in C_{\pm}$  and  $z_2 = t_2 \in C_{\mp}$ . In equilibrium,  $D_{\mu\nu}^{\geq}(t_1, t_2)$  depends on  $t_1 - t_2$  only, allowing to perform the Fourier transformation  $D_{\mu\nu}^{\geq}(\omega) = \int_{-\infty}^{\infty} dt e^{i\omega t} D_{\mu\nu}^{\geq}(t)$ . For instance, the resulting spectral function for the noninteracting case  $\Pi_{\mu\nu} = 0$  reads  $b_{\mu\nu}(\omega) = \pi \delta_{\mu\nu} [\delta(\omega - \Omega_{\nu}) - \delta(\omega + \Omega_{\nu})]$ . The appearance of the two peaks is a consequence of the second-order EOM Eq. (20). Further properties of the boson propagators are summarized in Appendix B.

As detailed in Appendix A, the expression for the electron self-energy due to the electron-boson interaction is given by

$$\begin{aligned} \Sigma_{ij}^{\text{el-bos}}(z_1, z_2) &= i s(z_1) \sum_{\mu\nu} \sum_{nk} \sum_{ab} \Gamma_{ik}^{\mu} \Gamma_{ab}^{\nu} \int_C d(z_3 z_5) G_{kn}(z_1, z_3) \\ &\quad \times \Lambda_{njab}(z_3, z_2; z_5) D_{\mu\nu}(z_5, z_1^+) s(z_5), \end{aligned} \quad (21)$$

where  $\Lambda_{njab}$  denotes the three-point vertex function obeying the standard Bethe-Salpeter equation (BSE) with the four-point kernel  $K_{abcd}(z_1, z_2; z_3, z_4) = \delta \Sigma^{\text{el-bos}}(z_1, z_2) / \delta G_{cd}(z_3, z_4)$  obtained from the functional derivative of the self-energy with respect to the electron GF (details in Appendix A). The bosonic self-energy is determined by the electron (irreducible) polarization,

$$\begin{aligned} P_{abcd}(z_1, z_2) &= -i \sum_{pq} \int_C d(z_3 z_4) G_{ap}(z_1, z_3) G_{qb}(z_4, z_1^+) \Lambda_{pqcd}(z_3, z_4; z_2), \end{aligned} \quad (22)$$

by

$$\Pi_{\mu\nu}^{\text{p}}(z_1, z_2) = s(z_1) s(z_2) \sum_{abcd} \Gamma_{ba}^{\mu} P_{abcd}(z_1, z_2) \Gamma_{cd}^{\nu}. \quad (23)$$

The simplest possible conserving approximation [81] emerges from invoking the zeroth-order approximation to the vertex function, that is,

$$\Lambda_{abcd}(z_1, z_2; z_3) = \delta_{ac} \delta_{bd} \delta(z_1, z_2) \delta(z_1, z_3). \quad (24)$$

Analogously to Hedin's equations for electronic systems (Fig. 2), we designate the resulting second-order (in  $\Gamma$ ) approximations to both the electron and the boson self-energy as  $GW$  approximation:

$$\Sigma^{(2)}(z_1, z_2) = i s(z_1) s(z_2) \sum_{\mu\nu} \Gamma^{\mu} \mathbf{G}(z_1, z_2) \Gamma^{\nu} D_{\mu\nu}(z_1, z_2), \quad (25a)$$

$$\Pi_{\mu\nu}^{(2)}(z_1, z_2) = -i s(z_1) s(z_2) \text{Tr}[\Gamma^{\mu} \mathbf{G}(z_1, z_2) \Gamma^{\nu} \mathbf{G}(z_2, z_1)]. \quad (25b)$$

The contribution to the respective self-energies arising from the environmental coupling (embedding self-energies) are expressed in the standard way in terms of the bath propagators for electrons,

$$\Sigma_{ij}^{\text{em}}(z_1, z_2) = s(z_1) s(z_2) \sum_k V_{ik} V_{kj}^* g_k^{\mathcal{B}}(z_1, z_2), \quad (26)$$

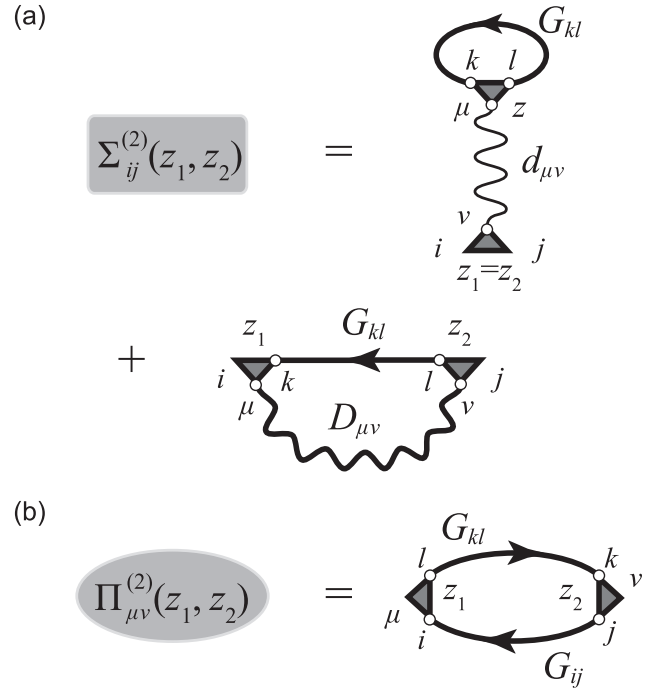


FIG. 2. Approximations for the fermionic (a) and bosonic (b) self-energy operators employed in this work. All self-energies are of the second order in  $\Gamma^{\mu}$  and are expressed in terms of full electronic  $\mathbf{G}$  and bare  $d_{\mu\nu}$  and full  $D_{\mu\nu}$  boson propagators. The first term in the fermionic self-energy is local in time and therefore is included [see Eq. (17)] in MF Hamiltonian  $\mathbf{h}^{\text{MF}}$ .

and for bosons

$$\Pi_{\nu}^{\text{em}}(z_1, z_2) = s(z_1) s(z_2) \sum_{\alpha} |\gamma_{\alpha, \nu}|^2 d_{\alpha}^{\mathcal{B}}(z_1, z_2). \quad (27)$$

Here  $g_k^{\mathcal{B}}$  and  $d_{\alpha}^{\mathcal{B}}$  are the bare GFs of the respective baths. It should be noted that here the bosonic embedding self-energy is labeled by a single mode index  $\nu$ . In general, nondiagonal terms can occur due to indirect coupling via the bath. Thus, Eq. (27) relies on the assumption that such effects can be neglected. As usual, the full self-energy is obtained by summing the system and the bath contributions, that is,  $\Sigma = \Sigma^{\text{el-bos}} + \Sigma^{\text{em}}$  and  $\Pi_{\mu\nu} = \Pi_{\mu\nu}^{\text{p}} + \Pi_{\mu\nu}^{\text{em}}$ , respectively.

Equation (20) for the coordinate-coordinate correlator  $D_{\mu\nu}(z_1, z_2)$  is not sufficient to fully describe the bosonic dynamics, as the MF Hamiltonian (17) explicitly depends on  $\langle \hat{Q}_{\nu}(z) \rangle$  [this quantity cannot be inferred from  $D_{\mu\nu}(z_1, z_2)$ ]. An additional EOM is therefore required and can be derived from Eqs. (18) and (19). Eliminating the bath amplitudes  $\hat{q}_{\alpha}(z)$  by the standard embedding technique, one obtains

$$\begin{aligned} & -\frac{1}{\Omega_{\nu}} \left( \frac{\partial^2}{\partial z^2} + \Omega_{\nu}^2 \right) \langle \hat{Q}_{\nu}(z) \rangle \\ &= -i \text{Tr}[\Gamma^{\nu} \mathbf{G}(z, z^+)] + \int_C d\bar{z} \Pi_{\nu}^{\text{em}}(z, \bar{z}) \langle \hat{Q}_{\nu}(\bar{z}) \rangle. \end{aligned} \quad (28)$$

The EOM (16), (20), (28) for the quantities on the contour is to be solved together with the Kubo-Martin-Schwinger (KMS) boundary conditions [82]. For Eq. (28) this implies that the solution is separated into a boundary-value problem for

$z = -i\tau \in C_{\text{im}}$ , as  $\langle \hat{Q}_v(0) \rangle = \langle \hat{Q}_v(-i\beta) \rangle$ , whereas for  $z \in C_{\pm}$  Eq. (28) represents an initial-value problem.

In the absence of environmental coupling (i.e.,  $\Pi_v^{\text{em}} = 0$ ), Eq. (28) can be solved in terms of the noninteracting boson propagators  $d_v(z_1, z_2)$ , yielding

$$\langle \hat{Q}_v(z) \rangle = -i \int_C d\bar{z} d_v(z, \bar{z}) \text{Tr}[\Gamma^v \mathbf{G}(\bar{z}, \bar{z}^+)]. \quad (29)$$

Substituting Eq. (29) back into the MF Hamiltonian (17), we obtain the first diagram depicted in Fig. 2(a). Thus, the first-order (in  $\Gamma^v$ ) MF expression has been transformed to a (formally) second-order self-energy, which is often referred to as Hartree term [44,83]. We stress that this transition is not possible in the presence of a bosonic bath ( $\Pi_v^{\text{em}} \neq 0$ ). The MF part is hence kept in the more general form Eq. (17). This is analogous to Ref. [84].

Furthermore, propagating the boson amplitude  $\langle \hat{Q}_v(z) \rangle$  is necessary for computing the boson occupation number  $N_v$ :

$$\begin{aligned} N_v(z) &= \langle \hat{a}_v^\dagger(z) \hat{a}_v(z) \rangle = \frac{1}{2} [\langle \hat{P}_v(z)^2 \rangle + \langle \hat{Q}_v(z)^2 \rangle - 1] \\ &= \frac{i}{2} [D_{vv}(z, z^+) + D_{vv}^{PP}(z, z^+)] \\ &\quad + \frac{1}{2} [\langle \hat{P}_v(z)^2 \rangle + \langle \hat{Q}_v(z)^2 \rangle - 1]. \end{aligned} \quad (30)$$

### III. NUMERICAL IMPLEMENTATION

In this section we revisit the formulation of the KBE from the contour EOM. Since the general solution strategy in the case of the electron GFs is quite established [35–37], we keep the discussion brief and rather focus on the modifications to be made for calculating the bosonic time evolution.

Together with the corresponding adjoint EOM, Eqs. (16) and (20) represent the KBEs for the coupled electron-boson system that needs to be solved along with Eq. (28). For a numerical approach, the general complex contour arguments are mapped onto observable times by splitting the general GFs into their respective Keldysh components. Let us introduce the convolution operations

$$[f \cdot g](t, t') \equiv \int_{t_0}^{\infty} d\bar{t} f(t, \bar{t}) g(\bar{t}, t'), \quad (31)$$

$$[f \star g](t, t') \equiv -i \int_0^{\beta} d\bar{t} f(t, \bar{t}) g(\bar{t}, t'). \quad (32)$$

Applying the Langreth rules [79], the KBEs for the greater/lesser electron GF become

$$i \frac{\partial}{\partial t_1} \mathbf{G}^{\gtrless}(t_1, t_2) = \mathbf{h}^{\text{MF}}(t_1) \mathbf{G}^{\gtrless}(t_1, t_2) + \mathbf{X}_L^{\gtrless}(t_1, t_2), \quad (33a)$$

$$-i \frac{\partial}{\partial t_2} \mathbf{G}^{\gtrless}(t_1, t_2) = \mathbf{G}^{\gtrless}(t_1, t_2) \mathbf{h}^{\text{MF}}(t_2) + \mathbf{X}_R^{\gtrless}(t_1, t_2), \quad (33b)$$

$$i \frac{\partial}{\partial t} \mathbf{G}^{\text{I}}(t, \tau) = \mathbf{h}^{\text{MF}}(t) \mathbf{G}^{\text{I}}(t, \tau) + \mathbf{X}_L^{\text{I}}(t, \tau), \quad (33c)$$

with the standard collision integrals

$$\mathbf{X}_L^{\gtrless}(t_1, t_2) = [\Sigma^{\text{R}} \cdot \mathbf{G}^{\gtrless} + \Sigma^{\gtrless} \cdot \mathbf{G}^{\text{A}} + \Sigma^{\text{I}} \star \mathbf{G}^{\text{I}}](t_1, t_2), \quad (34a)$$

$$\mathbf{X}_R^{\gtrless}(t_1, t_2) = [\mathbf{G}^{\text{R}} \cdot \Sigma^{\gtrless} + \mathbf{G}^{\gtrless} \cdot \Sigma^{\text{A}} + \mathbf{G}^{\text{I}} \star \Sigma^{\text{I}}](t_1, t_2), \quad (34b)$$

$$\mathbf{X}_L^{\text{I}}(t, \tau) = [\Sigma^{\text{R}} \cdot \mathbf{G}^{\text{I}} + \Sigma^{\text{I}} \star \mathbf{G}^{\text{M}}](t, \tau). \quad (34c)$$

Similarly to Eq. (33), one finds the KBEs for the boson propagators,

$$-\frac{1}{\Omega_\mu} \left( \frac{\partial^2}{\partial t_1^2} + \Omega_\mu^2 \right) D_{\mu\nu}^{\gtrless}(t_1, t_2) = Y_{L,\mu\nu}^{\gtrless}(t_1, t_2), \quad (35a)$$

$$-\frac{1}{\Omega_\nu} \left( \frac{\partial^2}{\partial t_2^2} + \Omega_\nu^2 \right) D_{\mu\nu}^{\gtrless}(t_1, t_2) = Y_{R,\mu\nu}^{\gtrless}(t_1, t_2), \quad (35b)$$

$$-\frac{1}{\Omega_\mu} \left( \frac{\partial^2}{\partial t^2} + \Omega_\mu^2 \right) D_{\mu\nu}^{\text{I}}(t, \tau) = Y_{L,\mu\nu}^{\text{I}}(t, \tau), \quad (35c)$$

where the collision integrals are obtained by applying the Langreth rules analogously as in Eq. (34). The symmetry properties of the GFs (and of the respective self-energies) lead to similar relations for the collision integrals:

$$\mathbf{X}_L^{\gtrless}(t_1, t_2) = -[\mathbf{X}_R^{\gtrless}(t_2, t_1)]^\dagger, \quad Y_{L,\mu\nu}^{\gtrless}(t_1, t_2) = -[Y_{R,\nu\mu}^{\gtrless}(t_2, t_1)]^*.$$

Let us now assume that the Matsubara GF for both electrons [ $\mathbf{G}^{\text{M}}(\tau)$ ] and bosons [ $D_{\mu\nu}^{\text{M}}(\tau)$ ] has been determined by solving the respective Matsubara Dyson equation. Note that the solution has to be carried out self-consistently with the EOM for the boson amplitude [Eq. (28)]. From the KMS conditions one finds

$$\begin{aligned} &\frac{1}{\Omega_\nu} \left( \frac{d^2}{d\tau^2} - \Omega_\nu^2 \right) Q_\nu^{\text{M}}(\tau) \\ &= -i \text{Tr}[\Gamma^v \mathbf{G}^{\text{M}}(0)] + [\Pi_v^{\text{em,M}} \star Q_\nu^{\text{M}}](\tau). \end{aligned} \quad (36)$$

Here  $Q_\nu^{\text{M}}(\tau) = \langle \hat{Q}_v(t_0 - i\tau) \rangle$ . Solving the imaginary track  $C_{\text{im}}$  is straightforward if one discards initial correlations, as done in the adiabatic switching method. Once the GFs at  $t_0$  have been initialized from the Matsubara components, Eqs. (33) and (35) can be propagated for real times together with the boson amplitude,

$$\begin{aligned} &-\frac{1}{\Omega_\nu} \left( \frac{d^2}{dt^2} + \Omega_\nu^2 \right) \langle \hat{Q}_v(t) \rangle \\ &= -i \text{Tr}[\Gamma^v \mathbf{G}^<(t, t)] + [\Pi_v^{\text{em,R}} \cdot \langle \hat{Q}_v \rangle](t). \end{aligned} \quad (37)$$

The KBEs (33) for the electrons can be solved by standard techniques. Specifically, we implemented a predictor-corrector Heun method similar to Ref. [85]. Equation (33a) is used for propagating  $\mathbf{G}^>(t_1, t_2)$  for  $t_1 > t_2$ , while  $\mathbf{G}^<(t_1, t_2)$  is obtained from Eq. (33b) for  $t_1 < t_2$  [see Fig. 3(a)]. Equations (33) are combined at  $t_1 = t_2 = t$  into the time-diagonal EOM,

$$i \frac{d}{dt} \mathbf{G}^<(t, t) = [\mathbf{h}^{\text{MF}}(t), \mathbf{G}^<(t, t)] + [\mathbf{X}_L^<(t, t) + \text{H.c.}]. \quad (38)$$

For propagating the boson KBEs (35) we have chosen the Numerov method, as it provides a fourth-order scheme with minimal number of function evaluations for this specific type of differential equations. Generally, the method

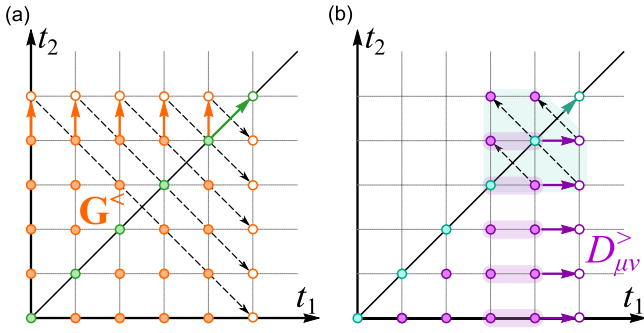


FIG. 3. Propagation scheme for solving the KBEs Eqs. (33) and (35). The time coordinates are discretized into a uniform mesh  $\{t_n\}$ , such that discrete-difference approximations can be applied to the derivatives. (a) Solution scheme for the electron KBEs.  $\mathbf{G}^<(t_k, t_{n+1})$  is computed from (33b) (orange arrows). Analogously,  $\mathbf{G}^>(t_n, t_k)$  is obtained from Eq. (33a) in the lower part of the time plane. Equation (38) is used for propagating on the time diagonal (green arrows). (b) Propagation method for the boson KBEs:  $D_{\mu\nu}^>(t_{n+1}, t_k)$ ,  $k \leq n$ , is determined from  $D_{\mu\nu}^>(t_{n-1}, t_k)$  and  $D_{\mu\nu}^>(t_n, t_k)$ , while the diagonal points are obtained from the surrounding grid points by a partial differential equation (see text). Symmetry relations between of greater/lesser components are denoted by dashed arrows.

applies to

$$\left[ \frac{d^2}{dt^2} + W(t) \right] F(t) = S(t), \quad (39)$$

which is transformed (after equidistant discretization  $t_{n+1} - t_n = \Delta t$ ) into the recursive relation

$$\tilde{F}_{n+1} - U_n \tilde{F}_n + \tilde{F}_{n-1} = \frac{\Delta t^2}{12} (S_{n+1} + 10S_n + S_{n-1}). \quad (40)$$

Here  $S_n = S(t_n)$ ,  $\tilde{F}_n = (1 - T_n)F(t_n)$ ,  $U_n = (2 + 10T_n)/(1 - T_n)$  and  $T_n = -(\Delta t^2/12)W(t_n)$ . When applying the Numerov method to the KBEs (35),  $S(t)$  plays the role of the collision integral. From Eq. (40) we see that  $S(t_{n+1})$  required to perform the step  $t_n \rightarrow t_{n+1}$  is unknown at this point (similar to the Heun propagation scheme). However, as  $S(t_n)$  carries the dominant weight, we can substitute  $(S_{n+1} + 10S_n + S_{n-1}) \approx 12S_n$  when executing  $t_n \rightarrow t_{n+1}$  for the first time. The precision of Eq. (40) is thereby reduced from fourth to second order. Once the boson propagators are known up to  $t_1, t_2 \leq t_{n+1}$ , the new collision integrals can be computed and the time step  $t_n \rightarrow t_{n+1}$  can be carried out in fourth order according to Eq. (40). The analogous strategy applies to Eq. (37). We combine this corrector step with the one needed for propagating the electron GF, as the electron (boson) self-energy depends on the boson (electron) GF, and iterate until self-consistency at each time step is achieved.

There is no need for computing  $D_{\mu\nu}^<(t_1, t_2)$  for  $t_1 < t_2$  from Eq. (35b), as  $D_{\mu\nu}^<(t_1, t_2) = D_{\nu\mu}^>(t_2, t_1) = -[D_{\mu\nu}^>(t_1, t_2)]^*$  (cf. Appendix B). Therefore, the propagation scheme can be restricted to the lower time half plane  $t_2 \leq t_1$  for the greater boson correlator [see Fig. 3(b)]. At variance with the electron KBEs it is not possible to formulate the time-diagonal EOM in the form of Eq. (38), as it relies on the notion of first derivatives. We solve this issue by adding Eqs. (35a) and (35b) to obtain

the Poisson-type equation

$$-\frac{1}{\Omega_\mu + \Omega_\nu} \left( \frac{\partial^2}{\partial t_1^2} + \frac{\partial^2}{\partial t_2^2} + \Omega_\mu^2 + \Omega_\nu^2 \right) D_{\mu\nu}^>(t_1, t_2) = Z_{\mu\nu}^>(t_1, t_2), \quad (41)$$

$$(\Omega_\mu + \Omega_\nu) Z_{\mu\nu}^>(t_1, t_2) = \Omega_\mu Y_{L,\mu\nu}^>(t_1, t_2) + \Omega_\nu Y_{R,\mu\nu}^>(t_1, t_2). \quad (42)$$

Next we apply the two-dimensional extension of the Numerov method (see Appendix C), expressing the Laplacian  $\nabla_{t_1, t_2}^2 D_{\mu\nu}^>(t_n, t_n)$  by the nine surrounding grid points  $D_{\mu\nu}^>(t_{n+i}, t_{n+j})$ ,  $i, j = -1, 0, 1$ . The resulting equation can then be solved for  $D_{\mu\nu}^>(t_{n+1}, t_{n+1})$  [sketched in Fig. 3(b)]. Similar to the one-dimensional case, the right-hand side of Eq. (41) has to be known at all these time points as well in order to achieve fourth order. Analogously, we can approximate  $Z_{\mu\nu}^>(t_{n+i}, t_{n+j})$  ( $i, j = -1, 0, 1$ ) by  $Z_{\mu\nu}^>(t_n, t_n)$  when carrying out  $D_{\mu\nu}^>(t_n, t_n) \rightarrow D_{\mu\nu}^>(t_{n+1}, t_{n+1})$  for the first time (predictor step) and apply several corrector steps after computing  $Z_{\mu\nu}^>(t_{n+1}, t_{n+1})$ .

Collision integrals are computed by either Durand's rule (even number of grid points) or Simpson's rule (odd number of points). The momentum-momentum correlator required for calculating the boson occupation Eq. (30) is obtained from the mixed derivative  $\Omega_\mu \Omega_\nu D_{\mu\nu}^{PP, >}(t, t') = [\partial_t \partial_{t'} D_{\mu\nu}^>(t, t')]_{t=t'}$ .

#### IV. APPLICATION TO PHOTOEMISSION FROM MAGNESIUM $2p$ CORE STATE

In order to illustrate our propagation method for coupled electron-boson Hamiltonians and, furthermore, explore the physics of such systems in the time domain, we apply the theory developed in Sec. II to a typical process described by the  $S$ -model: the photoemission from a deep core state.

In particular, we consider bulk Mg, a system where recent attosecond streaking experiments [9] were able to measure the time delay of photoemission between to the  $2p$  core state and the corresponding PS. The system is modeled by the Hamiltonian (11) with the static part Eq. (8). We account for the  $2p$  state,  $\mathcal{E}_{i=2p}$  and two virtual states  $\mathcal{E}_{i=k_{1,2}}$  representing photoelectrons, which is inspired by the minimal treatment of electronic states in the density matrix approach to time-resolved two-photon photoemission [86]. We consider one boson mode (bulk plasmon) with energy  $\Omega_{\text{pl}} \simeq 10$  eV (subscript  $\nu$  is dropped). This mode provides the dominant contribution to the scattering channels for the emanating photoelectrons [87]. The excitation of surface plasmons on the other hand is suppressed as the photoelectrons are generated relatively deep within the sample for the energy scale considered here. Furthermore, the energy and momentum conservation imposes restrictions on the momentum  $q$  of density fluctuations from which the photoelectrons may scatter [9]. For small  $q$ , the plasmon dispersion can be neglected, reducing the excitation channels to the incorporated bulk plasmon mode. For the electron-plasmon interaction (4) we distinguish intrinsic ( $\Gamma_{\text{in}}$ ) and extrinsic ( $\Gamma_{\text{ex}}$ ) mechanisms:

$$\hat{H}_{\text{el-pl}} = \Gamma_{\text{in}} \hat{c}_{2p} \hat{c}_{2p}^\dagger \hat{Q} + \sum_{i,j \neq 2p} (\Gamma_{\text{ex}})_{ij} \hat{c}_i^\dagger \hat{c}_j \hat{Q}. \quad (43)$$

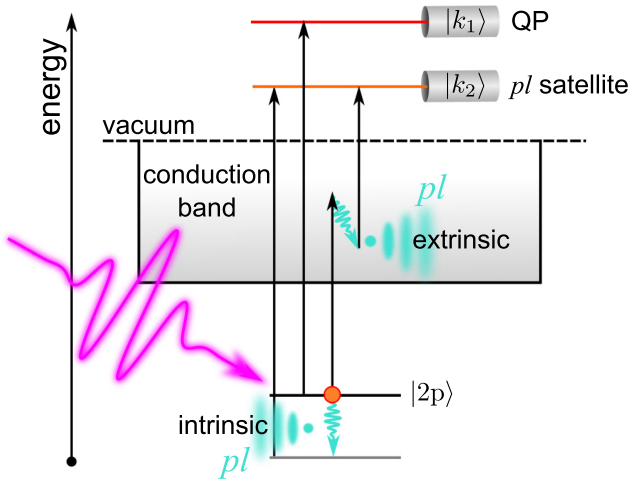


FIG. 4. Sketch of the model system for photoemission from the Mg  $2p$  core state. Besides the core level  $|2p\rangle$  the model comprises two continuum states  $|k_{1,2}\rangle$  at fixed detector energy and the intrinsic and extrinsic scattering channels upon plasmon generation. The energy  $\mathcal{E}_{k_1}$  is adjusted to the emission from the QP peak, while the energy  $\mathcal{E}_{k_2}$  selects the emission from the first plasmon satellite.

The latter accommodate postemission effects, that is inelastic scattering of the emerging photoelectron from the electron sea upon converting a part of their energy into a plasmon. The ingredients to the model are illustrated in Fig. 4.

The  $S$ -model describes two phenomena: Upon x-ray absorption, an excited core electron loses a part of its energy and excites a plasmon. This process is manifested as a sequence of PSs in the spectral function occurring at lower energies. For fixed detector energy, larger photon energy is needed to produce a photoelectron from PS as compared to QP. In the reciprocal process the core hole is filled upon emitting an x-ray photon. This process can be again accompanied by creating plasmons, such that the electron loses a part of its energy and emits a photon with smaller energy when recombining. For brevity we denote PSs at lower (higher) energies as  $PS^-$  ( $PS^+$ ). Furthermore, the position of the QP peak  $\mathcal{E}_{QP}$  is shifted by  $\Gamma_{in}^2/2\Omega_{pl}$  (correlation shift) [74] to larger energy with respect to the noninteracting value  $\mathcal{E}_{2p}$  when the core state is occupied, whereas  $\mathcal{E}_{QP} = \mathcal{E}_{2p} - \Gamma_{in}^2/2\Omega_{pl}$  for the empty core state. The spectral functions for the two scenarios are shown in Fig. 5(a).

#### A. Time-dependent spectral function

It is now interesting to investigate the time evolution in an intermediate case, where the initially occupied  $2p$  state is partially photoionized, in real time. The spectral function is expected to reorganize transiently, showing (i) a shift of the QP peak and (ii) appearance of plasmonic satellites ( $PS^+$ ). The energetic position of these features in the spectral function varies in time primarily reflecting changes in the core state occupation and in the number of bosons in the system.

We solved the KBEs Eqs. (33) and (35) with the algorithm from Sec. III. Instead of initializing with the interacting Matsubara GFs, we switch on the interaction adiabatically by defining  $s(t) = \{1 + \exp[\alpha(t_{sw} - t)]\}^{-1}$  [ $s(z) = 0$  for  $z \in C_{im}$ ]. Hence, initial correlations can be disregarded ( $\Sigma^{1,\uparrow} = 0$ ,

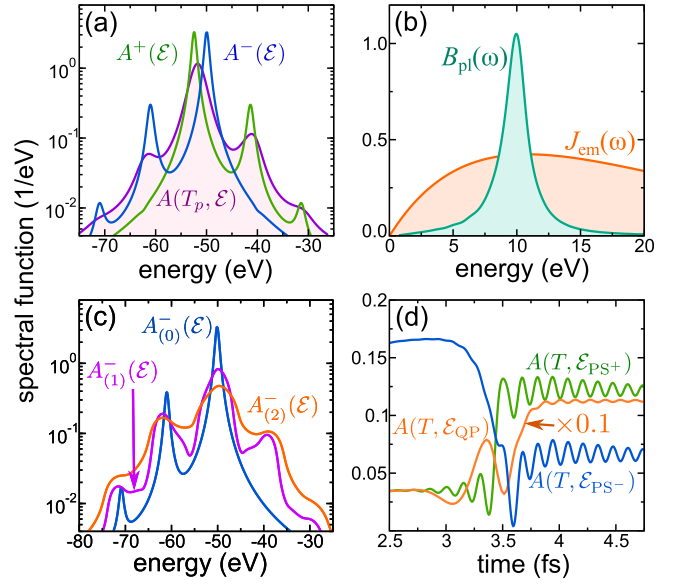


FIG. 5. (a) Spectral function  $A^-(\mathcal{E})$  [ $A^+(\mathcal{E})$ ] of occupied (empty) core state, obtained by time propagation, along with  $A(T, \mathcal{E})$ . (b) Interacting plasmon spectral function  $B_{pl}(\omega)$  and, for comparison, the embedding density  $J_{em}(\omega)$ . (c) Electron spectral function  $A_{(n)}^-(\mathcal{E})$  (occupied core state) with fixed plasmon occupation  $N_{pl} = 0, 1, 2$ . (d) Dynamics of  $A(T, \mathcal{E})$  for energy at the PSs and QP peak after the excitation,  $\mathcal{E} = \mathcal{E}_{PS^+} = -41.23$  eV,  $\mathcal{E} = \mathcal{E}_{PS^-} = -61.44$  eV, and  $\mathcal{E} = \mathcal{E}_{QP} = -51.76$  eV.

$\Pi_{\mu\nu}^{1,\uparrow} = 0$ ), simplifying the propagation scheme. We only consider intrinsic losses in this subsection, so  $\Gamma_{ex} = 0$ .

Plasmons typically decay by exciting particle-hole (p-h) pairs (Landau damping). Beside the states already incorporated in our model, there might be other electronic transitions limiting the plasmon lifetime. p-h excitations in the conduction band in the case of metals are a typical mechanism. In order to account for this plasmon decay channel in a simple way, we add a bosonic bath. For the latter we assume that the bath boson occupation number is zero, such that we obtain

$$\begin{aligned} \Pi^{em, \geq}(t_1, t_2) &= \sum_{\alpha} |\gamma_{\alpha}|^2 d_{\alpha}^B \geq(t_1, t_2) \\ &= -\frac{i}{2} \sum_{\alpha} |\gamma_{\alpha}|^2 e^{\mp i\omega_{\alpha}(t_1 - t_2)} \\ &\equiv -\frac{i}{2} \int_0^{\infty} d\omega J_{em}(\omega) e^{\mp i\omega(t_1 - t_2)}, \end{aligned} \quad (44)$$

where  $J_{em}(\omega)$  denotes the spectral density of the bath (it includes the coupling). For a simple Ohmic bath [88] adopted here, Eq. (44) can be analytically integrated:

$$J_{em}(\omega) = g_0 \frac{\omega}{\omega_c^2} e^{-\omega/\omega_c}, \quad \Pi^{em, \geq}(t_1, t_2) = \frac{ig_0}{2[\omega_c(t_1 - t_2) \mp i]^2}. \quad (45)$$

The transition  $\omega_c \rightarrow \infty$  represents the counterpart to the wide-band limit approximation (WBLA) often encountered for the electron embedding self-energy, as  $\Pi^{em, R}(t_1, t_2) \rightarrow -\pi(g_0/2\omega_c^2)\delta'(t)$ , turning the EOM (37) for the boson am-

plitude into the equation for the ordinary damped driven oscillator [similarly for the bosonic KBEs (35)], which has no memory. Adiabatic switching is realized by  $g_0 \rightarrow g_0 s(t_1) s(t_2)$ .

We propagated the KBEs up to  $T_p = 15$  fs (time step  $\Delta t = 0.024$  fs) with a switch-on time  $t_{sw} = 5$  fs and  $\alpha = 0.1$ . The inverse temperature is set to  $\beta = 50$  a.u., simulating the zero-temperature case. Initially, the electronic levels are occupied according to the Fermi function with the chemical potential  $\mu = 0$ , while we assume for the plasmon occupation  $N_{pl}(t = 0) = 0$ . The environmental coupling leads to a nonzero steady-state boson number as a result of the broadening of the spectral function. For  $g_0 = 1$  eV and  $\omega_c = 10$  eV we find  $N_{pl} = 0.012$  for  $t > t_{sw}$ . This is in accordance with the thermodynamical equilibrium value obtained from solving the Matsubara Dyson equation for the plasmon mode (including embedding only). The bosonic spectral function, calculated analogously to Eq. (46), is shown together with the Ohmic spectral density of the bath in Fig. 5(b).

To simulate the ultrafast photoionization dynamics, a laser pulse of 0.5 fs length and frequency  $\omega_L = 55$  eV (see Fig. 6, top panel) is applied after the system is fully thermalized. For this quasiresonant transition, we include one continuum state  $|k\rangle$  at  $\mathcal{E}_k = \mathcal{E}_{QP} + \omega_L$ , where  $\mathcal{E}_{QP} = -50$  eV is the QP energy for the no-hole ground state. The light-matter interaction is simplified to  $F_{2p,k}(t) = F_{k,2p}(t) \equiv F(t)$ . Electron-plasmon coupling is set to  $\Gamma_{in} = 5$  eV. We employ the self-energy Eq. (25).

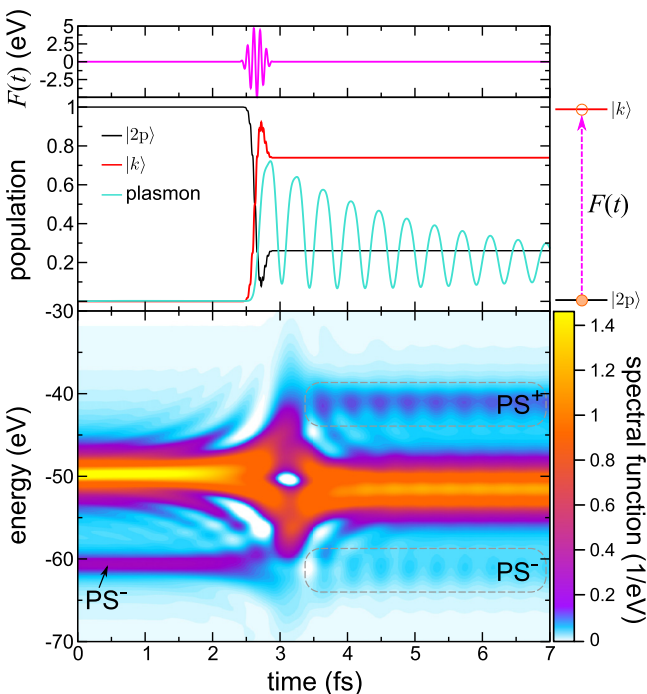


FIG. 6. (Top) Laser matrix element  $F(t)$ . (Middle) Population dynamics of the  $2p$  and the photoelectron state along with the plasmon occupation. (Bottom) Time-dependent spectral function  $A(T, \mathcal{E})$  of the core state. The Fourier transformation Eq. (46) was slightly smoothed by including an exponential damping.

Once the solution of the KBEs has been obtained, the time-resolved spectral function can be computed by

$$\mathbf{A}(T, \mathcal{E}) = i \int dt e^{i\mathcal{E}t} \left[ \mathbf{G}^> \left( T + \frac{t}{2}, T - \frac{t}{2} \right) - \mathbf{G}^< \left( T + \frac{t}{2}, T - \frac{t}{2} \right) \right]. \quad (46)$$

The laser-induced dynamics is presented in Fig. 6. The laser pulse (Fig. 6, top panel) partially ionizes the core state [the amplitude of  $F(t)$  has been chosen to maximize the depopulation] upon inducing plasmonic dynamics (Fig. 6, middle panel). The creation of the core hole is faster than the plasmon time scale  $\tau_{pl} = 2\pi/\Omega_{pl}$ , indicating a strongly nonadiabatic limit [19] of intrinsic plasmon excitation. The sudden change in the plasmon population is followed then by oscillations in the plasmon occupation. This nonequilibrium dynamics also becomes manifest in the time-resolved spectral function  $A(T, \mathcal{E}) \equiv A_{2p,2p}(T, \mathcal{E})$  (Fig. 6, bottom panel). The QP peak shifts transiently in about 1.5 fs from the initial configuration (QP peak at  $\mathcal{E} = \mathcal{E}_{QP}$ ,  $PS^-$  at  $\mathcal{E}_{PS^-} = 60.3$  eV [89]) to the new QP position at  $\mathcal{E} = -51.76$  eV. The shift is less than expected from the equilibrium spectral function for the completely empty core state [ $A^+(\mathcal{E})$ , Fig. 5(a)]. The spectral density quenches transiently into the new equilibrium position. In this way the  $PS^-$  splits into a branch coalescing in the QP and a second one merging with the shifted  $PS^-$  after the pulse. A  $PS^+$  above the QP appears ( $PS^+$ ) as expected. Furthermore, the strength of the  $PS^\pm$  oscillates in time. In order to understand this behavior, one needs to take the bosonic occupation into account as well. Revisiting the equilibrium case, Fig. 5(c) depicts the spectral function of the occupied core state with fixed integer plasmon number  $N_{pl} = n$ ,  $A_{(n)}^-(\mathcal{E})$ . The presence of a plasmon gives rise to a  $PS$  on the right-hand side of the QP peak, describing plasmon-assisted photoemission (i.e., a plasmon can be absorbed, transferring its energy to the photoelectron). Increasing  $n$  leads to stronger bosonic fluctuations (cf. Appendix B) and hence enhances the magnitude of the imaginary part of the self-energy, leading to broadened spectral features. This is consistent with the broadening observed in Fig. 5(c). Returning to the time-dependent scenario, these features are indeed manifested in  $A(T, \mathcal{E})$  (Fig. 6): The spectral strength of the  $PS^\pm$  displays oscillations in phase with the time-dependent plasmon occupation  $N_{pl}(t)$ . Furthermore, the weight of the QP peak is suppressed antiphase-wise to the variations of the  $PS$ s weight, as apparent from cuts of  $A(T, \mathcal{E})$  at the characteristic energies [Fig. 5(d)]. Hence, the spectral function exhibits an oscillatory transfer of spectral weight from the QP peak to the  $PS$ s. The enhanced broadening expected from Fig. 5(c) is clearly visible in the spectral function at the end of the propagation  $A(T_p, \mathcal{E})$ , as compared to the equilibrium spectra  $A^\pm(\mathcal{E})$  in Fig. 5(a).

## B. Time-resolved photoelectron spectra

After analyzing the intrinsic effects upon removing the electron from the core level, we proceed by incorporating extrinsic effects into the electron-plasmon coupling (43). Extrinsic plasmon losses are postemission, or, in other words, scattering effects. This goes beyond the standard treatment of (time-resolved) photoemission in terms of the lesser GF

restricted to bound states. Extrinsic effects can be incorporated by explicitly including (at least) two states  $|k_1\rangle$ ,  $|k_2\rangle$  representing photoelectrons and assign the plasmonic matrix element  $\Gamma_{\text{ex}} \equiv (\Gamma_{\text{ex}})_{k_1 k_2} = (\Gamma_{\text{ex}})_{k_2 k_1}$  (diagonal elements are set to zero). As photoelectrons propagate to infinity, the system is treated as open in their subspace. This is accomplished by including embedding self-energies. Because the continuum of photoelectron states describes electron propagating outside the sample, a noninteracting basis can be chosen. Defining the coupling density  $U_{ij}(\mathcal{E}) = \sum_k V_{i,k} V_{k,j}^* \delta(\mathcal{E} - \epsilon_k)$ , the continuum embedding self-energy can be expressed in spectral representation as

$$\Sigma^{\text{em},\gtrless}(t_1, t_2) = \int_0^\infty \frac{d\mathcal{E}}{2\pi} \Sigma^{\text{em},\gtrless}(\mathcal{E}) e^{-i\mathcal{E}(t_1 - t_2)}, \quad (47)$$

with

$$\Sigma^{\text{em},<}(\mathcal{E}) = i \mathbf{U}(\mathcal{E}) N_F(\mathcal{E} - \mu), \quad (48)$$

$$\Sigma^{\text{em},>}(\mathcal{E}) = -i \mathbf{U}(\mathcal{E}) [1 - N_F(\mathcal{E} - \mu)], \quad (49)$$

where  $N_F(\mathcal{E})$  denotes the Fermi distribution function.  $\mathbf{U}(\mathcal{E})$  accommodates the density of continuum states (e.g., proportional to  $\sqrt{\mathcal{E}}$  for free particles) and matrix element effects. We simplify the expressions by approximating  $\mathbf{U}(\mathcal{E}) \approx U_0 \mathbf{I}$  as a constant (WBLA). The retarded embedding self-energy attains  $\Sigma^{\text{em},\text{R}}(t_1, t_2) = -(i/2) U_0 \mathbf{I} \delta(t_1 - t_2)$  in this case. In accordance with the physical picture, we furthermore assume that no electrons can return from the continuum, leading to  $\Sigma^{\text{em},<}(\mathcal{E}) \approx 0$ . The WBLA has an advantage that all states, regardless of their energy, are damped uniformly. Such structureless embedding does not introduce any additional energy-dependent time delays.

The embedding self-energy for continuum states furthermore allows for computing the photocurrent (the number of electrons emitted per unit of time)  $J(\mathcal{E}, t) = dn(\mathcal{E}, t)/dt$  by the transient Meir-Wingreen formula [36,90] often used in transport calculations. The Meir-Wingreen expression for the total electron current flowing out of system reads

$$\frac{dn(t)}{dt} = 4\text{Re}\{\text{Tr}_k[\Sigma^{\text{em},\text{R}} \cdot \mathbf{G}^< + \Sigma^{\text{em},<} \cdot \mathbf{G}^{\text{A}} + \Sigma^{\text{em},\cdot} \star \mathbf{G}^{\text{r}}](t, t)\}. \quad (50)$$

Here  $\text{Tr}_k$  stands for the partial trace over the photoelectron states  $|k_{1,2}\rangle$ . Equation (50) is simplified in our case as  $\Sigma^{\text{em},\cdot} = 0$  due to the adiabatic switching procedure and  $\Sigma^{\text{em},<} = 0$  by the assumptions above. If we further resolve with respect to the photoelectron energies  $\mathcal{E}$ , we obtain

$$J(\mathcal{E}, t) = 4U_0 \text{Im} \int_0^t d\bar{t} e^{-i\mathcal{E}(t-\bar{t})} \text{Tr}_k[\mathbf{G}^<(\bar{t}, t)]. \quad (51)$$

We solved the KBEs Eqs. (33) and (35) for the three-level system as in Sec. IV A (with the additional embedding self-energy included). In order to reflect the experimental situation [9], the photoelectron states are assigned energies  $\mathcal{E}_{k_1} = 68$  eV and  $\mathcal{E}_{k_2} = 58$  eV ( $\mathcal{E}_{k_1} - \mathcal{E}_{k_2} = \Omega_{\text{pl}}$ ). The laser frequency is chosen  $\omega_L = 118$  eV, corresponding to the transition  $|2p\rangle \rightarrow |k_1\rangle$ . The pulse length is set to  $\tau_p = 1.2$  fs, corresponding to the full width at half maximum of 450 as in the experiment. The laser field amplitude is adjusted to

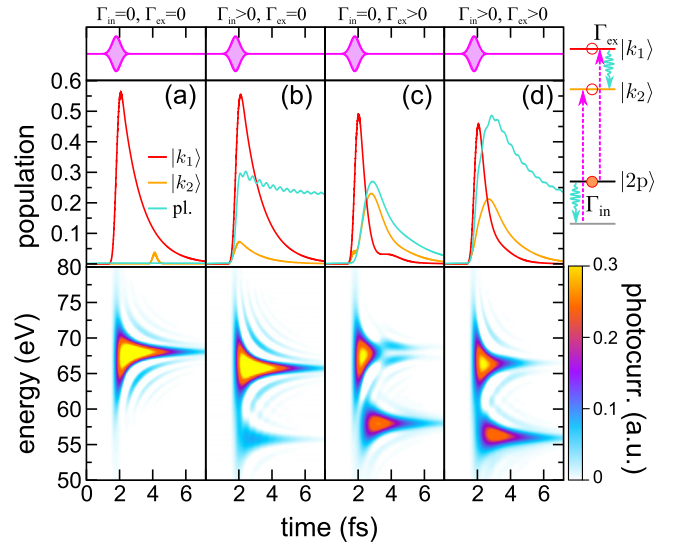


FIG. 7. Laser-induced KBE dynamics for the three-level system (see sketch on the right-hand side). (Top panels) Envelope of the laser pulse. (Middle panels) Population dynamics of  $|k_{1,2}\rangle$  and the plasmon occupation. (Bottom panels) Time-resolved photocurrent  $J(\mathcal{E}, t)$ . The electron-plasmon interaction is set to (a)  $\Gamma_{\text{in}} = \Gamma_{\text{ex}} = 0$ , (b)  $\Gamma_{\text{in}} = 5$  eV,  $\Gamma_{\text{ex}} = 0$ , (c)  $\Gamma_{\text{in}} = 0$ ,  $\Gamma_{\text{ex}} = 1$  eV, and (d)  $\Gamma_{\text{in}} = 5$  eV,  $\Gamma_{\text{ex}} = 1$  eV.

perform a complete population transfer in a noninteracting reference system.

Both intrinsic and extrinsic losses can result in the population of  $|k_2\rangle$  continuum state with a lower energy, which translates to a peak of  $J(\mathcal{E}, t)$  around  $\mathcal{E} \sim 58$  eV (see illustration in Fig. 7). The interplay between the two channels can be studied by turning either  $\Gamma_{\text{in}}$  or  $\Gamma_{\text{ex}}$  on or off (Fig. 7). In the case that the electron-plasmon interaction is switched off completely,  $|k_2\rangle$  acquires only a negligible occupation, while the transient photoelectron spectrum  $J(\mathcal{E}, t)$  converges to a dominant peak around  $\mathcal{E} \sim 68$  eV [Fig. 7(a)]. The plasmon number  $N_{\text{pl}}$  stays, of course, constant. When including intrinsic losses [Fig. 7(b)],  $J(\mathcal{E}, t)$  displays a peak originating from the emission from  $\text{PS}^-$ . Note that the  $N_{\text{pl}}(t)$  exhibits only small onset oscillations as compared to Fig. 6 because of the slower ionization process due to the increased laser pulse duration. Pure extrinsic electron-plasmon interaction [Fig. 7(c)] gives rise to similar spectral features, the occurrence of a peak in the time-resolved spectra, however, is delayed with respect to the intrinsic case. This is clear since  $|k_2\rangle$  can only be populated as a result of an additional scattering of  $|k_1\rangle$  involving the creation of a plasmon. This transition rate is set by (i)  $\Gamma_{\text{ex}}$ , (ii) the plasmon frequency, and (iii) the population of  $|k_1\rangle$ . Turning to the case of comparable intrinsic and extrinsic losses [Fig. 6(d)] the total number of photoelectrons detectable around  $E \sim 56$  eV increases beyond the previous cases. Interestingly, the bump in the population of  $|k_2\rangle$  due to extrinsic losses is less pronounced as in Fig. 7(c) and delayed by  $\sim 120$  as. On the other hand, the photocurrent extends over a longer period of time before approaching zero. Both factors are expected to influence the observed streaking time delay [9]. Moreover, the extrinsic process is weakened by the presence of

intrinsic losses. This is evidenced by that the maximum in the population of  $|k_2\rangle$  is slightly less pronounced when comparing Figs. 7(c) and 7(d). The intrinsic channel is already creating a plasmon, which acts as driving against extrinsic losses. This is a manifestation of quantum interference between intrinsic and extrinsic losses, analogous to Ref. [14]. The plasmon dynamics is quite different in the intrinsic and extrinsic cases as well. For intrinsic coupling only, the plasmon occupation quickly rises and is weakly damped due to the bosonic embedding self-energy. At variance, the plasmon creation is delayed in the extrinsic case and the plasmon occupation vanishes rapidly. The dynamics is governed by a dynamical balance  $|k_1\rangle \rightarrow |k_2\rangle$  upon creating plasmons and by the inverse process (visible in, e.g., the nonmonotonic behavior of the population of the upper continuum state for  $t > 2$  fs). As both continuum states are subject to environmental coupling, the transition  $|k_2\rangle \rightarrow |k_1\rangle$  due to plasmon absorption leads to an effective plasmon damping.

## V. CONCLUSIONS

In this work we developed a formalism for simultaneous propagation of the coupled fermionic and bosonic KBEs. The marked feature of our scheme is the treatment of bosonic correlators: Coupled first-order EOMs for  $\langle \Delta \hat{Q}_\mu(z) \Delta \hat{Q}_\nu(z') \rangle$ ,  $\langle \Delta \hat{Q}_\mu(z) \Delta \hat{P}_\nu(z') \rangle$ , and  $\langle \Delta \hat{P}_\mu(z) \Delta \hat{P}_\nu(z') \rangle$  correlators are reformulated as a second-order equation of motion for the coordinate-coordinate correlator and is efficiently propagated using the two-dimensional Numerov formula. The two-times nonequilibrium Green's functions, which are the solutions of these equations, completely describe the transient spectral density of both subsystems and make it possible to obtain the time-resolved photoemission spectra. Several competing scattering mechanisms result in a photoelectron arriving at the detector with a lower energy and time delay as compared to the unscattered one. In our calculations of the photoemission from the  $2p$  core state of bulk Mg we put apart scattering processes taking place before the photon interaction with the material and after the photoionization event on the electron's way to the detector. The time delay between the unscattered and scattered electrons is determined by the strength of the electron-plasmon interaction, which is the dominant scattering mechanism for electrons excited by XUV photons as in the experiment [9]. Interference between these two scattering pathways has already been theoretically predicted to modify the spectral strength of PSS. Here we demonstrate that the interference has also profound impact on the time dependence of the photoelectron current.

Future studies will focus on including the short-range part of the Coulomb interaction as well. This will allow for a many-body description of recent experiments such as the time-resolved Auger effect [91], where plasmonic effects are expected to play an important role [87,92].

## ACKNOWLEDGMENTS

This work is supported by the German Research Foundation (DFG) Collaborative Research Centre SFB 762 Functionality of Oxide Interfaces (J.B. and Y.P.) and Grant No. PA 1698/1-1 (M.S. and Y.P.).

## APPENDIX A: SOURCE-FIELD METHOD FOR DERIVING THE EQUATIONS OF MOTION

Let us assume that our system is initially prepared in some canonical ensemble set by the inverse temperature  $\beta$ . Using the contour-evolution operator, we can express the expectation value of any operator  $\hat{O}$  by

$$\langle \hat{O}(z) \rangle = \frac{\text{Tr}\{\mathcal{T} \exp[-i \int_C d\bar{z} \hat{H}(\bar{z})] \hat{O}(z)\}}{\text{Tr}\{\mathcal{T} \exp[-i \int_C d\bar{z} \hat{H}(\bar{z})]\}}. \quad (\text{A1})$$

Since embedding contributions to the self-energy are additive and straightforward to construct, we can focus on the electron-boson part, described by the general Hamiltonian

$$\begin{aligned} \hat{H}_0(z) = & \sum_{ij} h_{ij}(z) \hat{c}_i^\dagger \hat{c}_j + \sum_\nu \sum_{ij} \Gamma_{ij}^\nu(z) \hat{c}_i^\dagger \hat{c}_j \hat{Q}_\nu \\ & + \sum_\nu \frac{\Omega_\nu(z)}{2} (\hat{P}_\nu^2 + \hat{Q}_\nu^2). \end{aligned} \quad (\text{A2})$$

The Hamiltonian is now modified by adding time-dependent fields coupled to the bosons; that is,

$$\hat{H}_\xi(z) = \hat{H}_0(z) + \sum_\nu \xi_\nu(z) \hat{Q}_\nu. \quad (\text{A3})$$

The Heisenberg representation of all operators is now to be understood with respect to  $\hat{H}_\xi(z)$ . The way the source field couples to the system, the bosonic propagators can directly be obtained by

$$D_{\mu\nu}(z_1, z_2) = \left. \frac{\delta \langle \hat{Q}_\mu(z_1) \rangle}{\delta \xi_\nu(z_2)} \right|_{\xi_\nu=0}, \quad (\text{A4})$$

showing again that the boson GF describes the fluctuation of the amplitude  $\langle \hat{Q}_\nu(z_1) \rangle$ . In the following, all functional derivatives with respect to  $\xi_\nu(z)$  are understood to be taken at  $\xi_\nu = 0$ .

### 1. Fermionic Green's function and self-energy

With the help of the Heisenberg EOM, we obtain the fermion GF,

$$\begin{aligned} & \left[ i \frac{\partial}{\partial z_1} - \mathbf{h}(z_1) \right] \mathbf{G}(z_1, z_2) \\ & = \mathbf{I} \delta(z_1, z_2) + \sum_\nu \Gamma^\nu(z_1) \Upsilon^\nu(z_1, z_1^+, z_2), \end{aligned} \quad (\text{A5})$$

with the higher-order correlator  $\Upsilon_{kj}^\nu(z_1, z_2, z_3) = -i \langle \mathcal{T} \hat{c}_k(z_1) \hat{Q}_\nu(z_2) \hat{c}_j^\dagger(z_3) \rangle$ . The superscript  $+$  denotes an infinitesimal shift to later times. It is straightforward to see that it can be obtained by varying the fermionic GF with respect to the source field:

$$\Upsilon^\nu(z_1, z_3, z_2) = i \frac{\delta \mathbf{G}(z_1, z_2)}{\delta \xi_\nu(z_3)} + \langle \hat{Q}_\nu(z_3) \rangle \mathbf{G}(z_1, z_2). \quad (\text{A6})$$

Formally, we can identify the correlator term on the right-hand side of Eq. (A5) with the self-energy term; i.e.,

$$\sum_\nu \Gamma^\nu(z_1) \Upsilon^\nu(z_1, z_1^+, z_2) = \int_C d z_3 \Sigma(z_1, z_3) \mathbf{G}(z_3, z_2).$$

In order to access the self-energy directly, we need the inverse GF. In particular, let us define the right inverse by

$$\int_C d z_3 \mathbf{G}(z_1, z_3) \overleftarrow{\mathbf{G}}^{-1}(z_3, z_2) = \mathbf{I} \delta(z_1, z_2). \quad (\text{A7})$$

Multiplying by  $\overleftarrow{\mathbf{G}}^{-1}(z_3, z_2)$  and integrating over  $z_3$  yields for the self-energy

$$\begin{aligned} \Sigma(z_1, z_2) &= \sum_\nu \Gamma^\nu(z_1) \int_C d(z_3 z_4) \Upsilon^\nu(z_1, z_4, z_3) \overleftarrow{\mathbf{G}}^{-1}(z_3, z_2) \\ &\quad \times \delta(z_1^+, z_4). \end{aligned}$$

Equation (A6) suggests a separation of the self-energy into two terms. For reasons that become clear below, this distinction amounts to splitting the self-energy into a MF and correlation (c) part. The MF part gives

$$\Sigma^{\text{MF}}(z_1, z_2) = \delta(z_1, z_2) \sum_\nu \Gamma^\nu(z_1) \langle \hat{Q}_\nu(z_1) \rangle.$$

The correlation part of the self-energy so far reads

$$\begin{aligned} \Sigma^c(z_1, z_2) &= i \sum_\nu \Gamma^\nu \int_C d(z_3 z_4) \frac{\delta \mathbf{G}(z_1, z_3)}{\delta \xi_\nu(z_4)} \overleftarrow{\mathbf{G}}_{nj}^{-1}(z_3, z_2) \delta(z_1^+, z_4). \end{aligned}$$

Let us introduce the new source field,

$$\zeta_{ab}(z) = \sum_\nu \Gamma_{ab}^\nu(z) \langle \hat{Q}_\nu(z) \rangle, \quad (\text{A8})$$

which is exactly the MF contribution to the fermionic self-energy. This is analogous to the case of Hedin's equations, where the original source field (coupling to the density) is replaced by the total electronic energy. The reasons for the modification is to carry out the variation of the fermionic GF with respect to fermionic quantities only. Using the chain rule for functional derivatives, we obtain

$$\begin{aligned} \Sigma_{ij}^c(z_1, z_2) &= i \sum_\nu \sum_{nk} \sum_{ab} \Gamma_{ik}^\nu(z_1) \int_C d(z_3 z_4 z_5) \frac{\delta G_{kn}(z_1, z_3)}{\delta \zeta_{ab}(z_5)} \\ &\quad \times \overleftarrow{G}_{nj}^{-1}(z_3, z_2) \frac{\delta \zeta_{ab}(z_5)}{\delta \xi_\nu(z_4)} \delta(z_1^+, z_4). \end{aligned}$$

Invoking the functional variation analog of integration by parts, we can transfer the variation with respect to  $\zeta_{ab}(z_5)$  to the inverse GF. Noting further  $\delta \zeta_{ab}(z_5) / \delta \xi_\nu(z_4) = \Gamma_{ab}^\mu(z_5) D_{\mu\nu}(z_5, z_4)$  one arrives at

$$\begin{aligned} \Sigma_{ij}^c(z_1, z_2) &= i \sum_{\mu\nu} \sum_{nk} \sum_{ab} \int_C d(z_3 z_5) \Gamma_{ab}^\mu(z_5) G_{kn}(z_1, z_3) \\ &\quad \times \Lambda_{njab}(z_3, z_2; z_5) D_{\mu\nu}(z_5, z_1^+) \Gamma_{ik}^\nu(z_1), \end{aligned}$$

where we have introduced the three-point vertex

$$\Lambda_{abcd}(z_1, z_2; z_3) = - \frac{\delta \overleftarrow{G}_{ab}^{-1}(z_1, z_2)}{\delta \zeta_{cd}(z_3)}. \quad (\text{A9})$$

## 2. Vertex function and Bethe-Salpeter equation

The definition of the vertex function Eq. (A9) is completely analogous to the derivation of Hedin's equations by the source-field method. Beside this correspondence, treating the object

$\Lambda_{abcd}(z_1, z_2; z_3)$  as the usual vertex function is justified as it obeys the BSE. In order to show this property, we first realize that

$$\begin{aligned} \overleftarrow{G}_{ab}^{-1}(z_1, z_2) &= \left( -i \frac{\overleftarrow{\partial}}{\partial z_1} \delta_{ab} - \zeta_{ab}(z_1) \right) \delta(z_1, z_2) \\ &\quad - \epsilon_a \delta_{ab} - \Sigma_{ab}^c(z_1, z_2) \end{aligned}$$

and thus

$$\Lambda_{abcd}(z_1, z_2; z_3) = \delta_{ac} \delta_{bd} \delta(z_1, z_2) \delta(z_1, z_3) + \frac{\delta \Sigma_{ab}^c(z_1, z_2)}{\delta \zeta_{cd}(z_3)}. \quad (\text{A10})$$

Similar to the strategy above, we employ the chain rule for functional variation for the second term in Eq. (A10) to transform

$$\frac{\delta \Sigma_{ab}^c(z_1, z_2)}{\delta \zeta_{cd}(z_3)} = \sum_{mn} \int_C d(z_4 z_5) \frac{\delta \Sigma_{ab}^c(z_1, z_2)}{\delta G_{mn}(z_4, z_5)} \frac{\delta G_{mn}(z_4, z_5)}{\delta \zeta_{cd}(z_3)}.$$

As usual, we introduce the four-point kernel for BSE as

$$K_{abcd}(z_1, z_2; z_3, z_4) = \frac{\delta \Sigma_{ab}^c(z_1, z_2)}{\delta G_{cd}(z_3, z_4)}. \quad (\text{A11})$$

Next we would like to express the variation  $\delta G_{mn}(z_4, z_5) / \delta \zeta_{cd}(z_3)$  by the inverse GF in order to close the equation. This can be achieved by inserting the unity relation Eq. (A7). We thus obtain

$$\begin{aligned} \frac{\delta \Sigma_{ab}^c(z_1, z_2)}{\delta \zeta_{cd}(z_3)} &= \sum_{mn} \sum_p \int_C d(z_4 z_5 z_6) K_{abmn}(z_1, z_2; z_4, z_5) \\ &\quad \times \frac{\delta G_{mp}(z_4, z_6)}{\delta \zeta_{cd}(z_3)} \delta_{pn} \delta(z_5, z_6) \\ &= \sum_{mn} \sum_{pq} \int_C d(z_4 z_5 z_6 z_7) K_{abmn}(z_1, z_2; z_4, z_5) \\ &\quad \times \frac{\delta G_{mp}(z_4, z_6)}{\delta \zeta_{cd}(z_3)} G_{pq}(z_5, z_7) \overleftarrow{G}_{qn}^{-1}(z_7, z_6). \end{aligned}$$

Now we apply the variation to  $\overleftarrow{G}_{qn}^{-1}(z_7, z_6)$ , which then amounts to  $\Lambda_{qncd}(z_7, z_6; z_3)$ . Finally, we obtain the BSE

$$\begin{aligned} \Lambda_{abcd}(z_1, z_2; z_3) &= \delta_{ac} \delta_{bd} \delta(z_1, z_2) \delta(z_1, z_3) \\ &\quad + \sum_{mn} \sum_{pq} \int_C d(z_4 z_5 z_6 z_7) K_{abmn}(z_1, z_2; z_4, z_5) \\ &\quad \times G_{mp}(z_4, z_6) G_{pq}(z_5, z_7) \Lambda_{qncd}(z_7, z_6; z_3). \quad (\text{A12}) \end{aligned}$$

## 3. Boson Green's function and polarization

By differentiating the position-position correlator twice using EOM for position (18) and momentum (19) operators we arrive at the second-order differential equation

$$\begin{aligned} - \frac{1}{\Omega_\mu(z_1)} \left[ \frac{\partial^2}{\partial z_1^2} + \Omega_\mu^2(z_1) \right] D_{\mu\nu}(z_1, z_2) \\ = \delta_{\mu\nu} \delta(z_1, z_2) + \text{Tr} \left[ \Gamma^\mu(z_1) \frac{i \delta \mathbf{G}(z_1, z_1^+)}{\delta \xi_\nu(z_2)} \right]. \end{aligned}$$



Here we omit the terms originating from the bath bosonic coordinates. They can be added straightforwardly. In order to close the EOM, we introduce the irreducible polarization

$$P_{abcd}(z_1, z_2) = -i \frac{\delta G_{ab}(z_1, z_1^+)}{\delta \zeta_{cd}(z_2)}. \quad (\text{A13})$$

Like for the fermion GF we introduce the (right) inverse boson GF according to

$$\sum_{\xi} \int_C d z_3 D_{\mu\xi}(z_1, z_3) [\overleftarrow{D}^{-1}]_{\xi\nu}(z_3, z_2) = \delta_{\mu\nu} \delta(z_1, z_2). \quad (\text{A14})$$

Hence, we can express the polarization part of self-energy  $\Pi_{\mu\nu}^p(z_1, z_2)$  for the bosons, implicitly defined by

$$\text{Tr} \left[ \Gamma^\mu(z_1) i \frac{\delta \mathbf{G}(z_1, z_1^+)}{\delta \xi_\nu(z_2)} \right] = \sum_{\xi} \int_C d z_3 \Pi_{\mu\xi}^p(z_1, z_3) D_{\xi\nu}(z_3, z_2), \quad (\text{A15})$$

as

$$\begin{aligned} \Pi_{\mu\nu}^p(z_1, z_2) &= \text{Tr} \left\{ \Gamma^\mu(z_1) \int_C d z_3 \frac{i \delta \mathbf{G}(z_1, z_1^+)}{\delta \xi_\xi(z_3)} [\overleftarrow{D}^{-1}]_{\xi\nu}(z_3, z_2) \right\} \\ &= \sum_{mn} \sum_{ij} \Gamma_{ij}^\mu(z_1) \int_C d(z_3 z_4) \frac{i \delta G_{ji}(z_1, z_1^+)}{\delta \zeta_{mn}(z_4)} \\ &\quad \times \frac{\delta \zeta_{mn}(z_4)}{\delta \xi_\xi(z_3)} [\overleftarrow{D}^{-1}]_{\xi\nu}(z_3, z_2) \end{aligned}$$

and thus

$$\Pi_{\mu\nu}^p(z_1, z_2) = \sum_{mn} \sum_{ij} \Gamma_{ij}^\mu(z_1) \Gamma_{mn}^\nu(z_2) P_{jimm}(z_1, z_2). \quad (\text{A16})$$

Finally, we investigate how the polarization  $P_{abcd}(z_1, z_2)$  can be correlated to the fermionic GF. For this purpose we invoke the rule

$$\begin{aligned} \frac{\delta G_{ab}(z_1, z_2)}{\delta \zeta_{cd}(z_5)} &= - \sum_{pq} \int_C d(z_3 z_4) G_{ap}(z_1, z_3) \\ &\quad \times \frac{\delta \overleftarrow{G}_{pq}^{-1}(z_3, z_4)}{\delta \zeta_{cd}(z_5)} G_{qb}(z_4, z_2), \quad (\text{A17}) \end{aligned}$$

from which we obtain

$$\begin{aligned} P_{abcd}(z_1, z_2) &= -i \sum_{pq} \int_C d(z_3 z_4) G_{ap}(z_1, z_3) G_{qb}(z_4, z_2) \Lambda_{pqcd}(z_3, z_4; z_2). \quad (\text{A18}) \end{aligned}$$

## APPENDIX B: BASIC PROPERTIES OF THE BOSON PROPAGATOR

From the definition Eq. (13) one infers  $D_{\mu\nu}(z_1, z_2) = D_{\nu\mu}(z_2, z_1)$ . This implies for the greater/lesser Keldysh components

$$D_{\mu\nu}^{\gtrless}(t_1, t_2) = D_{\nu\mu}^{\lesseqgtr}(t_2, t_1), \quad (\text{B1})$$

such that the retarded boson propagator becomes a real function:

$$\begin{aligned} D_{\mu\nu}^R(t_1, t_2) &= \theta(t_1 - t_2) [D_{\mu\nu}^{\gtrless}(t_1, t_2) - D_{\mu\nu}^{\lesseqgtr}(t_1, t_2)] \\ &= 2\theta(t_1 - t_2) \text{Re}[D_{\mu\nu}^{\gtrless}(t_1, t_2)]. \quad (\text{B2}) \end{aligned}$$

Similarly, one obtains  $D_{\mu\nu}^A(t_1, t_2) = [D_{\nu\mu}^R(t_2, t_1)]^* = D_{\nu\mu}^R(t_2, t_1)$  for the advanced GF. For the Matsubara component, on the other hand,  $D_{\mu\nu}^M(\tau_1 - \tau_2) = D_{\mu\nu}(t_0 - i\tau_1, t_0 - i\tau_2)$ , the symmetry

$$D_{\mu\nu}^M(\tau) = D_{\nu\mu}^M(-\tau) \quad (\text{B3})$$

holds. Hence, as compared to fermions or bosons with a single peak in a spectral function representing one QP, there is no discontinuity in the diagonal Matsubara function for the transition  $\tau = 0^-$  to  $\tau = 0^+$ .

In equilibrium one can, as usual, assume that the greater/lesser propagators (and thus the retarded and advanced, as well) depend on the time difference  $t_1 - t_2$  only. Therefore, we can switch to frequency space  $D_{\nu}^{\gtrless}(\omega) = \int dt e^{i\omega t} D_{\nu}^{\gtrless}(t)$ . The symmetry relation Eq. (B1) implies

$$D_{\mu\nu}^{\gtrless}(\omega) = D_{\nu\mu}^{\lesseqgtr}(-\omega). \quad (\text{B4})$$

The spectral function is obtained from

$$B_{\mu\nu}(\omega) = i[D_{\mu\nu}^{\gtrless}(\omega) - D_{\mu\nu}^{\lesseqgtr}(\omega)], \quad (\text{B5})$$

which, in turn, makes it possible to characterize the greater/lesser boson GF by the fluctuation-dissipation theorem

$$D_{\mu\nu}^{\lesseqgtr}(\omega) = -i N_B(\omega) B_{\mu\nu}(\omega), \quad (\text{B6a})$$

$$D_{\mu\nu}^{\gtrless}(\omega) = -i [N_B(\omega) + 1] B_{\mu\nu}(\omega), \quad (\text{B6b})$$

where  $N_B(\omega)$  is the Bose distribution function. For illustration, let us consider the noninteraction case. From the definition Eq. (13) the bare boson GF follows as

$$\begin{aligned} d_{\nu}^{\gtrless}(t_1, t_2) &= -\frac{i}{2} [(N_{\nu} + 1)e^{\mp i\Omega_{\nu}(t_1 - t_2)} + N_{\nu} e^{\pm i\Omega_{\nu}(t_1 - t_2)}] \\ &= \mp \frac{1}{2} \sin[\Omega_{\nu}(t_1 - t_2)] \\ &\quad - i \left( N_{\nu} + \frac{1}{2} \right) \cos[\Omega_{\nu}(t_1 - t_2)] \quad (\text{B7}) \end{aligned}$$

[in thermal equilibrium  $N_{\nu} = N_B(\Omega_{\nu})$ ] and

$$d_{\nu}^R(t_1, t_2) = -\theta(t_1 - t_2) \sin[\Omega_{\nu}(t_1 - t_2)]. \quad (\text{B8})$$

Fourier transforming Eq. (B7) yields

$$d_{\nu}^{\gtrless}(\omega) = -i\pi [(N_{\nu} + 1)\delta(\omega \mp \Omega_{\nu}) + N_{\nu}\delta(\omega \pm \Omega_{\nu})], \quad (\text{B9})$$

from which the spectral function follows as

$$b_{\mu\nu}(\omega) = \pi \delta_{\mu\nu} [\delta(\omega - \Omega_{\nu}) - \delta(\omega + \Omega_{\nu})]. \quad (\text{B10})$$

Using the property  $N_B(-\omega) = -[N_B(\omega) + 1]$  the normalization of the spectral function can be verified:

$$\int_{-\infty}^{\infty} \frac{d\omega}{2\pi} N_B(\omega) b_{\mu\nu}(\omega) = \delta_{\mu\nu} N_B(\Omega_{\nu}) + \frac{1}{2}. \quad (\text{B11})$$

The retarded GF reads

$$d_{\nu}^R(\omega) = \frac{\Omega_{\nu}}{(\omega + i\eta)^2 - \Omega_{\nu}^2}, \quad (\text{B12})$$

where  $\eta$  is a positive infinitesimal. By complex continuation one finds, analogously to Eq. (B7), the noninteracting boson Matsubara function as

$$\begin{aligned} d_v^M(\tau) &= -\frac{i}{2}[(N_v + 1)e^{-\Omega_v|\tau|} + N_v e^{\Omega_v|\tau|}] \\ &= \frac{i}{2} \sinh(\Omega_v|\tau|) - i \left( N_v + \frac{1}{2} \right) \cosh(\Omega_v\tau). \end{aligned} \quad (\text{B13})$$

### APPENDIX C: TWO-DIMENSIONAL NUMEROV FORMULA

Consider the differential equation

$$\left( \frac{\partial^2}{\partial t_1^2} + \frac{\partial^2}{\partial t_2^2} \right) F(t_1, t_2) + S(t_1, t_2) = 0, \quad (\text{C1})$$

which we would like to solve numerically on a uniform two-dimensional mesh up to the fourth order in the grid spacing  $\Delta t$ .

This can be achieved by applying the Numerov discretization method, which can be summarized in a compact way [93] by

$$\begin{aligned} \sum_{i=-1}^1 \sum_{j=-1}^1 [(\Delta t)^2 (A_i B_j + A_j B_i) F(t_1 + i \Delta t, t_2 + j \Delta t) \\ + (\Delta t)^4 B_i B_j S(t_1 + i \Delta t, t_2 + j \Delta t)] = 0. \end{aligned} \quad (\text{C2})$$

The coefficients are defined by

$$A_{-1} = 12, \quad A_0 = -24, \quad A_1 = 12, \quad (\text{C3a})$$

$$B_{-1} = 1, \quad B_0 = 10, \quad B_1 = 1. \quad (\text{C3b})$$

For our numerical scheme we need  $F(t_1 + \Delta t, t_2 + \Delta t)$ . A corresponding fourth-order forward recursion formula is derived by solving Eq. (C2):

$$\begin{aligned} -F_{1,1} &= F_{-1,-1} + F_{-1,1} + F_{1,-1} + 6(F_{-1,0} + F_{0,-1} + F_{0,1} + F_{1,0}) + 20F_{0,0} \\ &\quad + \frac{(\Delta t)^2}{24} [S_{-1,-1} + S_{1,1} + 10(S_{-1,0} + S_{0,-1} + S_{1,0} + S_{0,1}) + 100S_{0,0}], \end{aligned} \quad (\text{C4})$$

where we abbreviated  $F_{i,j} = F(t_1 + i \Delta t, t_2 + j \Delta t)$  and  $S_{i,j} = S(t_1 + i \Delta t, t_2 + j \Delta t)$ . In case the source term  $S$  is not known at  $t_1 + \Delta t, t_2 + \Delta t$ , Eq. (C4) can be reduced to a second-order recursing by replacing the term in the square brackets in Eq. (C4) with  $144S_{0,0}$ .

- 
- [1] M. Kling and M. Vrakking, *Annu. Rev. Phys. Chem.* **59**, 463 (2008).
- [2] F. Krausz and M. Ivanov, *Rev. Mod. Phys.* **81**, 163 (2009).
- [3] S. Nagele, R. Pazourek, J. Feist, K. Doblhoff-Dier, C. Lemell, K. Tórkési, and J. Burgdörfer, *J. Phys. B* **44**, 081001 (2011).
- [4] R. Pazourek, S. Nagele, and J. Burgdörfer, *Faraday Discuss.* **163**, 353 (2013).
- [5] E. Goulielmakis, Z.-H. Loh, A. Wirth, R. Santra, N. Rohringer, V. S. Yakovlev, S. Zherebtsov, T. Pfeifer, A. M. Azzeer, M. F. Kling, S. R. Leone, and F. Krausz, *Nature (London)* **466**, 739 (2010).
- [6] F. Lépine, G. Sansone, and M. J. J. Vrakking, *Chem. Phys. Lett.* **578**, 1 (2013).
- [7] A. L. Cavalieri, N. Müller, T. Uphues, V. S. Yakovlev, A. Baltuška, B. Horvath, B. Schmidt, L. Blümel, R. Holzwarth, S. Hendel, M. Drescher, U. Kleineberg, P. M. Echenique, R. Kienberger, F. Krausz, and U. Heinzmann, *Nature (London)* **449**, 1029 (2007).
- [8] S. Neppel, R. Ernstorfer, A. L. Cavalieri, C. Lemell, G. Wachter, E. Magerl, E. M. Bothschafter, M. Jobst, M. Hofstetter, U. Kleineberg, J. V. Barth, D. Menzel, J. Burgdörfer, P. Feulner, F. Krausz, and R. Kienberger, *Nature (London)* **517**, 342 (2015).
- [9] C. Lemell, S. Neppel, G. Wachter, K. Tórkési, R. Ernstorfer, P. Feulner, R. Kienberger, and J. Burgdörfer, *Phys. Rev. B* **91**, 241101 (2015).
- [10] M. Lucchini, L. Castiglioni, L. Kasmi, P. Kliuiev, A. Ludwig, M. Greif, J. Osterwalder, M. Hengsberger, L. Gallmann, and U. Keller, *Phys. Rev. Lett.* **115**, 137401 (2015).
- [11] S. Hüfner, *Photoelectron Spectroscopy: Principles and Applications* (Springer Science & Business Media, Berlin, 2003).
- [12] C. N. Berglund and W. E. Spicer, *Phys. Rev.* **136**, A1030 (1964).
- [13] D. C. Langreth, *Phys. Rev. B* **1**, 471 (1970).
- [14] L. Campbell, L. Hedin, J. J. Rehr, and W. Bardyszewski, *Phys. Rev. B* **65**, 064107 (2002).
- [15] M. Guzzo, G. Lani, F. Sottile, P. Romaniello, M. Gatti, J. J. Kas, J. J. Rehr, M. G. Silly, F. Sirotti, and L. Reining, *Phys. Rev. Lett.* **107**, 166401 (2011).
- [16] E. Klevak, J. J. Kas, and J. J. Rehr, *Phys. Rev. B* **89**, 085123 (2014).
- [17] J. Lischner, D. Vigil-Fowler, and S. G. Louie, *Phys. Rev. Lett.* **110**, 146801 (2013).
- [18] Y. Pavlyukh, M. Schüler, and J. Berakdar, *Phys. Rev. B* **91**, 155116 (2015).
- [19] L. Hedin, J. Michiels, and J. Inglesfield, *Phys. Rev. B* **58**, 15565 (1998).
- [20] B. I. Lundqvist, *Phys. kondens. Materie* **9**, 236 (1969).
- [21] P. Minnhagen, *J. Phys. C* **8**, 1535 (1975).
- [22] F. Aryasetiawan and O. Gunnarsson, *Rep. Prog. Phys.* **61**, 237 (1998).
- [23] M. Cini and A. D'Andrea, *J. Phys. C* **21**, 193 (1988).
- [24] P. Lipavsky, V. Spicka, and B. Velicky, *Phys. Rev. B* **34**, 6933 (1986).
- [25] M. Bonitz, *Quantum Kinetic Theory* (Springer, Berlin, 2015).
- [26] J. Freericks, H. R. Krishnamurthy, and Th. Pruschke, *Phys. Rev. Lett.* **102**, 136401 (2009).
- [27] C. Sohr, A. Stange, M. Bauer, and K. Rossnagel, *Faraday Discuss.* **171**, 243 (2014).
- [28] S. Wall, D. Wegkamp, L. Foglia, K. Appavoo, J. Nag, R. F. H. Jr, J. Stähler, and M. Wolf, *Nat. Commun.* **3**, 721 (2012).
- [29] R. Huber, F. Tausser, A. Brodschelm, M. Bichler, G. Abstreiter, and A. Leitenstorfer, *Nature (London)* **414**, 286 (2001).

- [30] R. Huber, C. Kübler, S. Tübel, A. Leitenstorfer, Q. T. Vu, H. Haug, F. Köhler, and M.-C. Amann, *Phys. Rev. Lett.* **94**, 027401 (2005).
- [31] H. Haug, *Phys. Status Solidi B* **173**, 139 (1992).
- [32] L. Bányai, Q. T. Vu, B. Mieck, and H. Haug, *Phys. Rev. Lett.* **81**, 882 (1998).
- [33] Q. T. Vu and H. Haug, *Phys. Rev. B* **62**, 7179 (2000).
- [34] E. Perfetto, A.-M. Uimonen, R. van Leeuwen, and G. Stefanucci, *Phys. Rev. A* **92**, 033419 (2015).
- [35] N. E. Dahlen and R. van Leeuwen, *Phys. Rev. Lett.* **98**, 153004 (2007).
- [36] P. Myöhänen, A. Stan, G. Stefanucci, and R. van Leeuwen, *Phys. Rev. B* **80**, 115107 (2009).
- [37] K. Balzer and M. Bonitz, *Nonequilibrium Green's Functions Approach to Inhomogeneous Systems* (Springer, Berlin, 2012).
- [38] M. P. von Friesen, C. Verdozzi, and C.-O. Almbladh, *Phys. Rev. Lett.* **103**, 176404 (2009).
- [39] M. Puig von Friesen, C. Verdozzi, and C.-O. Almbladh, *Phys. Rev. B* **82**, 155108 (2010).
- [40] C. Verdozzi, D. Karlsson, M. Puig von Friesen, C. O. Almbladh, and U. von Barth, *Chem. Phys.* **391**, 37 (2011).
- [41] A. J. White and M. Galperin, *Phys. Chem. Chem. Phys.* **14**, 13809 (2012).
- [42] G. D. Mahan, *Many-Particle Physics* (Springer Science & Business Media, Berlin, 2000).
- [43] M. Galperin, M. A. Ratner, and A. Nitzan, *Nano Lett.* **4**, 1605 (2004).
- [44] L. K. Dash, H. Ness, and R. W. Godby, *J. Chem. Phys.* **132**, 104113 (2010).
- [45] M. Sukharev and M. Galperin, *Phys. Rev. B* **81**, 165307 (2010).
- [46] H. Ness and L. K. Dash, *Phys. Rev. B* **84**, 235428 (2011).
- [47] S. W. Koch, *Microscopic Theory of Semiconductors: Quantum Kinetics, Confinement and Lasers* (World Scientific, Singapore, 1996).
- [48] Y. Murakami, P. Werner, N. Tsuji, and H. Aoki, *Phys. Rev. B* **91**, 045128 (2015).
- [49] M. Schüler, Y. Pavlyukh, and J. Berakdar, *J. Phys. Chem. Lett.* **4**, 1131 (2013).
- [50] E. Boström, A. Mikkelsen, and C. Verdozzi, [arXiv:1507.06975](https://arxiv.org/abs/1507.06975).
- [51] C. Pellegrini, J. Flick, I. V. Tokatly, H. Appel, and A. Rubio, *Phys. Rev. Lett.* **115**, 093001 (2015).
- [52] A. J. White, B. D. Fainberg, and M. Galperin, *J. Phys. Chem. Lett.* **3**, 2738 (2012).
- [53] K. Kaasbjerg and A. Nitzan, *Phys. Rev. Lett.* **114**, 126803 (2015).
- [54] Q. T. Vu, H. Haug, and S. W. Koch, *Phys. Rev. B* **73**, 205317 (2006).
- [55] M. Sentef, A. F. Kemper, B. Moritz, J. K. Freericks, Z.-X. Shen, and T. P. Devereaux, *Phys. Rev. X* **3**, 041033 (2013).
- [56] M. Eckstein and P. Werner, *Phys. Rev. Lett.* **110**, 126401 (2013).
- [57] M. Guzzo, J. J. Kas, L. Sponza, C. Giorgetti, F. Sottile, D. Pierucci, M. G. Silly, F. Sirotti, J. J. Rehr, and L. Reining, *Phys. Rev. B* **89**, 085425 (2014).
- [58] J. Vinson, J. J. Rehr, J. J. Kas, and E. L. Shirley, *Phys. Rev. B* **83**, 115106 (2011).
- [59] J. J. Kas, F. D. Vila, J. J. Rehr, and S. A. Chambers, *Phys. Rev. B* **91**, 121112 (2015).
- [60] J. J. Kas, A. P. Sorini, M. P. Prange, L. W. Campbell, J. A. Soininen, and J. J. Rehr, *Phys. Rev. B* **76**, 195116 (2007).
- [61] C. O. Almbladh and P. Minnhagen, *Phys. Rev. B* **17**, 929 (1978).
- [62] C.-O. Almbladh, *Phys. Rev. B* **34**, 3798 (1986).
- [63] J. E. Inglesfield, *J. Phys. C* **16**, 403 (1983).
- [64] D. R. Penn, *Phys. Rev. Lett.* **40**, 568 (1978).
- [65] D. R. Penn, *Phys. Rev. Lett.* **38**, 1429 (1977).
- [66] C.-O. Almbladh, *Phys. Scr.* **32**, 341 (1985).
- [67] T. Fujikawa, *J. Electron Spectrosc. Relat. Phenom.* **173**, 51 (2009).
- [68] J.-J. Chang and D. C. Langreth, *Phys. Rev. B* **8**, 4638 (1973).
- [69] T. Fujikawa and H. Arai, *J. Electron Spectrosc. Relat. Phenom.* **123**, 19 (2002).
- [70] L. Hedin and J. D. Lee, *Phys. Rev. B* **64**, 115109 (2001).
- [71] A.-M. Uimonen, G. Stefanucci, and R. v. Leeuwen, *J. Chem. Phys.* **140**, 18A526 (2014).
- [72] D. Pines and D. Bohm, *Phys. Rev.* **85**, 338 (1952).
- [73] A. W. Overhauser, *Phys. Rev. B* **3**, 1888 (1971).
- [74] Introducing the electron-plasmon interaction via the electrostatic component of the quantized electromagnetic field as in Ref. [25] entails a careful gauge consideration. The density and current operators, on the other hand, are gauge invariant [75], such that the resulting electron-boson Hamiltonian is independent of the gauge.
- [75] G. Giuliani and G. Vignale, *Quantum Theory of the Electron Liquid* (Cambridge University Press, Cambridge, U.K., 2005).
- [76] G. Pal, Y. Pavlyukh, H. C. Schneider, and W. Hübner, *Eur. Phys. J. B* **70**, 483 (2009).
- [77] G. Pal, Y. Pavlyukh, W. Hübner, and H. C. Schneider, *Eur. Phys. J. B* **79**, 327 (2011).
- [78] A. S. Moskalenko, Y. Pavlyukh, and J. Berakdar, *Phys. Rev. A* **86**, 013202 (2012).
- [79] G. Stefanucci and R. v. Leeuwen, *Nonequilibrium Many-Body Theory of Quantum Systems: A Modern Introduction* (Cambridge University Press, Cambridge, U.K., 2013).
- [80] G. Strinati, *Riv. Nuovo Cimento* **11**, 1 (1988).
- [81] G. Baym and L. P. Kadanoff, *Phys. Rev.* **124**, 287 (1961).
- [82] L. P. Kadanoff and G. Baym, *Quantum Statistical Mechanics* (Addison-Wesley, Boston, 1994).
- [83] J. K. Viljas, J. C. Cuevas, F. Pauly, and M. Häfner, *Phys. Rev. B* **72**, 245415 (2005).
- [84] N. Säkkinen, Y. Peng, H. Appel, and R. van Leeuwen, *J. Chem. Phys.* **143**, 234102 (2015).
- [85] A. Stan, N. E. Dahlen, and R. v. Leeuwen, *J. Chem. Phys.* **130**, 224101 (2009).
- [86] H. Ueba and B. Gumhalter, *Prog. Surf. Sci.* **82**, 193 (2007).
- [87] C. Lemell, B. Solleder, K. Tótkési, and J. Burgdörfer, *Phys. Rev. A* **79**, 062901 (2009).
- [88] U. Weiss, *Quantum Dissipative Systems* (World Scientific, Singapore, 2012).
- [89] Note the distance between QP peaks and PSs is overestimated by the GW approximation and slightly modified by the finite width of the boson spectral function due to embedding.
- [90] A.-P. Jauho, N. S. Wingreen, and Y. Meir, *Phys. Rev. B* **50**, 5528 (1994).
- [91] M. Drescher, M. Hentschel, R. Kienberger, M. Uiberacker, V. Yakovlev, A. Scrinzi, T. Westerwalbesloh, U. Kleineberg, U. Heinzmann, and F. Krausz, *Nature (London)* **419**, 803 (2002).
- [92] M. Cini, *Phys. Rev. B* **17**, 2486 (1978).
- [93] P. L. Bartlett, *J. Phys. B* **39**, R379 (2006).



## Conclusions and perspectives

It has been the main topic of this thesis to establish the link between state-of-the-art theoretical tools and typical spectroscopies in order to contribute to the understanding of complex many-body compounds. The synergy between theory and experiment was given a special attention. The main spectroscopy studied theoretically by the works in this thesis is photoemission and its variants. In particular, we worked out the effects of correlations in many-body systems as manifested in spectroscopic quantities.

### 7.1 Summary

In [E1] and [E2], the coupling of the electronic degrees of freedom – the photoelectron properties, in particular – to the nuclear motion was studied in depth. The novel aspects hereby were how to extract the information on the dynamics of molecules from the *spatial* distribution of the photoelectrons. In [E1] we showed that, in principle, femtosecond time-resolved photoemission from single adsorbed molecules can be studied by using atomic-sized tips as used in the AFM setup as nano-sized photoelectron detector. A very useful and efficient tool to compute the scattering wave-functions – an important ingredient of the theory of photoemission – was presented in [E2]. We applied the theory to the photoionization of the diatomic  $\text{HeH}^{2+}$  molecule and established a direct link between the two-center interference effects and the PAD, from which we suggested a scheme to reconstruct the full NWP associated with the laser-driven molecular dynamics.

The electron-electron interaction and, in particular, dynamical correlation effects determined the remainder of our works and represent a central topic of this thesis. The advantages of the NEGF formalism and the underlying powerful machinery of the MBPT inspired us to develop the formal NEGF theory of photoemission further with [E3]. We elucidated the connection of the formal concepts of the FPA to the standard MBPT, allowing for a practical implementation of the theory. The main advances were achieved by the extension of the theoretical description of DPE, which we advocate as a very useful sensor for the many facets of correlations in many-body systems. The effective electron-electron interaction in more complex systems comprises, besides the Coulomb repulsion, fluctuation-mediated effects due to the dynamical environment. As an important example, we focused on dynamical screening mediated by charge-density fluctuations. We have chosen the Buckminster fullerene as a concrete system for its pronounced plasmon resonances and generally rich physics. In [E4] we rigorously categorized the collective modes, based on full-fledged *ab initio* calculations, with the help of the NMF. The obtained model for the DD response function – whose accuracy is corroborated by the comparison to EELS data – was then employed to characterize the dynamically screened interaction in the  $\text{C}_{60}$  molecule. With these tools at hand, we were able to elucidate the role of electronic correlations mediated by the density oscillations in DPE in our joint theoretical and experimental work [E5]. The distinct feature of the experiment – the significant narrowing of the coincidence spectrum – is in agreement with our *ab initio* description and so endorses the plasmon-assisted DPE as a novel aspect of releasing two correlated electrons from complex systems.

As an important aspect for experiments, we investigated the stability and decay dynamics of electronic excitations in the  $\text{C}_{60}$  molecule due thermally activated vibrations by means for 2PPE in our joint experiment-theory work [E6]. The theoretical modeling was based on an *ab initio* computation of the excited states in combination with non-hermitian quantum kinetics, yielding realistic insights into the laser- and vibration-driven electron dynamics.

The impact of electron-plasmon interactions on photoemission includes, besides the extrinsic (post-

emission) effects giving rise to the plasmon-mediated DPE process, also intrinsic losses. The latter occurs due to the electron-plasmon coupling in the initial state, which manifests by the typical satellite structure of the spectral function. Intrinsic and extrinsic losses compete for the same final state by the different pathways, resulting in quantum interference. These effects are particularly pronounced for the photoemission from core levels of simple metals. In [E7] we showed that intrinsic and extrinsic losses can be separated by means of transient photoemission due to their different time scales. The time-dependent NEGF treatment of the underlying EB model required important modifications of the established schemes and hence represents a methodological advancement.

With the suitable time-dependent treatment of EB models, the physics investigated in this thesis can be described in a unified way. Both, molecular vibrations (or phonons in the solid-state case) *and* the effective electron-electron interaction can be incorporated into the EB Hamiltonian simultaneously. The corresponding quantum kinetics opens the door to the correlated dynamics of electronic systems and may thus become an important aid for future experiments. In particular, we advocate DPE as a tool to "zoom" into the electron-electron interactions. Beside the effective interaction mediated by dynamical screening, other types of fluctuations may have similar effects and lead to strong mediated correlations, as well. This includes, for instance, the formation of Cooper pairs due to electron-phonon coupling or spin-spin fluctuations. Studying, based on the NEGF approach and its time-dependent formulation by the KBEs, such correlations in the time domain can contribute to a better understanding of the underlying processes.

## 7.2 Outlook

Despite the exciting perspective offered by the NEGF dynamics, its applicability to transient many-body spectroscopies is still in its infancy, leaving a lot of room for future research. Let us have a look at some selected points.

**Continuum embedding approach.** A major drawback of KBE-based quantum dynamics is the enormous computational effort arising due to the propagation along two time directions. Since the collision integrals entail memory effects, saving the full two-time GFs is required, which can easily consume terabytes of data for realistic simulations. One important step to reduce the computational costs is choosing the appropriate SP basis. While a real-space basis as employed in ref. [225] provides an appropriate description of the continuum, an application to realistic systems is clearly out of reach. Using a discrete basis according to a reference (e. g. HF) Hamiltonian and adding a few scattering states in the relevant energy region effectively limits the applicability to weak-field ionization <sup>1</sup>. Furthermore, the distinct feature of photoemission – the creation of an electron wave-packet which propagates to infinity – can only be retained if a continuum of scattering states enters the formulation. We suggest the following solution to this problem: a few scattering states are selected and incorporated into the full KBE scheme. This allows for treating extrinsic effects, as well. Moreover, the subspace of scattering states is treated as embedded in an open system, i. e., the electrons can vanish into a true continuum. This approach does not add any difficulty to the KBE scheme. We have used a simple version of the embedding method in [E7]. An extension based on a rigorous mathematical formulation is straightforward and will be the topic of future work.

**Generalized Kadanoff-Baym ansatz.** The main source of the computational complexity is, however, the dependence of the GFs on two time arguments. For this reason, approximation schemes reducing the two-times KBEs to a one-time master equation for the RDM  $\gamma(t)$  have been introduced early [75]. The so-called generalized Kadanoff-Baym ansatz (GKBA) [236] approximates the off-diagonal time points by

$$-i\mathbf{G}^{\lessgtr}(t_1, t_2) = \mathbf{G}^{\text{R}}(t_1, t_2)\mathbf{G}^{\lessgtr}(t_2, t_2) - \mathbf{G}^{\lessgtr}(t_1, t_1)\mathbf{G}^{\text{A}}(t_1, t_2) \quad (7.1)$$

and so decouples the spectral information (encoded in  $\mathbf{G}^{\text{R/A}}(t_1, t_2)$ ) from the population dynamics (captured by  $\mathbf{G}^{\lessgtr}(t, t) = i\gamma(t)$ ). The retarded/advanced GFs are no longer computed from the greater and lesser GFs (which are known on the time diagonal  $t_1 = t_2$  only), but have to be constructed before the time propagation (i. e., only the static correlation enters) or determined dynamically by, for example, the HF approximation [237] or advanced schemes [226].

<sup>1</sup>Under moderate to strong driving, the final states compete for the population. Reducing the number of final states to a discrete set thus severely overestimates their population.

For our idea of employing EB models to describe the quantum kinetics of transient spectroscopies, a counterpart to the GKBA for the electronic GF (7.1) would be required to obtain a one-time EOM for the boson propagators, as well. Replacing the electronic GFs in eq. (7.1) by the bosonic GFs is meaningless<sup>2</sup>. Hence, how to construct a GKBA for the bosons is still an open question which we are planning to answer by future works.

**Non-linear electron-boson coupling.** So far, we have considered EB models with linear coupling between the two subsystems only. While this is indeed the leading order term for electron-phonon interaction, corrections become necessary in case of stronger excitations or a deviation of the underlying PESs from the harmonic approximation. Furthermore, there are typical examples (Mott-insulating molecular crystals [238]) where the coupling term also includes higher-order terms in the electronic degrees of freedom, such as the double-occupation (doublon) of lattice sites. Due to selection rules, the scenario where the linear term (in the phonon coordinates) vanishes can occur, leaving the quadratic term as the dominant contribution. However, very little is known how the dynamics of such Hamiltonians can be treated within the KBEs framework. A first step would be to identify the suitable bosonic correlators and find a functional form (similar to appendix C.2) of the self-energy as a starting point for a diagrammatic perturbation theory. This might be an important contribution to the modeling of transient THz experiments on molecular crystals [239].

---

<sup>2</sup>The GKBA is exact for non-interacting fermions. An ansatz of the same form for the boson GFs violates the equality, even in the non-interacting case.





# Appendices



## Geometric classification of many-body states

In subsec. 2.4.1 we introduced the classification of SP states according to their geometric character into bound or scattering states. In this appendix we provide the details how to generalize this classification to the many-body states.

A mathematically rigorous definition of bound states is analogous to the SP case. Defining the density  $n_\alpha(\mathbf{r}, t) = \langle \Psi_\alpha | \hat{n}(\mathbf{r}, t) | \Psi_\alpha \rangle$  (the density operator  $\hat{n}(\mathbf{r})$  is in the Heisenberg picture with respect to the time-independent electronic Hamiltonian  $\hat{H}_e$ ), the state  $|\Psi_\alpha\rangle \in \mathcal{H}_0$  is called bound if for any  $\delta > 0$  there is a compact set  $B \subset \mathbb{R}^3$  so that

$$\int_{B^c} d\mathbf{r} n_\alpha(\mathbf{r}, t) < \delta, \quad B^c = \mathbb{R}^3 \setminus B. \quad (\text{A.1})$$

The subspace of all bound states of the  $N_e$ -electron Hilbert space ( $\mathcal{H}$ ) is denoted by  $\mathcal{H}_0$ , while we assign the (discrete) set of quantum numbers  $\alpha \in \mathcal{B}_{N_e}$ . A straightforward generalization of the criterion (2.26) to the many-body case is possible, but does not specify how many electrons are in scattering states. This deficiency is repaired by the notion of Feshbach projection operators. For the case of exactly one continuum electron, we define

$$\hat{\mathcal{P}}_\alpha^{(1)} = \sum_\sigma \int d\mathbf{k} \hat{c}_{\mathbf{k}\sigma}^\dagger |\Psi_\alpha^{(N_e-1)}\rangle \langle \Psi_\alpha^{(N_e-1)}| \hat{c}_{\mathbf{k}\sigma}, \quad \hat{\mathcal{P}}^{(1)} = \sum_{\alpha \in \mathcal{B}_{N_e-1}} \hat{\mathcal{P}}_\alpha^{(1)} \quad (\text{A.2})$$

with  $(\mathbf{k}\sigma)$  corresponding to a SP scattering state and require

$$\hat{c}_{\mathbf{k}\sigma} |\Psi_\alpha^{(N_e-1)}\rangle = 0 \quad \text{for } \alpha \in \mathcal{B}_{N_e-1}. \quad (\text{A.3})$$

The condition (A.3) guarantees that all properties of projection operators are fulfilled (see [E3] for a detailed discussion).  $\hat{\mathcal{P}}^{(1)}$  spans the subspace  $\mathcal{H}_1$  including all states with  $(N_e - 1)$  bound and exactly one scattering electron. It is well-defined since the SP scattering states are rigorously defined by the criterion (2.26). The state-specific version  $\hat{\mathcal{P}}_\alpha^{(1)}$  offers some flexibility with respect to the bound states, which is used in [E3]. The generalization of the projector (A.2) to  $n \geq 1$  scattering electrons is straightforward:

$$\hat{\mathcal{P}}_\alpha^{(n)} = \frac{1}{n!} \sum_{\sigma_1 \dots \sigma_n} \int d\mathbf{k}_1 \dots \int d\mathbf{k}_n \hat{c}_{\mathbf{k}_1 \sigma_1}^\dagger \dots \hat{c}_{\mathbf{k}_n \sigma_n}^\dagger |\Psi_\alpha^{(N_e-n)}\rangle \langle \Psi_\alpha^{(N_e-n)}| \hat{c}_{\mathbf{k}_n \sigma_n} \dots \hat{c}_{\mathbf{k}_1 \sigma_1} \quad (\text{A.4})$$

and

$$\hat{\mathcal{P}}^{(n)} = \sum_{\alpha \in \mathcal{B}_{N_e-n}} \hat{\mathcal{P}}_\alpha^{(n)}. \quad (\text{A.5})$$

As above, the condition

$$\hat{c}_{\mathbf{k}\sigma} |\Psi_\alpha^{(N_e-n)}\rangle = 0 \quad \text{for } \alpha \in \mathcal{B}_{N_e-n} \quad (\text{A.6})$$

is required to ensure the idempotency of the projectors. The projection operators (A.5) now permit a general classification as used in subsec. 2.4.1. A generic state  $|\Psi_\lambda\rangle \in \mathcal{H}$  is designated as  $n$ -electron scattering state, denoted by  $|\Psi_\lambda\rangle \in \mathcal{H}_n$ , if  $\hat{\mathcal{P}}^{(n)} |\Psi_\lambda\rangle = |\Psi_\lambda\rangle$ . For quantum numbers we write  $\lambda = (\alpha, \mathbf{k}_1, \dots, \mathbf{k}_n) \in \mathcal{B}_{N_e-n} \cup \mathcal{E}_n$  with  $\alpha \in \mathcal{B}_{N_e-n}$  and  $(\mathbf{k}_1, \dots, \mathbf{k}_n) \in \mathcal{E}_n \subset \mathbb{R}^{3n}$ . The subspaces  $\mathcal{H}_n$  spanned by the projection operators (A.5) are pair-wise orthogonal:  $\mathcal{H}_n \perp \mathcal{H}_m$  for  $n \neq m$ . Further consequences and the connection to the MBPT are presented in [E3].



## Quantum chemistry methods

**Configuration interaction (CI).** Although single the determinant form (2.38) is only an approximation to the many-body state, it represents a basis for expanding the exact many-body wave-function. The configuration interaction (CI) [240] method constructs, in principle, an infinite series of excited determinants starting from the HF reference state  $|\Psi_0^{\text{HF}}\rangle$  by successively exchanging occupied ( $i, j, \dots \in \text{occ}$ ) by virtual ( $p, q, \dots \in \text{virt}$ ) orbitals. The full-CI wave-function is expanded as

$$|\Psi^{\text{CI}}\rangle = \left[ 1 + \sum_{i \in \text{occ}} \sum_{p \in \text{virt}} C_i^p \hat{d}_p^\dagger \hat{d}_i + \sum_{\substack{i, j \in \text{occ} \\ i > j}} \sum_{\substack{p, q \in \text{virt} \\ p > q}} C_{ij}^{pq} \hat{d}_p^\dagger \hat{d}_q^\dagger \hat{d}_i \hat{d}_j + \dots \right] |\Psi_0^{\text{HF}}\rangle, \quad (\text{B.1})$$

where the fermionic creation and annihilation operators refer to the HF orbitals:  $\hat{d}_i^\dagger = \int d\mathbf{r} \psi_i^{\text{HF}}(\mathbf{r}) \hat{\psi}^\dagger(\mathbf{r} \sigma_i)$ . The spin dependence has been incorporated into the indices. The CI wave-function (B.1) is an exact solution to the many-body TISE, provided the expansion is not truncated and complete basis set is used for describing the orbitals. It is therefore also referred to as exact diagonalization.

For the practical implementation of CI scheme, the sum in eq. (B.1) has to be truncated after a few terms<sup>1</sup>. Restricting the expansion to single excitations is addressed as CIS (S for single), for single and double excitations one refers to CISD and so on. Forming the CI matrix, where the matrix elements of the Hamiltonian with respect to the individual terms in eq. (B.1), the energy correction (correlation energy) is found as eigenvalue of the CI matrix, where as the coefficients  $C_{i, \dots}^{p, \dots}$  are obtained by solving the resulting eigenvector problem. The (truncated) CI method displays the disadvantage of not being size consistent, i. e. of not showing the correct behavior when duplicating the system<sup>2</sup>.

**Coupled-cluster (CC) theory.** In order to assure the size-consistency and to reduce the substantial computational cost of higher-order CI expansion, several methods including the successful coupled-cluster (CC) method have been developed. Based on the linked-diagram theorem [240], the excitations with respect to the HF reference wave-function (2.38) are introduced as

$$|\Psi^{\text{CC}}\rangle = \exp(\hat{T}) |\Psi_0^{\text{HF}}\rangle = \left[ 1 + \hat{T} + \frac{1}{2!} \hat{T}^2 + \frac{1}{3!} \hat{T}^3 + \dots \right] |\Psi_0^{\text{HF}}\rangle. \quad (\text{B.2})$$

Here, the excitation operator  $\hat{T} = \hat{T}_1 + \hat{T}_2 \dots$  comprises the  $n$ -fold excitations (exchanging  $n$  orbitals in the reference determinant) similar to the CI expansion (B.1):

$$\hat{T}_1 = \sum_{i \in \text{occ}} \sum_{p \in \text{virt}} t_i^p \hat{d}_p^\dagger \hat{d}_i, \quad \hat{T}_2 = \sum_{\substack{i, j \in \text{occ} \\ i > j}} \sum_{\substack{p, q \in \text{virt} \\ p > q}} t_{ij}^{pq} \hat{d}_p^\dagger \hat{d}_q^\dagger \hat{d}_i \hat{d}_j, \dots \quad (\text{B.3})$$

Inserting the expansion of the CC wave-function (B.2) into the TISE yields a set of self-consistent equations for the coefficients  $t_i^p, t_{ij}^{pq}$  and so on. When restricting the computation to single and double excitations, the CC is then referred to as CCSD. Higher orders of the CC theory are denoted similarly. The CCSD wave function is thus defined by

$$|\Psi^{\text{CCSD}}\rangle = \exp(\hat{T}_1 + \hat{T}_2) |\Psi_0^{\text{HF}}\rangle. \quad (\text{B.4})$$

<sup>1</sup>For smaller systems, as, for instance, the  $\text{Na}_9^+$  cluster or similar systems, the full CI is within reach of computational resources [241].

<sup>2</sup>Imagine, for instance, two hydrogen molecules separated by a very large distance. The total energy should amount to twice the energy of the individual molecules.

In contrast to the CI approach, the CC theory, even if restricted to CCSD, accounts for *all* non-linear terms such as  $\hat{T}_1^2/2$ ,  $\hat{T}_1\hat{T}_2$  and higher excitations due to the exponentiation. Hence, CCSD already includes triple, quadruple and even higher excitations. This way of incorporating the successive excitation of the reference state is the reason for the CC theory to be size-consistent.

**Equation-of-motion (EOM) and Symmetry-adapted-cluster-configuration-interaction (SAC-CI) approach.** Quantum chemistry methods are not limited to ground-state properties, albeit this where their primary strength lies. In order to access excited-state properties, the equation-of-motion (EOM) approach has proven effective. Let us consider a ground-state wave-function  $\hat{H}_e|\Psi_0\rangle = E_0|\Psi_0\rangle$ , which is, for example, obtained by the CI or CC method<sup>3</sup>, and a target excited wave-function  $\hat{H}_e|\Psi_\alpha\rangle = E_\alpha|\Psi_\alpha\rangle$ . Introducing the excitation operator  $\hat{F}_\alpha$  by  $\hat{F}_\alpha|\Psi_0\rangle = |\Psi_\alpha\rangle$ , one obtains the relation

$$[\hat{H}_e, \hat{F}_\alpha]|\Psi_0\rangle = (E_\alpha - E_0)\hat{F}_\alpha|\Psi_0\rangle \equiv \Omega_\alpha \hat{F}_\alpha|\Psi_0\rangle,$$

which underlines the connection to the Heisenberg EOM for operators and thus explains the name EOM method [242]. Projecting and rearranging one transforms the EOM into the Rayleigh quotient

$$\Omega_\alpha = \frac{\langle \Psi_0 | \hat{F}_\alpha^\dagger [\hat{H}_e, \hat{F}_\alpha] | \Psi_0 \rangle}{\langle \Psi_0 | \hat{F}_\alpha^\dagger \hat{F}_\alpha | \Psi_0 \rangle}, \quad (\text{B.5})$$

from which the excitation energy is directly obtained. The computational effort goes into determining the excitation operator  $\hat{F}_\alpha$ . Representing it in the simplest case by single excitations,

$$\hat{F}_\alpha = \sum_{\sigma} \sum_{i \in \text{occ}} \sum_{p \in \text{virt}} X_i^p \hat{d}_p^\dagger \hat{d}_i, \quad (\text{B.6})$$

requiring  $\Omega_\alpha$  to be stationary leads to a generalized eigenvalue equation for the excitation amplitudes  $X_i^p$ . Note that also excitations removing or adding one electron from the system are possible to incorporate.

In order to reduce the in some cases immense computational costs of the CC and, in particular, the EOM-CC methods, two types of approximation are invoked: (i) some classes of unimportant unlinked terms are neglected from the beginning, and (ii) a perturbation selection of the linked operators and further selection of unlinked terms built from selected linked terms are performed. This preselection is the basis of the symmetry-adapted cluster (SAC) approach [243]. The SAC ground-state wave-function is, analogous to the CC construction, given by

$$|\Psi^{\text{SAC}}\rangle = \hat{Q} \exp(\hat{T}') |\Psi_0^{\text{HF}}\rangle, \quad (\text{B.7})$$

where  $\hat{Q}$  is a symmetry projection operator, while the excitation operator  $\hat{T}'$  differs from the CC excitation operator  $\hat{T}$  by the selection rules (i) and (ii). From the SAC wave-function, one can obtain the SAC-CI excited states  $|\Psi_\alpha^{\text{SAC-CI}}\rangle$  by applying a symmetry-adapted excitation operator  $\hat{F}'_\alpha$ , which is subjected to (i) and (ii), as well [243, 244].

<sup>3</sup>The EOM approach based on the CI theory is addressed as EOM-CI and, similarly, EOM-CC(SD) when the CC(SD) theory is used to compute the reference state.

## Source-field method and Hedin's equations

### C.1 Hedin's equations

An alternative to the diagrammatic approach to MBPT (see subsec. 2.5.2), is given by Hedin's equations. They can be derived – we follow ref. [80] here – by extending the Hamiltonian of an interacting fermionic or bosonic system by an artificial driving field  $\varphi(1) = \varphi(x_1, z_1)$ :

$$\begin{aligned} \hat{H}_\varphi(z) = & \int dx \int dx' h(x, x'; z) \hat{\psi}^\dagger(x) \hat{\psi}(x') + \frac{1}{2} \int dx \int dx' v(x, x') \hat{\psi}^\dagger(x) \hat{\psi}^\dagger(x') \hat{\psi}(x') \hat{\psi}(x) \\ & + \int dx \varphi(x, z) \hat{\rho}(x) \end{aligned} \quad (\text{C.1})$$

with  $h(x, x'; z) = h(x, x'; t_\pm)$  for  $z = t_\pm \in C_\pm$  and  $h(x, x'; z) = h(x, x'; t_0) - \mu\delta(x, x')$  (see subsec. 2.5.1) and  $\hat{\rho}(x) = \hat{\psi}^\dagger(x)\hat{\psi}(x)$ . Taking  $\varphi = 0$  reduces the Hamiltonian back to its original form. Revisiting the definition of expectation values on the contour, eq. (2.51), the Hamiltonian appears via the contour evolution operator  $\hat{U}_C(z_1, z_2)$ , which are functionals of  $\varphi$ . The corresponding derivatives are

$$\begin{aligned} \left. \frac{\delta \langle \hat{A}_H(z) \rangle}{\delta \varphi(x', z')} \right|_{\varphi=0} &= \frac{1}{\delta \varphi(x', z')} \text{Tr} [\mathcal{T} \hat{U}_C(z, z_i) \hat{U}_C(z_f, z) \hat{A}] = \text{Tr} [\mathcal{T} \hat{A}_H(z) \hat{\rho}(x', z')] , \\ \left. \frac{\delta \text{Tr} [\hat{U}_C(z_f, z_i)]}{\delta \varphi(x', z')} \right|_{\varphi=0} &= \text{Tr} [\hat{\rho}(x', z')] . \end{aligned}$$

The variation of the any correlator can now be executed. For instance, the relation between reducible polarizability and GF is simply given by

$$\chi(1; 2) = -i \left. \frac{\delta G(1, 1+)}{\delta \varphi(2)} \right|_{\varphi=0} = G_2(1, 2; 1+, 2+) - G(1, 1+)G(2, 2+) \quad (\text{C.2})$$

$$\Leftrightarrow -iG(1, 1+) = \int d2 \chi(1; 2) \varphi(2) \quad (\text{C.3})$$

Since  $\rho(x_1, z_1) = -iG(1, 1+)$ , eq. (C.2) underpins the interpretation of  $\chi(1; 2)$  as (spin-resolved) DD response function. Taking the electrostatic rearrangement of the system into account, one defines the total (external plus induced) field and the dielectric matrix  $\epsilon^{-1}(1; 2)$

$$V(1) = \varphi(1) + \int d2 v(1; 2) \rho(2) , \quad \epsilon^{-1}(1; 2) = \left. \frac{\delta V(1)}{\delta \varphi(2)} \right|_{\varphi=0} = \delta(1; 2) + \int d3 v(1; 3) \chi(3; 2) . \quad (\text{C.4})$$

The relation to the screened interaction is given by  $W(1; 2) = \int d3 \epsilon^{-1}(1; 3) v(3; 2)$  and thus  $W(1; 2) = v(1; 2) + \int d(34) v(1; 3) \chi(3; 4) v(4; 2)$ . Continuing the analysis of the functional derivatives of screened interaction  $W(1; 2)$ , GF  $G(1; 2)$ , self-energy  $\Sigma(1; 2)$  and polarization  $P(1; 2)$  reveals their close connection, which is expressed by Hedin's equations:

$$\Sigma^{\text{xc}}(1; 2) = \text{i} \int \text{d}(34) G(1; 3) W(1; 4) \Gamma(3, 2; 4), \quad (\text{C.5a})$$

$$W(1; 2) = \nu(1; 2) + \int \text{d}(34) W(1; 3) P(3; 4) \nu(4; 2). \quad (\text{C.5b})$$

$$P(1; 2) = -\text{i} \int \text{d}(34) G(1; 3) G(4; 1) \Gamma(3, 4; 2), \quad (\text{C.5c})$$

$$\Gamma(1, 2; 3) = \delta(1; 2) \delta(1; 3) + \int \text{d}(4567) K(1, 2; 4, 5) G(4; 6) G(7; 5) \Gamma(6, 7; 3). \quad (\text{C.5d})$$

For concreteness, we have formulated Hedin's equations (C.5) for a fermionic system. They have to be solved self-consistently along with the contour Dyson equation for the GF

$$G(1; 2) = g(1; 2) + \int \text{d}(34) g(1; 3) [\Sigma^{\text{H}}(3; 4) + \Sigma^{\text{xc}}(3; 4)] G(4; 2). \quad (\text{C.6})$$

The last equation (C.5d) constitutes the Bethe-Salpeter equation (BSE) for the vertex function;  $K(1, 2; 3, 4) = \delta \Sigma_{\text{xc}}(1; 2) / \delta G(3; 4)$  denotes the BSE kernel. The approximation  $\Gamma(1, 2; 3) \approx \delta(1; 2) \delta(1; 3)$  simplifies the expressions (C.5a) and (C.5c) for the self-energy and the polarization, respectively, to the well-known GW approximation

$$\Sigma^{\text{xc}}(1; 2) = \text{i} G(1; 2) W(1; 2) = \text{i} G(1; 2) \nu(1, 2) + \text{i} G(1; 2) \delta W(1; 2), \quad P(1; 2) = -\text{i} G(2; 1) G(1; 2). \quad (\text{C.7})$$

The exchange part  $\Sigma^{\text{x}}(1; 2) = \text{i} G(1; 2) \nu(1, 2)$  is a MF contribution and can be incorporated by redefining the reference GF. Choosing the HF GF  $g(1; 2) \rightarrow g^{\text{HF}}(1; 2)$  simplifies the Dyson equation into

$$G(1; 2) = g^{\text{HF}}(1; 2) + \int \text{d}(34) g^{\text{HF}}(1; 3) \Sigma^{\text{c}}(3; 4) G(4; 2) \quad (\text{C.8})$$

with the correlation self-energy  $\Sigma^{\text{c}}(1; 2) = \text{i} G(1; 2) \delta W(1; 2)$ .

## C.2 Generating functionals for electron-boson models

The source-field method summarized in sec. C.1 offers a useful toolbox for EB systems, as well. Let us consider the EB Hamiltonian

$$\hat{H}_0(z) = \int \text{d}x \int \text{d}x' h(x, x'; z) + \sum_{\nu} \int \text{d}x v_{\nu}(x) \hat{\rho}(x) \hat{Q}_{\nu} + \frac{1}{2} \sum_{\nu} \Omega_{\nu} (\hat{P}_{\nu}^2 + \hat{Q}_{\nu}^2) \quad (\text{C.9})$$

and modify it by two external fields acting on the electrons *and* the quasi-bosons, respectively:

$$\hat{H}_{\varphi \xi}(z) = \hat{H}_0(z) + \int \text{d}x \varphi(x, z) \hat{\rho}(x) + \sum_{\nu} \xi_{\nu}(z) \hat{Q}_{\nu}. \quad (\text{C.10})$$

As in sec. C.1, all quantities are treated as implicit functionals of the source fields  $\varphi(x, z)$  and  $\xi_{\nu}(z)$ . For functional derivatives, we assume taking  $\varphi = 0$ ,  $\xi_{\nu} = 0$  in what follows. Like for fermionic system, we introduce the total field including the MF induced field – which is the counterpart to the electrostatic potential in eq. (C.4) – by

$$V(x, z) = \varphi(x, z) + \sum_{\nu} \int \text{d}x v_{\nu}(x) \langle \hat{Q}_{\nu} \rangle \equiv \varphi(x, z) + \zeta(x, z). \quad (\text{C.11})$$

The bosonic degrees of freedom can be accessed via the functional derivative with respect to the source fields  $\xi_{\nu}(z)$ . First one notices

$$D_{\mu\nu}(z_1, z_2) = -\text{i} [\langle \hat{Q}_{\mu}(z_1) \hat{Q}_{\nu}(z_2) \rangle - \langle \hat{Q}_{\mu}(z_1) \rangle \langle \hat{Q}_{\nu}(z_2) \rangle] = \frac{\delta \langle \hat{Q}_{\mu}(z_1) \rangle}{\delta \xi_{\nu}(z_2)}. \quad (\text{C.12})$$



The quasi-boson GF thus describes the fluctuations of the coordinates  $\langle \hat{Q}_\mu \rangle$  due to coupling to external (or internal) fields. Mixed electronic-bosonic correlators lead to the notion of the self-energy for both the electrons and the bosons, respectively. Adopting a similar strategy for connecting the relevant correlators by functional derivatives as for Hedin's equations (see sec. C.1), one finds the analogue of Hedin's equations for the EB model:

$$\Sigma^c(1; 2) = i \int d(34) G(1; 3) \mathcal{W}(1; 4) \Lambda(3, 2; 4), \quad (\text{C.13a})$$

$$P(1; 2) = -i \int d(34) G(1; 3) G(4; 1) \Lambda(3, 4; 2), \quad (\text{C.13b})$$

$$\Lambda(1, 2; 3) = \delta(1; 2) \delta(1; 3) + \int d(4567) K(1, 2; 4, 5) G(4; 6) G(7; 5) \Lambda(6, 7; 3). \quad (\text{C.13c})$$

The details of the derivation can be found in our work [E7]. Note the one-to-one correspondence of the Hedin's equations (C.5) and their EB version (C.13). If we identify the screened interaction  $W(1; 2)$  with the EB effective interaction  $\mathcal{W}(1; 2)$  (and the respective vertex functions), the Hedin's equations for the EB model (C.13) are exactly reproduced. The four-point kernel appearing in the BSE (C.13c) is defined analogously. The boson-mediated interaction, on the other hand, is determined by the boson GF:

$$\mathcal{W}(1; 2) = \sum_{\mu\nu} v_\nu(x_1) D_{\mu\nu}(z_1, z_2) v_\mu(x_2). \quad (\text{C.14})$$

As for the purely fermionic case, the Dyson equations for the GF and the boson correlator (which plays the role of the screened interaction) are required to complement Hedin's equations (C.13):

$$G(1; 2) = g(1; 2) + \int d(34) g(1; 3) [\Sigma^{\text{MF}}(3; 4) + \Sigma^c(3; 4)] G(4; 2) \quad (\text{C.15})$$

for the electrons (with  $\Sigma^{\text{MF}}(1, 2) = \zeta(x_1, z_1) \delta(z_1, z_2)$ ) and, for the bosons,

$$D_{\mu\nu}(z_1, z_2) = d_{\mu\nu}(z_1, z_2) + \sum_{\mu'\nu'} \int_C d(z_3 z_4) d_{\mu\mu'}(z_1, z_3) \Pi_{\mu'\nu'}(z_3, z_4) D_{\nu'\nu}(z_4, z_2). \quad (\text{C.16})$$

The bosonic self-energy appearing in eq. (C.16) is directly related to the irreducible polarization (C.13b) by

$$\Pi_{\mu\nu}(z_1, z_2) = - \int dx_1 \int dx_2 v_\mu(x_1) P(1; 2) v_\nu(x_2). \quad (\text{C.17})$$

As usual, the GFs labelled by small letters refer to the non-interacting case ( $v_\nu = 0$ ). While the fermionic reference GF obeys, as usual  $i\partial_{z_1} g(1; 2) = \delta(1; 2) + \int d3 h(x_1, x_3; z_1) \delta(z_1, z_3) g(3; 2)$ , the non-interacting bosonic GF is subject to the second-order EOM

$$-\frac{1}{2\Omega_\mu} \left[ \partial_{z_1}^2 + \Omega_\mu^2 \right] d_{\mu\nu}(z_1, z_2) = \delta_{\mu\nu} \delta(z_1, z_2). \quad (\text{C.18})$$

For this reason, transforming the Dyson equation (C.16) into the contour EOM results in a *second-order* EOM for  $D_{\mu\nu}(z_1, z_2)$ .

### C.3 Electron-boson models and screened interaction

How can a purely electronic system be mapped onto an EB model? This question was first answered by Pines and Bohm [99] for the homogeneous electron gas in equilibrium, where a unitary transformation leads to the EB Hamiltonian similar to eq. (C.9) after neglecting fluctuating terms (RPA) [66]. A one-to-one correspondence can also be established for a general system under similar conditions. To be precise, we consider an electronic system in equilibrium at zero temperature. Via the FDT for the GF<sup>1</sup> the relevant Keldysh components of the GF in frequency space can be represented by the spectral function  $A(x, x'; \omega)$ :

$$G^{\gtrless}(x, x'; \omega) = \mp i \theta(\pm \omega \mp \mu) A(x, x'; \omega), \quad G^{\text{R}}(x, x'; \omega) = \int_{-\infty}^{\infty} \frac{d\omega'}{2\pi} \frac{A(x, x'; \omega')}{\omega - \omega' + i\eta}. \quad (\text{C.19})$$

<sup>1</sup>The concept of the FDT is more general than presented in subsec. 2.6.1 for the response functions. Generally, the FDT allows to determine greater/lesser components of some correlator in Keldysh space from the corresponding spectral function.

The spectral function is, in turn, obtained from the retarded GF (which is computed by solving the retarded Dyson equation (2.68)). Hence, the retarded GF determines all other Keldysh components. A similar statement can be made for the screened interaction. Employing the Lehmann representation of the equilibrium DD response function (2.89) with a slight extension by the spin degree of freedom yields, via eq. (2.61), for dynamical part of the screened interaction:

$$\chi^R(x, x'; \omega) = \sum_{\nu} \frac{2\omega_{\nu}}{(\omega + i\eta)^2 - \omega_{\nu}^2} \rho_{\nu}(x) \rho_{\nu}(x') \Rightarrow \delta W^R(x, x'; \omega) = \sum_{\nu} \frac{2\omega_{\nu}}{(\omega + i\eta)^2 - \omega_{\nu}^2} V_{\nu}(x) V_{\nu}(x').$$

Here,  $V_{\nu}(\mathbf{r}\sigma) = \int d\mathbf{r}' v(\mathbf{r} - \mathbf{r}') \rho_{\nu}(\mathbf{r}'\sigma)$  denote the fluctuation potentials. The many-body excitation energies are labelled by  $\omega_{\nu} = E_{\nu} - E_0$  to avoid any confusion with the bosonic frequencies.

Let us now turn to the EB Hamiltonian. The retarded component of the effective interaction (C.14) is given by

$$\mathcal{W}^R(x, x'; \omega) = \sum_{\mu\nu} v_{\mu}(x) D_{\mu\nu}^R(\omega) v_{\nu}(x'). \quad (\text{C.20})$$

Ignoring the back-action of the electrons onto the bosons (neglecting the boson self-energy (C.17), that is), one finds  $d_{\mu\nu}^R(\omega) = \delta_{\mu\nu} \Omega_{\nu} / ((\omega + i\eta)^2 - \Omega_{\nu}^2)$  for the non-interaction boson GF and thus

$$\mathcal{W}^R(x, x'; \omega) = \sum_{\mu} v_{\mu}(x) \frac{\Omega_{\mu}}{(\omega + i\eta)^2 - \Omega_{\mu}^2} v_{\mu}(x'). \quad (\text{C.21})$$

Choosing  $v_{\mu}(x) = \sqrt{2} V_{\mu}(x)$  and the boson frequencies  $\Omega_{\mu}$  to be identical to the excitation energies of the electronic system  $\omega_{\mu}$ , the equivalence  $\delta W^R(x, x'; \omega) = \mathcal{W}^R(x, x'; \omega)$  is guaranteed. By virtue of the FDT, this statement can be extended to the other Keldysh components. Therefore, the correlation self-energy within the GWA is exactly reproduced. Choosing the one-body Hamiltonian in eq. (C.9) as the HF Hamiltonian, the GFs obtained for the electronic and for the EB system, respectively, are identical.

Within a time-dependent scenario, this one-to-one correspondence is not preserved. This can be seen from the (i) the varying MF contributions for the EB, which differs from the HF term, and (ii) the different time evolution of the screened interaction as compared to the fully-interacting boson propagators (including the back-action of the electronic polarization onto the bosons). While point (i) may not be very important in case of strong dynamical screening (i. e. close to plasmon resonances), (ii) is an important point to be clarified by future studies.

## Markovian quantum kinetics

In this appendix we briefly introduce the description of the dissipative quantum kinetics used to model the electron-vibron interaction in [E6]. Suppose a small subsystem (Hilbert space  $\mathcal{H}_0$ ) is coupled to a thermal bath (Hilbert space  $\mathcal{H}_B$ ). The generic Hamiltonian reads

$$\hat{H}(t) = \hat{H}_0(t) + \hat{H}_{\text{int}} + \hat{H}_B, \quad \hat{H}_{\text{int}} = \sum_{\mu} \hat{M}_{\mu} \otimes \hat{B}_{\mu}, \quad (\text{D.1})$$

where  $\hat{H}_0(t) = \hat{H}_0^{(0)} + \hat{V}_0(t)$  describes the system (operating in  $\mathcal{H}_0$ ),  $\hat{H}_B$  stands for the bath Hamiltonian and  $\hat{H}_{\text{int}}$  accounts for the interaction. The eigenstates of the static system Hamiltonian are denoted by  $\hat{H}_0^{(0)}|a\rangle = E_a|a\rangle$ . We assume linear coupling with  $\hat{M}_{\mu}$  acting in  $\mathcal{H}_0$ , whereas  $\hat{B}_{\mu}$  denote the bath operators. The goal is to find an effective EOM for the system density matrix  $\hat{\rho}_0(t) = \text{Tr}_B[\hat{\rho}(t)]$ , which is obtained by tracing the full density matrix  $\hat{\rho}(t)$  over the bath degrees of freedom. For convenience, we switch to the interaction picture with respect to the non-interacting Hamiltonian  $\hat{H}_0(t) + \hat{H}_B$ . From the Heisenberg EOM for the density matrix, one finds

$$\frac{d}{dt}\hat{\rho}_0(t) = -i\text{Tr}_B[[\hat{H}_{\text{int}}(t), \hat{\rho}^{(0)}]] - \int_0^t dt' \text{Tr}_B[[\hat{H}_{\text{int}}(t), [\hat{H}_{\text{int}}(t'), \hat{\rho}(t')]]], \quad \hat{\rho}^{(0)} = \hat{\rho}(t=0). \quad (\text{D.2})$$

Eq. (D.2) is still exact, but entails the full (generally unknown) density matrix  $\hat{\rho}(t)$ . This dependence is removed by the Born approximation  $\hat{\rho}(t) \approx \hat{\rho}_0(t) \otimes \hat{\rho}_B^{(0)}$  ( $\hat{\rho}_B^{(0)}$  is the equilibrium bath density matrix). The EOM (D.2) is thus transformed into an integro-differential equation for the system density matrix  $\hat{\rho}_0(t)$  only. Similarly to the KBEs (see sec. 6.1), the memory effects due to the integration represent a substantial complication, both for analytical and numerical considerations. Ignoring the memory completely is known as the Markovian approximation [245] (the time evolution is treated as Markov process). Within the Markovian approximation,  $\hat{\rho}_0(t')$  is replaced by  $\hat{\rho}_0(t)$  under the integral. Furthermore, the upper bound for of the integration is extended to infinity. After some algebra and removing highly-oscillatory terms (secular approximation), the EOM attains the form of the Lindblad master equation [223] in the Heisenberg picture:

$$\frac{d}{dt}\hat{\rho}_0(t) = -i[\hat{H}_0(t) + \hat{H}_{\text{LS}}, \hat{\rho}_0(t)] + \sum_{abcd} \gamma_{abcd} \left( \langle b|\hat{\rho}_0(t)|d\rangle|a\rangle\langle c| - \frac{1}{2}\delta_{ca} \{ |d\rangle\langle b|, \hat{\rho}_0(t) \} \right). \quad (\text{D.3})$$

Here, the curly brackets denote the anti-commutator. The Lamb-shift Hamiltonian  $\hat{H}_{\text{LS}}$  describes the renormalization of the system levels due to the presence of the bath and is defined by

$$\langle a|\hat{H}_{\text{LS}}|b\rangle = \frac{1}{2i} \sum_{\mu\nu} \sigma_{\mu\nu}(E_b - E_c) \delta_{E_b, E_c} \langle c|\hat{M}_{\nu}|b\rangle \langle a|\hat{M}_{\mu}^{\dagger}|c\rangle. \quad (\text{D.4})$$

Dephasing and relaxation effects are incorporated by

$$\gamma_{abcd} = \sum_{\mu\nu} \gamma_{\mu\nu}(E_b - E_a) \delta_{E_b - E_a, E_d - E_c} \langle a|\hat{M}_{\nu}|b\rangle \langle d|\hat{M}_{\mu}^{\dagger}|c\rangle. \quad (\text{D.5})$$

The energy-dependent functions  $\sigma_{\mu\nu}(E)$  and  $\gamma_{\mu\nu}(E)$  are related by the Hilbert transformation as they are the imaginary and real part, respectively, of the bath correlation function

$$\Gamma_{\mu\nu}(E) = \int_0^{\infty} dt \text{Tr}_B [e^{i\hat{H}_B t} \hat{B}_{\mu} e^{-i\hat{H}_B t} \hat{B}_{\nu} \hat{\rho}_B^{(0)}] e^{iEt} \equiv \int_0^{\infty} dt \langle \hat{B}_{\mu}(t) \hat{B}_{\nu} \rangle_B e^{iEt}. \quad (\text{D.6})$$

An important special case is a bosonic bath  $\hat{H}_B = \frac{1}{2} \sum_{\mu} \Omega_{\mu} (\hat{P}_{\mu}^2 + \hat{Q}_{\mu}^2)$  (see subsec. 2.5.6) and linear coupling to the coordinates  $\hat{B}_{\mu} = \hat{Q}_{\mu}$ . It is straightforward to see that the integrand in eq. (D.6) then equals <sup>1</sup>  $iD_{\mu\nu}^>(t, 0)$  (see subsec. 2.5.6). Fourier transforming yields

$$\Gamma_{\mu\nu}(E) = - \int_{-\infty}^{\infty} \frac{dE'}{2\pi} \frac{D_{\mu\nu}^>(E')}{E - E' + i\eta} = i \int_{-\infty}^{\infty} \frac{dE'}{2\pi} (N_B(E') + 1) \frac{A_{\mu\nu}(E')}{E - E' + i\eta}, \quad \eta \rightarrow 0+ . \quad (\text{D.7})$$

Here, the greater GF is represented in terms of the bosonic spectral function (which is defined analogously to eq. (2.72)) and the Bose distribution  $N_B(E)$  (for details see [E7]). In particular, the relaxation rates and the level renormalization are found from

$$\gamma_{\mu\nu}(E) = (N_B(E) + 1) A_{\mu\nu}(E), \quad \sigma_{\mu\nu}(E) = \frac{i}{\pi} \mathcal{P} \int_{-\infty}^{\infty} dE' \frac{\gamma_{\mu\nu}(E')}{E - E'}, \quad (\text{D.8})$$

where  $\mathcal{P}$  denotes the principal part.

---

<sup>1</sup>We assume  $\langle \hat{B}_{\mu}(t) \rangle_B = 0$ . This, in fact, also required to derive the Lindblad equation (D.3).

---

## Bibliography

- [1] F. Krausz and M. Ivanov, *Rev. Mod. Phys.* **81**, 163 (2009).
- [2] H. A. Bethe and E. E. Salpeter, *Quantum mechanics of one-and two-electron atoms* (Plenum Pub. Corp, New York, 1977).
- [3] K. Yabana, T. Sugiyama, Y. Shinohara, T. Otobe, and G. F. Bertsch, *Phys. Rev. B* **85**, 045134 (2012).
- [4] C. Pellegrini, J. Flick, I. V. Tokatly, H. Appel, and A. Rubio, *Phys. Rev. Lett.* **115**, 093001 (2015).
- [5] P. M. M. C. de Melo and A. Marini, *Phys. Rev. B* **93**, 155102 (2016).
- [6] R. Miller, T. E. Northup, K. M. Birnbaum, A. Boca, A. D. Boozer, and H. J. Kimble, *Journal of Physics B-Atomic Molecular and Optical Physics* **38**, S551 (2005).
- [7] M. J. Hartmann, F. G. S. L. Brandao, and M. B. Plenio, *Laser & Photonics Reviews* **2**, 527 (2008).
- [8] W. Lange, *Nature Phys.* **5**, 455 (2009).
- [9] H. Tanji-Suzuki, I. D. Leroux, M. H. Schleier-Smith, M. Cetina, A. T. Grier, J. Simon, and V. Vuletic, in *Advances in Atomic, Molecular, and Optical Physics, Vol 60*, Vol. 60, edited by E. Arimondo, P. R. Berman, and C. C. Lin (Elsevier Academic Press Inc, San Diego, 2011) pp. 201–237.
- [10] M. F. Ciappina, S. S. Aćimović, T. Shaaran, J. Biegert, R. Quidant, and M. Lewenstein, *Opt. Express* **20**, 26261 (2012).
- [11] R. W. Bowman and M. J. Padgett, *Rep. Prog. Phys.* **76**, 026401 (2013).
- [12] J. Wätzel, Y. Pavlyukh, A. Schäffer, and J. Berakdar, *Carbon* **99**, 439 (2016).
- [13] F. Remacle and R. D. Levine, *Int. J. Quantum Chem.* **67**, 85 (1998).
- [14] R. P. Feynman, *Phys. Rev.* **56**, 340 (1939).
- [15] G. W. F. Drake, *Springer Handbook of Atomic, Molecular, and Optical Physics* (Springer, 2006).
- [16] D. A. Micha and I. Burghardt, *Quantum Dynamics of Complex Molecular Systems* (Springer Science & Business Media, 2006).
- [17] O. Svelto, S. D. Silvestri, and G. Denardo, *Ultrafast Processes in Spectroscopy* (Springer Science & Business Media, 2012).
- [18] M. D. Fayer, *Ultrafast Infrared Vibrational Spectroscopy* (CRC Press, 2013).
- [19] M. Gruebele and A. H. Zewail, *J. Chem. Phys.* **98**, 883 (1993).
- [20] Q. Wang, R. Schoenlein, L. Peteanu, R. Mathies, and C. Shank, *Science* **266**, 422 (1994).
- [21] A. H. Zewail, *J. Phys. Chem. A* **104**, 5660 (2000).
- [22] E. B. W. Jr, *J. Chem. Phys.* **9**, 76 (1941).

- [23] J. M. Hollas, *Modern spectroscopy*, 3rd ed. (J. Wiley, Chichester ; New York, 1996).
- [24] P. W. Atkins and J. De Paula, *Physical chemistry* (Oxford University Press, Oxford, 2006).
- [25] E. B. Wilson, J. C. Decius, and P. C. Cross, *Molecular vibrations: the theory of infrared and Raman vibrational spectra* (Dover Publications, New York, 1980).
- [26] F. T. Smith, *Phys. Rev.* **179**, 111 (1969).
- [27] A. Abedi, N. T. Maitra, and E. K. U. Gross, *Phys. Rev. Lett.* **105**, 123002 (2010).
- [28] S. K. Min, F. Agostini, and E. Gross, *Phys. Rev. Lett.* **115**, 073001 (2015).
- [29] J. M. Ziman, *Electrons and Phonons: The Theory of Transport Phenomena in Solids* (OUP Oxford, 1960).
- [30] R. van Leeuwen, *Phys. Rev. B* **69**, 115110 (2004).
- [31] K.-H. Bennemann and J. B. Ketterson, *Superconductivity: Volume 1: Conventional and Unconventional Superconductors Volume 2: Novel Superconductors* (Springer Science & Business Media, 2008).
- [32] M. Demuth and M. Krishna, *Determining Spectra in Quantum Theory* (Springer Science & Business Media, 2006).
- [33] C. J. Joachain, *Quantum collision theory* (North-Holland, 1975).
- [34] A. R. Edmonds, *Angular Momentum in Quantum Mechanics* (Princeton University Press, 1996).
- [35] F. W. J. Olver, D. W. Lozier, R. F. Boisvert, and C. W. Clark, *NIST Handbook of Mathematical Functions* (Cambridge University Press, 2010).
- [36] T. N. Rescigno, M. Baertschy, W. A. Isaacs, and C. W. McCurdy, *Science* **286**, 2474 (1999).
- [37] C. W. McCurdy, M. Baertschy, and T. N. Rescigno, *J. Phys. B* **37**, R137 (2004).
- [38] C. W. McCurdy, D. A. Horner, T. N. Rescigno, and F. Martín, *Phys. Rev. A* **69**, 032707 (2004).
- [39] D. A. Horner, F. Morales, T. N. Rescigno, F. Martín, and C. W. McCurdy, *Phys. Rev. A* **76**, 030701(R) (2007).
- [40] F. L. Yip, T. N. Rescigno, C. W. McCurdy, and F. Martín, *Phys. Rev. Lett.* **110**, 173001 (2013).
- [41] D. R. Hartree, *Math. Proc. Cambridge* **24**, 89 (1928).
- [42] D. R. Hartree, *Math. Proc. Cambridge* **24**, 426 (1928).
- [43] K. Gavroglou and A. Simões, *Neither Physics Nor Chemistry: A History of Quantum Chemistry* (MIT Press, 2012).
- [44] A. Szabó and N. S. Ostlund, *Modern Quantum Chemistry: Introduction to Advanced Electronic Structure Theory* (Courier Dover Publications, 1996).
- [45] E. J. Brändas, E. S. Kryachko, and P. O. Löwdin, *Fundamental World of Quantum Chemistry (Volume 3): A Tribute to the Memory of Per-Olov L Wdin* (Springer, 2004).
- [46] L. Piela, *Ideas of Quantum Chemistry* (Elsevier, 2007).
- [47] D. Vanfleteren, D. V. Neck, P. W. Ayers, R. C. Morrison, and P. Bultinck, *J. Chem. Phys.* **130**, 194104 (2009).
- [48] P. Hohenberg and W. Kohn, *Phys. Rev.* **136**, B864 (1964).
- [49] S. F. Sousa, P. A. Fernandes, and M. J. Ramos, *J. Phys. Chem. A* **111**, 10439 (2007).

- [50] T. Tsuneda, J.-W. Song, S. Suzuki, and K. Hirao, *J. Chem. Phys.* **133**, 174101 (2010).
- [51] S. Kummel and L. Kronik, *Rev. Mod. Phys.* **80**, 3 (2008).
- [52] X. Andrade and A. Aspuru-Guzik, *Phys. Rev. Lett.* **107**, 183002 (2011).
- [53] R. van Leeuwen and E. J. Baerends, *Phys. Rev. A* **49**, 2421 (1994).
- [54] P. R. T. Schipper, O. V. Gritsenko, S. J. A. v. Gisbergen, and E. J. Baerends, *J. Chem. Phys.* **112**, 1344 (2000).
- [55] T. Yanai, D. P. Tew, and N. C. Handy, *Chem. Phys. Lett.* **393**, 51 (2004).
- [56] M. A. L. Marques and E. K. U. Gross, *Annu. Rev. Phys. Chem.* **55**, 427 (2004).
- [57] R. M. Dreizler and E. K. U. Gross, *Density Functional Theory: An Approach to the Quantum Many-Body Problem* (Springer Science & Business Media, 2012).
- [58] M. A. L. Marques, N. T. Maitra, F. M. S. Nogueira, E. K. U. Gross, and A. Rubio, *Fundamentals of Time-Dependent Density Functional Theory* (Springer, 2012).
- [59] E. Runge and E. K. U. Gross, *Phys. Rev. Lett.* **52**, 997 (1984).
- [60] R. van Leeuwen, *Phys. Rev. Lett.* **76**, 3610 (1996).
- [61] G. Onida, L. Reining, and A. Rubio, *Rev. Mod. Phys.* **74**, 601 (2002).
- [62] C. Verdozzi, D. Karlsson, M. Puig von Friesen, C. O. Almbladh, and U. von Barth, *Chem. Phys.* **391**, 37 (2011).
- [63] J. I. Fuks and N. T. Maitra, *Phys. Chem. Chem. Phys.* **16**, 14504 (2014).
- [64] W. H. Dickhoff and D. V. Neck, *Many-body Theory Exposed!: Propagator Description of Quantum Mechanics in Many-body Systems* (World Scientific, 2008).
- [65] T. Seideman, *Current-Driven Phenomena in Nanoelectronics* (CRC Press, 2016).
- [66] E. K. U. Gross, E. Runge, and O. Heinonen, *Many-Particle Theory*, (Taylor & Francis, 1991).
- [67] G. D. Mahan, *Many-Particle Physics* (Springer Science & Business Media, 2000).
- [68] A. L. Fetter and J. D. Walecka, *Quantum Theory of Many-particle Systems* (Courier Corporation, 2003).
- [69] A. A. Abrikosov, L. P. Gorkov, and I. E. Dzyaloshinski, *Methods of Quantum Field Theory in Statistical Physics* (Courier Corporation, 2012).
- [70] M. Bonitz, *Quantum Kinetic Theory* (Springer, 2015).
- [71] N. E. Dahlen and R. van Leeuwen, *Phys. Rev. Lett.* **98**, 153004 (2007).
- [72] K. Balzer and M. Bonitz, *Nonequilibrium Green's Functions Approach to Inhomogeneous Systems* (Springer, 2012).
- [73] M. P. von Friesen, C. Verdozzi, and C.-O. Almbladh, *Phys. Rev. Lett.* **103** (2009).
- [74] G. Stefanucci and R. v. Leeuwen, *Nonequilibrium Many-Body Theory of Quantum Systems: A Modern Introduction* (Cambridge University Press, 2013).
- [75] L. P. Kadanoff and G. Baym, *Quantum Statistical Mechanics* (Addison-Wesley, 1994).
- [76] G. Baym and L. P. Kadanoff, *Phys. Rev.* **124**, 287 (1961).
- [77] K. A. Müller and A. Bussmann-Holder, *Superconductivity in Complex Systems* (Springer Science & Business Media, 2005).

- [78] M. Puig von Friesen, C. Verdozzi, and C.-O. Almbladh, *Phys. Rev. B* **82**, 155108 (2010).
- [79] N. Schlünzen, S. Hermanns, M. Bonitz, and C. Verdozzi, *Phys. Rev. B* **93**, 035107 (2016).
- [80] G. Strinati, *Riv. Nuovo Cimento* **11**, 1 (1988).
- [81] F. Aryasetiawan and O. Gunnarsson, *Rep. Prog. Phys.* **61**, 237 (1998).
- [82] R. A. Evarestov, *Quantum Chemistry of Solids: The LCAO First Principles Treatment of Crystals* (Springer Science & Business Media, 2007).
- [83] P. Fulde, *Correlated Electrons in Quantum Matter* (World Scientific, 2012).
- [84] H. Ebert, D. Koedderitzsch, and J. Minar, *Rep. Prog. Phys.* **74**, 096501 (2011).
- [85] Y. Pavlyukh and J. Berakdar, *J. Chem. Phys.* **135**, 201103 (2011).
- [86] J. Freericks, H. Krishnamurthy, and T. Pruschke, *Phys. Rev. Lett.* **102**, 136401 (2009).
- [87] E. Goulielmakis, Z.-H. Loh, A. Wirth, R. Santra, N. Rohringer, V. S. Yakovlev, S. Zherebtsov, T. Pfeifer, A. M. Azzeer, M. F. Kling, S. R. Leone, and F. Krausz, *Nature* **466**, 739 (2010).
- [88] R. Huber, F. Tauser, A. Brodschelm, M. Bichler, G. Abstreiter, and A. Leitenstorfer, *Nature* **414**, 286 (2001).
- [89] R. Huber, C. Kübler, S. Tübel, A. Leitenstorfer, Q. T. Vu, H. Haug, F. Köhler, and M.-C. Amann, *Phys. Rev. Lett.* **94**, 027401 (2005).
- [90] L. Campbell, L. Hedin, J. J. Rehr, and W. Bardyszewski, *Phys. Rev. B* **65**, 064107 (2002).
- [91] H. Fröhlich, H. Pelzer, and S. Zienau, *The London, Edinburgh, and Dublin Philosophical Magazine and Journal of Science* **41**, 221 (1950).
- [92] H. Fröhlich, *Proceedings of the Royal Society of London A: Mathematical, Physical and Engineering Sciences* **215**, 291 (1952).
- [93] H. Fröhlich, *Advances in Physics* **3**, 325 (1954).
- [94] W. Schmidt and M. Schreiber, *J. Chem. Phys.* **86**, 953 (1987).
- [95] D. Feinberg, S. Ciuchi, and F. de Pasquale, *International Journal of Modern Physics B* **04**, 1317 (1990).
- [96] T. Holstein, *Annals of Physics* **281**, 706 (2000).
- [97] A. J. White, B. D. Fainberg, and M. Galperin, *J. Phys. Chem. Lett.* **3**, 2738 (2012).
- [98] K. Kaasbjerg and A. Nitzan, *Phys. Rev. Lett.* **114**, 126803 (2015).
- [99] D. Pines and D. Bohm, *Phys. Rev.* **85**, 338 (1952).
- [100] P. Minnhagen, *J. Phys. C* **8**, 1535 (1975).
- [101] L. Hedin, J. Michiels, and J. Inglesfield, *Phys. Rev. B* **58**, 15565 (1998).
- [102] B. I. Lundqvist, *Phys. Kondens. Mater.* **9**, 236 (1969).
- [103] D. C. Langreth, *Phys. Rev. B* **1**, 471 (1970).
- [104] Y. Pavlyukh, J. Berakdar, and A. Rubio, arXiv:1601.04285 [cond-mat] (2016).
- [105] Q. T. Vu, H. Haug, and S. W. Koch, *Phys. Rev. B* **73**, 205317 (2006).
- [106] M. Eckstein and P. Werner, *Phys. Rev. Lett.* **110**, 126401 (2013).
- [107] Y. Murakami, P. Werner, N. Tsuji, and H. Aoki, *Phys. Rev. B* **91**, 045128 (2015).



- [108] G. Giuliani and G. Vignale, *Quantum Theory of the Electron Liquid* (Cambridge University Press, 2005).
- [109] A. Sakko, A. Rubio, M. Hakala, and K. Hämäläinen, *J. Chem. Phys.* **133**, 174111 (2010).
- [110] D. P. Chong, *Recent Advances in Density Functional Methods* (World Scientific, 1995).
- [111] Y. Pavlyukh, J. Berakdar, and K. Köksal, *Phys. Rev. B* **85**, 195418 (2012).
- [112] A. Verkhovtsev, A. V. Korol, and A. V. Solov'yov, *Eur. Phys. J. D* **66**, 253 (2012).
- [113] P. B. Corkum, *Phys. Rev. Lett.* **71**, 1994 (1993).
- [114] K. Zhao, Q. Zhang, M. Chini, Y. Wu, X. Wang, and Z. Chang, *Optics Lett.* **37**, 3891 (2012).
- [115] J. Itatani, F. Quere, G. L. Yudin, M. Y. Ivanov, F. Krausz, and P. B. Corkum, *Phys. Rev. Lett.* **88**, 173903 (2002).
- [116] C. Lemell, S. Neppl, G. Wachter, K. Tókési, R. Ernstorfer, P. Feulner, R. Kienberger, and J. Burgdörfer, *Phys. Rev. B* **91**, 241101 (2015).
- [117] P. Willmott, *An Introduction to Synchrotron Radiation: Techniques and Applications* (John Wiley & Sons, 2011).
- [118] A. A. Zholents and M. S. Zolotarev, *Phys. Rev. Lett.* **76**, 912 (1996).
- [119] R. R. Blyth, R. Delaunay, M. Zitnik, J. Krempasky, R. Krempaska, J. Slezak, K. C. Prince, R. Richter, M. Vondracek, R. Camilloni, L. Avaldi, M. Coreno, G. Stefani, C. Furlani, M. de Simone, S. Stranges, and M. Y. Adam, *J. Electron. Spectrosc. Relat. Phenom.* **101-103**, 959 (1999).
- [120] M. Gell-Mann and M. L. Goldberger, *Phys. Rev.* **91**, 398 (1953).
- [121] P. W. Atkins and R. S. Friedman, *Molecular quantum mechanics*, 3rd ed. (Oxford Univ. Press, Oxford, 2001).
- [122] J. Berakdar, *Concepts of Highly Excited Electronic Systems* (John Wiley & Sons, 2006).
- [123] B. Henke, E. Gullikson, and J. Davis, *Atomic Data and Nuclear Data Tables* **54**, 181 (1993).
- [124] U. Fano, *Phys. Rev.* **124**, 1866 (1961).
- [125] E. Prodan and P. Nordlander, *Chem. Phys. Lett.* **352**, 140 (2002).
- [126] E. Prodan and P. Nordlander, *Nano Lett.* **3**, 543 (2003).
- [127] H. Wang, D. W. Brandl, P. Nordlander, and N. J. Halas, *Accounts of Chemical Research* **40**, 53 (2007).
- [128] N. J. Halas, S. Lal, W.-S. Chang, S. Link, and P. Nordlander, *Chem. Rev.* **111**, 3913 (2011).
- [129] C. Caroli, D. Lederer-Rozenblatt, B. Roulet, and D. Saint-James, *Phys. Rev. B* **8**, 4552 (1973).
- [130] C. N. Berglund and W. E. Spicer, *Phys. Rev.* **136**, A1030 (1964).
- [131] A. D. Bandrauk and M. Ivanov, *Quantum Dynamic Imaging: Theoretical and Numerical Methods* (Springer Science & Business Media, 2011).
- [132] D. Hochstuhl, C. M. Hinz, and M. Bonitz, *The European Physical Journal Special Topics* **223**, 177 (2014).
- [133] H. R. Larsson, S. Bauch, L. K. Sørensen, and M. Bonitz, *Phys. Rev. A* **93**, 013426 (2016).
- [134] E. Stechel, R. Walker, and J. Light, *J. Chem. Phys.* **69**, 3518 (1978).
- [135] K. Berrington, P. Burke, M. Ledourneuf, W. Robb, K. Taylor, and V. Lan, *Comp. Phys. Commun.* **14**, 367 (1978).

- [136] M. Y. Amusia, *Atomic Photoeffect* (Springer Science & Business Media, 2013).
- [137] G. W. F. Drake, *Springer Handbook of Atomic, Molecular, and Optical Physics* (Springer, 2005).
- [138] C.-O. Almladh, *Phys. Scr.* **32**, 341 (1985).
- [139] P. Bolognesi, M. Coreno, G. Alberti, R. Richter, R. Sankari, and L. Avaldi, *J. Electron. Spectrosc. Relat. Phenom. Frontiers of Coincidence Experiments*, **141**, 105 (2004).
- [140] C. N. Yang, *Phys. Rev.* **74**, 764 (1948).
- [141] V. Schmidt, *Electron Spectrometry of Atoms using Synchrotron Radiation* (Cambridge University Press, Cambridge, 1997).
- [142] A. Eppink and D. H. Parker, *Review of Scientific Instruments* **68**, 3477 (1997).
- [143] W. Schattke and M. A. V. Hove, *Solid-State Photoemission and Related Methods: Theory and Experiment* (John Wiley & Sons, 2008).
- [144] J. Berakdar and J. S. Briggs, *Phys. Rev. Lett.* **72**, 3799 (1994).
- [145] J. S. Briggs and V. Schmidt, *J. Phys. B* **33**, R1 (2000).
- [146] L. Avaldi and A. Huetz, *J. Phys. B* **38**, S861 (2005).
- [147] N. Fominykh, J. Henk, J. Berakdar, P. Bruno, H. Gollisch, and R. Feder, *Solid State Commun.* **113**, 665 (2000).
- [148] B. D. Napitu and J. Berakdar, *Phys. Rev. B* **81**, 195108 (2010).
- [149] F. O. Schumann, L. Behnke, C. H. Li, and J. Kirschner, *Journal of Physics: Condensed Matter* **25**, 094002 (2013).
- [150] M. Drescher, M. Hentschel, R. Kienberger, M. Uiberacker, V. Yakovlev, A. Scrinzi, T. Westerwalbesloh, U. Kleineberg, U. Heinzmann, and F. Krausz, *Nature* **419**, 803 (2002).
- [151] O. Smirnova, V. S. Yakovlev, and A. Scrinzi, *Phys. Rev. Lett.* **91**, 253001 (2003).
- [152] W. Werner, W. Smekal, H. Störi, H. Winter, G. Stefani, A. Ruocco, F. Offi, R. Gotter, A. Morgante, and F. Tommasini, *Phys. Rev. Lett.* **94**, 038302 (2005).
- [153] C. Verdozzi, M. Cini, and A. Marini, *J. Electron. Spectrosc. Relat. Phenom. Strongly correlated systems*, **117-118**, 41 (2001).
- [154] R. Herrmann, S. Samarin, H. Schwabe, and J. Kirschner, *Phys. Rev. Lett.* **81**, 2148 (1998).
- [155] H. Ueba and B. Gumhalter, *Prog. Surf. Sci.* **82**, 193 (2007).
- [156] U. De Giovannini, D. Varsano, M. A. L. Marques, H. Appel, E. K. U. Gross, and A. Rubio, *Phys. Rev. A* **85**, 062515 (2012).
- [157] F. Schmitt, P. S. Kirchmann, U. Bovensiepen, R. G. Moore, L. Rettig, M. Krenz, J.-H. Chu, N. Ru, L. Perfetti, D. H. Lu, M. Wolf, I. R. Fisher, and Z.-X. Shen, *Science* **321**, 1649 (2008).
- [158] M. Sentef, A. F. Kemper, B. Moritz, J. K. Freericks, Z.-X. Shen, and T. P. Devereaux, *Physical Review X* **3**, 041033 (2013).
- [159] A. F. Kemper, M. Sentef, B. Moritz, C. C. Kao, Z. X. Shen, J. K. Freericks, and T. P. Devereaux, *Phys. Rev. B* **87**, 235139 (2013).
- [160] M. Lein, *Phys. Rev. Lett.* **94** (2005).
- [161] J. H. Posthumus, *Rep. Prog. Phys.* **67**, 623 (2004).
- [162] H. Stapelfeldt, E. Constant, and P. B. Corkum, *Phys. Rev. Lett.* **74**, 3780 (1995).

- [163] S. Chelkowski and A. Bandrauk, *Phys. Rev. A* **65**, 023403 (2002).
- [164] S. Barmaki and H. Bachau, *J. Phys. B* **40**, 463 (2007).
- [165] R. D. Birkhoff, in *Corpuscles and Radiation in Matter II / Korpuskeln und Strahlung in Materie II*, Encyclopedia of Physics / Handbuch der Physik No. 6 / 34, edited by S. Flügge (Springer Berlin Heidelberg, 1958) pp. 53–138.
- [166] P. M. Echenique, J. Bausells, and A. Rivacoba, *Phys. Rev. B* **35**, 1521 (1987).
- [167] R. F. Egerton, *Rep. Prog. Phys.* **72**, 016502 (2009).
- [168] F. J. García de Abajo, *Rev. Mod. Phys.* **82**, 209 (2010).
- [169] J. Verbeeck, H. Tian, and P. Schattschneider, *Nature* **467**, 301 (2010).
- [170] M. v. Veenendaal, *Theory of Inelastic Scattering and Absorption of X-rays* (Cambridge University Press, 2015).
- [171] H. Hayashi, Y. Udagawa, J. M. Gillet, W. A. Caliebe, and C. C. Kao, *Chemical Application of Synchrotron Radiation* **2**, 850 (2002).
- [172] J. A. Bradley, G. T. Seidler, G. Cooper, M. Vos, A. P. Hitchcock, A. P. Sorini, C. Schlimmer, and K. P. Nagle, *Phys. Rev. Lett.* **105**, 053202 (2010).
- [173] E. Boström, A. Mikkelsen, and C. Verdozzi, *Phys. Rev. B* **93**, 195416 (2016).
- [174] C. Bai, *Scanning Tunneling Microscopy and Its Application* (Springer Science & Business Media, 2000).
- [175] S. N. Magonov and M.-H. Whangbo, *Surface Analysis with STM and AFM: Experimental and Theoretical Aspects of Image Analysis* (John Wiley & Sons, 2008).
- [176] P. Samori, *STM and AFM Studies on (Bio)molecular Systems: Unravelling the Nanoworld* (Springer Science & Business Media, 2009).
- [177] S. Katano, Y. Kim, Y. Kagata, and M. Kawai, *The Journal of Physical Chemistry C* **114**, 3003 (2010).
- [178] S. R. Burema and M.-L. Bocquet, *J. Phys. Chem. Lett.* **3**, 3007 (2012).
- [179] N. Jiang, E. T. Foley, J. M. Klingsporn, M. D. Sonntag, N. A. Valley, J. A. Dieringer, T. Seideman, G. C. Schatz, M. C. Hersam, and R. P. Van Duyne, *Nano Lett.* **12**, 5061 (2012).
- [180] S. Grafström, *Journal of Applied Physics* **91**, 1717 (2002).
- [181] S. Loth, M. Etzkorn, C. P. Lutz, D. M. Eigler, and A. J. Heinrich, *Science* **329**, 1628 (2010).
- [182] P. Yu and J. Kirschner, *Appl. Phys. Lett.* **102**, 063111 (2013).
- [183] C. J. Milne, T. J. Penfold, and M. Chergui, *Coordination Chemistry Reviews Following Chemical Structures using Synchrotron Radiation*, **277-278**, 44 (2014).
- [184] J. J. Rehr, R. C. Albers, and S. I. Zabinsky, *Phys. Rev. Lett.* **69**, 3397 (1992).
- [185] T. Pfeifer, C. Spielmann, and G. Gerber, *Rep. Prog. Phys.* **69**, 443 (2006).
- [186] H. D. Cohen and U. Fano, *Phys. Rev.* **150**, 30 (1966).
- [187] X.-J. Liu, N. A. Cherepkov, S. K. Semenov, V. Kimberg, F. Gel'mukhanov, G. Prümper, T. Lischke, T. Tanaka, M. Hoshino, H. Tanaka, and K. Ueda, *J. Phys. B* **39**, 4801 (2006).
- [188] B. Zimmermann, D. Rolles, B. Langer, R. Hentges, M. Braune, S. Cvejanovic, O. Geßner, F. Heiser, S. Korica, T. Lischke, A. Reinköster, J. Viehhaus, R. Dörner, V. McKoy, and U. Becker, *Nature Phys.* **4**, 649 (2008).

- [189] D. Akoury, K. Kreidi, T. Jahnke, T. Weber, A. Staudte, M. Schöffler, N. Neumann, J. Titze, L. P. H. Schmidt, A. Czasch, O. Jagutzki, R. A. C. Fraga, R. E. Grisenti, R. D. Muiño, N. A. Cherepkov, S. K. Semenov, P. Ranitovic, C. L. Cocke, T. Osipov, H. Adaniya, J. C. Thompson, M. H. Prior, A. Belkacem, A. L. Landers, H. Schmidt-Böcking, and R. Dörner, *Science* **318**, 949 (2007).
- [190] M. Ilchen, L. Glaser, F. Scholz, P. Walter, S. Deinert, A. Rothkirch, J. Seltmann, J. Viehhaus, P. De-cleva, B. Langer, A. Knie, A. Ehresmann, O. M. Al-Dossary, M. Braune, G. Hartmann, A. Meissner, L. C. Tribedi, M. AlKhalidi, and U. Becker, *Phys. Rev. Lett.* **112**, 023001 (2014).
- [191] J. H. Posthumus, A. J. Giles, M. R. Thompson, and K. Codling, *J. Phys. B* **29**, 5811 (1996).
- [192] H. W. Kroto, J. R. Heath, S. C. O'Brien, R. F. Curl, and R. E. Smalley, *Nature* **318**, 162 (1985).
- [193] V. K. Voora, L. S. Cederbaum, and K. D. Jordan, *J. Phys. Chem. Lett.* **4**, 849 (2013).
- [194] V. K. Voora and K. D. Jordan, *Nano Lett.* **14**, 4602 (2014).
- [195] S. Klaiman, E. V. Gromov, and L. S. Cederbaum, *Phys. Chem. Chem. Phys.* **16**, 13287 (2014).
- [196] S. Pittalis, A. Delgado, J. Robin, L. Freimuth, J. Christoffers, C. Lienau, and C. A. Rozzi, *Advanced Functional Materials* **25**, 2047 (2015).
- [197] T. Mori, J. Kou, Y. Haruyama, Y. Kubozono, and K. Mitsuke, *J. Electron. Spectrosc. Relat. Phenom.* **144-147**, 243 (2005).
- [198] E. Sohmen, J. Fink, and W. Krätschmer, *Z. Phys. B: Condens. Matter* **86**, 87 (1992).
- [199] A. W. Burose, T. Dresch, and A. M. G. Ding, *Z. Phys. D: At. Mol. Clusters* **26**, 294 (1993).
- [200] S. Lee, R. Nicholls, D. Nguyen-Manh, D. Pettifor, G. Briggs, S. Lazar, D. Pankhurst, and D. Cockayne, *Chem. Phys. Lett.* **404**, 206 (2005).
- [201] P. Bolognesi, L. Avaldi, A. Ruocco, A. Verkhovtsev, A. V. Korol, and A. V. Solov'yov, *Eur. Phys. J. D* **66**, 254 (2012).
- [202] I. V. Hertel, H. Steger, J. de Vries, B. Weisser, C. Menzel, B. Kamke, and W. Kamke, *Phys. Rev. Lett.* **68**, 784 (1992).
- [203] S. W. J. Scully, E. D. Emmons, M. F. Gharaibeh, R. A. Phaneuf, A. L. D. Kilcoyne, A. S. Schlachter, S. Schippers, A. Müller, H. S. Chakraborty, M. E. Madjet, and J. M. Rost, *Phys. Rev. Lett.* **94**, 065503 (2005).
- [204] M. Feng, J. Zhao, and H. Petek, *Science* **320**, 359 (2008).
- [205] L. Zoppi, L. Martin-Samos, and K. K. Baldridge, *Phys. Chem. Chem. Phys.* **17**, 6114 (2015).
- [206] M. Boyle, T. Laarmann, K. Hoffmann, M. Hedén, E. E. Campbell, C. P. Schulz, and I. V. Hertel, *Eur. Phys. J. D* **36**, 339 (2005).
- [207] B. Mignolet, R. D. Levine, and F. Remacle, *Phys. Rev. A* **89**, 021403 (2014).
- [208] E. Bohl, K. P. Sokół, B. Mignolet, J. O. F. Thompson, J. O. Johansson, F. Remacle, and E. E. B. Campbell, *J. Phys. Chem. A* **119**, 11504 (2015).
- [209] M. Brack, *Rev. Mod. Phys.* **65**, 677 (1993).
- [210] O. Kidun and J. Berakdar, *Phys. Rev. Lett.* **87**, 263401 (2001).
- [211] M. E. Madjet, H. S. Chakraborty, J. M. Rost, and S. T. Manson, *J. Phys. B* **41**, 105101 (2008).
- [212] E. Maurat, P.-A. Hervieux, and F. Lépine, *J. Phys. B* **42**, 165105 (2009).
- [213] D. Östling, S. P. Apell, G. Mukhopadhyay, and A. Rosen, *J. Phys. B* **29**, 5115 (1996).
- [214] D. D. Lee and H. S. Seung, *Nature* **401**, 788 (1999).

- [215] A. D. Shiner, B. E. Schmidt, C. Trallero-Herrero, H. J. Wörner, S. Patchkovskii, P. B. Corkum, J.-C. Kieffer, F. Légaré, and D. M. Villeneuve, *Nature Phys.* **7**, 464 (2011).
- [216] F. U. Hillebrecht, A. Morozov, and J. Kirschner, *Phys. Rev. B* **71**, 125406 (2005).
- [217] S. Ullrich, T. Schultz, M. Z. Zgierski, and A. Stolow, *Phys. Chem. Chem. Phys.* **6**, 2796 (2004).
- [218] X. Roy, C.-H. Lee, A. C. Crowther, C. L. Schenck, T. Besara, R. A. Lalancette, T. Siegrist, P. W. Stephens, L. E. Brus, P. Kim, M. L. Steigerwald, and C. Nuckolls, *Science* **341**, 157 (2013).
- [219] G. Orlandi and F. Negri, *Photochemical & Photobiological Sciences* **1**, 289 (2002).
- [220] J. O. Johansson, G. G. Henderson, F. Remacle, and E. E. B. Campbell, *Phys. Rev. Lett.* **108**, 173401 (2012).
- [221] P. Myöhänen, A. Stan, G. Stefanucci, and R. van Leeuwen, *Phys. Rev. B* **80**, 115107 (2009).
- [222] P. Myöhänen, A. Stan, G. Stefanucci, and R. v. Leeuwen, *EPL (Europhysics Letters)* **84**, 67001 (2008).
- [223] H.-P. Breuer and F. Petruccione, *The Theory of Open Quantum Systems* (Oxford University Press, 2002).
- [224] K. Balzer, S. Bauch, and M. Bonitz, *Phys. Rev. A* **82**, 033427 (2010).
- [225] K. Balzer, S. Bauch, and M. Bonitz, *Phys. Rev. A* **81**, 022510 (2010).
- [226] E. Perfetto, A.-M. Uimonen, R. van Leeuwen, and G. Stefanucci, *Phys. Rev. A* **92**, 033419 (2015).
- [227] J. Viljas, J. Cuevas, F. Pauly, and M. Häfner, *Phys. Rev. B* **72**, 245415 (2005).
- [228] L. K. Dash, H. Ness, and R. W. Godby, *J. Chem. Phys.* **132**, 104113 (2010).
- [229] H. Ness, L. K. Dash, M. Stankovski, and R. W. Godby, *Phys. Rev. B* **84**, 195114 (2011).
- [230] L. K. Dash, H. Ness, and R. W. Godby, *Phys. Rev. B* **84**, 085433 (2011).
- [231] D. Golež, J. Bonča, L. Vidmar, and S. A. Trugman, *Phys. Rev. Lett.* **109**, 236402 (2012).
- [232] N. Säkkinen, Y. Peng, H. Appel, and R. v. Leeuwen, *J. Chem. Phys.* **143**, 234101 (2015).
- [233] M. Guzzo, G. Lani, F. Sottile, P. Romaniello, M. Gatti, J. J. Kas, J. J. Rehr, M. G. Silly, F. Sirotti, and L. Reining, *Phys. Rev. Lett.* **107**, 166401 (2011).
- [234] M. Guzzo, J. J. Kas, L. Sponza, C. Giorgetti, F. Sottile, D. Pierucci, M. G. Silly, F. Sirotti, J. J. Rehr, and L. Reining, *Phys. Rev. B* **89**, 085425 (2014).
- [235] E. Klevak, J. J. Kas, and J. J. Rehr, *Phys. Rev. B* **89**, 085123 (2014).
- [236] P. Lipavsky, V. Spicka, and B. Velicky, *Phys. Rev. B* **34**, 6933 (1986).
- [237] K. Balzer, S. Hermanns, and M. Bonitz, *J. Phys. Conf. Ser.* **427**, 012006 (2013).
- [238] S. Kaiser, S. R. Clark, D. Nicoletti, G. Cotugno, R. I. Tobey, N. Dean, S. Lupi, H. Okamoto, T. Hasegawa, D. Jaksch, and A. Cavalleri, *Scientific Reports* **4**, 3823 (2014).
- [239] R. Singla, G. Cotugno, S. Kaiser, M. Först, M. Mitrano, H. Liu, A. Cartella, C. Manzoni, H. Okamoto, T. Hasegawa, S. Clark, D. Jaksch, and A. Cavalleri, *Phys. Rev. Lett.* **115**, 187401 (2015).
- [240] R. Bartlett and M. Musiał, *Rev. Mod. Phys.* **79**, 291 (2007).
- [241] Y. Pavlyukh, J. Berakdar, and A. Rubio, *Phys. Rev. B* **87**, 125101 (2013).
- [242] D. J. Rowe, *Rev. Mod. Phys.* **40**, 153 (1968).
- [243] H. Nakatsuji, *Chem. Phys. Lett.* **67**, 329 (1979).
- [244] H. Nakatsuji and K. Hirao, *J. Chem. Phys.* **68**, 2053 (1978).
- [245] U. Weiss, *Quantum Dissipative Systems* (World Scientific, 2012)



---

## Acknowledgements

It is a great pleasure for me to be able to acknowledge all the people who supported me on the quest to write this thesis. My special thanks and deep appreciation go to my supervisor *Yaroslav Pavlyukh*, who was always willing to spend his precious time on my questions. Our discussions have always been very inspiring and constructive and taught me how important effective communication is for scientific work. Furthermore, I would like to acknowledge my mentoring professor and supervisor *Jamal Berakdar* for the great opportunity of conducting my PhD studies in his group. I learned a great deal of things from him in our very productive discussions; most importantly to think "out of the box" and how much joy sharing ideas brings! I cannot be grateful enough for the possibility to attend many inspiring conferences and the opportunities to present our work.

Of course, I would like to express my gratitude to our research group as a fantastic working environment. In particular, working with *Stefan Stagraczyński* and *Levan Chotorlishvili* has been very productive and enjoyable. I am further indebted to *Alexander Sukhov*, *Seyyed Ruholla Etasami*, *Jonas Wätzel*, *Maryam Azimi*, *Khompat Satitkovitchai*, *Alexander Schäffer* and *Dominik Schulze* for the many fruitful discussions and the great time we spent together. Further collaborators I had the pleasure to work with are *Andriy Klavsukh*, *Paola Bolognesi*, *Lorenzo Avaldi*, *Michael Stöger-Pollach* and *Tim Laarman*. I would also like to thank Stefan, Levan and Maryam for joining our chess team. With their efforts, winning the championship in Halle has been an exciting and successful endeavor.

Finally, I would like to express my appreciation for my parents who supported me all the way to this stage.

The research presented in this thesis has been supported by German Research Foundation (DFG) Collaborative Research Centre SFB 762 Functionality of Oxide Interfaces and Grant Number PA 1698/1-1.





---

## List of publications

1. M. Schüler, Y. Pavlyukh, J. Berakdar, *Ultrafast control of inelastic tunneling in a double semiconductor quantum well*, Appl. Phys. Lett. **97**, 172103 (2010)
2. M. Schüler, Y. Pavlyukh, J. Berakdar, *A theoretical analysis of the spin dynamics of magnetic adatoms traced by time-resolved scanning tunneling spectroscopy*, New Journ. Phys. **14**, 043027 (2012)
3. M. Schüler, Y. Pavlyukh, J. Berakdar, *Local Ionization Dynamics Traced by Photoassisted Scanning Tunneling Microscopy: A Theoretical Approach*, J. Phys. Chem. Lett. **4**, 1131 (2013)
4. P. Bolognesi, Y. Pavlyukh, M. Schüler, J. Berakdar, L. Avaldi, *(e,2e) and ( $\gamma$ ,2e) experiments on C<sub>60</sub>*, Journ. Phys.: Conf. Ser. **488**, 022018 (2014)
5. M. Schüler, Y. Pavlyukh, J. Berakdar, *Nuclear-wave-packet dynamics mapped out by two-center interference in the HeH<sup>2+</sup> molecule*, Phys. Rev. A **89**, 063421 (2014)
6. M. Schüler, J. Berakdar, *Generation and coherent control of pure spin currents via terahertz pulses*, Appl. Phys. Lett. **104**, 162409 (2014)
7. Y. Pavlyukh, M. Schüler, J. Berakdar, *Single and double electron emission: combination of projection operator and nonequilibrium Green's function approaches*, Phys. Rev. B **91**, 155116 (2015)
8. M. Schüler, J. Berakdar, Y. Pavlyukh, *Disentangling multipole contributions to collective excitations in fullerenes*, Phys. Rev. A **92**, 021403(R) (2015)
9. M. Schüler, J. Berakdar, Y. Pavlyukh, *Time-dependent many-body treatment of electron-boson dynamics: Application to plasmon-accompanied photoemission*, Phys. Rev. B **93**, 054303 (2016)
10. M. Schüler, Y. Pavlyukh, P. Bolognesi, L. Avaldi, J. Berakdar, *Electron pair escape from fullerene cage via collective modes*, Sci. Rep. **6**, 24396 (2016)
11. M. Schüler, Y. Pavlyukh, *Second-order bosonic Kadanoff-Baym equations for plasmon-accompanied optical absorption*, Journ. Phys.: Conf. Ser. **696**, 012006 (2016)
12. S. Usenko, M. Schüler, A. Azima, M. Jakob, L. L. Lazzarino, Y. Pavlyukh, A. Przystawik, M. Drescher, T. Laarmann, J. Berakdar, *Femtosecond dynamics of correlated many-body states in C<sub>60</sub> fullerenes*, New J. Phys. **18**, 113055 (2016)
13. L. Chotorlishvili, M. Azimi, S. Stagraczyński, Z. Toklikishvili, M. Schüler, J. Berakdar, *Superadiabatic quantum heat engine with a multiferroic working medium*, Phys. Rev. E **94**, 032116 (2016)
14. M. Schüler, J. Berakdar, *Energy-loss spectroscopy of C<sub>60</sub> fullerenes with twisted electrons: Influence of orbital-angular-momentum transfer on plasmon generation*, Phys. Rev. A **94**, 052710 (2016)



---

## Lebenslauf / Curriculum vitae

### **Persönliche Daten / Personal data**

GEBURTSDATUM / BIRTH DATE: 16. Juli 1988 / July 16, 1988  
GEBURTSORT/ BIRTH PLACE: Halle (Saale), Germany  
ADRESSE / ADDRESS: Große Wallstraße 1, 06108 Halle, Germany

### **Bildung / Education**

OKT. 2010 – SEP. 2012 Master of Science in Physik / Physics  
Martin-Luther-Universität Halle-Wittenberg, Halle, Germany  
Masterarbeit / Master thesis: “Spatio-temporal dynamics in magnetic nanostructures”  
GESAMTNOTE / TOTAL GRADE: 1.0 (very good)

OKT. 2007 – SEP. 2010 Bachelor of Science in Physik / Physics  
Martin-Luther-Universität Halle-Wittenberg, Halle, Germany  
Bachelorarbeit / Bachelor thesis: “Dissipation and coherence in excited quantum systems”  
GESAMTNOTE / TOTAL GRADE: 1.0 (very good)

JUL. 2002 – JUL. 2007 Abitur / Higher School Certificate  
Johann-Gottfried-Herder Gymnasium / grammar school , Halle, Germany  
GESAMTNOTE / TOTAL GRADE: 1.0 (very good)

Halle (Saale),

---

Michael Schüler



---

## Eidesstattliche Erklärung / Statutory statement

Ich erkläre an Eides statt, dass ich die von mir vorgelegte Arbeit

### Tracking inter-particle correlations by many-body spectroscopies from complex systems

selbstständig und ohne fremde Hilfe verfasst, keine anderen als die von mir angegebenen Quellen und Hilfsmittel benutzt und die den benutzten Werken wörtlich oder inhaltlich entnommenen Stellen als solche kenntlich gemacht habe.

I declare under penalty of perjury that this thesis

### Tracking inter-particle correlations by many-body spectroscopies from complex systems

is entirely my own work and has been written without any help of others. I only used the mentioned sources and indicated all kind of citations correctly.

Halle (Saale),

---

Michael Schüler